DTU Library

Cu$_2$ZnSnS$_4$ solar cells: Physics and technology by alternative tracks

Crovetto, Andrea

Publication date:
2016

Document Version
Publisher's PDF, also known as Version of record

[Link back to DTU Orbit](#)

Citation (APA):
Crovetto, A. (2016). *Cu$_2$ZnSnS$_4$ solar cells: Physics and technology by alternative tracks*. DTU Nanotech.

Cu$_2$ZnSnS$_4$ solar cells:

Physics and technology by alternative tracks

Andrea Crovetto
PhD Thesis August 2016

DTU Nanotech
Department of Micro- and Nanotechnology

DTU Nanotech
Department of Micro- and Nanotechnology

Technical University
of Denmark

Cu_2ZnSnS_4 solar cells:
Physics and technology by alternative tracks

Andrea Crovetto

Main Supervisor
Prof. Ole Hansen

Co-Supervisor
Dr. Scient. Jørgen Schou

In collaboration with:

DTU Fotonik
Department of Photonics Engineering

DTU Danchip
National Center for Micro- and Nanofabrication

DTU Energy
Department of Energy Conversion and Storage

THE UNIVERSITY OF
NEW SOUTH WALES

Preface

This thesis is written to fulfill the requirements for a Doctor of Philosophy degree at the Technical University of Denmark. The work presented in this thesis is part of the larger research project "CHALSOL", financed by the Danish Council for Strategic Research (grant number 12-132644). The CHALSOL project has included 4 doctoral students in total at the DTU Fotonik and DTU Nanotech departments at the Technical University of Denmark, together with several senior advisors and international partners. The scope of the project has been to explore some relatively off-the-beaten-track deposition methods for the promising solar energy material Cu_2ZnSnS_4 (CZTS). The main method investigated in this project is pulsed laser deposition, even though a parallel track has been pursued with non-vacuum methods involving CZTS nanoparticles. My official responsibilities have been: to produce all the layers in a standard CZTS-based solar cell, *with the exception of CZTS itself*, to characterize the resulting solar cell devices, and to contribute to materials characterization as needed. Fortunately for myself, I have been free to shape my own project and look for anything interesting within the context of CZTS-based solar cells, as long as I would abide to my official project duties.

This has had an unfortunate consequence when it comes to writing a thesis: most of my results are not related to each other but are instead rather isolated studies. For this reason, I have decided to structure this thesis in four main parts: (1) a very broad introduction to the problem of CZTS solar cells (Chapter 1); (2) a collection of the results of my work, mostly written in the form of self-contained studies in article form (published, submitted or to be submitted - Chapters 2-7); (3) a conclusion, both about the outcome of my PhD project and about the future of CZTS and new solar energy materials in general (Chapter 8); (4) an appendix, where I briefly present positive and negative results related to the more regular work done on a daily basis with the technological goal of establishing a reliable CZTS solar cell baseline fabrication process at our university.

I have worked a lot with other people in my PhD project and most of the presented results have been achieved through collaboration with others. Since the particular goal of this thesis is to show what my own contribution has been, I will do my best to specify which ideas I got myself and what work I did myself.

Some notes on style. Since this should be an original piece of work, I have decided to illustrate the theory a bit differently than standard textbook treatment. I like to give concepts priority over formal mathematical treatment, so in this thesis I have used equations only when really necessary. Also, I have tried to be as explicit as possible in my writing, to answer the question "why?" as much as possible, and to express my opinion on many debated topics instead of just listing the different existing interpretations.

DTU Nanotech
Department of Micro-and Nanotechnology
Ørsteds Plads, Building 344
Technical University of Denmark
2800 Kgs. Lyngby, Denmark

Contents

Abstract

In this thesis I shall present the most scientifically interesting and/or practically useful results achieved in my PhD project. Such results are related to fundamental properties and technological aspects of Cu_2ZnSnS_4 (CZTS) and related materials for solar cells. By "related materials" I mean two things: i) alternative solar absorbers (notably, Cu_2SnS_3) that are chemically related to CZTS and that have similar selling points; ii) other materials included in the device stack of CZTS solar cells. Here I list what I believe the main highlights of my work are.

First, we achieve the highest reported power conversion efficiency (5.2%) for a CZTS solar cell using pulsed laser deposition as a fabrication method for CZTS precursors. This is thanks to to joint work of PhD student Andrea Cazzaniga, PhD student Chang Yan (University of New South Wales, Australia) and myself. Perhaps more importantly, we finally understand, albeit very roughly, the "rules of the game" for successful pulsed laser deposition of high-quality chalcogenide precursors for solar cells. This kind of understanding is not evident in the existing literature and is mostly the result of the work of PhD student Andrea Cazzaniga.

Second, I propose and test experimentally a modification of the standard CZTS solar cell architecture by inserting a very thin (few nm) CeO_2 layer between the CZTS absorber and the CdS buffer. Despite being already known in the fields of catalysis and fuel cells, application of CeO_2 in CZTS solar cells is completely new, even though the two materials have a nearly perfect lattice match. In a first investigation over a two-month external research stay at the University of New South Wales, I demonstrate that the open circuit voltage of standard CZTS solar cells fabricated by PhD student Chang Yan is boosted when I include a CeO_2 interface passivation layer.

Third, I critically examine one of the mechanisms that are believed to be the major current issues of CTZS solar cells, namely recombination at the CZTS/CdS heterointerface. An initial outcome is a comprehensive review of the existing studies on the band alignment between the two materials, to which I add my own analysis and interpretation. I argue that, unlike what is often stated in the CZTS community, CdS does not necessarily have an unfavorable conduction band alignment with CZTS. Actually, the band alignment may to some extent be engineered by formation of secondary phases at the interface through controlled interdiffusion and due to orientation-dependent band alignment effects that are absent in the (otherwise very similar) $Cu(In,Ga)Se_2$ solar cells. Another outcome of this sub-project is a collaboration with computational material scientists, mostly PhD student Mattias Palsgaard, to improve our theoretical understanding of the CZTS/CdS interface. A new computational method is applied to calculate some interface properties that are of interest but cannot be readily extracted by established methods. From a combination of atomistic- and device simulation it appears as if surface-state-induced band gap narrowing at the CZTS/CdS interface may be the main reason behind the poorer interface properties of CZTS/CdS solar cells compared to CZTSe/CdS solar cells. Interestingly, this problem may be solved by passivating those states with a Zn-based chalcogenide.

Fourth, I measure for the first time the dielectric function of a monoclinic Cu_2SnS_3 thin film by spectroscopic ellipsometry. Cu_2SnS_3 is gaining some interest as a solar absorber

and is produced by pulsed laser deposition by PhD student Rebecca Ettlinger. What is special about this study is the comparison with the dielectric function of Cu_2SnS_3 calculated from first principles by external collaborators Rongzhen Chen and Clas Persson. We find that the characteristic double absorption onset of monoclinic Cu_2SnS_3 is due to optical transitions from three closely spaced valence bands to a single conduction band. The different transitions are excited by different light polarization directions with respect to the crystal lattice, and this subtle distinction can only be resolved in the calculation when dense sampling in reciprocal space is employed.

Fifth, I undertake a comprehensive investigation of the properties of radio-frequency sputtered ZnO:Al thin films used as a lateral electron transport layer on top of CZTS solar cells. With considerable fabrication help from M.Sc. student Tobias Ottsen, I demonstrate that compressive stress in the films is clearly correlated to several other properties (carrier concentration and mobility, grain size, orientation, and Al content) regardless of deposition pressure and position in the sputtering setup. Also, I show that spatial inhomogeneity in the electrical properties is mostly due to particle bombardment effects and only weakly to inhomogeneous oxygen distribution.

All the aforementioned results were achieved in the third and last year of my PhD project. In the first two years of my project I established a CZTS solar cell device fabrication process flow at a university, and in a country, with zero experience with chalcogenide solar cells. The process includes deposition of all necessary thin-film materials in a CZTS device stack, CZTS excluded, and has so far resulted in 2.6% efficient in-house CZTS solar cells by pulsed laser deposition.

Throughout this thesis I try, when possible, to connect the physics and chemistry of the individual component materials to the resulting device physics, since the existing literature of CZTS solar cells is heavily biased toward the former aspect. The relationship between the two aspects is one of my main research interests.

Dansk Resumé

I denne afhandling præsenterer jeg de mest interessante resultater – videnskabelige såvel som praktiske – fra mit PhD-projekt. Disse resultater omfatter fundamentale egenskaber og teknologiske aspekter af Cu_2ZnSnS_4 (CZTS) og relaterede materialer til solceller.

For det første har vi opnået den højest rapporterede energikonverteringseffektivitet (5.2%) for en CZTS solcelle hvor CZTS er fremstillet med pulseret laser deponering. Dette er opnået som resultatet af en fælles indsats fra PhD studerende Andrea Cazzaniga, PhD studerende Chang Yan (University of New South Wales, Australien) og mig selv.

For det andet har jeg foreslået og eksperimentelt testet en modifikation af standard CZTS solcellearkitekturen, hvor et meget tyndt (få nm) CeO_2 lag blev indsat mellem CZTS absorberen og CdS bufferen. I en indledende undersøgelse, udført under et to-måneders eksternt forskningsophold ved University of New South Wales, demonstrerede jeg at tomgangsspændingen for standard CZTS solceller (fremstillet af PhD studerende Chang Yan) blev forbedret når jeg inkluderede et lag af CeO_2 til grænseflade-passivering.

For det tredje har jeg kritisk analyseret rekombinationen ved CZTS/CdS grænsefladen, der opfattes som et af de største problemer ved CZTS for tiden. Et resultat heraf er et omfattende review af de eksisterende studier af båndtilpasningen mellem de to materialer, suppleret med min egen originale analyse. Jeg argumenterer for at i modsætning til den gængse opfattelse i CZTS-kredse, så har CdS ikke nødvendigvis en ufordelagtig tilpasning af ledningsbåndet til CZTS. I tilknytning hertil har jeg også forklaret resultaterne fra nogle materialeberegninger for CZTS/CdS grænsefladen udført af PhD studerende Mattias Palsgaard. Resultaterne tyder på at en ufordelagtig (intrinsisk) overfladetilstand kunne være den primære årsag til de dårligere grænseflade-egenskaber for CZTS/CdS solceller sammenlignet med CZTSe/CdS solceller.

Med hensyn til andre materialer relaterede til CZTS, har jeg målt den dielektriske funktion for en monoklinisk Cu_2SnS_3 tyndfilm med spektroskopisk ellipsometri, hvilket ikke er gjort før. Der er stigende interesse for Cu_2SnS_3 som absorber for sollys. Vores samarbejdspartnere Rongzhen Chen og Clas Persson har brugt resultaterne til at konkludere, at den karakteristiske dobbelte absorptionsbåndkant for monoklinisk Cu_2SnS_3 skyldes de optiske overgange fra tre tætliggende valensbånd til et enkelt ledningsbånd.

Endelig foretog kandidatstuderende Tobias Ottsen og jeg en omfattende undersøgelse af egenskaberne for sputterdeponeret ZnO:Al tyndfilm, der benyttes som lateralt elektron-transportlag oven på CZTS solcellerne. I studiet demonstrerer jeg at kompressiv mekanisk spænding i filmene er tydeligt korreleret med flere andre væsentlige egenskaber for filmene uafhængigt af deponeringstryk og position. Alle de beskrevne resultater er fremkommet i det tredje og sidste år af mit PhD projekt. De første to år brugte jeg på at etablere en proces til at fremstille CZTS solceller, på et universitet (og i et land) uden erfaring indenfor chalcogenid-baserede solceller. Processen inkluderer deponering af alle nødvendige tyndfilmsmaterialer i en CZTS solcelle, undtagen selve CZTS filmen. Indtil videre giver processen en effektivitet på 2.6% på "in-house" CZTS solceller fremstillet med pulset laser deponering.

Målet med afhandlingen er at diskutere relationen mellem materialeegenskaberne og komponentfysikken, da den eksisterende litteratur er mangelfuld på det område.

Abstract for solar cell dummies

In the past three years I have worked on a new type of solar cell technology, which has some advantages with respect to the technology that is currently dominating the market. The main difference lies in the materials that are used to build the solar cell. While established technology is based on the best-understood material in the world (silicon), the technology I have worked on is based on a mysterious material that has not yet been used for anything else (Cu_2ZnSnS_4, nicknamed "CZTS"). Some advantages of CZTS with respect to silicon are: it can *potentially* be cheaper (because it requires 200 times less material and can be produced with low-cost methods); it requires *potentially* less energy in production (because the required processing temperature is lower); and it can *potentially* make a unobtrusive-looking solar cell just by coating any regular or irregular surface.

This sounds good of course, but what do all those *potentiallies* mean? They mean that, right now, top-of-the-class CZTS solar cells convert only 9% of light into electricity, compared to over 25% for silicon solar cells. Therefore, CZTS solar cells are still in an early research phase and it is not clear how much money and energy one can save, nor what limitations exist in the types of surfaces they can coat. The main goal now must be to improve that 9%, otherwise we will never see CZTS solar cells in the real world.

Now, a solar cell is not made by one material, but by a number of different materials in contact with each other, which serve different purposes within the cell. In the cases presented above, CZTS and silicon are simply the *light-absorbing* materials of their respective solar cell. Then, solar cell performance can be improved by: i) improving the quality of each material by fabricating it in the best way for solar cell applications; ii) *knowing* what "the best way" means; iii) selecting a smart combination of materials that work well together in a solar cell; iv) constructing the solar cell with an appropriate *architecture*, meaning the amounts of each material, the order in which they are stacked, the way in which they are patterned and so on; and v) ensuring that no bad things happen while making the solar cell and taking actual advantage of the good work done in points 1) to 4).

Pretty much everything that is presented in this thesis in technical language relates somehow to the above points. My collaborators and I have produced the best-performing CZTS solar cell ever reported made by the particular technique chosen in this project, converting 5.2% of light into electricity. While I am proud of that, I have also looked at more fundamental problems where I asked myself: how does this part of the solar cell *really* work? Where does this strange property of this material come from? What happens if we put two similar materials next to each other, instead on just one?
While results of this kind are of less immediate utility, fundamental understanding is ultimately what allows us to envision great new things, so I am very happy to give even a small contribution to understanding something that one day may change the lives of many people. Even though the content of this thesis is a bit technical, I have made an effort to make Section 1.1 understandable for everyone. Enjoy!

List of Abbreviations

AZO	ZnO doped with Al
BIPV	building-integrated photovoltaics
CBD	chemical bath deposition
CBM	conduction band minimum
CBO	conduction band offset
CIGS	$Cu(In,Ga)Se_2$
CTS	Cu_2SnS_3
CV	capacitance-voltage
CZTS	Cu_2ZnSnS_4
CZTSe	$Cu_2ZnSnSe_4$
CZTSSe	$Cu_2ZnSn(S,Se)_4$, an alloy of the previous two compounds
CZTS(e)	the class of kesterite materials Cu_2ZnSnS_4, $Cu_2ZnSnSe_4$ and $Cu_2ZnSn(S,Se)_4$
DC	direct current
DI	deionized
DFT	density functional theory
DTU	Technical University of Denmark
EDX	energy-dispersive x-ray spectroscopy
EQE	external quantum efficiency
ITO	Sn-doped In_2O_3
JV	current density vs. voltage
KCN	potassium cyanide (watch out - dangerous!)
OVC	ordered vacancy compound
PL	photoluminescence
PLD	pulsed laser deposition
PV	photovoltaics
QE	quantum efficiency
RF	radio-frequency
SCAPS	Solar Cell Capacitance Simulator in One Dimension
SEM	scanning electron microscopy
SLG	soda lime glass
SQ	Shockley Queisser limit
SRH	Shockley-Read-Hall
STM	scanning tunneling microscopy
UNSW	University of New South Wales
VBM	valence band maximum
VBO	valence band offset
XPS	x-ray photoelectron spectroscopy
XRD	x-ray diffraction
ZnO:Al	ZnO doped with Al

List of Symbols

E	photon energy
E_A	activation energy of the main recombination path
$E_\mathrm{A,def}$	activation energy deficit, defined as $E_\mathrm{g} - E_\mathrm{A}$
E_g	band gap
F	electric field
FF	fill factor
J	current density
J_0	dark saturation current (density)
J_{00}	prefactor of the dark saturation current (density)
J_d	recombination current (density), or diode current (density)
J_m	current density at maximum power point
J_sc	short circuit current (density)
k_B	Boltzmann's constant
L_D	diffusion length
m_e, m_h	electron (hole) effective mass
n_d	diode ideality factor
n_ph	photon number density
N_A	acceptor doping density
N_C, N_V	effective density of states in the conduction (valence) band
N_i	density of interface defects
P_m	maximum power
q	elementary charge
R_s	series resistance
R_sh	shunt resistance
S_n, S_p	interface recombination velocity for electrons (holes)
T	temperature
V	voltage
V_m	voltage at maximum power point
V_oc	open circuit voltage
v_th	thermal velocity of electrons and holes
η	power conversion efficiency
μ_e	electron mobility
σ_n, σ_p	electron (hole) capture cross section
τ	electron lifetime

Thesis outline

In **Chapter 1 - The scene**, I give an introduction to the problem in the form of a "critical review", i.e., I present my own interpretation of some of the trends behind data, ideas, and models that have mostly been published by others. I start by explaining why I think it is a good idea to do research on CZTS solar cells (Section 1.1). Then I introduce CZTS as a material by reviewing its main properties and summarize the history and current state of the art of CZTS solar cell research (Section 1.2). From this background knowledge I introduce the standard CZTS solar cell architecture and explain, in ideal and slightly personal terms, how that architecture allows electrical power generation (Section 1.3). However, a number of non-idealities exist in CZTS solar cells with respect to "textbook" solar cells, and they are presented in Section 1.4. Some of such non-idealities can be identified as the main reason why performance of CZTS(e) solar cells lags far behind that of the closely related CIGS solar cells. Therefore, I also provide a direct point-by-point analysis of the shortcomings of CZTS(e) solar cells with respect to CIGS solar cells (Section 1.5). Because CZTS solar cells also lag behind CZTS(e) solar cells with a low S content, I repeat the procedure for CZTS versus CZTSe (Section 1.6). Finally, before presenting my actual results, I tediously list what my own contribution has been in the work that led to those results (Section 1.7).

In **Chapter 2 - Record efficiency for a CZTS solar cell by pulsed laser deposition**, I show the most important result related to the *original* goal of the CHALSOL research project, to which my own PhD project belongs. That is, development of solar cells from pulsed-laser-deposited CZTS.

In **Chapter 3 - CeO$_2$: a novel heterojunction partner for CZTS**, I present a proof-of-concept study for the idea I am most proud of, among all the ideas I got through my PhD project. That is, searching materials databases for a completely new heterojunction partner of CZTS, ending up with CeO$_2$ as an interesting candidate, and actually inserting it in a CZTS solar cell with promising results.

In **Chapter 4 - Aspects of the heterointerface physics of CZTS solar cells**, I put together a few studies that use atomistic simulation, device-level simulation, or simply critical literature review to draw some conclusions on some important topics revolving around the physics of the heterojunction in CZTS solar cells.

In **Chapter 5 - Growth and fundamental properties of ZnO:Al**, I present a fundamental study on some trends I observed in the properties of RF-sputtered ZnO:Al films used in our in-house CZTS solar cell stack. A number of ZnO:Al film properties can be correlated to the compressive stress in the film, some even quantitatively.

In **Chapter 6 - Growth and fundamental properties of Cu$_2$SnS$_3$**, I present two separate studies on a secondary phase of the Cu-Zn-Sn-S phase diagram (Cu$_2$SnS$_3$) that can also be used as an absorber material in photovoltaics. The first is a combined experimental/theoretical study, where the dielectric function of Cu$_2$SnS$_3$ is measured for the first time, and its puzzling double absorption onset is explained from first principles. The other is about the challenges of growing Cu$_2$SnS$_3$ precursors by pulsed laser deposition.

In **Chapter 7 - Growth and fundamental properties of CZTS**, I present some specific studies on the growth and properties of CZTS deposited either by pulsed laser

deposition or by a nanoparticle-based approach.

Finally, In **Chapter 8 - The take home messages**, I hope my readers will wake up and bear with me as I draw some conclusions on CZTS as a solar energy material in general and on CZTS by pulsed laser deposition specifically. I provide a prioritized list of what, in my view, future development of CZTS should focus on, and I give an outlook on what I think is most exciting about the field of new materials for photovoltaics.

Finally finally, in **Appendix A - Establishing a CZTS solar cell fabrication process flow at the Technical University of Denmark**, I want to show some details of our in-house solar cell fabrication process, and especially focus on the errors I made so that hopefully they are not repeated by others in the future.

Chapter 1

The scene

I do not need (he does not need)
a microphone (a microphone)
My voice is f'ing (f'ing)
powerful!
Tenacious D, 2006

Disclaimer: in this chapter I mix a literature review with my own ideas. Such ideas are the rather speculative outcome of looking at a lot of papers and digging into other people's data. Therefore I do not make any claim to the existence of a *solid* scientific foundation behind them, even though all those ideas are ultimately based on data.

1.1 Why bother?

Close to the end of my PhD project, news came that Prof. George Whitesides from Harvard would give a talk at our department called "Simplicity as a strategy in research". I was intrigued and went to the talk. Main point: the researcher is hired by the taxpayers and is thus expected to do something to the advantage of the taxpayers. More specifically, something that is simple enough so that the taxpayers can understand how they can eventually benefit from it. The details of the implementation may be a nightmare (that's the researcher's problem) but the final product of research must be clear and usable. Not really big news, but he said it in a cooler way than most others and got me thinking. With that in mind, I will try to convince the taxpayers that it's a good idea to finance work on CZTS solar cells. For this reason, I have tried to make this section more or less understandable to the non-specialists.

1.1.1 Why solar cells?

Hopefully it is now nearly universally accepted that energy production by burning things does not give very bright prospects for the next generations. That is mostly because of the less-than-infinite availability on Earth of materials that release a lot of energy when burning (oil, gas, coal) and the detrimental effects of CO_2 as a product of the combustion reaction [1].

Global reliance on renewable energy sources is the key to this problem. Among the solutions that are seriously being considered, photovoltaics (PV) involves direct energy conversion from solar radiation into electrical energy. The PV "product" is, at its most fundamental level, an optoelectronic device called a solar cell. Most solar cells reach their best conversion efficiency when they work at a voltage between 0.6 V and 1.1 V [2]. Because of how electrical energy is transported and supplied, this relatively low voltage

must be increased by connecting several solar cells in series to reach an output voltage of about 12 V [3]. This means that the typical panels we see in PV plants and on rooftop installations are "solar modules" which include several individual solar cells connected together to reach the desired output voltage of the energy system. Because the solar cell is a direct current (DC) device but electrical energy is normally distributed in alternate current (AC) mode, an additional device called an inverter is required to transform the DC signal into an AC signal before it can feed the distribution system.

PV is a particularly attractive option for many reasons:

1. solar energy is a lot. Other renewable energy sources simply cannot compete with the sheer amount of solar energy out there. The current energy per unit time needed to power the world is about 20 TW, and it is of course increasing. Assuming that PV can convert the energy from the sun into electricity at an average efficiency of 20% during the day and 0% at night (reasonable with today's standard technology), the whole demand could be met by PV alone if 0.6% of the Earth's landmass was covered by solar panels [4].

2. solar energy is cheap, finally. It used to be pricey but, as you can see from Figure 1.1(a), it is now more than ten times cheaper than thirty years ago. In the parts of the world of highest solar irradiance, solar energy has already reached grid parity, which means that it has become cheaper than the electrical energy provided by the existing electrical distribution systems. More on money later.

3. solar energy is safe, doesn't require extensive modifications of the landscape, and looks reasonably good (also, more on this later). Nuclear, hydro, and wind energy respectively may have some issues here.

4. solar energy is versatile, in the sense that it can be applied in actual GW-sized power plants and feed the grid system, or it can be mounted on a rooftop or private land and provide a few kW power to a houseowner or a factory who can then sell the rest to the national grid. It can be used in calculators and backpacks to power small devices with less than a W, or as a micro-energy harvester to power microchips in wireless sensor networks, which require power in the μW range. There already exist different PV technologies based on different materials, and each of them has an application in which it performs best [4,5].

With some exceptions (like hydroelectricity), a problem of most renewable energy sources is that it is subject to fluctuations in availability. It the wind doesn't blow, no energy. If it's dark, no energy. On the other hand, conventional fuels do not go on holiday so you can burn stuff at your command any time of the day or of the night, which gives great flexibility. For this reason, significant advances in energy storage technology must be made before CO_2-producing fuels can be phased out. Nevertheless, it can be envisioned that, in a first stage, conventional power plants can provide backup energy when the energy provided by renewable sources is insufficient.

1.1.2   Why *thin-film* solar cells?

The main difference among the most popular solar cell technologies lies in their constituent materials. An excellent and concise review of solar cell materials was published this year [8]. The indisputable king of solar cell materials is silicon (Si), which is at the same time the best understood and the most earth-abundant material in the world. Mastering the physics and technological processing of silicon has allowed the electronics industry to become the largest industry in the world by using very high quality Si as a basis for the majority of its components. All this can nowadays be achieved at a ridiculously low price.
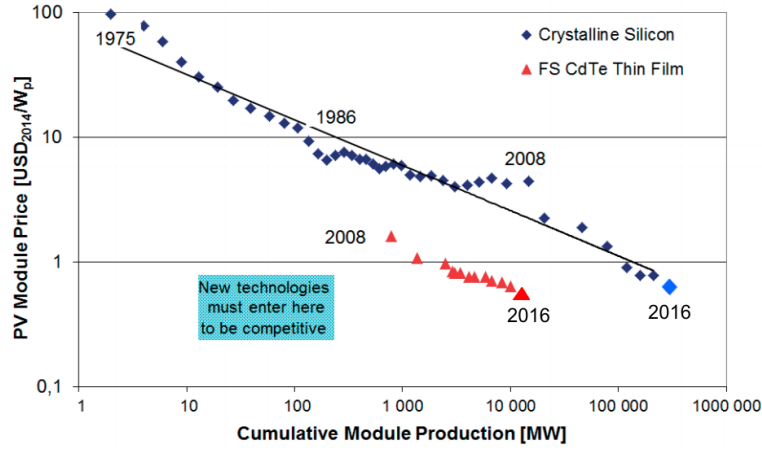
(a)
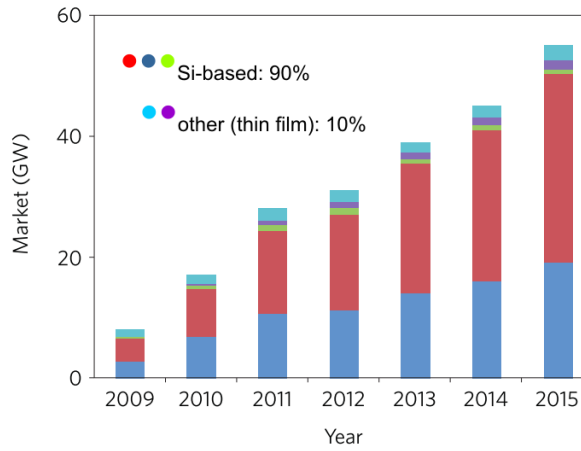
(b)

Figure 1.1: (a): Learning curve for Si modules and the most successful thin-film modules (CdTe-based), expressed as module price per unit of generated power. The price of thin-film modules has consistently been lower than that of Si modules, even though parity has almost been reached due to a recent price drop in Si modules. The lines are a guide to the eye. Adapted from [6,7].
(b): Breakdown of the PV market in recent years. The position of Si-based technology as market leader has strengthened over those years with respect to thin-film-based technology. Adapted from [5].

Making single-crystal silicon at the current market price is somewhat equivalent to having Michelangelo paint the ceiling of your living room and handing him a couple of dollars for the job. Fortunately Si is not as rebellious as Michelangelo.

Solar cells based on single-crystal or multicrystalline Si (c-Si and mc-Si respectively) are the market workhorse (Figure 1.1(b)) with a 90% market share. They are *wafer-based* technologies, meaning that the material is manufactured in the form of a big chunk (a couple of meters tall) and then cut into thin slices, called wafers. They are the building block of Si solar cells. Wafers are thin but not that thin: a typical Si solar cell employs a rigid 200 μm-thick wafer.

What should alternative technologies try to do to compete with silicon solar cells? The answer to this question is somewhat subjective and the typical answer has possibly changed over time. Researchers often focus on materials that can be fabricated easily using cheap techniques with less materials consumption, so that PV can cost less and be more convenient than fossil fuels. This way of thinking is currently taking some blows, as the conventional Si solar cells have become extremely cheap after impressive price drops between 2008 and 2012 (Figure 1.1(a)). Many experts in the field are then now
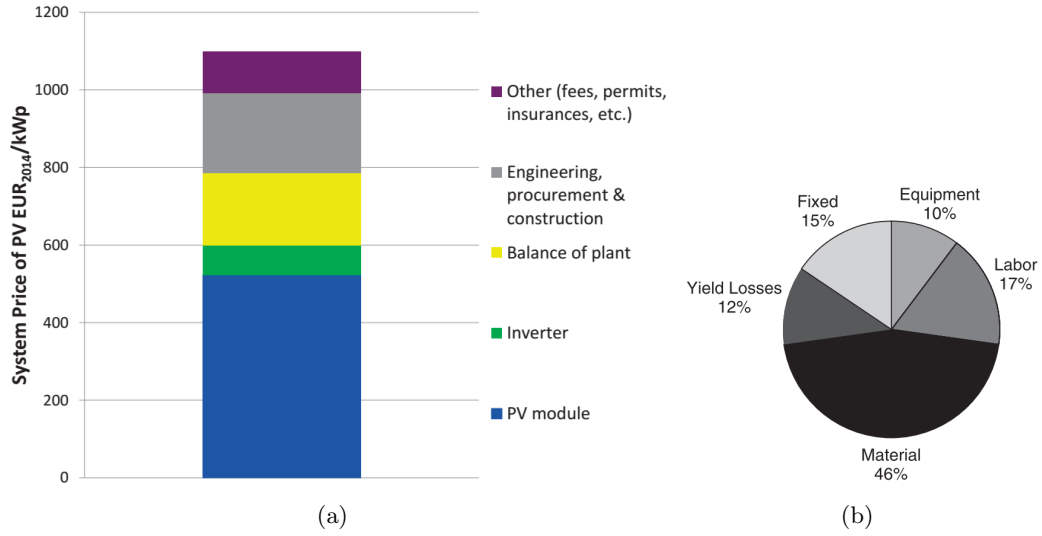
Figure 1.2: (a): Price breakdown of a medium-sized PV project based on Si modules. Taken from [6]. (b): Breakdown of costs in the fabrication of Si modules. Taken from [4].

convinced that the secret to future progress in PV lies in efficiency improvement more than in materials-related cost reduction [5]. This view is supported by the cost analysis of a PV power plant project based on Si solar cells, presented in Figure 1.2 per unit of power produced. The cost of the module is about one half of the total costs (blue region in Figure 1.2(a)). By further breaking down module costs, we see that materials costs contribute to about half of the module expenses (Figure 1.2(b)). So using cheaper materials and processing can change a fraction of the 25% remaining costs in the project. In practice, it is even less since some materials costs (metal contacts, encapsulating materials) cannot be decreased significantly with respect to Si technology as they are needed with any solar cell configuration. Conversely, an efficiency increase leads to strong cost reductions simply because the same power can be produced in a smaller area. Then, when evaluating the cost per unit of power produced (which is what matters economically) from Figure 1.2(b), area-dependent costs go down proportionally to the efficiency. PV module (blue), balance of plant (yellow), and engineering (grey) costs are approximately proportional to the size of the project and together account for about 85% of the total costs. Then, improving efficiency or decreasing materials costs by 10% (relative) imply a cost reduction of 8.5% and 2.5% respectively.

For now, the only real competitors of Si solar cells on a global scale are the so-called thin film technologies, which today have around 10% market share (Figure 1.1(b)). Differently from Si, they are not sliced from big chunks but instead form a thin coating (or film) on a rigid material that normally only serves as a support structure ("substrate"). A number of thin films of different materials deposited on top of each other can form a solar cell. The most important of them ("absorber") can be chosen among a class of materials that strongly absorb light (much more strongly than Si) called "direct band gap semiconductors". Then, the solar cell can be just a couple of μm thick - about 200 times thinner than a Si solar cell - with less materials consumption. Also, cell fabrication and module fabrication need not be two separate steps as with Si: a thin-film module can be produced by processing several identical solar cells in parallel, by depositing one film after the other in a continuous process. Finally, Si solar cells require some very high temperature processing steps, in excess of $1000°$C, first to form a Si crystal then to tune its electronic properties. Most thin-film technologies need less than $600°$C.

There are two particular markets where thin-film solar cells are expected to excel.

The first is building-integrated photovoltaics (BIPV), where some unique capabilities of thin-film technologies are very desirable: coating of rough or flexible surfaces, reduced weight, and options for semi-transparency simply by depositing thinner films that do not absorb all sunlight. In this respect, thin film technologies also have a much more pleasant appearance than Si solar cells, which are clearly not the hotties in the classroom.

The second market is the one based on the, still immature, "tandem solar cell" technology. This technology consists of putting two different solar cells on top of each other: one that is better at converting power in a certain region of the light spectrum, and another that is better in another spectral region. The theoretical efficiency of a tandem cell is much higher than that of just one solar cell ("single-junction solar cell") - 45% versus 33% [9]. While a Si solar cell can be one of the two, thin-film technologies are perfect candidates to be the other. The Si solar cell can then itself be the "substrate" onto which the second thin-film solar cell is deposited.

Excitingly, over the last few years two different thin-film technologies based on $Cu(In,Ga)Se_2$ (CIGS) and CdTe absorbers have almost closed the gap with Si solar cells in terms of their record efficiency. CIGS has reached 22.6% [10], CdTe 22.1%, whereas Si is at 25.6% (Figure 1.3 and [2]). Note that the maximum theoretical efficiency achievable by those direct band gap thin-film materials is higher than that achievable by Si (33% versus 29%) due to the slightly different physics of their ultimate loss mechanisms [5]. Therefore, it has been proven that there are no reasons to think that thin film technologies are inherently less efficient than Si and can therefore compete with Si even for bulk energy production. As seen in Figure 1.1(a), CdTe modules have been the ones delivering the most "power for the buck" for the last ten years, despite their relatively small market share. Thin film solar cell plants do exist, and I regularly get news by mail on the constructions of new plants based either on CIGS or CdTe.

1.1.3 Why CZTS(e)?

CIGS- and CdTe solar cells have 40 years behind their back. Therefore, with the current production volumes and with the existing legislation, they are inevitably dominating the thin-film PV market. However, there are serious concerns about the availability of the relatively rare elements In, Ga, Te, and Se in the case thin-film solar cell demand should experience a manifold increase [11,12]. Furthermore, Cd is a heavy metal that is toxic for humans. Legislation in some parts of the world is already taking steps toward banning Cd altogether. In Japan, CdTe modules are not allowed on residential rooftops. In the European Union, the Restriction on Hazardous Substances (RoHS) legislation [13] explicitly banned heavy metals like Cd and Pb from commercial products unless in trace amounts. For now, PV modules are exempted from complying to the RoHS requirements, but the situation may change. It seems, therefore, as if neither CIGS nor CdTe solar cells are a realistic long-term solution to the global energy hunger. The reasons for that are intrinsic to their constituent elements, so they can only be solved by switching to other materials.

A recent contender is the class of mixed organic-inorganic metal halide perovskite solar cells [14]. Virtually unknown before the year 2006, perovskite solar cells experienced the fastest efficiency improvement ever seen for a solar energy material. Between 2011 and 2016, their record efficiency went up from a moderately promising 6.5% to a dazzling 22.1% (Figure 1.3 and [2]). Efficient perovskite solar cells can be miraculously fabricated with very simple and low-cost methods. However, their fantastic efficiencies usually become far less fantastic within a matter of minutes due to various instabilities. Furthermore, it has so far been necessary to include the heavy metal Pb and the extremely expensive spiro-MeOTAD material in efficient perovskite solar cells. While those are serious problems, it is by no means impossible that they can be worked around by further development, so it is my opinion that perovskite solar cells can potentially play an important role in future

energy supply.

Finally, there are various thin-film materials with record efficiency between 10% and 15% (Figure 1.3) and various strengths and weaknesses. Among them, I shall use CZTS(e) as a general acronym to refer to all the following materials: the pure-selenide $Cu_2ZnSnSe_4$ ("CZTSe"), the pure-sulfide Cu_2ZnSnS_4 ("CZTS"), and their alloy $Cu_2ZnSnS_xSe_{4-x}$ ("CZTSSe"). The historical origin of CZTS(e) as a solar cell material is due to its similarity to CIGS, with the bonus of the rare elements In and Ga replaced by the more abundant Zn and Sn. This is why CZTS(e)-based PV is sometimes referred to as "earth-abundant photovoltaics". However, this label is misleading: while it is true that the thin-film giants CIGS and CdTe contain some rather scarce elements, silicon is the second most earth-abundant element available on earth after oxygen and no alternative technology can beat that. Further, the earth-abundance argument is not particularly strong for Se-containing CZTS(e), as the availability of Se is also an issue for ultra-large scale deployment [11, 12]. CZTS(e) solar cells are also often marketed as "non-toxic", because they supposedly do not contain toxic elements. However, this is not correct in most cases, as the typical architecture of a CZTS(e) solar cell includes a thin Cd-containing layer (CdS). While it is true that about 20 times less Cd is present in a CZTS solar cell than in a CdTe solar cell, it is still more than a trace amount and it is not unlikely that it will be hit by Cd-restraining legislation as much as CdTe solar cells. Still, there are alternative materials that can replace the CdS layer with a very limited efficiency loss, so this is unlikely to be an insurmountable problem.

What is my conclusion then? I believe that Se-containing CZTS(e) does not have any significant advantage over the (much better-performing) CIGS technology. If the goal of CZTS(e) is to enter a market niche that only demands moderate production volumes, then the scarcity of the CIGS elements is unlikely to be a limiting factor. A CZTS(e) solar cell may be slightly cheaper due to more inexpensive constituent metals but, as we have seen, there is not much money to be saved by that in an actual PV installation (Figure 1.2). On the other hand, if the goal of CZTS(e) is to become a serious candidate material for Terawatt-sized energy production, then the relative scarcity of Se will most likely limit its possibilities.

1.1.4 Why (pure-sulfide) CZTS?

The story is very different, in my opinion, when it comes to pure-sulfide CZTS. Compared to Se-containing CZTS(e), the following advantages can be identified:

1. S is a very abundant element [11, 12].

2. while most researchers still rely on a CdS layer in the CZTS solar cell architecture, it has been demonstrated that replacement of CdS by non-toxic materials such as (Zn,Sn)O [15] can actually improve solar cell efficiency.

3. due to its particular properties, CZTS is a type of material which is in principle appropriate both for a single-junction solar cell and for the top cell in a tandem architecture [5].

4. the distance between the CZTS atoms and the way in which they are arranged are very similar to those of silicon. This is called "lattice matching". This is very interesting because lattice-matched material pairs often give very clean interfaces when put on top of each other. Therefore, it can be envisioned that CZTS is an ideal partner of silicon in a tandem cell architecture. Indeed, research on Si/CZTS tandem solar cells has already started, mostly by groups with a strong Si solar cell track record [16].

For the above reasons, pure-sulfide CZTS solar cells may be considered a true earth-abundant and non-toxic PV solution that has very interesting medium- and long-term prospects. It can have its own existence as a single-junction solar cell or it can boost the efficiency of the well-established Si solar cells in a tandem architecture, without obvious barriers to the huge production volumes that are soon to be needed. The main problem that separates this dream prospect from reality is the comparably low efficiency achieved so far by this type of technology. The record laboratory efficiency achieved by CZTS solar cells is only 9.1% [17], with a bit higher efficiency (12.6%) achieved by Se-containing CZTSSe [18].

Most of this thesis will be about my attempt to understand the root causes of that problem and to experimentally evaluate new tracks to improve the efficiency of CZTS. Those root causes are related, at a lower level, to the physics and chemistry of the CZTS material alone and, at a higher level, to the teamwork of all the thin-film materials present in the solar cell (still physics and chemistry).
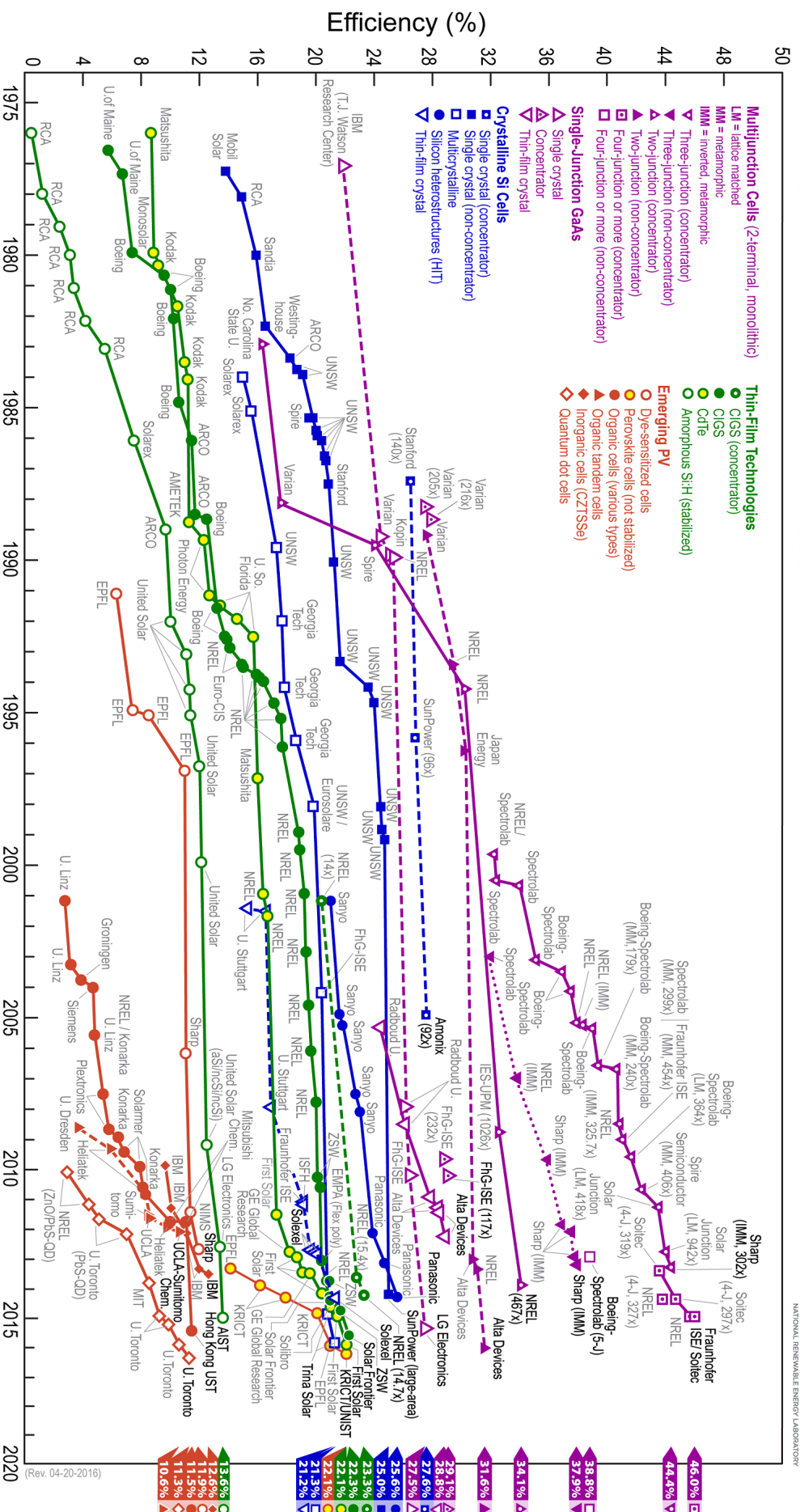
Figure 1.3: Record efficiency of the main solar cell technologies through the years [19]. Note that all the purple data points are related to very expensive technologies used in niche applications (e.g. power generation in space). Also,"concentrator"-based technologies are simply a boosted version of their parent materials, achieved through a rather expensive optical trick.

1.2 CZTS as a solar energy material

1.2.1 Properties of CZTS

From a crystallographical point of view, CZTS (Cu_2ZnSnS_4) can be derived from the zincblende structure of ZnS by keeping the S anion and substituting the Zn cation with Cu, Zn, and Sn cations in the relative amounts that ensure charge neutrality in the crystal. Specifically, if ZnS has a 2^+ cation (a group II element) and a 2^- anion (a group VI element), substituting four Zn ions in ZnS with two 1^+ Cu ions, one 2^+ Zn ion, and one 4^+ ion ensures charge neutrality with the S anion. Thus, starting from a [II-VI] compound (ZnS), a [I_2-II-IV-VI_4] is obtained (CZTS). Regarding the arrangement of the atoms in the crystal structure, two CZTS phases with very similar formation energy exist: kesterite (space group I$\bar{4}$) and stannite (space group I$\bar{4}2m$). The kesterite structure has been found to be favored both experimentally [20] and theoretically [21]. Note that CZTS is lattice-matched within less than 1% to materials of significant technological importance, first and foremost Si, but also CeO_2 (see Study 3) and ZnS. CZTS is a semiconductor that occurs naturally with p-type conductivity, that is, with more free holes than free electrons under equilibrium conditions. This happens due to the high probability of formation of defects that add free holes to the crystal (acceptor defects). This matter will be discussed in more detail in Section 1.4.

Most people quote 1.5 eV as the nominal band gap of CZTS, or "band gap of the extended states". However, the ideal band gap of a perfect CZTS crystal decreases by a couple hundred meV with increasing disorder in the material (more on this later). In any case, the band gap of CZTS is usually measured in the 1.4-1.6 eV range (real synthesized material), and calculated in the 1.5-1.65 eV range (ideal, ordered material). From both theory [21, 22] and experiment [23], the valence band of CZTS consists primarily of the antibonding state of hybridized Cu 3d and S 3p orbitals, whereas the conduction band consists of the antibonding state of hybridized Sn 5s and S 3p orbitals. The band gap of the stannite phase is about 0.1-0.2 eV lower than kesterite CZTS. The smaller band-gap brother of CZTS is CZTSe, which has a band gap of about 1.0 eV.

From thermodynamical considerations expressed in the detailed balance theory [24], the maximum efficiency theoretically achievable by a single-junction solar cell is only a function of the temperature, the illuminating spectrum, and the band gap of the absorber material. This is called the Shockley-Queisser limit. It turns out that, for a standard AM1.5 solar spectrum [25], any semiconductor with a direct band gap between 1.1 eV and 1.5 eV has a maximum theoretical efficiency of 32-34%. Indirect band gaps semiconductors like Si have a slightly lower theoretical efficiency (29-30% [5]). As mentioned in Section 1.1.4, a peculiar strength of a 1.5 eV band gap material like CZTS is that it is an optimal material not only for a single-junction solar cell but also as a top absorber in a double-junction (tandem) solar cell architecture [26] using Si as a bottom absorber.

1.2.2 History of CZTS solar cells and state of the art

The early history of CZTS solar cells is summarized in [27, 28]. Two broad reviews of the many different tracks that have led to reasonably efficient devices were published in 2012 and 2013 [29, 30]. More schematic information was compiled in 2013 [31]. An update on recent progress was published this year (2016) [32]. Briefly, the pioneers of CZTS solar cells are Kentaro Ito and Hironori Katagiri. The former was the first to report synthesis of CZTS thin films and suggest their potential photovoltaics application [33]. The latter was the first to fabricate a CZTS solar cell, by CZTS evaporation, with an efficiency of 0.66% [34]. Katagiri identified three important trends for future CZTS work: (i) reproducing the standard CIGS device architecture in CZTS solar cells, (ii) forming

9

CZTS in a S-containing atmosphere, and (iii) synthesizing CZTS with a Cu-poor, Zn-rich composition [35]. Until 2008, research on CZTS solar cells was limited to a few groups in Japan with the exception of an isolated attempt in Stuttgart. Then, a few European groups started reporting results on CZTS in 2008-2009, followed by some great successes by IBM, which convinced the rest of the world to join the race. As of 2016, the best solar cell of the CZTS(e) family (IBM - hydrazine solution) has a low S content, $[S]/([S]+[Se]) \approx 0.3$, a band gap of 1.13 eV, and an efficiency of 12.6% [18]. Pure-selenide CZTSe solar cells are almost as good, with a record efficiency (IBM - coevaporation) of 11.6% [36]. Interestingly, CZTS(e) solar cells with a low S content and efficiencies between 11% and 12.6% can be fabricated by a variety of techniques, including the two "vacuum giants" evaporation [36] and sputtering [37], and a variety of non-vacuum methods [18, 38–40]. The situation is a bit different for (pure sulfide) CZTS, as the highest certified record efficiency (Toyota - sputtering) is only 9.1% [2, 17]. Other high efficiencies I know of are a non-certified 9.2% (Solar Frontier - sputtering [41]), 8.6% (UNSW - sputtering [42]), 8.4% (IBM - coevaporation [43]), and 7.9% (Uppsala University - sputtering [44]). Therefore, there seems to be some advantage related to vacuum techniques, and sputtering in particular, for CZTS precursor deposition. Note that the CZTS precursors in almost all the high efficiency devices are annealed between 500°C and 600°C in a S(e)-containing atmosphere, obtained either by $H_2S(e)$ gas or by sublimation of solid S(e). Notable exceptions are the overall world record CZTSSe solar cell, which was annealed in N_2 [18], and some of the cells by coevaporation [45, 46], where the annealing step is skipped altogether as S can be supplied in the desired amount already during deposition by using a S cracking source.

How about pulsed laser deposition of CZTS? Ironically, it was already attempted in the early days of CZTS research at the institute of Katagiri, with a 1.74% efficiency reported in 2007 by Moriya and coworkers [47]. The only two other groups to have shown CZTS solar cells by PLD are Moholkar and coworkers, who reported a 4.13% efficiency in 2012 [48], and Jin and coworkers, who reported a 4.94% efficiency in 2016 [49] a couple of weeks before we submitted our work on a 5.2% solar cell presented in this thesis as Study 2.1 (timing is everything). There is also a claim to a 5.85% efficiency [50], which is however based on a measured short circuit current of 38.9 mA/cm^2, a physically impossible result using a 1.5 eV absorber. Work on PLD of CZTS is summarized in a review article [50].

1.3   How does a CZTS solar cell ideally work?

The standard device architecture of CZTS solar cells, shown in Figure 1.4, is borrowed exactly from the highly successful CIGS device architecture, with CIGS replaced by CZTS. The combination of materials was invented by the company ARCO in 1987 [51]. It can be labeled as a planar p-n heterojunction solar cell. The CZTS/CdS interface is labeled "heterointerface". The general device physics of this kind of heterojunction solar cells is treated in classic semiconductor books [52] and, in greater detail, in a specialized book on the physics of heterojunction solar cells [53] (watch out - pretty advanced). Besides that, I have also produced some structured original work myself, which are presented in the studies of Chapter 4.
For now, I will just present the principles that make a CZTS solar cell work. This will on purpose be done in a very loose and non-rigorous way, because my goal here is to maximize understanding in a limited space and not to repeat what has already been said by others [52, 53]. As I present the physics and the main issues and non-idealities of a CZTS solar cell, I hope that the choice of the particular device architecture shown in Figure 1.4 will become apparent. I like to divide operation of a CZTS solar cell into three basic processes.
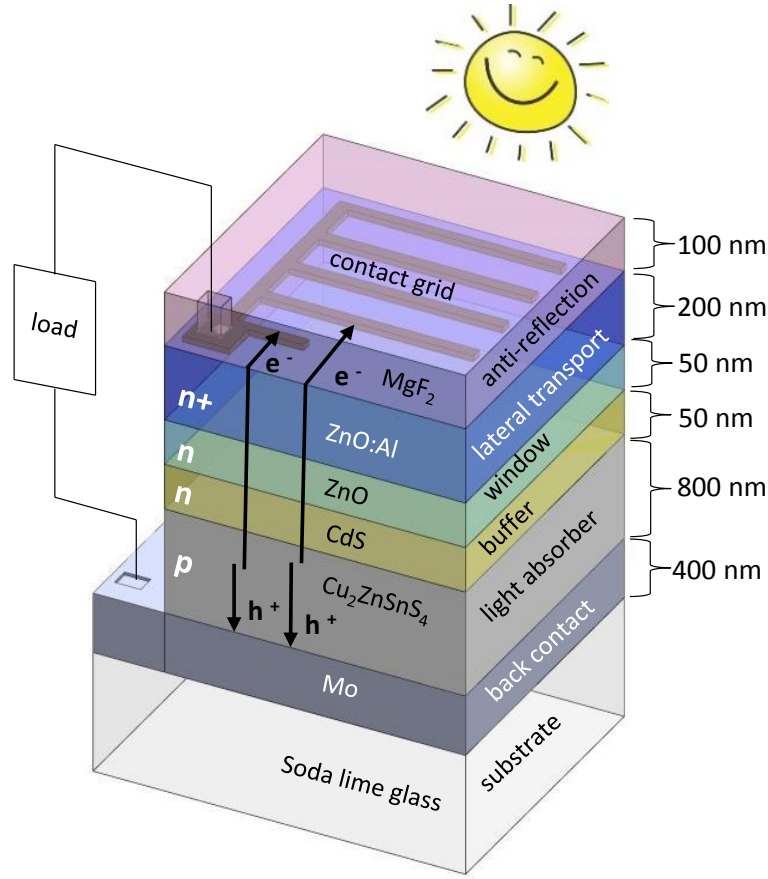
Figure 1.4: The standard device architecture of a CZTS solar cell. Layer thicknesses are indicative. the e^- and h^+ symbols represent electrons and holes photogenerated in CZTS by photon absorption which are effectively separated and reach their respective contacts. The p, n, and n^+ symbols refer to the doping type of the materials.

1.3.1 Photon absorption

The first process is absorption of photons. CZTS does the job very well thanks to its direct band gap and high absorption coefficient (Study 7.1 and [54]). Hence, a 800 nm CZTS thickness is enough to absorb nearly all incoming light [55]. Note that, even for a 400 nm absorber, the expected fraction of non-absorbed light is just 10% (Study 2.1). The spectral region of light that is absorbed in the solar cell is that with photon energy above ∼1.5 eV, corresponding to the band gap E_g of CZTS. Up to an energy of ∼2.4 eV, corresponding to the band gap of CdS, the result is generation of electron-hole pairs in CZTS only. Above ∼2.4 eV, some photon absorption and electron-hole generation occurs in CdS as well, and above ∼3.3 eV (band gap of ZnO) a contribution from the top ZnO and ZnO:Al layers is also present [56]. Most of the natural reflection at the air-solar cell interface is suppressed by the MgF_2 anti-reflection coating at the very front of the solar cell stack. Finally, the front contact grid shadows part of the incoming light but, for a well designed contact grid and a reasonably conductive lateral transport layer, such an optical loss can be kept below 2% [56].

1.3.2 Carrier separation and collection under short circuit conditions

Since electrons and holes carry charge of opposite signs, they need to be collected at two separate contacts in the solar cells for a net current to flow into the external load. An initial requirement is that such a carrier separation/collection process works well under

short circuit conditions, i.e., without an applied voltage. This the second physical process. The goal of the standard CZTS solar cell architecture is to drive holes to the Mo back contact and electrons to the front contact grid. Gradients in the *electrochemical* potentials of holes and electrons, i.e. in their quasi-Fermi levels, are the driving force behind separation of electrons and holes toward their respective contacts. For the electron-hole pairs generated within the depletion region of the p-n heterojunction (Figure 1.5), separation is ensured by the "built-in" *electrostatic* potential gradient formed across the p-n junction as a consequence of junction formation. Such an electrostatic potential gradient induces a gradient in the quasi-Fermi levels under illumination, so that the carriers are swept in opposite directions. This phenomenon occurs for carriers generated in the depletion region, and the width of the depletion region depends on the doping density and relative permittivity of CZTS, CdS, and ZnO, as well as on the thicknesses of the CdS and ZnO layers (Study 4.4, [52]). In state-of-the-art CZTS solar cells, the depletion region extends about 180-200 nm from the p-n junction into CZTS (Study 2.1, [17, 43]). Note that the electrostatic built-in potential itself is not the cause of charge separation, as pointed out by two generations of Würfels [57], and in fact the free carriers in the dark under zero bias are not preferentially going anywhere, even though the electrostatic built-in potential is still there. What happens to carriers generated out of the depletion region? There, no quasi-Fermi level gradient exists to drive the photogenerated carriers toward a particular direction. Therefore, electrons and holes will move randomly (Figure 1.5). The question is where they will end up. The closer to the p-n junction they are generated, the more likely it is for them to be successfully separated by the built-in electrochemical potential. Likewise, the closer to the back contact they are generated, the more likely it is for electrons to reach the (wrong) Mo contact. The latter (detrimental) effect can be avoided by a sufficiently thick absorber layer or by introduction of a back surface field to bend the bands upward next to back contact and thus create an electron barrier (Figure 1.5, [58]). Note that, in general, electrons generated out of the depletion region do not have an infinite amount of time to reach the edge of the depletion region and separate. The quantity that determines how well such electrons are collected is the electron diffusion length L_D

$$L_\mathrm{D} = \sqrt{\frac{k_\mathrm{B} T \mu_\mathrm{e} \tau}{q}} \tag{1.1}$$

where τ is the lifetime of electrons in the CZTS conduction band before they recombine, μ_e is the mobility of electrons in CZTS, k_B is Boltzmann's constant, T is the temperature, and q is the elementary charge. Regarding the front and back contacts, they have to be designed differently from each other. This is because, to a first approximation, the only critical properties of the back contact are the electrical properties so the back contact can be a highly conductive metal. On the other hand, the front contact has to both collect the carriers *and* let sunlight through. This is why a transparent conductive material like ZnO:Al is needed. However, even though the conductivity of transparent conductors can be surprisingly close to the conductivity of metals [59], it is still not enough to allow current collection over a large area without significant series resistance losses. That is why a metal contact grid is usually added on top of the transparent conductor to provide an average shorter path for the collected carriers in the lateral (in-plane) direction and decrease series resistance losses with only a minimal decrease in the fraction of photons reaching the absorber.

There is one quantity that reveals whether the solar cell is doing a good job at the tasks listed in this and in the previous section (photon absorption and carrier separation/collection). Such quantity is the short circuit current J_sc. Luckily for solar cell researchers, the origin of the short circuit current can be tracked all the way down to the photon spectrum by measuring the "photon to collected charge carrier conversion efficiency" for
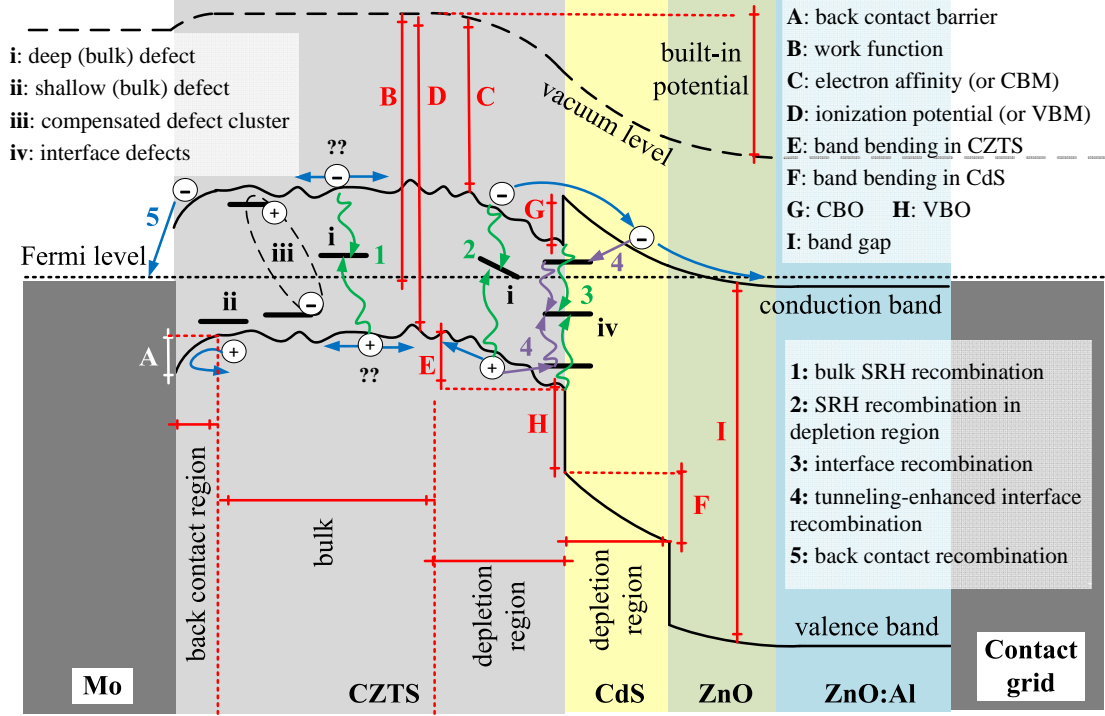
Figure 1.5: Schematic band diagram of a CZTS solar cell for purely illustrative purposes (not quantitative and not to scale). The x axis is position in the out-of-plane direction in the standard solar cell architecture of Figure 1.4, and the y axis is electron energy. Most of the semiconductor device terminology used in this thesis is introduced here. In the specific case of this figure, I have assumed a positive (spike-like) CBO and downward (detrimental) band bending at the CZTS/Mo interface, which creates a hole barrier. Even though I present transport and recombination processes typical of non-equilibrium conditions (applied bias and/or illumination) I still draw a single Fermi level instead of two quasi-Fermi levels for the sake of simplicity. For the same reason, I omit the MoS_2 layer that is typically formed between Mo and CZTS. The irregular bands in CZTS are meant to illustrate the band gap- or electrostatic potential fluctuations that are present in CZTS (see Section 1.4).

each photon energy, known as the external quantum efficiency spectrum $\mathrm{EQE}(E)$ of the device.

$$J_{sc} = \int_{E_g}^{\infty} q\, n_{ph}(E)\, A(E)\, C(E)\, dE \equiv \int_{E_g}^{\infty} q\, n_{ph}(E)\, \mathrm{EQE}(E)\, dE \qquad (1.2)$$

Here, E is the photon energy, E_g is the band gap of the absorber, q is the elementary charge, $A(E)$ is the photon absorbance, i.e., the fraction of incoming photons that are absorbed in the solar cell and generate an electron-hole pair, $C(E)$ is the collection efficiency, i.e., the fraction of photogenerated electron-hole pairs that are collected at their respective contact, and $n_{ph}(E)$ is the photon density of the measured solar spectrum that is generally taken as a standard (the AM1.5 spectrum). Therefore, it is relatively easy to diagnose problems in the absorption or collection behavior of solar cells. My guess is that this is part of reason why the short circuit current of CZTS solar cells, normalized to the theoretical maximum predicted by the Shockley-Queisser limit, is nearly as good as the much more efficient CIGS solar cells [60].

1.3.3 Carrier separation and collection under an applied voltage

For electrical work to be done and thus electrical power to be generated, the photo-generated current must flow *against* an applied voltage V that reduces the built-in potential of the junction, which is called - in p-n junction language - forward bias. For

increasing forward bias, the favorable gradients in the quasi-Fermi levels will decrease and finally change sign so there will be a voltage at which the current through the device changes sign and power is consumed instead of generated. Such a voltage is the open circuit voltage of the solar cell, and the details of carrier separation and collection under forward bias are the third process. In practice, it may be easier to look at the problem of a biased solar cell by means of a mathematical trick, where the current is modeled as the sum of two currents of opposite signs. The first is the photocurrent, equal to the short-circuit current J_{sc}, that is constant at any voltage bias and flows from the front contact to the back contact as we wish. The second is the diode current J_d, or recombination current, that flows in the opposite direction and increases with voltage. With this type of model, the current-voltage (JV) characteristic of the solar cell can be expressed by the following equation:

$$J(V) = J_{sc} - J_d(V) \tag{1.3}$$

where $J(V)$ is the net current flowing in the device. The voltage-dependent recombination current $J_d(V)$ can be expressed as

$$J_d(V) = J_0 \left[\exp\left(\frac{qV}{n_d k_B T} \right) - 1 \right] \tag{1.4}$$

Here, J_0 and n_d are parameters called dark saturation current and diode ideality factor. I postpone an explanation of their physical meaning to later on in this section. Following the discussion in the previous section, J_{sc} is hopefully a quantity greater than zero at zero voltage. Instead, $J_d(V)$ is zero at zero voltage according to Equation 1.4, but its magnitude increases exponentially with voltage. The voltage at which $J_{sc} = J_d(V)$ is the open circuit voltage.

If illumination is removed, $J_{sc} = 0$ and the current-voltage behavior of the solar cell becomes that of a p-n junction diode

$$J(V) = -J_d(V) \tag{1.5}$$

Maximum power can be extracted by biasing the solar cell at a certain voltage, corresponding to the voltage where the JV product is maximized. This particular voltage can be labeled V_m, and the corresponding current density can be labeled J_m. Then, the maximum power obtainable (P_m) is

$$P_m = A V_m J_m \tag{1.6}$$

where A is the area of the solar cell. The efficiency of the solar cell η is determined by how well the power from the sun is converted into electrical power, that is

$$\eta = \frac{V_m J_m}{\int_0^\infty n_{ph}(E) \, E \, dE} \tag{1.7}$$

where the denominator is the total intensity of the standard AM1.5 solar spectrum. Because J_{sc} and V_{oc} are key parameters in a solar cell, it is convenient to express the efficiency as a function of them. This can be done by defining the "fill factor" FF as

$$FF = \frac{V_m J_m}{V_{oc} J_{sc}} \tag{1.8}$$

The more the illuminated JV characteristic of the solar cell approximates a square, the closer the fill factor is to 100%. With the FF defined, the efficiency of a solar cell can be rewritten in a very practical form as

$$\eta = \frac{V_{oc} J_{sc} FF}{\int_0^\infty n_{ph}(E) \, E \, dE} \tag{1.9}$$

Clearly, an improvement of, say 10%, in either V_{oc}, J_{sc}, or FF has the same beneficial effect on the efficiency (10% relative increase). Therefore, improvement in V_{oc}, J_{sc}, and FF in a solar cell are all of equal importance.

What does the value of the open circuit voltage depend on? It can be expressed empirically as

$$V_{oc} = \frac{E_A}{q} - \frac{n_d k_B T}{q} \ln\left(\frac{J_{00}}{J_{sc}}\right) \tag{1.10}$$

Here, E_A is the activation energy of the main recombination path and the other terms have the same meaning as in Equation 1.4. J_{00} is the prefactor of the dark saturation current J_0 introduced in Eq. 1.4, which can be expressed as

$$J_0 = J_{00} \exp\left(\frac{-E_A}{n_d k_B T}\right) \tag{1.11}$$

Equation 1.10 is my favorite expression of the open-circuit voltage of a moderately crappy solar cell (such as a CZTS solar cell) because it is very practical. It says that the open circuit voltage is limited by a quantity E_A, and that it deteriorates with temperature with a temperature coefficient that depends on the quantities n_d, J_{00}, and J_{sc}. Now we can start to understand the physical meaning of the parameters used in the previous equations.

- E_A is the distance, in energy, between recombining electrons and holes in the point of the device where the main recombination path is located. Hence, in a solar cell where the main recombination mechanism is band-to-band recombination in the absorber bulk or depletion region, E_A should be equal to E_g. In a solar cell with a reduced interface band gap due to a cliff-like band alignment or other mechanisms (Study 4.1), and where interface recombination is the dominant recombination mechanism, E_A should be equal to the interface band gap [61]. It follows that the absolute limit for the open circuit voltage at 0 K is the absorber's band gap.

- n_d expresses the voltage dependence of the main recombination path between short circuit conditions and the open circuit voltage point. The higher its value, the more gradually the recombination current increases between zero bias and the open circuit voltage. Therefore, the higher n_d, the lower the fill factor and the lower the open circuit voltage (Equation 1.10). In principle, the value of n_d is fixed by the type of recombination that is dominant. For example, in an ideal solar cell with pure band-to-band recombination $n_d = 1$; in a solar cell with dominating Shockley-Read-Hall (SRH) recombination in the depletion region through a defect state near the absorber's midgap $n_d = 2$ [62]. The lower the ideality factor, the sharper the onset of the recombination current. Since n_d was originally introduced to describe reasonably well-behaved diodes, some caution must be taken when using it to describe not-so-well-behaved solar cells [63]. For example, recombination may be dominated by a mechanism that implies a diode ideality factor greater than 2, or the origin of the main recombination path may change with voltage. The latter case even occurs in well-behaved solar cells, where $n_d = 2$ at a low voltage due to dominance of Shockley-Read-Hall recombination through a midgap defect state, and $n_d = 1$ at higher voltage [64]. Finally, the ideality factor alone may not completely capture the essence of the voltage-dependence of recombination, for example when the collection efficiency $C(E)$ varies with voltage close to short-circuit conditions.

- having identified the dominant recombination path, J_{00} is basically a measure of how bad recombination is within that path. J_{00} has a different functional form for each recombination mechanism [65, 66], and the relevant one is that of the dominant recombination path. J_{00} and n_d both act to reduce the open circuit voltage of the

solar cell with respect to the zero-temperature case E_A/q. Here I list the expressions of J_{00} related to some common recombination mechanisms assuming a p-type absorber as CZTS [65, 66]. All such mechanisms are based on Shockley-Read-Hall (SRH) recombination, which means that recombination is mediated by defect states located in the band gap, which can efficiently capture electrons and holes. Because those defects are abundant in thin-film polycrystalline materials, SRH recombination is generally assumed to be dominating in most thin-film solar cell technologies. In general, the SRH recombination rate is maximized when: (i) the energy position of the defect state is near the middle of the band gap of the material; (ii) the density of free electrons and holes at a certain position are equal; and (iii) the density of both holes and electrons at a certain position is high [62].

For SRH recombination in the CZTS absorber (outside of the depletion region), $n_d = 1$ and

$$J_{00} = \frac{N_C N_V}{N_a} \sqrt{\frac{q \mu_e k_B T}{\tau}} \tag{1.12}$$

Here, N_C and N_V are the conduction- and valence band effective density of states, which increase with increasing effective mass of electrons and holes respectively [52]; N_a is the (p-type) doping density of CZTS, μ_e is the electron mobility of CZTS, and τ is the lifetime of electrons in the CZTS conduction band.

For SRH recombination in the CZTS absorber (within the depletion region), $n_d = 2$ and

$$J_{00} = \frac{\pi k_B T \sqrt{N_C N_V}}{F \tau} \tag{1.13}$$

where F is the electric field at the position with highest recombination rate.

For SRH recombination at the heterointerface, $n_d = 1$. If the interface is strongly n-type (i.e., electrons are "majority carriers"):

$$J_{00} = q \, S_p \, N_V \tag{1.14}$$

Here, $S_p = \sigma_p N_i v_{th}$ is the interface recombination velocity of holes at the heterointerface, which depends on the thermal velocity of holes v_{th}, on the surface density of interface states within the band gap N_i that can act as recombination centers, and on the capture cross section of holes by those states σ_p, which determines how likely it is for a free hole to be captured by those states. Occupied acceptor states can have large capture cross sections because they are negatively charged and attract holes electrostatically. If the interface is strongly p-type (i.e., electrons are "minority carriers"), the expression for J_{00} is the same but the relevant quantities become those of electrons (S_n, N_C, σ_n).

If the origin of the main recombination path is known (or guessed) Equation 1.10 and Equations 1.12-1.14 show which properties of the solar cell materials influence that recombination path, and how. This is my favorite way of looking at the recombination problems of a solar cell from a theoretical point of view because it helps identify where the problems are. This is particularly important for CZTS solar cells as their biggest problem is clearly their behavior under an applied voltage, i.e., the recombination current $J_d(V)$. Indeed, CZTS solar cells have more severe recombination problems in comparison with CIGS solar cells and even in comparison with CZTSe solar cells. This will become evident in the next sections and leads to open circuit voltage losses and fill factor losses. Unfortunately, characterization of recombination losses is more difficult than characterization of short circuit current losses because there is no such a thing as a "recombination equivalent of the EQE". Hence, characterization of recombination losses relies inevitably

on a plethora of indirect techniques such as transient photocapacitance spectroscopy to find the energy position of deep defect levels [67], steady-state PL to characterize radiative recombination [68], time-resolved-PL to extract the electron lifetime in the absorber [45], photoemission spectroscopy to measure interface band gap narrowing [69], JV curve analysis to extract n_d [70], and temperature-dependent open circuit voltage measurement to extract E_A [66]. Understanding the origin of recombination and trying to mitigate it with new fabrication strategies is currently the main challenge in CZTS solar cell research, as will be shown in the next two sections.

1.3.4 Resistive effects

In practice, the solar cell equation has to be adjusted to account for parasitic resistance losses. They can be either series resistance losses, modeled by a single resistor R_s in series with the solar cell, or shunt resistance losses, modeled by a single resistor R_sh in parallel with the solar cell. Both are area-specific resistances. Contributions to series resistance can be: bulk resistivity of the absorber, sheet resistance of the lateral transport layer (ZnO:Al), of the back contact (Mo) or of the contact grid, or presence of barriers to carrier transport somewhere in the device. Contributions to shunt resistance can be: pinholes in the absorber layer where the back contact touches the top layers, presence of high conductivity secondary phases within the CZTS layer (such as Cu_2S - see Section 1.4) or shunt paths at the edges of the solar cell. The solar cell equation (Eq. 1.3) should then be rewritten as

$$J(V) = J_\mathrm{sc} - J_0 \left[\exp\left(\frac{q(V - R_\mathrm{s}J)}{n_\mathrm{d}k_\mathrm{B}T} \right) - 1 \right] - \frac{V - R_\mathrm{s}J}{R_\mathrm{sh}} \tag{1.15}$$

Unless series resistance and shunt resistance are very bad (meaning very high and very low, respectively), they do not affect J_sc and V_oc significantly. However, they will of course degrade the fill factor. To a first approximation, R_s and R_sh are equal to the inverse of the slope of the JV curve of a solar cell at the open circuit voltage point and at under short circuit conditions respectively.

A final note on the fill factor: if parasitic resistance losses are negligible, the fill factor of a solar cell with a certain open-circuit voltage is basically determined by the voltage dependence of the recombination current, that is, on the diode ideality factor n_d. If n_d is fixed, the higher the open circuit voltage of a solar cell, the more "space" there is between zero voltage and the open circuit voltage. Therefore, solar cells with a higher open circuit voltage should in principle yield a higher fill factor [71].

1.4 Non-idealities in CZTS solar cells

In this section, my goal is to try and fill in the gap between what you read in books about the physics of solar cells and the hard reality of CZTS solar cells. Note: such books can be excellent [3, 64, 72] but are usually designed with good, well understood materials in mind such as Si or GaAs. Welcome to the CZTS wasteland.

1.4.1 Is CZTS a single-phase material?

The answer is not just "yes" or "no". Also, like most issues with CZTS, it is still in part an open problem. It was recognized already in the early days of CZTS that the single-phase region of the material is pretty small, and from the early phase diagrams [73] it was believed that only about 1% absolute deviation from the ideal, stoichiometric composition 25%-12.5%-12.5%-50% for Cu-Zn-Sn-S could be tolerated by single-phase CZTS at typical annealing temperatures [74]. However, later studies gave a more complex picture. The

most important question is: what happens when CZTS is grown far from the stoichiometric point, as necessary for efficient solar cells, where Cu/(Zn+Sn) ≈ 0.8 and Zn/Sn ≈ 1.2? It was shown that CZTS could exist as a non-stoichiometric phase when the *overall* stoichiometry (i.e., CZTS plus any other phases) was Cu/(Zn+Sn)=0.79 and Zn/Sn=1.19 - basically the optimal stoichiometry for solar cells - which means 6% absolute deviation in Zn and Cu content from the stoichiometric point. This non-stoichiometric phase had very similar structural properties to the stoichiometric phase [75]. However, non-stoichiometry resulted in ZnS segregation [76] as expected from the earlier phase diagrams. In a more recent study [77] it was shown that, if single-phase CZTS is desired, there is some space on the Zn-rich side of the phase diagram, even though not much more than 2% deviation in Zn content is tolerated. This means that, to obtain single-phase, Zn-rich CZTS, it must be ensured that Cu/(Zn+Sn)>0.95 and Zn/Sn>1.1 or ZnS will form. Note that the same study detected some Cu_xS even when Cu/(Zn+Sn)<0.95, but only when Zn/Sn was high enough (>1.1). It is then inevitable that some ZnS will precipitate when CZTS is synthesized under the necessary conditions for efficient solar cells. However, what is the stoichiometry *of the CZTS phase* when the *overall stoichiometry* is Cu/(Zn+Sn) ≈ 0.8 and Zn/Sn ≈ 1.2? An answer to this question was provided very recently by experiment on actual CZTS thin films [78]: the Zn/Sn ratio in CZTS never exceeds 1 and all the excess Zn is present in the form of ZnS. Therefore, ZnS is always expected to be present *somewhere* in high-efficiency CZTS solar cells, and it seems indeed as if in many cases ZnS segregates at the back contact [43] or at the heterointerface [79–81]. In the latter case, it may be convenient to etch it with a HCl solution [82]. Fortunately, ZnS is probably the least harmful of the competing phases around the stoichiometric point of CZTS in the phase diagram. It has a large band gap (about 3.7 eV) and a large conduction band spike with CZTS [83]. Therefore the main risks are current losses in the case of a continuous ZnS layer (because of the electron barrier between CZTS and ZnS) and series resistance losses in the case of scattered ZnS phases. Other competing phases with a lower band gap than CZTS (such as Cu_xS, SnS, Cu_2SnS_3) can be very dangerous for the open circuit voltage of the solar cell. That is because they can trap free carriers due to the potential well they form with the valence band or conduction band of CZTS. This would lead to a lower E_A because it would lower the minimum energy distance for recombination in absorber, with consequent V_{oc} losses.

1.4.2 Defects

Point defects and defect clusters are extremely important in CZTS solar cells. Shallow defects determine the doping density in CZTS, CdS, ZnO, ZnO:Al, and cause structural disorder in the kesterite structure of CTZS. Deep defects cause Shockley-Read-Hall recombination in the CZTS bulk. Defects may be isolated or they may form defect *clusters* consisting of a combination of acceptors and donors with net zero charge (see Figure 1.5). The case of defect clusters is significantly different than the case of isolated defects. While the latter class "only" forms energy levels in the band gap of CZTS (shallow or deep), the former class can also locally change the band edge positions in the material and thus modify the band gap, electron affinity and other key electronic properties [84].

Shallow defects: why is CZTS p-type?

Some semiconductors (for example, Si and GaAs) can be produced under such well-controlled conditions that their crystals are nearly free of point defects, that is, every Si, Ga, As atom is located exactly where it should in the ideal crystal. The story is very different for materials with a shorter history behind them, and especially for multinary compounds like CZTS where the number of possible point defects explodes simply for

permutational reasons. An important consequence is that the former class of very pure materials is of intrinsic nature, i.e. with the Fermi level located near the middle of the band gap, unless foreign atoms of difference valence are intentionally introduced to substitute a fraction of the original atoms (extrinsic doping). Conversely, the second class of materials often exhibits "natural" p- or n-type doping simply due to the combined effect of all the point defects present unintentionally in the synthesized material. The closer in energy an acceptor (donor) defect lies with respect to the valence (conduction) band edge, and the larger its volume density, the more free carriers it adds to the valence (conduction) band, the more it tends to move the Fermi level downward (upward) and dope CZTS p-type (n-type). The effective doping density is then determined by the net effect of all defects present in the lattice. Acceptors (donors) located within 0.2 eV from the VBM (CBM) can be labeled as "shallow". The acceptor Cu_{Zn} antisite (i.e., Cu substituting Zn) is the defect with the lowest formation energy within the single-phase region of CZTS [84], however it is not extremely close to the VBM (about 0.15 eV distance). The V_{Cu} defect (Cu vacancy, i.e., empty Cu lattice site) is a less abundant acceptor in single-phase CZTS but it is very close to the VBM (less than 0.05 eV). As empirically discovered by Katagiri in the early days [35], the best photovoltaic performance of CZTS is always achieved with a Zn-rich and Cu-poor absorber (Cu/(Zn+Sn) $\approx$ 0.8 and Zn/Sn $\approx$ 1.2). Under those conditions, the V_{Cu} defect is actually predicted to have even a lower formation energy than the Cu_{Zn} defect, therefore one can conclude that both may contribute to p-type doping in CZTS. On the other hand, all donor defects are predicted to have relatively high formation energies [84], so their contribution to n-type conductivity should be small. This can explain the common observation that CZTS is "naturally" a p-type material, regardless of preparation conditions. Dominant acceptor levels compatible with both the shallow V_{Cu} and the not-so-shallow Cu_{Zn} have been identified experimentally in CZTS [85].

Deep defects: recombination centers in CZTS

Unfortunately, shallow defects responsible for the natural p-type doping of CZTS are not the only ones. There are also some truly evil defects close to the middle of the band gap ("deep defects"). Why evil? Because the SRH recombination rate versus energy position of the recombination center has a maximum when the position is equal to the middle of the band gap [62]. Unless interface recombination is dominating, it makes sense to expect the main recombination path to be located in the depletion region of the absorber. That is because the recombination rate is maximized when the electron and hole population are equal [62]. Then, unless CZTS has very small band bending, there is a place somewhere in the depletion region where a crossover in the electron and hole population occurs [64]. What are the evil defects in CZTS and where are they located energetically? Even though it is very difficult to characterize deep defects experimentally, some defect-related signals have been detected by capacitance techniques. For CZTS(e) with a low S content, deep defects at around 0.5 eV [86] and around 0.8 eV above the VBM [67] have been found. For CZTS, a signal centered at 1.0 eV above the VBM has been found [87]. Identification of such signals with specific point defects is still very much a matter of taste. The matter is complicated by the fact that the formation energy of most defects depends strongly on the stoichiometry of CZTS [84]. Based on their predicted energy position and their predicted formation energy under Cu-poor, Zn-rich conditions, a selection of candidates could be V_S, Sn_{Zn}, Sn_{Cu} (isolated deep donor defects) and the ($2Cu_{Zn}+Sn_{Zn}$) cluster [88, 89].

Defect clusters: structural disorder

Cu and Zn are adjacent elements in the periodic table, meaning that they have similar size and mass. Therefore it is perhaps not surprising that they like to take each other's spot in a

crystal. In more scientific terms, CZTS is prone to disorder in the Cu/Zn cation sublattice, which means that the $(Cu_{Zn}+Zn_{Cu})$ defect cluster occurs with a very high density. This type of disorder was observed experimentally in the early days of CZTS research [20], then confirmed to have a very low formation energy by first-principles calculations [22], and it was finally discovered that the density of the $(Cu_{Zn}+Zn_{Cu})$ clusters could to some extent be controlled by the temperature and cooling rate of the CZTS annealing step [90].

Even if care is taken to prepare CZTS under conditions that maximize the order state of the material, i.e., minimize the density of $(Cu_{Zn}+Zn_{Cu})$ clusters, an unrealistically slow cooling step is needed to achieve anything better than 80% ordering (unless you are ok with waiting 30 years [91]). Hence, synthesized CZTS always features a certain amount of cation disorder in practice [92, 93]. Interestingly, the $(Cu_{Zn}+Zn_{Cu})$ clusters are predicted to lower the band gap of CZTS a bit, mostly by an upward shift of the VBM [84]. A completely disordered structure, corresponding to one $(Cu_{Zn}+Zn_{Cu})$ cluster per CZTS unit cell, is predicted to decrease the band gap by 0.24 eV [94]. This fits nicely with experiment, as the band gap of CZTS(e) was shown to decrease by 0.20 eV [95] when the order parameter of the materials decreased from a realistically achievable high-order state to a fully disordered state. Does structural disorder limit the efficiency, and not just the band gap, of a CZTS solar cell? When an order range between complete disorder and 80% order is explored, the answer is no. In fact, V_{oc} improves with ordering as a result of the higher band gap, but J_{sc} decreases (also as a result of the higher band gap), so in the end the efficiency remains basically the same [32]. The question is: what if someone could synthesize 100% ordered CZTS? Would the efficiency improve? I will propose an answer in Chapter 8.

Defect clusters: tail states

By comparison of optical measurements (reflection/transmission, ellipsometry, PL) and device quantum efficiency measurements, it is evident that CZTS(e) suffers from band tailing problems [96, 97], that is, there is a decay of the allowed states into the CZTS band gap instead of a sharp cut-off as in idealized semiconductors. It is widely accepted that this is due to band gap fluctuations or electrostatic potential fluctuations, or a combination of both. They are illustrated by the irregular band edges in Figure 1.5. If we take the offset between the optical band gap of the material (i.e. the gap between "extended states" in valence and conduction bands) and the position of the PL peak maximum at room temperature (i.e. the energy of the dominant recombination transition) as a rough estimate of the fluctuations' amplitude, then state-of-the-art CIGS, CZTSe, and CZTS feature fluctuations of the order of 0.02 eV [98], 0.02 eV [36], and 0.15 eV [43] respectively. Models exist that can relate the measurable characteristics of the tails to specific characteristics of either band gap fluctuations [98] or electrostatic potential fluctuations [99]. Both models have been checked against experimental data and they have both been found to be compatible, [96]. Therefore, identification of one of the two fluctuation mechanisms as dominant is mostly a matter of taste.

The "American school" [96] provides some indirect evidence in favor of electrostatic potential fluctuations based on the temperature dependence of time-resolved PL. The much slower decay of the CZTS(e) PL signal at low temperature with respect to room temperature is interpreted as the result of spatial separation of the local maxima (minima) of the valence (conduction) band in the material, which is compatible with electrostatic potential fluctuations but not with band gap fluctuations. In general, electrostatic potential fluctuations can be due to the spatial charge distribution caused by charge-compensated defects clusters (see previous section). They can be mitigated by a high relative permittivity and a high free carrier concentration, both of which increase the screening capability of the material [99].

On the other hand, the "European school" [32] leans toward band gap fluctuations, as electrostatic potential fluctuations are often quenched at room temperature in other materials (notably CIGS [100]) due to the large amount of free carriers available to screen the fluctuations. Band gap fluctuations could be caused by a number of mechanisms, all suspected to occur in CZTS: (i) secondary phase inclusions - binaries, ternaries as well as stannite CZTS all have different band gaps; (ii) spatial non-uniformity in the order parameter; (ii) again, defect clusters, as some of them are expected to change the band gap of CZTS significantly [84]. We have seen that the ($Cu_{Zn}+Zn_{Cu}$) cluster, at the origin of structural disorder, can decrease the band gap and could therefore be an option. However, the energy distance between the PL peak and the band gap of the extended states remains pretty much constant upon the band gap changes induced by different ordering degrees [95, 101], so it appears as if the reason for band tailing must be found elsewhere, if the band gap fluctuation model is correct. A candidate defect cluster in ($2Cu_{Zn}+Sn_{Zn}$), because it has a low formation energy and it narrows the band gap of CZTS significantly even with a small defect density [84]. Note, then, that such a defect cluster would most likely result in *both* band gap and electrostatic potential fluctuations, so I actually believe that both schools of thought presented above can be correct.

The device-level effect of fluctuations (of any kind) on device performance is a decrease in the transport band gap, roughly corresponding to the magnitude of band tailing [97, 102, 103]. Therefore, the open circuit voltage is expected to decrease (with respect to a fluctuation-free material) by an amount roughly equal to the fluctuations amplitude. The corresponding gain in short circuit current due to increased absorption below the band gap of the extended states is expected to be minimal, because the corresponding unlucky electron-hole pairs find themselves trapped in the potential wells of those tail states, where they can only rely on thermal energy to escape. Therefore, fluctuations can in principle limit the open circuit voltage (and the efficiency) of the solar cell by decreasing E_A, as demonstrated by device simulation [102]. Indeed, a correlation has been found by several studies between the depth of tail states and the open circuit voltage of CZTS(e) solar cells [67, 87]. A correlation has also been found between the estimated density of defect clusters and both the open circuit voltage and fill factor [104]. The question is whether such fluctuations are a limiting factor in the current state-of-the-art solar cells. I will give my opinion on this in Chapter 8.

1.4.3   Why three n-type layers?

In the early months of my PhD project, I would play with solar cell simulation tools [105], remove CdS and ZnO from the standard architecture, and inevitably see the simulated efficiency go up. What the heck? This issue has bothered me a lot throughout my PhD project. I have to admit I am still not entirely sure of the answer to this section's title now (three years later), but I think I have made some progress.

ZnO:Al

At a first glance, it appears as if the ZnO:Al layer is the only one that is *really* necessary. Such a layer is equivalent to the "emitter" in Si homojunction solar cells, that is, the thin and highly doped top layer that allows p-n junction formation and lateral carrier transport to the contact grid [64]. The fact that the Fermi level in ZnO:Al, or in any good transparent conductive material, is *above* the conduction band maximum (Figure 1.5) is beneficial for the device because it maximizes the built-in potential of the junction, which has a beneficial effect on the open circuit voltage in the case of depletion region recombination (Equation 1.13).

CdS

What is then the role of the CdS "buffer layer"? Before trying to answer this question, let me point out that, if you try to skip the buffer layer altogether, your CZTS solar cell will most likely not be very good. As a matter of fact, introduction of a CdS buffer layer grown by chemical bath deposition was a key milestone in the development of CIGS solar cells in the second half of the 1980s [53]. CdS is a direct wide-band gap (2.4-2.6 eV) semiconductor of "natural" n-type doping, i.e. doped n-type as a result of its intrinsic defect chemistry. Its doping density depends on deposition conditions, on presence or absence of illumination (more on this below), and is in general rather low [106, 107]. As mentioned above, the choice of CdS as a buffer layer in CZTS solar cells is basically due to its success in CIGS solar cells. Therefore, many of the explanations I have found for its beneficial role are related to CIGS solar cells. Popular explanations are:

- shunt protection. If there is a rough defect in the absorber layer (pinhole or similar), the (not too conductive) CdS barrier avoids direct contact between the Mo back contact and the ZnO:Al transparent conductor [108] which would otherwise decrease the shunt resistance of the solar cell and the fill factor.

- sputter damage protection. The standard technique for depositing ZnO and ZnO:Al is sputtering, which is a rather brutal method involving bombardment of the growing film with a variety of high-energy species, in particular negative oxygen ions and derivatives thereof (Study 5.1 and [109]). Such a high-energy bombardment is detrimental for the absorber surface, as clearly demonstrated in [110]. A buffer layer of at least 10 nm in thickness must then be deposited by a "soft" deposition technique that does not bombard the absorber surface with energetic species [110] and allows complete coverage already at a small film thickness. Keeping the thickness reasonably small is important in order to limit parasitic light absorption, series resistance losses, and negative effects on the electrostatics of the junction. Appropriate techniques can be atomic layer deposition and solution-based methods. Within the latter class, chemical bath deposition [111] is the most popular.

- diffusion barrier. Inclusion of a CdS layer has been shown to suppress diffusion of Al (or any element used as a ZnO dopant) from ZnO:Al into the absorber [112]. It is, however, unclear whether presence of Al in CZTS near the heterojunction is detrimental for solar cell performance.

- formation of a heterointerface of a high crystallographic quality with the absorber. This can decrease the interface recombination velocity (S_p and S_n in Equation 1.14) due to fewer defect states in the band gap at the interface. Even though there can be many factors determining the defect density of an interface, close lattice matching between the interface materials is expected to greatly reduce the defect density, as demonstrated by the successful history of lattice-matched III-V semiconductor heterostructures. ZnO has a very large lattice mismatch with CIGS. However, the lattice mismatch between CdS and CIGS (with the optimal Ga/(In+Ga)=0.3) is 1.5%, which is reasonably low and allows formation of an epitaxial interface [113,114]. A fact that is not often addressed in the literature is that the CdS/CZTSe lattice mismatch is larger (2.4%), and it becomes even larger in the CdS/CZTS system (7.0%). More on this issue later in this section.

- formation of a wide enough depletion region to minimize tunneling-enhanced recombination. The absence or insufficient thickness of a CdS buffer layer was correlated with the occurrence of a lower breakdown voltage under reverse bias in CIGS solar cells [115]. Because reverse breakdown is associated with tunneling [52], it is likely

that a sufficiently thick CdS buffer layer reduces tunneling-enhanced recombination on the n-side on the junction (Figure 1.5). This probably occurs because the presence of a lightly doped CdS layer widens the depletion region on the n-side of the junction, so that band bending occurs less abruptly and the tunneling probability decreases.

- optical gain in the device. If a buffer layer with intermediate refractive index is added between ZnO and the absorber, the fraction of light that is reflected before reaching the absorber decreases. This is an effect that can overcompensate the loss in short circuit current due to parasitic light absorption in the buffer, even in a not-too-high band gap material like CdS, as long as the buffer thickness does not exceed 40 nm [116]. An analogous effect is expected in CZTS solar cells, as the refractive indexes of CIGS and CZTS are rather similar [54, 117]

- achievement of an optimal conduction band alignment at the heterointerface. It is well known [53,118] that the efficiency of heterojunction solar cells is maximized when the conduction band maximum (CBM) of the absorber lies about 0-0.4 eV below the CBM of its heterojunction partner at the interface (spike-like band alignment). While CdS appears to have an optimal band alignment with CIGS [119], it is widely believed that this is not true for CZTS. I don't necessarily agree with this, and I will tackle this issue in detail in Study 4.1.

- when CdS is deposited by chemical bath deposition, there are some beneficial side effects of the solution that is typically used to deposit CdS on CIGS absorbers. The solution will: (i) remove the native oxide layer from the CIGS surface, and (ii) remove elemental Se from the CIGS surface [120]. Mechanism (i) was demonstrated to be active also in CZTS(e) with a low S content, due to the tendency of ammonium hydroxide (present in the solution) to etch metal oxides [121]. Because elemental Se can also be present at the CZTSe surface [122], it is likely that mechanism (ii) is also valid for chemical bath deposition of CdS on CZTSe. However, I do not know of any study showing sulfur removal from CZTS due to the chemical bath.

- It has also been proposed that Cd diffusion into the absorber can lead to n-type doping of the absorber close to the interface due to the Cd_{Cu} antisite defect of donor character [123]. This would lead to formation of a "buried" p-n homojunction in the CIGS bulk, close to the heterointerface. However, it was proven that this would lead to poor collection efficiency in the low wavelength region of the spectrum [124], which is not compatible with the high EQE observed in CIGS solar cells in that spectral region. As a result, now many experts in the field reject the buried homojunction model [125]. Even though the matter has not been specifically investigated on kesterites, I find it very unlikely that a buried homojunction exists in CZTS because it is challenging to dope CZTS n-type (Sections 1.5 and 1.6).

ZnO

The ZnO layer, which is often referred to as "undoped" or "intrinsic", can actually be produced with a wide range of "natural" (n-type) doping densities due to its (not really understood, as far as I can read) defect chemistry [126]. Actual doping can be anywhere between a too low value to be measured and as high as above 10^{20} dopants/cm^{-3} [127]. The conductivity of the latter not-so-intrinsic ZnO can be so good to allow replacement of ZnO:Al with simply ZnO as a lateral transport layer in CIGS solar cells [127]. What is then the role of the (nominally undoped) ZnO layer? Like for CdS, inclusion of this layer is basically as a result of copying and pasting the standard CIGS solar cell architecture

onto CZTS, so most of the studies have been performed on CIGS solar cells. I have found the following explanations:

- jointly with CdS, shunt protection. While in principle a single shunt barrier should be sufficient, inclusion of the ZnO layer has been shown by several authors to improve reproducibility of solar cell performance over a fabrication batch [108, 128]. This is possibly a reason why academic researchers often report that the ZnO layer can be omitted, whereas industrial researchers insist on its inclusion [41, 56].

- growth initiation of ZnO:Al. There are some hints that growing ZnO:Al on undoped ZnO may improve its electrical properties [129, 130]. This is because growth of ZnO:Al on a foreign substrate often results in an Al-enriched seed layer at the initial stages of the deposition, which includes Al-based secondary phases that deteriorate the electrical properties of the film [131]. While this can be an important factor in pushing the electrical performance of ZnO:Al to its theoretical limit, I am not aware of any study proving that the ZnO:Al resistivity in solar cells can be reduced when it is deposited on top of ZnO.

1.4.4 Na incorporation, grain boundaries, and surfaces

Under somewhat legendary circumstances, it was discovered in the early 1990s that CIGS solar cells performed better when deposited on soda lime glass (SLG) rather than any other kind of glass [132]. This was found to be related to Na diffusion from the glass, through the Mo back contact, and into the absorber. Still today, the highest efficiency CIGS and CZTS(e) solar cells are either deposited on SLG or they have Na incorporation from a thin Na-containing layer (usually NaF [133]), which is typically deposited between the back contact and the absorber. The main solar cell parameter to be positively affected by Na diffusion is the open circuit voltage. Despite the rather high maturity level of CIGS technology, it is not clear yet what mechanism lies behind the V_{oc} boost. Rather than Na incorporation in the CIGS bulk, Na segregation at grain boundaries and/or at the heterointerface seems to be responsible [53, 125]. A quite comprehensive model based on experimental findings was developed for Na-related effects in CZTS [133], according to which small amounts of Na quench non-radiative recombination processes at grain boundaries. This is likely to be a crucial mechanism in the open circuit voltage improvement. Note that formation of SnO_x at grain boundaries after air annealing of CTZS has also been observed to have a positive impact in grain boundary passivation [121]. Larger amounts of Na lead to a significant increase in the CZTS grain size, combined with increased Zn segregation at the heterojunction and at the back contact. However, it is unclear whether very large grains are really needed for good solar cell performance, as long as the grain boundaries are effectively passivated by Na/SnO_x. In fact, very high efficiencies can be achieved in CIGS solar cells with relatively small grains [134]. I need to emphasize that the electrical behavior of CZTS(e) grain boundaries and bare surfaces is very controversial. At CZTS(e) grain boundaries, the bands have been observed to be bent upwards in some studies [121] and downwards in other studies [135, 136], all resulting in devices with reasonable efficiency. One the other hand, the bands of bare CZTS(e) surfaces have only been found to be bent upwards [137, 138]. For p-type materials, upward band bending can be labeled as "accumulation" (more majority carriers than in the bulk) and downward band bending can be labeled as "depletion" (fewer majority carriers than in the bulk). The only two theoretical studies I am aware of are also somewhat contradictory: one concludes that unpassivated CZTSe grain boundaries must feature a high density of defect states within the band gap [139]; the other concludes that unpassivated CZTS bare surfaces favor formation of Cu-poor point defects (such as V_{Cu}), which neutralize surfaces that would otherwise be polar, and do *not* result in detrimental gap states [140]. Study 4.3 is a new

addition to the field, which may help resolve some of the existing contradiction. Perhaps the only matter on which most studies actually agree on is that CZTS(e) surfaces are even more Cu-poor than the CZTS(e) bulk [121, 137, 141]. I believe that surfaces and grain boundaries are of paramount importance in CZTS(e) solar cells: it was demonstrated that the efficiency of CZTS(e) solar cells could be reversibly switched from 11% to 0.1% just by cyclically oxidizing and etching CZTS(e) surfaces and grain boundaries [121].

1.4.5 Back contact chemistry and physics

In Figure 1.4 a layer that is always present in the solar cell stack is actually omitted from the drawing. Such a layer is MoS_2, which inevitably forms between Mo and CZTS when CZTS is annealed. Obviously, for MoS_2 to form, Mo needs to react with S. This can occur through the CZTS-back contact decomposition reactions summarized in [142, 143] and/or through the gaseous S that is always supplied in a CZTS annealing process. Typical annealing processes are designed to ensure a high S partial pressure in order to (i) prevent the CZTS *surface* decomposition reaction [144] which involves SnS evaporation, and to (ii) compensate the CZTS-back contact decomposition reaction through a supply of S, so that MoS_2 is supposedly formed without CZTS decomposition [44]. Insufficient S partial pressure has disastrous consequences on solar cell efficiency, and it was possible to relate part of the disaster to the CZTS-back contact decomposition reaction [44]. It is not well understood (at least by me) whether suppression of the CZTS-back contact decomposition reaction is properly taken care of by the current state-of-the-art annealing processes. Certainly, some of the binary chalcogenides expected from the back contact decomposition reaction are found even in the best CZTS devices [43, 44] Unfortunately, it seems as if the detrimental effects of the CZTS-back contact decomposition reaction are invisible to standard characterization techniques [44], as many other unfavorable properties of CZTS are. In any case, the nature of the back contact is a major difference between CIGS and CZTS solar cells. In the former, Mo is advantageous because it does not react with CIGS [145], but this is certainly not the case in CZTS solar cells. As reviewed very recently, several attempts have been made to prevent the CZTS-back contact decomposition reaction by introduction of a thin barrier layer (TiN is the most popular), but in practice the highest efficiency solar cells remain the ones without any interlayers [17, 42–44]. Besides purely chemical issues, formation of MoS_2, even without any decomposition reaction of CZTS, adds a new material to the band diagram of a CZTS solar cell. The main problem that may occur is a non-ohmic contact featuring a hole barrier (i.e., downward band bending, Figure 1.5), which would partially block hole transport to the back contact. This seems indeed to be the case for the $Mo/MoS_2/CZTS$ system, mostly based on results from suns-V_{oc} measurements [146, 147]. This is a difference with both pure-selenide CIGS and CZTSe, where $MoSe_2$ does not prevent a quasi-ohmic back contact, and may even aid its formation [146, 148]. A small back contact barrier of 0.13 eV has been explicitly measured [149] for the $Mo/MoSe_2/CZTSe$ system, which should not deteriorate device performance significantly according to device simulation [53]. Regarding the $Mo/MoS_2/CZTS$ system, I am not aware of any study showing whether the reason for an increased back contact barrier is a non-ohmic MoS_2/Mo contact or a non-ohmic CZTS-MoS_2 contact. Since pure-sulfide CIGS solar cells have reached relatively high fill factors of 72-74% [150], I would not expect a large barrier in the MoS_2/Mo contact. Instead, I hypothesize that downward band bending at the CZTS-MoS_2 interface may exist simply because of a higher work function in CZTS than in CZTSe. Even though I am not aware of work function measurements on neither pure CZTS nor pure CZTSe, kelvin probe microscopy measurements have revealed that increasing the S content in CZTSSe increases its work function [151]. The difference in work function between CZTS and CZTSe can be estimated as the difference in CBM position with respect to a common reference minus the difference in the distance

between the CBM and the Fermi level. Taking the former to be 0.07 eV and the latter to be 0.3 eV based on photoemission spectroscopy results [69], CZTS is predicted to have a work function that is about 0.2 eV higher than CZTSe. To a first approximation, this should result in a back contact barrier that is 0.2 eV larger in CZTS than in CZTSe, which may contribute to the series resistance losses in CZTS. Finally, Zn segregation at the back contact (and, as a matter of fact, at the heterointerface) may increase the series resistance of the device through scattered formation of the ZnS high-band gap phase, which locally blocks carrier transport due to its large band offsets with CZTS, resulting in an energy barrier for both electrons and holes [79].

1.4.6 Light-dark JV curve crossover

In solar cell textbooks and in Section 1.3, you learn that a solar cell under illumination is basically the same thing as a solar cell in the dark [3, 64] because the only term you have to add to the diode equation when you turn the light on is the photocurrent, which is constant with voltage (Equation 1.4). Then, in principle, the JV curves of the solar cell in the dark and under illumination should never cross. However, they certainly do cross in nearly all CZTS solar cells with a CdS buffer layer, often already at a voltage just slightly larger than the open circuit voltage (Study 2.1, [43]). By splitting the currents into a constant photocurrent and a voltage-dependent recombination current of opposite sign, as illustrated in Section 1.3, the reason behind light-dark JV crossover is then that a larger recombination current exists under illumination than in the dark. Why does this happen? Based on several studies on CIGS solar cells, the most likely model involves the different occupation probability - in the dark and under illumination - of acceptor defects in the CdS bulk that compensate the dominant n-type doping. Such defects are mostly occupied by electrons in the dark because the Fermi level of CdS is above mid gap (n-type material), hence they compensate the dominant n-type (donor) doping in CdS. However, under illumination with photon energy larger than the band gap of CdS, the acceptors may become mostly unoccupied due to the excess photogenerated holes, which are captured by the negatively charged defect and neutralize its charge [152]. This means that the net charge on the n-side of the junction becomes more positive with illumination due to the decreasing contribution from ionized acceptors. As illustrated in [153], this decreases the barrier of the recombination current, i.e., the barrier in quasi-Fermi level that electrons on the n-side of the junction have to overcome to reach the absorber. Therefore, the onset of the recombination current occurs at a lower voltage under illumination. The thicker the CdS layer, the more total positive charge exists, and the larger the difference in the electron barrier between dark and illuminated conditions. Hence, it should be no surprise that devices with a thicker buffer layer have a more pronounced cross over effect. Is the cross over effect unique to CdS buffer layers? No. It depends on the density of (compensating) p-type acceptor defects in the (predominantly n-type) buffer layer material. Different materials have different tendencies to form compensating acceptors [154]. For example, in ZnO it is extremely energetically unfavorable to form compensating acceptors (incidentally, this is why ZnO can be doped so heavily n-type and can be an excellent transparent conductor). As a consequence, CZTS solar cells with a ZnO buffer layer exhibit almost no cross-over effect, whereas, for example, crossover is observed with a Zn(O,S) buffer layer [155].

1.4.7 Heterointerface band alignment

This is a popular topic, and for good reasons. In any heterojunction solar cell where the heterojunction partner of the absorber has a wider band gap than the absorber itself, the conduction band alignment between the two can have a significant impact on the

performance of the solar cell. A significant fraction of the electron photocurrent is blocked if the CBM of the buffer lies more than about 0.4 eV higher than the CBM of CZTS of the interface (large spike-like CBO, Figure 1.5) due to the large electron barrier. The result is first a fill factor loss when the spike is not large enough to block the current under short-circuit conditions but it is large enough to block it at a certain forward bias. As the spike increases, the current is blocked regardless of the applied bias, leading to complete suppression of the photovoltaic effect [118, 156].

What happens with a cliff-like CBO, i.e., when the CBM of the buffer layer lies at a lower energy than the CBM of CZTS at the heterointerface, depends on the how bad the interface is. "Bad" means "with a high interface recombination velocity" (large S_p and S_n parameters). That velocity depends on the properties of the recombination centers present at the interface due to perturbation in the band structure of the two bulk materials caused by interface formation. If there are many such centers within the band gap, and if carriers are easily captured by them, the recombination velocity is high and the interface is bad. In any case, a cliff-like CBO is a dangerous thing because it opens up a new recombination path with a lower activation energy than the bulk regardless of how good the interface is. This path involves electrons on the CdS side of the junction recombining with holes on the CZTS side of the junction. Will that lower E_A and the open circuit voltage? Yes, but only if the interface recombination velocity is high enough to make interface recombination the dominant recombination path. The lower the recombination velocity, the more a cliff-like CBO can be tolerated. For a fixed CBO, the open circuit voltage will decrease with increasing interface recombination velocity. All this can be easily demonstrated by device simulation [156]. Of course, it is very likely that interface recombination velocities are high enough in CZTS solar cells, where no particular care is taken to grow interfaces with low defect densities so I do not doubt that a cliff-like CBO is detrimental. However, it should be kept in mind that, even if an optimal CBO is achieved, this does not guarantee that interface recombination becomes negligible in the solar cell. Interface recombination can still be dominant if the interface is really bad (high recombination velocities). I emphasize this as I suspect that interface quality may play an important role in CZTS solar cells. I show the reasons why in the next section.

CZTS is often believed to have an unfavorable cliff-like band alignment with CdS, which would explain why the measured values of E_A in CZTS solar cells are always significantly lower than the absorber's band gap. While I do believe that many lower-performance CZTS solar cells are negatively affected by a cliff-like CBO, I strongly doubt that a cliff-like CBO exists in state-of-the-art CZTS solar cells. Justification of this view is the topic of Study 4.1.

Finally, it is not clear in the literature whether the band structure of CZTS experiences some significant changes near the heterointerface. Just like a cliff-like band alignment decreases the energy distance for recombination at the interface, thus a potentially lower E_A, the same may occur through band gap narrowing on the CZTS side through an upshift of its valence band near the interface. Even though this hypothesis has not been investigated yet in the CZTS community, in Study 4.3 I will provide some evidence that CZTS band gap narrowing at the interface has some theoretical foundations.

1.4.8 Heterointerface quality

Following the discussion of the previous section, the quantitative equivalent of "heterointerface quality" is the value of the recombination velocities S_p and S_n at the interface between CZTS and the buffer layer. The lower the value, the better the interface. As discussed above, interface quality can indeed influence the efficiency of the solar cell, even though its influence can to a significant extent be "turned off" by an optimal CBO. This is a point where the literature is, in my opinion, surprisingly silent. This is unfortunate, as

I believe there are some clues in the literature that point to the importance of obtaining a decent quality interface. Here I provide examples:

1. To my knowledge, there are only two groups [81, 157] that have demonstrated epitaxial CZTS/CdS interfaces. Interestingly, those groups are the ones who have produced the highest-efficiency CTZS/CdS solar cells reported so far [17, 157]. One of the groups also achieved the highest value of E_A (1.18 eV) ever reported in a CZTS solar cell with a CdS buffer layer [17]. From decades of experience with heterojunction devices based on III-V semiconductors, it is well known that epitaxial interfaces have lower defect densities and thus lead to lower interface recombination velocities.

2. There is a study [15] that compares the performance of CZTS solar cells with a Zn(O,S) buffer layer and with a $(Zn,Sn)O_x$ buffer layer. The CBM position of those two materials can be controlled by the degree of alloying for Zn(O,S) [155] and by the deposition temperature for $(Zn,Sn)O_x$ [158]. Therefore, an optimal CBO with CZTS can be reached merely by empirical optimization, as shown in [158]. Nevertheless, the result of the buffer comparison study was that solar cells with a Zn(O,S) buffer layer yielded a lower E_A and a lower open circuit voltage than solar cells with a $(Zn,Sn)O_x$ buffer layer. Extensive experience of that research team with both materials makes it very unlikely to attribute such an outcome to a less-than-optimal CBO in one of the two materials, as pointed out by the authors themselves.

3. The lattice mismatch of CdS with CIGS (with the optimal Ga/(In+Ga)=0.3) is 1.5%, and it increases to 2.4% with CZTSe, and to 7.0% with CZTS. Intuitively, it is then very likely that an epitaxial interface is easier to achieve with CIGS than CZTS. In fact, pseudo-epitaxial growth is observed for CdS on CIGS without any post-annealing treatment [113, 114]. Conversely, epitaxy of CdS on CZTS has only been demonstrated with annealing temperatures above 200°C [81] and/or with significant Cd diffusion into CZTS [157], which is expected to expand its lattice constant and thus reduce the lattice mismatch with CdS [159].

For these reasons, I believe that the role of the buffer layer as an "interface passivation" layer is more important than what is normally stated in the literature, which focuses almost exclusively on the band alignment issue. In this respect, a CdS buffer layer may not be as effective in CZTS solar cells as it is in CIGS solar cell because it is more difficult to obtain a high-quality (psudo-epitaxial) interface with CZTS due to the larger lattice mismatch. Study 3.1 supports this statement, as the introduction of a thin lattice-matched CeO_2 passivation layer between CZTS and CdS improved the open circuit voltage in a reproducible manner. Study 4.3 also supports the importance of interface passivation, albeit from another perspective.

One fair question to ask when talking about passivation is whether the CZTS interface with the buffer layer can be considered an "ideal" abrupt interface without any intermediate layer. If by "intermediate layer" a native CZTS oxide is intended, then I believe the answer is yes. That is because, even though CZTS is often re-annealed in air after post-deposition annealing in sulfur, the ammonium hydroxide species usually present in the CdS deposition solution etch metal oxides, as mentioned earlier in this section. Therefore, while grain boundaries can be regarded as oxidized after air annealing, the heterointerface is probably not. However, if by "intermediate layer" a graded junction is intended, then I believe the answer is no. By graded junction, I simply mean an interface region where some constituents of CZTS and CdS interdiffuse, thereby forming an interface phase with a continuous gradient in the content of its constituents, especially Cd and Zn. More on interdiffusion and its consequences in Study 4.1. For now, I just want to emphasize that,

in my opinion, it is very likely that Cd and Zn interdiffusion is an absolute requirement for achieving an epitaxial CZTS/CdS interface despite the very large lattice mismatch. In fact, Cd substitution in CZTS and Zn substitution in CdS tend to increase the lattice constant of CZTS and decrease the lattice constant of CdS respectively, thus resulting in an "engineered lattice matching" of the two materials.

1.4.9 Adhesion

Adhesion problems of CZTS on MoS_2 are well known from informal communication channels and are sometimes reported *en passant* in the literature [146, 160]. It seems as if the most important parameter that determines the adhesion properties is the preferential c-axis orientation of MoS_2 with respect to the substrate plane. MoS_2 oriented with the c-axis perpendicular to the substrate has lubricating properties [161], which is clearly not very good for adhesion of CZTS. A different preferential c-axis orientation is therefore highly desirable. It has been reported that c-axis orientation parallel to the substrate plane increases with increasing porosity of the underlying Mo layer, which in turn can be achieved by a higher sputtering pressure in the Mo deposition process [162]. Note that adhesion problems are more rarely reported for the selenide materials $CZTSe/MoSe_2$ and, when both CZTS and CZTSe were investigated in the same study, the thickness of CZTS had to be limited to 900 nm to avoid adhesion problems, whereas no thickness limitations were reported for CZTSe [146]. Even though the reason is unclear, I suspect there are some differences between MoS_2 and $MoSe_2$ in terms of preferential orientation of their c-axis, which may also depend on the details of the CZTS(e)-back contact decomposition reaction [143]. However, I am not aware of any published explanation of the issue and I do not have a better explanation myself. From personal experience, it seems as if the adhesion properties of CZTS on Mo are significantly worsened by increasing the CZTS thickness (as noted in [146]) and by a large CZTS grain size (say more than 500 nm).

1.5 Main differences between CIGS and CZTS(e) that affect solar cell performance

Now that I have given an overview of the main non-idealities that exist in CZTS solar cells, I would like to be more practical now and ask: which of those non-idealities are the main loss mechanims in CZTS solar cells? To try and answer that question, I think it is a good idea to start by listing all important differences in the materials- and device properties between CZTS(e) and CIGS solar cells. Here, by CZTS(e) solar cells I mean the *best* CZTS(e) solar cells, that is, those with a low S content. This is a popular topic for very good reasons and a number of excellent review articles focus on many aspects of the subject [30, 163, 164], even though they are already getting old, as new things have been discovered in the meantime. Some trends presented in this section have already explicitly pointed out by others. Other trends are the result of my analysis.

1.5.1 Compound formation and phase purity

- CIGS is not subject to decomposition reactions at the surface or at the back contact. Conversely, CZTS(e) is subject to (i) decomposition into binary chalcogenides and loss of SnS at the surface due to the volatility of SnS [144], and (ii) decomposition into binary chalcogenides by reacting with the Mo back contact [143].

- CIGS has a wider single-phase region in chemical potential space than CTZS(e). In fact, CIGS can tolerate about 4% (absolute) deviations in stoichiometry, whereas CZTS(e) can only tolerate about 2% (absolute) deviations without precipitating

secondary phases [74]. The least dangerous secondary phase that can be formed is ZnS(e), which is part of the reason why Zn-rich Cu-poor growth conditions are necessary for high-efficiency CZTS(e).

- CZTS(e) can exist in two phases, kesterite and stannite, with very similar formation energies, kesterite being slightly favored [21]. Because the stannite phase has a narrower band gap by about 0.1 eV, it can trap carriers and reduce the effective recombination gap in the CZTS(e) bulk. Conversely, stoichiometric CIGS exists in the chalcopyrite structure with no competing CIGS phases.

1.5.2 Bulk properties

- in CIGS, the dangerous deep donor defect In_{Cu} is removed from the band gap when it is compensated by the V_{Cu} acceptor defect to form the $(2V_{Cu}+In_{Cu})$ cluster. The compensation process is very likely to occur, as the formation energy of the defect cluster is significantly lower than the formation energy of the isolated In_{Cu} defect. This is a beneficial mechanism that, however, does not seem to occur with the dangerous CZTS(e) defects when they form defect clusters [84].

- minority carrier lifetimes are, in general, measured to be shorter in CZTS(e) than in CIGS. Comparing different sources, I would settle on about one order of magnitude shorter [30, 45, 164]. This indicates that the SRH recombination rate is probably higher in CZTS(e) than in CIGS, according to Equations 1.12, 1.13.

- CZTS(e) has always some degree of structural disorder from Cu/Zn mixing, related to the low formation energy of the $(Cu_{Zn}+Zn_{Cu})$ defect cluster (see Section 1.4). There is no equivalent mechanism in CIGS.

- the very shallow V_{Cu} defect is very abundant in CIGS and is the main source of p-type conductivity in the material. V_{Cu} also exists in CZTS(e). However, the Cu_{Zn} acceptor, not as shallow as V_{Cu}, is also expected to play an important role as it has a lower formation energy than V_{Cu} in stoichiometric CZTS. Under the typical Zn-rich Cu-poor growth conditions, V_{Cu} should become more abundant but, in any case, a dominant defect level compatible with Cu_{Zn} is often found experimentally [85].

- The relative permittivity of CZTS(e) is lower than that of CIGS (8-9 versus 12-14), at least according to the few available reports [85, 165]. Negative effects of a lower absorber permittivity can be: (i) smaller depletion region width in the absorber; (ii) increase of the electric field in the depletion region, which can promote tunneling-enhanced recombination; (iii) decreasing of the screening capability of the absorber against electrostatic potential fluctuations due to charge-compensated defect clusters [96]. A positive effect can be the increase of the potential drop in the CZTS depletion region compared to the potential drop in the CdS depletion region, as explained in greater detail in Study 4.4 and as shown in the regions of band bending in Figure 1.5.

1.5.3 Surfaces and grain boundaries

- There is strong evidence that a Cu-poor ordered vacancy compound (OVC) forms spontaneously at CIGS surfaces [125, 164]. A first feature of the OVC is band gap broadening by means of a valence band downshift on the CIGS side of the heterointerface, which can be detected by photoemission measurements [166] and also predicted by first principles [167]. This decreases the hole population at the interface. A second feature of the OVC is that its defect chemistry seems to make it less p-type than CIGS, or even n-type. This increases band bending and the electron

population at the interface. The combined effect of the two OVC features is a decrease in the SRH interface recombination rate because, at the heterointerface, the electron population is much larger than the hole population ("type inversion").

CZTS(e) surfaces have also been found to be Cu-poor, after removal of the native oxide [137, 141]. However, the consequences of a Cu-poor surface do not seem to be as favorable as in CIGS. First of all, there is no evidence yet for formation of a wider band-gap surface phase with a down-shifted VBM. On the contrary, it seems as if the surface band gap of CZTS is similar to its bulk band gap [168, 169]. I don't know of any similar study on CZTSe. Secondly, it seems as if the defect chemistry of CZTS(e) Cu-poor surfaces favors an increase in p-type conductivity at the surface instead of a natural inversion to n-type as in CIGS. In other words, CZTS(e) surfaces are in accumulation, whereas CIGS surfaces are in inversion. Accumulation was observed experimentally in a few different studies, both by photoemission and by STM [121, 137, 138]. The STM-based study [138] found surface accumulation for CZTS(e) and surface inversion for CIGS within the same experiment. Surface accumulation is compatible with theory, as Cu-poor CZTS is predicted to become more p-type [84]. However, I have not yet found any convincing physical explanation of the different behavior of CIGS and CZTS(e).

- There is an interesting difference in the crystal structures of CIGS and CZTS(e). The (001) direction in CIGS features only two types of atomic planes: cationic planes containing Cu-In-Ga and anionic planes containing Se. The same direction in CZTS(e) features three types of atomic planes: cationic planes containing Cu-Zn, cationic planes containing Cu-Sn, and anionic planes containing S(e). Since Zn and Sn have different oxidation states, the two cationic planes can be labeled as "heterovalent" [170]. Similarly, in the (110) direction, CZTS(e) has two heterovalent atomic planes, whereas CIGS has just one type of atomic plane. This implies that in CZTS(e) there are more surface orientations that are of polar character than in CIGS. Therefore, CZTS(e) may have more complex surface reconstruction phenomena through defects to avoid polar surfaces [140, 171]. Another consequence is that, at the very particular "surface" found at the heterointerface with the buffer layer, there is a higher chance of obtaining an electric dipole. This would imply that the band alignment of CZTS(e) with other materials may be different than expected, as interface dipoles at polarized interfaces would shift the "natural" band alignment that can be calculated from theory based on bulk material properties [172]. This is explained more in detail in Study 4.1. For completeness, notice that in the common growth direction (112) for CIGS and CZTS(e) thin films [36], there are no heterovalent cationic planes in either CIGS and CZTS(e) so (112) surfaces may have a similar qualitative behavior in the two materials.

- While grain boundaries in CIGS are consistently found to be depleted (downward band bending), both depletion and accumulation have been measured at CZTS(e) grain boundaries [121, 135, 136]. This hints to the fact that grain boundary passivation is more difficult and probably not optimal in the current generation of devices.

1.5.4 Compatibility with standard device structure

- It seems to me as if the standard CIGS device structure fits CZTS(e) well. Indeed, CZTS(e) has proven to be compatible with the other layers in the device in a number of ways. First, the back contact is found to be reasonably ohmic [149], with only a small barrier that should not be detrimental for performance. Second, the CBO with CdS is consistently reported to be optimal (see Study 4.1). Third, the doping densities of CZTS(e) and CIGS appear to be similar [18] so the n-type side of the

junction optimized for CIGS should also fit a CZTS(e) absorber. Fourth, lattice-matching with CdS is still reasonable, even though it is not as good as for CIGS. Fifth, E_A in good CZTSe solar cells is roughly equal to the band gap [79], indicating that no band gap narrowing occurs at interfaces.

1.6 Main differences between CZTSe and CZTS that affect solar cell performance

Unfortunately, I do not know of any single paper that comprehensively reviews the differences between the selenide and sulfide kesterite materials. There is, however, a very nice work comparing defects in CZTS and CZTSe directly [84]. Again, some information contained here has already been presented explicitly by others, whereas other points are the result of my analysis.

1.6.1 Bulk properties

- CZTS has deeper tail states than CZTSe. This is clear from the larger mismatch between the band gap of the extended states (extracted from the EQE) and the recombination band gap (extracted by the steady-state PL peak position). In good CZTS solar cells, the mismatch is always around 0.15-0.20 eV. In good CZTSe solar cells, the mismatch can be very low: 0.02 eV is the lowest I have seen [36]. When the depth of tailing is formally quantified by the Urbach energy parameter, a linear trend with increasing S content can be seen [67, 87].

- The formation energy of the dangerous defect cluster ($2Cu_{Zn}+Sn_{Zn}$) is predicted to be lower in CZTS than in CZTSe. Such a defect cluster can narrow the CZTS(e) band gap dramatically, even when present in relatively small amounts. The narrowing effect is more pronounced in CZTS than in CZTSe at constant density of ($2Cu_{Zn}+Sn_{Zn}$) clusters [84].

- in CZTS, a lower formation energy is expected for the dangerous deep (isolated) defects Sn_{Zn} and $V_{S(e)}$ [84].

- The antisite defect Cu_{Zn}, which may play a role in determining the doping density of CZTS(e), is shallower in CZTSe than in CZTS. According to [85], the distance of the dominant acceptor from the valence band is 0.13 eV for CTZSe and 0.18 eV for CZTS. Hence, Cu_{Zn} can be a more effective dopant in CTZSe than in CZTS, if present in similar amount.

- Compatibly with the point above, the doping density of CZTS appears to be about an order of magnitude lower than in CZTSe from Hall measurements [146]. However, this is not necessarily confirmed by capacitive techniques, where the opposite trend can be observed [36, 43, 85].

- The relative permittivity [85] of CZTS is lower than that of CZTSe, 6.7 versus 8.4 respectively. This can have the same consequences as those listed in the CIGS/CZTSe comparison.

- The effective masses of electrons and holes (m_e and m_h respectively) are predicted to be larger in CZTS than in CZTSe. In CZTS, $m_e = 0.19$ and $m_h = 0.47$. In CZTSe, $m_e = 0.08$ and $m_h = 0.21$ [21]. Then the effective density of states of the respective bands, N_C and N_V, are larger in CZTS than in CZTSe as they are proportional to $m_e^{3/2}$ and $m_h^{3/2}$. This increases J_{00} for any type of SRH recombination

(Equations 1.12-1.14). It also has a negative impact on the electron mobility μ_e, since the latter is inversely proportional to m_e. To conclude, the larger effective masses in CZTS can have a negative impact on both the recombination properties and the collection efficiency of carriers generated out of the depletion region, according to Equation 1.1.

- despite the apparently more adverse defect chemistry in CZTS, its minority carrier lifetimes τ are often found to be very similar to those in CZTSe [36]. However, the diffusion length L_D is reported to be smaller in CZTS than in CZTSe [173]. Lifetimes being equal, this can only be due to a lower mobility in CZTS than in CZTSe, which is compatible with existing mobility measurements [174] and with the effective mass trends discussed above.

1.6.2 Surfaces and grain boundaries

- According to theoretical predictions for the doping limits of semiconductors [154, 175], it is more difficult to achieve n-type doping in CZTS than in CZTSe because of the more energetically favored formation of compensating acceptors as the Fermi level shifts upward. This means that it is more difficult to obtain large band bending in CZTS and have electrons as majority carriers at the heterointerface. From SRH recombination theory, the ability of a p-type absorber to become inverted to n-type at the heterointerface can largely suppress interface recombination, even if S_p is large, due to the large mismatch between the electron and hole population [156]. This is a fundamental limitation that makes CZTS more susceptible than CZTSe to interface recombination problems.

- The band gap of CZTS has a tendency to narrow at surfaces and interfaces that are not properly passivated. The same effect does not occur in CZTSe. This is one of the original results of this thesis and is presented in Study 4.3.

1.6.3 Compatibility with standard device structure

- Both band edges (CBM and VBM) of CZTSe are predicted to lie at about the same energy as CIGS, and both materials seem to have an optimal band alignment with CdS. However, the CBM of CZTS is expected to lie at a higher energy than that of CTZSe [175]. The main risk of a higher-lying CBM is that the CBO with CdS changes from spike-like to cliff-like. This point is treated in detail in Study 4.1.

- The lattice mismatch of CZTS with CdS is 7.0%, which is much worse than the lattice mismatch of 2.4% for the CZTSe/CdS interface.

- In 2014, a smart optical simulation study was carried out on CZTS(e) solar cells. It proved that using thinner CdS (25 nm) and ZnO (10 nm) layers minimizes optical losses without sacrificing other device parameters [56]. This was an important milestone in reaching the very good J_{sc} of the current state-of-the-art CZTS(e) solar cells with a low S content [18, 36]. Something interesting happened afterwards. Other groups working on CZTS(e) with a low S content also switched to thin buffer-window layers and their J_{sc} improved [36,40]. However, to my knowledge, none of the groups working on CZTS switched to the thinner CdS/ZnO architecture. In fact, the CdS/ZnO thicknesses of the best CZTS solar cells are 100/0 nm [17], 100/80 nm [43], 50/90 nm [44], and 60/60 nm [42]. Incidentally, a 25 nm-thick CdS buffer layer was tested on a CZTS solar cell in [155] but it degraded the open circuit voltage.

- As mentioned in Section 1.4 there is some evidence of a significant back contact hole barrier in CZTS (Figure 1.5), whereas CZTSe features only a small barrier. Such a barrier is possibly a reason for the high series resistance measured in all state-of-the-art CZTS solar cells [146].

1.7 Areas covered in my PhD project

This will be a tedious section but, as my PhD project has been part of a joint project, I want to be as clear as possible about what others did and what I did.

1.7.1 What I did not do

- I did not make CZTS or CTS, by any means

- I did not post-anneal CZTS or CTS

- I did not do part of the characterization of CZTS and CTS

- I did not do atomistic calculations, except for my own educational purposes

- there are many other things I did not do, but I will tackle them by exclusion in the next section and in each particular study that I shall present.

1.7.2 What I did do

- The deposition processes for all materials used in the standard CZTS solar cell architecture (except for CZTS itself) are relatively well-established in the materials science community. However, experience with such materials was not available at our institution. Therefore, I had the (more technical than scientific) responsibility for process development of those layers. I worked on the following:

  - Mo back contact by DC magnetron sputtering, with sheet resistance, ellipsometry, SEM, EDX, and XRD (only phase analysis) characterization. In certain periods of time, I received help from B.Sc. students Philip Rasmussen (fabrication), Lars Kildebro (process development, ellipsometry, sheet resistance, SEM), intern Edoardo Bosco (sheet resistance), and PhD students Andrea Cazzaniga and Rebecca Ettlinger (XRD measurement)

  - CdS buffer layer by chemical bath deposition, with sheet resistance, SEM, EDX, and ellipsometry characterization. Here I want to acknowledge the important work of B.Sc. student Tobias Mouritzen, who, in his thesis project, studied systematically the effect on different deposition conditions on different film properties.

  - ZnO window and the AZO transparent conductor by DC- and RF magnetron sputtering. This took up a significant fraction of my PhD time, as the initial sputtering setup I used did not yield satisfactory results (more details in Appendix A). I assembled a new dedicated setup under the guidance of Senior Researcher Eugen Stamate, who also provided invaluable technical assistance. I also want to acknowledge the crucial work of M.Sc. student Tobias Ottsen, who, in his thesis project, studied systematically the effect on different deposition conditions on different film properties, thus providing a database of measurement results that helped me make sense of a lot of trends that were initially obscure.

- other practicalities such as an evaporated Al dot structure used as a front contact, design of the related shadow mask, etching CZTS in a KCN solution, automating the chip cutting process.

- I executed all device fabrication steps except for deposition and annealing of CZTS. They include: cleaning glass, depositing Mo, cutting glass/Mo into chips, depositing CdS, depositing ZnO and ZnO:Al, depositing an Al dot contact or silver paste, defining the solar cell area and exposing the back contact.

- I did device-level simulation with the software SCAPS [105]. Some help was provided by B.Sc. student Mattias Huss-Hansen.

- I did a considerable amount of CZTS and CTS characterization: ellipsometry (all); XPS (all); Raman (all); steady-state PL mapping (with some help from B.Sc. students Tomas Youngman, Lasse Ravnkilde and intern Edoardo Bosco); SEM/EDX (with considerable help from B.Sc. students Philip Rasmussen, Tomas Youngman, Lasse Ravnkilde and intern Edoardo Bosco).

- I did nearly all device characterization (JV, EQE, and CV measurements) with some help from intern Edoardo Bosco. An exception is the illuminated JV and EQE characterization shown in Study 2.1 and Study 3.1.

- I got the following new ideas:

  - to try CeO_2 in CZTS solar cells
  - to plot the film properties of sputtered ZnO:Al as a function of compressive stress regardless of position and deposition pressure
  - to measure the CTS dielectric function on a device-relevant Mo substrate
  - to interpret the surface state predicted at the CZTS/CdS interface as detrimental for performance
  - to apply a forward bias in first-principles interface calculations in order to decouple interface alignment from electrostatic band bending

- I established the collaboration will all the international coauthors of the studies printed in this thesis, with the exception of Yeng Ming Lam (Nanyang University). Furthermore, I established the collaboration with the theoreticians at DTU Nanotech and QuantumWise A/S that resulted in Study 4.2 and Study 4.3.

- I went to UNSW for two months, where I developed the CeO_2 deposition recipe and executed it on actual solar cell devices. I also took to UNSW some CZTS precursors deposited at DTU, which are those that resulted in the champion solar cell presented in Study 2.1. I did most of the characterization of CeO_2 films: SEM, EDX, ellipsometry, and XPS (partly at UNSW and partly at DTU).

1.7.3 Note about the "studies" presented in this thesis

As you will see, I have decided to present the results of my PhD project in the form of articles, and in a few cases posters, which I all labeled "studies". I made this choice because, like you just read, in the majority of cases I have not worked alone through my PhD project. Hence I find it both logical and fair to present the results in a way in which the all collaborators can be acknowledged by simply having them as coauthors in each study. Also, even if some of those studies have not been sent out for publication, they will at some point in the near future.

Because it makes referencing much easier, I have labeled those studies with the notation "Study x.y", for example Study 2.1, Study 3.2 and so on. The first number (x) is the chapter number; the second number (y) is the ID of the study within that chapter. *Those studies should not be directly identified with publications.* That is because some of those studies have been published, some are under review, some will be submitted as soon as I recover from the classic mental breakdown associated to writing a thesis, and some are not quite complete yet.

Therefore, if you are interested in my publication record, I made a List of Publications section at the end of this thesis for that purpose. I hope you enjoy going through the next chapters. If you feel sleepy, sleep now but please set your alarm clock to Chapter 8 - The take-home messages.

Chapter 2

Record efficiency for a CZTS solar cell by pulsed laser deposition

I'm walking on sunshine, woooah
Katrina and the Waves, 1985

2.1 Study 2.1: Ultra-thin Cu_2ZnSnS_4 solar cell prepared by pulsed laser deposition

- Cazzaniga A*, <u>Crovetto A*</u>, Yan C, Sun K, Hao X, Estelrich J R, Canulescu S, Stamate E, Pryds N, Hansen O and Schou J, Ultra-thin Cu_2ZnSnS_4 solar cell prepared by pulsed laser deposition, submitted

  * These authors contributed equally to this work

The study presented in this chapter is truly a joint effort. Besides my own contribution, it is the combined outcome of (i) three years of attempts to understand how to obtain high-quality CZTS precursors by pulsed laser deposition of a sintered target with overall CZTS stoichiometry, done entirely by PhD student Andrea Cazzaniga at DTU; (ii) the highly successful baseline fabrication process for CZTS solar cells (implemented here from the CZTS annealing step onwards), developed at UNSW by PhD student Chang Yan. The result is the highest efficiency ever reported for a CZTS solar cell by pulsed laser deposition.

My contribution (detailed):
• Proposal of collaboration with UNSW, actual research stay at UNSW, and management of collaboration • Fabrication of Mo back contact (at DTU) and of CdS buffer layer (at UNSW, with C. Yan) • Choice and execution of SEM, Raman, steady-state PL, CV, and dark IV measurement with related data analysis • Idea and implementation of optical loss analysis and series resistance investigation • Writing of "Solar cell characterization" section • Co-writing (with A. Cazzaniga) of abstract, conclusions, introduction, and experimental section

Coauthors' contribution (brief):
• A. Cazzaniga: all development work on PLD of CZTS and writing of "Precursors preparation" section • C. Yan: development and execution of device fabrication from CZTS post-annealing onwards • K. Sun: time-resolved PL measurement, help with JV and EQE characterization • J.R. Estelrich: fabrication of CZTS precursors used in this study • S. Canulescu: technical assistance with PLD • E. Stamate: technical assistance with ZnO:Al deposition in test solar cells at DTU • X. Hao, N. Pryds, O. Hansen, J. Schou: funding, discussions, and commenting the manuscript

Ultra-thin Cu₂ZnSnS₄ solar cell prepared by pulsed laser deposition

Andrea Cazzaniga[†1], Andrea Crovetto[†*2,3], Chang Yan[3], Kaiwen Sun[3], Xiaojing Hao[3], Joan Ramis Estelrich[1], Stela Canulescu[1], Eugen Stamate[4], Nini Pryds[4], Ole Hansen[2,5], and Jørgen Schou[1]

[1]DTU Fotonik, Technical University of Denmark, DK-4000 Roskilde, Denmark
[2]DTU Nanotech, Technical University of Denmark, DK-2800 Kgs. Lyngby, Denmark
[3]School of Photovoltaic and Renewable Energy Engineering, University of New South Wales, NSW 2052, Sydney Australia
[4]DTU Energy, Technical University of Denmark, DK-4000 Roskilde, Denmark
[5]CINF, Center for Individual Nanoparticle Functionality, Technical University of Denmark, DK-2800 Kgs. Lyngby, Denmark

[†] The authors A. Cazzaniga and A. Crovetto contributed equally to this work
[*] Correspondence: ancro@nanotech.dtu.dk

Abstract

We report on the fabrication of a 5.2% efficiency Cu₂ZnSnS₄ (CZTS) solar cell made by pulsed laser deposition (PLD) featuring an ultra-thin absorber layer (less than 450 nm). Solutions to the issues of reproducibility and micro-particulate ejection often encountered with PLD are proposed. At the optimal laser fluence, amorphous CZTS precursors with optimal stoichiometry for solar cells are deposited from a single target. Such precursors do not result in detectable segregation of secondary phases after the subsequent annealing step. In the analysis of the solar cell device, we focus on the effects of the finite thickness of the absorber layer. Depletion region width, carrier diffusion length, and optical losses due to incomplete light absorption and back contact reflection are quantified. We conclude that material and junction quality is comparable to that of thicker state-of-the-art CZTS devices.

1 Introduction

Considerable research effort is presently devoted to alternative earth-abundant and non-toxic materials for photovoltaic applications. In this context, the p-type chalcogenide semiconductor Cu₂ZnSnS₄ (CZTS) has become very popular due optimal direct bandgap at 1.5 eV, high absorption coefficient $> 10^4$ cm^{-1} and its rapid technological development in the last decade [1, 2]. Still, the current record efficiency of 12.6% for CZTSSe [3] and of 9.1% for pure-sulfide CZTS [4] is far below the 21.7% efficiency demonstrated by the very similar CIGS technology [5], from which they borrow most of the device architecture. Regarding the pure sulfide CZTS, different vacuum deposition techniques have been successfully employed, such as co-sputtering [4, 6–8] and co-evaporation [9–12]. The most successful strategies to date consist of a two stage process, where precursors are prepared at a substrate temperature below 300°C, followed by a high temperature annealing (>500°C) done separately at much higher pressures. Among vacuum techniques, pulsed laser deposition (PLD) was firstly studied in 2007-08 by Moriya et al. [13, 14], who demonstrated a power conversion efficiency up to 1.74% with a two stage approach consisting of room temperature deposition of the precursors

followed by high temperature annealing in a mixture of N₂ and H₂S. With a similar approach, but using a quaternary oxide target, a power conversion efficiency of 4.94% was claimed very recently by Jin et al. [15]

Pulsed laser deposition is a non-equilibrium technique that enables the fabrication of high quality thin films with complex stoichiometry, particularly oxides, nitrides, and amorphous materials [16–18]. Briefly, a pulsed UV laser beam is focused onto a solid target and laser ablation occurs, which result in highly non-thermal removal of the target material. The ablated material, which is an expanding plasma cloud, is finally collected onto a substrate placed a few cm away. The fact that the energy source is outside of the vacuum chamber and decoupled from the deposition process enables one to investigate many experimental parameters (background gas pressure, substrate temperature, ablation energy density) over a wider physical range than with other vacuum techniques. Since the laser heating and subsequent plasma formation are confined in a very small region of the target, there is no risk of contaminating the growing film with materials coming from components of the chamber other than the target itself. The kinetic energy of the atoms and ions in the deposition flux is related to the laser fluence and is usually of few eV. Particularly relevant to this
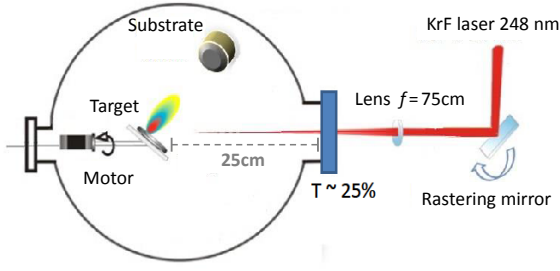
Figure 1: Sketch of the PLD setup. The laser pulses are focused on the target at 45 degrees from normal incidence with a focal lens. The fluence on the target was 0.6 J/cm^2 with a spot size of 4 mm^2.
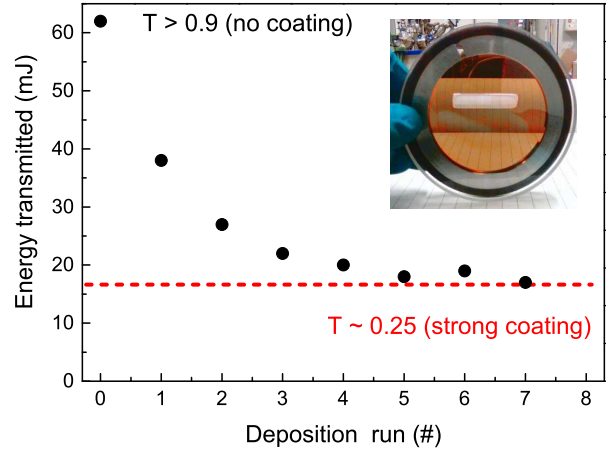

Figure 2: Laser energy transmitted through the viewport as a function of cumulative number of CZTS deposition runs. In the inset: photograph of the viewport after more than five deposition runs, when transmission of the laser through the viewport has reached an equilibrium value of about 25%. One deposition run corresponds to a 20 min deposition at 10 Hz pulse repetition rate.

work, PLD has proven to be a very successful technique in the growth of high quality films of amorphous structure [18,19]. This ability comes from a few combined features: the possibility to keep the substrate at room temperature with relative ease, the sticking coefficient close to unity for all incoming species, and both compactness and flatness of deposited films due to the highly energetic instantaneous material flux [16, 19]. However, reproducibility is often reported to be an issue, mostly because it is difficult to keep the laser ablation parameters within the desired range throughout the whole deposition process, especially in the case of strong coating on the laser view-port [20]. Droplet production and target deterioration are also issues in PLD [16]. Such problems have already been recognized as hurdles to production of high-efficiency solar cells by PLD [21].

However, in this work we demonstrate that it is possible to circumvent most of the above problems and obtain a CZTS solar cell efficiency above 5%. Interestingly, this result is achieved with an "ultra-thin" absorber layer, with thickness below 450 nm.

2 Experimental Details

A 10×10 cm^2 soda lime glass (SLG) substrate was sequentially cleaned in acetone and isopropanol in an ultrasonic bath (5 min each), rinsed in deionized water, and dried with nitrogen. A Mo bilayer was deposited by DC magnetron sputtering at 10 W/cm^2 power density. The first layer was 200 nm thick and deposited at a working pressure of 1.3×10^{-2} mbar for good adhesion to the substrate. The second layer was 300 nm thick and deposited at a working pressure of 3.9×10^{-3} mbar to achieve a lower sheet resistance. The sheet resistance of the Mo bilayer was 0.7 Ω/sq $\pm 50\%$ depending on position on the SLG substrate. The Mo-coated glass was cut into 1.5×3 cm^2 substrates, which were cleaned in the same way as above prior to pulsed laser deposition of CZTS precursors. Precursors were deposited with our PLD equipment, depicted schematically in Figure 1, under high vacuum with $p < 5 \times 10^{-6}$ mbar. The KrF excimer laser beam (248 nm wavelength, 20 ns pulse-width, 15 Hz

pulse repetition rate) was focused onto a sintered target with overall CZTS stoichiometry (2.5 cm diameter, Testbourne Ltd, 2CuS:ZnS:SnS) at a laser fluence of 0.6 J/cm^2 and a spot size of 4 mm^2.

The laser energy on the target was measured inside the chamber to avoid errors due to strong coating of the viewport with ablated material. The depositions were done after the laser beam-viewport system had reached equilibrium, as shown in Figure 2.

Rastering of the laser and rotation of the target were used to maximize film uniformity and target utilization. The target-substrate distance was set to 4 cm and the substrate was kept at room temperature. Morphology of the precursors, and of the finished solar cell devices, was examined with a scanning electron microscope (SEM) equipped with a field emission gun (Supra 60VP, Zeiss). The chemical composition of the precursors was measured in the same instrument by energy dispersive X-ray spectroscopy (EDX) using a silicon drift detector (X-Max^N 50, Oxford Instruments) and a beam voltage of 15 kV. The CZTS precursors were vacuum packed and taken to the University of New South Wales for the sulfurization treatment and the buffer/window layer deposition. Sulfurization was conducted at 560°C in the presence of S and SnS powder in a rapid thermal processor (AS-One 100). The CdS buffer layer (60 nm) was deposited by a standard chemical bath deposition process [22], followed by RF magnetron sputtering of 50 nm intrinsic ZnO (i-ZnO) and 200 nm indium tin oxide (ITO) having a sheet resistance around 30 Ω/sq. A 1.5 mm^2 dot-shaped silver paste contact was applied on the ITO layer, followed by evaporation of 100 nm MgF$_2$ as an anti-reflection coating. Solar cell devices of 0.2 cm^2 were defined by mechanical scribing.

Illuminated current-voltage (J-V) measurements were performed after 5 min light soaking under stan-
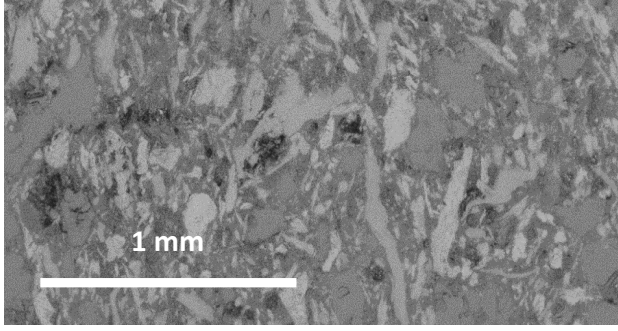
Figure 3: SEM image of the 2CuS:ZnS:SnS sintered target. The different phases are clearly visible and extend over a typical length scale of a few hundred μm. The melting point and the vapor pressure of the main phases are summarized in Table 1. The ablated area corresponds to a beam spot size of 4 mm^2.
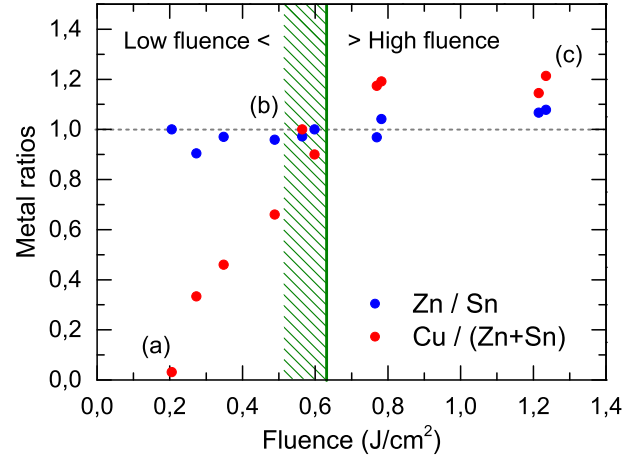

Figure 4: The metal ratios as a function of laser fluence as measured by EDX in the films deposited at room temperature. Letters denote the films shown in Figure 5. The fluence range used for preparing the solar cells precursors is indicated by the green shaded area. The fluence value (approximately 0.6 J/cm^2) that results in stoichiometric transfer is marked with a green line. Below and above this reference fluence, we speak of "low fluence" and "high fluence" in the main text.

dard AM 1.5 solar spectrum (100 mW/cm^2) using a solar simulator from PV Measurement calibrated with a standard Si reference and a Keithley 2400 source meter. Due to the coarse nature of the top contact, in this work we present the active area efficiency of the solar cell instead of the total area efficiency. Dark J-V and capacitance-voltage (C-V) curves were measured with an Agilent B1500A semiconductor device analyzer. C-V scans were performed between -4 V (reverse bias) and +2 V at a frequency of 100 kHz and an AC voltage of 50 mV.

External quantum efficiency (EQE) curves were measured at 0V and -1V dc bias in the range 300 to 1000 nm with a QEX10 spectral response system (PV measurements, Inc.) calibrated by the National Institute of Standards and Technology (NIST)-certified reference Si and Ge photodiodes. The band gap of CZTS was extracted from the inflection point of the EQE curve, i.e., as the photon energy at which $-\mathrm{d(EQE)}/\mathrm{d}\lambda$ has a maximum [23].

Steady-state photoluminescence (PL) spectra were measured on completed solar cells with an Accent RPM2000 system at an excitation wavelength of 532 nm and power density 100 W/cm^2. Raman spectra and time-resolved photoluminescence (TR-PL) decay were measured on a bare absorber layer fabricated similarly to those used for the solar cell.

Raman spectra with multiple excitation wavelengths (455, 532, and 780 nm) were measured on a similarly fabricated CZTS film using a DXR Raman microscope (Thermo Scientific) in backscattering configuration, with a laser power of 1.6 mW and a spot size of approximately 2×2 μm^2.

TR-PL was measured using the time-correlated single photon counting (TCSPC) technique (Microtime200, Picoquant). The excitation wavelength was 470 nm and the power density was 1 W/cm^2, with a pulse frequency of 10 MHz and a 780-820 nm detection range.

3 Results and discussion

3.1 Precursors preparation

In this study we aimed for maximally amorphous precursors by keeping the substrate at room temperature during deposition. Thus, stoichiometry and morphology of the films are primarily related to the laser beam-target interaction, which is very complex here due to the multi-phase structure of the target, as shown in Figure 3. Since a single crystal target is not commercially available, the target used in this work is made from sintered powders (2CuS:ZnS:SnS). The different phases extend over many hundreds of μm and have very different physical properties in terms of energy absorption, decomposition mechanisms and volatility in vacuum, as summarized in Table 1.

As a matter of fact, the Cu/(Zn+Sn) and Zn/Sn ratios in the precursors are of paramount importance to achieve good quality devices [27]. Therefore, we start our discussion with the stoichiometry of films deposited in the laser fluence range from 0.2 to 1.2 J/cm^2, as shown in Figure 4. Noteworthy, the copper content in the as-deposited films is found to be strongly related to the laser fluence, while the Zn/Sn ratio is always close to the target stoichiometry. First, a threshold fluence for copper transfer is clearly visible at 0.2 J/cm^2. In the "low fluence" range from 0.2 to 0.8 J/cm^2, the Cu content steadily increases from 0% to its stoichiometric value, same as the target. In the "high fluence" range above 0.6 J/cm^2 the films become Cu-rich and the Cu content saturates above its stoichiometric value. The sulfur content is not shown here, but a behaviour opposite to copper is seen, i.e., it steadily

Solid Phase	Specific heat C_p J/(K*mol)	Melting point °C	Heat of Fusion kJ/mol	Heat of vaporization kJ/mol	Vapor products
CuS	47.8	220*	s.s.r 1		$S_{2(g)}$
$Cu_{1.75}S$	76.3	507*	s.s.r 2		$S_{2(g)}$
Cu_2S	76.3	1129	9.62	N.A.	N.A.
SnS	49.3	881	31.6	220 (subl.)	$SnS_{(g)}$
ZnS	46.0	1827	30.0	206 (subl.)	$ZnS_{(g)}$, Zn, $S_{2(g)}$

Table 1: Physical properties of the most relevant solid state phases in the sintered target. Other binary and ternary chalcogenide phases are not excluded, but no metallic phases were found. Subscripts (s)/(g) indicate solid/gas. Melting temperatures marked with * relate to the solid state reaction (s.s.r.) mentioned in the text. Heat of vaporization is only given for compounds that can be fully evaporated, either congruently or via dissociation product. Data from [24–26].
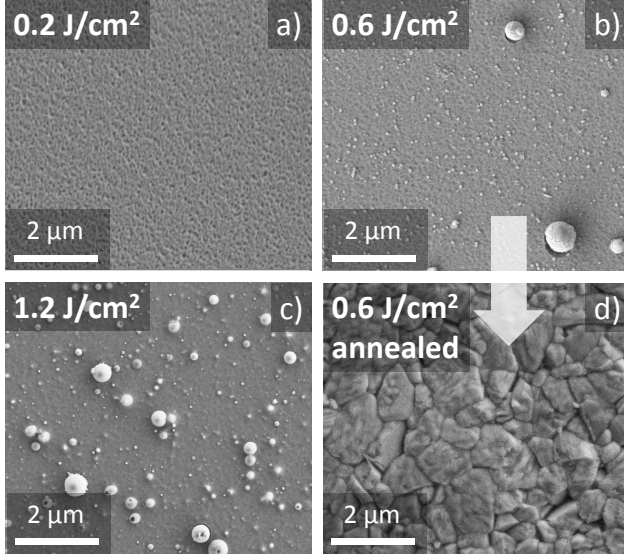

Figure 5: (a to c): top view of as-deposited films using three different laser fluences. (a) 0.2 J/cm^2 (low fluence); (b) 0.6 J/cm^2 (intermediate fluence); and (c) 1.2 J/cm^2 (high fluence). No peaks are detected in the XRD pattern (not shown here), indicating that the films and the droplets are amorphous. Image (d) represents film (b) after annealing in sulfurized atmosphere as used for making solar cells.

decreases from low to high laser fluences. Changes in films composition are also followed by changes in films morphology. SEM images of three films deposited with different laser fluences are shown in Figure 5. The as-deposited films are amorphous and, in particular, (b) and (c) are studded with micron-sized droplets which are primarily a mixture of copper and sulfur [28]. From Figures 4 and 5 it is clear that, by increasing the laser fluence, both the copper content in the films and the amount of Cu-S droplets are increasing.

While laser ablation is not an evaporation process at thermodynamic equilibrium, still, a qualitative understanding of the fluence dependence of composition and morphology of the deposited films can be proposed on the account of thermodynamical parameters of the different phases in the target, which are listed in Table 1. As can be seen, ZnS and SnS phases readily sublime in vacuum, either congruently (SnS) or incongruently (ZnS), due to low enthalpy of evaporation. On the other hand, Cu-containing phases only release S$_2$ gas when heated above the melting point, see Equations 1, 2. Only when Cu$_2$S is formed it can then release gaseous Cu after dissociation. Hence the minimum temperature for Cu evaporation is above the melting point of Cu$_2$S, at 1129°C, and the process requires more energy than SnS and ZnS sublimation. Furthermore, the specific heat of ZnS and SnS phases is lower than those of Cu-S phases, meaning that the laser energy can be more effective in raising the local temperature of the volatile phases. Cu$_2$S formation from CuS and Cu$_{1.75}$S is a relatively energy-intensive process, which occurs through two sequential solid state reactions [25]:

$$CuS \rightarrow Cu_{1.75}S_{(s)} + S_{2(g)} \tag{1}$$
$$Cu_{1.75}S_{(s)} \rightarrow Cu_2S_{(s)} + S_{2(g)} \tag{2}$$
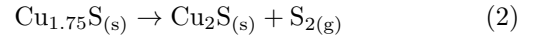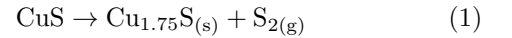
The enthalpies of formation of the reactions in Equations 1 and 2 are 178 ±4 kJ/mol and 268 ±7 kJ/mol, respectively [25].

We can speculate that at very low fluence, below 0.2 J/cm^2, all the energy is readily absorbed by the volatile phases ZnS and SnS, which very quickly dissociate and create the plasma, while the energy density on the target never reaches the critical value to dissociate Cu$_{2-x}$S phases and copper is not transferred to the films, as shown in Figure 4, sample (a). The relatively low heat of fusion of Cu$_2$S can partly explain why some of the material is not fully ablated, but instead transferred as a molten droplet when the hydrostatic pressure of the plasma on the target is enough for inducing material removal from the target. At very high fluence (>0.8 J/cm^2), we believe that the Cu-rich composition of the as-deposited films is a direct consequence of non-directional evaporation of volatile species ZnS and SnS from the target, while the ablated particles are emitted preferentially toward the substrate.

For the preparation of the solar cell absorbers we utilized precursors made at the laser fluence of 0.6 J/cm^2, which corresponds to sample (b) in Figure 5. The overall composition at this fluence, estimated by EDX, is Cu-poor Cu/(Zn + Sn) ∼ 0.85, as prescribed for high efficiency CZTS devices [27]. The Zn/Sn ratio is ∼ 1 and the S/(Cu+Zn+Sn) ratio is between
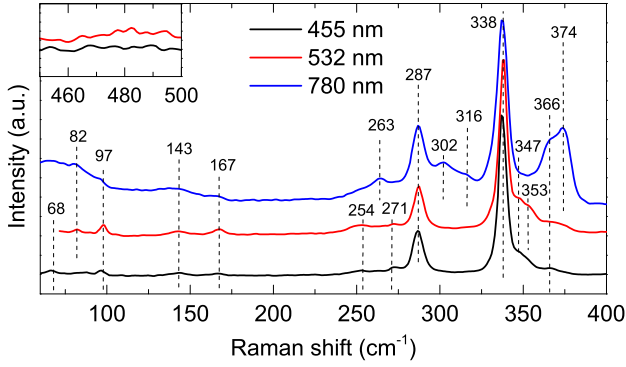
Figure 6: Raman spectra of the CZTS absorber layer at three different excitation wavelengths after high temperature sulfurization. Raman spectroscopy was also performed on the bottom surface of CZTS after lift-off from the Mo substrate, and no peaks related to secondary phases were found. The dashed bars indicate the identified peaks related to kesterite CZTS, according to [29]. The inset graph shows the spectral range where $Cu_{2-x}S$ has the strongest Raman peak.

Figure 7: SEM image of the cross section of our champion device.

0.9 and 1. We note that precursors (b) contain Cu-S droplets. We have verified that these droplets can be removed via KCN etching, but pinholes and voids are left in the precursors, which is not desirable for making solar cells. However, removal of droplets does not seem to be necessary. In fact, after high temperature sulfurization, no localized Cu excess is detected by EDX mapping (not shown), no traces of secondary phases are visually evident by SEM (Figure 5(d)), and no $Cu_{2-x}S$ is detected by Raman spectroscopy (inset of Figure 6). This indicates that the Cu atoms diffuse effectively in the film during annealing.

3.2 Solar cell characterization

3.2.1 Morphology and thickness

In Figure 7 a SEM cross section of our champion device with 5.2% active area efficiency is shown. The morphology is compact and most grains extend from bottom to top. No obvious segregation of smaller grains and secondary phases exists at the interfaces, and no voids are visible, in contrast to what is often observed even in state-of-the-art devices [9, 30]. We emphasize that these features are common to all our annealed films, regardless of the specific point where the image is taken. We speculate that the absence of voids and secondary phases in the annealed films may be a consequence of the compact and maximally disordered structure of the precursors obtained by PLD. The CZTS absorber layer rests on a relatively thick (390 nm) MoS_2 layer. The image was taken about 2-3 mm from the solar cell area and, with a conservative estimate on the expected thickness gradient, the CZTS layer in the solar cell does not exceed a thickness of 450 nm, which is among the lowest values reported for high efficiency CZTS devices [15, 30].

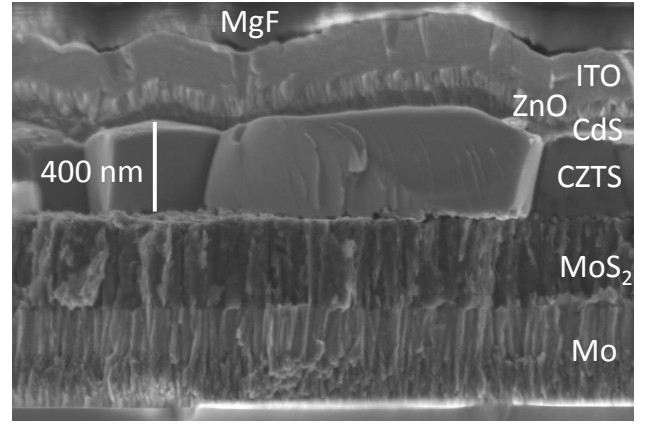Chalcogenide absorbers below 700 nm thickness are sometimes referred to as "ultra-thin" in the literature [31, 32]. In general, if the material properties of the absorber were independent of thickness, one would expect only the short circuit current to be reduced in an ultra-thin absorber, due to 1) incomplete light absorption, and 2) lower collection efficiency, as more minority carriers are generated near the back contact where they can recombine. However, keeping a high material quality in ultra-thin absorbers has been proven to be very challenging for CdTe [31], CIGS [33] and CZTS [30]. Even though back contact recombination can be successfully reduced by introduction of a back surface passivation layer [33], device efficiencies at thicknesses below 500 nm are still consistently lower than expected from short circuit current losses alone [31]. In fact, in all the above studies there was a noticeable decrease in both the open circuit voltage and the fill factor. A common observation was that the morphology of ultra-thin absorbers was inferior to that of thicker films grown under the same conditions, mainly in terms of reduced grain size and increased density of shunt paths. While it is difficult to evaluate the effect of the former on device efficiency, the latter is documented by a decrease of the device shunt resistance with decreasing thickness [30, 31, 33]. The only systematic investigation of CZTS thickness effects on device efficiency was done for co-sputtered CZTS [30]. There, the effect was particularly strong: a 500 nm absorber achieved only 50% of the efficiency of a 2 μm absorber, compared to 80% for both CdTe and CIGS [31, 33]. This was attributed to the increasing role played by secondary phases (SnS, ZnS), both at the front and back interface of CZTS. In the following section these issues will be quantified in our own device.

3.2.2 Electrical and optical properties

The dark and illuminated (1 sun) J-V curves, steady state PL, and EQE (at zero and reverse bias) are shown in Figures 8 and 9. The CZTS band gap of 1.53 eV, indicated in Figure 9, corresponds to to the inflection point of the EQE curve. The PL spectrum has a peak
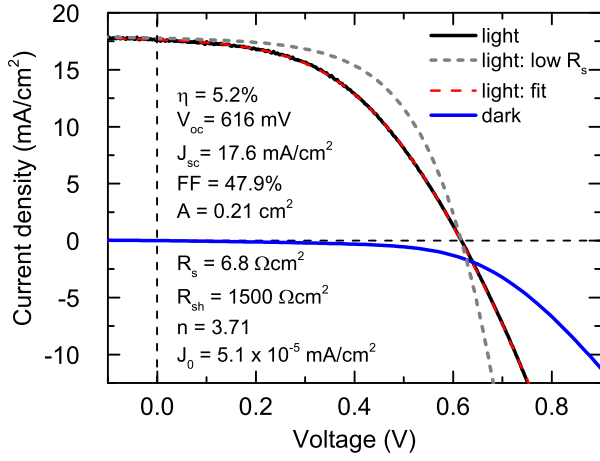
Figure 8: The dark and illuminated (1 sun) J-V curve of our champion device fitted with a single diode model (red dashed curve). All parameters, with the exception of the dark saturation current density J_0, were extracted by fitting the illuminated J-V curve. The high series resistance is due to non-ideal top contact geometry, as discussed in Section 3.3.3. Assuming a series resistance of $1\,\Omega\,cm^2$ (grey dashed curve), the fill factor and efficiency increase to 58% and 6.3%, respectively.
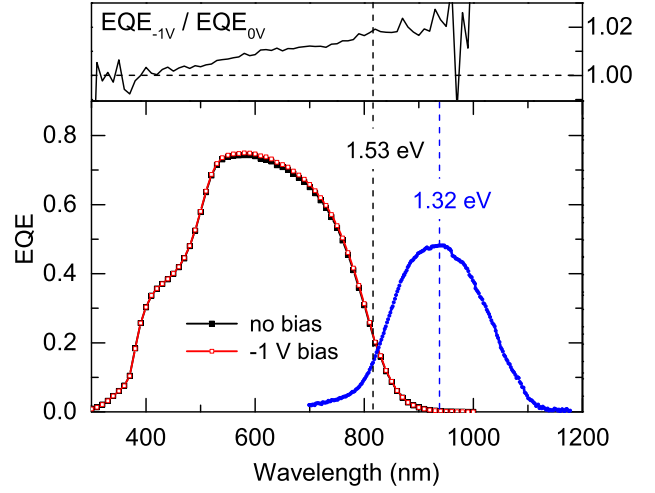

Figure 9: External Quantum Efficiency curves under 0 V bias (black symbols) and -1 V bias (red symbols). The inflection point of the $EQE_{0V}(\lambda)$ curve at 810 nm (1.53 eV) is indicated with a black dashed line. The inset shows the ratio $EQE_{-1V}(\lambda)/EQE_{0V}(\lambda)$. The PL spectrum at room temperature of the finished device (blue symbols) has a maximum at 1.32 eV (blue dashed line).

at a lower energy (1.32 eV), similarly to previous investigations on CZTS devices [9, 34]. This is believed to be due to a high density of band-edge tail states that reduces the achievable open circuit voltage [23].

The short circuit current $J_{sc} = 17.6\,mA/cm^2$ derived from the illuminated J-V curve is in good agreement with the value of $17.4\,mA/cm^2$ obtained by integration of the EQE measured under white light bias. Despite the very thin absorber, this is a fairly high value for CZTS solar cells, which hints to a high collection efficiency, as will be discussed later. The shunt resistance R_{sh} and the dark saturation current J_0 are also comparable to state-of-the-art CZTS devices with larger thickness and efficiency > 7% [4,6,7,9]. The high shunt resistance is consistent with the absence of voids and shunting paths as revealed by SEM imaging (Figure 7). On the other hand, the open circuit voltage $V_{oc} = 616$ mV is somewhat lower and the fill factor $FF = 47.9\%$ is much lower than in benchmark devices. The latter is mostly due to high series resistance R_s and a high diode ideality factor n.

As mentioned above, short circuit current losses are always expected in ultra-thin absorbers, so it can be instructive to quantify them. The calculated losses due to incomplete light absorption are reported in Figure 10 and explained in the caption. The potential gain in short circuit current by complete light absorption due to the extra generated carriers is not negligible ($+1.9\,mA/cm^2$). This could be achieved either by a thicker absorber, or by an ideal back reflector, and would result in a 10% relative gain in efficiency, up to 5.7%. The J_{sc} would then be close to $20\,mA/cm^2$, which is comparable to the state-of-the-art CZTS solar cells [4,6,7,9].

However, with our back contact structure (390 nm MoS_2/Mo), the calculated contribution of back contact reflection to the short circuit current is as low as $0.04\,mA/cm^2$, which is negligible. This difference can be explained as follows. The reflection at the $CZTS/MoS_2$ interface is negligible due to the small mismatch between the optical functions of the two materials. While the MoS_2/Mo reflectivity is higher (about 20% in the high wavelength range), still the remaining 80% is completely absorbed in the Mo and there is a large additional contribution from absorption in the thick MoS_2 layer. Even if the MoS_2 was only 50 nm thick, the contribution of back contact reflection would still be relatively low ($0.3\,mA/cm^2$). In the limiting case of a direct CZTS/Mo interface, the contribution would increase slightly to $0.5\,mA/cm^2$.

The fact that our measured short circuit current, corrected for optical losses due to finite thickness, is comparable to state-of-the-art CZTS devices, points to the fact that collection efficiency is reasonably high and not significantly degraded by the small thickness of the absorber. To confirm this hypothesis, we investigated the ratio between the EQE at zero voltage bias (EQE_{0V}) and at -1 V reverse bias (EQE_{-1V}) of our device, as shown in the upper panel of Figure 9. Remarkably, the two curves never differ by more than 2% for photon energies above the CZTS band gap and the difference steadily reduces at shorter wavelengths. This resembles closely the measurement in [9], where the maximum difference in EQE at 0 V and -1 V was slightly more than 3% for a 600 nm-thick, 8.6%-efficient device. In [30], a deviation of more than 10% was observed even at a reverse bias of only -0.5 V, indicating dramatic problems with collection efficiency attributed by the authors to secondary phases at the
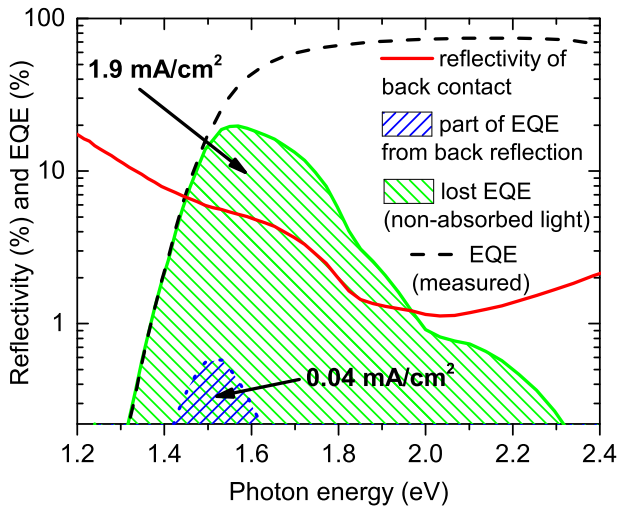
Figure 10: Calculated losses on the short circuit current due to the limited thickness of the device. In dashed green the current loss due to non absorbed light (assuming 90% collection efficiency). In dashed blue the contribution to current gain from reflection at the CZTS/MoS$_2$ interface. Note the logarithmic scale. The solid red curve is the calculated reflectivity of the back contact, which includes contributions from a single CZTS-MoS$_2$ reflection and a single MoS$_2$-Mo reflection minus absorbtion in the MoS$_2$ layer. The optical functions of CZTS, MoS$_2$ and Mo were taken from the literature [35, 36]. The thickness of MoS$_2$ in the calculation is 390 nm as in our solar cell. The reflectivities of the two interfaces were calculated using the Fresnel reflection coefficient.

interfaces. These results suggest that our device is relatively unaffected by collection losses, and that the diffusion length L$_d$ of minority carriers is larger than the quasi-neutral region W$_N$ of our absorber. We attribute the small increase in EQE at reverse bias to back surface recombination losses that are inevitable for a thin absorber in the absence of a back surface field.
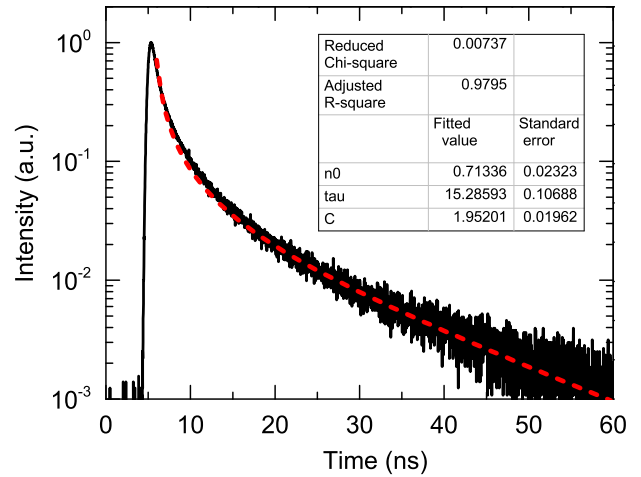
A diffusion length greater than the quasi-neutral region, $L_D > W_N$, is also supported by the analysis of time-resolved photoluminescence (TR-PL), as illustrated in Figure 11. The TR-PL signal does not follow a simple exponential decay and is best described by a rate equation which contains both a linear and a quadratic term in the excess carrier density n:

$$\frac{dn}{dt} = -An - Cn^2 \qquad (3)$$

Following [37], and substituting $A = 1/\tau$ for the linear term, which represents the minority-carrier lifetime in the low injection regime, the solution to Equation 3 is:

$$n(t) = \frac{n_0 \exp(-t/\tau)}{1 + n_0 C\tau[1 - \exp(-t/\tau)]} \qquad (4)$$

By fitting the whole range of the PL decay according to this model, we obtain a value of about 15 ns for the carrier lifetime. We note that, if the same fitting
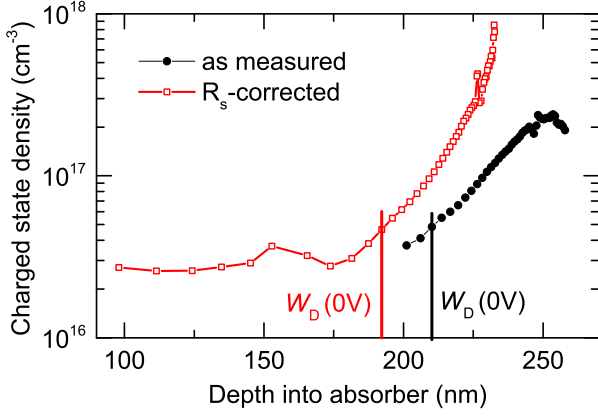

Figure 11: Time-resolved photoluminescence of a bare CZTS film after sulfurization. The red dashed line is the fit following Equation 4 with the coefficients n_0, τ, and C as indicated in the figure.

method as [9] is applied, we obtain about 10 ns lifetime. While carrier lifetimes reported in the literature cannot always be compared directly due to the different models used by different authors to fit the TR-PL data, we emphasize that this value is at the high end for CZTS absorbers [9].

To provide a lower bound value for the minority carrier diffusion length, we estimate the width of the depletion region by means of C-V scan measurements. In Figure 12 we show the density of charged states at different depths into the CZTS absorber, which constitutes an upper limit to its real doping density. The plot has been derived from C-V scans by applying a standard model for a p-n$^+$ junction, where all the measured capacitance is due to ionized acceptors in the depletion region, which is assumed to extend exclusively in the p-type absorber. Due to the significant series resistance present in the device, we corrected the measured capacitance and conductance at each DC voltage bias based on an equivalent circuit with an AC resistance in series with the junction [38]. The value of the AC resistance was estimated as 8.1 Ω cm^2 from the characteristics of the capacitance decline at high frequency in a separate capacitance-frequency (C-f) measurement. The resulting charged state density stabilizes to about 3×10^{16} cm^{-3} within the depletion region, which is interpreted as an upper limit for the true doping density of CZTS. Outside the depletion region, the charged state density seems to increase rapidly. We believe this to be a data analysis artifact due to the simplified model for the device response to the C-V measurement. Indeed, in thin-film materials trap states can be an additional sources of capacitance besides the ionized shallow acceptors. [39]. Following [38], the width of the depletion region at zero bias W_D is estimated to be 190 nm, similarly to that in Ref. [9]. However, this value is obtained under the strong assumptions that both the CdS and the i-ZnO layers are much more heavily doped than the CZTS absorber, which is ques-

Figure 12: Depth profile of the density of charged states in the CZTS absorber extracted from a capacitance-voltage measurement. Black filled symbols: uncorrected data assuming zero series resistance. Open red symbols: data corrected for an AC series resistance of 8.1 Ω cm^2. W_D is the width of the depletion region at zero bias, assuming that the CdS and i-ZnO layers have much heavier doping than CZTS.

Figure 13: Dependance of dark series resistance on device area, with a linear fit to the measured points. The area of the silver paste dot contact is 0.015 cm^2. The area-independent dark series resistance is extrapolated as 2.1 Ω cm^2. This corresponds to the case where the lateral spreading resistance of the ITO layer is no longer the limiting factor for the series resistance.

tionable [40, 41]. In the case of a completely depleted 60 nm-thick CdS layer, the depletion region width in CZTS can be extracted by assuming the measured capacitance C_m to be due to two equivalent capacitors in series: one encompasses the full CdS buffer layer (C_b), and the other is due to the depletion region of the CZTS absorber (C_a), so that:

$$\frac{1}{C_m} = \frac{1}{C_a} + \frac{1}{C_b} \qquad (5)$$

Here $C_a = \varepsilon_0 \varepsilon_a \Sigma / W_D$ and $C_b = \varepsilon_0 \varepsilon_b \Sigma / d$, where ε_0 is the vacuum permittivity, ε_a (ε_b) is the relative permittivity of the absorber (buffer) layer, Σ is the solar cell area, and d is the thickness of the buffer layer. Under these assumptions, the extracted CZTS depletion region width reduces to 150 nm, and further to 110 nm if both the CdS and the i-ZnO layers are assumed to be completely depleted. Hence, we estimate an interval from 110 to 190 nm for the depletion width in CZTS. From this we conclude that the minority carrier diffusion length must be at least 300 nm. Indeed, if the diffusion length is simply calculated using the measured lifetime of 15 ns and a CZTS electron mobility of 3 cm^2/Vs [42], the result is 350 nm.

3.2.3 Performance limitations

The main deficit of our device with respect to state-of-the-art CZTS solar cells is the low fill factor of 47.9%, which is due to a high ideality factor and high series resistance. To investigate the possible origin of the latter, we studied the dependence of series resistance on device area. This was done on an adjacent solar cell on the same chip (with similar series resistance) by measuring its dark J-V characteristic after reducing its total area A by mechanical scribing. Four scribing-measurement iterations were performed. As
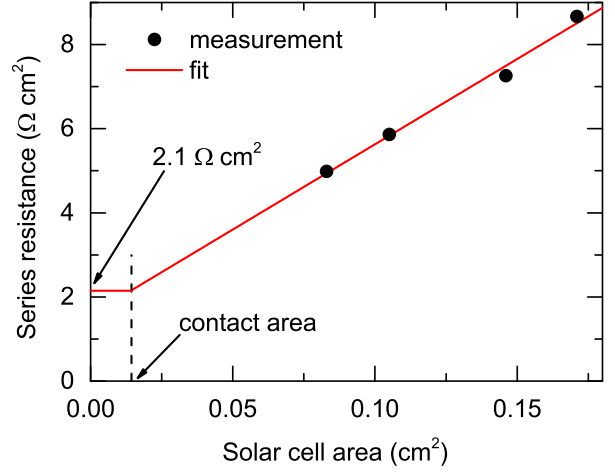
shown in Figure 13, the series resistance of the solar cell increases linearly with area. Hence, we conclude that the main contribution to the high series resistance must be the lateral spreading resistance of the ITO layer. By proper design of a top contact grid, this contribution can be minimized with a minimal loss in short circuit current due to shadowing. Therefore, we plotted in Figure 8 also the simulated J-V curve under illumination with the same parameters of the fitted experimental J-V curve but a lower realistic series resistance of 1 Ω cm^2. As a result the fill factor improves up to a value of 58%, close to the values reported for state-of-the-art CZTS solar cells, which would lead to a device efficiency of 6.3% (Figure 8).

The origin of the high ideality factor can only be speculated at the moment. However, it was observed in a study on ultra-thin CdTe solar cells [43] that the ideality factor increased with decreasing absorber thickness, up to a value of 3.9 for a thickness of 500 nm. The authors attributed the fact to voltage-dependent collection in the thin solar cell. This explanation may apply to our device as well, since our estimated collection depth is not much larger than the thickness of the absorber. This implies that significant collection losses may occur under forward bias, where the depletion region shrinks.

The V_{oc} of our device is inferior to [9] by about 50 mV. Since our carrier lifetimes are relatively high, this discrepancy could be due to enhanced back surface recombination in the thin absorber, or alternatively to a voltage-dependent collection efficiency under forward bias as proposed above.

4   Conclusion

We reported a pure-sulfide CZTS solar cell device with 5.2% active area efficiency using an ultra-thin absorber (< 450 nm) prepared by pulsed laser deposition. Careful control of the laser fluence allows deposition of high-quality amorphous CZTS precursors with the optimal stoichiometry for solar cells. Such precursors do not result in detectable segregation of secondary phases in the subsequent annealing step. We believe this is the main reason why the present device performs well compared to previously reported CZTS devices of similar thickness. In particular, the short circuit current is comparable to (thicker) state-of-the-art CZTS devices, when the losses related to incomplete light absorption are taken into account. Despite the small absorber thickness, there are no signs that material and junction quality are significantly lower than that of thicker absorbers: grain size, carrier lifetimes, collection efficiency, shunt resistance, and dark saturation current are all similar to benchmark CZTS solar cells. The main deficit compared to benchmark CZTS solar cells is in the fill factor, which, however, does not appear to be a thickness-related effect. Instead, it is mostly due to non-optimal contact geometry, which should not represent a severe development roadblock. In absolute terms, the low open circuit voltage remains the main problem preventing $> 10\%$ efficiencies to be achieved in CZTS solar cells.

Acknowledgements

References

[1] Ito K. *Copper Zinc Tin Sulfide-Based Thin-Film Solar Cells.* Wiley, 2015.

[2] Liu X, Feng Y, Cui H, Liu F, Hao X, Conibeer G, Mitzi DB, Green M. The current status and future prospects of kesterite solar cells: a brief review. *Progress in Photovoltaics: Research and Applications* 2016; doi: 10.1002/pip.2741.

[3] Wang W, Winkler MT, Gunawan O, Gokmen T, Todorov TK, Zhu Y, Mitzi DB. Device Characteristics of CZTSSe Thin-Film Solar Cells with 12.6% Efficiency. *Advanced Energy Materials* 2013; **4**(7):1301 465, doi:10.1002/aenm.201301465.

[4] Tajima S, Itoh T, Hazama H, Ohishi K, Asahi R. Improvement of the open-circuit voltage of Cu$_2$ZnSnS$_4$ solar cells using a two-layer structure. *Applied Physics Express* 2015; **8**(8):082 302, doi:10.7567/APEX.8.082302.

[5] Jackson P, Hariskos D, Wuerz R, Kiowski O, Bauer A, Friedlmeier TM, Powalla M. Properties of Cu(In,Ga)Se$_2$ solar cells with new record efficiencies up to 21.7%. *physica status solidi (RRL) - Rapid Research Letters* 2015; **9**(1):28–31, doi:10.1002/pssr.201409520.

[6] Sun K, Yan C, Liu F, Huang J, Zhou F, Stride JA, Green M, Hao X. Over 9% Efficient Kesterite Cu$_2$ZnSnS$_4$ Solar Cell Fabricated by Using Zn$_{1-x}$Cd$_x$S Buffer Layer. *Advanced Energy Materials* 2016; doi:10.1002/aenm.201600046.

[7] Scragg JJ, Kubart T, Wätjen JT, Ericson T, Linnarsson MK, Platzer-Björkman C. Effects of Back Contact Instability on Cu$_2$ZnSnS$_4$ Devices and Processes. *Chemistry of Materials* 2013; **25**(15):3162–3171, doi:10.1021/cm4015223.

[8] Fairbrother A, Fontané X, Izquierdo-Roca V, Espíndola-Rodríguez M, López-Marino S, Placidi M, Calvo-Barrio L, Pérez-Rodríguez A, Saucedo E. On the formation mechanisms of Zn-rich Cu$_2$ZnSnS$_4$ films prepared by sulfurization of metallic stacks. *Solar Energy Materials and Solar Cells* 2013; **112**:97–105, doi:10.1016/j.solmat.2013.01.015.

[9] Shin B, Gunawan O, Zhu Y, Bojarczuk NA, Chey SJ, Guha S. Thin film solar cell with 8.4% power conversion efficiency using an earth-abundant Cu$_2$ZnSnS$_4$ absorber. *Progress in Photovoltaics: Research and Applications* 2011; **21**(1):72–76, doi:10.1002/pip.1174.

[10] Wang K, Gunawan O, Todorov T, Shin B, Chey SJ, Bojarczuk NA, Mitzi D, Guha S. Thermally evaporated Cu$_2$ZnSnS$_4$ solar cells. *Applied Physics Letters* 2010; **97**(14):143 508, doi:10.1063/1.3499284.

[11] Mise T, Tajima S, Fukano T, Higuchi K, Washio T, Jimbo K, Katagiri H. Improving the photovoltaic performance of co-evaporated Cu$_2$ZnSnS$_4$ thin-film solar cells by incorporation of sodium from NaF layers. *Progress in Photovoltaics: Research and Applications* 2016; :n/a–n/adoi: 10.1002/pip.2745.

[12] Schubert BA, Marsen B, Cinque S, Unold T, Klenk R, Schorr S, Schock HW. Cu$_2$ZnSnS$_4$ thin film solar cells by fast coevaporation. *Progress in Photovoltaics: Research and Applications* 2011; **19**(1):93–96, doi:10.1002/pip.976.

[13] Moriya K, Tanaka K, Uchiki H. Fabrication of Cu$_2$ZnSnS$_4$ Thin-Film Solar Cell Prepared by Pulsed Laser Deposition. *Japanese Journal of Applied Physics* 2007; **46**(9A):5780–5781, doi:10.1143/JJAP.46.5780.

[14] Moriya K, Tanaka K, Uchiki H. Cu$_2$ZnSnS$_4$ Thin Films Annealed in H$_2$S Atmosphere for Solar Cell Absorber Prepared by Pulsed Laser Deposition. *Japanese Journal of Applied Physics* 2008; **47**(1):602–604, doi:10.1143/JJAP.47.602.

[15] Jin X, Yuan C, Zhang L, Jiang G, Liu W, Zhu C. Pulsed laser deposition of Cu$_2$ZnSn(S$_x$Se$_{1-x}$)$_4$ thin film solar cells using quaternary oxide target prepared by combustion method. *Solar Energy Materials and Solar Cells* 2016; **155**:216–225, doi:10.1016/j.solmat.2016.06.022.

[16] Willmott PR. Deposition of complex multielemental thin films. *Progress in Surface Science* 2004; **76**(6-8):163–217, doi:10.1016/j.progsurf.2004.06.001.

[17] Norton D. Pulsed Laser Deposition of complex materials: Progress towards applications. *Pulsed Laser Deposition of Thin Films*, Eason R (ed.). John Wiley & Sons, Inc.: Hoboken, NJ, USA, 2008; 3–31, doi:10.1002/0470052120.

[18] Frumar M, Frumarova B, Nemec P, Wagner T, Jedelsky J, Hrdlicka M. Thin chalcogenide films prepared by pulsed laser deposition – new amorphous materials applicable in optoelectronics and chemical sensors. *Journal of Non-Crystalline Solids* 2006; **352**(6):544–561, doi: 10.1016/j.jnoncrysol.2005.11.043.

[19] Krebs H. Characteristic properties of laser-deposited metallic systems. *International Journal of Non-equilibrium Processing* 1997; **10**(1).

[20] Ohnishi T, Lippmaa M, Yamamoto T, Meguro S, Koinuma H. Improved stoichiometry and misfit control in perovskite thin film formation at a critical fluence by pulsed laser deposition. *Applied Physics Letters* 2005; **87**(24):1–3, doi: 10.1063/1.2146069.

[21] Dittrich H, Klose M, Brieger M, Schaffler R, Schock H. CuInSe$_2$ thin film solar cells by pulsed laser deposition. *Conference Record of the Twenty Third IEEE Photovoltaic Specialists Conference*, 1993; 617–620, doi: 10.1109/PVSC.1993.347022.

[22] Yan C, Liu F, Sun K, Song N, Stride JA, Zhou F, Hao X, Green M. Boosting the efficiency of pure sulfide CZTS solar cells using the In/Cd-based hybrid buffers. *Solar Energy Materials and Solar Cells* 2016; **144**:700–706, doi: 10.1016/j.solmat.2015.10.019.

[23] Gokmen T, Gunawan O, Todorov TK, Mitzi DB. Band tailing and efficiency limitation in kesterite solar cells. *Applied Physics Letters* 2013; **103**(10):103 506, doi: 10.1063/1.4820250.

[24] Piacente V, Foglia S, Scardala P. Sublimation study of the tin sulphides SnS$_2$, Sn$_2$S$_3$ and SnS. *Journal of Alloys and Compounds* 1991; **177**(1):17–30, doi:10.1016/0925-8388(91)90053-X.

[25] Brunetti B, Piacente V, Scardala P. Study on sulfur vaporization from covellite (CuS) and anilite (Cu$_{1.75}$S). *Journal of Alloys and Compounds* 1994; **206**(1):113–119, doi: 10.1016/0925-8388(94)90018-3.

[26] Haynes WM. *CRC Handbook of Chemistry and Physics, 96th Edition*. CRC Press, 2015.

[27] Katagiri H. Survey of development of CZTS-based thin film solar cells. *IEEE 3rd International Conference on Photonics*, 2012; 345–349, doi:10.1109/ICP.2012.6379533.

[28] Ettlinger RB, Crovetto A, Canulescu S, Cazzaniga A, Ravnkilde L, Youngman T, Hansen O, Pryds N, Schou J. Formation of copper tin sulfide films by pulsed laser deposition at 248 and 355 nm. *Applied Physics A* 2016; **122**(4):466, doi:10.1007/s00339-016-9939-4.

[29] Dimitrievska M, Fairbrother A, Fontané X, Jawhari T, Izquierdo-Roca V, Saucedo E, Pérez-Rodríguez A. Multiwavelength excitation Raman scattering study of polycrystalline kesterite Cu$_2$ZnSnS$_4$ thin films. *Applied Physics Letters* 2014; **104**(2):021 901, doi:10.1063/1.4861593.

[30] Ren Y, Scragg JJS, Frisk C, Larsen JK, Li SY, Platzer-Björkman C. Influence of the Cu$_2$ZnSnS$_4$ absorber thickness on thin film solar cells. *physica status solidi (a)* 2015; **212**(12):2889–2896, doi:10.1002/pssa.201532311.

[31] Paudel N, Wieland K, Compaan A. Ultrathin CdS/CdTe solar cells by sputtering. *Solar Energy Materials and Solar Cells* 2012; **105**:109–112, doi:10.1016/j.solmat.2012.05.035.

[32] Li-Kao ZJ, Naghavi N, Erfurth F, Guillemoles JF, Gérard I, Etcheberry A, Pelouard JL, Collin S, Voorwinden G, Lincot D. Towards ultrathin copper indium gallium diselenide solar cells: proof of concept study by chemical etching and gold back contact engineering. *Progress in Photovoltaics: Research and Applications* 2012; **20**(5):582–587, doi:10.1002/pip.2162.

[33] Lundberg O, Bodegård M, Malmström J, Stolt L. Influence of the Cu(In,Ga)Se$_2$ thickness and Ga grading on solar cell performance. *Progress in Photovoltaics: Research and Applications* 2003; **11**(2):77–88, doi:10.1002/pip.462.

[34] Larsen JK, Li SY, Scragg JJS, Ren Y, Hägglund C, Heinemann MD, Kretzschmar S, Unold T, Platzer-Björkman C. Interference effects in photoluminescence spectra of Cu2ZnSnS4 and Cu(In,Ga)Se2 thin films. *Journal of Applied Physics* 2015; **118**(3):035 307, doi:10.1063/1.4926857.

[35] Li SY, Hägglund C, Ren Y, Scragg JJ, Larsen JK, Frisk C, Rudisch K, Englund S, Platzer-Björkman C. Optical properties of reactively sputtered Cu$_2$ZnSnS$_4$ solar absorbers determined by spectroscopic ellipsometry and spectrophotometry. *Solar Energy Materials and Solar Cells* 2016; **149**:170–178, doi:10.1016/j.solmat.2016.01.014.

[36] Crovetto A, Chen R, Ettlinger RB, Cazzaniga AC, Schou J, Persson C, Hansen O. Dielectric function and double absorption onset of monoclinic Cu$_2$SnS$_3$: Origin of experimental features explained by first-principles calculations. *Solar Energy Materials and Solar Cells* 2016; **154**:121–129, doi:10.1016/j.solmat.2016.04.028.

[37] Ohnesorge B, Weigand R, Bacher G, Forchel A, Riedl W, Karg FH. Minority-carrier lifetime and efficiency of Cu(In,Ga)Se$_2$ solar cells. *Applied Physics Letters* 1998; **73**(9):1224–1226, doi:10.1063/1.122134.

[38] Schroder DK. *Semiconductor material and device characterization*. John Wiley & Sons: Hoboken, New Jersey, 2006; 63–84.

[39] Hegedus SS, Shafarman WN. Thin-film solar cells: device measurements and analysis. *Progress in Photovoltaics: Research and Applications* 2004; **12**(23):155–176, doi: 10.1002/pip.518.

[40] Misic B, Pieters BE, Theisen JP, Gerber A, Rau U. Shunt mitigation in ZnO:Al/i-ZnO/CdS/Cu(In,Ga)Se$_2$ solar modules by the i-ZnO/CdS buffer combination. *physica status solidi (a)* 2015; **212**(3):541–546, doi: 10.1002/pssa.201431496.

[41] Shafarman WN, Siebentritt S, Stolt L. Cu(InGa)Se$_2$ Solar Cells. *Handbook of Photovoltaic Science and Engineering*, Luque A, Hegedus S (eds.). chap. 13, John Wiley & Sons, Ltd: Chichester, UK, 2010; 579, doi: 10.1002/9780470974704.

[42] Shin B, Gershon T, Guha S. CZTS-Based Thin-Film Solar Cells Prepared via Coevaporation. *Copper Zinc Tin Sulfide-Based Thin-Film Solar Cells*, Ito K (ed.). chap. 15, Wiley, 2015; 344–345.

[43] Bai Z, Yang J, Wang D. Thin film CdTe solar cells with an absorber layer thickness in micro- and sub-micrometer scale. *Applied Physics Letters* 2011; **99**(14):143 502, doi: 10.1063/1.3644160.

Chapter 3

CeO$_2$: a novel heterojunction partner for CZTS

Don't ever let nothing ever get you down
Cause it's so so new new
Bob Sinclair, 2009

3.1 Study 3.1: Lattice-matched CZTS/CeO$_2$ solar cell with open circuit voltage boost

- Crovetto A, Yan C, Iandolo B, Zhou F, Stride J, Schou J, Hao X, Hansen O, Lattice-matched Cu$_2$ZnSnS$_4$/CeO$_2$ solar cell with open circuit voltage boost, submitted

Here I present a proof-of-concept study for the idea I am most proud of, among all the ideas I got through my PhD project. That is, searching materials databases for a completely new heterojunction partner of CZTS, ending up with CeO$_2$ as an interesting candidate, and actually inserting it in a CZTS solar cell.
Basically, I felt genuinely excited about finding and trying out a *really* new material that was not one of the "classic" candidate buffer layers for CIGS or CZTS solar cells, i.e., the pure or alloyed compounds that share some elements with CZTS or CIGS like Zn(O,S), (Zn,Sn)O, In$_2$S$_3$, or (Zn,Cd)S. Here I will explain my search strategy. Since there is a very comprehensive database of structural properties of materials out there (the Inorganic Crystal Structure Database on icsd.fiz-karlsruhe.de), I decided to search for compounds that are somehow structurally related to CZTS. Thus, to start out with, I made a query for any binary compound with a cubic crystal structure and a lattice constant contained within a $\pm 1\%$ range from the CZTS lattice constant of 5.43 Å. I filtered out any compound that contained any amount of toxic, radioactive, or scarce material, so no cadmium, no indium, no gold, no uranium and so on. Despite the abundance of filters, a lot of binaries popped up: some sounded reasonable, some were just plain weird. I excluded some options just because they didn't appear to be stable or wouldn't form at a reasonable temperature and atmospheric pressure. Then I put the remaining materials in an Excel sheet and looked up additional properties in the scientific literature, Springer Materials (materials.springer.com), The Materials Project (materialsproject.org), AFLOW (aflowlib.org), Wikipedia, Google, anything. The most obvious properties that needed to be checked were, in my view: wide band gap (let's say at least 2.5 eV - not too hard to find); natural n-type conductivity (often difficult to find); electron affinity (also rather difficult to find); and possibility of growth by chemical bath deposition (reference [111] was of great help). In the end, only one material survived: CeO$_2$. I did look into

ternaries and hexagonal materials as well, but I realized that things can quickly explode when doing database searches so eventually I was content with CeO_2. It sounded like a solid material (no pun intended - I mean trustworthy) and there existed some reports on chemical bath deposition of CeO_2 [176–182]. At that point in time, I was not aware of a potential issue due to the poor transport properties of the 4f "conduction band" in CeO_2 [183], so I believed that CeO_2 could be a stand-alone buffer layer and replace CdS altogether.

Shortly after I settled on CeO_2, I managed to arrange a two-month external stay at the University of new South Wales in Sydney, Australia, which I thought would be the perfect setting to try out the new buffer (and, of course, to become involved in slightly less scientific activities involving floating boards). So I went to UNSW, developed a chemical bath deposition recipe for CeO_2 that seemed to work well with a CZTS substrate, and introduced such a CeO_2 layer to the baseline device fabrication process of PhD student Chang Yan. I tried both to completely replace CdS with CeO_2 and to insert a thin CeO_2 layer between CZTS/CdS as a "passivation" layer. The results were very different and then, after some thinking and reading, the problem about the poor transport properties of the 4f conduction band of CeO_2 became clear [183]. The most interesting results of my brief work on CeO_2 is summarized in this Study 3.1.

My contribution (detailed):
• Idea, search strategy, literature review, and decision to try CeO_2 as a heterojunction partner of CZTS • Proposal of collaboration with UNSW, actual research stay at UNSW, and management of collaboration • Development of CeO_2 growth recipe and its execution on CZTS for solar cells • Choice and execution of SEM and XPS characterization. • Development of band alignment measurement strategy • All data analysis • Writing the full manuscript

Coauthors' contribution (brief):
• C. Yan: development and execution of all device fabrication except for the CeO_2 buffer layer; measurement of JV curves; Raman measurement. • B. Iandolo: TEM/STEM/STEM-EDX characterization with corresponding FFT analysis and making of Figure 2 • F. Zhou: XRD measurement (not included), assistance with device fabrication and JV measurement • J. Stride: provision of lab space and training • X. Hao, O. Hansen, J. Schou: funding, discussions, and commenting the manuscript

Lattice-matched Cu_2ZnSnS_4/CeO_2 solar cell with open circuit voltage boost

Andrea Crovetto,[1,2,a)] Chang Yan,[2] Beniamino Iandolo,[3] Fangzhou Zhou,[2] John Stride,[4] Jørgen Schou,[5] Xiaojing Hao,[2,b)] and Ole Hansen[1,6]

[1)] *DTU Nanotech, Technical University of Denmark, DK-2800 Kgs. Lyngby, Denmark*
[2)] *School of Photovoltaic and Renewable Energy Engineering, University of New South Wales, NSW 2052 Sydney, Australia*
[3)] *DTU CEN, Center for Electron Nanoscopy, DK-2800 Kgs. Lyngby, Denmark*
[4)] *School of Chemistry, University of New South Wales, NSW 2052 Sydney, Australia*
[5)] *DTU Fotonik, Technical University of Denmark, DK-4000 Roskilde, Denmark*
[6)] *V-SUSTAIN, Villum Center for the Science of Sustainable Fuels and Chemicals, Technical University of Denmark, DK-2800 Kgs. Lyngby, Denmark*

We report a reproducible enhancement of the open circuit voltage in Cu_2ZnSnS_4 solar cells by introduction of a very thin CeO_2 interlayer between the Cu_2ZnSnS_4 absorber and the conventional CdS buffer. CeO_2, a non-toxic earth-abundant compound, has nearly optimal band alignment with Cu_2ZnSnS_4 and the two materials are lattice-matched within 0.4%. This makes it possible to achieve an epitaxial interface when growing CeO_2 by chemical bath deposition at temperatures as low as 50°C. The open circuit voltage improvement is then attributed to a decrease in the interface recombination rate through formation of a high-quality heterointerface.

$Cu_2ZnSn(S,Se)_4$ compounds are among the materials that are currently considered as potentially suitable for terawatt-scale solar energy production. The pure-sulfide material Cu_2ZnSnS_4 (CZTS) is particularly interesting because it avoids the relatively scarce element Se and it has a larger band gap (1.5 eV) which is appropriate both for a single-junction solar cell and for a top absorber in a tandem solar cell architecture.[1] Even though its highest reported power conversion efficiency so far (9.1%) was achieved with a CdS heterointerface partner, or buffer layer,[2] interface recombination is still the dominant voltage loss mechanism in the solar cell,[3] which suggests that CdS is not the ideal partner of CZTS. Despite promising results achieved with (Zn,Cd)S and (Zn,Sn)O buffer layers,[4,5] no alternative materials to date have outperformed the highest efficiency[2] or the highest open circuit voltage[6] achieved with a CdS heterojunction partner.

The open circuit voltage V_{oc} of a solar cell limited by interface recombination can be expressed as

$$V_{oc} = \frac{E_i}{q} - \frac{kT}{q} \ln\left(\frac{q S_p N_v}{J_{sc}}\right) \qquad (1)$$

for a p-type absorber with an inverted heterointerface, i.e., with holes as minority carriers at the interface.[7] E_i is the interface band gap, q is the elementary charge, k is Boltzmann's constant, T is temperature, N_v is the effective density of states in the valence band, J_{sc} is the short circuit current, and S_p is the interface recombination velocity of holes. By modeling interface recombination as Shockley-Read-Hall recombination through a single interface defect level, S_p can be expressed as

$$S_p = N_i \sigma_p v_{th} \qquad (2)$$

where N_i is the area density of interface defects, σ_p is a cross section describing how efficiently the holes are captured by the defect, and v_{th} is the thermal velocity.

Eqs. 1, 2 show that decreasing the interface defect density N_i can be a way to improve the open circuit voltage in a solar cell limited by interface recombination. By analogy to high-efficiency solar cell technology based on III-V semiconductors,[8] this can be achieved by ensuring epitaxial growth of the buffer material on the absorber material. In the absence of epitaxial growth, a large density of atomic dislocations will exist at the interface, which leads to formation of allowed electronic states within the interface band gap, thus increasing N_i and enhancing interfacial Shockley-Read-Hall recombination. Epitaxial growth is facilitated by a small lattice mismatch between the two heterojunction materials.[8] While CdS has a reasonably small lattice mismatch with some absorber materials such as $Cu(In,Ga)Se_2$ ($\sim$ 1.5%) and $Cu_2ZnSnSe_4$ ($\sim$ 2.4%), its mismatch with CZTS is much larger ($\sim$ 7%). A high value of N_i can therefore be anticipated at the CZTS/CdS interface.

To address this problem, we carry out an initial investigation of the non-toxic, earth abundant material[9] CeO_2 as a heterojunction partner of CZTS. CeO_2 has a nearly perfect lattice match[10] with CZTS (lattice constant of CZTS: 5.43 Å; lattice constant of CeO_2: 5.41 Å; thus a lattice mismatch under 0.4%). This opens the possibility for a high-quality epitaxial interface, which may alleviate the interface recombination problem. CeO_2 also has a wide indirect band gap[11,12] of 3.3 eV, which minimizes parasitic light absorption. We note that, based on Eq. 1, the lattice mismatch at the CeO_2/CdS interface is not expected to limit V_{oc}, since E_i is much larger at the CeO_2/CdS interface than at the CZTS/CeO_2 interface.

CZTS films were prepared by co-sputtering Cu/ZnS/SnS precursors on Mo-coated soda lime glass using a magnetron sputtering system (AJA Inter-

[a)] Electronic mail: ancro@nanotech.dtu.dk
[b)] Electronic mail: xj.hao@unsw.edu.au

national, Inc., model ATC-2200) as presented in detail before.[13] Two types of elemental compositions were targeted in different CZTS precursors within the same batch: the first (C1) with Cu/Sn = 1.9 and Zn/Sn = 1.25; the second (C2) with Cu/Sn = 1.8 and Zn/Sn = 1.25. C1 and C2 were chosen because the final solar cell efficiency is very sensitive to the sample stoichiometry, especially to the Cu/Sn ratio.[14] These precursors were then annealed using Rapid Thermal Processor (AS-One 100) in a S- and Sn-containing atmosphere at 560°C. The S atmosphere compensates for S substoichiometry in the precursors and the addition of Sn stabilizes CZTS against decomposition reactions.[15] CeO_2 films were deposited on CZTS by chemical bath deposition (CBD) at 50°C in a weakly acidic solution (pH: 6) containing 10 mM $Ce(CH_3COO)_3$ and 5 mM $KClO_3$ in Milli-Q water under mild stirring. The expected chemical reactions resulting in thin film deposition are those presented in previous work.[16] CdS (60 nm) was deposited by CBD with a previously described process.[13] ZnO (60 nm) and indium tin oxide (ITO, 200 nm) layers were deposited by RF magnetron sputtering, followed by an Al contact grid. No anti-reflection coating was applied. The total area of the final cells (0.23 cm^2) was defined by mechanical scribing. Three different solar cell architectures were fabricated in this work as shown in Fig. 1. In the first architecture (A1), CdS is completely replaced by a stand-alone 30 nm CeO_2 buffer layer deposited with a 100 min process. In the second architecture (A2), a thin CeO_2 layer of estimated thickness between 1 and 5 nm is inserted between CZTS and the standard CdS buffer layer using a 10-20 min deposition process. The reference architecture (Fig. 1) is a conventional CZTS solar cell structure without CeO_2. Only very weak n-type conductivity has been reported[17] for CeO_2 and, in fact, the resistivity of the films synthesized in this work was too high to be measured with conventional four-point probe apparatus. Therefore, the CeO_2 layer in the solar cell can be regarded as completely depleted. In the case of architecture A2, the CeO_2 layer is so thin that it is not expected to modify significantly the original electric field profile of the reference architecture. Scanning electron microscope images were taken with a FEI-Nova NanoSEM 450 instrument at 2 kV beam voltage. High-resolution bright-field transmission electron microscope images (HRTEM) were taken with a FEI-Titan 80-300 TEM, at 300 kV beam voltage. X-ray photoelectron spectroscopy (XPS) was performed with a Thermo Scientific K-Alpha instrument with a monochromatized Al K_α x-ray source. The binding energy scale was calibrated using the adventitious C 1s peak at 284.8 eV. An electron flood source was employed to limit charging effects in CeO_2.[18] CeO_2 was found by others to be reduced to Ce_2O_3 both under prolonged x-ray exposure[19] and under ion beam sputtering.[18] Indeed, by inspection of the Ce 3d spectrum and of the valence band edge, reduction effects were evident in our films even at the lowest ion beam energy (200 eV) available in the XPS
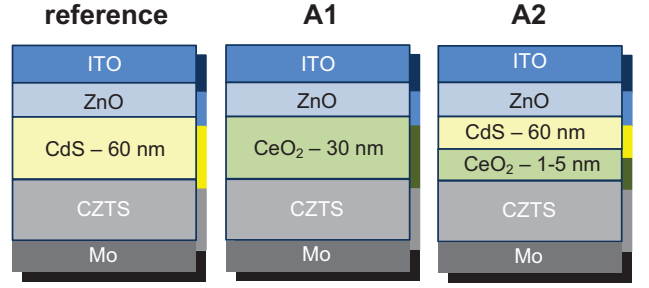

FIG. 1. Schematic drawing of the A1 architecture with a 30 nm stand-alone CeO_2 buffer layer and the A2 architecture with a 1-5 nm CeO_2 interlayer between CZTS and CdS. The reference architecture is a standard CZTS solar cell structure.

setup. Therefore no sputter cleaning was performed on our samples. XPS data analysis was performed with the Avantage 5.948 software (Thermo Scientific). Current-voltage (JV) characteristics on finished devices were measured under AM 1.5G illumination with a solar simulator from PV Measurement and a Keithley 2400 source meter calibrated with a standard Si reference.

Before discussing solar cell results, we want to answer some basic questions about the quality of deposited CeO_2 films. The first question is adhesion. By depositing CeO_2 on glass/Mo substrates, it was found that the films deposited from a solution with a $KClO_3$ concentration of 10 mM or above were easily peeled off by scotch tape. However, already at a $KClO_3$ concentration of 5 mM, the films were strongly adherent with no peel-off by repeated scotch tape application. A $KClO_3$ concentration of 5 mM was therefore chosen for the deposition process. The maximum CeO_2 thickness on CZTS that could be achieved in a single chemical bath deposition run was about 30 nm with a 100 min process (Fig. S1(a)).

The second question is whether the deposited film indeed consists of the desired CeO_2 material. The fast Fourier transform (FFT) of cross-sectional TEM images of the deposited film yields a pattern that is compatible with CeO_2 and not with the main competing phase Ce_2O_3 (Fig. 2(c)). However, TEM analysis involves very small regions (few nm). Raman spectroscopy was then performed over a much larger analysis area (about 2 μm diameter). Only one additional Raman peak at 461 cm^{-1} was revealed on CZTS/CeO_2 bilayers compared to a bare CZTS spectrum (Fig. S2). The peak corresponds to the first-order-allowed Raman mode of CeO_2, with a small red shift due to size effects.[20] Finally, XPS characterization was performed over an even larger analysis area (about 400 μm diameter). All the XPS peaks corresponding to Ce 3d core levels were fitted and attributed to either CeO_2 or Ce_2O_3 according to reference spectra[21] (Fig. S3). The fraction of CeO_2 present in the deposited film is estimated as 70.4% with this method. Hence, some Ce_2O_3 inclusion should be expected. Since Ce_2O_3 is not lattice-matched to CZTS and it has a band gap[12] almost 1 eV lower than that of CeO_2, we assume that Ce_2O_3
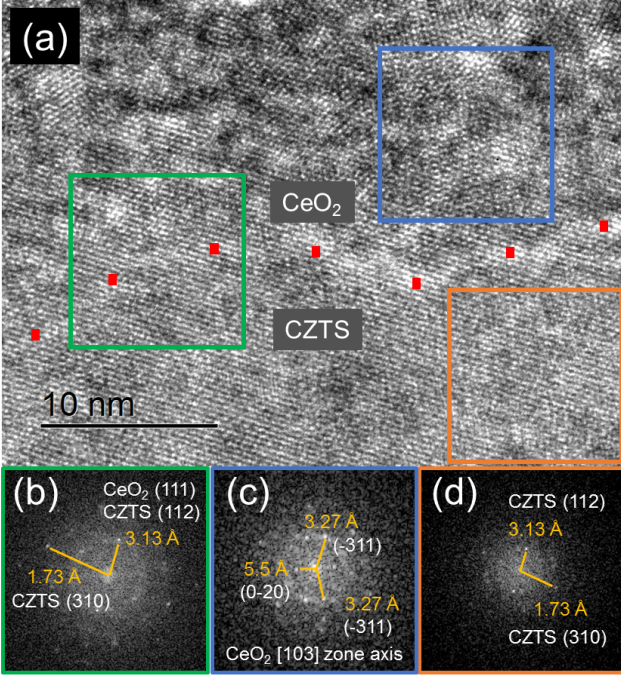
FIG. 2. (a) Cross-sectional HRTEM image across the interface between CeO_2 (top) and CZTS (bottom). (b) FFT of a selected region across the interface. A reflection at 3.13 Å is visible, corresponding to the distance between (111) planes of CeO_2 and between the (112) planes of CZTS. (c) FFT of a selected region within CeO_2. The diffractogram can be indexed as a CeO_2 crystal along with [103] as zone axis. (d) FFT of a selected region within CZTS. Reflections corresponding to the (112) and (310) planes are visible.
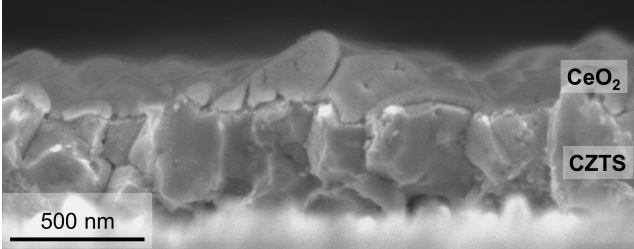

FIG. 3. Cross sectional SEM image of a CeO_2 film grown on CZTS used for architecture A1. The film is about 30 nm thick, which is the maximum thickness that could be achieved with a single CBD process in this work. Some scattered pinholes and inhomogeneous coverage of the grain boundaries are seen.

inclusions promote interface recombination and limit the open circuit enhancement that could be achieved with a pure CeO_2 layer.

The third question is whether the deposited film provides complete coverage of the underlying CZTS layer. SEM images of a 30 nm-thick CeO_2 film (Fig. 3) show some non-uniform coverage in correspondence of CZTS grain boundaries and some smaller isolated dips in the CeO_2 film profile, which may be interpreted as pinholes.
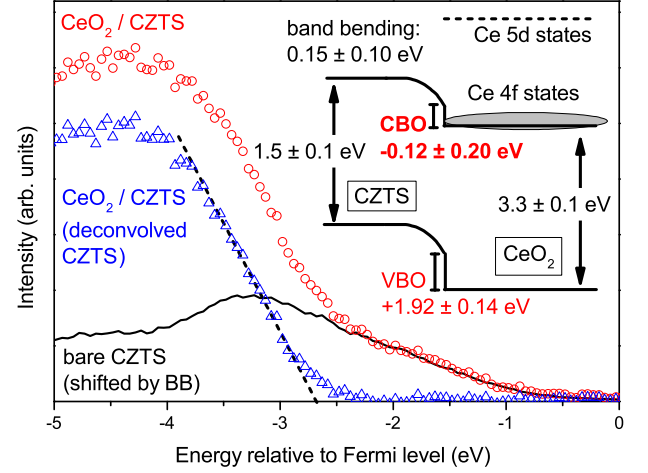

FIG. 4. $CZTS/CeO_2$ band alignment extracted by XPS. The valence band maximum (VBM) of CZTS with respect to the Fermi level is -0.60 ± 0.10 eV in a bare CZTS sample and -0.75 ± 0.10 eV in a CZTS sample coated with a thin CeO_2 layer (20 min deposition time, red circles). From this, band bending (BB) in CZTS is estimated as 0.15 ± 0.10 eV. This is also confirmed from the average shift in the Cu 2p, Zn 2p, and Sn 3d core levels between the bare CZTS sample and the $CeO_2/CZTS$ sample. Shifting the XPS spectrum of the bare CZTS sample by the BB (black line) allows deconvolution of the CeO_2 valence band signal (blue triangles), located -2.67 ± 0.10 eV below the Fermi level. The shifted spectrum of bare CZTS (black line) fits well with the $CeO_2/CZTS$ spectrum until the onset of the CeO_2 valence band, as expected.

The area fraction of CZTS that is covered by CeO_2 can be estimated by comparing the peak intensity of Ce, Cu, Zn, and Sn core levels by XPS, as explained in the Supplementary Material. The covered area is then estimated as 62%, 94% and 95% for the films deposited for 20, 60, and 90 min, with estimated thicknesses 1-5, 15, and 25 nm, respectively. Thus, it seems as if the very thin films (20 min deposition time) employed in architecture A2 may have rather poor coverage. However, in that case the CeO_2 thickness is comparable to the XPS probing depth (about 2 nm). Therefore, part of the CZTS signal is likely to originate from CZTS buried under CeO_2 so that the covered fraction is in reality higher. The consequence of incomplete coverage is simply the coexistence of $CZTS/CeO_2$ and CZTS/CdS heterojunctions in parallel in the solar cells.

The fourth question is whether CeO_2 forms an epitaxial interface with CZTS, as may be expected by their excellent lattice match. The HRTEM image in Fig. 2(a) shows that the atomic arrangement on the CZTS side continues on the CeO_2 side for a few nm, thus demonstrating that an epitaxial interface *can* be achieved despite the low deposition temperature. Analysis of the FFT pattern across the interface (Fig. 2(b)) reveals that epitaxy occurs along the $CZTS(112)$-$CeO_2(111)$ direction, similarly to what was recently observed on a
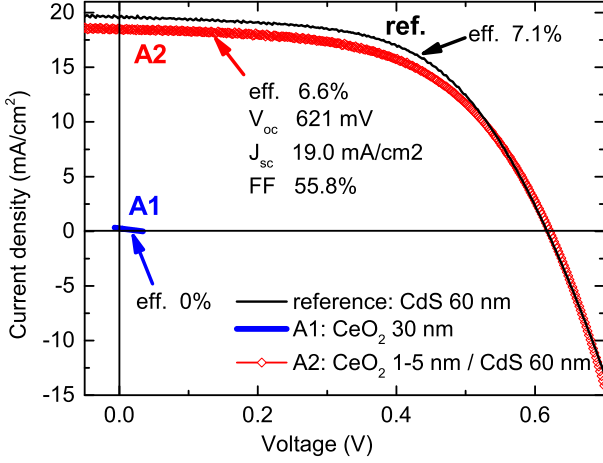
FIG. 5. Illuminated current-voltage characteristics of the best solar cells with the A1 and A2 architectures, together with the best solar cell with the reference architecture.
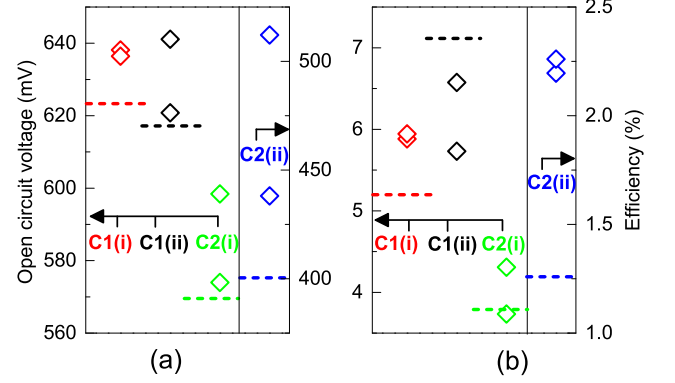

FIG. 6. Comparison of open circuit voltage (a) and conversion efficiency (b) between solar cells with the A2 architecture (diamond data points) and a reference solar cell with a pure CdS buffer layer (dashed line) within the same batch. C1 and C2 are two different CZTS compositions; (i) and (ii) are two different batches. Each data point represents the highest-efficiency solar cell within a chip containing 12 devices.

CZTS/CdS interface.[22] A few nm away from the interface, CeO_2 is nanocrystalline with average grain size less than 5 nm, as inferred from TEM images (Fig. 2(a)) and by quantitative analysis of Raman peak broadening (Fig. S2). We emphasize, however, that epitaxial growth was *not* observed at most interface locations imaged by TEM in this work, as shown for example in Fig. S1(b).

The fifth and final question is the band alignment of CeO_2 with CZTS. It is well known that a moderate spike-like conduction band offset (CBO) at the heterointerface, in the 0-0.4 eV range, is optimal as it reduces interface recombination without blocking photocurrent transport.[23] The valence band offset (VBO) was estimated by XPS as shown in Fig. 4. The experimental (bulk) band gaps of the two materials were then added to the VBO to finally obtain a CBO of -0.12 ± 0.20 eV. For the CeO_2 indirect gap, we used a value of 3.3 ± 0.1 eV measured by internal photoemission yield.[11] The extracted CBO is only slightly below the optimal range and it is actually more favorable than the previously measured CZTS/CdS band offset.[24] Considering the many possible sources of error in the measurement, including the use of as-deposited surfaces for analysis, this is considered a promising result. We also note that the CeO_2 Fermi level lies about 2.7 eV above the valence band, which indicates that CeO_2 is n-type in the analysis region, similarly to previous reports.[21,25]

The current-voltage characteristics of the three best solar cells fabricated with the three different architectures are shown in Fig. 5. A small improvement in open circuit voltage is achieved by architecture A2 with respect to the reference architecture. The accompanying degradation in short circuit current will be discussed in the following. Interestingly, the statistics shown in Fig. 6 indicate that the V_{oc} boost is reproducible over two separate batches (i) and (ii) regardless of precursor composition (C1 or C2). In all those cases, the open circuit voltage

of the solar cells with A2 architecture is always between 20 mV and 100 mV higher than in the corresponding solar cells with the standard CdS architecture. Additional statistics in Fig. S6 confirm this trend. The highest open circuit voltage achieved in this study with the A2 architecture was 641 mV, and the highest efficiency was 6.6% (Fig. 5). Conversely, complete current blocking and no photovoltaic effect was observed in the solar cells with a stand-alone CeO_2 buffer layer (architecture A1 in Fig. 5).

To interpret these results, we refer to the band structure of CeO_2.[12] What has been referred to as the "conduction band" in this work is a band consisting of highly localized Ce 4f states, 3.3 eV above the valence band as mentioned before.[11] However, localization of states in this band implies that the electron effective mass is very high, and hence the electron mobility is very low. This can be inferred by a nearly complete lack of dispersion of those states in reciprocal space.[12] For this reason, a band consisting mostly of Ce 5d states, which lies about 6 eV above the valence band and has lighter effective masses, is often quoted as the conduction band of CeO_2. From our band alignment study (Fig. 4), we found that the 4f band has a nearly optimal CBO with the CZTS conduction band, while the 5d band lies at much higher energy. Then, we can attribute the complete lack of photocurrent in architecture A1 to the very poor transport properties of the 4f band. A 30 nm CeO_2 layer is therefore thick enough to completely impede electron transport. Instead, when CeO_2 is very thin as in architecture A2 (1-5 nm), short circuit current and fill factor losses are greatly diminished and in some cases eliminated (Fig. 5) and Fig. S5). This is possibly due to tunneling-based transport between the CZTS and CdS conduction bands through the thin interlayer. Residual current losses, as in Fig. 5, are probably due to thickness inhomogeneity

of CeO_2, or to the fact that an even thinner layer is necessary. Growth of CeO_2 by atomic layer deposition may be beneficial in this respect.

We conclude that inserting a thin lattice-matched CeO_2 layer between CZTS and CdS alleviates interface recombination and results in a reproducible open circuit voltage boost in the solar cell. This is attributed to the formation of a high-quality $CZTS/CeO_2$ heterointerface, with instances of epitaxial growth observed in some regions. We suggest that the open circuit voltage could be further improved if epitaxy could be obtained on a larger scale, if Ce_2O_3 inclusions could be decreased, and if surface coverage could be improved. Etching the CZTS surface immediately prior to CeO_2 deposition may facilitate formation of an epitaxial interface. It should be kept in mind that the very large electron effective mass in the CeO_2 conduction band puts a severe constraint on the maximum thickness of the CeO_2 film, which should only be a couple of nm thick in order to avoid dramatic current losses.

SUPPLEMENTARY MATERIAL

See supplementary material for additional TEM images, phase analysis of the CeO_2 layer, compositional analysis across the interface, estimation of CeO_2 coverage, and more detailed statistics on the solar cell parameters for the reference architecture and architecture A2.

ACKNOWLEDGMENTS

[1] M. A. Green, Nat. Energy **1**, 1 (2016).

[2] S. Tajima, T. Itoh, H. Hazama, K. Ohishi, and R. Asahi, Appl. Phys. Express **8**, 082302 (2015).

[3] M. Courel, J. A. Andrade-Arvizu, and O. Vigil-Galán, Applied Physics Letters **105**, 233501 (2014).

[4] K. Sun, C. Yan, F. Liu, J. Huang, F. Zhou, J. A. Stride, M. Green, and X. Hao, Adv. Energy Mater. **6**, 1600046 (2016).

[5] C. Platzer-Björkman, C. Frisk, J. K. Larsen, T. Ericson, S.-Y. Li, J. J. S. Scragg, J. Keller, F. Larsson, and T. Törndahl, Appl. Phys. Lett. **107**, 243904 (2015).

[6] H. Hiroi, N. Sakai, T. Kato, and H. Sugimoto, in *2013 IEEE 39th Photovoltaic Specialists Conference (PVSC)* (IEEE, 2013) pp. 0863–0866.

[7] U. Rau and H. Schock, Appl. Phys. A **69**, 131 (1999).

[8] D. J. Friedman, J. M. Olson, and S. Kurtz, in *Handbook of Photovoltaic Science and Engineering*, edited by A. Luque and S. Hegedus (John Wiley & Sons, Ltd, Chichester, UK, 2011) 2nd ed., Chap. 8, p. 338.

[9] U.S. Geological Survey, Fact Sheet 087-02 (2005).

[10] M. Yashima, S. Kobayashi, and T. Yasui, Solid State Ionics **177**, 211 (2006).

[11] V. V. Afanas'ev, S. Shamuilia, A. Stesmans, A. Dimoulas, Y. Panayiotatos, A. Sotiropoulos, M. Houssa, and D. P. Brunco, Appl. Phys. Lett. **88**, 132111 (2006).

[12] R. Gillen, S. J. Clark, and J. Robertson, Phys. Rev. B **87**, 125116 (2013).

[13] C. Yan, F. Liu, K. Sun, N. Song, J. A. Stride, F. Zhou, X. Hao, and M. Green, Sol. Energy Mater. Sol. Cells **144**, 700 (2016).

[14] C. Yan, K. Sun, F. Liu, J. Huang, F. Zhou, and X. Hao, Sol. Energy Mater. Sol. Cells **160**, 7 (2017).

[15] A. Redinger, D. M. Berg, P. J. Dale, and S. Siebentritt, J. Am. Chem. Soc. **133**, 3320 (2011).

[16] H. Unuma, T. Kanehama, K. Yamamoto, K. Watanabe, T. Ogata, and M. Sugawara, J. Mater. Sci. **38**, 255 (2003).

[17] R. N. Blumenthal and R. L. Hofmaier, J. Electrochem. Soc. **121**, 126 (1974).

[18] D. Mullins, S. Overbury, and D. Huntley, Surf. Sci. **409**, 307 (1998).

[19] E. Paparazzo, G. M. Ingo, and N. Zacchetti, J. Vac. Sci. Technol. A **9**, 1416 (1991).

[20] G. Graham, W. Weber, C. Peters, and R. Usmen, J. Catal. **130**, 310 (1991).

[21] Y. Zhu, N. Jain, M. K. Hudait, D. Maurya, R. Varghese, and S. Priya, J. Vac. Sci. Technol. B **32**, 011217 (2014).

[22] F. Liu, C. Yan, J. Huang, K. Sun, F. Zhou, J. A. Stride, M. A. Green, and X. Hao, Adv. Energy Mater. **6**, 1600706 (2016).

[23] M. Gloeckler and J. Sites, Thin Solid Films **480-481**, 241 (2005).

[24] C. Yan, F. Liu, N. Song, B. K. Ng, J. A. Stride, A. Tadich, and X. Hao, Appl. Phys. Lett. **104**, 173901 (2014).

[25] H. F. Wardenga and A. Klein, Appl. Surf. Sci. **377**, 1 (2016).

Lattice-matched Cu$_2$ZnSnS$_4$/CeO$_2$ solar cell with open circuit voltage boost

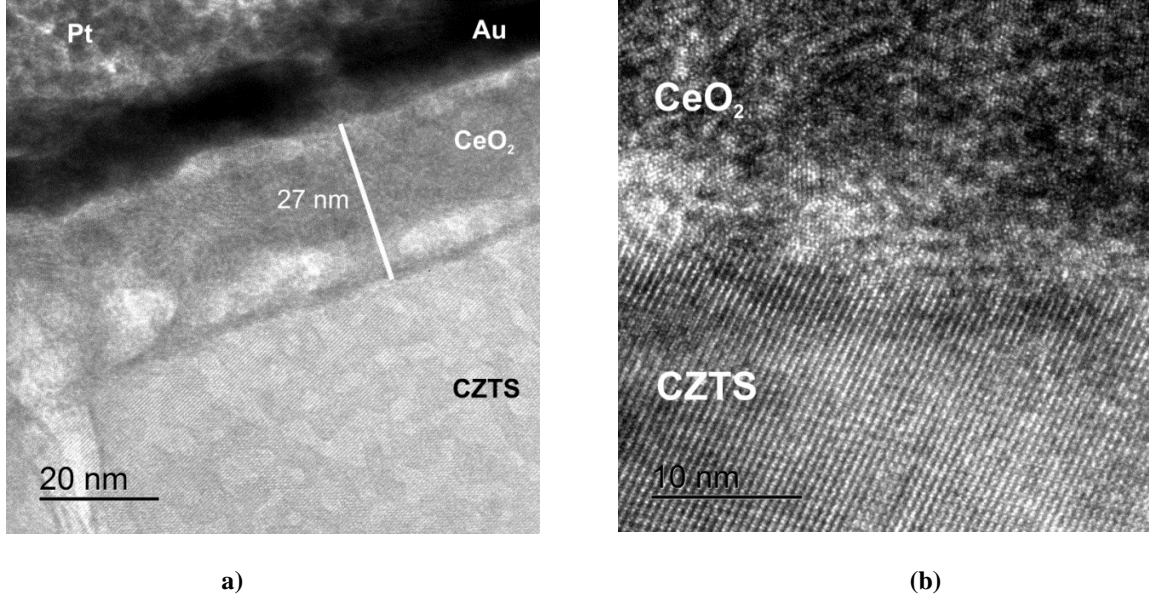A. Crovetto, C. Yan, B. Iandolo, F. Zhou, J. Stride, J. Schou, X. Hao, O. Hansen

a)   **(b)**

Fig. S1: Cross-sectional TEM images at the CZTS/CeO$_2$ interface of a sample where CeO$_2$ was deposited for 100 min. **(a)** Low-magnification image showing the approximate maximum thickness of the CeO$_2$ layer achievable by the deposition recipe employed in this work. The Au and Pt layers were deposited to avoid charging and image drift when preparing the cross-sectional TEM sample by focused ion beam. **(b)** High-magnification image showing a region without any epitaxial growth. The CeO$_2$ layer is nanocrystalline with average grain size estimated around 3 nm.
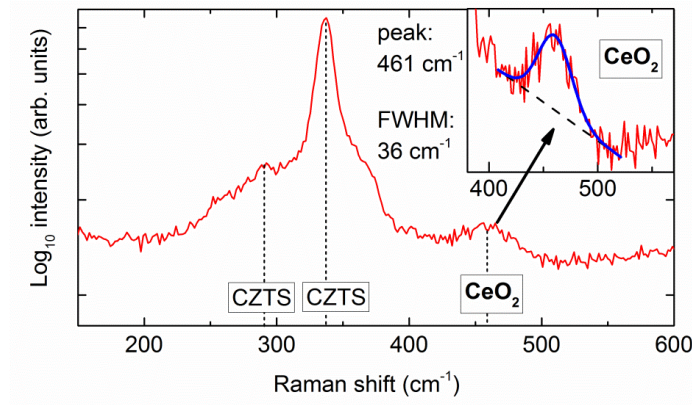
Fig. S2: Raman spectrum of a on a 30-nm CeO$_2$ film on CZTS taken with a Renishaw inVia instrument at a laser wavelength of 514 nm. Besides the characteristic peaks of CZTS, a peak at 461 cm^{-1} is present, which can be attributed to the first-order-allowed Raman mode of CeO$_2$ (reference 15 in the main article). The full-width-half-maximum (FWHM) of 36 cm^{-1} for the CeO$_2$ peak allows indirect estimation of a crystallite size of roughly 4 nm (reference 15 in the main article), which is compatible with the direct TEM results (Fig. S1(b)).

Fig. S3: Binding energy of the Ce 3d core levels measured by XPS on a 30-nm CeO_2 film on CZTS, as in architecture A1. The spectrum (black dots) is fitted with nine pseudo-Voigt peaks over a Shirley background. Each peak is assigned either to the desired CeO_2 phase (red) or to an unwanted Ce_2O_3 phase (blue) based on the well-known core level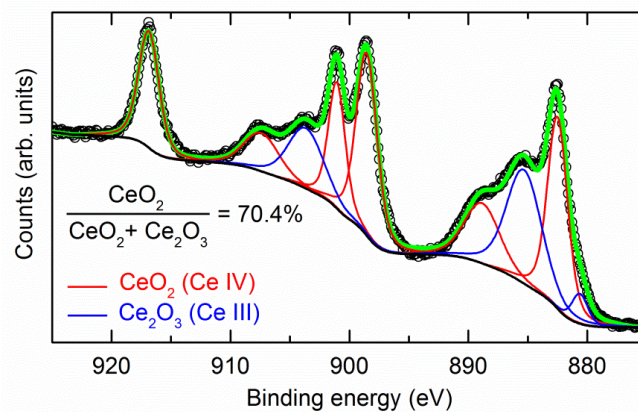 positions of each compound (reference 16 in the main text). The resulting phase composition is derived by summing the integrated area of all the peaks belonging to each oxidation state.
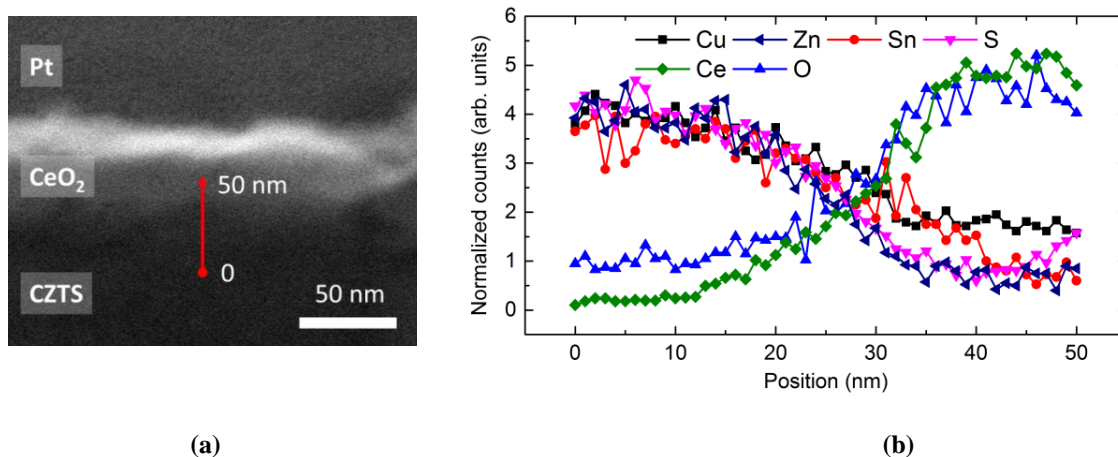

(a)   **(b)**

Fig. S4: **(a)** Scanning transmission microscope (STEM) image of the CZTS/CeO_2 interface. **(b)** Energy-dispersive X-ray spectroscopy (EDX) line scan performed along the line highlighted in Fig. S4(a). STEM/EDX analysis was performed with the same microscope used for TEM imaging (FEI-Titan 80-300 TEM) at 300 kV beam voltage. The EDX line scan was performed with a step size of 1 nm using an INCA x-sight detector (Oxford Instruments) with an integration time of 20 s for each spectrum. EDX spectra were fitted using the TEM Imaging and Analysis software v. 4.2 (FEI).

Procedure for the estimation of CZTS coverage by CeO_2 using XPS

Due to the nearly identical lattice constants of CeO_2 and CZTS, the relative volume fraction of CeO_2 within the XPS probing depth (about 2 nm) can be simply estimated by quantifying the overall atomic composition of the cations of the two materials. Based on the chemical formulas of the two compounds, the expression

$$\frac{3Ce}{3Ce + 2(Cu + Zn + Sn)}$$

can be used to evaluate the fraction of CeO_2 with respect to the total composition. Ce, Cu, Zn, and Sn are the integrated intensities of the Ce 3d, Cu 2p, Zn 2p, and Sn 3d core levels multiplied by a sensitivity factor typical of each peak, which is taken from the XPS analysis software database.
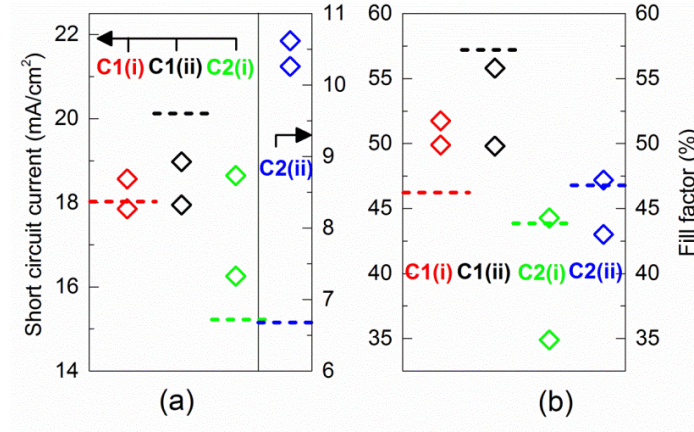
Fig. S5: Comparison of short circuit current **(a)** and fill factor **(b)** between solar cells with the A2 architecture (diamond data points) and a reference solar cell with a pure CdS buffer layer (dashed line) within the same batch. C1 and C2 are two different CZTS compositions; (i) and (ii) are two different batches. Each data point represents the <u>highest-efficiency</u> solar cell within a chip containing 12 devices.
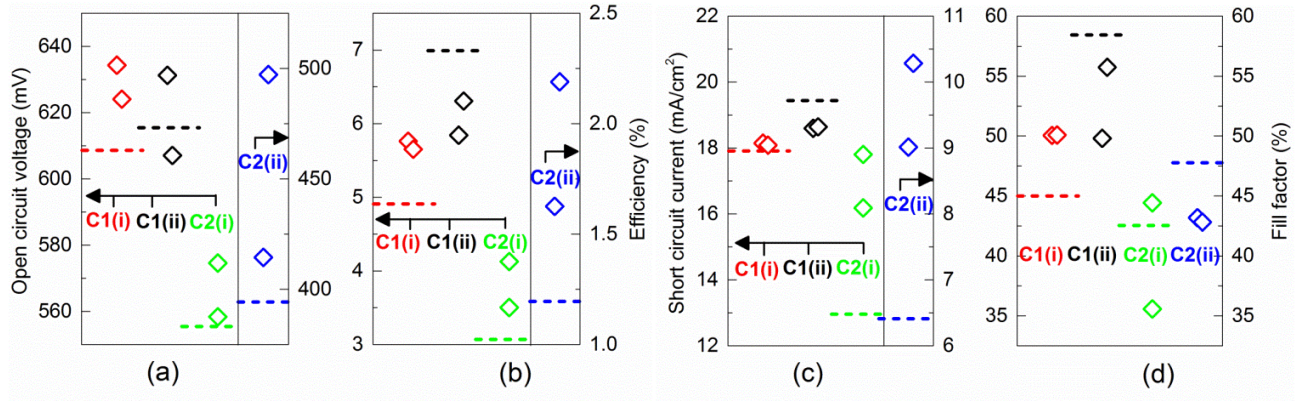
Fig. S6: Comparison of open circuit voltage **(a)**, conversion efficiency **(b)**, short circuit current **(c)** and fill factor **(d)** between solar cells with the A2 architecture (diamond data points) and a reference solar cell with a pure CdS buffer layer (dashed line) within the same batch. C1 and C2 are two different CZTS compositions; (i) and (ii) are two different batches. Each data point represents the <u>average value from the five best solar cells</u> within a chip containing 12 devices.

Chapter 4

Aspects of the heterointerface physics of CZTS solar cells

Let him who hath understanding
reckon the number of the beast
Iron Maiden, 1982

4.1 Study 4.1: What is the real band alignment of CZTS solar cells?

- <u>Crovetto A</u> and Hansen O, What is the band alignment of $Cu_2ZnSn(S,Se)_4$ solar cells?, under preparation

The conduction band offset (CBO) at the heterointerface is a parameter of crucial importance for maximizing the efficiency of any heterojunction solar cell [53]. However, the actual CBO of the CZTS/CdS interface is still debated, as different measurements and calculations carried out by many groups have yielded contradictory results. Here I present a review, combined with my own analysis, of the band alignment of the CZTS/CdS and CZTSe/CdS interfaces. I compile all the experimental and theoretical values I am aware of and propose some reasons why those values are often contradictory. I argue that state-of-the-art CZTS solar cells probably do *not* have an unfavorable band alignment.

My contribution (detailed):
• Idea for the study, literature review, analysis, and development of all theories presented in the manuscript • Writing the full manuscript
Coauthors' contribution (brief):
• O. Hansen: discussions and commenting the manuscript;

4.2 Study 4.2: A new band alignment calculation method applied to the CZTS/CdS interface

- Palsgaard M L N, <u>Crovetto A</u>, Gunst T, Markussen T, Hansen O, Stokbro K and Brandbyge M, 2016 Semiconductor band alignment from first principles: a new nonequilibrium Green's function method applied to the CZTS/CdS interface for photovoltaics, *2016 International Conference on Simulation of Semiconductor Processes and Devices (SISPAD),* pp 377–380

There are several methods to calculate the band alignment from first principles [184]: some are based on purely bulk properties of the two materials, other explicitly construct an interface consisting of some unit cells of both materials placed next to each other. The latter approach has given convincing results [172] but the size of the interface region ("supercell") that can be modeled at a reasonable computational cost is often too small to separate the effect of interface states from the "true" band edges when looking at the calculated density of states at the interface. Therefore, when using those methods, one cannot extract the CBO directly from the interface calculation. Instead, it is necessary to extract the energy difference between the core levels of the two materials in the interface calculation and use those to align the VBM and CBM found in separate bulk calculations to a common energy reference. While this trick allows calculation of the band offsets indirectly, the actual electronic structure of the interface is not clearly revealed due to the small supercell size. In this study, PhD student Mattias Palsgaard tries to overcome this limitation by employing a less computationally demanding approach that allows a much larger supercell size. Pure interface states can then be separated from bulk states and interface band bending can be explicitly modeled, so atomistic simulation starts to look more like true device simulation. The effect of adding a certain doping density in the materials and applying a voltage bias are also discussed.

My contribution (detailed):
• Proposal of collaboration with theoreticians and preliminary device-level simulation (Figure 1(a,b)) • Support and advice on the device-relevance and the overall direction of the atomistic study • Idea for the calculation under forward bias to obtain flat-band conditions • Writing the bulk of the introduction and some passages of the other sections • Commenting the manuscript

4.3 Study 4.3: Surface states behind open circuit voltage losses in CZTS solar cells

- Crovetto A, Palsgaard M L N, Gunst T, Markussen T, Stokbro K, Brandbyge M and Hansen O, Interface gap narrowing behind open circuit voltage losses in Cu_2ZnSnS_4 solar cells, submitted

The previous study described a method to discern interface properties from bulk properties. Here is where the actual fun starts, as we take advantage of the strengths of that method to look at the differences in the interface properties of CZTS and CZTSe when they are coupled to a CdS buffer layer. By performing the same calculation on the CZTS/CdS interface and on the CZTSe/CdS interface, a significant difference occurs. Localized electronic states, which are not present in the CZTS(e) bulk, pop up in the band gap at the interface, just above the valence band of the bulk absorber: this occurs in CZTS but not in CZTSe. Those states are not related to formation of the specific interface with CdS, but are simply a surface modification of the CZTS band structure that shifts its valence band upwards at the surface, thus narrowing the band gap there. This mechanism can have very interesting consequences on the device physics of CZTS solar cells. I show by device simulation that band gap narrowing due to the presence of the surface states can explain, even quantitatively, why E_A in CZTS solar cells is always found to be lower than the band gap when a CdS buffer layer is used, *without assuming a cliff-like band alignment*. Excitingly, the first-principles calculations predict that Zn is able to passivate the surface states, thus opening a possible path to V_{oc} improvement in CZTS solar cells by using a Zn-based chalcogenide as an interface passivation layer.

My contribution (detailed):
• Interpretation of the surface state as potentially detrimental for solar cell performance

60

• Modeling the surface state as a simple valence band upshift. • Idea and execution of device-level simulation (temperature-dependent open circuit voltage) to confirm the effect of the surface state and its compatibility with experiment • Simulated band structure and carrier population versus position • Writing most of the manuscript

Coauthors' contribution (brief):

• M. Palsgaard: execution and analysis of all DFT calculations, and idea of associating bulk CZTS point defects to the first atomic layer of the heterojunction partner; • T. Gunst, T. Markussen: technical assistance with DFT calculations and discussions; • O. Hansen, K. Stokbro, M. Brandbyge: discussions and commenting the manuscript;

4.4 Study 4.4: The relative permittivity of heterojunction solar cell materials

- <u>Crovetto A</u>, Huss-Hansen M K and Hansen O, How the relative permittivity of heterojunction solar cell materials influences solar cell performance, submitted

This study is about what I consider an often forgotten detail in heterojunction solar cells in general. In books and articles on the physics and design principles of solar cells, the relative permittivity of solar cell materials is often overlooked when discussing the "optimal" parameters of heterojunction solar cells. Is that justified? The study I present in this manuscript tries to answer that question. I became curious about the subject after B.Sc. student Mattias Huss-Hansen showed me that the relative permittivity was the parameter that affected the efficiency the most when he tried to simulate different buffer layers in a CIGS solar cell. I found that quite surprising so, after he was done with his thesis, I dug a bit more into the subject as a side project. While there are indeed a number of situations where the buffer permittivity is nearly irrelevant, I concluded that useful design rule does exist: a high buffer permittivity with respect to the absorber permittivity ensures the most robust design of the solar cell against a number of non-idealities. Since CZTS has a rather low permittivity (around 7), this design rule is easily satisfied, as most buffer layer materials (including CdS) have permittivities above 9.

My contribution (detailed):

• Idea for the study, development of the baseline parameters, execution, and analysis of device simulation • Writing the full manuscript

Coauthors' contribution (brief):

• M. K. Huss-Hansen: preliminary device simulation studies; • O. Hansen: discussions and commenting the manuscript;

What is the band alignment of Cu$_2$ZnSn(S,Se)$_4$ solar cells?

Andrea Crovetto[a,*], Ole Hansen[a,b]

[a]*DTU Nanotech, Technical University of Denmark, DK-2800 Kgs. Lyngby, Denmark*
[b]*V-SUSTAIN, Villum Center for the Science of Sustainable Fuels and Chemicals, Technical University of Denmark, DK-2800 Kgs. Lyngby, Denmark*

Abstract

By analyzing published data on the band alignment at the Cu$_2$ZnSn(S,Se)$_4$/CdS solar cell heterojunction, we argue that two physical mechanisms play a major role in the large deviation of the reported conduction band offsets. The first is Fermi level pinning, which tends to decrease the conduction band offset. The second is interdiffusion across the heterointerface, which tends to increase the conduction band offset and can, to some extent, be controlled to engineer the desired band alignment through interface phase formation. Presence of polar interfaces, quantum confinement in the CdS seed layer, and formation of an epitaxial interface possibly play a significant role in the band alignment as well, but their effects are, for now, rather difficult to quantify. The above mechanisms result in genuine variations in the conduction band offset depending on preparation conditions, as well as in errors in its experimental determination due to the mismatch between the bulk (or surface) band gaps of the materials and their corresponding interface band gaps. Achievement of an optimal spike-like conduction band offset seems to be both possible and necessary for high efficiency Cu$_2$ZnSnS$_4$/CdS solar cells, even though in many lower-efficiency devices the conduction band offset is indeed cliff-like. The existence of a spike-like conduction band offset differentiates Cu$_2$ZnSnS$_4$/CdS solar cells with reported efficiency above 7% from those below 5%.

Keywords:
CZTS, CZTSe, band alignment, conduction band offset

1. Introduction

The p-type semiconductor Cu$_2$ZnSn(S,Se)$_4$ (CZTS(e)) is among the most promising solar absorber materials on the path to thorough deployment of solar energy [1]. CZTS(e) is usually coupled to an n-type CdS partner to form a heterojunction solar cell. While absorbers with a high Se content (CZTSe) have achieved a promising power conversion efficiency of 12.6% at the laboratory scale [2], the record efficiency of higher-band gap absorbers with a low Se content (CZTS) lags at 9.1% [3]. In both cases, the most urgent issue to be solved is the low open circuit voltage (V_{oc}) of the solar cell compared to its theoretical maximum given by the Shockley-Queisser limit [1].

The origin of the large V_{oc} deficit, though, appears to be different in CZTSe- and CZTS solar cells. In fact, temperature-dependent V_{oc} measurements have shown that, in CZTSe solar cells of reasonable efficiency, extrapolation of the open circuit voltage to a temperature of 0 K yields a value that is just a few tens meV lower than the band gap of CZTSe [4]. As the extrapolated V_{oc} at 0 K corresponds to the activation energy of the dominant recombination path in the solar cell (E_A), it is reasonable to conclude that CZTSe solar cells are limited by bulk recombination, and that the small mismatch between V_{oc} and E_A exists because most bulk recombination occurs to/from bulk tail states [5].

Conversely, the same type of measurement done on CZTS solar cells yields values of E_A that are consistently lower than the CZTS band gap by about 0.3-0.4 eV [6–8]. This is significantly larger than the depth of tail states in CZTS, so it seems as if the dominant recombination path is not located in the CZTS bulk but at some interface instead. There can be different reasons for E_A being lower than the absorber's band gap when interface recombination is dominant [9]. Among them, a cliff-like conduction band offset (CBO) between CZTS and its typical heterojunction partner CdS ("buffer layer") is often invoked due to some experimental and theoretical evidence. Such evidence will be examined throughout this paper. Here, by "cliff-like" or "negative" CBO we intend a lower-lying conduction band maximum of CdS with respect to CZTS(e) at the heterointerface. In a generic heterojunction solar cell with a cliff-like CBO at the heterointerface, the activation energy of interface recombination becomes equal to the energy difference between the conduction band maximum (CBM) of CdS and the valence band maximum (VBM) of CZTS due to cross-recombination [9]. Therefore, if interface recombination is the dominant recombination path, a cliff-like CBO will result in a lower E_A than the absorber's band gap and in a lower V_{oc}, as shown in device simulation work [10–12]. The ideal CBO for heterojunction solar cells is a moderately positive (spike-like) CBO between +0 eV and +0.4 eV in magnitude [10–12]. If the spike becomes too large (>+0.4 eV) the light-generated electrons flowing from CZTS toward the top contact are blocked by the large electron barrier at the heterointerface. The valence band offset (VBO)

*Corresponding author, email: ancro@nanotech.dtu.dk, Ørsteds Plads, building 345 East, DK-2800 Kgs. Lyngby, Denmark, Tel.: +45 4525845

at the heterointerface is not of primary importance as long as the band gap of the buffer is significantly larger than that of the absorber.

There are two main reasons why it is attractive to explain the low E_A and V_{oc} of CZTS/CdS heterojunction solar cells - even of the best ones - by a cliff-like CBO. The first is the results of measurements [13–24] and calculations [10, 23, 25–30] of the band alignment at the CZTS(e)/CdS heterointerface, which are compiled in Fig. 1. The majority of those studies found a cliff-like CBO at the CZTS/CdS interface, whereas all studies on the CZTSe/CdS interface found spike-like CBO. The second reason is actual demonstrations of a higher V_{oc} and a higher E_A by replacing CdS with alternative buffer layer materials. A higher V_{oc} has been obtained with $Zn_{0.35}Cd_{0.65}S$ [31], $Zn_{0.8}Sn_{0.2}O_x$ [32], In_2S_3 [33], and CeO_2 [34]. A higher E_A has been obtained with $Zn_{0.8}Sn_{0.2}O_x$ [32]. In all those cases, the improvement with respect to the baseline CdS buffer layer was attributed to a more favorable CBO of the alternative materials with CZTS. The above arguments may lead to the conclusion that the CZTS/CdS interface *always* has a cliff-like CBO. In this work we will investigate the limits of those arguments and argue that CZTS does not *necessarily* have a cliff-like CBO with CdS. We will suggest the reasons behind such a lack of generality and the consequent deviation of measured and calculated values of the CBO of CZTS/CdS solar cells.

2. Theory of band alignment of semiconductor heterojunctions

Most of the basic models of heterojunction band alignment are based on ideas developed in the 1970s and 1980s. A recent review can be found in [35]. A specific review on chalcogenide semiconductors for solar cells can be found in [36]. It is now generally accepted that, in most situations, the band alignment between two ideal semiconductors is just a function of their bulk properties [35, 37–39]. By this it is intended that any contribution to the band alignment due to interfacial charge transfer can be predicted from bulk properties of the two materials without explicitly modeling the interface itself. Two limiting cases are the "electron affinity rule", which aligns semiconductors based on the distance χ between their conduction band and the vacuum level, and the "charge neutrality rule", which aligns semiconductors based on the distance ϕ_{CNL} between their conduction band and their charge neutrality level (CNL). Those two limiting cases are contained in the following generalized expression for the CBO between semiconductors a and b [35].

$$\text{CBO} = (\chi_a - \phi_{CNL,a}) - (\chi_b - \phi_{CNL,b}) - S(\phi_{CNL,b} - \phi_{CNL,a}) \quad (1)$$

The dimensionless screening parameter S ($0 \leq S \leq 1$) is a bulk property of each semiconductor, which depends on its high-frequency dielectric constant ε_∞ according to an expression shown in [40]. If $S = 0$, we are in the limiting case of the charge neutrality rule and the semiconductors can be aligned against a common CNL. If $S = 1$, we are in the limiting case of the electron affinity rule and the semiconductors can be aligned against a common vacuum level. For intermediate S values,

there is not a universal reference level and Eq. 1 must be used. Based on this theory and on measured ε values [41, 42], one expects $S = 0.23$ for CZTS ($\varepsilon_\infty = 6.7$), $S = 0.15$ for CZTSe ($\varepsilon_\infty = 8.4$), and $S = 0.08$ for CIGS ($\varepsilon_\infty = 12$). Therefore, the charge neutrality rule is more appropriate than the electron affinity rule for those materials, as is generally the case for most covalently-bonded semiconductors of not too large band gap [35]. The charge neutrality level of CIGS has been calculated [37]. By substituting it in Eq. 1, one obtains very good agreement with experimental band offsets on CIGS/CdS interfaces without process-induced non-idealities (e.g. interdiffusion or interface defects) [36, 37, 43]. Unfortunately, the charge neutrality levels of CZTS and CZTSe have not been explicitly calculated yet and theoretical predictions of the CZTS(e)/CdS band alignment have so far been based on the computation of the full electronic structure of explicit CZTS(e)/CdS interface models. Those models will be introduced in Sec. 4.

As mentioned already, Eq. 1 is expected to be valid for "ideal" interfaces. However, a number of non-idealities can occur at real interfaces. Two widely discussed non-idealities are polar interfaces and Fermi level pinning by interface defects. Some types of polar interfaces can result in a nonzero dipole moment in addition to the general, orientation-independent dipole component predicted by Eq. 1. The types of polar interfaces that can give rise to such an additional dipole have been identified in the literature [39, 44, 45]. As discussed later in this paper, those interfaces may be present in CZTS(e)/CdS solar cells, even though their presence is not expected in CIGS/CdS solar cells [37, 43]. A second widely discussed non-ideality is Fermi level pinning by interface defects. Briefly, a high density of electrically active defects, either in the materials' bulk or at the interface, can constrain the natural movement of the Fermi level within the band gap arising from electrostatic band bending caused by the doping type difference between the two heterojunction materials. In the simplest case of a single acceptor (donor) state at a certain energy level within the band gap, the Fermi level cannot move further above (below) the acceptor (donor) level. One can then say that the Fermi level is "pinned" by the defect level. The reason for the constraint is the very high additional charge density that appears when the Fermi level crosses those defect levels due to defect ionization. If the Fermi level is pinned by a certain defect level on one side of the junction and by another defect level on the other side of the junction, then there will be two sheet charge layers at the interface at a very small distance from each other due to ionization of those defects at the interface. This is equivalent to a dipole moment and will shift the natural band alignment at the interface given by Eq. 1, similarly to the case of a polar interface. Fermi level pinning has already been found to influence the band alignment of some absorber/buffer combinations in CIGS solar cells [36] so it deserves special attention. Other mechanisms that may change the natural band alignment of the CZTS(e)/CdS interface involve changes in the band edge positions, band gap changes, alloying between the two materials at the interface, and formation of interface phases. Those mechanisms are not often discussed in relation to band alignment but they will be covered in this work for completeness.

3. Experimental methods

With only two exceptions [15, 18], all the CBO measurements on CZTS(e)/CdS interfaces reported so far were performed with photoemission-based techniques. A photoemission experiment can be of standard or inverse type. Standard photoemission spectroscopy probes the density of occupied states (valence band) with respect to the Fermi level. Hence, the leading edge of the spectrum is a measure of the VBM of the material with respect to the Fermi level. Standard photoemission spectroscopy methods can differ in terms of the analysis depth of the experiment, that is, how deep from the material's surface the valence band signal comes from. The analysis depth increases from about a nm to about 20 nm as the wavelength of the excitation radiation is decreased from ultraviolet photons (UPS), soft x-rays (XPS) or hard x-rays (HAXPES). Conversely, inverse photoemission spectroscopy (IPES) probes the density of unoccupied states (conduction band) with respect to the Fermi level. Hence, the leading edge of the spectrum is a measure of the CBM of the material with respect to the Fermi level.

Standard and inverse photoemission spectroscopy can determine band offsets with two measurement approaches. With the "bulk band edge + band bending" approach (VBM+BB or CBM+BB), one measures the VBM (CBM) of CZTS(e) and CdS in bulk samples by standard (inverse) photoemission. The VBO (CBO) at the interface is then derived by measuring band bending in the junction. Band bending can be extracted by comparing the position of the core levels of the two materials in the respective bulk samples and in a sample with a very thin CdS overlayer on top of CZTS(e). If the CdS overlayer is thinner than the analysis depth of the technique, the core levels of both materials can be resolved. Another way to extract band bending is to measure the shift of the whole photoemission spectrum between equilibrium conditions and flat-band conditions, which can be achieved in a special setup where the bands can be flattened through optical pumping [19]. With the "direct" approach, one simply tries to deconvolve an interface photoemission spectrum (CZTS(e) sample with thin CdS overlayer) into the CZTS(e) and CdS band edge components.

Therefore, valence band offsets can be obtained by standard photoemission with the VBM+BB approach or with the direct VBO approach. Conduction band offsets are derived by adding the bulk band gap of the two materials, as determined by a complementary technique. In the case of inverse photoemission, conduction band offsets can be obtained with the CBM+BB approach or with the direct CBO approach, without relying on separate band gap measurements. All the above possible types of measurement differ in the assumptions needed to derive the actual CBM positions of CZTS(e) and CdS *at the heterointerface*. Those positions are, strictly speaking, only measured directly with the direct CBO method. The consequence of those assumptions on the accuracy of the measurement will be discussed in Sec. 10.

For completeness, we briefly discuss the non-photoemission based techniques used to measure the CZTS(e)/CdS band alignment in the two remaining cases [15, 18]. They are: (i) near-edge x-ray absorption fine structure (NEXAFS) with the CBM+BB approach (band bending obtained by XPS [15]); and (ii) electrochemical measurement, from which the VBM of a single bulk material can be determined with respect to a universal energy scale [18].

4. Computational methods

Methods to obtain valence- and conduction band offsets (VBO and CBO) from first principles have been recently reviewed [46]. Among them, an explicit interface modeling method inspired by the photoemission measurement has gained significant popularity due to its excellent agreement with experimental data [47–49]. In this method, the energy positions of the valence bands of CZTS(e) and CdS are first calculated separately in the two unstrained bulk materials with respect to a reference energy unique to each bulk calculation (for example, the position of a core level). Then, an explicit model of the interface is built, where CdS is artificially strained to match the lattice constant of CZTS(e). The electronic structure of such an interface region is calculated, which allows alignment of the two previously determined valence band positions to a common energy reference, typically a core level just like in a photoemission experiment. Even though many computational details differ in each study, those theoretical investigations can be conceptually divided into two categories. In the first category [10, 27, 30] the goal is to model an epitaxial interface, so it is assumed that the lattice constant of CdS is also strained in the real interface. This means that the band gap of CdS in the interface region can be different from that in the bulk due to the slightly deformed lattice. This class of models allows for interface band gap changes. In the second category [25, 26], even though CdS is still strained in the calculation to match the lattice constant of CZTS, the effect of strain on the electronic structure is subtracted by using a volume deformation potential correction. Therefore, this category calculates the band alignment of strain-free interfaces assuming that no band gap changes occur at the interface. Especially for CZTS, which has a lattice mismatch around 7% with CdS, this corresponds to a non-epitaxial interface. The remaining studies are similar to the first category but they do not allow the interface gap to vary with respect to the bulk band gap [23, 28, 29].

5. Review of band alignment between CZTS(e) and CdS

A summary of all previous work on band alignment of the CZTS(e)/CdS interface known to the authors is provided in Fig. 1. The following general trends can be observed:

1. The CZTSe/CdS interface has a larger CBO than the CZTS/CdS interface.
2. The CBO of both CZTS/CdS and CZTSe/CdS determined experimentally under flat-band conditions (**F**) is larger than nearly all other experimental data points, where the measurement was taken under equilibrium conditions.
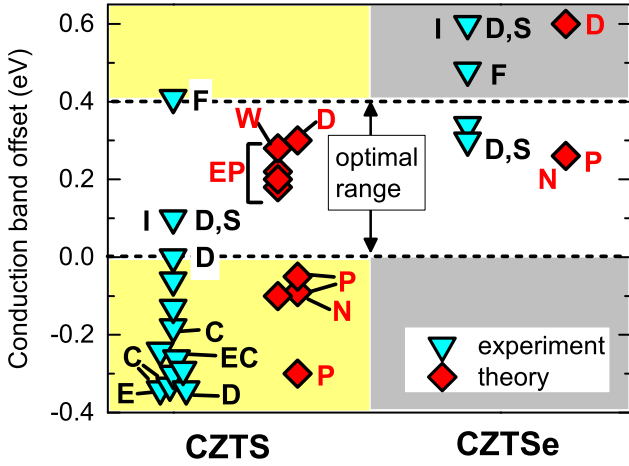
Figure 1: Conduction band offset (CBO) between CZTS (CZTSe) and CdS as determined in experimental and theoretical work. Unless otherwise specified, the measured quantity in experimental work is the VBO, and the CBO is derived by adding the experimental band gap of the materials. Unless otherwise specified, the measurement technique is photoemission spectroscopy (standard or inverse). Finally, calculations are performed with cubic (zincblende) CdS, unless otherwise specified. **F**: measurement taken under flat-band conditions. **D**: direct VBO measurement/calculation at the interface without the need for an indirect band bending correction. **D,S**: direct VBO measurement (as **D**) obtained through destructive sputter etching of the CdS overlayer. **C**: "conduction band" type of measurement, where the measured quantity is the CBM, but where an indirect band bending correction is still needed. **I**: significant interdiffusion identified by the authors at the interface. **E**: absorber intentionally etched before CdS deposition. **EC**: eletrochemical measurement. **P**: calculation performed on a polar interface. **W**: calculation performed with wurtzite CdS instead of zincblende CdS. **EP**: modeling of an epitaxial junction with corresponding band gap changes. **N**: calculation of "natural" band alignment, where interface-specific effects are subtracted. References: [13–24] for experimental CBOs, and [10, 23, 25–30] for calculated CBOs.

3. There is a significant deviation in the reported CBO values at the CZTS/CdS interface (note that there exist about three times as many studies on CZTS/CdS than on CZTSe/CdS).

In the next sections, we will examine the above points one by one by analyzing the existing band alignment studies. In particular, we will evaluate the possible reasons for the large deviation in the reported CBO values for the CZTS/CdS interface.

5.1. Larger conduction band offset for CZTSe than for CZTS

This is qualitatively consistent with theory and can be explained by the nature of the valence- and conduction band of CZTS(e). The conduction band is the antibonding state of Sn *s* and S(Se) *s* orbitals. The valence band is an antibonding state of Cu *d* and S(Se) *p* orbital hybridization [26, 50]. The *s* and *p* orbitals of S are at a lower energy than the corresponding Se orbitals, which tends to shift the bands of CZTS to a lower energy than in CZTSe. However, the Cu-S and Sn-S bonds are shorter than the Cu-Se and Sn-Se bonds respectively, which increases level repulsion and tends to shift the bands of CZTS to a higher energy than in CZTSe. In the valence band, the downshift tendency is stronger, so the valence band is expected to

lie at a lower energy in CZTS than in CZTSe. Conversely, in the conduction band the up-shift tendency is stronger, so the conduction band is expected to lie at a higher energy in CZTS than in CZTSe [26]. From this theoretical argument, the CBO of CZTS/CdS is expected to be lower than the CBO of CZTSe/CdS in the absence of interface-specific effects such as an interface dipole. However, the difference between the CBOs of the two material pairs is expected to be *smaller* than the difference in band gap between CZTS and CZTSe (0.5 eV) due to the valence band down-shift in CZTS. Indeed, the difference in CBO for the two material pairs was found to be 0.35 eV and 0.3 eV in two independent computational studies [26, 30].

This leads to a first inconsistency: most experimental studies on CZTS/CdS report a CBO < −0.2 eV, and all experimental studies on CZTSe/CdS report a CBO ≥ +0.3 eV (Fig. 1). The difference between the two sets of CBOs is indeed larger than the band gap difference (0.5 eV). As this contrasts with theory, it is likely that the experimental band alignment depends on some non-idealities in the materials or at the interface, or that it is affected by measurement errors. In the next sections we will examine such possibilities.

5.2. Larger conduction band offset under flat-band conditions

The band alignment measurement method employed in [19] resulted in some of the highest reported CBOs for both interfaces under consideration (data points labeled **F** in Fig. 1). Interestingly, the measurement was performed on the materials that yielded world-record efficiency solar cells, so the results will be discussed in detail here. The main difference between the measurement method in [19] and all the other experimental studies is that [19] performed a photoemission-based band alignment measurement under optical pumping instead of under equilibrium conditions. The photon energy of the optical excitation was below the band gap of CdS but above the CZTS(e) band gap, which resulted in an excess carrier population in CZTS(e). If the excess carriers density is high enough, the built-in electric field of the p-n junction on the CZTS(e) side is screened by the excess free carriers and the bands on the CZTS(e) side of the junction flatten, as shown in [51]. The thickness of the CdS layer was kept to a minimum in order to obtain approximately flat bands on the CdS side as well. As mentioned above, this method yielded higher CBOs than nearly all other measurement methods for both the CZTS/CdS and the CZTSe/CdS interface. A proposed explanation [52] invokes a measurement error introduced if the pump intensity is not sufficient to generate an excess carrier density large enough to completely screen the built-in electric field. However, incomplete screening would actually result in *underestimation* of the CBO, because of the following concurrent effects: (1) overestimation of the distance between the VBM of CdS and the Fermi level under pumping (because the upward VBM shift of CdS would be less than under true flat band conditions), and (2) underestimation of band bending (because of a smaller overall energy shift between a pumped spectrum and an unpumped spectrum). Therefore, it is unlikely that the high measured CBO under flat band conditions is simply due to a measurement error.
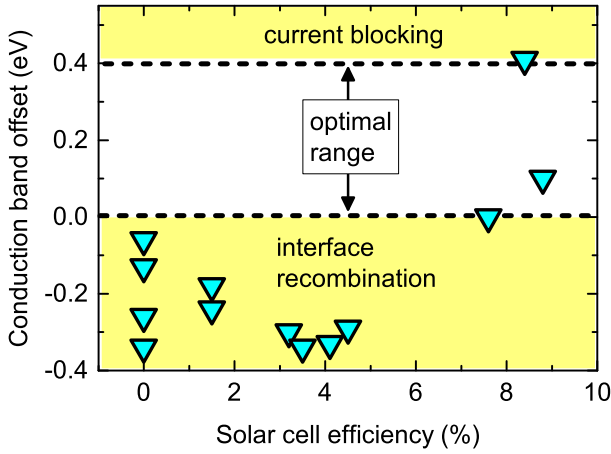
Figure 2: Correlation between the CBO at the CZTS-CdS interface with the corresponding device efficiency. In the cases where no devices were characterized in parallel with the band alignment measurement, we refer to devices reported in the same period of time by the same groups who fabricated the films used in the measurements [53–55]. In the cases where no device reports could be found, 0% efficiency is assumed.
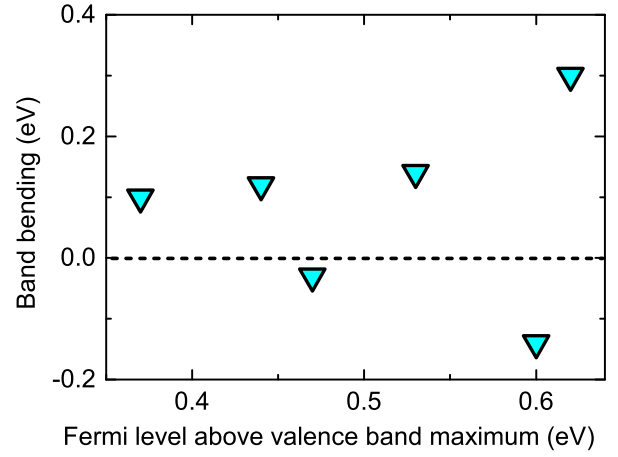
Figure 3: Total band bending over both sides of the CZTS/CdS interface versus Fermi level position of CZTS above the valence band maximum. Data taken from existing photoemission measurements [13, 15, 17, 19, 23]. No clear dependence of band bending on the Fermi level position can be identified.

5.3. Deviation in measured and calculated band offsets

We divide the possible causes of variation into two categories: the first category is related to *real* variations in the CBO depending on the particular preparation conditions of CZTS(e) and CdS. Within this category we include: (1) Fermi level pinning through defects; (2) orientation-dependent band alignment; (2) variations in the bulk- or interface band gap of CZTS(e) or CdS; and (4) formation of interface phases, e.g. by interdiffusion. The second category is related to errors in the *evaluation* of the CBO. Within this category we include: (5) incorrect assumptions used to derive the CBO from other measured or calculated quantities, most notably the the assumed equivalence between bulk-, surface-, and interface band gaps; (6) pure measurement or computational errors intrinsic to the techniques used to measure or calculate the CBO. Those six possibilities will be discussed in the following sections.

We already note at this point that measurement errors are very unlikely to be the main reason for the wide range of measured CBOs. This becomes evident by plotting the measured CBO of each CZTS-CdS heterojunction as a function of the conversion efficiency of the resulting solar cell (Fig. 2). In all the fabricated heterojunctions that resulted in efficiencies above 7% [14, 21, 53], the measured CBO was a moderate spike (between 0 eV and +0.41 eV), as required for efficient solar cells. Conversely, all devices based on heterojunctions with a cliff-like CBO (between −0.34 eV and −0.06 eV) had efficiencies below 5%. Hence, it appears as if obtaining a spike-like conduction band is both *possible* and *necessary* for high-efficiency devices.

6. Role of Fermi level pinning

This has been shown to be the physical mechanism behind the large band alignment deviation in Cu$_2$O/ZnO solar cells.

In Cu-rich Cu$_2$O, interface band bending was quenched due to bulk pinning of the Fermi level to a fixed energy determined by the particular bulk electronic structure of the Cu-rich material [56]. This resulted in a different interface CBO with respect to stoichiometric Cu$_2$O [56]. The influence of bulk Fermi level pinning on the CBO of CZTS(e)/CdS solar cells can be investigated by plotting the measured band bending on the CZTS side versus the Fermi level position of CZTS in a bare CZTS sample, referenced to respect to its VBM. Unfortunately, only the total band bending over both sides of the junction is reported in the existing studies, with the exception of [19]. Under the approximation that most band bending occurs on the CZTS side, it does not appear as if there is a universal Fermi level position at which band bending is quenched for all samples. However, the measured band bending values are rather small for a 1.5 eV band gap material like CZTS, so it is likely that the Fermi level is pinned in a significant fraction of the CZTS/CdS interfaces subject of previous studies. More specifically, inspection of Fig. 1 reveals that there are a lot of measured CBO values in the limited -0.35 eV to -0.25 eV range. We speculate that this corresponds to specific pinning energies of the Fermi level on the CZTS side and on the CdS side, which are achieved unintentionally but easily. Therefore, we propose that Fermi level pinning can decrease the CBO with respect to most theoretical predictions.

7. Role of interface orientation

Orientation-dependent band alignment has been mentioned before as a potential cause of variability in the CBO of the CZTS(e)/CdS interface, without further investigation [57]. To the authors' knowledge, no studies exist on this subject. Regardless of the materials in question, orientation-dependent band alignment can occur when a nonzero orientation-specific dipole moment exists at the interface [44]. Specific conditions

Mechanism	Location	Influence on band offset		Error in determination of CBO, by method			
		CBO (eV)	VBO (eV)	VBM+BB (eV)	CBM+BB (eV) **C**	direct VBO (eV) **D D,S**	direct CBO (eV)
1)Disorder	CZTS(e) bulk	+0.0(+0.0)	+0.2(+0.1)	+0.0(+0.0)	+0.0(+0.0)	+0.0(+0.0)	+0.0(+0.0)
2)Wurtzite CdS **W**	CdS bulk	+0.1(+0.1)	+0.0(+0.0)	+0.0(+0.0)	+0.0(+0.0)	+0.0(+0.0)	+0.0(+0.0)
3)Quant. confinement	CdS interface	+0.2(+0.2)	+0.0(+0.0)	+0.2(+0.2)	+0.2(+0.2)	+0.2(+0.2)	+0.0(+0.0)
4)Epitaxy **EP**	CdS interface	+0.0(+0.0)	-0.2(-0.1)	-0.2(-0.1)	-0.2(-0.1)	-0.2(-0.1)	+0.0(+0.0)
5)Interdiffusion **I**	interface	+0.3(+0.3)	-0.2(-0.5)	+0.1(-0.2)	+0.1(-0.2)	+0.1(-0.2)	+0.0(+0.0)
6)Etching (KCN) **E**	CZTS(e) surf.	+0.0(+0.0)	-0.4(-0.3)	-0.4(-0.3)	+0.0(+0.0)	-0.4(-0.3)	+0.0(+0.0)
7)Polar surface **P**	CZTS(e) interf.	-0.2(-0.2)	+0.2(+0.2)	+0.0(+0.0)	+0.0(+0.0)	+0.0(+0.0)	+0.0(+0.0)
8)Fermi level pinning	CZTS(e) interf.	-0.2(-0.2)	+0.2(+0.2)	+0.0(+0.0)	+0.0(+0.0)	+0.0(+0.0)	+0.0(+0.0)
9)Measurement error				±0.1(±0.1)	±0.1(±0.1)	±0.1(±0.1)	±0.1(±0.1)

Table 1: Estimated consequences of various physical mechanisms on the CBO and VBO at the CZTS(e)/CdS interface, based on the discussion in the main text. The *real* changes in the CBO and VBO are estimated with reference to a baseline case consisting of ordered, non-etched CZTS(e) with non-polar surfaces and a non-epitaxial zincblende CdS buffer layer with no quantum confinement nor interdiffusion effects. If the value is positive (negative), it means that the mechanism increases (decreases) the CBO or the VBO. The expected experimental error in the evaluation of the CBO with four different techniques (VBM+BB, CBM+BB, direct VBO, and direct CBO) is also provided, assuming that the bulk band gap of both CZTS(e) and CdS has been measured correctly with a complementary technique. VBM+BB: measurement of the VBM in two bulk samples and band bending correction in a sample with a thin CdS overlayer (all experimental data points in Fig. 1 except for those labeled **C**, **D**, and **D,S**). CBM+BB: measurement of the CBM in two bulk samples and band bending correction in a sample with a thin CdS overlayer (labeled **C** in Fig. 1). Direct VBO: direct measurement of the VBO at the interface without the need for band bending correction (labeled **D** or **D,S** in Fig. 1). Direct CBO: direct measurement of the CBO at the interface without the need for band bending correction (no existing measurements known to the authors). A positive (negative) experimental error means that the real CBO is higher (lower) than the outcome of the measurement. The format of all listed changes and errors is $x_i(y_i)$, where x_i is the change or error at the CZTS/CdS heterojunction and y_i is the change or error at the CZTSe/CdS heterojunction due to Mechanism i. The bold letters refer to the labeling introduced in Fig. 1.

need to be met for this to occur. They are the following: (i) the surface of at least one of the two heterojunction materials must be polar [44]; (ii) the atomic layers on the two sides of interface plane must be heterovalent [39]; and (iii) any dipole-compensating interface reconstruction must not proceed to the point where the dipole moment is completely canceled [45]. Condition (i) is met, for example, at (001) surfaces of compound zincblende semiconductors [44]. In CZTS(e), the condition is met at the (001), (110), (112), and (100) surfaces due to the presence of alternating cationic and anionic layers in the surface plane. Condition (ii) is met in the classical example of a Ge/GaAs(001) interface from which the band alignment theory of polar interfaces was originally developed [45]. In CZTS(e)/CdS system, the condition is met at the (001) and (110) interfaces as explained later in this section. Condition (iii) is in practice very difficult to check experimentally, even on monocrystalline interfaces. However, convincing experimental evidence of orientation-dependent band alignment has been shown for other zincblende semiconductor pairs from which the CZTS(e) kesterite structure is derived. Example are Ge/GaAs(001) [58] and GaAs/ZnSe(001) [59]. The measured dipole contribution to the band alignment (up to a few hundred meV) was compatible with certain interface reconstruction patterns that did not cancel the dipole moment of the ideal unreconstructed interface completely [37].

It must be emphasized that the theory developed to model the influence of interface orientation on band alignment was intended for abrupt monocrystalline heterojunctions [45]. Thus, such a theory cannot be rigorously applied to the CZTS(e)/CdS system, which is a polycrystalline heterojunction with different grain orientations within the same sample and interdiffusion over regions of several tens of nm. Also, transmission electron microscopy images of the CZTS(e)/CdS interface suggest that, even within a single CZTS(e) grain, the CZTS(e) surfaces at the heterojunction are not necessarily single-orientation, atomically smooth facets but that, instead, their orientation varies continuously [34, 60]. Nevertheless, based on qualitative arguments, here we suggest that there are two reasons to suspect that the band alignment of CZTS(e) solar cells is more likely to have some orientation dependence than the band alignment of CIGS solar cells.

The first reason is that condition (ii) is not satisfied by any low-Miller index interface in the CIGS/CdS system, but it is satisfied by some low-Miller-index interfaces in the CZTS(e)/CdS system, namely the (001) and (110) interfaces. This happens because in CZTS(e) the (001) and (110) directions feature cationic planes that consist either of 50%Cu-50%Zn or of 50%Cu-50%Sn [27]. The former planes have valence 1.5, the latter have valence 2.5. The corresponding planes in CIGS all contain the same amounts of Cu, In and Ga, so their valence is 2, which matches the valence of Cd in CdS. Then, the (001) and (110) interfaces are isovalent in the CIGS/CdS system but heterovalent in the CZTS/CdS system. Therefore, the CZTS(e)/CdS band alignment can in principle be orientation-dependent, even though several authors have correctly remarked that this is not the case for the CIGS/CdS system [36, 37, 43].

The second reason is that the band alignment shift due to an orientation-specific dipole moment is inversely proportional to the average dielectric constant of the two heterojunction materials [37]. Therefore, everything else being equal, materials with a lower dielectric constant will have a larger band alignment shift from the interface dipole layer. Experimental values of the dielectric constant of CIGS, CZTSe and CZTS are 12,

8.4 and 6.7 respectively [41, 42], so CZTS is the most sensitive material to interface dipoles. Even though *unreconstructed* (001) and (110) CZTS(e)/CdS interfaces are high-energy (unstable) interfaces [27] just like the classical Ge/GaAs(001) interface [44], it is perfectly possible, in principle, that certain reconstruction patterns stabilize such interfaces without completely canceling the interface dipole moment, as demonstrated for Ge/GaAs(001) [58] and GaAs/ZnSe(001) [59]. A specific computational study is needed to confirm this hypothesis.

Some published first-principles calculations were performed on isovalent interfaces such as the (100), (102), and (112) CZTS(e) surfaces coupled, respectively, with commensurate CdS (100), (101), and (111) surfaces [10, 27, 29, 30]. Other interface calculations were performed using the heterovalent CZTS(e)/CdS(001) interface [23, 26, 28, 29] and they are labeled as **P** in Fig. 1. All calculated interfaces are non-reconstructed. In the case of the heterovalent interface, it was found that the CBO depends strongly on the chosen CZTS atomic layer at the interface (Cu-Zn or Cu-Sn) as expected from the above discussion [28]. The computed CBO was negative in both cases but it was less negative for the Cu-Zn-terminated CZTS, implying a dipole with negative charge on the CdS side and positive charge on the CZTS side. The opposite dipole is then expected for the Cu-Sn terminated CZTS.

In our view it is, however, unlikely that orientation-dependent band alignment is a major reason behind the deviation of the measured CBOs in CZTS(e)/CdS solar cells. That is because the preferential CZTS(e) orientation in the substrate normal direction does not differ much among thin films grown by different groups and the preferential orientation is actually very similar for CIGS, CZTSe, and CZTS [61]. Also, the exposed CZTS(e) facets do not appear to be atomically smooth but their orientation varies continuously within the same grain, as mentioned before. A more likely effect is that the band alignment varies laterally from grain to grain, because grains that differ in orientation with respect to the substrate plane are also likely to differ in the orientation of the exposed facets. In a photoemission experiment the single grains cannot be resolved because the lateral resolution of the technique is not better than tens of μm. Then, grain-to-grain band alignment variations would result in broadening of the core level peaks and tailing of the valence band spectrum when a CZTS(e) sample with a thin CdS overlayer is measured, for example to obtain the band bending correction in a VBM+BB measurement.

If preferential orientation of the exposed CZTS(e) surfaces could be controlled to produce (001) or (110) polar facets that are heterovalent with the buffer layer, the CBO of CZTS(e)/CdS interfaces could in principle be engineered by the interface dipole layer. This could be achieved, for example, by development of an orientation-dependent etchant, similarly to potassium hydroxide etching of Si, which is routinely used to produce (111) Si surfaces.

8. Role of band gap changes

Synthesized CZTS(e) always features some cation disorder in the Cu/Zn sublattice, due to the low formation energy of the ($Zn_{Cu}+Cu_{Zn}$) defect pair. The degree of disorder can be quantified by the order parameter of the material [62, 63]. The band gap of CZTS(e) was shown to decrease by 0.20 eV in CZTS [64] and by 0.11 eV in CZTSe [63] when the order parameter of the materials decreased from a realistically achievable high-order state to a fully disordered state. The effect of those changes on the interface CBO can be predicted by estimating the corresponding band edge shifts with respect to the vacuum level. According to calculations [65], the band gap decrease should occur mostly through an upward shift of the VBM rather than through a downward shift of the CBM. This is consistent with the fact that the a Cu orbital is responsible for formation of the CZTS(e) valence band, whereas no Cu nor Zn orbitals are involved in formation of the CZTS(e) conduction band to a first approximation [26, 50]. Therefore, the CBO should not be affected significantly by the order parameter, see Mechanism 1 in Table 1.

In the case of CdS, a number of physical mechanisms have been shown to alter its band gap. First of all, there exist two CdS phases, cubic (zincblende) and hexagonal (wurtzite), with very similar formation energies. The wurtzite phase has a band gap that is about 0.1 eV larger than the zincblende phase (roughly 2.5 eV versus 2.4 eV). Such two phases are often found to co-exist in CdS made by chemical bath deposition [66], the standard technique used to deposit CdS in CZTS(e) solar cells. According to first-principles calculations [27, 67], the band shift occurs primarily in the conduction band, which is expected to lie 0.1 eV higher in wurtzite CdS. This corresponds to the data point labeled as **W** in Fig. 1 for the only calculation performed with wurtzite CdS. See Mechanism 2 in Table 1.

Secondly, the band gap of CdS may expand due to quantum confinement effects if the crystallite size is small enough to be comparable to the Bohr radius of the material (about 3 nm [68]). This can potentially be a crucial effect: band gap changes due to quantum confinement in (Zn,Sn)O films grown by atomic layer deposition are so large that they have been successfully controlled to engineer the desired CBO in Cu(In,Ga)Se$_2$/(Zn,Sn)O heterojunction solar cells [69]. It has been shown that the band gap of CdS starts to increase at a particle size of 6 nm and reaches roughly 3.5 eV for a crystallite size of 1 nm [70]. We note that CdS films by chemical bath deposition are always nanocrystalline and that the "seed layer" that first forms on the CZTS surface typically has a smaller crystallite size than the final film [66, 71]. Because the band gap that determines the band alignment with CZTS(e) is that of the seed layer, the interface band gap is possibly higher than that measured in the film with the desired thickness by optical measurements. In fact, in [72] the band gap of CdS increased by 0.15 eV as film thickness decreased from 200 nm to 35 nm, possibly due to quantum confinement effects from the smaller crystallite size in the thinner films. Unfortunately, no studies on the corresponding band edge shifts are known to the authors. By assuming variations up to 0.2 eV in the band gap of the CdS seed layer depending on preparation conditions, and by assuming that band gap expansion occurs through an upward shift of the conduction band as demostrated, for example, in (non-hydrogenated) amorphous Si [73] and amorphous (Zn,Sn)O [69] a rather speculative ±0.1 eV

deviation in the CBO is derived. See Mechanism 3 in Table 1.

A third mechanism that may modify the interface band gap of CdS is strain in the CdS lattice induced by formation of the interface with CZTS(e). This mechanism depends strongly on the growth mode of CdS, especially on whether CdS grows epitaxially on CZTS(e). Despite the relatively large lattice mismatch with CZTS (7%), epitaxial CZTS(100)/CdS(100) and CZTS(112)/CdS(111) interfaces have been demonstrated by some authors in actual solar cells [60, 74]. An epitaxial interface is always assumed in first-principle calculations as it permits much smaller periodic structures to be used, thus reducing computational time. However, most studies force the interface band gaps to be equal to the bulk band gaps. One exception is [27], where the interface band gap of CdS was explicitly calculated by fixing the CdS lattice constant in the interface plane to a value equal to the CZTS lattice constant and relaxing the CdS lattice constant in the direction perpendicular to the interface. The result (labeled **EP** in Fig. 1) was that the CdS band gap was narrowed by a significant amount (0.2-0.5 eV) depending on the interface under consideration. This effect occurred primarily through an upward shift of the VBM. Hence, we estimate that an epitaxial CZTS/CdS interface has a VBO that is 0.2 eV smaller than a non-epitaxial interface, but the CBO remains the same. See Mechanism 4 in Table 1. Note that, even though the group that reported epitaxial growth also performed a band alignment measurement [14], the CdS film in that measurement was annealed at 200°C, which does not result in an epitaxial interface.

Finally, both CZTS(e) and CdS feature tail states within the band gap of the extended states due to band gap- or electrostatic potential fluctuations caused by secondary phase inclusions or acceptor-donor defect clusters. In top-performing CZTS (CZTSe), the band gap including tail states is roughly 0.15 eV lower (0.02 eV lower) than the band gap of extended states [53, 75]. In CdS, the density and depth of tail states into the band gap may be even larger, simply based on comparison of the photoemission tails of CZTS(e) and CdS [13]. If the CBO is defined and measured as the offset between the bands of the extended states, then the tail states have no influence on the CBO, as long as they can be discerned from the extended states in a band alignment measurement. This conclusion is, however, partly misleading. Just as tail states reduce the effective recombination band gap in the bulk of the material [76], they also cause local narrowing of the effective interface band gap. Then, a large density and depth of tail states can aggravate the effects of a negative CBO, i.e., decrease the activation energy of the dominant recombination path and, ultimately, the open circuit voltage.

9. Role of interdiffusion and interface phases

Formation of interface phases that modify the expected band alignment has strong experimental evidence. It may occur due to (1) secondary phase formation at the CZTS(e) surface as a result of growth conditions, annealing or etching, or alternatively due to (2) chemical interdiffusion during deposition of CdS. The first mechanism is well known in CIGS solar cell technology, where a Cu-poor surface causes the surface VBM to decrease in energy and the band gap to expand [77]. In CIGS, a Cu-poor surface can be achieved either by tuning the growth conditions or by performing a potassium cyanide (KCN) etching step before CdS deposition. It was similarly shown that a KCN etching treatment on CZTS increased its surface band gap to 1.9 eV: the VBO with CdS became larger but the CBO remained nearly unaffected [13], see the data point labeled **E** in Fig. 1. We then conclude that, while a KCN etching step does not appear to modify the CBO, it cannot be excluded that other types of surface treatments [78] affect the CBO by a significant amount, even though the band alignment of CZTS(e) etched with alternative etching agents has not yet been measured. See Mechanism 6 in Table 1.

The secondary phase that is most likely to be present at the CZTS(e)/CdS heterojunction simply as a result of the absorber growth and annealing is ZnS(e), due to the Cu-poor Zn-rich growth conditions required to achieve efficient solar cells [4, 79, 80]. In some cases, ZnS(e) is intentionally etched with HCl [80]. There are two qualitatively different mechanisms of ZnS(e) segregation: the first is formation of a thin continuous layer, the second is formation of isolated ZnS(e) grains at a surface that mostly consists of CZTS(e). We argue that the latter is more likely for three reasons. The first is that isolated segregation has been observed directly by microscopy [79, 80]. The second is that a continuous thin ZnS(e) layer at the CZTS surface should be detected indirectly by the absence of a Cu and Sn signal using highly surface-sensitive composition-probing techniques such as x-ray photoemission spectroscopy (XPS) or secondary ion mass spectroscopy (SIMS). However, studies performed with such techniques consistently reveal a significant amount of Cu and Sn in Zn-rich CZTS(e) films [4, 81]. The third reason is that a ZnS(e) surface layer should be easily detected when measuring the VBM of a bulk CZTS sample with respect to the Fermi level, as routinely done in most band alignment studies shown in Fig. 1. This is because ZnS(e) has a much higher band gap than CZTS(e) and is n-type instead of p-type, hence its VBM should be much more distant from the Fermi level than in CZTS(e), in the case of a continuous ZnS(e) surface layer. Assuming that the above argument is correct, the measured CBO is expected to be that of the actual CZTS(e)/CdS interface. However, since the CZTS(e)/ZnS(e) interface features a very large spike [27, 79], the actual behavior of the solar cell will depend on the geometrical details of the ZnS(e) phases. The main expected consequence of scattered ZnS(e) phases at the heterointerface is an increase in series resistance with respect to the ZnS(e)-free case, as often discussed in the literature [4, 82, 83]. One may also expect a modification in the band alignment by oxide phases at the CZTS(e) surface. However, it has been shown that the alkaline NH₄OH-based chemical bath used by most researchers to deposit the CdS buffer layer removes almost completely the surface oxide grown by air exposure or air annealing [84].

The second possible mechanism leading to the formation of interface phases is chemical interdiffusion across the CZTS(e)/CdS interface. The reported CBO values labeled **I** in Fig.1 refer to interfaces where significant interdiffusion was
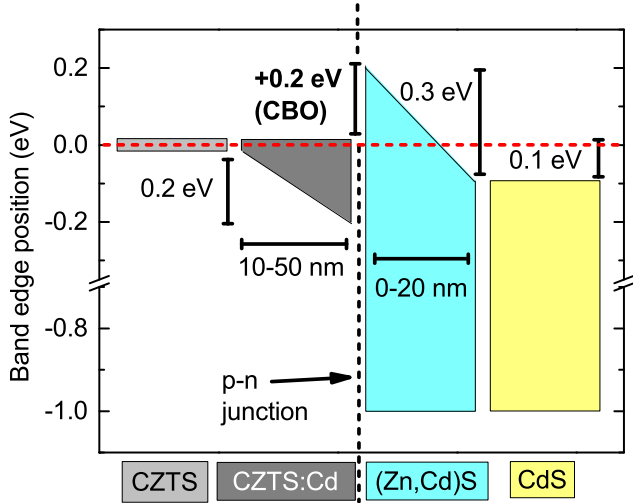
Figure 4: Semi-quantitative model of a (favorable) engineered band alignment at the CZTS/CdS interface achievable in the presence of significant interdiffusion and assuming an unfavorable cliff-like CBO of -0.1 eV at the original CZTS/CdS interface without interdiffusion. This is proposed as part of the reason behind the optimal band alignment achieved in state-of-the-art CZTS/CdS solar cells [14, 19, 21]. The (Zn,Cd)S phase is assumed to be $Zn_{0.35}Cd_{0.65}S$ at the heterointerface and to gradually decrease in Zn content toward CdS, consistently with a Zn diffusion tail. Its band edge positions are based on the results in [31]. The CZTS:Cd phase is assumed to have one $Cd_{Zn} + V_{Cu}$ defect pair per two unit cells. Its band edge positions are based on the results in [21, 90].
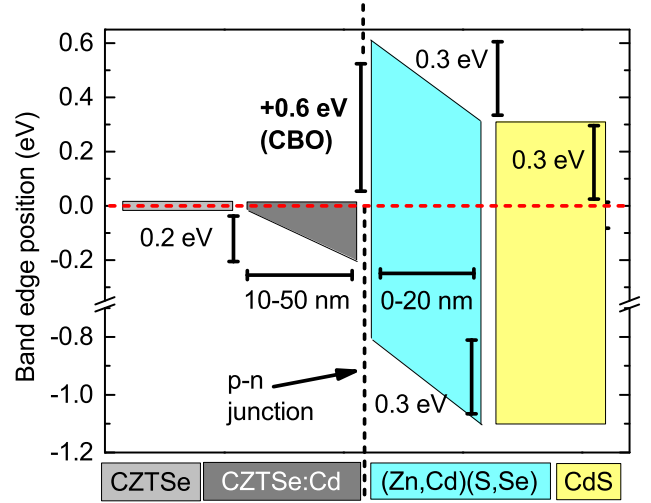

Figure 5: Semi-quantitative model of an (unfavorable) engineered band alignment at the CZTSe/CdS interface achievable in the presence of significant interdiffusion and assuming an favorable spike-like CBO of +0.3 eV at the original CZTSe/CdS interface without interdiffusion. The main difference with the CZTS/CdS interface is Se diffusion into CdS, which is predicted to shift the VBM upward [49]. The band gap increase due to Cd alloying with Zn is assumed to be compensated by the band gap decrease due to S alloying with Se.

documented. Interdiffusion has already been proven to be a major force in determining the band alignment of many other heterojunction solar cells, often beneficially. In Cu_2O/ZnO solar cells, significant CBO variation (up to 0.4 eV) was observed depending on the presence or absence of a CuO interface phase induced by the particular process conditions chosen for deposition of the ZnO heterojunction partner [85]. In CIGS/CdS solar cells, Cd and S can diffuse into CIGS, and In and Se can diffuse into CdS [86, 87]. Especially Se inclusion into CdS was shown to decrease its band gap (from 2.4 eV to 2.2 eV) 20 nm away from the interface [88]. In CdTe/CdS solar cells, S and Te can interdiffuse to a depth over 200 nm and form a $CdTe_{1-x}S_x$ interface phase with an intermediate band gap [89].

In CZTS(e) solar cells, diffusion of Cd into the absorber is ubiquitously observed as a tail in the Cd signal into the CZTS(e) layer in elemental depth profiling experiments [21, 33, 53]. Tails between 10 nm long [2, 31, 74] and 50 nm long [33, 53] have been reported. Of the possible defects related to Cd diffusion into CZTS(e) from a chemical bath, the one with the lowest formation energy is the $(Cd_{Zn} + V_{Cu})$ neutral pair [90]. According to theoretical work, such a defect pair increases the band gap of CZTS by roughly 0.1 eV in the case of one defect pair per four CZTS unit cells [90]. Since a Cu orbital is involved in the formation of the CZTS(e) valence band, we assume that it is the VBM that is mostly affected by the band gap change. This would imply that the VBM shifts to a lower energy in proximity of the interface in the presence of Cd interdiffusion, but the CBO would not be affected. Indeed, a VBM down-shift by 0.2 eV in CZTS in proximity of the interface was observed experimentally in [21]. However, the authors did not discuss the

matter further and assumed the same interface band gap as the bulk band gap to determine the CBO indirectly.

The situation on the CdS side of the junction is even more interesting. Zn and, to a lesser extent, Se in selenium-containing absorbers, are often observed to diffuse from CZTS(e) into CdS [2, 21, 31, 33, 53, 74]. In some cases, a maximum in Zn concentration at the interface was found [31, 33, 74] instead of just a tail into CdS. This is compatible with Zn segregation at the heterointerface. Furthermore, Zn was found to diffuse more from CZTSe than from CZTS [21]. This affected the band edge positions at the interface and increased the CBO of CZTSe/CdS above the optimal range, which resulted in clear current blocking in the solar cell. However, Zn diffusion from CZTSe was finally suppressed by changing the preparation conditions of the CdS film. From the results in [74], we assume that temperature, either of CdS deposition or of a subsequent annealing step, is the main parameter that can be tuned to control Zn interdiffusion. It can be interesting to analyze in detail the consequences of Zn interdiffusion on the interface band edge positions determined in [21]. We note that the energy position of the VBM on the CdS side increased significantly close the interface (by about +0.6 eV) in the case when Zn diffusion was significant. The width of the region where the gradient occurred corresponds almost perfectly with the depth of Zn diffusion measured in the same study. This provides evidence for formation of a Zn-containing interface phase that changes the expected band alignment. A candidate phase is $Zn_{1-x}Cd_xS$, which has been shown to have a larger band gap and higher-lying VBM and CBM than CdS already at $x = 0.65$ [31]. Se interdiffusion may also contribute to a higher-lying VBM at the interface because the VBM of selenides is predicted to be at a higher energy than that of the sulfides with the same metal cations [49]. Com-

patibly with this explanation, the VBM increase of CdS close to the interface in [21] was greatly mitigated (down to +0.2 eV) when Zn interdiffusion was suppressed by switching to the alternative CdS preparation recipe. Since oxides have a lower-lying VBM than the corresponding sulfides [49], the residual VBM gradient in the case of no Zn interdiffusion may be explained by a sharper gradient in O content observed near the interface, together with small residual amounts of interdiffused Se and Zn. In any case, far enough away from the interface, the VBM on the CdS side was about the same for both CdS preparation recipes, a sign that any changes in the electronic structure are primarily confined to the region over which interdiffusion occurs. See Mechanism 5 in Table 1. We finally note that the band edge gradients observed in [21] on both sides of the heterojunction cannot be simply attributed to electrostatic band bending due to p-n junction formation. That is because the length scale of band bending would be much larger than the observed VBM gradient in CdS (which occurs over just a few nm) especially in a lightly doped material like CdS [72]. In CZTS(e), the gradient occurred over a wider region but p-n junction-induced band bending is also excluded simply because the junction did not exist when the VBM of CZTS(e) was measured, as it had been previously removed by ion beam etching in the photoemission spectroscopy depth profile.

10. Role of some experimental and computational assumptions

The expected errors in the determination of the CBO by each of the measurement methods outlined in Sec. 3 are summarized in Table 1 and justified in the following.

The VBM+BB method, employed in most reports [15–17, 19, 20, 23, 24] uses the bulk band gap of the materials, measured with a complementary technique (optical absorption, ellipsometry, or quantum efficiency), as an approximation of the band gaps at the interface. Therefore, any mechanism that changes the band gap at the surface or interface, such as Mechanisms (3-6) in Table 1, will result in a measurement error.

The direct VBO method [14, 21, 22] is based on the same approximation; however, when used in combination with ion beam sputtering [21, 22], it has the advantage of measuring a depth-dependent VBM profile. This can help identify, if only qualitatively, changes in the electronic properties close to the interface, such as Mechanisms (3-6) in Table 1.

The CBM+BB method [13, 15] measures the CBM position at the *surface* of bulk samples and adds an interface band bending correction. However, such a correction is based on core level shifts, which are not sensitive to *interface*-induced changes in the CBM, but only in the VBM. Therefore, the main advantage of the CBM+BB method is detection of surface changes in the band gaps independently of interface formation, for example Mechanism (6) in Table 1. Note that in one of the existing studies where the CBO can be derived both by a VBM+BB and by a CBM+BB measurement method [13], the CBO of a KCN-etched sample would indeed be overestimated by 0.3 eV by a VBM+BB measurement due to KCN-induced surface band

gap expansion. Note also that, in the cases where a comparison can be made between the results of VBM+BB and the CBM+BB method on non-etched samples, a good agreement is found, with differences of only 0.03 eV [13] and 0.06 eV [15] between the two methods. However, this only means that the bulk band gaps are similar to the surface band gaps, but the extracted CBO might still suffer from an error due to *interface* band gap changes, for example due to Mechanisms (3-5) in Table 1.

Finally, the direct CBO method (not employed in any study known to the authors) involves measuring the CBM of the two heterointerface materials *at the interface*. This could be possible, for example, with a CBM depth profile performed by IPES through consecutive ion beam sputtering steps, similarly to what was done in the studies employing the direct VBO method [21, 22]. We note that the direct CBO method greatly reduces the experimental error in the determination of the CBO down to the "pure" measurement error, which is discussed in the next section.

The calculated band offsets suffer from the same uncertainty in the interface band gap as the measured band offsets. In most reported calculations the interface band gaps were simply assumed to be equal to the bulk band gaps. Exceptions are [10, 27, 30], where the effect of epitaxial growth on the interface band gap was investigated. The calculation that is expected to best approximate the band alignment of the CZTS(e)/CdS interface in the absence of interface-specific effects is the one in [26], because it accounts for the changes in the energy levels that occur when the lattice constant of each material is stretched to form an epitaxial interface. This procedure yields the "natural" (i.e., unstrained) band offsets of each material pair [49].

11. Role of measurement errors

A source of measurement error in photemission-based measurements could be the use of sputter etching in the direct VBO and direct CBO methods. It is well known that prolonged energetic ion beam sputtering can lead to surface modifications that may affect the position of the band edges in the materials [88]. Ion beam profiling was deliberately avoided in the majority of the cited studies except for two [17, 21], labeled as **D,S** in Fig. 1. Those studies measured a +0.1 eV and a -0.34 eV offset, which lie rather far apart among the reported values. Therefore, a systematic error in the determination of the band offsets due to sputtering damage is regarded as unlikely, as long as the sputtering parameters are kept within a safe range [91]. For example, the authors in [17] explicitly verified that their 1 kV Ar$^+$ beam etching did not lead to modifications in the band edge positions and, in fact, the VBO measured directly with the aid of ion beam sputtering and the VBO measured with two bulk samples and a band bending correction agreed within 0.04 eV in that study.

The measurements of band edges mentioned in this work are in most cases reported with an estimated error of ±0.1 eV, which encompasses the typical sources of error in photoemission experiments [92]. See Mechanism 9) in Table 1. Note that one of the sources of the ±0.1 eV experimental error is uncertainty in

the linear extrapolation of the leading band edge signal, a task that may be further complicated by the presence of a high density of tail states or by a mix of phases at the interface, both of which are expected in CZTS(e).

12. CZTS/CdS band alignment engineering by interdiffusion

Having ascertained that there can be many possible sources of variation in the CBO of CZTS(e)/CdS heterojunctions, we conclude that the CBO is not a fixed property of those material pairs. In the case of CZTS, the risk is to obtain a too low CBO (cliff-like). In CZTSe, the risk is to obtain a too high CBO (spike-like). Both such non-ideal cases have been documented in the literature, as shown in Fig. 1. While most of the CBO-varying mechanisms presented in the previous sections are not easily controllable by the experimentalist, here we propose how control of interdiffusion at the heterointerface can be used to engineer the desired band alignment. It is proposed that interdiffusion can be controlled by the temperature of the CdS deposition process or of any subsequent annealing step.

CZTS From the measured and calculated CBOs of the CZTS/CdS interface (Fig. 1), it seems as if this interface can easily have a cliff-like CBO. However, interdiffusion may improve the situation. A shown before, the main species that are expected to interdiffuse are Cd and Zn [21, 33, 53, 74]. Assuming that a $Zn_{1-x}Cd_xS$ interface phase forms on the CdS side of the junction, the CBM on that side will shift upward. The magnitude of the shift depends on the value of x at the interface. On the other side of the junction, Cd interdiffusion is expected to shift the CZTS valence band downward and thus not affect the CBO [21, 90]. Note, however, that this can still be a beneficial effect, as a lower-lying VBM at the CZTS interface will decrease the hole population, which is one of the main factors controlling the interface recombination rate [12, 93]. The combined effect of both types of interdiffusion on the position of the band edges at the heterointerface is modeled schematically in Fig. 4. We then conclude that interdiffusion can actually be *beneficial* in CZTS solar cells as it may increase an originally cliff-like CBO to a value that lies within the optimal range for photovolataics. This can explain the success of solar cells based on the CZTS-$Zn_{1-x}Cd_xS$ heterojunction, where Zn was deliberately alloyed with Cd to increase the CBO. Note however that, while Zn diffusion into the buffer is a positive effect, excessive Zn segregation on the CZTS(e) side of the interface leads to fill factor losses, probably due to formation of spatially scattered ZnS(e) phases which locally block the photocurrent as discussed before. This has been documented by several authors with different investigation methods [4, 74, 82].

CZTSe The CBOs that are usually obtained at the CZTSe/CdS interface (Fig. 1) are close to the upper limit of the optimal range for photovoltaics. Cd interdiffusion is simply expected to lower the VBM of CZTSe as in the case of CZTS [21, 90]. However, Zn interdiffusion can worsen the situation, as already demonstrated in [21]. As discussed in the CZTS case, Cd alloying with Zn is expected to raise the CBM of CdS. In CZTSe, there is an additional effect related to Se diffusion.

S alloying with Se should narrow the band gap of CdS by raising the VBM with respect to the corresponding sulfide material [49]. CdS band gap narrowing due to Se interdiffusion has already been observed in CIGS solar cells [88]. As long as the shift only occurs in the VBM, it will not have a large influence on the physics of the interface [43]. A resulting model for the CZTSe/CdS heterointerface under significant interdiffusion is shown schematically in Fig. 5. We conclude that interdiffusion is most likely to be *detrimental* in CZTSe solar cells, since it is expected to increase a CBO that is already close to the upper limit of its optimal range. A CBO above the optimal range is, however, easier to diagnose than a CBO below the optimal range because of its peculiar effects on the illuminated current-voltage (JV) curve of the solar cell, i.e., a kink or nearly full current blockage [8, 21].

13. Alternative buffer materials

In the previous sections we have provided evidence that both a cliff-like and a spike-like CBO can *actually* exist at the CZTS/CdS hetrojunction and this deviation is not simply the result of measurement or calculation errors. Now we briefly examine the cases where alternative buffer layer materials resulted in open circuit voltage improvement in CZTS solar cells, which has often been interpreted as a sign of a more appropriate CBO at the heterojunction. A higher V_{oc} was achieved with In_2S_3 [33], $Zn_{0.35}Cd_{0.65}S$ [31], $Zn_{0.8}Sn_{0.2}O_x$ [32], and CeO_2 [34]. A higher E_A was only achieved with $Zn_{0.8}Sn_{0.2}O_x$ [32].

In the cases of In_2S_3 [33] and $Zn_{0.35}Cd_{0.65}S$ [31], the improvement can be ascribed at least partially to a more appropriate CBO at the heterojunction. Indeed, the baseline CZTS/CdS heterojunction fabricated by the same group who reported the results had a cliff-like CBO (-0.18 eV by a CBM-probing technique). This explanation is corroborated by the report of a different group that observed a spike-like CBO at the CZTS/CdS interface (+0.1 eV [21]) and did not observe a V_{oc} improvement for a CZTS/In_2S_3 heterojunction, even though V_{oc} did improve when In_2S_3 was inserted between CdS and ZnO [22].

The case of $Zn_{0.8}Sn_{0.2}O_x$ is of less straightforward interpretation. The CBO of the CZTS/$Zn_{0.8}Sn_{0.2}O_x$ interface in [32] was most likely optimal because the CBM of $Zn_{0.8}Sn_{0.2}O_x$ can be engineered by tuning x and the atomic layer deposition (ALD) temperature [69]. However, the band alignment of CZTS with the standard CdS layer resulting from the particular fabrication process of that group is not known. While it can be speculated that part of the improvement is due to a (possibly) non-optimal CBO of their CZTS/CdS heterojunction, we propose another, possibly coexisting, explanation.

Because E_A measurements on CZTS/CdS solar cells consistently yield E_A values that are at least 0.3 eV lower than the CZTS band gap [6–8], interface recombination is likely the dominant recombination path [4]. E_A determines the activation energy of whatever recombination path is dominant in the device. It can be lower than the absorber's band gap due to Fermi level pinning by charged interface states [9] or due to interface band gap narrowing from a negative CBO or a higher-lying VBM in CZTS [30]. However, the fact that interface

recombination is *dominating* implies that the interface recombination velocities for electrons and holes must be sufficiently high for this type of recombination to dominate. This is shown graphically in [12], where it is clear that variations in interface recombination velocity can lead to significant variations in V_{oc} at constant CBO, especially at the lower end of the "optimal" 0-0.4 eV CBO range.

This point is exemplified well by the significant differences between Zn(O,S) and $Zn_{0.8}Sn_{0.2}O_x$ buffer layers on the same CZTS absorber [8, 32]. While Zn(O,S) with an appropriate (O,S) mix apparently satisfies all requirements of a good buffer layer and has been employed in record CIGS solar cells [94], it was largely outperformed by $Zn_{0.8}Sn_{0.2}O_x$ in CZTS solar cells [8, 32]. It appears, therefore, as if $Zn_{0.8}Sn_{0.2}O_x$ is more effective at passivating interface states within the gap and results in lower interface recombination velocities, even though the actual passivation mechanism is not clear. Note that, even in the case of the $Zn_{0.35}Cd_{0.65}S$ buffer, part of the V_{oc} improvement may be attributed to a higher-quality passivated interface, possibly due to the better lattice matching of CZTS with ZnS than with CdS.

Finally, even though an optimal spike-like CBO has been obtained in CZTS solar cells with a variety of buffer layer materials including CdS and Zn(O,S), an E_A reasonably close to the absorber band gap was found only in the case of a $Zn_{0.8}Sn_{0.2}O_x$ buffer. This means that a negative CBO is unlikely to be the only reason behind the low E_A reported in nearly all CZTS solar cells with any buffer layer material. An alternative explanation involving an upward shift of the CZTS valence band at the interface is provided elsewhere on the basis of first-principles calculations [30].

14. Conclusion

We have shown that obtaining an optimal spike-like CBO at CZTS/CdS heterojunctions is both *possible* and *necessary* for high-efficiency solar cells, even though in many lower-efficiency devices the CBO is indeed cliff-like. Achievement of a spike-like CBO differentiates CZTS/CdS solar cells with reported efficiency above 7% from those below 5%. After analyzing the possible sources of experimental CBO variation, we have concluded that interdiffusion at the heterointerface can increase the CBO by a significant amount and may be controlled to engineer the desired band alignment through interface phase formation. On the other hand, it seems as if other phenomena exist that *decrease* the CBO in some CZTS/CdS heterojunctions. We attribute this to Fermi level pinning at the heterointerface in the samples of lower quality, which have a higher defect density. A large deviation in the measured CBOs is also expected simply due to incorrect assumptions regarding the interface band gap of the heterojunction materials, which depend on preparation conditions. A measurement method that probes the interface CBM of the materials directly should improve the accuracy of CBO determination considerably. A conduction band profile performed by inverse photoemission spectroscopy through sputter etching of the heterointerface satisfies such requirements, but it has not yet been demonstrated on CZTS(e)/CdS. Finally, the demonstrations of higher open circuit voltage in CZTS solar cells using alternative buffer materials have been attributed to a cliff-like CBO in the reference CZTS/CdS solar cell used by in those studies and to better passivation properties of some of the alternative buffers.

15. Acknowledgments

References

[1] A. Polman, M. Knight, E. C. Garnett, B. Ehrler, W. C. Sinke, Photovoltaic materials: Present efficiencies and future challenges, Science 352 (6283) (2016) aad4424. doi:10.1126/science.aad4424.

[2] W. Wang, M. T. Winkler, O. Gunawan, T. Gokmen, T. K. Todorov, Y. Zhu, D. B. Mitzi, Device Characteristics of CZTSSe Thin-Film Solar Cells with 12.6% Efficiency, Advanced Energy Materials 4 (7) (2013) 1301465. doi:10.1002/aenm.201301465.

[3] S. Tajima, M. Umehara, M. Hasegawa, T. Mise, T. Itoh, Cu_2ZnSnS_4 photovoltaic cell with improved efficiency fabricated by high-temperature annealing after CdS buffer-layer deposition, Progress in Photovoltaics: Research and Applicationsdoi:10.1002/pip.2837.

[4] A. Redinger, M. Mousel, M. H. Wolter, N. Valle, S. Siebentritt, Influence of S/Se ratio on series resistance and on dominant recombination pathway in $Cu_2ZnSn(S,Se)_4$ thin film solar cells, Thin Solid Films 535 (2013) 291–295. doi:10.1016/j.tsf.2012.11.111.

[5] T. Gokmen, O. Gunawan, D. B. Mitzi, Semi-empirical device model for $Cu_2ZnSn(S,Se)_4$ solar cells, Applied Physics Letters 105 (3) (2014) 033903. doi:10.1063/1.4890844.

[6] S. Tajima, T. Itoh, H. Hazama, K. Ohishi, R. Asahi, Improvement of the open-circuit voltage of Cu_2ZnSnS_4 solar cells using a two-layer structure, Applied Physics Express 8 (8) (2015) 082302. doi:10.7567/APEX.8.082302.

[7] K. Wang, O. Gunawan, T. Todorov, B. Shin, S. J. Chey, N. A. Bojarczuk, D. Mitzi, S. Guha, Thermally evaporated Cu_2ZnSnS_4 solar cells, Applied Physics Letters 97 (14) (2010) 143508. doi:10.1063/1.3499284.

[8] T. Ericson, J. J. Scragg, A. Hultqvist, J. T. Watjen, P. Szaniawski, T. Torndahl, C. Platzer-Björkman, Zn(O, S) Buffer Layers and Thickness Variations of CdS Buffer for Cu_2ZnSnS_4 Solar Cells, IEEE Journal of Photovoltaics 4 (1) (2014) 465–469. doi:10.1109/JPHOTOV.2013.2283058.

[9] R. Scheer, Activation energy of heterojunction diode currents in the limit of interface recombination, Journal of Applied Physics 105 (10) (2009) 104505. doi:10.1063/1.3126523.

[10] M. Palsgaard, A. Crovetto, T. Gunst, T. Markussen, O. Hansen, K. Stokbro, M. Brandbyge, Semiconductor band alignment from first principles: A new nonequilibrium Green's function method applied to the CZTSe/CdS interface for photovoltaics, in: 2016 International Conference on Simulation of Semiconductor Processes and Devices (SISPAD), IEEE, Nuremberg, Germany, 2016, pp. 377–380. doi:10.1109/SISPAD.2016.7605225.

[11] T. Minemoto, T. Matsui, H. Takakura, Y. Hamakawa, T. Negami, Y. Hashimoto, T. Uenoyama, M. Kitagawa, Theoretical analysis of the effect of conduction band offset of window/CIS layers on performance of CIS solar cells using device simulation, Solar Energy Materials and Solar Cells 67 (1) (2001) 83–88.

[12] M. Gloeckler, J. Sites, Efficiency limitations for wide-band-gap chalcopyrite solar cells, Thin Solid Films 480-481 (2005) 241–245. doi:10.1016/j.tsf.2004.11.018.

[13] M. Baer, B.-A. Schubert, B. Marsen, R. G. Wilks, S. Pookpanratana, M. Blum, S. Krause, T. Unold, W. Yang, L. Weinhardt, C. Heske, H.-W. Schock, Cliff-like conduction band offset and KCN-induced recombination barrier enhancement at the CdS/Cu_2ZnSnS_4 thin-film solar cell heterojunction, Applied Physics Letters 99 (22) (2011) 222105. doi:10.1063/1.3663327.

[14] S. Tajima, K. Kataoka, N. Takahashi, Y. Kimoto, T. Fukano, M. Hasegawa, H. Hazama, Direct measurement of band offset at the interface between CdS and Cu_2ZnSnS_4 using hard X-ray photoelectron spectroscopy, Applied Physics Letters 103 (24) (2013) 243906. doi:10.1063/1.4850235.

[15] C. Yan, F. Liu, N. Song, B. K. Ng, J. A. Stride, A. Tadich, X. Hao, Band alignments of different buffer layers (CdS, Zn(O,S), and In_2S_3) on Cu_2ZnSnS_4, Applied Physics Letters 104 (17) (2014) 173901. doi:10.1063/1.4873715.

[16] J. Li, Q. Du, W. Liu, G. Jiang, X. Feng, W. Zhang, J. Zhu, C. Zhu, The band offset at CdS/Cu_2ZnSnS_4 heterojunction interface, Electronic Materials Letters 8 (4) (2012) 365–367. doi:10.1007/s13391-012-2023-0.

[17] A. Santoni, F. Biccari, C. Malerba, M. Valentini, R. Chierchia, A. Mittiga, Valence band offset at the CdS/Cu_2ZnSnS_4 interface probed by x-ray photoelectron spectroscopy, Journal of Physics D: Applied Physics 46 (17) (2013) 175101. doi:10.1088/0022-3727/46/17/175101.

[18] S. Huang, W. Luo, Z. Zou, Band positions and photoelectrochemical properties of Cu_2ZnSnS_4 thin films by the ultrasonic spray pyrolysis method, Journal of Physics D: Applied Physics 46 (23) (2013) 235108. doi:10.1088/0022-3727/46/23/235108.

[19] R. Haight, A. Barkhouse, O. Gunawan, B. Shin, M. Copel, M. Hopstaken, D. B. Mitzi, Band alignment at the $Cu_2ZnSn(S_xSe_{1-x})_4/CdS$ interface, Applied Physics Letters 98 (25) (2011) 253502. doi:10.1063/1.3600776.

[20] J. Li, M. Wei, Q. Du, W. Liu, G. Jiang, C. Zhu, The band alignment at $CdS/Cu_2ZnSnSe_4$ heterojunction interface, Surface and Interface Analysis 45 (2) (2013) 682–684. doi:10.1002/sia.5095.

[21] T. Kato, H. Hiroi, N. Sakai, H. Sugimoto, Buffer/Absorber Interface Study on Cu_2ZnSnS_4 and $Cu_2ZnSnSe_4$ Based Solar Cells: Band Alignment and Its Impact on the Solar Cell Performance, in: 28th European Photovoltaic Solar Energy Conference and Exhibition, WIP, 2013, pp. 2125–2127. doi:10.4229/28thEUPVSEC2013-3AO.5.1.

[22] H. Hiroi, N. Sakai, T. Kato, H. Sugimoto, High voltage Cu_2ZnSnS_4 submodules by hybrid buffer layer, in: 2013 IEEE 39th Photovoltaic Specialists Conference (PVSC), IEEE, 2013, pp. 0863–0866. doi:10.1109/PVSC.2013.6744281.

[23] Z.-Y. Dong, Y.-F. Li, B. Yao, Z.-H. Ding, G. Yang, R. Deng, X. Fang, Z.-P. Wei, L. Liu, An experimental and first-principles study on band alignments at interfaces of Cu_2ZnSnS_4 /CdS/ZnO heterojunctions, Journal of Physics D: Applied Physics 47 (7) (2014) 075304. doi:10.1088/0022-3727/47/7/075304.

[24] M. Than Htay, R. Fujimura, R. Hasuike, K. Takei, N. Momose, Y. Hashimoto, K. Ito, Effect of ultrasonically generated water vapor treatment on the Cu_2ZnSnS_4/CdS heterojunction-based photovoltaic cells, Solar Energy Materials and Solar Cells 157 (2016) 765–776. doi:10.1016/j.solmat.2016.07.014.

[25] S. Chen, J. Yang, X. Gong, A. Walsh, S. Wei, Intrinsic point defects and complexes in the quaternary kesterite semiconductor Cu_2ZnSnS_4, Physical Review B 81 (24) (2010) 245204.

[26] S. Chen, A. Walsh, J.-H. Yang, X. G. Gong, L. Sun, P.-X. Yang, J.-H. Chu, S.-H. Wei, Compositional dependence of structural and electronic properties of $Cu_2ZnSn(S,Se)_4$ alloys for thin film solar cells, Physical Review B 83 (12) (2011) 125201. doi:10.1103/PhysRevB.83.125201.

[27] A. Nagoya, R. Asahi, G. Kresse, First-principles study of Cu_2ZnSnS_4 and the related band offsets for photovoltaic applications., Journal of physics. Condensed matter : an Institute of Physics journal 23 (40) (2011) 404203. doi:10.1088/0953-8984/23/40/404203.

[28] W. Bao, M. Ichimura, Prediction of the Band Offsets at the CdS/Cu_2ZnSnS_4 Interface Based on the First-Principles Calculation, Japanese Journal of Applied Physics 51 (10S) (2012) 10NC31. doi:10.1143/JJAP.51.10NC31.

[29] W. Bao, M. Ichimura, First-Principles Study on Influences of Crystal Structure and Orientation on Band Offsets at the CdS/Cu_2ZnSnS_4 Interface, International Journal of Photoenergy 2012 (Article ID 619812) (2012) 5 pages.

[30] A. Crovetto, M. L. N. Palsgaard, T. Gunst, T. Markussen, K. Stokbro, M. Brandbyge, O. Hansen, A surface state at the origin of interface losses in Cu_2ZnSnS_4 solar cells, to be published.

[31] K. Sun, C. Yan, F. Liu, J. Huang, F. Zhou, J. A. Stride, M. Green, X. Hao, Over 9% Efficient Kesterite Cu_2ZnSnS_4 Solar Cell Fabricated by Using $Zn_{1-x}Cd_xS$ Buffer Layer, Advanced Energy Materials 6 (12) (2016) 1600046. doi:10.1002/aenm.201600046.

[32] C. Platzer-Björkman, C. Frisk, J. K. Larsen, T. Ericson, S.-Y. Li, J. J. S. Scragg, J. Keller, F. Larsson, T. Törndahl, Reduced interface recombination in Cu_2ZnSnS_4 solar cells with atomic layer deposition $Zn_{1x}Sn_xO_y$ buffer layers, Applied Physics Letters 107 (24) (2015) 243904. doi:10.1063/1.4937998.

[33] C. Yan, F. Liu, K. Sun, N. Song, J. A. Stride, F. Zhou, X. Hao, M. Green, Boosting the efficiency of pure sulfide CZTS solar cells using the In/Cd-based hybrid buffers, Solar Energy Materials and Solar Cells 144 (2016) 700–706. doi:10.1016/j.solmat.2015.10.019.

[34] A. Crovetto et al., Lattice-matched Cu_2ZnSnS_4/CeO2 solar cell with open circuit voltage boost, Applied Physics Letters in press.

[35] J. Robertson, Band offsets, Schottky barrier heights, and their effects on electronic devices, Journal of Vacuum Science & Technology A: Vacuum, Surfaces, and Films 31 (5) (2013) 050821. doi:10.1116/1.4818426.

[36] A. Klein, Energy band alignment in chalcogenide thin film solar cells from photoelectron spectroscopy, Journal of Physics: Condensed Matter 27 (13) (2015) 134201. doi:10.1088/0953-8984/27/13/134201.

[37] W. Monch, Electronic Properties of Semiconductor Interfaces, Springer, Heidelberg, 2004.

[38] J. Tersoff, The theory of heterojunction band lineups, in: G. Capasso, G. Margaritondo (Eds.), Heterojunction band discontinuities: Physics and device applications, North-Holland, Amsterdam, 1987, Ch. 1.

[39] W. R. L. Lambrecht, B. Segall, Interface-bond-polarity model for semiconductor heterojunction band offsets, Physical Review B 41 (5) (1990) 2832–2848. doi:10.1103/PhysRevB.41.2832.

[40] W. Mönch, Role of virtual gap states and defects in metal-semiconductor contacts, Physical Review Letters 58 (12) (1987) 1260–1263. doi:10.1103/PhysRevLett.58.1260.

[41] O. Gunawan, T. Gokmen, C. W. Warren, J. D. Cohen, T. K. Todorov, D. A. R. Barkhouse, S. Bag, J. Tang, B. Shin, D. B. Mitzi, Electronic properties of the $Cu_2ZnSn(Se,S)_4$ absorber layer in solar cells as revealed by admittance spectroscopy and related methods, Applied Physics Letters 100 (25) (2012) 253905. doi:10.1063/1.4729751.

[42] J. Lee, J. D. Cohen, W. N. Shafarman, The determination of carrier mobilities in CIGS photovoltaic devices using high-frequency admittance measurements, Thin Solid Films 480-481 (2005) 336–340. doi:10.1016/j.tsf.2004.11.087.

[43] R. Scheer, H.-W. Schock, Chalcogenide Photovoltaics, Wiley-VCH Verlag, Weinheim, Germany, 2011. doi:10.1002/9783527633708.

[44] P. W. Tasker, The stability of ionic crystal surfaces, Journal of Physics C: Solid State Physics 12 (22) (1979) 4977–4984. doi:10.1088/0022-3719/12/22/036.

[45] W. A. Harrison, E. A. Kraut, J. R. Waldrop, R. W. Grant, Polar heterojunction interfaces, Physical Review B 18 (8) (1978) 4402–4410. doi:10.1103/PhysRevB.18.4402.

[46] Y. Hinuma, A. Grüneis, G. Kresse, F. Oba, Band alignment of semiconductors from density-functional theory and many-body perturbation theory, Physical Review B 90 (15) (2014) 155405. doi:10.1103/PhysRevB.90.155405.

[47] S.-H. Wei, A. Zunger, Calculated natural band offsets of all IIVI and IIIV semiconductors: Chemical trends and the role of cation d orbitals, Applied Physics Letters 72 (16) (1998) 2011. doi:10.1063/1.121249.

[48] A. Alkauskas, P. Broqvist, F. Devynck, A. Pasquarello, Band Offsets at Semiconductor-Oxide Interfaces from Hybrid Density-Functional Calculations, Physical Review Letters 101 (10) (2008) 106802. doi:10.1103/PhysRevLett.101.106802.

[49] Y.-H. Li, A. Walsh, S. Chen, W.-J. Yin, J.-H. Yang, J. Li, J. L. F. Da Silva, X. G. Gong, S.-H. Wei, Revised ab initio natural band offsets of all group IV, II-VI, and III-V semiconductors, Applied Physics Letters 94 (21) (2009) 212109. doi:10.1063/1.3143626.

[50] M. Bär, B.-A. Schubert, B. Marsen, S. Schorr, R. G. Wilks, L. Weinhardt, S. Pookpanratana, M. Blum, S. Krause, Y. Zhang, W. Yang, T. Unold, C. Heske, H.-W. Schock, Electronic structure of Cu_2ZnSnS_4 probed by soft x-ray emission and absorption spectroscopy, Physical Review B 84 (3) (2011) 035308. doi:10.1103/PhysRevB.84.035308.

[51] D. Lim, R. Haight, In situ photovoltage measurements using femtosecond pump-probe photoelectron spectroscopy and its application to metalHfO2Si structures, Journal of Vacuum Science & Technology A: Vacuum, Surfaces, and Films 23 (6) (2005) 1698. doi:10.1116/1.2083909.

[52] S. Siebentritt, Why are kesterite solar cells not 20% efficient?, Thin Solid Films 535 (2013) 1–4.

75

[53] B. Shin, O. Gunawan, Y. Zhu, N. A. Bojarczuk, S. J. Chey, S. Guha, Thin film solar cell with 8.4% power conversion efficiency using an earth-abundant Cu_2ZnSnS_4 absorber, Progress in Photovoltaics: Research and Applications 21 (1) (2013) 72–76. doi:10.1002/pip.1174.

[54] B.-A. Schubert, B. Marsen, S. Cinque, T. Unold, R. Klenk, S. Schorr, H.-W. Schock, Cu_2ZnSnS_4 thin film solar cells by fast coevaporation, Progress in Photovoltaics: Research and Applications 19 (1) (2011) 93–96. doi:10.1002/pip.976.

[55] C. Malerba, Cu2ZnSnS4 thin films and solar cells: material and device characterization, PhD thesis, University of Trento (2014).

[56] S. Siol, J. C. Hellmann, S. D. Tilley, M. Grätzel, J. Morasch, J. Deuermeier, W. Jaegermann, A. Klein, Band Alignment Engineering at Cu_2O/ZnO Heterointerfaces.

[57] A. Polizzotti, I. L. Repins, R. Noufi, S.-H. Wei, D. B. Mitzi, The state and future prospects of kesterite photovoltaics, Energy & Environmental Science 6 (11) (2013) 3171–3182. doi:10.1039/c3ee41781f.

[58] R. W. Grant, J. R. Waldrop, E. A. Kraut, Observation of the Orientation Dependence of Interface Dipole Energies in Ge-GaAs, Physical Review Letters 40 (10) (1978) 656–659. doi:10.1103/PhysRevLett.40.656.

[59] R. Nicolini, L. Vanzetti, G. Mula, G. Bratina, L. Sorba, A. Franciosi, M. Peressi, S. Baroni, R. Resta, A. Baldereschi, J. E. Angelo, W. W. Gerberich, Local interface composition and band discontinuities in heterovalent heterostructures, Physical Review Letters 72 (2) (1994) 294–297. doi:10.1103/PhysRevLett.72.294.

[60] F. Liu, C. Yan, J. Huang, K. Sun, F. Zhou, J. A. Stride, M. A. Green, X. Hao, Nanoscale Microstructure and Chemistry of Cu_2ZnSnS_4/CdS Interface in Kesterite Cu 2 ZnSnS 4 Solar Cells, Advanced Energy Materials 6 (15) (2016) 1600706. doi:10.1002/aenm.201600706.

[61] D. B. Mitzi, O. Gunawan, T. K. Todorov, K. Wang, S. Guha, The path towards a high-performance solution-processed kesterite solar cell, Solar Energy Materials and Solar Cells 95 (6) (2011) 1421–1436. doi:10.1016/j.solmat.2010.11.028.

[62] J. J. S. Scragg, L. Choubrac, A. Lafond, T. Ericson, C. Platzer-Björkman, A low-temperature order-disorder transition in Cu_2ZnSnS_4 thin films, Applied Physics Letters 104 (4) (2014) 041911. doi:10.1063/1.4863685.

[63] G. Rey, A. Redinger, J. Sendler, T. P. Weiss, M. Thevenin, M. Guennou, B. El Adib, S. Siebentritt, The band gap of $Cu_2ZnSnSe_4$: Effect of order-disorder, Applied Physics Letters 105 (11) (2014) 112106. doi:10.1063/1.4896315.

[64] M. Valentini, C. Malerba, F. Menchini, D. Tedeschi, A. Polimeni, M. Capizzi, A. Mittiga, Effect of the order-disorder transition on the optical properties of Cu_2ZnSnS_4, Applied Physics Letters 108 (21) (2016) 211909. doi:10.1063/1.4952973.

[65] S. Chen, A. Walsh, X.-G. Gong, S.-H. Wei, Classification of Lattice Defects in the Kesterite Cu_2ZnSnS_4 and $Cu_2ZnSnSe_4$ Earth-Abundant Solar Cell Absorbers, Advanced Materials 25 (11) (2013) 1522–1539. doi:10.1002/adma.201203146.

[66] G. Hodes, Chemical solution deposition of semiconductor films, Marcel Dekker, New York, Basel, 2002.

[67] M. Murayama, T. Nakayama, Chemical trend of band offsets at wurtzite/zinc-blende heterocrystalline semiconductor interfaces, Physical Review B 49 (7) (1994) 4710–4724. doi:10.1103/PhysRevB.49.4710.

[68] K. I. Kang, B. P. McGinnis, Sandalphon, Y. Z. Hu, S. W. Koch, N. Peyghambarian, A. Mysyrowicz, L. C. Liu, S. H. Risbud, Confinement-induced valence-band mixing in CdS quantum dots observed by two-photon spectroscopy, Physical Review B 45 (7) (1992) 3465–3468. doi:10.1103/PhysRevB.45.3465.

[69] J. Lindahl, J. Keller, O. Donzel-Gargand, P. Szaniawski, M. Edoff, T. Törndahl, Deposition temperature induced conduction band changes in zinc tin oxide buffer layers for $Cu(In,Ga)Se_2$ solar cells, Solar Energy Materials and Solar Cells 144 (2016) 684–690. doi:10.1016/j.solmat.2015.09.048.

[70] Y. Wang, N. Herron, Quantum size effects on the exciton energy of CdS clusters, Physical Review B 42 (11) (1990) 7253–7255. doi:10.1103/PhysRevB.42.7253.

[71] S. Tajima, H. Katagiri, K. Jimbo, N. Sugimoto, T. Fukano, Temperature Dependence of Cu_2ZnSnS_4 Photovoltaic Cell Properties, Applied Physics Express 5 (8) (2012) 082302. doi:10.1143/APEX.5.082302.

[72] F. Liu, Y. Lai, J. Liu, B. Wang, S. Kuang, Z. Zhang, J. Li, Y. Liu, Characterization of chemical bath deposited CdS thin films at different deposition temperature, Journal of Alloys and Compounds 493 (1) (2010)

305–308. doi:10.1016/j.jallcom.2009.12.088.

[73] C. G. Van de Walle, L. H. Yang, Band discontinuities at heterojunctions between crystalline and amorphous silicon, Journal of Vacuum Science & Technology B: Microelectronics and Nanometer Structures 13 (4) (1995) 1635. doi:10.1116/1.587870.

[74] S. Tajima, R. Asahi, D. Isheim, D. N. Seidman, T. Itoh, M. Hasegawa, K. Ohishi, Atom-probe tomographic study of interfaces of Cu_2ZnSnS_4 photovoltaic cells, Applied Physics Letters 105 (9) (2014) 093901. doi:10.1063/1.4894858.

[75] Y. S. Lee, T. Gershon, O. Gunawan, T. K. Todorov, T. Gokmen, Y. Virgus, S. Guha, $Cu_2ZnSnSe_4$ Thin-Film Solar Cells by Thermal Co-evaporation with 11.6% Efficiency and Improved Minority Carrier Diffusion Length, Advanced Energy Materials 5 (7) (2015) 1401372. doi:10.1002/aenm.201401372.

[76] T. Gokmen, O. Gunawan, T. K. Todorov, D. B. Mitzi, Band tailing and efficiency limitation in kesterite solar cells, Applied Physics Letters 103 (10) (2013) 103506. doi:10.1063/1.4820250.

[77] W. N. Shafarman, S. Siebentritt, L. Stolt, $Cu(InGa)Se_2$ Solar Cells, in: A. Luque, S. Hegedus (Eds.), Handbook of Photovoltaic Science and Engineering, John Wiley & Sons, Ltd, Chichester, UK, 2011, Ch. 13. doi:10.1002/9780470974704.

[78] S. López-Marino, Y. Sánchez, M. Placidi, A. Fairbrother, M. Espindola-Rodríguez, X. Fontané, V. Izquierdo-Roca, J. López-García, L. Calvo-Barrio, A. Pérez-Rodríguez, E. Saucedo, ZnSe etching of Zn-rich $Cu_2ZnSnSe_4$: an oxidation route for improved solar-cell efficiency., Chemistry (Weinheim an der Bergstrasse, Germany) 19 (44) (2013) 14814–22. doi:10.1002/chem.201302589.

[79] W. Li, J. Chen, C. Yan, X. Hao, The effect of ZnS segregation on Zn-rich CZTS thin film solar cells, Journal of Alloys and Compounds 632 (2015) 178–184. doi:10.1016/j.jallcom.2015.01.205.

[80] A. Fairbrother, E. García-Hemme, V. Izquierdo-Roca, X. Fontané, F. A. Pulgarín-Agudelo, O. Vigil-Galán, A. Pérez-Rodríguez, E. Saucedo, Development of a selective chemical etch to improve the conversion efficiency of Zn-rich Cu_2ZnSnS_4 solar cells., Journal of the American Chemical Society 134 (19) (2012) 8018–21. doi:10.1021/ja301373e.

[81] M. Bar, B.-A. Schubert, B. Marsen, S. Krause, S. Pookpanratana, T. Unold, L. Weinhardt, C. Heske, H.-W. Schock, Impact of KCN etching on the chemical and electronic surface structure of Cu_2ZnSnS_4 thin-film solar cell absorbers, Applied Physics Letters 99 (15) (2011) 152111. doi:10.1063/1.3650717.

[82] N. Sakai, H. Hiroi, H. Sugimoto, Development of Cd-free buffer layer for Cu_2ZnSnS_4 thin-film solar cells, in: 2011 37th IEEE Photovoltaic Specialists Conference, IEEE, 2011, pp. 003654–003657. doi:10.1109/PVSC.2011.6185941.

[83] K. F. Tai, O. Gunawan, M. Kuwahara, S. Chen, S. G. Mhaisalkar, C. H. A. Huan, D. B. Mitzi, Fill Factor Losses in $Cu_2ZnSn(S_xSe_{1-x})_4$ Solar Cells: Insights from Physical and Electrical Characterization of Devices and Exfoliated Films, Advanced Energy Materials 6 (3) (2016) 1501609. doi:10.1002/aenm.201501609.

[84] K. Sardashti, R. Haight, T. Gokmen, W. Wang, L.-Y. Chang, D. B. Mitzi, A. C. Kummel, Impact of Nanoscale Elemental Distribution in High-Performance Kesterite Solar Cells, Advanced Energy Materials 5 (10) (2015) 1402180. doi:10.1002/aenm.201402180.

[85] S. S. Wilson, J. P. Bosco, Y. Tolstova, D. O. Scanlon, G. W. Watson, H. A. Atwater, Interface stoichiometry control to improve device voltage and modify band alignment in ZnO/Cu_2O heterojunction solar cells, Energy Environ. Sci. 7 (11) (2014) 3606–3610. doi:10.1039/C4EE01956C.

[86] C. Heske, D. Eich, R. Fink, E. Umbach, T. van Buuren, C. Bostedt, L. J. Terminello, S. Kakar, M. M. Grush, T. A. Callcott, F. J. Himpsel, D. L. Ederer, R. C. C. Perera, W. Riedl, F. Karg, Observation of intermixing at the buried CdS/Cu(In, Ga)Se_2 thin film solar cell heterojunction, Applied Physics Letters 74 (10) (1999) 1451. doi:10.1063/1.123578.

[87] T. Nakada, Nano-structural investigations on Cd-doping into $Cu(In,Ga)Se_2$ thin films by chemical bath deposition process, Thin Solid Films 361 (2000) 346–352. doi:10.1016/S0040-6090(99)00767-1.

[88] M. Morkel, L. Weinhardt, B. Lohmueller, C. Heske, E. Umbach, W. Riedl, S. Zweigart, F. Karg, Flat conduction-band alignment at the CdS/$CuInSe_2$ thin-film solar-cell heterojunction, Applied Physics Letters 79 (27) (2001) 4482. doi:10.1063/1.1428408.

[89] J. P. Enríquez, E. Gómez Barojas, R. Silva González, U. Pal, S and Te inter-diffusion in CdTe/CdS hetero junction, Solar Energy Materials and

Solar Cells 91 (15) (2007) 1392–1397. doi:10.1016/j.solmat.2007.05.008.

[90] T. Maeda, S. Nakamura, T. Wada, First-Principles Study on Cd Doping in Cu_2ZnSnS_4 and $Cu_2ZnSnSe_4$, Japanese Journal of Applied Physics 51 (10S) (2012) 10NC11. doi:10.1143/JJAP.51.10NC11.

[91] M. Baer, B.-A. Schubert, B. Marsen, S. Krause, S. Pookpanratana, T. Unold, L. Weinhardt, C. Heske, H.-W. Schock, Native oxidation and Cu-poor surface structure of thin film Cu_2ZnSnS_4 solar cell absorbers, Applied Physics Letters 99 (11) (2011) 112103. doi:10.1063/1.3637574.

[92] G. Margaritondo, Heterojunction band discontinuities: A fundamental problem in solid-state science, Journal of Vacuum Science & Technology B: Microelectronics and Nanometer Structures 11 (4) (1993) 1362. doi:10.1116/1.586941.

[93] R. Klenk, Characterisation and modelling of chalcopyrite solar cells, Thin Solid Films 387 (1-2) (2001) 135–140. doi:10.1016/S0040-6090(00)01736-3.

[94] K. Kushiya, CIS-based thin-film PV technology in solar frontier K.K., Solar Energy Materials and Solar Cells 122 (2014) 309–313. doi:10.1016/j.solmat.2013.09.014.

Semiconductor band alignment from first principles: a new nonequilibrium Green's function method applied to the CZTSe/CdS interface for photovoltaics.

Mattias L. N. Palsgaard*[†], Andrea Crovetto[†], Tue Gunst[†], Troels Markussen*, Ole Hansen[†], Kurt Stokbro*
and Mads Brandbyge[†]

[†]Center for Nanostructured Graphene (CNG), Department of Micro- and Nanotechnology (DTU Nanotech)
*Quantumwise A/S, Fruebjergvej 3, Postbox 4, DK-2100 Copenhagen, Denmark

Abstract—In this paper we present a method to obtain the band offset of semiconductor heterointerfaces from Density Functional Theory together with the nonequilibrium Green's function method. Band alignment and detailed properties of the interface between $Cu_2ZnSnSe_4$ and CdS are extracted directly from first principles simulations. The interface is important for photovoltaics applications where in particular the band offsets are important for efficiency. The band bending pose a problem for accurate atomistic simulations of band offsets due to its long range. Here we investigate two different methods for dealing with band bending directly. One involves doping the materials to induce a shorter screening length. The other method is to apply a voltage bias across the interface to correct for the band bending. The calculated band offsets agree well with previous experimental and theoretical studies and, interestingly, the offset is seen to depend on whether or not the interface is under flat-band conditions.

I. INTRODUCTION

Semiconductor heterointerfaces play an increasingly important role in optical and electronic devices due to miniaturization and to the pervasive trend of introducing new materials to tailor the desired device properties [1]. In particular, the valence- and conduction band offsets (VBO and CBO) at the interface affect the transport properties and recombination rates at the interface [2].
Methods to obtain VBO and CBO from first principles have been recently reviewed [3]. Among them, an explicit interface modeling method inspired by the photoemission measurement has gained significant popularity due to its excellent agreement with experimental data [4]–[6]. In this method, the energy positions of the valence bands of materials A and B are first calculated separately in the two unstrained bulk materials with respect to a reference energy unique to each bulk calculation (for example, the position of a core level). Then, an explicit interface calculation is employed to align the two valence band positions to a common energy reference, which can be a core level or the averaged local potential.

Conversely, we propose a method where the band alignment can be obtained directly from the interface supercell

calculation containing both materials using Density Functional Theory (DFT) together with Nonequilibrium Green's functions (NEGF). In this way it is further possible to extract information about the atomic properties of the interface such as defects and tunneling of states over the interface and study transport phenomena. Similar methods have been used previously to study Schottky barriers [7].

To demonstrate this method, we have selected the CZTSe-CdS interface as a case study. $Cu_2ZnSnSe_4$ (CZTSe, band gap 1.0 eV), Cu_2ZnSnS_4 (CZTS, band gap 1.5 eV) and their alloy $Cu_2ZnSnS_xSe_{4-x}$ (CZTSSe, tunable band gap 1.0-1.5 eV) are promising p-type semiconductors for thin-film photovoltaics. To indicate all three materials in general terms we use the notation CZTS(e). In solar cell devices, their n-type heterojunction partner is typically CdS, with which the best conversion efficiencies reported so far have been achieved [8], [9]. A schematic band diagram is shown in Fig. 1(a).

As noted in a number of review papers [10]–[12], loss mechanisms at the CZTS(e)/CdS interface are believed to be one of the reasons why laboratory-scale CZTS(e) solar cells still lag far behind their theoretical maximum efficiency. To emphasize the potentially dramatic consequences of an unfavorable band alignment of the CZTSe/CdS interface on solar cell efficiency, we have carried out a device-level simulation (Fig. 1(b)). There, we have swept the electron affinity of CZTSe to recreate different hypothetical band alignments, according to Anderson's rule [2]. The results are shown in Fig. 1(b). A type I alignment, or conduction band "spike" with a height between +0.1 eV and +0.4 eV (Fig. 1) is found to be optimal, in agreement with similar studies on other solar cell heterointerfaces [13], [14].

Despite the importance of the offset values in device performance, only few reports of calculated band alignments are available in the literature and mostly with focus on CZTS. Only one report could be found on CZTSe [15]. To the best of our knowledge, only the photoemission-inspired calculation method [4] has been reported for any CZTS(e)/CdS interface [15]. The actual band alignment at the CZTS-CdS interface is still disputed, with experimental and theoretical offsets scat-
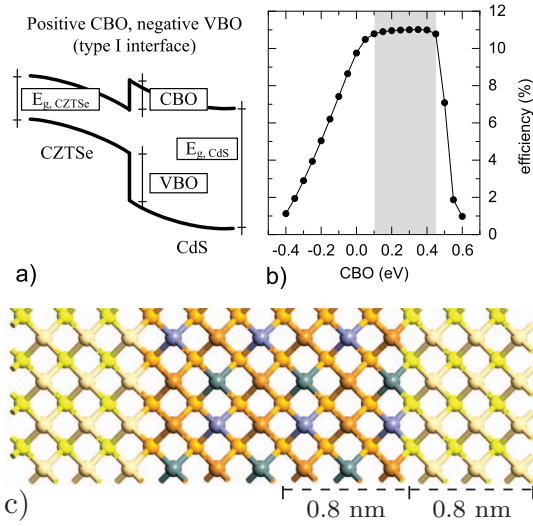
Figure 1: a) Schematic illustration of the sign conventions and symbols used for the band alignment problem. The signs of the CBO and VBO are referred to the lower band gap semiconductor, so that a positive CBO means that the CdS conduction band lies above the CZTSe conduction band. Assuming a negative VBO, a positive (negative) CBO results in a type I (II) interface, also known as conduction band spike (cliff). $E_{g,CZTSe}$ and $E_{g,CdS}$ are the band gaps of CZTSe and CdS respectively. b) Simulated CZTSe/CdS heterojunction solar cell efficiency as a function of the conduction band offset. The shaded region is the optimal CBO range for achieving maximum efficiency. c) Periodic supercell containing the (100)/(100) interface of CZTS and CdS, dimensioned as in previously reported calculations [15].

tered in a broad energy range -0.34 eV to +0.45 eV. However, the few existing studies for the CZTSe-CdS interface are in rather good agreement: Different photoemission experiments have measured +0.48 eV [16], +0.34 eV [17], and +0.3 eV offsets [18], while a theoretical study has calculated a +0.34 eV offset [15]. This provides a benchmark for our proposed method and allows adding new information to an interface in which the band alignment is relatively well established.

II. COMPUTATIONAL DETAILS

The preliminary device-level simulation was performed numerically with the finite-element method as implemented in the thin-film solar cell simulation software SCAPS [19] on a standard CZTSe/CdS/ZnO device structure. The material parameters were taken from various literature sources [20], [21]. The CBO between CZTSe and CdS was swept from -0.4 eV to +0.6 eV by sweeping the electron affinity of CZTS while maintaining the flat band conditions at the contacts.

All first-principles calculations in this study were performed with the ATK DFT software [22] using a double zeta polarized LCAO basis set [23], [24]. The combination of DFT with NEGF enables a device setup with semi-infinite electrodes on each side of the interface.
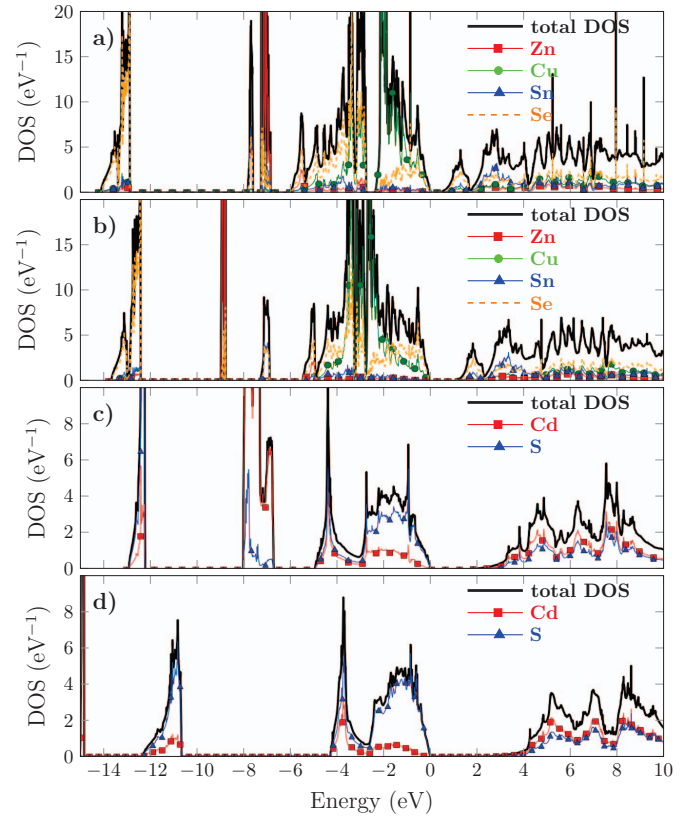

Figure 2: Total and projected density of states of bulk CZTSe calculated with GGA (a) and GGA + U (b) and for bulk CdS calculated with GGA (c) and GGA + U (d).

It is well known that the bandgaps of CZTSe and CdS are poorly reproduced with the conventional local density approximation (LDA) or generalized gradient approximation (GGA) approach to the exchange-correlation potential in DFT calculations [15]. We use the semi-empirical Hubbard correction where an additional energy term of the form

$$E_U = \frac{1}{2} \sum_\mu U_\mu \left(n_\mu - n_\mu^2 \right) \tag{1}$$

where n_μ is the projection onto an atomic shell and U is chosen to reproduce the experimental bandgap in the bulk unit cell of either material, is added to the usual GGA-PBE exchange-correlation functional. This method is a computationally cheap way to correct for the self interaction of localized electrons in strongly correlated systems [25]. In Fig. 2, we compare density of states (DOS) of bulk CZTSe calculated with and without the Hubbard correction term. As expected the bandgaps are opened and the valence bands of d-like character for Zn and Cd are downshifted in energy. This is very similar to the effects seen when using the G_0W_0(HSE) approach on CZTS [26] indicating a high degree of self interaction error in these systems. Previous theoretical studies [15] have been performed on interface supercells with up to 3 unit cells of either material. This means that dimensions only up to a few nm in the direction perpendicular to the interface plane have been used
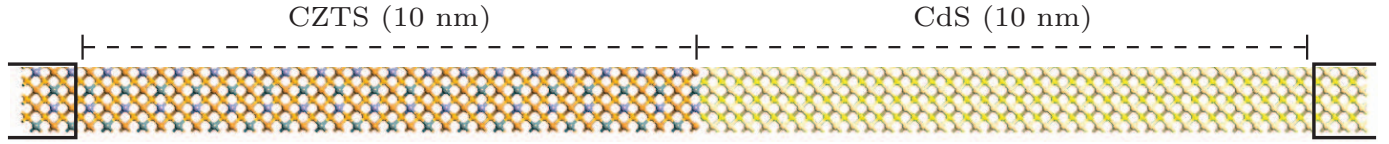
Figure 3: Structure used to simulate the 100/100 interface of CZTSe (left) and CdS (right). The supercell is more than five times larger than that used in previous work [15].

(Fig. 1). Furthermore these calculations were performed using periodic boundary conditions (PBC) in all directions resulting in interfaces separated by less than 2 nm as shown in Fig. 1.

Instead, in this work we employed a supercell that is 20 nm in length (Fig. 3) and semi-infinite boundary conditions in the direction perpendicular to the interface plane, as allowed by the DFT-NEGF approach. This assures that bulk-like conditions are met on either side. This approach can be justified as the thickness of each layer of material in real devices is tens of nm for CdS and hundreds of nm for CZTSe, so semi-infinite boundary conditions give a better description of the situation than PBC's [7]. The supercells employed in the calculation are periodic along the interface using 5x3 k-points. In the electrodes of the device a 3x5x100 k-point grid is used. K-points were chosen so that the total energy of the bulk materials was converged to within 0.5 meV. Several interfaces can be constructed with different surface geometries and formation energies. Here we consider the CZTSe(100)/CdS(100) interface, which has relatively low strain of ∼2.5%. GGA + U is known to overestimate lattice parameters for CZTS(e), we therefore keep the experimental lattice parameter for CZTSe. When setting up the interface the CdS bulk crystal is strained to fit that of CZTSe.

All relaxation where performed until interatomic force where below 0.02 eV/Å. Calculations of the local density of states (LDOS) in the device were performed using 11x11 k-points. Using this scheme we can for the first time study directly the effect of the interface on the band-alignment and transport properties in this system.

III. RESULTS

Fig. 4(a) shows the LDOS and the local potential across the intrinsic (non-doped) interface. We see a clear spike-like CBO in agreement with previous theoretical and experimental studies [15], [16]. The potential shows a residual slope towards the electrodes indicating that the screening is not contained within the supercell. Nevertheless, the CBO obtained with this method (∼0.3eV) is in good agreement with experimental data measured under equilibrium conditions [17], [18]. To address the problem of the residual slope in the potential, one can reduce the screening length by doping both materials. Our simulations include doping by adding a complementary charge to the atomic sites. Fig. 4(b) shows the LDOS and local potential across the interface where a p-type (n-type) charge density of 10^{18} cm^{-3} unit charges are added to CZTSe (CdS). Adding the charge removes the residual slope of the potential, however it also dramatically changes the electronic structure of
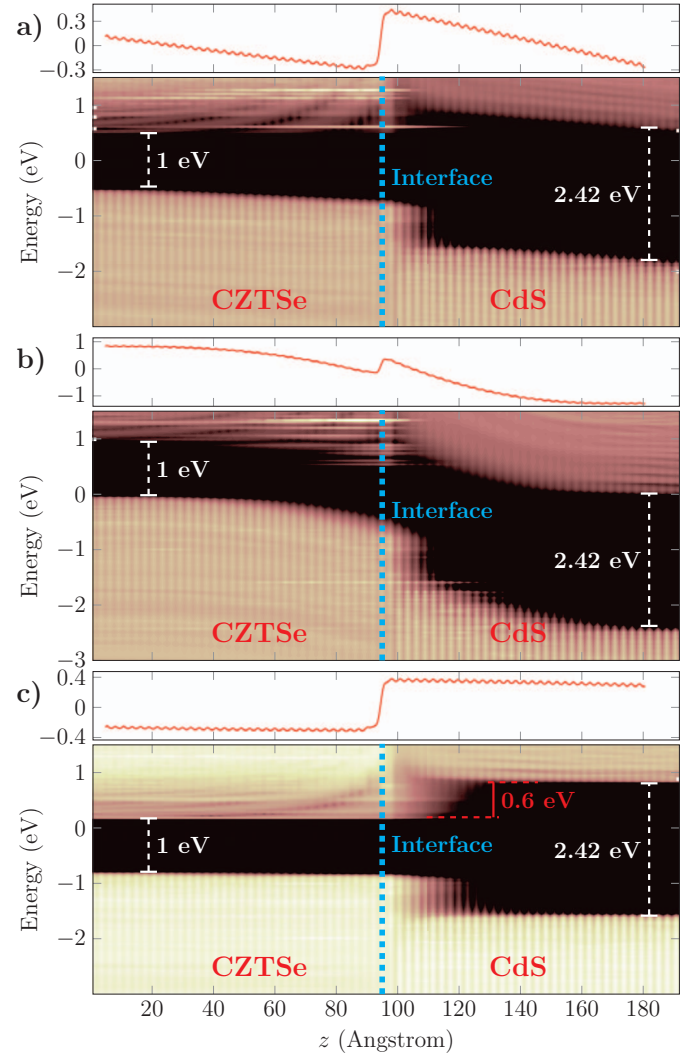
Figure 4: The local potential (top) and local density of states (bottom) of the CZTSe/CdS interface resolved along the direction perpendicular to the interface surface. (a) equilibrium conditions with zero bias and zero doping; (b) equilibrium conditions with zero bias and 10^{18} cm^{-3} doping density; (c) non-equilibrium conditions with an applied forward bias to achieve flat-band conditions and zero doping.

the interface. Further, it must be emphasized that the amount of charge needed here to contain the screening within the cell is very large compared to the real doping density of CZTSe, which is on the order of 10^{15}–10^{16} cm^{-3} [8]. In

fact, the experimental screening length of CZTSe (equivalent to the depletion region width in a p-n$^+$ junction device) is about 20 times larger than the width of the CZTSe layer in our supercell and consequently several hundred times larger than previous theoretical studies [8], [15]. To handle weakly screened materials, i.e. with band bending occurring over more than a few nm, we apply a small forward bias in the device simulations. Fig. 4(c) shows the LDOS and potential across such a system. Clearly we have in this way achieved flat band conditions on both sides of the device and at the same time removed the residual slope of the local potential. Such a calculation is only possible due to the device setup we have used here. The obtained CBO is +0.6 eV which agrees nicely with the only reported measurement done under flat-band conditions [16]. Note that the CBO is larger in the flat-band case than in the case of equilibrium band bending, which was also the case in experimental studies [16]–[18]. Finally in the LDOS for the undoped and doped systems at equilibrium, Fig. 4(a) and Fig. 4(b) respectively, localized states appear inside the gaps of either material. Localized states can have a crucial impact on the performance of any electronic device by e.g. increasing the recombination rate. They may also lead to errors in experimental measurements of band offsets due to lack of sufficient resolution to distinguish an interface state from its nearest bulk band. These states can be addressed directly in the device method as opposed to bulk supercell simulations. In particular, we note that the CBO in the doped system (Fig. 4(b)) is strongly influenced by the presence of localized states.

IV. Conclusion

We have successfully analyzed the electronic structure of the interface between CdS and $Cu_2ZnSnSe_4$ using first principles calculations. This interface is of particular interest for the photovoltaics community. The conduction band offset across the interface has been identified as a bottleneck for efficiency of a promising thin-film solar cell device, using device simulations. From DFT-NEGF calculations a CBO of +0.6 eV is found under flat-band conditions imposed by applying a forward bias over the interface to correct for band-bending. The results agree reasonably well with experiments under equilibrium and flat-band conditions.

Acknowledgment

References

[1] "The interface is still the device." *Nature materials*, vol. 11, no. 2, p. 91, mar 2012.

[2] G. Margaritondo, *Electronic structure of semiconductor heterojunctions*. Kluwer Academic Publishers.

[3] Y. Hinuma, A. Grüneis, G. Kresse, and F. Oba, "Band alignment of semiconductors from density-functional theory and many-body perturbation theory," *Physical Review B*, vol. 90, no. 15, p. 155405, oct 2014.

[4] S.-H. Wei and A. Zunger, "Calculated natural band offsets of all II–VI and III–V semiconductors: Chemical trends and the role of cation d orbitals," *Applied Physics Letters*, vol. 72, no. 16, p. 2011, apr 1998.

[5] A. Alkauskas, P. Broqvist, F. Devynck, and A. Pasquarello, "Band Offsets at Semiconductor-Oxide Interfaces from Hybrid Density-Functional Calculations," *Physical Review Letters*, vol. 101, no. 10, p. 106802, sep 2008.

[6] Y.-H. Li, A. Walsh, S. Chen, W.-J. Yin, J.-H. Yang, J. Li, J. L. F. Da Silva, X. G. Gong, and S.-H. Wei, "Revised ab initio natural band offsets of all group IV, II-VI, and III-V semiconductors," *Applied Physics Letters*, vol. 94, no. 21, p. 212109, may 2009.

[7] D. Stradi, U. Martinez, A. Blom, M. Brandbyge, and K. Stokbro, "General atomistic approach for modeling metal-semiconductor interfaces using density functional theory and nonequilibrium green's function," *Phys. Rev. B*, vol. 93, p. 155302, Apr 2016.

[8] Y. S. Lee, T. Gershon, O. Gunawan, T. K. Todorov, T. Gokmen, Y. Virgus, and S. Guha, "$Cu_2ZnSnSe_4$ Thin-Film Solar Cells by Thermal Co-evaporation with 11.6% Efficiency and Improved Minority Carrier Diffusion Length," *Advanced Energy Materials*, vol. 5, no. 7, p. 1401372, apr 2015.

[9] W. Wang, M. T. Winkler, O. Gunawan, T. Gokmen, T. K. Todorov, Y. Zhu, and D. B. Mitzi, "Device Characteristics of CZTSSe Thin-Film Solar Cells with 12.6% Efficiency," *Advanced Energy Materials*, vol. 4, no. 7, p. 1301465, nov 2013.

[10] S. Siebentritt, "Why are kesterite solar cells not 20% efficient?" *Thin Solid Films*, vol. 535, pp. 1–4, 2013.

[11] A. Polizzotti, I. L. Repins, R. Noufi, S.-H. Wei, and D. B. Mitzi, "The state and future prospects of kesterite photovoltaics," *Energy & Environmental Science*, vol. 6, no. 11, pp. 3171–3182, oct 2013.

[12] X. Liu, Y. Feng, H. Cui, F. Liu, X. Hao, G. Conibeer, D. B. Mitzi, and M. Green, "The current status and future prospects of kesterite solar cells: a brief review," *Progress in Photovoltaics: Research and Applications*, jan 2016.

[13] T. Minemoto, T. Matsui, H. Takakura, Y. Hamakawa, T. Negami, Y. Hashimoto, T. Uenoyama, and M. Kitagawa, "Theoretical analysis of the effect of conduction band offset of window/CIS layers on performance of CIS solar cells using device simulation," *Solar Energy Materials and Solar Cells*, vol. 67, no. 1, pp. 83–88, 2001.

[14] M. Gloeckler and J. Sites, "Efficiency limitations for wide-band-gap chalcopyrite solar cells," *Thin Solid Films*, vol. 480-481, pp. 241–245, jun 2005.

[15] S. Chen, A. Walsh, J.-H. Yang, X. G. Gong, L. Sun, P.-X. Yang, J.-H. Chu, and S.-H. Wei, "Compositional dependence of structural and electronic properties of $Cu_2ZnSn(S,Se)_4$ alloys for thin film solar cells," *Physical Review B*, vol. 83, no. 12, p. 125201, mar 2011.

[16] R. Haight, A. Barkhouse, O. Gunawan, B. Shin, M. Copel, M. Hopstaken, and D. B. Mitzi, "Band alignment at the $Cu_2ZnSn(S_xSe_{1-x})_4$/CdS interface," *Applied Physics Letters*, vol. 98, no. 25, p. 253502, jun 2011.

[17] J. Li, M. Wei, Q. Du, W. Liu, G. Jiang, and C. Zhu, "The band alignment at CdS/$Cu_2ZnSnSe_4$ heterojunction interface," *Surface and Interface Analysis*, vol. 45, no. 2, pp. 682–684, feb 2013.

[18] T. Kato, H. Hiroi, N. Sakai, and H. Sugimoto, "Buffer/Absorber Interface Study on Cu_2ZnSnS_4 and $Cu_2ZnSnSe_4$ Based Solar Cells: Band Alignment and Its Impact on the Solar Cell Performance." *28th European Photovoltaic Solar Energy Conference*, pp. 2125–2127, sep 2013.

[19] M. Burgelman, P. Nollet, and S. Degrave, "Modelling polycrystalline semiconductor solar cells," *Thin Solid Films*, vol. 361-362, pp. 527–532, feb 2000.

[20] M. Gloeckler, "Device physics of Cu(In,Ga)Se2 thin-film solar cells," PhD thesis, Colorado State University, 2005.

[21] K. Ito, *Copper Zinc Tin Sulfide-Based Thin-Film Solar Cells*. Wiley, 2015.

[22] Atomistix ToolKit version 2015.0, QuantumWise A/S.

[23] J. M. Soler, E. Artacho, J. D. Gale, A. García, J. Junquera, P. Ordejón, and D. Sánchez-Portal, "The siesta method for ab initio order- n materials simulation," *Journal of Physics: Condensed Matter*, vol. 14, no. 11, p. 2745, 2002.

[24] M. Brandbyge, J.-L. Mozos, P. Ordejón, J. Taylor, and K. Stokbro, "Density-functional method for nonequilibrium electron transport," *Phys. Rev. B*, vol. 65, p. 165401, Mar 2002.

[25] V. I. Anisimov, J. Zaanen, and O. K. Andersen, "Band theory and Mott insulators: Hubbard U instead of Stoner I," *Physical Review B*, vol. 44, no. 3, pp. 943–954, jul 1991.

[26] J. Paier, R. Asahi, A. Nagoya, and G. Kresse, "Cu_2ZnSnS_4 as a potential photovoltaic material: A hybrid hartree-fock density functional theory study," *Phys. Rev. B*, vol. 79, p. 115126, Mar 2009.

Surface states behind open circuit voltage losses in Cu_2ZnSnS_4 solar cells

Andrea Crovetto,[1, a)] Mattias Palsgaard,[1, 2, b)] Tue Gunst,[1] Troels Markussen,[2] Kurt Stokbro,[2] Mads Brandbyge,[1] and Ole Hansen[1, 3]

[1)] *DTU Nanotech, Technical University of Denmark, DK-2800 Kgs. Lyngby, Denmark*

[2)] *QuantumWise A/S, DK-2100 Copenhagen, Denmark*

[3)] *V-SUSTAIN, Villum Center for the Science of Sustainable Fuels and Chemicals, Technical University of Denmark, DK-2800 Kgs. Lyngby, Denmark*

We present evidence that band gap narrowing at the heterointerface may be a major cause of the large open circuit voltage deficit of Cu_2ZnSnS_4/CdS solar cells. Band gap narrowing is caused by surface states that extend the Cu_2ZnSnS_4 valence band into the forbidden gap. Those surface states are consistently found in Cu_2ZnSnS_4, but not in $Cu_2ZnSnSe_4$, by first-principles calculations. They do not simply arise from defects at surfaces but are an intrinsic feature of Cu_2ZnSnS_4 surfaces. By including those states in a device model, the outcome of previously published temperature-dependent open circuit voltage measurements on Cu_2ZnSnS_4 solar cells can be reproduced quantitatively without assuming a cliff-like conduction band offset at the heterointerface. Our first-principles calculations indicate that the success of Zn-based alternative heterojunction partner materials may be due to the ability of Zn to passivate those surface states. Improved passivation by novel Zn-based materials is expected to yield further improvement of the open circuit voltage.

Research on the p-type semiconductor $Cu_2ZnSn(S,Se)_4$ (CZTS(e)) for solar cells is driven by the hope of achieving similar performance to the highly successful $Cu(In,Ga)(S,Se)_2$ (CIGS) solar cells, without the need to rely on highly sought-after elements (In and Ga) that may face scarcity problems if solar cell production volumes should increase by manifold. The highest reported power conversion efficiencies of CZTS(e) solar cells have been achieved with a CdS heterointerface partner, also known as buffer layer.[1,2] However, CZTS(e) solar cells still suffer from a large voltage deficit, meaning that the open circuit voltage of the solar cell is much lower than the band gap of the material. The origin this loss may be elucidated by a temperature-dependent measurement of the open circuit voltage. The extrapolation of the open circuit voltage to 0 K is expected to yield the activation energy of the main recombination path. If the extracted activation energy is lower than the band gap of the absorber, interface recombination may be dominant because of two possible mechanisms:[3] i) interface gap narrowing, for example due to a cliff-like conduction band offset (CBO) at the heterointerface, or ii) Fermi level pinning due to charged interface- or bulk states. Both mechanisms limit the achievable quasi-Fermi level splitting at the interface at 0 K (activation energy of interface recombination) to a value below the band gap of the absorber. We define the difference between the bulk band gap of the absorber and the activation energy of the dominant recombination path "recombination energy deficit".

In CZTSe, that is, CZTS(e) with a high Se content, there is convincing evidence that most of the open circuit voltage deficit is not due to recombination at the heterointerface. Indeed, both current-voltage (JV) characteristics and device quantum efficiency (QE) could be reproduced by device-level simulation in the absence of any interface recombination mechanisms in two independent studies.[4,5] Instead, the voltage deficit could be reproduced by assuming narrowing of the recombination band gap due to fluctuations in the bulk band edges of CZTSe. Furthermore, the recombination energy deficit (0.11 eV) measured in state-of-the-art CZTSe devices fits nicely to the 0.10 eV offset between the band gap of the extended states in the bulk and the effective recombination band gap in the bulk, extracted respectively from the QE and photoluminescence (PL) spectra in the same devices.[6] This hints to the fact that interface recombination is not the main recombination mechanism in CZTSe solar cells and that electronic phenomena in the CZTS bulk can account alone for the open circuit voltage loss.

The situation is very different in state-of-the-art CZTS solar cells, that is, CZTS(e) with a low Se content. There, the recombination energy deficit is about 0.4 eV[7,8] but the bulk recombination band gap is only 0.1-0.2 eV lower than the band gap of the extended states in the CZTS bulk.[9,10] Such a mismatch means that bulk phenomena are unlikely to be the only reason for the large open circuit voltage deficit in CZTS solar cells. Indeed, two independent device simulation studies found it necessary to introduce a finite recombination velocity at the CZTS/CdS interface, coupled with a cliff-like CBO, to reproduce the electro-optical characteristics of the solar cells.[11,12] Even though a dominating contribution from interface recombination does not necessarily imply a cliff-like CBO at the heterointerface, the latter is still often assumed in the literature to be the main reason of the enhanced interface recombination.[11,13,14] Therefore, considerable research effort has been devoted to replacing CdS with other materials such as In_2S_3,[15,16] $Zn(O,S)$,[8] $(Zn,Cd)S$,[14] and $(Zn,Sn)O$,[10] with their selection criterion being a (supposedly) more favorable CBO

a)Electronic mail: ancro@nanotech.dtu.dk

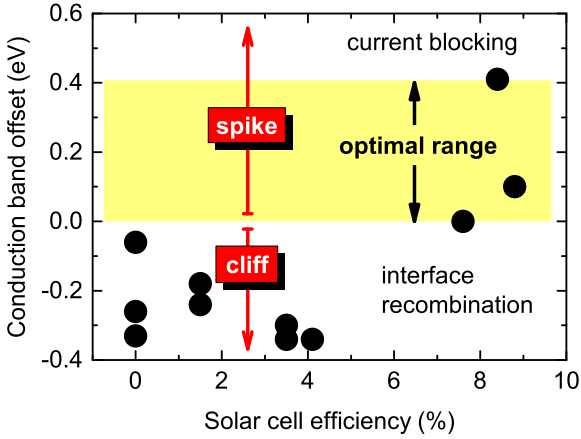b)Electronic mail: mattias.palsgaard@quantumwise.com

FIG. 1. Correlation between measured CBO values at the CZTS/CdS interface and corresponding solar cell efficiency. Data from Refs. 17–19, 22–26.

with CZTS. However, Fig. 1 illustrates that all the CBO measurements taken on CZTS/CdS heterointerfaces that resulted in solar cells above 7% efficiency yielded values between 0 and +0.4 eV.[17–19] This corresponds exactly to the optimal CBO range for photovoltaics.[20] It seems, therefore, as if obtaining an optimal CBO at the CZTS/CdS interface is possible. It is only in the lower-efficiency cells that the CBO was found to be negative. The favorable CBO obtained in the most successful solar cells is possibly due to interface phase formation caused by Zn and Cd interdiffusion at the heterointerface.[21] To sum up, Fig. 1 provides evidence in favor of an alternative interface phenomenon as responsible for the open circuit voltage limitation of state-of-the-art CZTS solar cells with efficiency above 7%.

In an attempt to identify such a phenomenon, we performed first-principles electronic structure calculations on the CZTS(100)/CdS(100) and CZTSe(100)/CdS(100) interfaces, as described in the Computational Details and in Ref. 27. The choice of interface orientation can be justified based on transmission electron microscopy results from some of the highest-efficiency CZTS solar cells reported in the literature, which consistently show a (100)-oriented epitaxial interface.[28,29] This also justifies modeling the CZTS/CdS interface as epitaxial in our calculation. Fig. 2(a,b) shows the calculated density of states (DOS) close to the band edges as a function of position along the direction perpendicular to the interface, for both the CZTSe/CdS and CZTS/CdS interface. The resulting CBOs are +0.2 eV for the CZTS/CdS interface and +0.6 eV for the CZTSe/CdS interface. Besides the differences in band alignment, we note that localized interface states are present at the CZTS/CdS interface but are absent from the CZTSe/CdS interface.

To quantify the depth of the localized states into the forbidden gap, we show in Fig. 2(c) the DOS of the
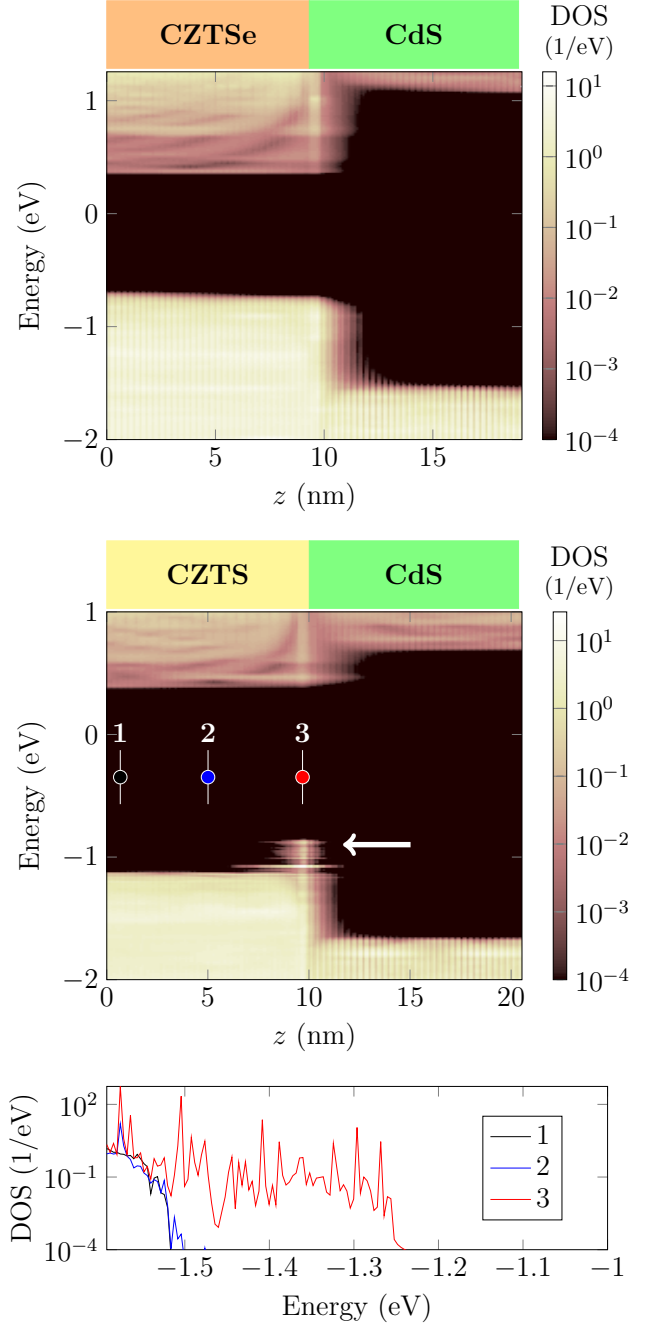
FIG. 2. Local density of states of the CZTSe/CdS interface (a) and of the CZTS/CdS interface (b) resolved along the direction perpendicular to the interface surface. (c) Local density of states at the three positions indicated in (b). Results are obtained under non-equilibrium conditions with an applied forward bias to achieve flat-band conditions.[27]

CZTS/CdS interface as a function of energy at the three positions indicated in Fig. 2(b). At positions 1 and 2, the valence band maximum (VBM) of CZTS is located at a value of about -1.5 eV on an arbitrary energy scale. However, at position 3 the presence of the localized states

results in an extension of the valence band up to 0.2-0.3 eV above the original VBM. It is desirable to verify whether the presence of the localized states (and their absence at the CZTSe/CdS interface) can be confirmed with a different computational method and under different modeling assumptions. For this purpose, we repeated the interface calculations with a standard GGA-PBE exchange-correlation potential by removing the Hubbard term used in our original calculation (see Computational Details). Furthermore, we performed an additional calculation where the distance between the CZTS and the CdS layers was relaxed in the direction perpendicular to interface, to account for any out-of-plane strain imposed by their 7% lattice mismatch. In both calculations, the localized states were still observed (not shown here). This indicates that their presence is independent of the computational approach and therefore they are expected to occur in real CZTS/CdS interfaces, at a minimum in those where (100)-oriented epitaxial growth is observed.

The next question is where the localized states come from. A first step is to understand if they are a feature of the CZTS surface alone, or if they are due to the interaction between the two materials at the heterointerface. Therefore we performed a S-terminated CZTS slab calculation, that is, a CZTS(100)/vacuum interface instead of a CZTS/CdS interface. When plotting the resulting spatially-resolved density of states, localized states above the VBM of CZTS are observed (not shown here), similarly to the interface calculation in Fig. 2(b). This suggests that the localized states are surface states intrinsic to the CZTS surface, and they do not originate from interaction with the heterojunction partner. In fact, focusing again on the CZTS/CdS interface calculation, it is evident that the localized states are situated exclusively on the CZTS side on the junction (Fig. 3). More specifically, the states are highly localized on Cu sites in the first cationic layer of CZTS and on their neighboring S atoms in the interface anionic layer (Fig. 3). Since the valence band of CZTS originates from Cu and S states,[27,30] it is logical that a modification in the local environment of those elements due to the presence of a surface or an interface will mostly affect the valence band.

In view of the above discussion, the localized states appearing in the CZTS/CdS interface calculation can be interpreted as surface states localized on Cu and S atoms due to dangling bonds on the S-terminated bare CZTS surface. Those dangling bonds are not adequately passivated by the adjacent CdS material, therefore their corresponding states remain when a CZTS/CdS interface is formed. Other surface- or interface states may exist at both the CZTS/CdS and at the CZTSe/CdS interfaces and they may be localized on different atoms than Cu and S. For example, a perturbation of the bulk DOS is clearly observed above the CZTS(e) conduction band at both interfaces under consideration (Fig. 2(a,b)). However, our calculation predicts that any additional states do not result in energy levels within the forbidden gap, so their potential impact on the final device is much lower
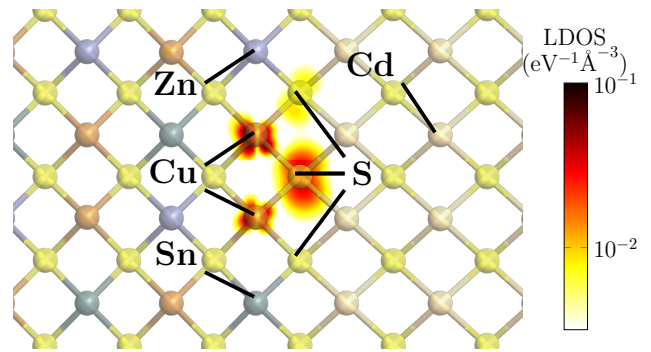

FIG. 3. Spatially-resolved DOS of the localized states at the CZTS/CdS interface. The DOS at a single energy, marked by the arrow in Fig. 2(b), is plotted in the figure. Such an energy is 0.2 eV above the VBM at positions 1 and 2. The localized states are situated on the Cu atoms in the first cationic layer on the CZTS side and on their neighboring S atoms in the interface anionic layer.

as they do not act as trapping levels for charge carriers. Note that, even though pure S-terminated CZTS surfaces are unlikely to occur due to surface reconstruction phenomena,[31] CZTS can be considered as S-terminated at the heterointerface with another sulfide material (like CdS) because the S atoms are shared between both materials. Interestingly, there exists some experimental evidence of the presence of electrically active surface states at the CZTS surface, and of their absence at the CZTSe surface, as predicted by our calculation. A surface photovoltage measurement by scanning tunneling microscopy[32] revealed that, while both CZTS and CZTSe surfaces appeared to be in accumulation (that is, with upward band bending), only in CZTS was the photocurrent dominated by surface electronic states.

The identification of localized states at the CZTS/CdS interface can help explain why CZTS solar cells are still limited by interface recombination, even in the case of an optimal band alignment with CdS. To demonstrate this quantitatively, we move from atomistic modeling to device-level simulation, as explained in the Computational Details. To model the localized interface states in a simulated CZTS device, we refer to the results of our first-principles calculation. According to the calculation, the DOS of the localized states is continuous in energy from the bulk-like VBM of positions 1 and 2, up to 0.2-0.3 eV into the forbidden gap with only limited decay (Fig. 2(c)). The depth of the localized states in real space is limited to an interface region less than 5 nm (Fig. 2(b)). Therefore, for device simulation purposes, the localized states are modeled as a 0.2 eV upward shift in the valence band over a 5 nm region at the interface, rather than a valence band tail or a single defect level within the gap. This is equivalent to narrowing the interface band gap from the CZTS side – the opposite assumption of a negative CBO, where the interface band gap is narrowed from the CdS side. The other materi-
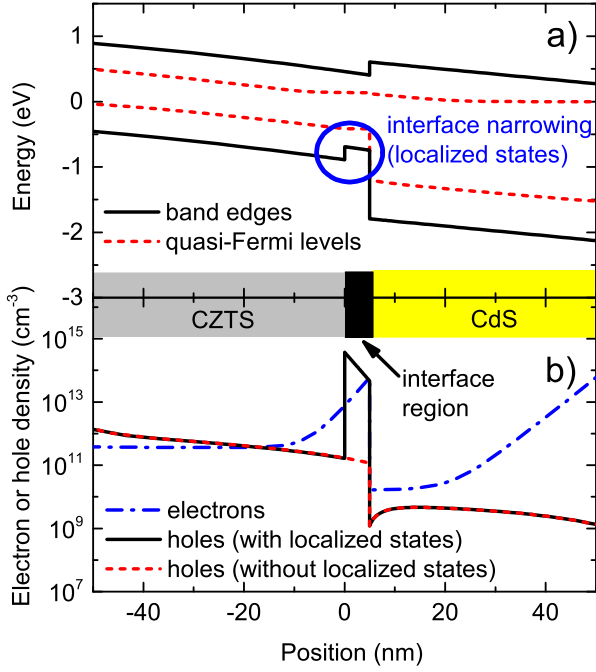
FIG. 4. Simulated properties of a CZTS/CdS heterojunction under AM1.5 illumination and no applied voltage, with interface narrowing due to localized states. (a) Band diagram and corresponding quasi-Fermi levels for electrons and holes. (b) Electron and hole density in the same region. When localized states are included in the simulation, the electron and hole densities at the interface are comparable, which maximizes the interface recombination rate. In a baseline case with no localized states, the hole density is much lower. The electron density is the same in both scenarios.
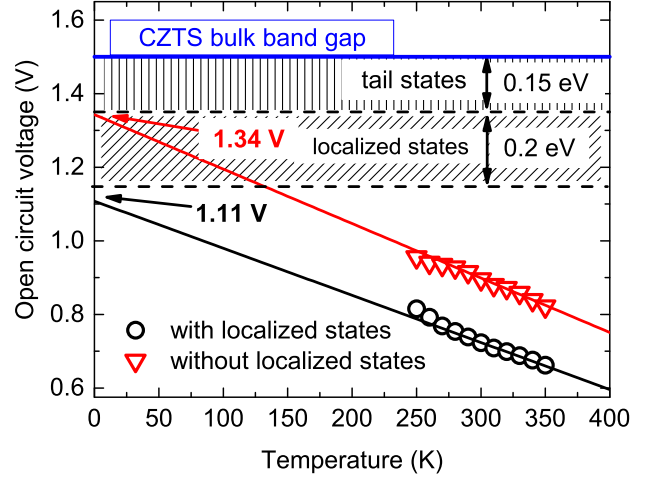

FIG. 5. Simulated open circuit voltage of complete CZTS/CdS solar cells as a function of temperature. The linearly extrapolated 0 K intercept of the data yields the activation energy of the dominant recombination path.

als parameters of this interface region are kept identical to the CZTS material properties in a baseline CZTS solar cell device simulated for comparison, as shown in Table I. Apart from interface gap narrowing, we note two important features our device model. The first is the assumption of a positive CBO between CZTS and CdS, consistently with state-of-the-art CZTS/CdS solar cells (Fig. 1). The second is the distinction between an optical band gap of 1.5 eV and a transport band gap of 1.35 eV. This approach has been suggested by other authors[4,11] to model the mismatch between the band gap of the extended states (which defines the optical absorption onset of CZTS after deconvolution of tail states), and the band gap from which bulk recombination occurs (which includes the tail states due to bulk fluctuations in the CZTS band edges).[33] 0.15 eV is a typical depth for the tail states of high-quality CZTS.[9,10]

The resulting band diagram of the simulated device with localized states is shown in Fig. 4(a). Two important device-level effects with respect to the baseline case without localized states: i) an increase in the hole density at the interface, and ii) a decrease in the effective recom-

bination band gap at the interface by 0.2 eV. Effect i) is demonstrated in Fig. 4(b), which shows the electron- and hole density near the interface without and with localized states. In the latter case the hole density at the interface increases by three orders of magnitude, up to values that are comparable to the electron density. This translates to a higher recombination rate at the interface, because the Shockley-Read-Hall recombination rate increases with increasing electron and hole densities, and is maximized when the two densities equal each other.[34,35] Note that it is the same principle, but in the opposite direction, that allows very favorable interface recombination properties in highly efficient CIGS/CdS solar cell: there, the VBM of CIGS is actually shifted *downwards* due to formation of the ordered vacancy compound at the Cu-poor CIGS surface, which effectively reduces the hole population at the interface.[36] Effect ii) will decrease the recombination barrier in the interface region to a value that is 0.2 eV lower than the CZTS band gap. As long as interface recombination is the dominant recombination path, this effect alone should result in a 0.2 eV recombination energy deficit in a temperature-dependent open circuit voltage measurement. However, the ubiquitous observation of a recombination energy deficit in real CZTS devices has usually been attributed to a negative CBO at the CZTS/CdS interface instead, even though a positive or null CBO is consistently reported in the highest-efficiency CZTS/CdS solar cells (Fig. 1).

To verify that interface narrowing by localized states can be a plausible explanation for the large recombination energy deficit of CZTS/CdS solar cells, we use our device model to simulate a temperature-dependent open circuit voltage measurement (Fig. 5). For the baseline case without localized states, extrapolation of the open

circuit voltage to 0 K yields a value of 1.34 V. This matches the value of the transport band gap (1.35 eV) defined in our model, and it means that such a baseline device is not limited by interface recombination but the activation energy of the domination recombination path is still lower than the CZTS optical band gap due to bulk tail states. For the case of interface narrowing through localized states, the open circuit voltage extrapolates to 1.11 V, which matches the value of the transport gap minus 0.2 eV narrowing at the interface as defined for the interface region (1.15 eV). The corresponding recombination energy deficit is 0.39 eV, which fits very well with the recombination energy deficits of 0.3 eV, 0.4 eV, and 0.4 eV found experimentally in the highest-efficiency CZTS solar cells with a CdS heterojunction partner.[2,7,8] This result shows that interface recombination is the dominant recombination path in the device with interface narrowing, as expected by the increased hole population (Fig. 4(b)). It also demonstrates that narrowing of the interface band gap through an upward shift of the CZTS valence band can explain existing temperature-dependent open circuit voltage measurements just as well as a negative CBO does. Finally, it implies that complete passivation of CZTS surface states could possibly yield a $\sim$200 mV boost in open circuit voltage.

This interesting prospect may be practically realized by replacing CdS with an appropriate passivation material, or by adding a thin layer of such a passivation material between CZTS and CdS. The question is which material would work. Limiting our analysis to a (100)-(100) interface with a metal chalcogenide (MX, where M is the metal and X is the chalcogen) with cubic or tetragonal structure, one approach could be to consider the first cationic layer of such a material. Such a cationic layer breaks the bulk crystal structure of CZTS by introducing a layer of $2M_{Cu} + M_{Zn} + M_{Sn}$ point defects. In the case of CdS, those defects are $2Cd_{Cu} + Cd_{Zn} + Cd_{Sn}$. Therefore, one strategy could be to search for a metal $\tilde{M}$ where the $2\tilde{M}_{Cu} + \tilde{M}_{Zn} + \tilde{M}_{Sn}$ defect complex does not narrow the CZTS band gap nor introduces discrete energy levels in the CZTS band gap. If one chooses M = Zn, the defect complex reduces to just $2Zn_{Cu} + Zn_{Sn}$. The effect of this particular defect complex on the electronic properties of CZTS has been investigated before.[37] The result was that the $2Zn_{Cu} + Zn_{Sn}$ complex does not narrow the band gap of CZTS. Therefore, there is hope that a Zn chalcogenide material could remove the surface states. To test this hypothesis with our first-principles interface calculation, an obvious choice for a Zn chalcogenide is ZnS, due to its simple cubic structure with nearly perfect lattice matching with CZTS. Therefore we repeated our CZTS interface calculation replacing CdS with ZnS. Strikingly, Fig. 6 shows that the surface states are indeed absent within the resolution of the calculation, which means that their DOS is at least three orders of magnitude smaller than in the case of a CdS heterojunction partner. This indicates that the ideal situation of a CZTS interface without band gap narrowing could be achieved by re-
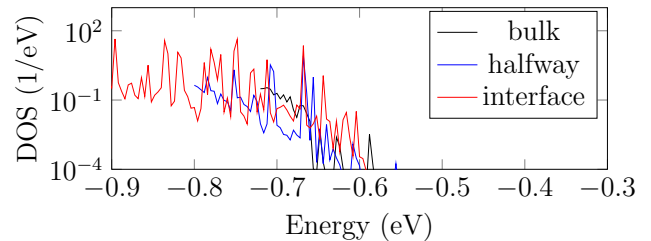

FIG. 6. Local density of states of the CZTS/ZnS interface calculated at positions equivalent to those in Fig. 2(a). Note that no distinct localized states can be seen in contrast to the result for the CZTS/CdS interface.

placement of CdS by a Zn chalcogenide, with a corresponding shift of the dominant recombination path from the interface to the bulk. Our results provide a theoretical foundation behind the empirical finding that Zn-based alternative heterojunction partners have so far resulted in the largest open circuit voltage improvement of CZTS/CdS solar cells. $Zn_{0.8}Sn_{0.2}O_x$ improved the open circuit voltage from 666 mV to 713 mV;[10] $Zn_{0.35}Cd_{0.65}S$ from 665 mV to 748 mV;[14] and a generic Zn-based buffer by an unspecified amount.[38] $Zn_{0.8}Sn_{0.2}O_x$ is also the only heterojunction partner material to date that has resulted in a decrease of the recombination energy deficit of CZTS solar cells from the typical 0.3-0.4 eV down to 0.16 eV,[10] which corresponds roughly to the depth of CZTS bulk tail states. Unfortunately, pure ZnS is not suitable due to its extremely large positive CBO with CZTS,[39] which blocks electron transport in solar cell devices.[8]

To conclude, we have shown that the interface band gap of CZTS/CdS solar cells is narrowed by localized states that shift the valence band maximum of CZTS to a higher energy. The same effect does not occur at the CZTSe/CdS interface. This phenomenon can explain why interface recombination is always observed to dominate in CZTS solar cells but not in CZTSe solar cells, a fact that has so far been attributed to differences in the conduction band alignment of the two interfaces with the CdS buffer layer. We have shown that a Zn-based chalcogenide can effectively passivate CZTS surfaces by removing the localized states. This can explain the success of Zn-based buffer layers in shifting the dominant recombination path of CZTS solar cells from the interface to the bulk and in improving their open circuit voltage. According to device simulation, the open circuit voltage of a CZTS/CdS solar cell could be boosted by about 200 mV if complete passivation of the localized states is achieved by an appropriate buffer layer material.

COMPUTATIONAL DETAILS

First principles calculations were performed with a density functional theory-nonequilibrium Green's function (DFT-NEGF) approach within the generalized gradient approximation (GGA-PBE) as implemented in the Atomistix ToolKit

(QuantumWise A/S). A semi-empirical Hubbard energy term (DFT+U approach) is added to the GGA-PBE exchange-correlation potential to correct for self-interaction of localized d-orbitals and yield accurate band gaps. All calculations were performed, with a double-zeta-polarized basis set based on linear combination of atomic orbitals (LCAO). Atomic positions of the CZTS(e) were relaxed keeping the experimental lattice parameters. For CdS and ZnS we relaxed the atomic positions until all forces were below 0.02 eV/Å in a cell strained to fit that of CZTS(e) in the directions parallel to the interface. The lattice parameter perpendicular to the interface was relaxed until the stress was below 0.005 eV/Å^3. For the bulk calculations of CZTS we used a $5 \times 5 \times 3$ Monkhorst-Pack $\mathbf{k}$-point grid. For the bulk calculations of CdS and ZnS we used a $5 \times 5 \times 5$ Monkhorst-Pack $\mathbf{k}$-point grid. For the device calculation of the interfaces we used 5×3 transverse $\mathbf{k}$-points. Density of states calculations were performed using 21×21 transverse $\mathbf{k}$-points. As explained in Ref. 27, we performed the calculation by applying a forward voltage bias across the supercell to remove residual slopes of the local potential near the electrodes. For an appropriate magnitude of the applied voltage, flat-band conditions are achieved. To justify this approach, we emphasize two points here: i) even though in a realistic band diagram of the heterojunction under equilibrium there is an electrostatic potential drop at the junction (Fig. 4(a)), the latter occurs over a much larger length scale than the supercell length, thus to a first order approximation the bands can be assumed to be flat within a few nm from the junction; and ii) the optimal working point of the solar cell device is indeed under forward bias, close to flat-band conditions. Device-level simulation in the interface-normal direction was carried out with the finite element method as implemented in the software SCAPS.[40] The device parameters are listed in Table I.

[1] W. Wang, M. T. Winkler, O. Gunawan, T. Gokmen, T. K. Todorov, Y. Zhu, and D. B. Mitzi, Advanced Energy Materials **4**, 1301465 (2013).
[2] S. Tajima, T. Itoh, H. Hazama, K. Ohishi, and R. Asahi, Applied Physics Express **8**, 082302 (2015).
[3] R. Scheer, Journal of Applied Physics **105**, 104505 (2009).
[4] T. Gokmen, O. Gunawan, and D. B. Mitzi, Applied Physics Letters **105**, 033903 (2014).
[5] J. E. Moore, C. J. Hages, R. Agrawal, M. S. Lundstrom, and J. L. Gray, Applied Physics Letters **109**, 021102 (2016).
[6] O. Gunawan, T. K. Todorov, and D. B. Mitzi, Applied Physics Letters **97**, 233506 (2010).
[7] K. Wang, O. Gunawan, T. Todorov, B. Shin, S. J. Chey, N. A. Bojarczuk, D. Mitzi, and S. Guha, Applied Physics Letters **97**, 143508 (2010).
[8] T. Ericson, J. J. Scragg, A. Hultqvist, J. T. Watjen, P. Szaniawski, T. Torndahl, and C. Platzer-Björkman, IEEE Journal of Photovoltaics **4**, 465 (2014).
[9] B. Shin, O. Gunawan, Y. Zhu, N. A. Bojarczuk, S. J. Chey, and S. Guha, Progress in Photovoltaics: Research and Applications **21**, 72 (2013).
[10] C. Platzer-Björkman, C. Frisk, J. K. Larsen, T. Ericson, S.-Y. Li, J. J. S. Scragg, J. Keller, F. Larsson, and T. Törndahl, Applied Physics Letters **107**, 243904 (2015).
[11] C. Frisk, T. Ericson, S. Y. Li, P. Szaniawski, J. Olsson, and C. Platzer-Björkman, Solar Energy Materials and Solar Cells **144**, 364 (2016).
[12] M. Courel, J. A. Andrade-Arvizu, and O. Vigil-Galán, Applied Physics Letters **105**, 233501 (2014).
[13] S. Bourdais, C. Choné, B. Delatouche, A. Jacob, G. Larramona, C. Moisan, A. Lafond, F. Donatini, G. Rey, S. Siebentritt, A. Walsh, and G. Dennler, Advanced Energy Materials, 1502276 (2016).
[14] K. Sun, C. Yan, F. Liu, J. Huang, F. Zhou, J. A. Stride, M. Green, and X. Hao, Advanced Energy Materials **6**, 1600046 (2016).
[15] D. A. R. Barkhouse, R. Haight, N. Sakai, H. Hiroi, H. Sugimoto, and D. B. Mitzi, Applied Physics Letters **100**, 193904 (2012).
[16] C. Yan, F. Liu, K. Sun, N. Song, J. A. Stride, F. Zhou, X. Hao, and M. Green, Solar Energy Materials and Solar Cells **144**, 700 (2016).
[17] R. Haight, A. Barkhouse, O. Gunawan, B. Shin, M. Copel, M. Hopstaken, and D. B. Mitzi, Applied Physics Letters **98**, 253502 (2011).
[18] S. Tajima, K. Kataoka, N. Takahashi, Y. Kimoto, T. Fukano, M. Hasegawa, and H. Hazama, Applied Physics Letters **103**, 243906 (2013).
[19] T. Kato, H. Hiroi, N. Sakai, and H. Sugimoto, in *28th European Photovoltaic Solar Energy Conference and Exhibition* (WIP, 2013) pp. 2125–2127.
[20] T. Minemoto, T. Matsui, H. Takakura, Y. Hamakawa, T. Negami, Y. Hashimoto, T. Uenoyama, and M. Kitagawa, Solar Energy Materials and Solar Cells **67**, 83 (2001).
[21] A. Crovetto and O. Hansen, to be published.
[22] M. Baer, B.-A. Schubert, B. Marsen, R. G. Wilks, S. Pookpanratana, M. Blum, S. Krause, T. Unold, W. Yang, L. Weinhardt, C. Heske, and H.-W. Schock, Applied Physics Letters **99**, 222105 (2011).
[23] C. Yan, F. Liu, N. Song, B. K. Ng, J. A. Stride, A. Tadich, and X. Hao, Applied Physics Letters **104**, 173901 (2014).
[24] J. Li, Q. Du, W. Liu, G. Jiang, X. Feng, W. Zhang, J. Zhu, and C. Zhu, Electronic Materials Letters **8**, 365 (2012).
[25] A. Santoni, F. Biccari, C. Malerba, M. Valentini, R. Chierchia, and A. Mittiga, Journal of Physics D: Applied Physics **46**, 175101 (2013).
[26] S. Huang, W. Luo, and Z. Zou, Journal of Physics D: Applied Physics **46**, 235108 (2013).
[27] M. Palsgaard, A. Crovetto, T. Gunst, T. Markussen, O. Hansen, K. Stokbro, and M. Brandbyge, in *2016 International Conference on Simulation of Semiconductor Processes and Devices (SISPAD)* (IEEE, Nuremberg, Germany, 2016) pp. 377–380.
[28] S. Tajima, R. Asahi, D. Isheim, D. N. Seidman, T. Itoh, M. Hasegawa, and K. Ohishi, Applied Physics Letters **105**, 093901 (2014).
[29] F. Liu, C. Yan, J. Huang, K. Sun, F. Zhou, J. A. Stride, M. A. Green, and X. Hao, Advanced Energy Materials **6**, 1600706 (2016).
[30] C. Persson, Journal of Applied Physics **107**, 053710 (2010).
[31] C. Persson and A. Zunger, Applied Physics Letters **87**, 211904 (2005).
[32] H. Du, M. J. Romero, I. Repins, G. Teeter, R. Noufi, and M. M. Al-Jassim, in *2011 37th IEEE Photovoltaic Specialists Conference* (IEEE, 2011) pp. 001983–001986.
[33] S. Siebentritt, G. Rey, A. Finger, D. Regesch, J. Sendler, T. P. Weiss, and T. Bertram, Solar Energy Materials and Solar Cells (2015), 10.1016/j.solmat.2015.10.017.
[34] C.-T. Sah, R. Noyce, and W. Shockley, Proceedings of the IRE **45**, 1228 (1957).
[35] M. Gloeckler and J. Sites, Thin Solid Films **480-481**, 241 (2005).
[36] R. Klenk, Thin Solid Films **387**, 135 (2001).
[37] S. Chen, A. Walsh, X.-G. Gong, and S.-H. Wei, Advanced Materials **25**, 1522 (2013).
[38] N. Sakai, H. Hiroi, and H. Sugimoto, in *2011 37th IEEE Photovoltaic Specialists Conference* (IEEE, 2011) pp. 003654–003657.
[39] A. Nagoya, R. Asahi, and G. Kresse, Journal of physics. Condensed matter : an Institute of Physics journal **23**, 404203 (2011).
[40] M. Burgelman, P. Nollet, and S. Degrave, Thin Solid Films **361-362**, 527 (2000).

A. Contact properties		Front	Back
S_{e} (cm/s)		10^7	10^7
S_{h} (cm/s)		10^7	10^7
$\phi_{\mathrm{Bn0}}, \phi_{\mathrm{Bp0}}$ (eV)		0	0
B. Layer properties	Window (ZnO)	Buffer (CdS)	Absorber (CZTS)
Thickness (nm)	50	60	1000
$E_{\mathrm{g,o}}$ (eV)	3.3	2.4	1.5
$E_{\mathrm{g,t}}$ (eV)	3.3	2.4	1.35
χ (eV)	4.5	4.5	4.7
ε_{r}	9.0	10.0	6.7
N_{C} (cm^{-3})	2.2×10^{18}	2.2×10^{18}	6.7×10^{17}
N_{V} (cm^{-3})	1.8×10^{19}	1.8×10^{19}	1.5×10^{19}
μ_{e} (cm^2/Vs)	100	100	3
μ_{h} (cm^2/Vs)	25	25	1
$N_{\mathrm{d/a}}$ (cm^{-3})	$N_{\mathrm{d}} = 1 \times 10^{20}$	$N_{\mathrm{d}} = 1 \times 10^{15}$	$N_{\mathrm{a}} = 3 \times 10^{16}$
C. Defect states	Window (ZnO)	Buffer (CdS)	Absorber (CZTS)
Type	Single donor	Single acceptor	Single donor
Energy distribution	Single level	Single level	Single level
N_{t} (cm^{-3})	1×10^{17}	2×10^{17}	1×10^{13}
E_{t} (eV)	$E_{\mathrm{C}} - 1.65$	$E_{\mathrm{C}} - 1.2$	$E_{\mathrm{C}} - 0.6$
σ_{e} (cm^2)	1×10^{-12}	1×10^{-17}	5×10^{-13}
σ_{h} (cm^2)	1×10^{-17}	1×10^{-12}	1×10^{-15}
D. Interface defect	ZnO/CdS	CdS/CZTS	
Type	N.A.	Neutral	
Energy distribution		Single level	
E_{t} (eV)		$E_{\mathrm{V,CZTS}} + 0.2$	
N_{t} (cm^{-3})		1×10^{12}	
σ_{e} (cm^2)		1×10^{-16}	
σ_{e} (cm^2)		1×10^{-14}	

TABLE I. The parameters used for device simulation of a baseline CZTS solar cell without interface narrowing. S_{e} and S_{h} are the interface recombination velocities for electrons and holes; ϕ_{Bn0} and ϕ_{Bp0} is the contact barrier height; $E_{\mathrm{g,o}}$ and $E_{\mathrm{g,t}}$ are the optical- and transport band gap respectively (see main text for explanation); χ is the electron affinity; ε_{r} is the static relative permittivity; N_{C} and N_{V} are the effective density of states in the conduction and valence band respectively; μ_{e} and μ_{h} are the electron and hole mobilities; $N_{\mathrm{d/a}}$ is the shallow dopant density in the case of donors and acceptors, respectively; N_{t} is the defect density; E_{t} is the defect energy level (referenced to the conduction band minimum E_{C} or the valence band maximum E_{V} of the material); σ_{e} and σ_{h} are the defect capture cross sections for electrons and holes respectively. In the simulation, the conduction band offsets (CBO) between layers are determined by the difference in their electron affinity. Hence, the CBO at the CZTS/CdS interface is a $+0.2$ eV spike, whereas the CBO at the CdS/ZnO interface is zero. In the case of interface narrowing, a 5 nm layer is included between CZTS and CdS. This layer has the same properties as CZTS, except for the fact that $E_{\mathrm{g,t}} = 1.15$ eV.

How the relative permittivity of heterojunction solar cell materials influences solar cell performance

Andrea Crovetto*[1], Mathias Kasper Huss-Hansen[1], and Ole Hansen[1,2]

[1]DTU Nanotech, Technical University of Denmark, DK-2800 Kgs. Lyngby, Denmark
[2]CINF, Center for Individual Nanoparticle Functionality, Technical University of Denmark, DK-2800 Kgs. Lyngby, Denmark

Abstract

The relative permittivity of the materials constituting heterojunction solar cells is usually not considered as a design parameter when searching for novel combinations of heterojunction materials. In this work, we investigate whether such an approach is valid. Using a $Cu(In,Ga)Se_2$ solar cell architecture as a template, we specifically show the effect of the materials permittivity on the physics and performance of the solar cell by means of numerical simulation supported by analytical relations. We demonstrate that, depending on the specific solar cell configuration and materials properties, there are scenarios where the relative permittivity has a major influence on the achievable conversion efficiency, and scenarios where its influence can be safely ignored. In particular, we argue that high-permittivity materials should always be the preferred choice as heterojunction partners of the absorber layer in early stage research on new solar cell materials. When the heterojunction partner has a high permittivity, solar cells are consistently more robust against several non-idealities that are especially likely to occur when the device is not yet optimized.

1 Introduction

Within the last few years, impressive power conversion efficiencies have been demonstrated by various heterojunction solar cell technologies. Si-based heterojunction intrinsic thin layer (HIT), CdTe, $Cu(In,Ga)Se_2$ (CIGS), and metal halide perovskite solar cells have all reached efficiencies above 20% [1] and can be manufactured at a relatively low cost. The earth-abundant and non-toxic absorber $Cu_2ZnSn(S,Se)_4$ (CZTS) has also been investigated extensively and has reached a promising 12.6% record efficiency [1].

Assuming a p-type absorber material, heterojunction solar cells typically feature a moderately doped thin layer (n-type), often called "buffer layer", as the immediate heterojunction partner of the absorber layer. This is followed by a heavily doped transparent conductive layer (n^+-type) for lateral current transport, often called "window layer". Especially for CIGS and CZTS solar cells, there is an ongoing effort to replace the standard CdS buffer layer with another material of equivalent or higher performance [2]. The reasons are the toxicity of Cd and relatively low band gap of CdS (2.4 eV), which means that an appreciable fraction of light is absorbed in this layer, where carrier collection efficiency is low.

Selection of potential candidates as buffer layer materials is typically based on criteria such as 1) wide band gap, 2) natural occurrence of doping of opposite type as the absorber layer, 3) favorable conduction band offset with absorber layer, 4) lattice matching with absorber layer, 5) good coverage of the absorber layer, 6) absence of detrimental chemical element interdiffusion with absorber layer. While all the above reasons are valid, efficiency limitations arising from an unfavorable relative permittivity of the buffer layer have not been discussed in detail. In this work, we take a standard CIGS solar cell architecture as a case study and we present scenarios where the relative permittivity of the solar cell materials affects the power conversion efficiency. We show which physical mechanisms are responsible for the observed changes in efficiency and we quantify such changes by device simulation. Based on those results, we suggest a design rule for the relative permittivity of novel heterojunction solar cell materials. The rule is relatively easy to implement since the relative permittivity of materials is usually known or easily measurable [3].

2 Simulation details

Device-level simulations were performed numerically in one dimension with the finite-element method as implemented in the thin-film solar cell simulation software SCAPS [4] on a standard CIGS absorber/CdS buffer/ZnO:Al window device structure with ideal flat-band contacts. For the sake of simplicity, we have omitted the intrinsic ZnO layer often used in this type of architecture, and we have selected the baseline thickness of the buffer layer to match the typical total thickness of the CdS-ZnO bilayer. Since it is important for the buffer layer to have a relatively high electrical resistance in order to prevent shunting between the bottom

91

and top contact [5], we have assigned it a relatively low donor doping density 10^{16} cm^{-3} as a baseline case. A full list of the baseline values of all device parameters is presented in Table 1. Those were chosen by comparing various comprehensive literature sources on CIGS solar cells [6–8]. We emphasize, however, that it is not our goal to accurately model CIGS solar cells with our baseline parameters. Instead, we want to provide a reasonable starting point that may apply to a generic novel heterojunction solar cell. The simulated conversion efficiency with our baseline device model is 14.6%, which is significantly lower than state-of-the-art CIGS solar cells. We attribute this to the lower interface recombination velocity and enhanced type inversion at the CIGS-CdS heterojunction due to formation of an ordered vacancy compound at the interface and Fermi level pinning by interface donors [8,9]. Except for the parameters varied in each simulation, and unless otherwise specified, the parameters used in all simulations are fixed to their baseline value.

3 Theory

Using standard equations for p-n heterojunctions in the depletion approximation with a p-type absorber and an n-type partner, the effect of the relative permittivity of the two heterojunction materials on device operation can be summarized by two mathematical relations [10]. The first is

$$W = \left[\frac{2V_{\mathrm{bi}} \epsilon_{\mathrm{n}} \epsilon_{\mathrm{p}} \left(N_{\mathrm{d}} + N_{\mathrm{a}}\right)^2}{e N_{\mathrm{d}} N_{\mathrm{a}} \left(\epsilon_{\mathrm{n}} N_{\mathrm{d}} + \epsilon_{\mathrm{p}} N_{\mathrm{a}}\right)} \right]^{1/2} \quad (1)$$

Here W is the width of the depletion region, ϵ_{n} and ϵ_{p} are the static permittivites of the n- and p-type semiconductors, V_{bi} is the built-in voltage in equilibrium, e is the elementary charge and N_{a} and N_{d} are the acceptor and donor densities of the p- and n-type material, respectively. In most practical cases, both light absorption and collection efficiency are low in the n-type heterojunction partner, so it can be more instructive to deal with the part of the depletion region that lies in the p-type absorber, which has a width

$$W_{\mathrm{p}} = \left[\frac{2V_{\mathrm{bi}} \epsilon_{\mathrm{n}} \epsilon_{\mathrm{p}} N_{\mathrm{d}}}{e N_{\mathrm{a}} \left(\epsilon_{\mathrm{n}} N_{\mathrm{d}} + \epsilon_{\mathrm{p}} N_{\mathrm{a}}\right)} \right]^{1/2} \quad (2)$$

Eq. 2 predicts that the width of the depletion region increases as the permittivity of the two heterojunction materials increases. Notice that, if one of the two sides of the junction is doped heavily with respect to the other, then it is only the permittivity of the lightly-doped side of the junction that contributes to depletion region widening. Since minority carriers are collected most efficiently within a depth corresponding to the depletion width in the absorber layer plus their diffusion length, widening of the depletion region increases the depth at which the carriers can be efficiently collected. This can noticeably increase the short circuit current density J_{sc} in the cases where the total width

of the two above regions is not enough to efficiently collect all photo-generated carriers, especially those due to long-wavelength photons. If the collection length is large compared to the light absorption depth in the absorber material, the short circuit current is unaffected by the permittivities.

The second relation describing the effect of the materials permittivity on device performance is the following (valid for a single heterojunction without interface charge):

$$\frac{V_{\mathrm{bi,n}}}{V_{\mathrm{bi,p}}} = \frac{\varepsilon_{\mathrm{p}} N_{\mathrm{a}}}{\varepsilon_{\mathrm{n}} N_{\mathrm{d}}} \quad (3)$$

where $V_{\mathrm{bi,n}}$ and $V_{\mathrm{bi,p}}$ are the built-in voltage drops in the n-type and p-type junction materials [10]. For an ideal heterointerface (i.e., with zero interface recombination velocity), the $V_{\mathrm{bi,n}}/V_{\mathrm{bi,p}}$ ratio does not affect the efficiency. However, in the presence of interface recombination, an increase in the $V_{\mathrm{bi,n}}/V_{\mathrm{bi,p}}$ ratio leads to a decrease in the open circuit voltage V_{oc} (for $0 < V_{\mathrm{bi,n}}/V_{\mathrm{bi,p}} < 1$) and in J_{sc} (for $V_{\mathrm{bi,n}}/V_{\mathrm{bi,p}} > 1$), due to trends in the relative abundance of electrons and holes at the interface [6]. Hence, it appears that increasing the ϵ_n/ϵ_p ratio is beneficial for increasing the solar cell efficiency. However, this statement must be qualified by several factors. First of all, if the n-type material is much more highly doped than the p-type material, $V_{\mathrm{bi,n}}$ will be very small compared to $V_{\mathrm{bi,p}}$ regardless of the permittivity ratio, as permittivities of most semiconductors only vary over one order of magnitude. This renders all buffer-free solar cell architectures, with the absorber in direct contact with a highly doped window layer, insensitive to the ϵ_n/ϵ_p ratio. On the other hand, if N_{d} is not much greater than N_{a}, then the permittivity ratio can significantly influence the voltage drop ratio. However, even under those conditions, if the lowly-doped buffer layer is thin enough it will be completely depleted, such that $V_{\mathrm{bi,n}}$ will be dictated solely by its doping density and thickness, and not by its permittivity. This will be shown numerically in the next section. In the limiting case of an infinitely thin buffer layer, we are again in the case of a direct heterojuntion discussed above. Finally, if interface charge is present in appreciable amount, Fermi level pinning occurs and Eq. 3 is again invalidated, because the relative voltage drops are now dictated by the (pinned) position of the Fermi level at the interface. Negative interface charge can be present in the form of occupied acceptor states, which have a detrimental effect on V_{oc} because they increase $V_{\mathrm{bi,n}}/V_{\mathrm{bi,p}}$. On the other hand, unoccupied donor states close to the conduction band (positive interface charge) have a beneficial effect on V_{oc} because they decrease $V_{\mathrm{bi,n}}/V_{\mathrm{bi,p}}$.

In the next section, we will quantify variations in solar cell performance in the cases where the permittivity does play a role. From now on, the p and n subscripts of the discussed physical quantities refer only to the absorber and buffer layers respectively. This is because the heavily doped window layer used in the model behaves similarly to a metal and does not contribute to any built-in voltage drop.
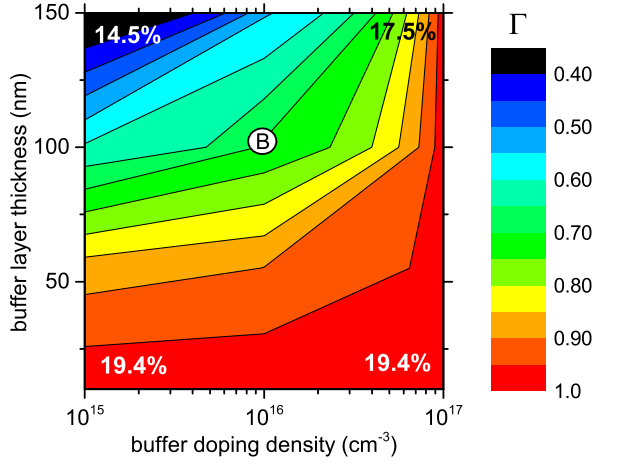
Figure 1: The effect of buffer layer thickness and doping level on the permittivity ratio sensitivity factor Γ. The circle with the "B" label indicates the baseline parameters. The overlaid numbers are the values of $\eta_{\epsilon_{\mathrm{B}}}$, i.e. the solar cell efficiency with a high buffer-to-absorber permittivity ratio, at the corresponding point in the parameter space.
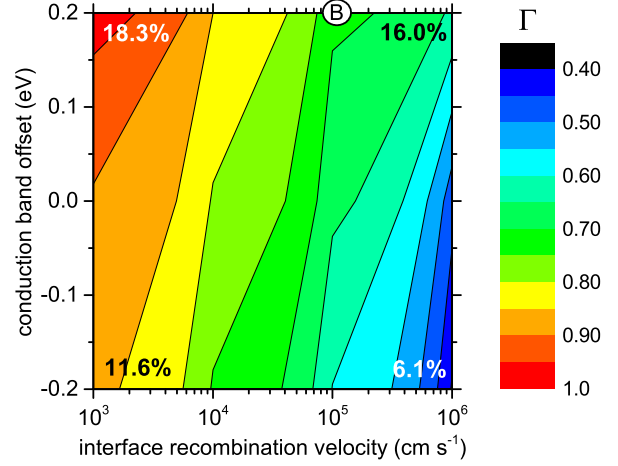
Figure 2: The effect of absorber-buffer interface recombination velocity and absorber-buffer conduction band offset on the permittivity ratio sensitivity factor Γ. The circle with the "B" label indicates the baseline parameters. The overlaid numbers are the values of $\eta_{\epsilon_{\mathrm{B}}}$, i.e. the solar cell efficiency with a high buffer-to-absorber permittivity ratio, at the corresponding point in the parameter space.

4   Results

Throughout this section, we employ the permittivity ratio sensitivity factor Γ as a measure of how solar cell performance is sensitive to changes in the $\varepsilon_{\mathrm{n}}/\varepsilon_{\mathrm{p}}$ ratio. Γ is defined as follows:

$$\Gamma = \frac{\eta_{\epsilon_{\mathrm{A}}}}{\eta_{\epsilon_{\mathrm{B}}}} \tag{4}$$

where $\eta_{\epsilon_{\mathrm{A}}}$ is the simulated power conversion efficiency of the solar cell for $\varepsilon_{\mathrm{n}}/\varepsilon_{\mathrm{p}} = 0.6$ (low buffer-to-absorber permittivity ratio), and $\eta_{\epsilon_{\mathrm{B}}}$ is the simulated efficiency for $\varepsilon_{\mathrm{n}}/\varepsilon_{\mathrm{p}} = 1.5$ (high buffer-to-absorber permittivity ratio). In short, if $\Gamma \sim 1$, the $\varepsilon_{\mathrm{n}}/\varepsilon_{\mathrm{p}}$ ratio does not affect the efficiency; if $\Gamma < 1$, the efficiency decreases as the $\varepsilon_{\mathrm{n}}/\varepsilon_{\mathrm{p}}$ ratio decreases. In practice, the absorber permittivity has been set to $\varepsilon_{\mathrm{p}} = 13.6$ (as in a CIGS absorber [11]), and the low (high) permittivity ratios have been achieved by setting the buffer permittivity to $\varepsilon_{\mathrm{n}} = 8$ ($\varepsilon_{\mathrm{n}} = 20$), corresponding to ZnS and to CdO respectively [12, 13]. The permittivity of commonly used buffer layer materials falls within this range.

In Figs. 1-4, we quantify variations in Γ due to the influence of the permittivity ratio $\varepsilon_{\mathrm{n}}/\varepsilon_{\mathrm{p}}$ on voltage drop ratio $V_{\mathrm{bi,n}}/V_{\mathrm{bi,p}}$ (Eq. 3). Fig. 1 demonstrates quantitatively what was qualitatively discussed in the previous section, i.e., that in the limit of high buffer doping or small buffer thickness, the efficiency is independent of the $\varepsilon_{\mathrm{n}}/\varepsilon_{\mathrm{p}}$ ratio. For high buffer doping, this occurs because $V_{\mathrm{bi,n}}$ remains small even in the case of a high $\varepsilon_{\mathrm{n}}/\varepsilon_{\mathrm{p}}$ ratio. For a thin buffer with low doping, on the other hand, this occurs because the buffer is completely depleted regardless of the permittivity ratio, and therefore $V_{\mathrm{bi,n}}$ is determined only by the donor doping density and buffer thickness.

In Fig. 2, we analyze the effect of interface quality on Γ. As discussed in the previous section, increasing interface recombination velocity increases the severity

of the losses related to the potential drop in the buffer, and Γ decreases accordingly due to Eq. 3. This effect becomes more severe as the conduction band offset decreases, because the device becomes more sensitive to the $V_{\mathrm{bi,n}}/V_{\mathrm{bi,p}}$ ratio [6, 7].

In Fig. 3, we examine the influence of Fermi level pinning on Γ. While keeping the (neutral) interface defects responsible for the baseline interface recombination velocity as in the above studies, we added a single interface donor state with different densities and at different energy levels. If the interface donors are sufficiently abundant and sufficiently close to the conduction band, the interface Fermi level is pinned to the donor level and the permittivity ratio does not influence the efficiency. At the other extreme (low donor density and low energy level), Γ approaches the baseline value of 71% shown in Fig. 1 regardless of the donor properties. This is because the amount of additional positive charge at the interface is not enough to influence the $V_{\mathrm{bi,n}}/V_{\mathrm{bi,p}}$ ratio significantly.

In a similar fashion, we examine in Fig. 4 the influence of an interface acceptor on Γ. If the energy level of the acceptor state is close enough to the conduction band for it to be mostly unoccupied, or if its density is too low to contribute with a appreciable amount of extra negative fixed charge, Γ is fixed to its baseline value as in the interface donor case. If the fixed negative charge provided by the acceptor becomes significant, Γ decreases without approaching a saturation value.

Finally, in Fig. 5 we show variations in Γ in connection to Eq. 2, i.e., related to variations in the depletion region width. To eliminate effects due to Eq. 3, we set the interface recombination velocity to zero, while all other parameters are kept at their baseline value. Then, unless the conduction band offset is large and
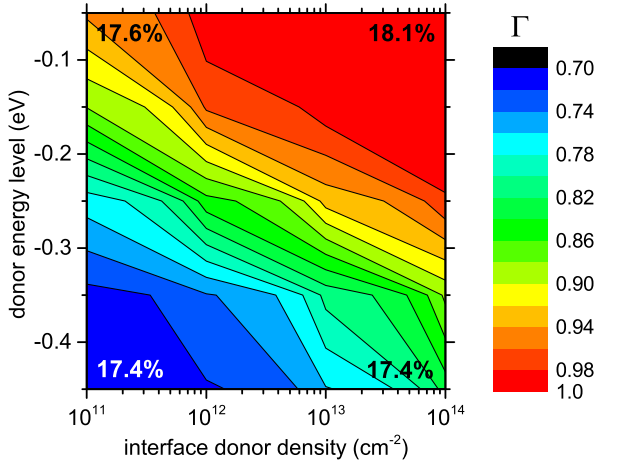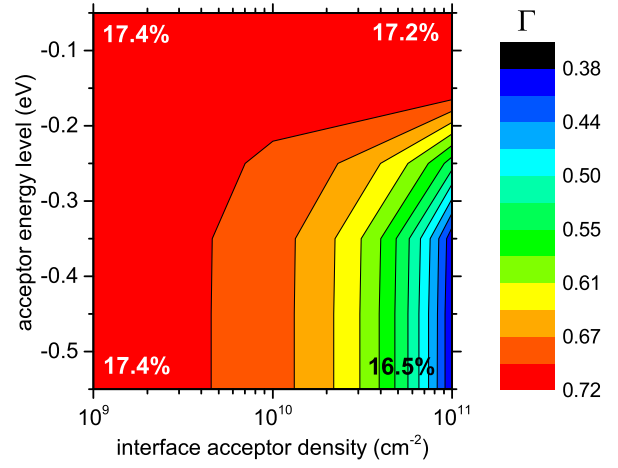
Figure 3: The effect of absorber-buffer interface donor density and energy level (referenced to the conduction band of the absorber layer) on the permittivity ratio sensitivity factor Γ. The overlaid numbers are the values of η_{ϵ_B}, i.e. the solar cell efficiency with a high buffer-to-absorber permittivity ratio, at the corresponding point in the parameter space.

Figure 4: The effect of absorber-buffer interface acceptor density and energy level (referenced to the conduction band of the absorber layer) on the permittivity ratio sensitivity factor Γ. The overlaid numbers are the values of η_{ϵ_B}, i.e. the solar cell efficiency with a high buffer-to-absorber permittivity ratio, at the corresponding point in the parameter space.

positive, Γ decreases as the minority carrier lifetimes in the absorber layer decrease. This is in accordance with Eq. 2 because, as lifetimes decrease, a larger fraction of J_{sc} comes from carrier generated in the depletion region, hence the variation in depletion region width by variation in buffer permittivity becomes more important. Note that, even though we keep using Γ as a measure of permittivity-related effects, here it is not the permittivity ratio $\varepsilon_n/\varepsilon_p$ that causes the observed effect but simply the permittivity of any of the two materials, according to Eq. 2. Since we keep ε_p constant in our simulation, it is ε_n alone that influences the solar cell efficiency. For a large positive conduction band offset, another mechanism limiting the short circuit current exists, i.e., the barrier to electron flow due to the conduction band spike. Electron transport through the spike depends on the kinetic energy of the electrons reaching the barrier from the absorber. This energy is, at maximum, equal to $eV_{bi,p}$ if electrons are generated outside the depletion region or at its edge. In case of generation within the depletion region, the expected value of the kinetic energy depends on the voltage drop between the point of generation and the heterojunction. That explains the drop of Γ at a conduction band offset of 0.4 eV for low lifetimes. In such a situation, most of the collected electrons come from the depletion region, so J_{sc} changes significantly due to changes in $V_{bi,p}$ by different permittivity ratios. For a spike larger that 0.5 eV, all electron current from the absorber is blocked regardless of how the voltage drop is distributed and the only (few) collected electrons are from the buffer layer. Hence, Γ becomes independent of the absorber lifetimes and, in the extreme case of a 0.6 eV barrier, Γ is larger than 1 because in such conditions it is beneficial to have a *high* $V_{bi,n}/V_{bi,p}$ ratio to maximize collection efficiency *in the buffer*.
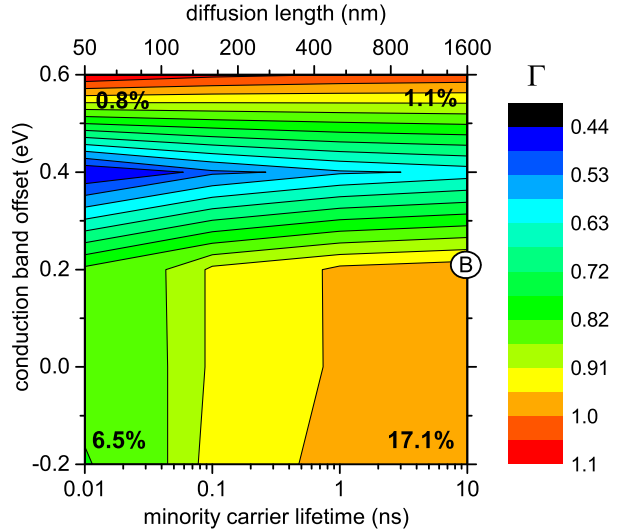

Figure 5: The effect of minority carrier lifetime in the absorber and conduction band offset at the absorber-buffer interface on the permittivity ratio sensitivity factor Γ. In this particular simulation, the interface recombination velocity due to neutral interface states was set to zero in order to separate effects due to depletion region widening from effects due to interface recombination. The circle with the "B" label indicates the baseline parameters. The overlaid numbers are the values of η_{ϵ_B}, i.e. the solar cell efficiency with a high buffer-to-absorber permittivity ratio, at the corresponding point in the parameter space.

5 Discussion

With the exception of this last rather unrealistic case, we note that $\Gamma \leq 1$ in all parameter ranges explored in Figs. 1-5. This means that a high $\varepsilon_n/\varepsilon_p$ ratio is, in general, either beneficial or irrelevant for device performance. In state-of-the-art Cu(In,Ga)Se$_2$ solar

cells it is most likely to be irrelevant. This is because high-efficiency Cu(In,Ga)Se$_2$ solar cells have sufficiently high (above 10 ns) minority carrier lifetimes, so that the $\varepsilon_n/\varepsilon_p$ is not expected to influence current collection. Further, ordered vacancy compound formation at the heterointerface and Fermi level pinning by interface donors [8, 9] are expected to lead to a low $V_{bi,n}/V_{bi,p}$ ratio regardless of the permittivity ratio. On the other hand, higher band gap absorbers such as Cu(In,Ga)S$_2$, CuInS$_2$, and Cu$_2$ZnSnS$_4$ are believed to be more sensitive to interface recombination [8, 9, 14], so a high permittivity buffer layer may be an advantage in those cases. It is clear that, for absorbers with a low permittivity (such as Cu$_2$ZnSnS$_4$, with $\varepsilon_p = 6.7$ [15]), a high $\varepsilon_n/\varepsilon_p$ can be obtained by a wider range of buffer materials.

6 Conclusion

When designing novel absorber-buffer-window combinations for heterojunction solar cells, it is advantageous to choose among high-permittivity buffer materials. This is because a high buffer-to-absorber permittivity ratio makes a solar cell more robust against non-idealities that may be encountered in early stage research, such as low buffer doping, large required buffer thickness, suboptimal band alignment, interface recombination, and negative interface charge. Even among existing heterojuction solar cell technologies, those that are limited by interface recombination may experience an improvement in open circuit voltage if a high-permittivity buffer material is used. Furthermore, a high permittivity in either the buffer or the absorber improves current collection when minority carrier lifetimes are low. Many oxide materials have a high permittivity, in addition to other desirable properties such as high band gaps and natural n-type doping. Hence, they may be the preferred class of materials as buffer layers for p-type absorbers.

Acknowledgments

References

[1] Green M A, Emery K, Hishikawa Y, Warta W and Dunlop E D 2016 *Progress in Photovoltaics: Research and Applications* **24** 905–913

[2] Naghavi N, Abou-Ras D, Allsop N, Barreau N, Bücheler S, Ennaoui A, Fischer C H, Guillen C, Hariskos D, Herrero J, Klenk R, Kushiya K, Lincot D, Menner R, Nakada T, Platzer-Björkman C, Spiering S, Tiwari A and Törndahl T 2010 *Progress in Photovoltaics: Research and Applications* **18** 411–433

[3] Tereshchenko O V, Buesink F J K and Leferink F B J 2011 An overview of the techniques for measuring the dielectric properties of materials *2011 XXX URSI General Assembly and Scientific Symposium* (IEEE) pp 1–4

[4] Burgelman M, Nollet P and Degrave S 2000 *Thin Solid Films* **361-362** 527–532

[5] Misic B, Pieters B E, Theisen J P, Gerber A and Rau U 2015 *physica status solidi (a)* **212** 541–546

[6] Scheer R and Schock H W 2011 *Chalcogenide Photovoltaics* (Weinheim, Germany: Wiley-VCH Verlag) pp. 133–136, pp. 137–139, p. 320

[7] Gloeckler M 2005 *Device physics of Cu(In,Ga)Se$_2$ thin-film solar cells* Phd thesis Colorado State University p. 31, p. 56

[8] Shafarman W N, Siebentritt S and Stolt L 2010 Cu(InGa)Se$_2$ Solar Cells *Handbook of Photovoltaic Science and Engineering* ed Luque A and Hegedus S (Chichester, UK: John Wiley & Sons, Ltd) chap 13 pp. 575–578, pp. 580–581

[9] Klenk R 2001 *Thin Solid Films* **387** 135–140

[10] Sze S and Ng K K 2004 *Physics of semiconductor devices* (Wiley) p. 126

[11] Li P, Anderson R and Plovnick R 1979 *Journal of Physics and Chemistry of Solids* **40** 333–334

[12] Samara G A 1983 *Physical Review B* **27** 3494–3505

[13] Finkenrath H and Uhle N 1967 *Solid State Communications* **5** 875–877

[14] Gunawan O, Todorov T K and Mitzi D B 2010 *Applied Physics Letters* **97** 233506

[15] Gunawan O, Gokmen T, Warren C W, Cohen J D, Todorov T K, Barkhouse D A R, Bag S, Tang J, Shin B and Mitzi D B 2012 *Applied Physics Letters* **100** 253905

A. Contact properties		Front	Back
S_{e} (cm/s)		10^7	10^7
S_{h} (cm/s)		10^7	10^7
Optical properties		Transmission $= 1$	Mo
$\phi_{\mathrm{Bn0}}, \phi_{\mathrm{Bp0}}$ (eV)		0	0

B. Layer properties	Window (ZnO:Al)	Buffer (CdS)	Absorber (CIGS)
Thickness (nm)	50	100	2500
E_{g} (eV)	3.3	2.4	1.15
χ (eV)	4.5	4.3	4.5
ϵ_{r}	9.0	10.0	13.6
N_{C} (cm^{-3})	2.2×10^{18}	2.2×10^{18}	6.7×10^{17}
N_{V} (cm^{-3})	1.8×10^{19}	1.8×10^{19}	1.5×10^{19}
μ_{e} (cm^2/Vs)	100	100	100
μ_{h} (cm^2/Vs)	25	25	10
$N_{\mathrm{d/a}}$ (cm^{-3})	$N_{\mathrm{d}} = 1 \times 10^{20}$	$N_{\mathrm{d}} = 1 \times 10^{16}$	$N_{\mathrm{a}} = 1 \times 10^{16}$

C. Defect states	Window (ZnO:Al)	Buffer (CdS)	Absorber (CIGS)
Type	N.A.	Neutral	Neutral
Energy distribution		Single level	Single level
N_{t} (cm^{-3})		2×10^{17}	2×10^{13}
E_{t} (eV)		$E_{\mathrm{V}} + 1.2$	$E_{\mathrm{V}} + 0.8$
σ_{e} (cm^2)		10^{-13}	5×10^{-13}
σ_{h} (cm^2)		10^{-13}	1×10^{-15}

D. Interface defect	ZnO:Al/CdS	CdS/CIGS
Type	N.A.	Neutral
Energy distribution		Single level
E_{t} (eV)		$E_{\mathrm{V,CIGS}} + 0.6$
N_{t} (cm^{-3})		10^{14}
$\sigma_{\mathrm{e}}, \sigma_{\mathrm{h}}$ (cm^2)		10^{-16}

Table 1: The baseline parameters used for simulation of a CIGS-type solar cell. S_{e} and S_{h} are the interface recombination velocities for electrons and holes; ϕ_{Bn0} and ϕ_{Bp0} is the contact barrier height; E_{g} is the band gap; χ is the electron affinity; ϵ_{r} is the static relative permittivity; N_{C} and N_{V} are the effective density of states in the conduction and valence band respectively; they are derived from the effective masses of electrons and holes, which are taken as $0.09m_0$ and $0.7m_0$ respectively (m_0 is the electron rest mass); μ_{e} and μ_{h} are the electron and hole mobilities; $N_{\mathrm{d/a}}$ is the shallow dopant density in the case of donors and acceptors, respectively; N_{t} is the defect density; E_{t} is the defect energy level (referenced to the valence band of the material); and σ_{e} and σ_{h} are the capture cross sections for electrons and holes respectively. In the simulation, the conduction band offsets (CBO) between layers are determined by the difference in their electron affinity. Hence, the baseline CBO at the CIGS-CdS (CdS-ZnO:Al) interface is $+0.2$ eV (-0.2 eV).

Chapter 5

Growth and fundamental properties of ZnO:Al

You know that we are living in a material world
And I am a material girl
Madonna, 1984

5.1 Study 5.1: Performance limitations and property correlations of ZnO:Al by radio-frequency sputtering

- <u>Crovetto A</u>, Ottsen T S, Stamate E, Kjær D, Schou J and Hansen O 2016 On performance limitations and property correlations of Al-doped ZnO deposited by radio-frequency sputtering *Journal of Physics D: Applied Physics* **49** 295101

  Received the "Young Scientist Award" at the European Materials Research Society 2016 Spring Meeting, Lille, France, May 2016.

Even though ZnO:Al (or AZO) is a much more mature material than CZTS, I still think there are discoveries to be made with this material. At a fundamental level, it is not clear yet what intrinsic defects allow such a high n-type doping density even in pure ZnO [126]. To me, this is very surprising. At a technological level, despite many years of experience with magnetron sputtering of ZnO:Al, it is not entirely clear yet why the electrical properties of the film depend on the position with respect to the sputtering source and on the deposition pressure. Furthermore, compressive stress in the film has often been associated to unfavorable electrical properties, but a quantitative relationship between stress, position, pressure, and electrical properties has not been identified.

In this work, I show a quantitative relationship between the compressive stress in the film and the electrical properties. I also demonstrate that there are clear qualitative relationships between the compressive stress and the structural and compositional properties. I conclude that position and pressure in the deposition process are very important because they determine the compressive stress in the film through the mechanism of particle bombardment.

Since I have decided to focus on CZTS in this thesis, I do not provide a review of ZnO:Al as a material. Comprehensive information on ZnO and ZnO:Al is available in two books [185, 186] and one extended review [187]. More specific information about magnetron sputtering of ZnO:Al is given in a slightly old but still excellent review [188]. Finally, the general status of transparent conductive materials was recently reviewed [59].

My contribution (detailed):

• Idea for the study • Building of a dedicated sputtering setup • Fabrication of half of the

AZO films used in the study • All characterization (except for micro four-point probe) and all analysis of experimental data, including XRD line profile analysis • Idea for expressing the measured properties as a function of compressive stress • Literature review • Writing the full manuscript

Coauthors' contribution (brief):
• T. Ottsen: fabrication of the other half of the AZO films, process development, preliminary characterization with a variety of methods • E. Stamate: technical assistance with building the sputtering setup • D. Kjær: micro four-point-probe characterization • J. Schou, O. Hansen: discussions and commenting the manuscript

5.2 Study 5.2: Electrical property mapping of ZnO:Al with micro four-point-probe technique

- Crovetto A, Kjær D, Petersen D H, Schou J and Hansen O, Electrical property mapping of ZnO:Al films with micro four-point-probe technique, *presented at the 5th International Symposium on Transparent Conductive Materials, Chania, Greece, October 2014*

In this poster I present graphically the only non-standard characterization technique used in the previous study, i.e., micro four-point probing. This method allows extraction of the carrier concentration and mobility with a very high spatial resolution. This is made possible by measuring the Hall parameters with collinear probes placed parallel to, and just a few micron away from, an insulating edge of the film. The method is described in [189].

Contributions (brief):
• A. Crovetto: ZnO:Al film deposition, ellipsometry and standard four-point probe characterization • D. Kjær: micro four-point-probe characterization • D. Petersen, J. Schou, O. Hansen: discussions and commenting the poster

On performance limitations and property correlations of Al-doped ZnO deposited by radio-frequency sputtering

Andrea Crovetto[1]**, Tobias Sand Ottsen**[1]**, Eugen Stamate**[2]**, Daniel Kjær**[1,3]**, Jørgen Schou**[4] **and Ole Hansen**[1,5]

[1] DTU Nanotech, Technical University of Denmark, DK-2800 Kgs. Lyngby, Denmark
[2] DTU Energy, Technical University of Denmark, DK-4000 Roskilde, Denmark
[3] CAPRES A/S, Scion-DTU, DK-2800 Kgs. Lyngby, Denmark
[4] DTU Fotonik, Technical University of Denmark, DK-4000 Roskilde, Denmark
[5] CINF, Center for Individual Nanoparticle Functionality, Technical University of Denmark, DK-2800 Kgs. Lyngby, Denmark

E-mail: ancro@nanotech.dtu.dk

Abstract
The electrical properties of RF-sputtered Al-doped ZnO are often spatially inhomogeneous and strongly dependent on deposition parameters. In this work, we study the mechanisms that limit the minimum resistivity achievable under different deposition regimes. In a low- and intermediate-pressure regime, we find a generalized dependence of the electrical properties, grain size, texture, and Al content on compressive stress, regardless of sputtering pressure or position on the substrate. In a high-pressure regime, a porous microstructure limits the achievable resistivity and causes it to increase over time as well. The primary cause of inhomogeneity in the electrical properties is identified as energetic particle bombardment. Inhomogeneity in oxygen content is also observed, but its effect on the electrical properties is small and limited to the carrier mobility.

Keywords: ZnO, AZO, sputtering, stress, correlations, line profile analysis, bombardment

(Some figures may appear in colour only in the online journal)

1. Introduction

Transparent conductive oxides (TCO) are thin-film materials that feature low electrical resistivity and high optical transmission in the visible region of light, which are requirements in applications such as flat panel displays, low emissivity coatings, and top electrodes in thin-film solar cells [1]. Currently, the best-performing TCO is Sn-doped In_2O_3 (ITO), which, however, suffers from the high cost and limited availability of indium [2]. This can be a problem for large-area applications such as photovoltaics. Therefore, Al-doped ZnO (AZO) has been widely used in research and industry as a top electrode in thin-film solar cells based on amorphous silicon or $Cu(In,Ga)Se_2$, which have recently reached more than 22% power conversion efficiency on the laboratory scale [3]. The main advantage of AZO over ITO is the greater abundance and lower cost of its component elements. AZO thin film deposition by RF- or DC magnetron sputtering technique combines high film quality with relatively high deposition rate, compatibility with large-area substrates, and is routinely employed in thin-film solar cell production [4, 5]. Resistivity in the 10^{-4} Ω cm range can be obtained by sputtering while retaining more than 80% average transmission in the visible region of light [6]. However, an issue related to sputter deposition of AZO is that the resistivity of the deposited films exhibits spatial inhomogeneity [7–13]. Mainly two explanations exist for this phenomenon: (1) bombardment of the film by inhomogeneously distributed energetic particles during deposition [7]; (2) inhomogeneity in the amount and activity of oxygen reaching the substrate, which results in non-optimal oxygen stoichiometry in certain regions of the film [8].

According to hypothesis (1), O^- and O_2^- ions (the former being more abundant) [9, 14, 15] are formed at the target and accelerated through the cathode sheath up to an energy corresponding to the target DC bias voltage. Upon leaving the cathode sheath, such a collimated beam of energetic ions travels mostly perpendicular to the target surface with a small collision cross section with the working gas [16]. In the plasma, O^- ions may undergo electron detachment and turn into equally energetic O neutrals [17]. Film bombardment by such energetic species leads to formation of crystal defects and deteriorates the electrical properties.

According to hypothesis (2), excess oxygen reaches the substrate in the regions of largest plasma density and causes the resistivity to increase or decrease in those regions, depending on whether the excess oxygen results in an oxygen content in the film that is above or below optimal, respectively [8, 18].

In an attempt to distinguish which mechanisms limit the minimum achievable resistivity under different deposition conditions, we systematically examine the spatial distribution of the electrical, structural, morphological, and compositional properties of RF-sputtered AZO at different deposition pressures. This investigation method also allows discrimination between property correlations that only exist under specific conditions, and correlations of a more general nature.

2. Experimental details

Thin AZO films were deposited by RF magnetron sputtering with a balanced cathode and a hot-pressed ceramic target (Lesker ZnO/Al_2O_3 98/2 wt%, 99.99% purity). The target had a circular shape with a diameter of 50.8 mm, a thickness of 3.2 mm, and was indium-bonded to a Cu backing plate. The experiments in this work were carried out when the depth of the erosion track on the target was approximately 0.2 mm. At the target surface, the component of the magnetic flux density along the x direction (figure 1) was approximately 57.5 mT.

One Si and one quartz substrate (size: 10 mm × 30 mm each) were directly facing the target at a target-substrate distance of 30 mm and kept at ground potential (figure 1). The two types of substrate were chosen for compatibility with the characterization techniques used in this work.

The chamber was pumped down to a base pressure of 5×10^{-7} Torr by a turbo pump, then pure Ar gas (99.999%) was introduced and the discharge RF power was set to 20 W with a 0.25 W s^{-1} ramp. The target was pre-sputtered at the desired deposition pressure by closing a shutter between the target and the substrate. In the meantime, the substrate stage was heated to 150 °C. After pre-sputtering for 15 min, the shutter was opened and film deposition took place. The measured target self-bias varied between 132 V (at 2.5 mTorr) and 146 V (at 15 mTorr). The temperature remained between 145 and 155 °C during deposition, as measured by a thermocouple. After deposition, the substrates were allowed to cool down naturally in vacuum, and they were taken out when the measured temperature was below 50 °C. The only parameter that was changed from one deposition to another was the deposition pressure. In the following sections, pressures of the
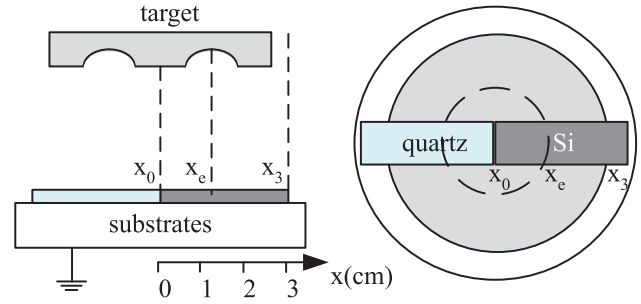

Figure 1. Schematic drawing of the sputtering geometry and the position of the substrates with respect to the target. All dimensions are to scale. x_0 is the symmetry axis of the magnetron, x_e is the radial distance corresponding to the maximum depth of the erosion track of the target. x_3 is the edge of the substrate.

order of 2.5 mTorr, 5 mTorr, and 15 mTorr are referred to as low-, intermediate-, and high-pressure regimes respectively.

We show different properties of the deposited films as a function of distance from the central symmetry axis of the magnetron $x = 0$ (labeled x_0) through the point directly facing the erosion track of the target at a radial distance $x = 1.2$ cm (labeled x_e) and up to the end of the substrate, at $x = 3$ cm (labeled x_3). Because the sputtering setup is center-symmetric, we also expect the film properties to be center-symmetric. This was confirmed by measuring thickness and resistivity on a film deposited on a 6 cm-long quartz substrate centered on $x = 0$. Hence, the distribution of properties is in fact a 'radial' distribution instead of simply a 'spatial' distribution.

The AZO/Si films were imaged with a scanning electron microscope (SEM) equipped with a field emission gun and an in-lens detector (FE-SEM, Supra 60VP, Zeiss). Energy dispersive x-ray spectroscopy (EDX) was performed in the same instrument on the AZO/Si films using a Si drift detector (X-Max^N 50, Oxford Instruments) and a beam voltage of 3 kV. If the beam voltage was higher, artifacts in the composition appeared due to x-ray generation in the Si substrate. On the other hand, strong Zn, O, and Al x-ray peaks are present at energies well below 3 keV.

X-ray diffraction (XRD) patterns were collected on the AZO/quartz films with a Bruker D8 Discover diffractometer equipped with a Göbel mirror for a parallel primary beam. The measurement was performed in Bragg–Brentano configuration using Cu-K$_\alpha$ radiation, a 0.001°(2θ) s^{-1} acquisition time, a 0.6 mm primary slit, a 0.6 mm anti-scatter slit, and a 0.2 mm detector slit. The slit sizes were selected in order to obtain as low instrumental broadening as possible, while still being able to detect a clear (0 0 2) peak. Instrumental broadening was measured using a standard LaB$_6$ sample. Out-of-plane crystallite size and micro-strain were calculated by fitting the (0 0 2) peak with a pseudo-Voigt function (i.e. a weighted sum of a Lorentzian and a Gaussian function) and by extracting the parameters of the Lorentzian and Gaussian contributions after subtracting instrumental broadening. The detailed procedure is described elsewhere [19]. The out-of-plane lattice shift ε was measured based on the position of the (0 0 2) XRD peak. In-plane stress σ was calculated from the measured lattice shift using a biaxial stress model and literature values for
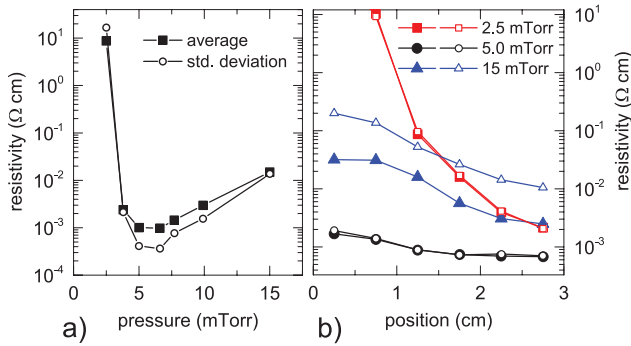
2

Figure 2. (a) Radially averaged resistivity between x_0 and x_3, and its inhomogeneity (expressed as the standard deviation of resistivity between x_0 and x_3) versus deposition pressure. (b) Radial distribution of resistivity from x_0 to x_3. A first measurement was taken within one day after depositing each film (closed symbols); a second measurement was taken after storage for seven months at atmospheric pressure and room temperature (open symbols).

the ZnO stress tensor elements [13]. The thickness and optical functions of the AZO/Si films were measured in reflection mode in the spectral range 0.7–5.9 eV on a rotating compensator spectroscopic ellipsometer (M-2000, J.A. Woollam Co.) using a collimated beam with a spot size of approximately 200 μm $\times$ 300 μm. Ellipsometry spectra were analyzed and fitted with the CompleteEase software package (version 5.06—J.A. Woollam Co.).

Sheet resistance was measured on the AZO/quartz films with a four-point probe with electrode spacing of 0.5 mm. Carrier concentration and Hall mobility were measured on the AZO/quartz films with an industrial micro-Hall setup (CAPRES A/S) including an equidistant, collinear micro 7-point probe with electrode spacing of 10 μm. The measurement principle and data analysis procedure have been described elsewhere [20, 21].

3. Results

In this section we present the radially resolved measurement of a few relevant properties of AZO films deposited at different pressures. The average of the radial measurements is also plotted against deposition pressure, in the cases where it provides useful information. The electrical properties are presented first, followed by other properties that provide insights into the mechanisms limiting the minimum achievable resistivity, or that may be directly correlated to the electrical properties.

3.1. Resistivity

Figure 2(a) shows that the resistivity of AZO is strongly dependent on deposition pressure, with the films exhibiting significant loss of electrical quality both in the low- and in the high-pressure regime. The radial standard deviation of resistivity for each of our deposited films follows a similar trend as the average resistivity, i.e. with a minimum at intermediate pressure. Therefore, the films deposited at the optimal pressure achieve both the lowest resistivity and the
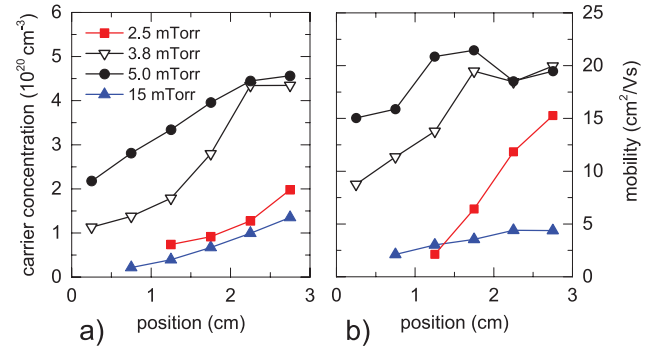

Figure 3. Radial distribution of carrier concentration and mobility from x_0 to x_3. Some data points are missing because mobilities lower than $\sim$2 cm^2 Vs^{-1} could not be measured with our Hall setup.

lowest inhomogeneity. The radial distribution of electrical resistivity for films deposited at different pressures is shown in figure 2(b). In all films, the resistivity has a maximum at x_0 and a minimum at x_3. Furthermore, we note that only the film deposited in the high-pressure regime experiences significant degradation in resistivity (approximately by a factor of 5) over a storage period of seven months. This has been observed in previous studies on AZO sputtered at high pressure by single-point measurements [22, 23]. From figure 2(b), we can conclude that resistivity degradation over time in samples deposited at a high pressure is a global phenomenon, i.e. it occurs to a similar extent at different positions of the film, and must be therefore related to a global property typical of the high-pressure films.

3.2. Carrier concentration and mobility

By inspection of figure 3, it is clear that the radial resistivity gradient is due to a gradient in both carrier concentration and mobility, which have a minimum at x_0 at all pressures. However, such gradients depend strongly on deposition pressure. For example, the mobility gradient in the low-pressure regime is much greater than in the other regimes. Note that mobility in the 2.5 mTorr sample near x_0 is even lower than on the other points on the same film, but such low mobilities cannot be measured with our setup due to their weak Hall signal. In contrast, in the high-pressure regime there is a weaker mobility gradient but the carrier concentration reaches by far the lowest values obtained in our experiments. Interestingly, a local mobility maximum is consistently found in the intermediate-pressure regime at positions close to x_e. Its origin will be discussed in the following sections.

3.3. Deposition rate

A maximum in the spatially averaged deposition rate (figure 4(a)) is found at about 5 mTorr, corresponding to the intermediate-pressure regime. This resembles the trend found in a previous study on certain sputter-deposited oxides [24], where two mechanisms limiting the deposition rate were identified. In the high-pressure regime, the deposition rate decreased with pressure due to thermalization of the sputtered species, as
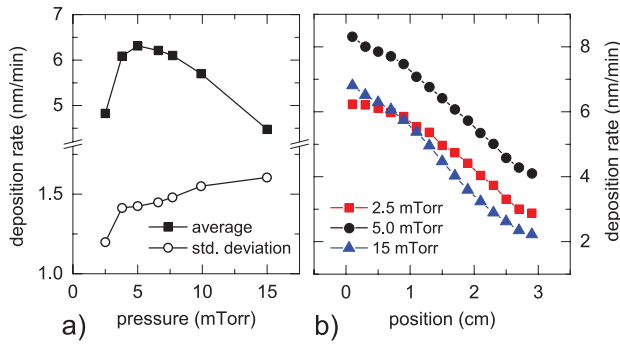
Figure 4. (a) Radially averaged deposition rate between x_0 and x_3, and its inhomogeneity (expressed as the standard deviation of deposition rate between x_0 and x_3) versus deposition pressure. (b) Radial distribution of deposition rate from x_0 to x_3.

Figure 5. (a) Radial distribution of out-of-plane lattice shift from x_0 to x_3. The shift is calculated based on the position of the fitted (0 0 2) XRD peak at each radial position and expressed as percentage of the lattice constant of a reference ZnO powder (JCPDS card 36-1451). A positive lattice shift stands for lattice expansion in the out-of-plane direction (compressive in-plane stress); a negative lattice shift signifies lattice compression (tensile in-plane stress). In-plane stress has been calculated based on a biaxial stress model with reference ZnO tensor elements [13]. (b) Radial distribution of root-mean-square micro-strain from x_0 to x_3 as determined by XRD line profile analysis after deconvoluting instrument- and size-related broadening effects. The micro-strain is expressed as a percentage of the lattice constant of a reference ZnO powder (JCPDS card 36-1451).

predicted by a general model of sputter deposition [25]. In the low-pressure regime the deposition rate dropped due to resputtering of the growing film caused by energetic ion bombardment. The (re)sputtering threshold of ZnO has been estimated to be 33–35 eV by semi-empirical formulas [10] and numerical simulation [26]. Typical energy distributions of the O^- ions impinging on growing AZO films in an RF discharge have been measured before [27] and are well above such a threshold. Due to a global drop in deposition rate in the low-pressure regime (figure 4), we conclude that our AZO film is partially resputtered by energetic particle bombardment in the low-pressure regime. Previous studies have shown that not only can resputtering effects exist in AZO, but they can also be spatially distributed: the regions of the film where a higher flux density of energetic ions is expected may have a higher resputtering rate [28, 29]. By inspection of the radial distribution of deposition rate in our films (figure 4(b)), we notice that the deposition rate profile flattens considerably near x_0 in the low-pressure regime, and a cross-over with the high-pressure regime curve occurs. This may be attributed to a higher resputtering rate near x_0.

3.4. Lattice shift and stress

Besides a drop in deposition rate from resputtering effects, energetic particle bombardment is expected to give rise to compressive stress due to the atomic peening mechanism [30]. According to quantitative models verified against a number of sputter-deposited materials [31], the in-plane compressive stress σ scales with the product of the flux density of the bombarding particles Γ times the square root of their *kinetic* energy E, that is, $\sigma \propto \Gamma\sqrt{E}$. This relation must be rewritten for RF-sputtered AZO, because the O^- flux is not monoenergetic, but it has an energy distribution function centered on the energy corresponding to the target self-bias voltage (about 140 V in our study) and is rather uniformly distributed from 0 eV up to approximately twice the value of the self-bias [9, 27]. Also, both Γ and E may depend on deposition pressure p and radial position x. Hence, we generalize the empirical formula [31] as

$$\sigma(p,x) \propto \int_{E_{\min}}^{E_{\max}} \Gamma(E,p,x)\; d(E^{1/2}(p,x)) \equiv \Sigma_{E^{1/2}}(p,x) \quad (1)$$
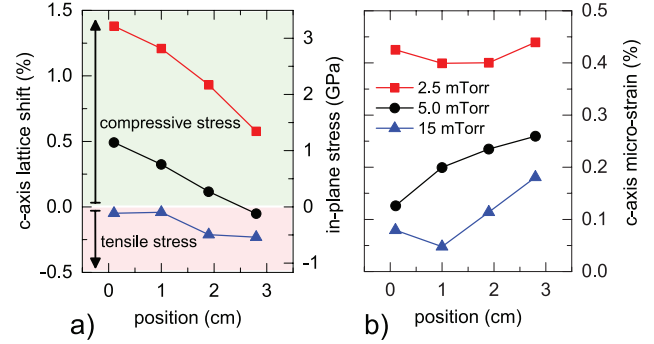
where $\Sigma_{E^{1/2}}$ is introduced by definition and is the flux density integrated with respect to the square root of the kinetic energy at pressure p and position x. In the following, we refer to it as 'energy flux' for simplicity, and will assume our measured lattice shift to be roughly proportional to it. This proportionality can be justified experimentally for sputter-deposited AZO based on the results of a recent study, where the measured energy-weighted O^- ion flux density and the measured lattice shift were found to be correlated for both DC- and RF sputtering [9].

The measured lattice shift and calculated stress of our AZO films in the three pressure regimes along the radial direction are shown in figure 5(a). In a biaxial stress model, a positive lattice shift ε in the out-of-plane direction (lattice expansion) corresponds to compressive in-plane stress, whereas a negative out-of-plane lattice shift (lattice compression) corresponds to tensile in-plane stress. In our films there are two tendencies: (1) the lattice shift increases by decreasing deposition pressure, and (2) the lattice shift increases by decreasing radial position from x_3 to x_0. As a consequence, in-plane stress in the films varies between the two extreme cases of a moderate tensile stress (-0.5 GPa at 15 mTorr at x_3) and a large compressive stress (3.2 GPa at 2.5 mTorr at x_0). The transition from tensile to compressive stress from the high- to low-pressure regime is not unique to AZO, but is well-known and quite general for sputter-deposited films [32]. These trends suggest that the energy flux, and the consequential lattice shift, are diminished both by increasing the deposition pressure and by moving away from x_0. We will demonstrate quantitatively in the next sections that this is uniquely reflected in the electrical properties of the films.

3.5. Micro-strain

Only very few works [33–35] have shown the root-mean square (RMS) micro-strain in AZO films. This quantity
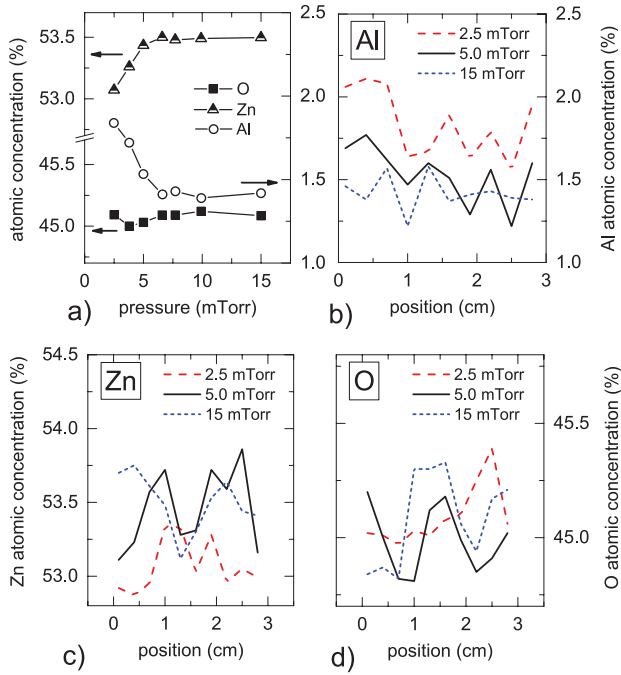
4

Figure 6. (a) Radially averaged atomic composition versus deposition pressure measured by EDX. ((b)–(d)) Radially resolved atomic composition of Al, Zn, and O from x_0 to x_3 measured by EDX.

is fundamentally different from the (macroscopic) strain discussed in the previous section. The micro-strain is the Gaussian-distributed variation of the lattice constant centered on the macroscopically strained lattice constant of the material. From the radially resolved measurement of micro-strain in figure 5(b) it is noted that the micro-strain globally increases as the pressure decreases. This is compatible with the higher probability of lattice dislocations and substitutional defects occurring in the low-pressure regime due to particle bombardment [30, 31] and it is also consistent with the increased Al content in the low-pressure regime (figure 6(b)). When doping ZnO with 2% Al, the latter is expected to substitute Zn in a small number of Zn sites (the absolute maximum is 4% of the Zn sites assuming 100% dopant activation). Because Al^{3+} has a smaller ionic radius than Zn^{2+} (53 pm and 72 pm respectively), the consequence of Al substitution should be that the ZnO lattice becomes strained in the vicinity of the Al lattice site. This should result in micro-strain instead of an overall lattice shift. The fact that different physical mechanisms may lie behind these two distinct types of strain is confirmed by the fact that in figure 5 there is no obvious relationship between the overall lattice shift and the micro-strain.

3.6. Elemental composition

In order to obtain excellent electrical properties in AZO films, it is crucial that the oxygen stoichiometry be optimal [36]. Amount and activation of the dopant Al is equally important [37, 38]. Before analyzing our compositional results, however, two warnings must be expressed: (1) a systematic error around ±5% (relative) should be expected for the absolute

composition ratios, due to the relatively low beam voltage and use of elemental standards in EDX analysis; (2) a random error around ±0.1% point (absolute) should also be expected, due to reproducibility limits of the EDX measurement. Since the deviations in atomic composition found in this study are always contained within a 1% point (absolute) range or less, care must be taken in interpreting weak trends in the radially resolved measurements. From figure 6(a), we note that the global Al content increases and the Zn content decreases in the low-pressure regime. In fact, resputtering effects in AZO films have been shown in previous work to be associated to preferential removal of Zn from the growing film [29]. As previously observed from figure 4, the largest resputtering rate in our films occurs in the low-pressure regime, which is consistent with the Zn depletion measured in the that regime. Al enrichment will be discussed in the following sections.

Even though the O content is roughly constant against pressure on an average level, O concentration exhibits a local maximum in the radially resolved measurement at all pressures (figure 6(d)). The maximum moves progressively from x_e to x_3 as the deposition pressure is decreased. We suggest that local maxima of the O content near x_e may be related to the local maxima in Hall mobility near x_e observed in figure 3(b). In fact, the electron mobility of AZO is known to exhibit a maximum in correspondence to the optimal oxygen content [36]. Besides that, no other measured quantity has a local maximum or minimum near x_e in our study. Finally, we note that it is difficult to establish any trends in the Zn and Al content against radial position (the dips in Zn content near x_e can be attributed to the local increase in O content).

3.7. Morphology

To investigate the influence of deposition pressure and radial position on film morphology, we examine SEM images in the top- and cross-sectional view of three representative films (figure 7). Interestingly, the cross-sectional images of the 2.5 mTorr film demonstrate that a phase with different morphology exists at the film top surface. This effect is greatly enhanced in the region near x_0 where, in the whole upper half of the film, columnar grains are replaced by a more homogeneous layer of nearly amorphous appearance. In fact, the XRD pattern of the 2.5 mTorr film near x_0 (not shown) has a very weak broad background hump around the (0 0 2) peak position, which is probably related to this nearly amorphous AZO phase. In the top-view images of the 2.5 mTorr film, the crystal grains are not as sharply defined as in the other films, probably because those grains do not extend all the way up to the film surface. As noted in previous reviews, heavy particle bombardment is known to be responsible for film amorphization effects [39, 40].

On the other hand, in the high-pressure regime the film has less dense, more porous morphology at all positions (figure 7(c)). This is generally expected for films sputtered at high pressure [32] and it is likely to play a role in the increase of resistivity occurring in this regime. It can also explain the global increase of resistivity over time shown in figure 2, since
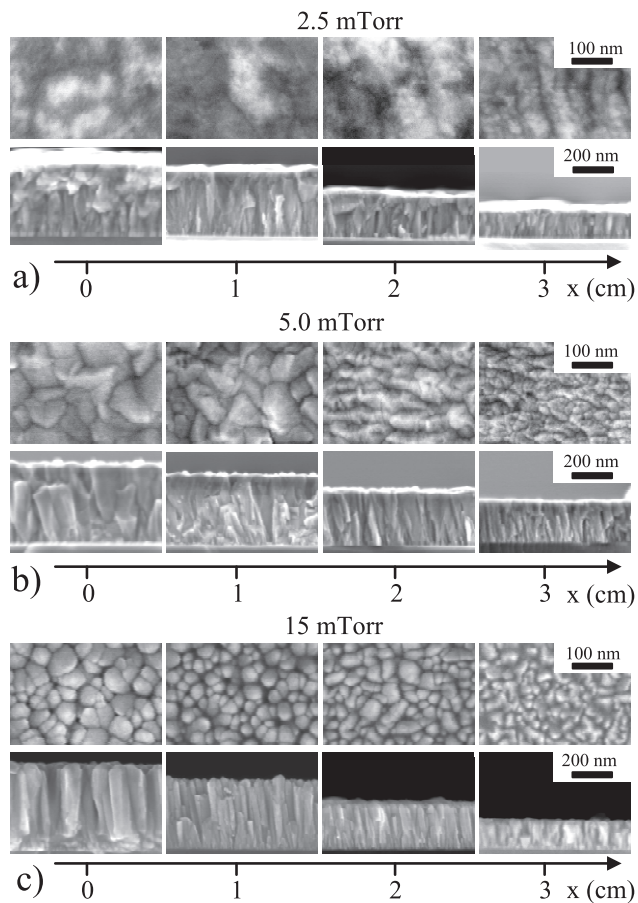
5

J. Phys. D: Appl. Phys. **49** (2016) 295101

A Crovetto *et al*

2.5 mTorr

5.0 mTorr

15 mTorr

Figure 7. SEM images in top- and cross-sectional view as a function of radial position from x_0 to x_3 at different deposition pressures. (a) 2.5 mTorr, (b) 5.0 mTorr, (c) 15 mTorr. The magnification is kept constant from left to right on each row.

a higher porosity can result in easier adsorption of oxygen and other detrimental chemical species at grain boundaries.

3.8. Grain size

The quantity that can be extracted by XRD is the out-of-plane crystallite size, which, especially in the case of columnar growth, is not necessarily related to the in-plane grain size. For this reason, we rely on SEM images in the top view to visualize the in-plane grain size and we employ a standard data analysis procedure in XRD line profile analysis to deconvolute microstrain and instrumental effects from the out-of-plane grain size [19]. Note that this method has been applied to AZO films in a very limited number of previous reports [33–35], with most studies not applying any kind of deconvolution. From the SEM images in the top view (figure 7) it is evident that the in-plane dimensions of the crystal grains decrease from x_0 to x_3 at all pressures. On the other hand, the out-of-plane grain size measured by XRD (figure 8(a)) does not point to a unique trend. In fact, the grain size decreases with increasing radial position in the low- and high-pressure regime in a similar fashion as the in-plane grain size, but the opposite is observed in the intermediate-pressure regime. Hence, an anomaly exists near x_0 in the intermediate-pressure regime. This is qualitatively confirmed by the SEM images in cross-sectional view for such a region
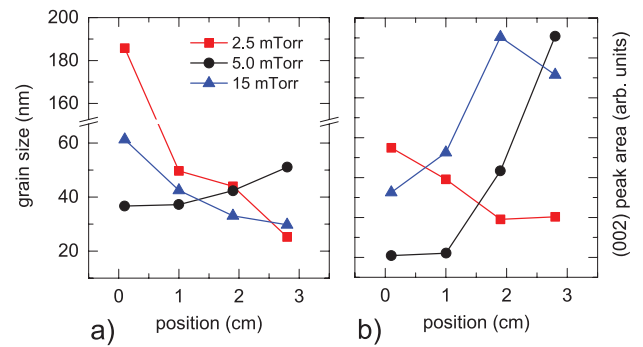

Figure 8. (a) Radial distribution of out-of-plane grain size from x_0 to x_3 as determined by XRD line profile analysis after deconvoluting instrument- and strain-related broadening effects. (b) Radial distribution of (0 0 2) peak area divided by film thickness at each point from x_0 to x_3. As a rough approximation, the (0 0 2) peak area is proportional to the degree of preferential *c*-axis orientation perpendicular to the substrate plane.

(figure 7b), showing V-shaped grains that do not extend all the way through the film. The origin of this type of morphology will be discussed in the following sections.

Finally, we note that at the x_0 position in the low-pressure regime a striking five-fold increase in grain size occurs with respect to the rest of the film. This corresponds to the position with the most severe amorphization effects at the film top. Further experiments are needed to understand such an abrupt increase. It must be emphasized, however, that this effect would not have been detected without deconvoluting the instrumental- and strain-related XRD line broadening from size-related broadening. In fact, direct grain size estimation with the Scherrer formula before deconvolution yields 24 nm for this data point, whereas the same formula after deconvolution yields 185 nm. Even though this is an extreme example, skipping the deconvolution step in our data results in an average underestimation of grain size by 43%.

3.9. Texture

It is well-known that sputter-deposited ZnO films often exhibit very strong *c*-axis texture, with the (0 0 1) planes of the hexagonal lattice mostly parallel to the plane of the substrate. In this study, we do not carry out a comprehensive texture analysis but we simply evaluate the integrated area of the (0 0 2) peak in the XRD pattern, normalized by the film thickness at each point, to give a rough estimate of the degree of preferential *c*-axis orientation. The results (figure 8(b)) demonstrate that completely different radial distributions exist in the different pressure regimes. Notably, the (0 0 1) texture is almost completely lost near x_0 in the intermediate-pressure regime. This effect will be discussed in the following sections in conjunction with the trends in grain size.

4. Discussion

4.1. Review of particle energy flux distributions in AZO sputter deposition

We have concluded that particle bombardment is likely to affect the properties of our AZO film to various extents

6

104

depending on deposition pressure and radial position. By compiling results from various existing works, we present in the following the expected trends for the total energetic particle flux density and average particle energy with respect to deposition pressure and radial position. The expected trends are then compared to our film characterization results.

4.1.1. Particle flux density. The energetic particle flux density dependence on deposition pressure was examined for DC sputtering of ZnO [17], where O^- ions were found to be the dominating species up to a pressure of about 5 mTorr, and O neutrals dominated above 5 mTorr. The summed flux density from the two species was only slightly decreasing with increasing pressure up to about 8 mTorr, then a faster exponential decay occurred, characterized by a 50% decrease every 10 mTorr.

The spatial distribution of the O^- ion flux density was investigated in several works, which generally found a larger flux density near x_e, corresponding to the largest plasma density or, equivalently, to the strongest magnetic field at the target [9, 28, 41]. It is difficult to extract quantitative trends, because the flux density distribution depends on the age of the target [9, 42], the strength of the magnetic field in the magnetron [10], the type of excitation [9] (RF or DC), and energy-dispersive measurements are typically affected by the limited acceptance angle of the probe [9, 15]. However, it can be assumed that increasing deposition pressure leads to a reduction in the flux density gradient due to a larger contribution from species with an off-normal incidence angle caused by more frequent collisions. This effect can be seen to some extent in angle-resolved flux density measurements [28].

4.1.2. Particle energy. The maximum energy of the negative ions at the substrate decreases with increasing deposition pressure, because the particle mean free path decreases with pressure due to collisions in the plasma. However, the decrease is not as strong as might be expected by the classical mean free path of Ar at room temperature, because the collision cross section of energetic species is considerably smaller than that of thermal species [43]. According to universal energy-dependent thermalization curves [44], species with an energy distribution centered at 150 eV (as expected from our measured target self-bias) reach the substrate with still 90%, 85%, and 70% of their initial energy at 2.5 mTorr, 5 mTorr, and 15 mTorr respectively. A rather similar pressure dependence has also been shown experimentally for O^- ions in RF sputtering of MgO [45].

Regarding the radial dependence, the maximum difference in ballistic path from target to substrate in our setup is from the center of the target to point x_0 and to point x_3 on the substrate. Those two distances are 3.0 and 4.2 cm respectively, i.e. a $\sim$ 30% difference in pressure-distance product. Using the same energy-dependent thermalization curves as above, an upper limit to particle energy gradients can be estimated. From this analysis, we conclude that particle energy at all radial positions should be within 90% of the energy at the shortest target-substrate path at all investigated pressures. A nearly uniform radial energy distribution

is confirmed by existing experimental data [9] and simulations [10, 26].

4.1.3. Comparison with our results. The lattice shift trends in our films (figure 5(a)) point to the fact that the particle energy flux is enhanced by decreasing the deposition pressure from 15 to 2.5 mTorr and by decreasing the radial position from x_3 to x_0. While the pressure trend is compatible with the above review, the radial trend is not. Specifically, we have indirectly found a maximum in the particle energy flux (and resistivity) at x_0 through equation (1), in contrast with the typical observation of a maximum at x_e.

Yet it must be emphasized that previously reported resistivity distributions do not necessarily follow the expected energetic particle distribution at the target. While resistivity maxima at x_e are most often reported [7–9, 11, 12, 29], resistivity minima at x_e [13] and resistivity maxima at x_0 were also observed [9–12]. In some cases [9, 11, 12], the resistivity maximum at x_0 was shown to occur only when an old, eroded target was used (roughly, for an erosion track deeper than 1 mm). This was related to an increased flux of high-energy oxygen ions in the region around x_0 due to a modified emission angle distribution of the ions from a target with an eroded profile [9]. However, this mechanism is unlikely to be active in our experiment because our target was nearly uneroded (depth of erosion track: 0.2 mm).

Another possible explanation for a resistivity maximum at x_0 could be the radial inhomogeneity of oxygen reaching the substrate, as clearly shown in a study on DC-sputtered $In_4Sn_3O_{12}$ [18]. There, a maximum at x_0 occurred when the oxygen content was closer to the optimal amount at x_e than at x_0. However, this is not the case in our experiments either, since the oxygen content in our films is not a monotonic function of radial position (figure 6(d)).

Yet a third possible cause for a resistivity maximum at x_0 could be specific plasma features at the target, influenced by parameters such as strength of the magnetic field, balanced/unbalanced type of cathode, or superposition of a capacitively coupled mode of discharge over the magnetron sputtering regime at low-pressure-distance product [46]. For example, it has been shown for DC-sputtered AZO that, upon enhancement of the magnetic field parallel to the target by an external magnetic field, the position of the resistivity maximum shifts from x_0 to x_e [10].

Note also that most previous studies have neglected the detrimental effect of positive ions (of which Ar^+ are the most abundant) on the basis that their average energy is much lower than that of the O^- ions. However, a flux density ratio between Ar^+ and O^- ions greater than 2 was measured for RF sputtering of AZO with a grounded substrate [27]. In the same study, the average energy of the Ar^+ ions impinging onto a grounded surface was 29 eV, with a significant tail above the 33–35 eV sputtering threshold of ZnO [10, 26]. The radial distribution of Ar^+ ion flux density features a maximum at x_0, corresponding to a maximum in plasma density at the substrate [9]. Therefore, it is not excluded that Ar^+ ions may play a role in the the energy flux and resistivity distributions in our experiments.

7

J. Phys. D: Appl. Phys. 49 (2016) 295101

A Crovetto *et al*

4.2. Correlations at low- and intermediate deposition pressure

In this section, we focus on deposition pressures lower than the optimal pressure in figure 2(a), i.e. on the left of the resistivity minimum at around 5 mTorr pressure. This corresponds to a process window where the resulting films are under compressive stress. We attempt to identify correlations between the compressive stress and some electrical, structural, and compositional properties. For each pair of correlated properties, we suggest a fitting function for the experimental data, which roughly describes the nature of the correlation. Also, we discuss the possible physical origin of the correlations and briefly mention the relationship between oxygen content and carrier mobility, which is an additional cause of inhomogeneity in AZO films.

4.2.1. Electrical properties and stress.
In this study, the electrical properties and the out-of-plane lattice shift (or in-plane compressive stress) of AZO are clearly correlated (figures 2 and 5). Since the latter is related to the energy E and flux density Γ of the bombarding particles [31] according to equation (1), there is strong evidence that particle bombardment has a major influence on the resistivity of RF-sputtered AZO, both in the radial direction and in the low-pressure regime.

To quantify this effect, we propose plotting $y(\bar{p}, \bar{x})$ versus $\varepsilon(\bar{p}, \bar{x})$ curves, where y is any measured quantity at point $(\bar{p}, \bar{x})$ in the pressure-position space. This should be equivalent to plotting quantity y versus a rough measure of the particle energy flux. The results are presented in figure 9 for resistivity ρ, carrier concentration N_c, and mobility μ. Strikingly, we find that all three electrical properties can be expressed as a function of the lattice shift alone, regardless of radial position or deposition pressure. By fitting the experimental data points in the three curves in figure 9, we obtain the following empirical relations between the electrical properties and the lattice shift:

$$N_c(\varepsilon) = N_0 + A_1 \exp\left(-\frac{(\varepsilon - \varepsilon_I)^2}{2B_1^2}\right) \quad (2)$$

$$\mu(\varepsilon) = A_2 \exp\left(\frac{B_2}{\varepsilon - \varepsilon_2}\right) \quad (3)$$

$$\rho(\varepsilon) = \frac{1}{qA_2 \exp\left(\frac{B_2}{\varepsilon - \varepsilon_2}\right)\left(N_0 + A_1 \exp\left(-\frac{(\varepsilon - \varepsilon_I)^2}{2B_1^2}\right)\right)} \quad (4)$$

where equation (4) was simply derived by applying the relation $\rho = (qN_c\mu)^{-1}$, q being the elementary charge. The fitted values of the free parameters are: $N_0 = 7.57 \times 10^{19}$ cm^{-3}, $A_1 = 3.01 \times 10^{20}$ cm^{-3}, $\varepsilon_1 = -0.151\%$, $B_1 = 0.465\%$, $A_2 = 28.9$ cm^2 Vs^{-1}, $\varepsilon_2 = 1.34\%$, $B_2 = 0.537\%$.

These results suggest that the lattice shift (and ultimately the energy flux of the bombarding particles) is correlated to the electrical properties in a more general way than the single deposition parameters or the radial position are. Namely, a certain value of the lattice shift may be obtained by different combinations of radial position, deposition pressure
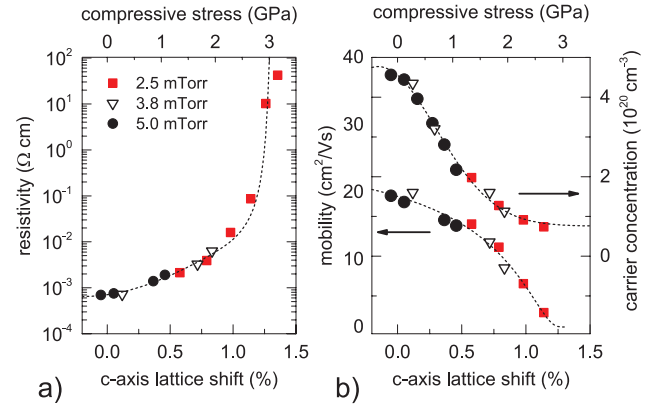

Figure 9. Resistivity, carrier concentration, and mobility of AZO films versus their corresponding lattice shift and stress. The plotted data points are from radial positions between x_0 and x_3 at three different deposition pressures in the low- and intermediate-pressure regime. The dashed curves are the fitting functions defined by equations (2)–(4) in the text.

and possibly other parameters, but the resistivity is ultimately determined by the lattice shift resulting from those deposition parameters. It is evident from figure 9(a) that lattice shift must be minimized in order to minimize the film resistivity. This can be achieved by minimizing the energy flux of bombarding particles as demonstrated, for example, by placing the substrate perpendicularly to the target [47, 48] or by a variety of other methods [16]. Note also that, in the case of a large compressive stress, the carrier concentration stabilizes to its asymptotic value given by N_0, while the mobility drops dramatically.

4.2.2. Structural properties and stress.
The out-of-plane grain size and the degree of preferential *c*-axis orientation are also correlated with compressive stress and thus with the particle energy flux (figure 10(a)). In this case, however, the correlation is only qualitative and the fitting functions are merely a guide to the eye. Both the grain size and (0 0 2) peak area have a minimum at a compressive stress of about 1–2 GPa. This is likely to correspond to the energy flux and temperature window typical of zone T in the Thornton structure zone diagram [32], where a mixed film texture and small out-of-plane grain size are expected due to competition between differently oriented V-shaped grains during film growth.

Here an interesting observation can be made. Most of the existing studies on sputtered AZO report an increase in grain size [7, 9, 49] and an increase in (0 0 1) texture coefficient [50] with decreasing resistivity, but inconsistent trends have been pointed out, especially for the case of RF sputtering [9, 33, 51]. From inspection of figure 10(a), we propose that the often-reported trend of increasing grain size with decreasing resistivity applies only under mild particle bombardment, i.e. for $\sigma < 1$ GPa, where resistivity is lowest. This possibly corresponds to zone 1 in the Thornton zone diagram. Conversely, the grain size increases for increasing energy flux and increasing resistivity when $\sigma > 2$ GPa, as the film structure possibly moves to zone 2 of the diagram. This may provide an explanation for the reported inconsistencies in the literature.
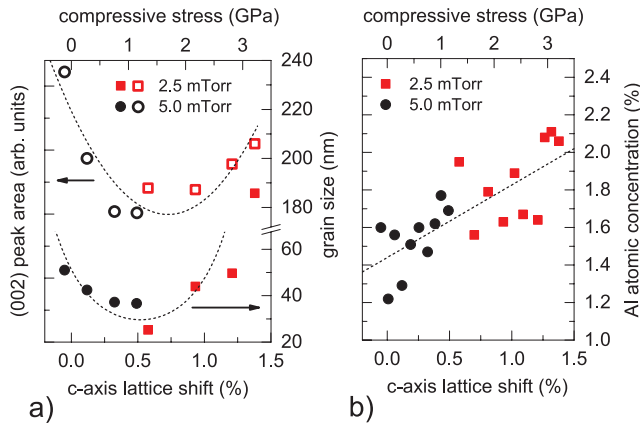
J. Phys. D: Appl. Phys. **49** (2016) 295101

A Crovetto *et al*

Figure 10. (a) Area of (0 0 2) peak and out-of-plane grain size of AZO films versus their corresponding lattice shift and stress. The plotted data points are from radial positions between x_0 and x_3 at two different deposition pressures in the low- and intermediate-pressure regime. The dashed curves are fitting functions to be interpreted only qualitatively. (b) Atomic Al concentration at different radial positions in the low- and intermediate-pressure regime versus their corresponding lattice shift and stress. The dashed curve is the fitting function defined by equation (5).

In fact, the lattice shift in one study that reported the anomalous trend of increasing grain size with increasing resistivity was in the 1.0–1.5% range [9], where that trend is actually predicted by our qualitative model.

4.2.3. Aluminum content and stress. While it is difficult to establish any trends in the Al content against radial position alone (figure 6(b)), the Al content c_{Al} seems to increase roughly linearly with lattice shift (figure 10(b)) and can be fitted as

$$c_{Al}(\varepsilon) = A_3 + B_3\,\varepsilon \qquad (5)$$

where $A_3 = 1.44\%$ and $B_3 = 0.387$. Al enrichment has been observed by several authors when the substrate temperature was increased above an optimal value [37, 52, 53]. Even though the substrate temperature was kept constant in this study, the actual temperature of the growing film is given by the substrate temperature plus a temperature shift proportional to the *potential* energy flux of the particles reaching the substrate. The latter depends on the number flux density of the species, their cohesive and ionization energy and work function, but not on their kinetic energy [40]. However, the potential energy flux is still expected to increase for decreasing pressure (due to less thermalization) [54] and for decreasing radial position (due to higher deposition rate, reflecting the higher number flux density of all species arriving at the substrate) similarly to the kinetic energy flux and the lattice shift [46]. Hence we may interpret the increase in Al content with lattice shift as due to a film temperature increase related to the increased potential energy flux density at the substrate.

4.2.4. Mobility and oxygen content. Besides the global resistivity maximum at x_0, weaker local maxima of the Hall mobility are also observed near x_e in the intermediate-pressure regime (figure 3(b)). We suggest that a correlation exists

between the local Hall mobility maxima and the maxima of the oxygen content near x_e found in the intermediate-pressure regime (figure 6(d)). If this hypothesis is true, the oxygen content in the other regions of the film must be slightly below the optimal value. Note, however, that the measured change in oxygen content near x_e is less than $+0.5\%$ (absolute), pointing to the high sensitivity of electron mobility on oxygen content. A local maximum in oxygen content is also present, at slightly different radial positions, in the low- and high-pressure regimes, which however do not exhibit an evident mobility spike. We presume that the mobility change is harder to detect in those regimes due to the steeper gradient or lower value of the mobility.

4.3. Correlations at high deposition pressure

In this section, we focus on deposition pressures higher than the optimal pressure in figure 2(a), i.e. on the right of the resistivity minimum at around 5 mTorr pressure. This corresponds to a process window where the resulting films are under tensile stress. No quantitative correlations were found in this process window, so a purely qualitative discussion is provided.

4.3.1. Electrical properties and porosity. SEM images confirm that a less dense, more porous film is formed in the high-pressure regime (figure 7(c)), accompanied by tensile in-plane stress (figure 5(a)). This can be attributed to thermalization of most sputtered species. In fact, the mean free path for neutrals (Zn, O, Al) is around 2.0 cm at 2.5 mTorr, comparable to our target-substrate distance, but it is only around 3.4 mm at 15 mTorr [43]. Porosity can explain the inferior electrical properties in the as-deposited films, because the electrical current has to flow around a larger number of voids. Since more grain boundaries are exposed to air than in an ideally compact film, a porous morphology can also explain the time-dependent degradation under ambient conditions (figure 2(b)) due to adsorbed species at grain boundaries. However, it is unlikely that the resistivity gradient in the radial direction is also due to an increase in porosity from x_3 to x_0. First of all, film density is more likely to increase near x_0, rather than the opposite, due to a larger expected energy flux of the bombarding particles, which is confirmed by a lower tensile stress in that region. Secondly, no significant difference in the refractive index and extinction coefficient was measured from from x_3 to x_0 (not shown), suggesting that film density is approximately constant in the radial direction. Finally, the resistivity degradation factor under ambient exposure is approximately constant in the radial direction (figure 2(a)), which also suggests that the density gradient is negligible.

5. Conclusion

We have investigated the spatial distribution of different electrical, structural, morphological, and compositional properties of RF-sputtered AZO at different deposition pressures. Based on a well-known relationship between the kinetic energy flux of the bombarding particles and the compressive stress in the film, we have correlated several properties of the films to the

9

energy flux. Generalized quantitative relationships have been established between the electrical properties (carrier concentration, mobility, and resistivity) and the compressive stress in the film. In general, the stress must be as low as possible in order to minimize resistivity. At a large stress (above 2 GPa) the carrier concentration stabilizes to an approximately constant value while the mobility drops dramatically.

On the other hand, preferential *c*-axis orientation and grain size both have a very different relationship to the compressive stress and the bombarding energy flux. They have a minimum at a compressive stress in the 1–2 GPa range, where the most random orientation and the smallest grain size are found, corresponding to zone T of the Thornton structure zone diagram. Moving away from this stress range, the grains increase in size and the preferential (0 0 1) orientation is restored. This can explain why inconsistent correlations between resistivity and grain size have often been found in previous work.

The Al content in the film also has an (approximately linear) relationship to the compressive stress. We attribute the Al enrichment to an increased potential energy flux from the species arriving at the substrate, resulting in a temperature increase of the growing film.

From the analysis of deposition rate, film morphology and stress, it is concluded that the main reason for spatial inhomogeneity and pressure dependence of the electrical properties is particle bombardment. However, we have also observed localized gradients in the electron mobility (but not in the carrier concentration) in an intermediate-pressure regime, which we attributed to inhomogeneous oxygen distribution. While this was found to be a minor effect under our deposition conditions, oxygen inhomogeneity may become a dominating factor if films with a uniform low-stress profile can be produced at a reasonably low pressure.

Finally, under process conditions where particle bombardment effects are negligible and in-plane tensile stress develops, a porous microstructure limits the achievable resistivity and causes it to increase over time as well.

Acknowledgments

References

[1] Ellmer K 2012 *Nat. Photon.* **6** 809–17
[2] Kumar A and Zhou C 2010 *ACS Nano* **4** 11–4
[3] Green M A, Emery K, Hishikawa Y, Warta W and Dunlop E D 2015 *Prog. Photovolt., Res. Appl.* **24** 3–11
[4] Herrmann D, Kratzert P, Weeke S, Zimmer M, Djordjevic-Reiss J, Hunger R, Lindberg P, Wallin E, Lundberg O and Stolt L 2014 CIGS module manufacturing with high deposition rates and efficiencies *IEEE 40th Photovoltaic Specialist Conf.* pp 2775–7
[5] Jackson P, Hariskos D, Wuerz R, Kiowski O, Bauer A, Friedlmeier T M and Powalla M 2015 *Phys. Status Solidi RRL* **9** 28–31
[6] Ellmer K 2000 *J. Phys. D: Appl. Phys.* **33** R17–32
[7] Tominaga K, Yuasa T, Kume M and Tada O 1985 *Japan. J. Appl. Phys.* **24** 944–9
[8] Minami T, Miyata T, Yamamoto T and Toda H 2000 *J. Vac. Sci. Technol.* A **18** 1584
[9] Bikowski A, Welzel T and Ellmer K 2013 *J. Appl. Phys.* **114** 223716
[10] Zhang X B, Pei Z L, Gong J and Sun C 2007 *J. Appl. Phys.* **101** 014910
[11] Szyszka B 2008 Magnetron sputtering of ZnO films *Transparent Conductive Zinc Oxide: Basics and Applications in Thin Film Solar Cells* ed K Ellmer *et al* (Berlin: Springer) p 221
[12] Dewald W, Sittinger V, Werner W, Jacobs C and Szyszka B 2009 *Thin Solid Films* **518** 1085–90
[13] Cebulla R, Wendt R and Ellmer K 1998 *J. Appl. Phys.* **83** 1087
[14] Tominaga K, Sueyoshi Y, Munfei C and Shintani Y 1993 *Japan. J. Appl. Phys.* **32** 4131–5
[15] Welzel T, Kleinhempel R, Dunger T and Richter F 2009 *Plasma Process. Polym.* **6** S331–6
[16] Ellmer K and Welzel T 2012 *J. Mater. Res.* **27** 765–79
[17] Tominaga K, Iwamura S, Shintani Y and Tada O 1982 *Japan. J. Appl. Phys.* **21** 688–95
[18] Minami T, Takeda Y, Takata S and Kakumu T 1997 *Thin Solid Films* **308–9** 13–8
[19] de Keijser T H, Langford J I, Mittemeijer E J and Vogels A B P 1982 *J. Appl. Crystallogr.* **15** 308–14
[20] Petersen D H, Hansen O, Lin R and Nielsen P F 2008 *J. Appl. Phys.* **104** 013710
[21] Henrichsen H H, Hansen O, Kjaer D, Nielsen P F, Wang F and Petersen D H 2014 Precision of single-engage micro Hall effect measurements *IEEE Int. Workshop on Junction Technology* pp 1–4
[22] Kluth O, Schöpe G, Rech B, Menner R, Oertel M, Orgassa K and Werner Schock H 2006 *Thin Solid Films* **502** 311–6
[23] Chung Y M, Moon C S, Jung M J and Han J G 2005 *Surf. Coat. Technol.* **200** 936–9
[24] Ngaruiya J M, Kappertz O, Mohamed S H and Wuttig M 2004 *Appl. Phys. Lett.* **85** 748
[25] Keller J H and Simmons R G 1979 *IBM J. Res. Dev.* **23** 24–32
[26] Carcia P F, McLean R S, Reilly M H, Li Z G, Pillione L J and Messier R F 2003 *J. Vac. Sci. Technol.* A **21** 745
[27] Welzel T and Ellmer K 2013 *J. Phys. D: Appl. Phys.* **46** 315202
[28] Tominaga K, Ueshiba N, Shintani Y and Tada O 1981 *Japan. J. Appl. Phys.* **20** 519–26
[29] Cai Y, Liu W, He Q, Zhang Y, Yu T and Sun Y 2010 *Appl. Surf. Sci.* **256** 1694–7
[30] DHeurle F M 1970 *Metall. Mater. Trans.* B **1** 725–32
[31] Windischmann H 1987 *J. Appl. Phys.* **62** 1800
[32] Thornton J A 1977 *Annu. Rev. Mater. Sci.* **7** 239–60
[33] Charpentier C, Prodhomme P, Maurin I, Chaigneau M and Roca i Cabarrocas P 2012 *EPJ Photovolt.* **2** 25002
[34] Charpentier C, Prod'homme P and Roca i Cabarrocas P 2013 *Thin Solid Films* **531** 424–9
[35] Bikowski A and Ellmer K 2012 *J. Mater. Res.* **27** 2249–56
[36] Ellmer K, Kudella F, Mientus R, Schieck R and Fiechter S 1994 *Thin Solid Films* **247** 15–23
[37] Cornelius S and Vinnichenko M 2016 *Thin Solid Films* **605** 20–29
[38] Agashe C, Kluth O, Schöpe G, Siekmann H, Hüpkes J and Rech B 2003 *Thin Solid Films* **442** 167–72
[39] Mattox D M 1989 *J. Vac. Sci. Technol.* A **7** 1105
[40] Anders A 2010 *Thin Solid Films* **518** 4087–90
[41] Toyoda H, Goto K, Ishijima T, Morita T, Ohshima N and Kinoshita K 2009 *Appl. Phys Express* **2** 126001
[42] Welzel T and Ellmer K 2011 *Surf. Coat. Technol.* **205** S294–8

10

J. Phys. D: Appl. Phys. **49** (2016) 295101

A Crovetto *et al*

[43] Harper J M E, Cuomo J J, Gambino R J, Kaufman H R and Robinson R 1978 *J. Vac. Sci. Technol.* **15** 1597

[44] Somekh R E 1984 *J. Vac. Sci. Technol.* A **2** 1285

[45] Ishijima T, Goto K, Ohshima N, Kinoshita K and Toyoda H 2009 *Japan. J. Appl. Phys.* **48** 116004

[46] Musil J 1998 *Vacuum* **50** 363–72

[47] Minami T, Sato H, Nanto H and Takata S 1985 *Japan. J. Appl. Phys.* **24** L781–4

[48] Jin Z C, Hamberg I and Granqvist C G 1988 *J. Appl. Phys.* **64** 5117

[49] Minami T, Nanto H, Sato H and Takata S 1988 *Thin Solid Films* **164** 275–9

[50] Prabhakar T, Dai L, Zhang L, Yang R, Li L, Guo T and Yan Y 2014 *J. Appl. Phys.* **115** 083702

[51] Jeong S and Boo J 2004 *Thin Solid Films* **447–8** 105–10

[52] Vinnichenko M, Gago R, Cornelius S, Shevchenko N, Rogozin A, Kolitsch A, Munnik F and Moller W 2010 *Appl. Phys. Lett.* **96** 141907

[53] Bikowski A, Rengachari M, Nie M, Wanderka N, Stender P, Schmitz G and Ellmer K 2015 *APL Mater.* **3** 060701

[54] Sahu B B, Han J G, Hori M and Takeda K 2015 *J. Appl. Phys.* **117** 023301

Electrical property mapping of ZnO:Al films with micro four-point-probe technique

Andrea Crovetto[1], Daniel Kjær[1,2], Dirch H. Petersen[1], Jørgen Schou[3] and Ole Hansen[1,4]

[1]DTU Nanotech, Technical University of Denmark; [2] CAPRES A/S, Kgs. Lyngby, Denmark;
[3]DTU Photonics, Technical University of Denmark; [4] CINF, Center for Individual Nanoparticle Functionality, Technical University of Denmark

Motivation

Demonstrating the advantages of a **micro-four-point probe** setup for mapping electrical properties of transparent conductive films:

1. High spatial resolution
2. Non-destructive
3. Compatible with in-line processes
4. No sample preparation for Hall measurement
5. Error suppression by combining measurements from 7 probes

Sheet resistance measurement

micro probe **10 µm** pitch
macro probe **1 mm** pitch

Micro probe: **10 µm** probe pitch — 1%

Micro probe **1.5 µm** probe pitch — 6%
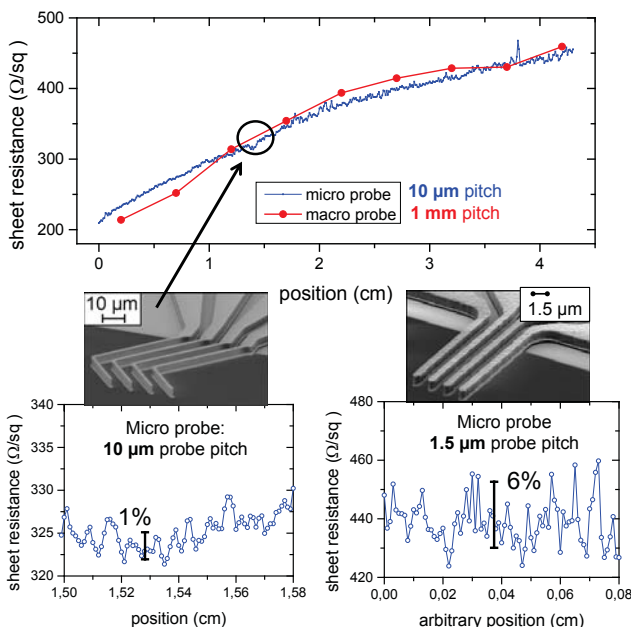
Probe with smaller pitch is more sensitive to local variations and reduces correlation effects

thickness ← optical mapping (ellipsometry) → **band gap**

film thickness
average resistivity
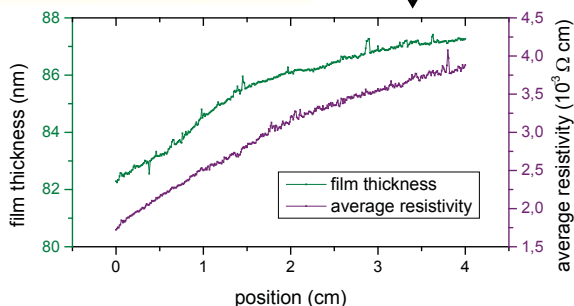
Hall measurement

measure V_B and $V_{B'}$ close to an insulating boundary

↓ ↓ ↓

determine Hall mobility and carrier density

B

B'

film | air
strain gauge
sample edge
probe tip
10 µm

carrier density
mobility
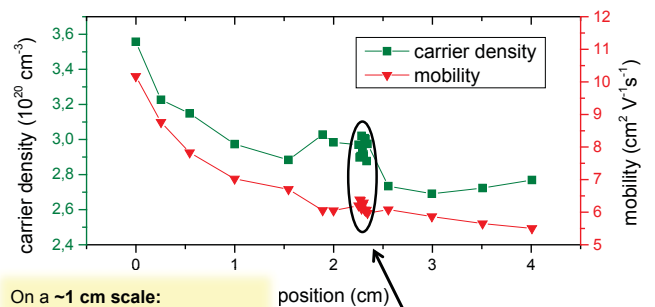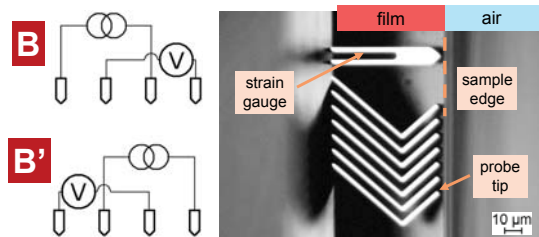
On a **~1 cm scale:**
Resistivity decreases due to increase in both carrier density and mobility

On a **~100 µm scale:**
carrier density and mobility vary in antiphase (measurement noise)

carrier density
mobility

Burstein-Moss effect mapping:

$$\Delta E_G = \text{const}\left(\frac{1}{m_c} + \frac{1}{m_v}\right) n^{2/3}$$

ΔE_G: (optical band gap of ZnO:Al) – (band gap of undoped ZnO)

n: carrier density

Contact

Andrea Crovetto
ancro@nanotech.dtu.dk

Daniel Kjær
DK@capres.com

Chapter 6

Growth and fundamental properties of Cu$_2$SnS$_3$

Oh, seeing double double
Oh, I have double vision, yeah, I'm getting double vision
Foreigner, 1978

6.1 Study 6.1: Dielectric function and double absorption onset in monoclinic Cu$_2$SnS$_3$

- <u>Crovetto A</u>, Chen R, Ettlinger R B, Cazzaniga A C, Schou J, Persson C and Hansen O 2016 Dielectric function and double absorption onset in monoclinic Cu$_2$SnS$_3$: Origin of experimental features explained by first-principles calculations *Solar Energy Materials and Solar Cells* **154** 121–129

You may wonder why I chose the above citation for this chapter. Is there something about Cu$_2$SnS$_3$ that is double? Or am I starting myself to see double after spending too much time in front of a computer, writing this thesis? Well, the answer is both.

Cu$_2$SnS$_3$ (CTS) is a secondary phase of the Cu-Zn-Sn-S phase diagram, which is sometimes unintentionally produced when aiming for a CZTS compound due to the narrow single-phase region of the latter. While CTS inclusions are most likely very bad for the efficiency of CZTS solar cells (see Section 1.4), CTS can be an absorber in its own right, and single-junction CTS solar cells have been fabricated with respectable efficiencies just below 5% [190]. The band gap of CTS (about 1.0 eV) is not too far off the optimal range for single-junction solar cells and is optimal for a bottom absorber in a tandem architecture [26].

Here I measure the dielectric function of CTS for the first time and observe a double onset in the imaginary part of the dielectric function, which describes light absorption in the material. Such a double onset was observed before by absorption measurements and quantum efficiency, but its origin was puzzling [191]. In the hope to find an answer to the interesting issue, I presented the problem to computational material scientists Rongzhen Chen and Clas Persson. What they found is that the double absorption onset is an intrinsic feature of CTS. CTS has three close-lying valence bands: because of different dipole selection rules for the optical transitions from such bands to the conduction band, the first onset can be attributed to a certain light polarization direction with respect to the CTS lattice, and the second onset to two other polarization directions. The double onset can only be resolved by computation if point sampling in the reciprocal space is dense enough.

My contribution (detailed):
• Preliminary characterization by Raman, SEM, AFM, and mechanical profilometry •
Idea for the study and establishment of the international collaboration • Ellipsometry
measurement, optical modeling, and data analysis • Fabrication of Mo back contact •
Preliminary SEM, Raman, AFM characterization and all related data analysis (including
XRD) • Literature review • Writing the manuscript, except for sections 3 and 4.3. Section
5 written with co-authors.

Coauthors' contribution (brief):
• R. Chen, C. Persson: executed the DFT calculations with different approaches, analyzed
the results and understood the physical reason behind the double absorption onset • R. B.
Ettlinger, A. Cazzaniga: deposited and annealed Cu_2SnS_3 by PLD • J. Schou, O. Hansen:
discussions and commenting the manuscript

6.2 Study 6.2: Growth of Cu_2SnS_3 precursors by pulsed laser deposition

- Ettlinger R B, <u>Crovetto A</u>, Canulescu S, Cazzaniga A, Ravnkilde L, Youngman T,
  Hansen O, Pryds N and Schou J 2016 Formation of copper tin sulfide films by pulsed
  laser deposition at 248 and 355 nm *Applied Physics A* **122** 466

This study, mostly the result of the work of PhD student Rebecca Ettlinger, demonstrates that growing Cu-containing chalcogenide films by pulsed laser deposition would be
a nightmare *if* the films were to be used without a (life-saving) post-annealing step. This
study focuses on CTS deposition. The trends in the stoichiometry and droplet density of
the CTS films as a function of laser fluence are similar to those of CZTS films. Two different laser sources with different laser properties were tested: the resulting film properties
were quite similar.

My contribution (detailed):
• Fabrication of Mo back contact • Compositional analysis of the CTS films and droplets
by EDX • Size analysis of the droplets • Part of the SEM characterization • Commenting
the manuscript

Dielectric function and double absorption onset of monoclinic Cu$_2$SnS$_3$: Origin of experimental features explained by first-principles calculations

Andrea Crovetto [a,*], Rongzhen Chen [b], Rebecca Bolt Ettlinger [c], Andrea Carlo Cazzaniga [c], Jørgen Schou [c], Clas Persson [b,d], Ole Hansen [a,e,*]

[a] DTU Nanotech, Technical University of Denmark, DK-2800 Kgs. Lyngby, Denmark
[b] Department of Materials Science and Engineering, Royal Institute of Technology, SE-100 44 Stockholm, Sweden
[c] DTU Fotonik, Technical University of Denmark, DK-4000 Roskilde, Denmark
[d] Department of Physics, University of Oslo, PO Box 1048 Blindern, NO-0316 Oslo, Norway
[e] CINF, Center for Individual Nanoparticle Functionality, Technical University of Denmark, Technical University of Denmark, DK-2800 Kgs. Lyngby, Denmark

ARTICLE INFO

ABSTRACT

In this work, we determine experimentally the dielectric function of monoclinic Cu$_2$SnS$_3$ (CTS) by spectroscopic ellipsometry from 0.7 to 5.9 eV. An experimental approach is proposed to overcome the challenges of extracting the dielectric function of Cu$_2$SnS$_3$ when grown on a glass/Mo substrate, as relevant for photovoltaic applications. The ellipsometry measurement reveals a double absorption onset at 0.91 eV and 0.99 eV. Importantly, we demonstrate that calculation within the density functional theory (DFT) confirms this double onset only when a very dense **k**-mesh is used to reveal fine details in the electronic structure, and this can explain why it has not been reported in earlier calculated spectra. We can now show that the double onset originates from optical transitions at the Γ-point from three energetically close-lying valence bands to a single conduction band. Thus, structural imperfection, like secondary phases, is not needed to explain such an absorption spectrum. Finally, we show that the absorption coefficient of CTS is particularly large in the near-band gap spectral region when compared to similar photovoltaic materials.

© 2016 Elsevier B.V. All rights reserved.

1. Introduction

The ternary chalcogenide semiconductor Cu$_2$SnS$_3$ (CTS) has attracted interest as a solar cell absorber material in the last half decade. Indeed, promising power conversion efficiencies of 4.63% and 4.29% have recently been reported by two independent groups [1,2]. The main potential advantage of CTS over quaternary absorbers Cu(In, Ga)Se$_2$ (CIGS), Cu$_2$ZnSnS$_4$ (CZTS), and Cu$_2$ZnSnSe$_4$ (CZTSe) is a relatively broad single-phase region and reduced fabrication complexity due to fewer chemical constituents [3]. Furthermore, the CTS compound consists of inexpensive and non-toxic chemical elements, unlike the common high-efficiency chalcogenide absorbers CIGS and CdTe. CTS is typically produced by high temperature sulfurization of metal precursors [1] or of a precursor S-containing compound [2,3].

Depending on the deposition parameters and sulfurization conditions, CTS can form with different crystal structures. Tetragonal, cubic, monoclinic, and triclinic phases have been reported. Despite such phase variety, a theoretical work [4] has shown that all the commonly observed crystal structures are based on the same zincblende pattern with tetrahedral coordination. The only difference between them is the degree of disorder in the cation sublattice, which results in different crystal symmetries. The monoclinic phase is a perfectly ordered phase, whereas the disordered cubic and tetragonal phases feature different arrangements of tetrahedral S-Cu$_2$Sn$_2$ and S-Cu$_3$Sn structural motifs. The best-performing CTS solar cells reported so far had a CTS absorber with monoclinic structure [1,2].

A double absorption onset of 0.90–0.93 eV and 0.97–1.02 eV [1,5,6] has consistently been reported in the literature for monoclinic CTS, on the basis of both optical absorption and quantum efficiency (QE) measurements. It has been shown [7] that the double onset is an intrinsic feature of monoclinic CTS and it does not arise from other CTS phases or other compounds. However, another study [8] has shown that a disordered structure can exist

---

locally even in single-phase monoclinic CTS due to the high density of structural defects such as stacking faults, which modify the local atomic coordination. This leaves the open question of whether the double onset is a feature of defect-free monoclinic CTS, or if it is a consequence of the high defect density found in CTS thin films, which locally alters its band structure and consequently its optical transitions. While the electronic structure and density-of-states of monoclinic CTS have earlier been analyzed theoretically [4,9–11] and the optical properties have been computed [4,9], the double onset phenomenon was not reported in those studies. Furthermore, no experimental data on the dielectric function of monoclinic CTS is found in the literature. Experimental dielectric functions have only been reported for multi-phase films identified as a mix of tetragonal and cubic CTS [12], where it is not possible to isolate the dielectric functions of the two single phases.

In this work, we synthesize thin films of monoclinic CTS by pulsed laser deposition (PLD) on Mo-coated glass in order to reproduce the conditions under which CTS is formed in solar cell devices. We extract the complex dielectric function $\varepsilon(E) = \varepsilon_1(E) + i\varepsilon_2(E)$ of CTS in the photon energy range from $E = 0.7$–5.9 eV by spectroscopic ellipsometry measurement, and compare it to the dielectric function calculated within the density functional theory (DFT) to corroborate the results and to investigate the origin of the double onset phenomenon. We find that the very details in the dielectric response at the band-gap energy are revealed only with a very dense **k**-point sampling. Then, the double onset phenomenon is explained as optical transitions from the three topmost bands at the valence band maximum (VBM) in a perfectly crystalline CTS. Thus, the phenomenon does not need to be due to structural imperfections, like a disordered structure or secondary phases. Also, with the dense **k**-mesh the shapes of both the real and imaginary parts of the dielectric function are improved considerably in the low energy region (i.e., below 1.5 eV).

2. Experimental details

Thin films of Mo (approximately 500 nm thick) were deposited on soda lime glass (SLG) by DC magnetron sputtering, with a sputtering pressure of 1.3×10^{-2} mbar for the first 200 nm (adhesion layer) and 3.9×10^{-3} mbar for the last 300 nm (low-resistivity layer).

Thin films of Cu_2SnS_3 were deposited at room temperature on Mo-coated soda lime glass substrates in a pulsed laser deposition (PLD) setup with a background pressure below 3×10^{-6} mbar. The substrates were cleaned sequentially by ultrasonic treatment for 5 min in acetone and isopropanol and finally rinsed in ultra-pure water. The laser beam from a Nd: YAG laser (355 nm wavelength, 7 ns pulse duration) with a repetition rate of 10 Hz was partly focused onto a beam-spot of 2.2 mm² with an angle of incidence of 45° with respect to the target normal and a target-substrate distance of 4.4 cm, as illustrated in Fig. 1. The laser fluence was set to 1.6 J/cm². The targets used are sintered powder disks provided by Testbourne Ltd. with the stoichiometry Cu_2SnS_3.

After deposition, the samples were annealed at 570 °C for 10 min in a sealed furnace evacuated down to 10^{-4} mbar and then filled with 100 mbar of N_2 gas. Samples were placed in a graphite box in the hot zone of the furnace together with 160 mg of sulfur.

The films were imaged with a scanning electron microscope (SEM) equipped with a field emission gun (FE-SEM, Supra 60 VP, Zeiss). Energy dispersive X-ray spectroscopy (EDX) was performed in the same instrument using a silicon drift detector (X-Max^N 50, Oxford Instruments) and a beam voltage of 15 kV. EDX spectra were taken on five different spots and averaged. The error bars are expressed as the standard deviation of the measurements. The EDX analysis software (AzTec, Oxford Instruments) was calibrated with elemental standards instead of with a reference compound.
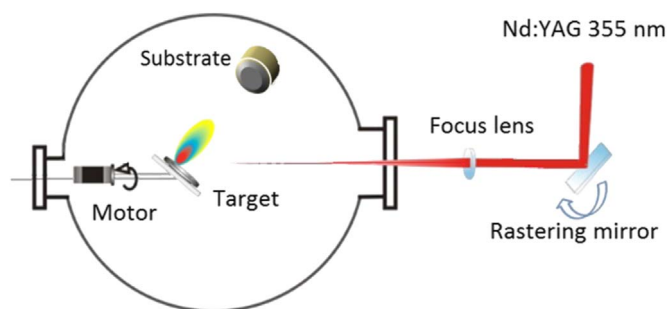

Fig. 1. Scheme of the pulsed laser deposition setup. The combination of target rotation and a rastering mirror ensures uniform ablation of the target. In a vacuum chamber a pulsed laser source (Nd: YAG, 355 nm, 7 ns pulses at 10 Hz) is focused onto a target, which is ablated by the laser.

Therefore, we expect the standard error due to an oversimplified EDX spectrum analysis to be larger than the standard deviation of the measurements.

X-ray diffraction (XRD) patterns were collected with a Bruker D8 powder diffractometer in Bragg-Brentano configuration using $Cu-K_\alpha$ radiation, a 0.009° step size, and a 1.5 s/step integration time. In order to avoid possible peak shifts due to sample alignment errors, the diffraction pattern was aligned using the peaks of standard Si powder.

Raman spectra were obtained in the backscattering configuration at a laser wavelength of 455 nm and laser power of 1.6 mW, using a 50× objective that resulted in a spot size of about 2 μm × 2 μm (DXR Raman Microscope, Thermo Scientific).

Ellipsometry measurements were performed in reflection mode in the spectral range 0.7–5.9 eV on a rotating compensator spectroscopic ellipsometer (M-2000, J.A. Woollam Co.) using a collimated beam with a spot size of approximately 200 μm × 300 μm. Ellipsometry spectra were analyzed and fitted with the CompleteEase software package (version 5.06- J.A. Woollam Co.). When properties of a thin film are to be extracted by an ellipsometry measurement, the reliability of the results depends strongly on the amount of unknown fitting parameters, versus the number of independent measured variables that can be used to fit such parameters [13]. In order to increase the number of measured variables, we measured the magnitude ($\tan \Psi$) and phase (Δ) of the ratio between p- and s- type polarization reflection coefficients for six angles of incidence (from 45 to 70° in steps of 5°), giving twelve measured variables at each wavelength, which were fitted simultaneously in the data analysis step. In order to decrease the number of fitting parameters, we extracted the dielectric function of each layer independently in a separate ellipsometry measurement, as explained in the following sections. A Kramers–Kronig-consistent b-spline model was used to model the shape of the dielectric functions, as demonstrated previously [14]. This means that the imaginary part $\varepsilon_2(E)$ was fitted by a b-spline function using control points spaced by 0.2 eV, whereas the real part $\varepsilon_1(E)$ was not fitted independently but was instead derived by Kramers–Kronig integration. This implies that the relation between $\varepsilon_1(E)$ and $\varepsilon_2(E)$ is a physical one, and that one fitting parameter, instead of two, is required at each control point. Bruggeman's effective medium theory [13] was employed to treat surface roughness as a 50%-solid-film-50%-air layer. Unless otherwise stated, the thickness of the films and of the surface roughness layer were treated as unknown parameters and fitted in the model. However, in order to constrain their range to realistic values and reduce potential correlation errors, their initial values were assigned on the basis of measurements done with other techniques. Since all the layers of interest for this study can be clearly identified in cross sectional SEM images (Fig. 2), pixel counting from high-resolution SEM images allowed us to estimate film thicknesses. In the case of surface roughness, the
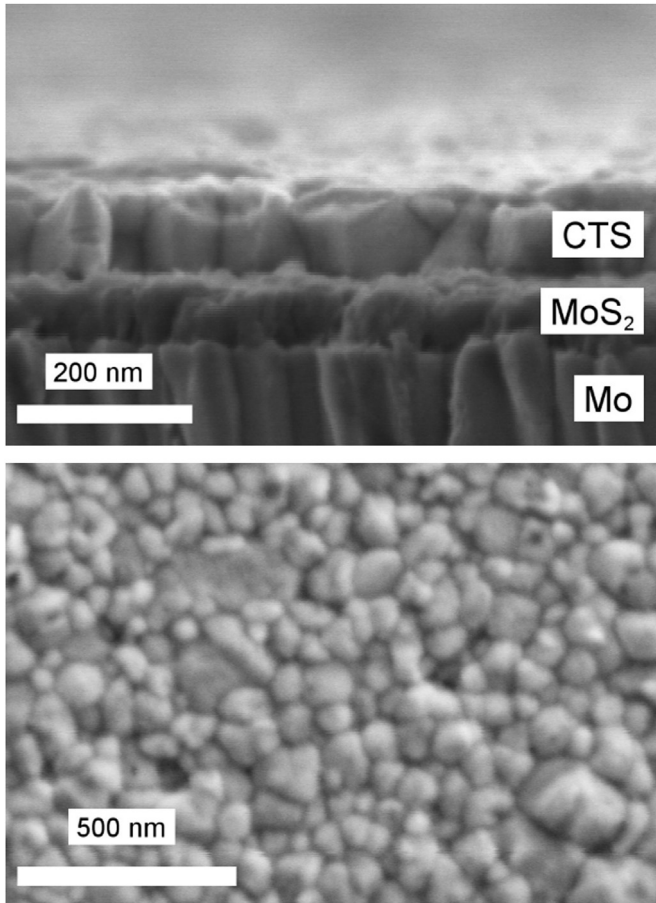
Fig. 2. Cross-sectional and top-view SEM images of the annealed CTS films on a glass/Mo/MoS$_2$ stack. The Mo, MoS$_2$ and CTS layers are clearly visible and are labeled in the cross-sectional image. Each film covers the underlying layers uniformly without obvious pinholes or intermixing. From the cross-sectional image, the estimated film thicknesses are 80 nm for the MoS$_2$ layer and 100 nm for the CTS layer.

measurement was done by atomic force microscopy (AFM) in tapping mode over a 2 μm × 2 μm area (Bruker Dimension Icon). The measured root-mean-square roughness value (R_q) was used to initialize the thickness of the surface roughness layer in the ellipsometry model (R_e), because a good correlation between the two quantities has been observed before, following the empirical formula $R_e \approx 1.5\,R_q + 4$ Å [15]. When fitting ellipsometry data, the allowed range for thickness and roughness values was then restricted to the estimated value $\pm$ 20%.

3. Computational details

The electronic and dielectric responses are theoretically analyzed by means of the plane augmented wave formalism within the DFT as implemented in the VASP program package [16,17]. We model the monoclinic Cu$_2$SnS$_3$ crystal with a 12 atom base-centered primitive cell, space group $Cc = C_s^4$ with unique axis b. The electron density and the optical properties are described with the exchange–correlation potential by Heyd et al., (HSE06) [18] using a $K = 5 \times 5 \times 5$ Γ-centered Monkhorst–Pack like **k**-mesh which implies $N_k = 39$ **k**-points in the irreducible Brillouin zone (IBZ). We use the standard mixing and range-separation parameter for HSE06. With these parameters, the estimated error bar of the band gap energy for similar compounds is about 0.1–0.2 eV [19,20]. All the calculations are performed with an energy cutoff of 420 eV. The structure of monoclinic CTS (4a site atom positions) is

fully relaxed using the HSE06 potential until the total energy and the residual force on each atom converge to 0.1 meV and 10 meV/Å, respectively. The relaxed lattice parameters of the monoclinic CTS are $a = 6.67$ Å, $b = 11.57$ Å, $c = 6.68$ Å, and $\beta = 109.41°$ for unique axis b, obtained with the HSE06 exchange–correlation potential with the standard parameter setting.

The imaginary part $\varepsilon_2(E)$ of the dielectric function is computed directly from the electronic structure and the optical matrix elements performing a tetrahedron integration, while the real part $\varepsilon_1(E)$ is obtained via the Kramers–Kronig transformation, similarly to the experimental approach.

In addition, we perform complementary calculations using the generalized gradient approximation (i.e., PBE [21]) and the PBE+U approach [22] with an onsite Coulomb interaction of U_d(Cu) = 6 eV on the Cu d-like orbitals. PBE implies zero gap energy. With the correction potential U_d(Cu), the energy gap is opened slightly and the d-like energy states are also corrected [23]. However, an additional constant upwards shift of the conduction band minimum (CBM) of Δ_g is needed to reproduce the HSE06 gap energy; we therefore denote this method PBE+U$_d$+Δ_g. With this PBE+U approach we can increase the density of the **k**-mesh to reveal details in the dielectric spectra.

4. Results

4.1. Sample preparation and phase analysis

The CTS deposition time was tuned in order to obtain relatively thin films for ellipsometry analysis (thickness after annealing: less than 100 nm). This approach has been demonstrated previously with other polycrystalline chalcogenide materials [24,25], and it has been shown as an effective way to keep the surface roughness low, which reduces light scattering and depolarization effects. This makes it simpler to analyze the as-annealed films without the need of altering the original surface by polishing [13].

When analyzing a CTS film grown and annealed on Mo-coated glass rather than on bare glass, a few precautions should be taken. By annealing Mo in a S-containing atmosphere, both with and without a sulfide film deposited on top, it is well known that a MoS$_2$ layer is formed on top of the Mo layer if the temperature is high enough [26]. By means of Raman spectroscopy and X-ray photoemission spectroscopy (not shown), we have confirmed the presence of a MoS$_2$ layer up to 100 nm thick in our samples after annealing. This layer is clearly visible when taking a cross-sectional SEM image (Fig. 2). Compositional analysis of such thin samples by EDX is inaccurate due to X-rays being generated in all the layers of the stack and due to the overlap of the Mo and S peaks in the X-ray spectrum. Therefore, thicker films (around 2 μm) were prepared using the same recipe and analyzed by EDX. The resulting atomic composition is Cu = (33.0 $\pm$ 0.3)%, Sn = (18.0 $\pm$ 0.1)%, S = (49.0 $\pm$ 0.3)% with Cu/Sn = 1.81 $\pm$ 0.02, similar to the composition of the best performing solar cells [1,2].

To confirm that a CTS phase is actually formed in the bulk of the film, X-ray diffraction (XRD) was performed on the same thicker film used for EDX measurements to increase the signal intensity. The detected peaks that are not related to Mo or MoO$_3$ can be attributed to monoclinic CTS based on the reference pattern JCPDS-01-070-6338 (Fig. 3). Such peaks are related to different CTS crystal planes, thus we conclude that our CTS film does not have a unique crystal orientation perpendicular to the substrate.

It should be emphasized that distinguishing between different CTS polymorphs by means of XRD alone is a difficult task due to the similarity of their crystal structures and, hence, of their XRD patterns [4]. On the other hand, the Raman spectra of the different CTS polymorphs are more characteristic [27,28]. Therefore, we
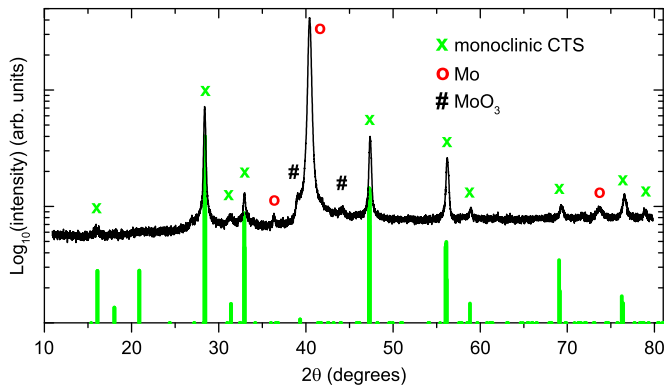
Fig. 3. X-ray diffraction pattern of a 2 μm-thick CTS film prepared with the same recipe as the film for ellipsometry analysis. All detected peaks but two can be attributed to monoclinic Cu_2SnS_3 (green - JCPDS-01-070-6338) and cubic Mo (red - JCPDS-01-071-3771; the peak at 36.4° is the k_β component of the strongest Mo peak). The two remaining peaks are also present in the XRD pattern of the bare Mo film (not shown) and are attributed to two MoO_3 phases (black - JCPDS-01-076-1003 and JCPDS-01-089-1554). The reference powder pattern of monoclinic CTS is displayed in green below the measured XRD pattern. (For interpretation of the references to color in this figure legend, the reader is referred to the web version of this article.)
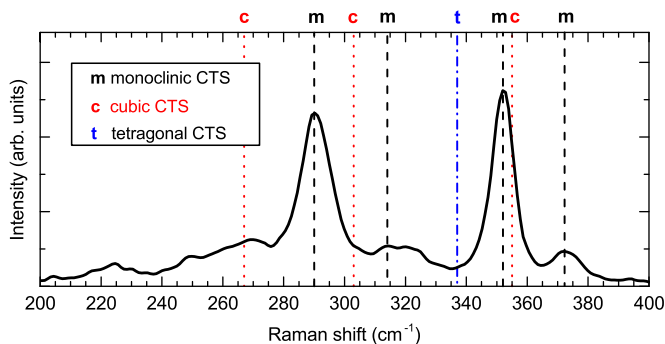

Fig. 4. Averaged Raman spectrum of the annealed CTS films on a glass/Mo/MoS₂ stack from five measurement points. The dashed lines correspond to the four main peaks identified by Berg et al. [28] as vibrational modes of monoclinic CTS. The dotted and dash-dotted lines correspond to vibrational modes attributed by Fernandes et al. [27] to cubic and tetragonal CTS respectively.

performed Raman spectroscopy on five different spots in the vicinity of the ellipsometry measurement area and plotted the average spectrum (Fig. 4). Due to the presence of the four characteristic Raman peaks of monoclinic CTS [28] and to the absence of both cubic- and tetragonal CTS peaks [27], it can be concluded that monoclinic CTS is the main phase in the deposited film.

4.2. Ellipsometry analysis

To measure the dielectric function of the Mo layer independently, we annealed a single Mo film grown on soda lime glass in the same deposition run as the investigated CTS stack. The annealing conditions were the same as those used for the CTS stack, with the exception that no sulfur was added, and that a clean quartz tube was used in the annealing furnace. Annealing the Mo film prior to ellipsometry measurement was necessary because it was observed that the dielectric function of Mo changed noticeably when annealed. The thickness of the films (500 nm) and its large absorption coefficient allows to neglect reflection at the Mo-SLG interface and only consider reflection at the Mo-air interface. Hence, the unknown parameters were the thickness of the surface roughness layer and the dielectric function of Mo. The latter was fitted using literature spectra [29] as an initial guess. The results are
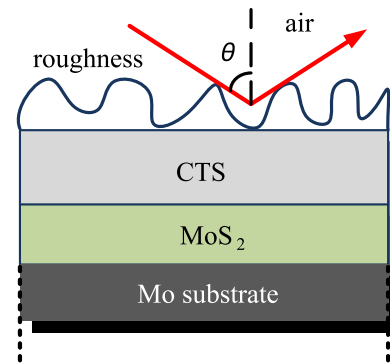

Fig. 5. Optical model used for data analysis of ellipsometry measurements on CTS. It consists of a Mo bulk substrate, a MoS₂ layer, and a CTS layer. From an optical point of view, a bulk substrate is a layer in which only the reflection from the top surface is considered. All layers are assumed to be uniform in the depth direction and without intermixing. Bruggeman's effective medium theory is employed to treat the surface roughness layer. The angle of incidence of polarized light in the measurement is labeled as θ.

shown in Fig. A.1, Appendix A. The mean square error of the fit is 2.834.

To measure the dielectric function of the MoS₂ layer, we annealed a Mo-coated glass substrate in a S atmosphere together with the CTS sample used for ellipsometry analysis. The dielectric function of Mo was treated as a known parameter, based on the previous measurement. On the other hand, the presence of the Mo–MoS₂ reflection makes it necessary to include the thickness of MoS₂ as a fitted parameter. The dielectric function of MoS₂ was fitted using literature spectra [26] as an initial guess. The mean square error of the fit is 3.362. Well-known excitonic features [30] are clearly visible in our measured dielectric function and are labeled in Fig. A.2, Appendix A. Even though single-crystal MoS₂ has an indirect band gap of about 1.2 eV [31], significant absorption occurs below the band gap energy in our film, as evident from the ε_2 spectrum in Fig. A.2, Appendix A. This has been observed before in multi-crystalline MoS₂ and has been attributed to defect absorption at surfaces [31].

Turning now to the full Mo/MoS₂/CTS layer stack of interest for this study, a relatively simple optical model was employed to fit ellipsometry data, in order to minimize the risk of obtaining artifacts in the dielectric function. The model (Fig. 5) consists of a Mo bulk substrate, a MoS₂ layer, a CTS layer and a surface roughness layer. All layers are assumed to be uniform in the depth direction and without intermixing. Cross-sectional SEM images (Fig. 2) indeed show a regular CTS surface roughness layer ($R_q = 9.5 \pm 0.5$ nm by AFM) and no clearly visible intermixing between the layers, which qualitatively justifies our assumptions. When fitting the ellipsometry spectra, the dielectric functions of both Mo and MoS₂ were treated as known parameters, based on the previous measurements. The fitted parameters were the thicknesses of the MoS₂ and CTS layers, the surface roughness layer thickness, and the dielectric function of the CTS layer. In order to increase sensitivity for the double absorption onset, the node spacing of the b-spline model of the CTS dielectric function was decreased to 0.02 eV in the 0.8–1.1 eV spectral region. The measured and fitted Ψ and Δ spectra, with a mean square error of 2.936, are shown in Fig. A.3, Appendix A. The value of the error is regarded as acceptably low. In fact, simultaneous fitting of measurements with less than six incidence angles lowers the mean square error but it also yields less robust results and increases the correlation between the estimated parameters. The fitted thickness of CTS is 92.07 ± 0.09 nm and the resulting CTS dielectric function is shown in Fig. 6. Note that two absorption onsets exist, compatible with previous reports on monoclinic CTS [1,5,6].
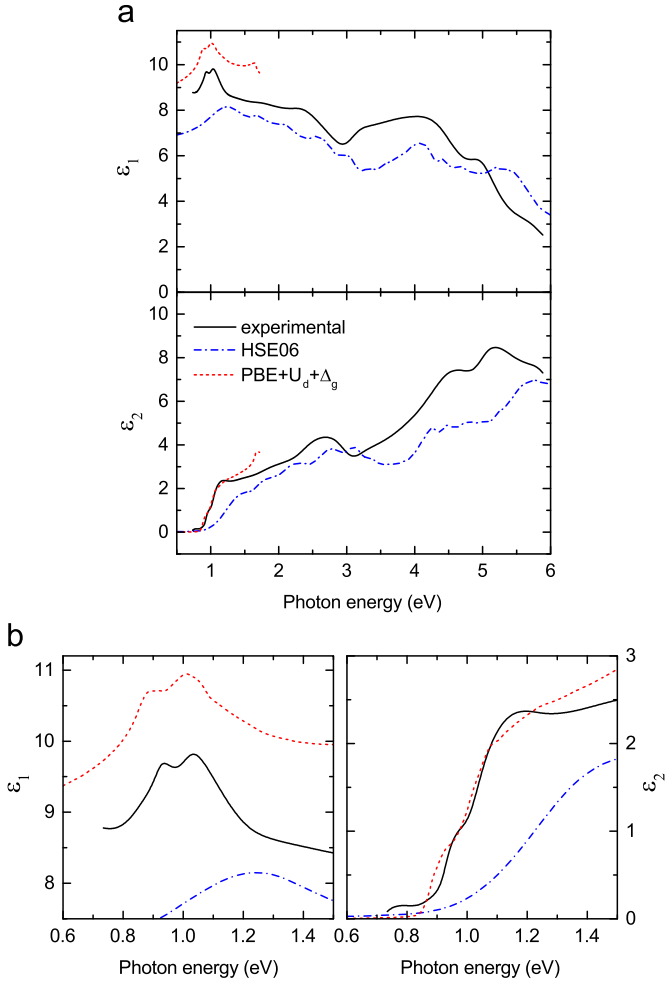
Fig. 6. (a) Real and imaginary parts of the dielectric function $\varepsilon(E) = \varepsilon_1(E) + i\varepsilon_2(E)$ for of monoclinic CTS, as determined by experimental and computational techniques. Black solid line: experimental spectra by spectroscopic ellipsometry. Blue dash-dotted line: calculated spectra with the HSE06 approach with a $5 \times 5 \times 5$ **k**−mesh ($N_k = 39$ **k**-points). Red dashed line: calculated spectra with the PBE+U$_d$+Δ_g with a denser $30 \times 30 \times 30$ **k**−mesh ($N_k = 6992$ **k**-points). (b) Detailed view of the near-band-gap spectral region. Note that the clear double absorption onset observed experimentally is revealed by computation only in the case of the denser **k**-mesh. (For interpretation of the references to color in this figure legend, the reader is referred to the web version of this article.)

The fitted value of the surface roughness layer R_e is 12.72 ± 0.03 nm. This is in good agreement with the value 14.6 nm predicted by the empirical formula $R_e \approx 1.5\,R_q + 4$ Å [15] using the value of R_q measured by AFM. Combined with the fact that our measured R_q is more than 10 times smaller than the minimum wavelength (210 nm) used in our ellipsometry measurement [13], this indicates that Bruggeman's effective medium theory is likely to be an acceptable method to treat the surface roughness layer in our analyzed sample.

Absorber layers in thin-film solar cells are normally made much thicker than our analyzed sample in order to allow full absorption of light and achieve larger crystal grains to facilitate electrical transport. However, the dielectric function is not expected to depend strongly on thickness as long as the film is crystalline [32] and the optical model employed for ellipsometry data analysis is correct [13]. In fact, throughout our experiments we observed significant distortion of the measured CTS dielectric function only for film thicknesses below 30 nm, due to partial loss of long-range order from partially amorphous structure, and above 150 nm, due to inaccurate modeling of surface roughness.

4.3. Electronic structure calculation

From the calculated electronic structure of monoclinic CTS, we observe a direct Γ-point band gap with the gap energy $E_g = 0.83$ eV. Similar theoretical results have been reported before: Zhai et al. [4] reported 0.84 eV also with the HSE functional, Shigemi et al. [11] got 0.88 eV using HSE with a larger Hartree–Fock exchange contribution, and Zawadzki et al. [9] found 0.63 eV with a beyond-DFT GW approach. Overall, these theoretical calculations [4,9–11] yield similar electronic band structure and/or density-of-states. Moreover, calculation of monoclinic Cu_2SnSe_3 by Choi et al. [33] with HSE showed improved dielectric response with a denser **k**-mesh. However, none of the earlier published works discusses any feature in the electronic structure that can explain a double onset phenomenon.

Computation of the dielectric function from HSE06 yields spectra that are overall in fairly good agreement with the experimental results in the whole energy region (Fig. 6). However, one observes that the calculated spectrum of $\varepsilon_2(E)$ has a weaker response just above the band gap energy. Also the peak at around 1.2 eV in the calculated $\varepsilon_1(E)$ spectrum is too small, too broad, and shifted to higher energies. These HSE06 calculations were done with a **k**-mesh of $K = 5 \times 5 \times 5$ (implying 39 **k**-points in the IBZ). Such **k**-mesh is commonly used, and it is usually dense enough to generate accurate total energy and an overall good electron density for semiconductors. However, in order to see details in the optical properties, a much denser mesh is needed. We therefore use the PBE+U$_d$+Δ_g method with correction of the Cu d-states and an additional constant upwards shift $\Delta_g = 0.52$ eV of the CBM to reproduce the HSE06 band gap energy. With this method we increase the **k**-mesh until the details of $\varepsilon_2(E)$ are revealed. We find an improved $\varepsilon_2(E)$ spectrum between E_g and $E_g + 0.5$ eV for a **k**-mesh of $K = 30 \times 30 \times 30$ (6992 **k**-points; red dotted line in Fig. 6). Two significant details are observed: first, the strength of the response function is much larger in this low-energy region and therefore the spectrum shows a strong absorption onset. Second, the double onset becomes visible. Both of these features are in very good agreement with the measured spectrum of $\varepsilon_2(E)$. With the improved $\varepsilon_2(E)$ spectrum for the low-energy region, also the real part of the dielectric function is improved considerably below $E_g + 0.5$ eV. The main peak in $\varepsilon_1(E)$ now has a reasonable size and
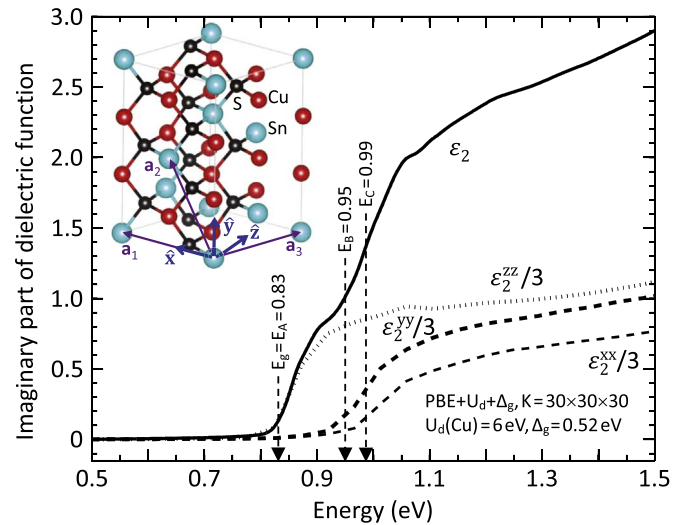

Fig. 7. Polarization dependency of the dielectric function of CTS with the PBE+U$_d$+Δ_g computational approach. The calculated dielectric response $\varepsilon_2(E)$ is very anisotropic in the near-band-gap spectral region. The primitive cell of the crystal is defined by the lattice vectors **a**$_1$, **a**$_2$, and **a**$_3$, and the orientation of the polarization is described in the Cartesian coordinate space ($\hat{\mathbf{x}}, \hat{\mathbf{y}}, \hat{\mathbf{z}}$).
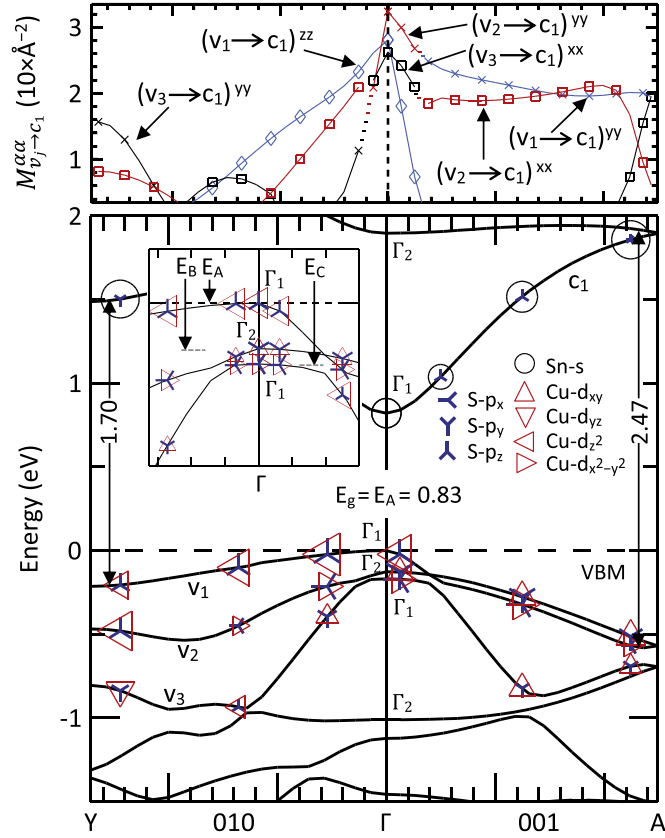
Fig. 8. Electronic band structure of monoclinic CTS along two main symmetry directions, computed with the HSE06 potential. At the Γ-point VBM, there are three close-lying valence bands (see inset figure) that contribute to the observed double absorption onset near the band gap energy. The marks indicate the main character of the energy states. The upper panel shows the optical interband matrix elements for electric dipole induced transitions. Each line color refers to a specific valence band for the transition $v_j \rightarrow c_1$, and each marker type refers to a specific polarization of the matrix element $M^{\alpha\alpha}$. Blue, red, and black lines represent transitions from the uppermost (v_1), the second uppermost (v_2), and the third uppermost (v_3) valence bands, respectively, to the lowest conduction band (c_1). Square, cross, and diamond markers represent x–, y–, and z–polarized transitions respectively. (For interpretation of the references to color in this figure legend, the reader is referred to the web version of this article.)

width, but is also correctly shifted to around 1.0 eV. Moreover, one observes that this peak is actually a double peak, which also is in agreement with the measured spectrum.

For CTS, as for similar photovoltaic materials, it is well known that the regular PBE generates zero, or almost zero, gap energy. That implies also that the band edges become somewhat distorted. The d-state correction in PBE+U is important not only to correct those orbitals but also to open the gap to 0.31 eV. Although a still too small gap energy, that is enough to describe the curvatures of the bands much better. In order to verify that the PBE+U method does not involve an incorrect model of the interaction potential, we analyze the computational method for monoclinic Cu_2SiS_3 (CSS). This compound is similar to CTS, however with a much larger gap ($E_g \approx 2.6$ eV) [34] and the regular PBE potential can therefore be used. In Fig. A.4, Appendix A, we demonstrate that both the regular PBE method and the PBE+U method generate similar dielectric response spectra $\varepsilon_2(E)$ as HSE06 for the sparse **k**-mesh of $K = 5 \times 5 \times 5$, although both methods have slightly larger responses than HSE06. Increasing the **k**-mesh improves the $\varepsilon_2(E)$ spectrum correspondingly for both PBE and PBE+U. Moreover, we find that also monoclinic CSS exhibits a double absorption onset similar to CTS.

Thus, the calculation confirms that monoclinic CTS has a strong dielectric response for photons with energies just above the gap

energy, and that the compound exhibits a double absorption onset.

5. Discussion

As demonstrated in Fig. 7, the calculation predicts that the dielectric function of monoclinic CTS is very anisotropic in the near-band gap region. In the very low energy region ($E_g \leq E < E_g + 0.15$ eV) the polarization in the z-direction is completely dominating, while for higher photon energies also the polarization in the y-direction (and partly the x-direction) contributes to the dielectric response. See Fig. 7 for definition of crystal orientation.

To explain these features, we analyze in Fig. 8 the electronic structure more in detail. One first observes the direct gap at the Γ-point. This gap energy between VBM (for band v_1) and CBM (for band c_1) is directly associated to the first absorption onset. The second and third uppermost valence bands (v_2 and v_3) have maxima also at the Γ-point, with the energies 0.12 and 0.16 eV below the VBM. These two bands are thus responsible for the second absorption onset. The three Γ-point transition energies are thus $E_A = E_g$ (equal to 0.83 eV in the HSE06 calculation), $E_B = E_g + 0.12$ eV (or 0.95 eV), and $E_C = E_g + 0.16$ eV (or 0.99 eV). One notices that the topmost valence band is very flat along the (010) direction (and also along the (100) direction; not displayed). Therefore, the absorption coefficient can be large near the gap energy, i.e., for $E_g \leq E < E_g + 0.5$ eV. The direct energy gap at the Y-point is only 1.70 eV $= E_g + 0.87$ eV, and the corresponding energy at the A-point is 2.47 eV $= E_g + 1.64$ eV. Optical transitions at these **k**-states generate the peaks in the dielectric function for energies from 1.8 to 2.5 eV. However, also **k**-states in other directions in the IBZ contribute to the spectrum in this energy range. For instance, the energy between the VBM and the second lowest conduction band is only 1.90 eV at the Γ-point.

The energy state at the CBM has the irreducible representation Γ_1 of C_2 point group. Also the VBM energy state has Γ_1 symmetry. The irreducible representations describe the allowed polarization of the allowed electric dipole induced transitions for that **k**-state. The lowest conduction band has a strong contribution of Sn s-like character. The conduction band contains also S p_y-like (S p_z-like) character along the (010) direction ((001) direction). Furthermore, the uppermost valence band has primarily Cu d_{z^2}-like and S p_z-like character. This explains the strong and in-plane z-polarized dielectric response related to the first absorption onset. The second uppermost valence band has Γ_2 symmetry at its maximum with primarily Cu d_{xy}-like and S p_y-like character, while the third band has Γ_1 symmetry at its maximum with primarily Cu $d_{x^2-y^2}$-like and S p_x-like character. Transitions from these two valence bands yield the pronounced x- and y-polarized dielectric response. Of the three topmost bands it is the third band that has most Sn s-like character away from the Γ-point, but the contribution is small (not displayed). Noticeably, along the (001) direction, the topmost valence bands (with Γ_1 symmetry at the VBM) and second valence band (with Γ_2 symmetry) cross about 18% away from the Γ-point, while the third band (with Γ_1 symmetry) "interacts" and bends downwards. At the cross-over point, the characters of the valence bands change symmetry, an effect which is typical for these types of band-band interactions.

The characters of the valence band states explain the optical transitions. In the top panel in Fig. 8, we present the optical matrix elements $M^{\alpha\alpha}_{v_j \rightarrow c_1} = |\langle \psi_{k_{c_1}} | \hat{p}_\alpha \psi_{k_{v_j}} \rangle|^2$, describing probability for optical transitions from the valence band v_j to the conduction band c_1. Note that here v_1 is the topmost valence state for each **k**-point, whether or not bands cross along the symmetry lines. One observes that close to the Γ-point the transitions from the
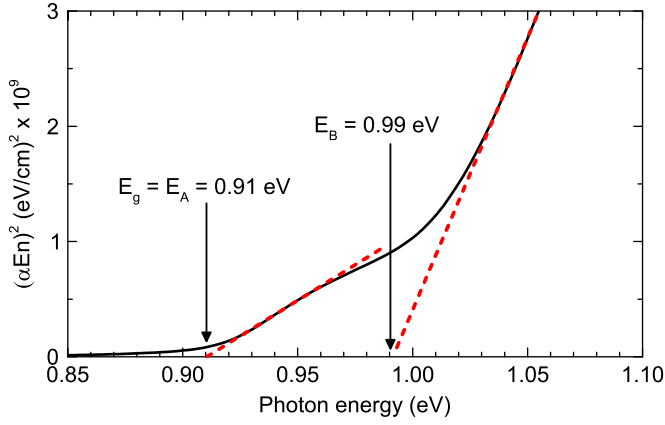
Fig. 9. $(\alpha En)^2$ versus E plot for monoclinic CTS, where the distance between the initial and final state of the two optical transitions responsible for the double absorption onset can be estimated from the linear regions of the plots. The absorption coefficient α and the refractive index n are derived from the experimentally determined dielectric function of monoclinic CTS.

Fig. 11. Absorption coefficient of different chalcogenide absorbers in the spectral region of most interest for solar cells. CTS: derived from the dielectric function measured in this work; CdTe: taken from Li et al. [36]; CIGS ($CuIn_{0.62}Ga_{0.38}Se_2$): taken from Minoura et al. [24]; CZTS (Cu_2SnZnS_4): taken from Li et al. [25]; CZTSe ($Cu_2SnZnSe_4$), taken from Choi et al. [37]. The absorption onset in CTS is relatively sharp and with a high intensity, even when compared to CZTSe, which has a similar band gap.
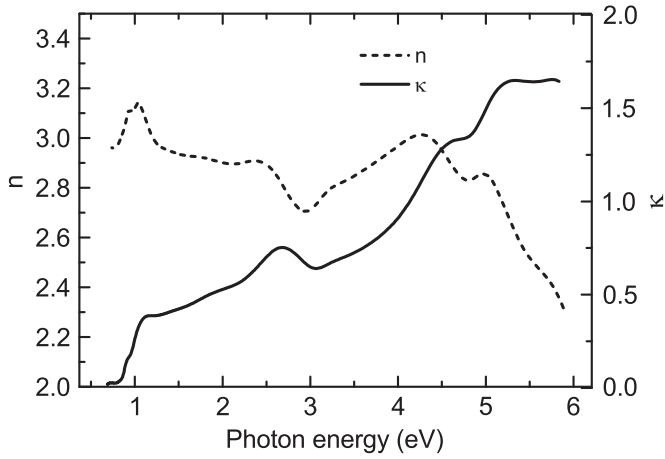

Fig. 10. Refractive index n and extinction coefficient κ for monoclinic CTS, derived by the experimental dielectric function spectra obtained by spectroscopic ellipsometry. The refractive index exhibits relatively low dispersion in the visible region of light.

topmost valence band (blue lines) have mainly $M^{zz}_{v_1 \to c_1}$ contribution. The other terms in the optical matrix are less than 0.03, and therefore not presented in the figure. Transitions from the second valence band (red lines) have mainly $M^{yy}_{v_2 \to c_1}$ contribution, while transitions from the third valence band (black lines) have mainly $M^{xx}_{v_3 \to c_1}$ contribution. It is also clear how the character of the band states affects the contribution of $M^{\alpha\alpha}_{v_j \to c_1}$ when a band crosses or interacts with another band. The character of the bands, and the corresponding optical matrix elements, are the origin of the anisotropy of the dielectric function $\varepsilon_2(E)$ spectrum, and it also may explain why the double onset phenomenon is so pronounced in monoclinic CTS.

Unfortunately, the strong polarization dependence of the calculated dielectric response of monoclinic CTS cannot be cross-checked experimentally in this work. The reason is that the crystal grains in our CTS film are not oriented along a single lattice direction, as is evident by the number of different peaks observed in the XRD pattern in Fig. 3. A spectroscopic ellipsometry measurement on a (001) surface in monoclinic CTS is needed to observe experimentally the polarization-dependent absorption onset.

Nevertheless, the shape of the dielectric function, the energy of the first absorption onset and the energy separation of the two onsets can be compared between experiment and theory.
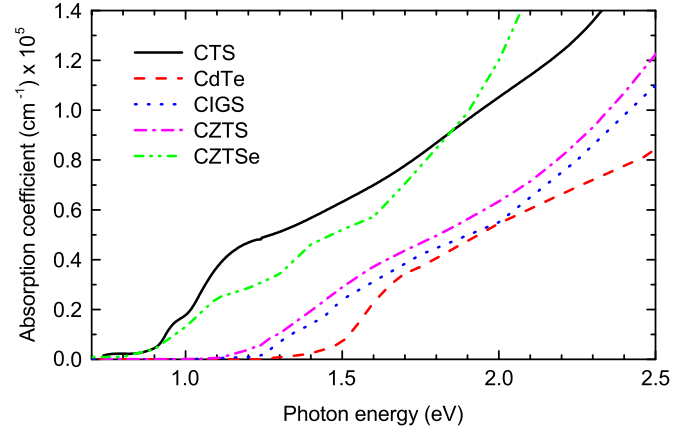
In general, the band gap of a crystalline direct semiconductor can be estimated experimentally by extrapolation of the linear region above the absorption onset in an $(\alpha En)^2$ versus E plot, where α and n are the absorption coefficient and refractive index of the material, and E is the photon energy [35]. Often, $(\alpha E)^2$ plots are used for this purpose in unpolarized transmission and reflection measurements because n is not easily derived from the measurement. However, it has been shown that band gap estimation can be difficult if n is omitted in the plot [29]. In the case of an ellipsometry measurement, α and n can be readily extracted from the measured dielectric function of CTS by employing the standard relations $\varepsilon_1 = n^2 - \kappa^2$, $\varepsilon_2 = 2n\kappa$, and $\alpha = 4\pi\kappa E/hc$, where κ is the extinction coefficient, h is Planck's constant and c is the speed of light in vacuum. Then, the distance between the initial and final state of the two direct transitions involved in the double onset can be estimated. This method yields $E_A = E_g = 0.91 \pm 0.01$ eV for the first onset and $E_B = 0.99 \pm 0.01$ eV for the second onset in monoclinic CTS (Fig. 9). The energy difference between the two onsets is therefore 0.12 eV by theory and 0.08 eV ± 0.01 eV by experiment. Then, the double-onset phenomenon observed experimentally can indeed be explained as caused by optical transitions from the three topmost bands at the VBM in a perfectly crystalline monoclinic CTS. The phenomenon does thus not need to be due to structural imperfections, like inclusion of disordered structures or secondary phases.

As for the energy of the first absorption onset, the HSE06 calculation predicts $E_A = E_g = 0.83$ eV, whereas the measurement yields $E_A = E_g = 0.91 \pm 0.1$ eV. It must be emphasized that the calculated value is obtained from the single-particle energies at the band edges, and one shall not expect that this Kohn–Sham gap energy be exactly equal to the true fundamental band gap energy. From similar calculations of CIGS and CZTS [19,20] we expect the HSE06 method to underestimate the actual band gap energy by about 0.1–0.2 eV.

Regarding the shape of the dielectric function, it shall be emphasized that only with a fine **k**-point sampling the shapes of both the real and imaginary parts of the computed dielectric function are improved considerably in the low energy region (i.e, for photon energies between 0 and $E_g + 1.5$ eV). Considering this, the computed dielectric response spectra are in good agreement with the experimental spectra from monoclinic CTS in the whole energy region from 0.7 to 5.9 eV. Based on the experimental spectra, the refractive index n of monoclinic CTS is between

2.7 and 3.2 over a broad spectral region, from below the band gap to about 5 eV (Fig. 10). Finally, we note that the absorption coefficient of monoclinic CTS is quite large in the spectral region of large solar irradiance (roughly 1.0–2.5 eV), when compared to the widely investigated chalcogenide thin film absorbers for photovoltaics CIGS, CdTe, and CZTS (Fig. 11). In particular, the near-band gap region between 1.0 and 1.5 eV features very strong absorption due to the contributions from multiple optical transitions, even when compared to similar low band gap materials such as CZTSe. This has two beneficial consequences: (1) the absorber layer can be thinner, resulting in lower material consumption, and (2) charge carriers are, on the average, generated closer to the p–n junction, where the collection probability is high. These features, together with the relatively low band gap, make CTS a promising candidate as a bottom absorber in tandem solar cells.

6. Conclusion

We have experimentally determined the dielectric function of monoclinic CTS by spectroscopic ellipsometry from 0.7 to 5.9 eV. An experimental procedure has been proposed to overcome the challenges of extracting the dielectric function of a CTS thin film grown on a glass/Mo substrate. This involves separate measurement of the dielectric function of each layer in the stack, and careful initialization of the unknown parameters in the data fitting step using the results from other measurement techniques. The experimental dielectric function has been compared to that obtained by computation using DFT with a satisfactory agreement also at a quantitative level. The calculation has confirmed a double absorption onset at 0.9–1.0 eV, which originates from direct optical transitions at the Γ-point from three energetically closely-spaced valence bands to a single conduction band in perfectly crystalline monoclinic CTS bulk. Thus, the phenomenon does not need to be due to structural imperfections, like inclusion of disordered structure or secondary phases. Importantly, the double onset can only be predicted in the case of using a dense **k**-mesh. We therefore use the PBE+U approach (with dense **k**-mesh, to reveal details in the dielectric function spectra) combined with the HSE06 hybrid functional (for better description of the overall spectra) to describe the optical properties. The calculation predicts that the response function of CTS is very polarization dependent near the band gap energy, and this will help future optical analysis of monocrystalline CTS samples. Finally, we note that the absorption coefficient of monoclinic CTS is particularly large in the near-band-gap region between 1.0 and 1.5 eV. This makes CTS an interesting option as a bottom absorber in tandem solar cells.

Acknowledgments

Appendix A. Supplementary figures

Supplementary data associated with this article can be found in the online version at http://dx.doi.org/10.1016/j.solmat.2016.04.028.

References

[1] M. Nakashima, J. Fujimoto, T. Yamaguchi, M. Izaki, Cu$_2$SnS$_3$ thin-film solar cells fabricated by sulfurization from NaF/Cu/Sn stacked precursor, Appl. Phys. Express 8 (4) (2015) 042303, http://dx.doi.org/10.7567/APEX.8.042303.

[2] A. Kanai, K. Toyonaga, K. Chino, H. Katagiri, H. Araki, Fabrication of Cu$_2$SnS$_3$ thin-film solar cells with power conversion efficiency of over 4%, Jpn. J. Appl. Phys. 54 (8S1) (2015) 08KC06, http://dx.doi.org/10.7567/JJAP.54.08KC06.

[3] L.L. Baranowski, P. Zawadzki, S. Christensen, D. Nordlund, S. Lany, A.C. Tamboli, L. Gedvilas, D.S. Ginley, W. Tumas, E.S. Toberer, A. Zakutayev, Control of doping in Cu$_2$SnS$_3$ through defects and alloying, Chem. Mater. 26 (17) (2014) 4951–4959, http://dx.doi.org/10.1021/cm501339v.

[4] Y.-T. Zhai, S. Chen, J.-H. Yang, H.-J. Xiang, X.-G. Gong, A. Walsh, J. Kang, S.-H. Wei, Structural diversity and electronic properties of Cu$_2$SnX$_3$ (X=S, Se): a first-principles investigation, Phys. Rev. B 84 (7) (2011) 075213, http://dx.doi.org/10.1103/PhysRevB.84.075213.

[5] N. Aihara, A. Kanai, K. Kimura, M. Yamada, K. Toyonaga, H. Araki, A. Takeuchi, H. Katagiri, Sulfurization temperature dependences of photovoltaic properties in Cu$_2$SnS$_3$-based thin-film solar cells, Jpn. J. Appl. Phys. 53 (5S1) (2014) 05FW13, http://dx.doi.org/10.7567/JJAP.53.05FW13.

[6] D.M. Berg, R. Djemour, L. Gütay, G. Zoppi, S. Siebentritt, P.J. Dale, Thin film solar cells based on the ternary compound Cu$_2$SnS$_3$, Thin Solid Films 520 (19) (2012) 6291–6294, http://dx.doi.org/10.1016/j.tsf.2012.05.085.

[7] J. de Wild, E.V.C. Robert, B. El Adib, P.J. Dale, Optical characterization of solution prepared Cu$_2$SnS$_3$ for photovoltaic applications, MRS Proc. (2015), http://dx.doi.org/10.1557/opl.2015.624, mrss15–2135683.

[8] L.L. Baranowski, K. McLaughlin, P. Zawadzki, S. Lany, A. Norman, H. Hempel, R. Eichberger, T. Unold, E.S. Toberer, A. Zakutayev, Effects of disorder on carrier transport in Cu$_2$SnS$_3$, arXiv:1504.01327.

[9] P. Zawadzki, L.L. Baranowski, H. Peng, E.S. Toberer, D.S. Ginley, W. Tumas, A. Zakutayev, S. Lany, Evaluation of photovoltaic materials within the Cu–Sn–S family, Appl. Phys. Lett. 103 (25) (2013) 253902, http://dx.doi.org/10.1063/1.4851896.

[10] L. Xi, Y.B. Zhang, X.Y. Shi, J. Yang, X. Shi, L.D. Chen, W. Zhang, J. Yang, D.J. Singh, Chemical bonding, conductive network, and thermoelectric performance of the ternary semiconductors Cu$_2$SnX$_3$ (X=Se, S) from first principles, Phys. Rev. B 86 (15) (2012) 155201, http://dx.doi.org/10.1103/PhysRevB.86.155201.

[11] A. Shigemi, T. Maeda, T. Wada, First-principles calculation of Cu$_2$SnS$_3$ and related compounds, Phys. Status Solidi (B) 252 (6) (2015) 1230–1234, http://dx.doi.org/10.1002/pssb.201400346.

[12] D. Tiwari, T.K. Chaudhuri, T. Shripathi, U. Deshpande, V.G. Sathe, Structural and optical properties of layer-by-layer solution deposited Cu$_2$SnS$_3$ films, J. Mater. Sci. Mater. Electron. 25 (9) (2014) 3687–3694, http://dx.doi.org/10.1007/s10854–014–2076–y.

[13] H. Fujiwara, Spectroscopic Ellipsometry – Principles and Applications, Wiley, 2007, (Chapter 5).

[14] A. Crovetto, A. Cazzaniga, R.B. Ettlinger, J. Schou, O. Hansen, Optical properties and surface characterization of pulsed laser-deposited Cu$_2$ZnSnS$_4$ by spectroscopic ellipsometry, Thin Solid Films 582 (2015) 203–207, http://dx.doi.org/10.1016/j.tsf.2014.11.075.

[15] J. Koh, Y. Lu, C.R. Wronski, Y. Kuang, R.W. Collins, T.T. Tsong, Y.E. Strausser, Correlation of real time spectroellipsometry and atomic force microscopy measurements of surface roughness on amorphous semiconductor thin films, Appl. Phys. Lett. 69 (9) (1996) 1297, http://dx.doi.org/10.1063/1.117397.

[16] G. Kresse, D. Joubert, From ultrasoft pseudopotentials to the projector augmented-wave method, Phys. Rev. B 59 (3) (1999) 1758–1775, http://dx.doi.org/10.1103/PhysRevB.59.1758.

[17] G. Kresse, J. Furthmüller, Efficient iterative schemes for ab initio total-energy calculations using a plane-wave basis set, Phys. Rev. B 54 (16) (1996) 11169–11186, http://dx.doi.org/10.1103/PhysRevB.54.11169.

[18] J. Heyd, G.E. Scuseria, M. Ernzerhof, Hybrid functionals based on a screened Coulomb potential, J. Chem. Phys. 118 (18) (2003) 8207, http://dx.doi.org/10.1063/1.1564060.

[19] L.E. Oikkonen, M.G. Ganchenkova, A.P. Seitsonen, R.M. Nieminen, Vacancies in CuInSe$_2$ new insights from hybrid-functional calculations, J. Phys. Condens. Matter 23 (42) (2011) 422202, http://dx.doi.org/10.1088/0953–8984/23/42/422202.

[20] H. Zhao, C. Persson, Optical properties of Cu(In, Ga)Se$_2$ and Cu$_2$ZnSn(S,Se)$_4$, Thin Solid Films 519 (21) (2011) 7508–7512.

[21] J.P. Perdew, K. Burke, M. Ernzerhof, Generalized gradient approximation made simple, Phys. Rev. Lett. 77 (18) (1996) 3865–3868, http://dx.doi.org/10.1103/PhysRevLett.77.3865.

[22] V.I. Anisimov, J. Zaanen, O.K. Andersen, Band theory and Mott insulators Hubbard U instead of Stoner I, Phys. Rev. B 44 (3) (1991) 943–954, http://dx.doi.org/10.1103/PhysRevB.44.943.

[23] C. Persson, C. Dong, L. Vayssieres, A. Augustsson, T. Schmitt, M. Mattesini, R. Ahuja, J. Nordgren, C. Chang, A. Ferreira da Silva, J.-H. Guo, X-ray absorption and emission spectroscopy of ZnO nanoparticle and highly oriented ZnO microrod arrays, Microelectron. J. 37 (8) (2006) 686–689, http://dx.doi.org/10.1016/j.mejo.2005.12.009.

[24] S. Minoura, K. Kodera, T. Maekawa, K. Miyazaki, S. Niki, H. Fujiwara, Dielectric function of Cu(In, Ga)Se$_2$-based polycrystalline materials, J. Appl. Phys. 113 (6) (2013) 063505, http://dx.doi.org/10.1063/1.4790174.

[25] J. Li, H. Du, J. Yarbrough, A. Norman, K. Jones, G. Teeter, F.L. Terry, D. Levi, Spectral optical properties of Cu$_2$ZnSnS$_4$ thin film between 0.73 and 6.5 eV, Opt. Express 20 (102) (2012) A327–A332, http://dx.doi.org/10.1364/OE.20.00A327.

[26] C. Yim, M. O'Brien, N. McEvoy, S. Winters, I. Mirza, J.G. Lunney, G.S. Duesberg, Investigation of the optical properties of MoS$_2$ thin films using spectroscopic ellipsometry, Appl. Phys. Lett. 104 (10) (2014) 103114, http://dx.doi.org/10.1063/1.4868108.

[27] P.A. Fernandes, P.M.P. Salomé, A.F. da Cunha, Cu$_x$SnS$_{x+1}$(x = 2, 3) thin films grown by sulfurization of metallic precursors deposited by dc magnetron sputtering, Phys. Status Solidi (C) 7 (2010) 901–904, http://dx.doi.org/10.1002/pssc.200982746.

[28] D.M. Berg, R. Djemour, L. Gütay, S. Siebentritt, P.J. Dale, X. Fontane, V. Izquierdo-Roca, A. Pérez-Rodriguez, Raman analysis of monoclinic Cu$_2$SnS$_3$ thin films, Appl. Phys. Lett. 100 (19) (2012) 192103, http://dx.doi.org/10.1063/1.4712623.

[29] S. Marsillac, N. Barreau, H. Khatri, J. Li, D. Sainju, A. Parikh, N.J. Podraza, R.W. Collins, Spectroscopic ellipsometry studies of In$_2$S$_3$ top window and Mo back contacts in chalcopyrite photovoltaics technology, Phys. Status Solidi (C) 5 (5) (2008) 1244–1248, http://dx.doi.org/10.1002/pssc.200777889.

[30] R.A. Neville, B.L. Evans, The band edge excitons in 2H-MoS$_2$, Phys. Status Solidi (B) 73 (2) (1976) 597–606, http://dx.doi.org/10.1002/pssb.2220730227.

[31] C.B. Roxlo, R.R. Chianelli, H.W. Deckman, A.F. Ruppert, P.P. Wong, Bulk and surface optical absorption in molybdenum disulfide, J. Vac. Sci. Technol. A Vac. Surf. Films 5 (4) (1987) 555, http://dx.doi.org/10.1116/1.574671.

[32] J. Tauc, R. Grigorovici, A. Vancu, Optical properties and electronic structure of amorphous germanium, Phys. Status Solidi (B) 15 (2) (1966) 627–637, http://dx.doi.org/10.1002/pssb.19660150224.

[33] S.G. Choi, J. Kang, J. Li, H. Haneef, N.J. Podraza, C. Beall, S.-H. Wei, S.T. Christensen, I.L. Repins, Optical function spectra and bandgap energy of Cu$_2$SnSe$_3$, Appl. Phys. Lett. 106 (4) (2015) 043902, http://dx.doi.org/10.1063/1.4907202.

[34] K. Toyonaga, H. Araki, Preparation and characterization of Cu$_2$Si$_x$Sn$_{1-x}$S$_3$, Physica Status Solidi (C) 12 (6) (2015) 753–756, http://dx.doi.org/10.1002/pssc.201400296.

[35] F. Stern, Elementary theory of the optical properties of solids, Solid State Phys. 15 (1963) 299–408.

[36] J. Li, J. Chen, M.N. Sestak, C. Thornberry, R.W. Collins, Spectroscopic ellipsometry studies of thin film CdTe and CdS: from dielectric functions to solar cell structures, in: Proceedings of the 2009 34th IEEE Photovoltaic Specialists Conference (PVSC), IEEE, 2009, pp. 001982–001987, http://dx.doi.org/10.1109/PVSC.2009.5411520.

[37] S.G. Choi, H.Y. Zhao, C. Persson, C.L. Perkins, A.L. Donohue, B. To, A.G. Norman, J. Li, I.L. Repins, Dielectric function spectra and critical-point energies of Cu$_2$ZnSnSe$_4$ from 0.5 to 9.0 eV, J. Appl. Phys. 111 (3) (2012) 033506, http://dx.doi.org/10.1063/1.3681814.

Dielectric function and double absorption onset of monoclinic Cu$_2$SnS$_3$: Origin of experimental features explained by first-principles calculations

Andrea Crovetto[a,*], Rongzhen Chen[b], Rebecca Bolt Ettlinger[c], Andrea Carlo Cazzaniga[c], Jørgen Schou[c], Clas Persson[b,d], Ole Hansen[a,e,**]

[a]*DTU Nanotech, Technical University of Denmark, DK-2800 Kgs. Lyngby, Denmark*
[b]*Department of Materials Science and Engineering, Royal Institute of Technology, SE-100 44 Stockholm, Sweden*
[c]*DTU Fotonik, Technical University of Denmark, DK-4000 Roskilde, Denmark*
[d]*Department of Physics, University of Oslo, PO Box 1048 Blindern, NO-0316 Oslo, Norway*
[e]*CINF, Center for Individual Nanoparticle Functionality, Technical University of Denmark, Technical University of Denmark, DK-2800 Kgs. Lyngby, Denmark*

Abstract

In this work, we determine experimentally the dielectric function of monoclinic Cu$_2$SnS$_3$ (CTS) by spectroscopic ellipsometry from 0.7 to 5.9 eV. An experimental approach is proposed to overcome the challenges of extracting the dielectric function of Cu$_2$SnS$_3$ when grown on a glass/Mo substrate, as relevant for photovoltaic applications. The ellipsometry measurement reveals a double absorption onset at 0.91 eV and 0.99 eV. Importantly, we demonstrate that calculation within the density functional theory (DFT) confirms this double onset only when a very dense **k**-mesh is used to reveal fine details in the electronic structure, and this can explain why it has not been reported in earlier calculated spectra. We can now show that the double onset originates from optical transitions at the Γ-point from three energetically close-lying valence bands to a single conduction band. Thus, structural imperfection, like secondary phases, is not needed to explain such an absorption spectrum. Finally, we show that the absorption coefficient of CTS is particularly large in the near-band gap spectral region when compared to similar photovoltaic materials.

Keywords:
CTS, Cu$_2$SnS$_3$, optical properties, band gap, ellipsometry

Appendix A. Supplementary figures

Figure A.1: Real and imaginary parts of the dielectric function $\varepsilon(E) = \varepsilon_1(E) + i\varepsilon_2(E)$ of the Mo layer from spectroscopic ellipsometry. The analyzed sample is a Mo film on glass after a 570°C anneal in N$_2$ without sulfur addition.
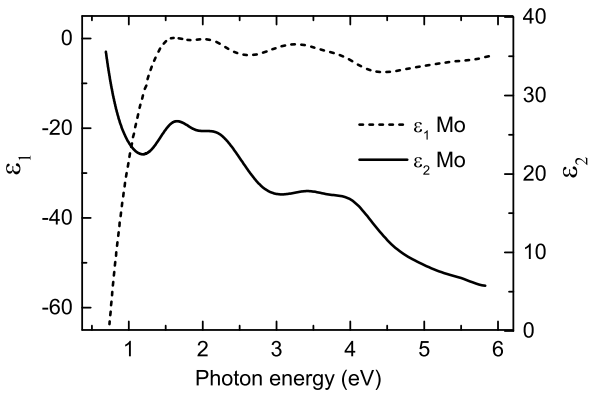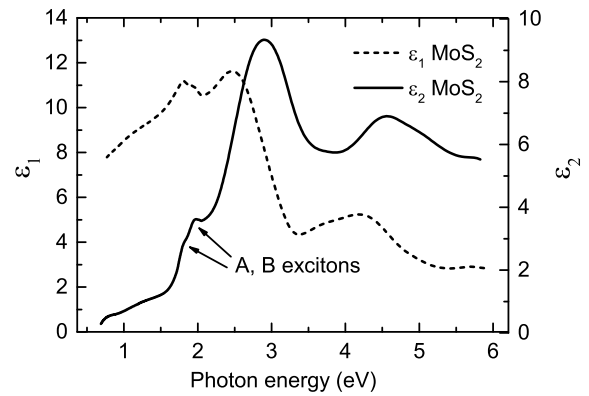

Figure A.2: Real and imaginary parts of the dielectric function $\varepsilon(E) = \varepsilon_1(E) + i\varepsilon_2(E)$ of the MoS$_2$ layer from spectroscopic ellipsometry. The analyzed sample is a Mo film on glass after a 570°C anneal in N$_2$ with 200 mg of sulfur, resulting in the formation of a MoS$_2$ layer at the surface, with a thickness of about 70 nm. Weak excitonic features, arising from direct d-d transitions split by spin-orbit interaction, are resolved and labeled A and B as in previous works (reference [30] in the main article).

*Corresponding author, email: ancro@nanotech.dtu.dk, Ørsteds Plads, building 345 East, DK-2800 Kgs. Lyngby, Denmark, Tel.: +45 4525845

**Principal corresponding author, email: ole.hansen@nanotech.dtu.dk, Ørsteds Plads, building 345 East, DK-2800 Kgs. Lyngby, Denmark, Tel.: +45 4525715
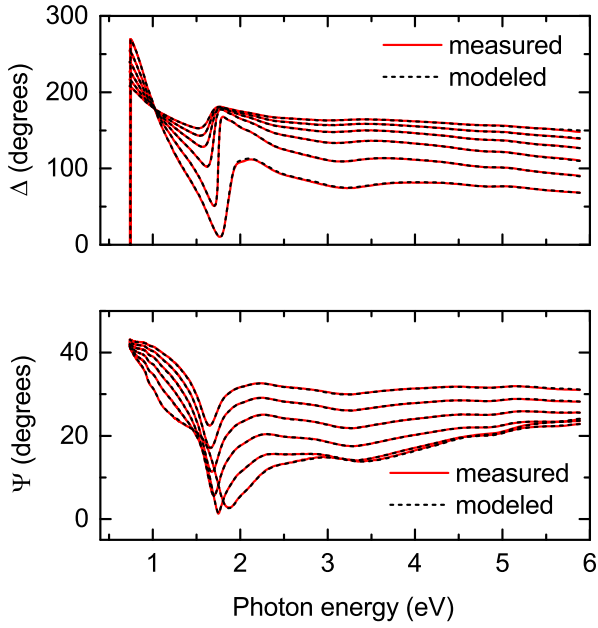
Figure A.3: Spectral magnitude $\Psi(E)$ and phase $\Delta(E)$ of the ratio between p- and s- type polarization reflection coefficients, measured on the glass/Mo/MoS$_2$/CTS stack by spectroscopic ellipsometry. For both $\Psi(E)$ and $\Delta(E)$, the measured and modeled spectra are shown at six angles of incidence, between 45° and 70°.
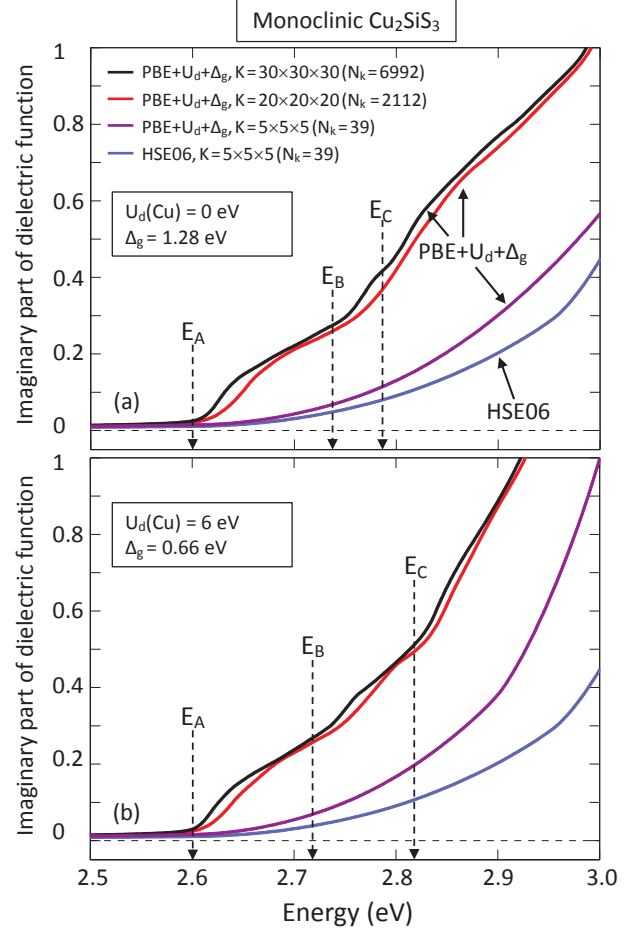

Figure A.4: The imaginary part ε_2 of the dielectric function for monoclinic Cu$_2$SiS$_3$ with the HSE06 and PBE+U$_d$+Δ_g computational approaches. All spectra has the onset at $E_g = E_A = 2.60$ eV, determined from a HSE06 calculation. First, we demonstrate that the PBE+Δ_g [i.e., with no onsite Coulomb potential, thus U_d(Cu)= 0 eV; see (a)] generates qualitatively the same near-gap spectra as PBE+U$_d$+Δ_g [with U_d(Cu)= 6 eV; see (b)] near the band-edge energy. Second, with a sparse $5 \times 5 \times 5$ k-mesh (implying $N_k = 39$ k-points in the IBZ) both HSE06 (light blue lines) and PBE+U$_d$+Δ_g (purple lines) show qualitatively the same spectra with no indication of a double onset near E_g. Third, with a denser $20 \times 20 \times 20$ k-mesh (2121 k-points; red lines) and $30 \times 30 \times 30$ k-mesh (6992 k-points; black lines) the double onset is clear, and one actually observes the contributions from the three transitions $E_A = 2.60$ eV, $E_B = 2.76$ eV, and $E_C = 2.83$ eV; compare with Fig. 7 in the main article.

2

125

Formation of copper tin sulfide films by pulsed laser deposition at 248 and 355 nm

Rebecca Bolt Ettlinger[1] · Andrea Crovetto[2] · Stela Canulescu[1] · Andrea Cazzaniga[1] ·
Lasse Ravnkilde[2] · Tomas Youngman[2] · Ole Hansen[2] · Nini Pryds[3] ·
Jørgen Schou[1]

Abstract The influence of the laser wavelength on the deposition of copper tin sulfide (CTS) and SnS-rich CTS with a 248-nm KrF excimer laser (pulse length $\tau = 20$ ns) and a 355-nm frequency-tripled Nd:YAG laser ($\tau = 6$ ns) was investigated. A comparative study of the two UV wavelengths shows that the CTS film growth rate per pulse was three to four times lower with the 248-nm laser than the 355-nm laser. SnS-rich CTS is more efficiently ablated than pure CTS. Films deposited at high fluence have submicron and micrometer size droplets, and the size and area density of the droplets do not vary significantly from 248 to 355 nm deposition. Irradiation at low fluence resulted in a non-stoichiometric material transfer with significant Cu deficiency in the as-deposited films. We discuss the transition from a non-stoichiometric material transfer at low fluence to a nearly stoichiometric ablation at high fluence based on a transition from a dominant evaporation regime to an ablation regime.

1 Introduction

Research in thin-film solar cells based on p-type semiconductors has mainly been focused on Cu(In,Ga)(S,Se)$_2$ (CIGS) and CdTe. However, due to the limited availability of elements such as In and Te and the toxicity of Cd, alternative absorbers such as Cu$_2$ZnSnS$_4$ (CZTS) are being investigated [1], and recently, a thin-film solar cell based on a CZTS absorber layer has reached an efficiency of 8.8 % [2]. Other p-type semiconductors with fewer elements are also available, including members of the ternary Cu–Sn–S system [3]. Among the Cu–Sn–S compounds, Cu$_2$SnS$_3$ (CTS) has been suggested as potential solar cell absorber because it has an absorption coefficient comparable to CZTS and a band gap of 0.9–1.35 eV depending on the crystal structure [4–6]. The highest efficiency of CTS solar cells of 4.65 % was achieved by thermal evaporation [7]. CTS thin films have also, more recently, been fabricated by pulsed laser deposition (PLD) [8]. Vanalakar

✉ Rebecca Bolt Ettlinger
reet@fotonik.dtu.dk

Andrea Crovetto
ancro@nanotech.dtu.dk

Stela Canulescu
stec@fotonik.dtu.dk

Andrea Cazzaniga
andcan@fotonik.dtu.dk

Lasse Ravnkilde
s122729@student.dtu.dk

Tomas Youngman
s123603@student.dtu.dk

Ole Hansen
ole.hansen@nanotech.dtu.dk

Nini Pryds
nipr@dtu.dk

Jørgen Schou
josc@fotonik.dtu.dk

[1] DTU Fotonik, Technical University of Denmark, Frederiksborgvej 399, 4000 Roskilde, Denmark

[2] DTU Nanotech, Technical University of Denmark, 2800 Kgs. Lyngby, Denmark

[3] DTU Energy, Technical University of Denmark, 4000 Roskilde, Denmark

🖄 Springer

et al. [9] have reported on the first CTS solar cell prepared by pulsed laser deposition with an efficiency of 0.82 %.

PLD is a suitable technique for the deposition of films with complex structures [10]. The presence of droplets (in some papers called particulates) in the growing films is a well-known problem, which can be addressed in a number of ways [11]. Particularly, droplets up to 1 micron in diameter or larger were observed in the films of CTS deposited by PLD [8, 9]. The influence of droplets on the overall efficiency of the solar cell is not well understood, but it is clear that it can be detrimental for the cell performance for the following reasons: (1) The droplet size can be larger than the overall thickness of the absorber layer, resulting in a rough interface and possible shunt paths between the CTS film and the subsequent solar cell layers [12], and (2) the droplets can have a different composition than the matrix of the CTS film [13, 14], resulting in non-homogeneity in composition and therefore different charge carrier transport properties.

Round droplets of micrometer or submicrometer size result from solidification of molten droplets ejected from the target by laser-induced recoil pressure or subsurface boiling [11]. A common approach to minimize droplets is to reduce the irradiation wavelength, as previously reported for Si [15], ZnO [16], and YBa$_2$Cu$_3$O$_{7-x}$ (YBCO) [17, 18] with comparisons of PLD using IR, visible, and UV laser wavelengths. Several mechanisms have been proposed to explain the better morphology of films deposited at UV wavelengths. First, the absorption depth (α^{-1}) in the material is usually short at UV wavelengths, resulting in a thin layer being ablated and thus formation of a hot plasma plume [17]. Second, if the absorption does not vary significantly with irradiation wavelength, droplet minimization may result from absorption of UV light by the droplets in the near-surface region, resulting in fragmentation down to a very small size. The second mechanism may be more dominant when comparing the morphology of films deposited at different UV wavelengths [17].

Apart from changing the laser wavelength, it is also known that a reduction in fluence can lead to a reduction in droplet area density and size [19]. A reduction in droplet density and size with a reduction of the fluence from 1.5 to 0.7 J/cm^2 has been seen in PLD of CZTS with a 248-nm laser by Moriya et al. [20] and with a reduction in fluence from 4 to 0.5 J/cm^2 on CZTS using a 355-nm laser by Sulaiman et al. [13]. Pawar et al. [21] also observed smaller and fewer droplets at 1 J/cm^2 than at 1.5 and 2 J/cm^2 using a 248-nm laser with CZTS. Similarly, Ujimoto et al. [22] observed a reduction in droplet density from 1.5 to 0.5 J/cm^2 using a 193-nm excimer laser to deposit BiFeO$_3$, while noting that in their case droplets could not be completely avoided simply by decreasing laser fluence.

The aim of this paper is to examine the influence of two different UV laser wavelengths on the deposition rate and the size, density, and composition of the droplets in films deposited by PLD from targets of CTS and SnS-enriched CTS. The SnS-rich composition was chosen for comparison because deficiency of Sn and S had previously been observed in CTS films deposited with 355-nm laser irradiation [8].

2 Materials and methods

2.1 Pulsed laser deposition

Pulsed laser deposition was carried out using a Nd:YAG laser operating at 355 nm (third harmonic) with a pulse duration of 5–7 ns and a KrF excimer laser operating at 248 nm with a pulse duration of 20 ns (see Fig. 1; Table 1). The depositions were made in vacuum at a pressure of 1–5 × 10^{-6} mbar. The target was placed at an angle of 45° with respect to the incoming laser beam, and the beam was rastered across the target. The substrate material was Mo-coated soda-lime glass, which is typically used for CTS solar cell preparation. The fluence was varied from 0.2 to 2.3 J/cm^2 and was calculated based on a measurement of the spot size on a Cu foil. The substrate–target distance was 4–4.5 cm due to constraints in the setups for ensuring similar deposition conditions. Films made using the 355 nm laser with target–substrate distances ranging from 4 cm to 7.5 cm were similar in composition and droplet density (not shown), as expected for depositions made in vacuum [19].

Single samples were made at different fluence values and spot sizes. The representativeness of the single samples was verified by repeated depositions of some of the films under identical circumstances. With the 355-nm laser and
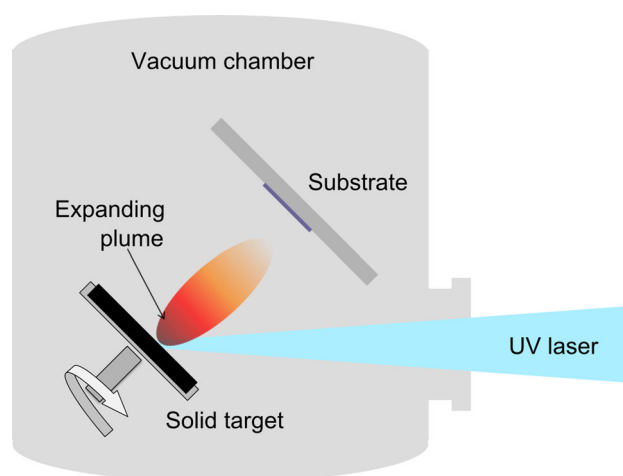

Fig. 1 Setup. See Table 1 for comparison of the 248 and 355 nm setups

Table 1 Laser and setup comparison

Wavelength (λ)	248 nm	355 nm
Laser type	KrF excimer	Nd:YAG solid-state
Pulse width (ns)	20	5–7
Frequency (Hz)	10	10
Target–substrate distance (cm)	4	4–4.5[a]
Spot size (mm^2)	2.2 ± 0.1[a]	2.2 ± 0.1[a]
Fluence range (J/cm^2)	0.2–2.1	0.2–2.4
Duration of deposition (min)	45–94	20–180

[a] All measurements with the quartz crystal microbalance were made with a target–substrate distance of 4 cm and a spot size of 2.2 ± 0.1 mm^2. The films at low fluence (0.2–0.5 J/cm^2) were made with a larger spot size (up to 5 ± 0.2 mm^2) in order to make a relatively thick film within a reasonable amount of time

the SnS-rich CTS target, nine films were made under exactly the same circumstances, confirming that the deposition rate, droplet density (appearance in SEM), and composition were reproducible. With the non-SnS-enriched CTS target, films made at 1.6 J/cm^2 were reproduced with both lasers and it was confirmed that samples produced under the same circumstances were similar regarding thickness, droplet density, and composition.

The number of pulses at the two different wavelengths was adjusted to deposit films sufficiently thick for reliable energy-dispersive X-ray spectroscopy (EDX) at most fluences. According to the model CASINO [23], 99 % of the EDX signal for CTS derives from below 900 nm thickness and 90 % from below 750 nm, assuming a smooth surface and a bulk density of 5.02 g/cm^3 for Cu_2SnS_3 [24].

Multicomponent targets of CTS and SnS-rich CTS were purchased from PVD products. The targets named "CTS" in the present work had a Cu:Sn:S ratio of about 2:1:2.5 (measured by EDX; see Table 2), while the one called "SnS-rich CTS" had a Cu:Sn:S ratio of about 1:2:3. The targets consisted of multiple crystalline phases identified by XRD including Cu_2SnS_3 (tetragonal, JCPDS 89-4714), SnS (cubic, JCPDS 89-2755, and orthorhombic, JCPDS

75-1803), CuS (cubic, JCPDS 78-877), and Cu_2S (cubic, JCPDS 53-522). EDX mapping of the targets showed regions of hundreds of micrometers in diameter with either Cu-rich composition, Sn-rich composition, or a mixture of different phases.

2.2 Characterization

The deposition rates were measured with quartz crystal microbalances (QCM, Colnatec, Inc) and converted to film thickness, assuming a bulk density of 5.02 g/cm^3 for both Cu_2SnS_3 and SnS-rich CTS (the bulk density of SnS of 5.08 g/cm^3 is similar to that of CTS) [24, 25]. The targets were pre-ablated by 15.000–18.000 pulses before the measurement of the deposition rate in order to ensure a stable deposition. As shown in Table 1, the ablation parameters were similar for the comparison of the deposition rate between the different wavelengths. The deposition rates measured by QCM were systematically larger (by about 20–30 %) than the deposition rates determined from thickness measurements of films made at different fluence values (data not shown). This was most likely due to the measurement method: In SEM, the measurement excluded droplets sticking up above the film surface, while Dektak measurements are not highly accurate for surfaces with a high density of micrometer-scale droplets.

X-ray diffraction (XRD) measurements were carried out with a Bruker D8 diffractometer in Bragg–Brentano configuration using Cu K$_\alpha$ and Cu K$_\beta$ radiation. The diffraction pattern of the as-deposited films was measured using a step size of 0.03° and a rate of 0.33 step/s.

Scanning electron microscopy was performed at 5–15 kV using the in-lens and secondary electron detectors of two SEMs equipped with field emission guns (FE-SEM, Supra 60VP and Supra 35, Zeiss). The droplet size distributions were determined by processing SEM images of 20 × 30 μm size with image analysis software (ImageJ). The droplets were discriminated from the homogeneous

Table 2 Composition of the CTS target and selected films deposited at room temperature

	Fluence (J/cm^2)	Spot size (mm^2)	Thickness (nm)	Cu (%)	Sn (%)	S (%)	Cu/Sn
CTS target	–	–	–	38.6 ± 1.0	17.1 ± 1.0	44.4 ± 0.3	2.3 ± 0.5
355-nm laser	1.6	2.5	1500	43.3 ± 0.4	18.7 ± 0.5	38.1 ± 0.1	2.3 ± 0.1
	0.5	5	1000	28.8 ± 0.5	25.8 ± 0.5	45.5 ± 0.1	1.1 ± 0.1
	0.2	3.3	1200	27.4 ± 0.7	25.3 ± 0.3	47.3 ± 0.5	1.1 ± 0.1
248-nm laser	1.6	2.2	850–900	38.9 ± 0.6	19.3 ± 0.2	41.8 ± 0.6	2.0 ± 0.1
	0.5	5	800	11.1 ± 1	29.2 ± 2.1	59.8 ± 2.3	0.4 ± 0.1
	0.2	4	450	*ND*	*ND*	*ND*	*ND*

Uncertainties are the standard error of repeated measurements with the same instrument. The standard error on the Cu/Sn ratio is calculated, assuming that the Cu and Sn content are fully anti-correlated. All the film measurements in this table were made with the Bruker detector

film using a semiautomatic procedure with the signal intensity contrast as selection criterion and the area of each droplet was calculated automatically. Energy-dispersive X-ray spectroscopy (EDX) was performed at 15 kV in a Hitachi TM3000 tabletop SEM using a built-in Bruker detector with Quantax 70 software that performed mapping and quantification of the element ratios with Cu K-lines. Additional EDX measurements were performed in the Supra 60VP SEM with a silicon drift detector (X-Man[N] 50, Oxford Instruments), which allowed measurement on specific areas identified in SEM images of the films including individual droplets. From the Supra/X-Man[N] 50 data, element ratios were calculated by Oxford Instrument's Aztec software using the Cu K-lines and deconvoluting any Mo contribution to the S peak.

3 Results

3.1 Deposition rates

The deposition rate of CTS and SnS-rich CTS as a function of laser fluence is shown in Fig. 2. At any given fluence, the deposition rate of CTS and SnS-rich CTS at 355 nm is three to four times higher than at 248 nm.

Two main factors may explain the difference in deposition rate between the two lasers. Firstly, the effective intensity at 248 nm (1.2×10^8 W/cm^2) was about three times lower than at 355 nm (3.8×10^8 W/cm^2) due to the longer pulse duration at 248 nm. Secondly, the photon energy of 5 eV (corresponding to 248 nm) and 3.5 eV (corresponding to 355 nm) is much larger that the band gap energy of the constituent phases of the target, which was

mainly composed of SnS, CuS, Cu$_2$S, and tetragonal-phase Cu$_2$SnS$_3$ (see Sect. 2.1) [4, 26, 27]. However, it is possible that the absorption coefficient of the individual phases varies from 248 to 355 nm even though the photon energies are greater than the band gap energy. For example, for a mixture of the two related phases, cubic-phase and monoclinic-phase Cu$_2$SnS$_3$, the absorption coefficient was found to vary by a factor 3 from 1.6×10^5 cm^{-1} at 3.5 eV to 4.3×10^5 cm^{-1} at 5 eV [28]. For SnS, the absorption coefficient varies less between the two wavelengths (both approx. 1×10^6 cm^{-1} as estimated from plots of the dielectric functions) [29]. The variation in the absorption coefficient means that the light penetration depth may vary from phase to phase in the target. Overall, the lower deposition yield at 248 nm compared to 355 nm probably may be attributed to the lower laser intensity, possibly in combination with a smaller light penetration depth in some of the phases in the target.

Figure 2 furthermore shows that the deposition of SnS-rich CTS (Cu:Sn:S 1:2:3) was faster than the deposition of CTS (Cu:Sn:S 2:1:2.5), independent of the irradiation wavelength. This is expected since both S and SnS have a higher vapor pressure than the copper-containing phases in the target [30, 31]. An increase in the concentration of high vapor pressure components in the target results in a higher ablation yield [10, 11].

3.2 Droplets

SEM images of several CTS and SnS-rich CTS films deposited at a laser fluence of 0.2–1.8 J/cm^2 are shown in Fig. 3a–f. The surface of the films is covered with large circular droplets ranging from tens of nanometers to

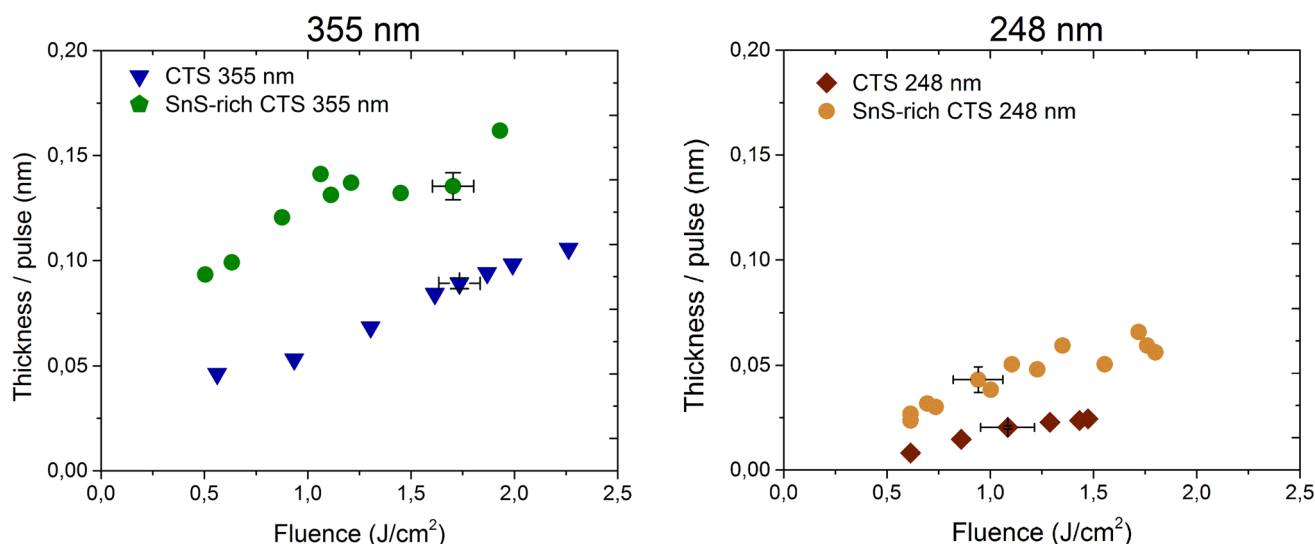**Fig. 2** Deposition rates of CTS and SnS-rich CTS at 355 nm (Nd:YAG laser, $\tau = 6$ ns) and 248 nm (KrF laser, $\tau = 20$ ns). The estimated error is similar for all the measurements, increasing

proportionally with the fluence. Due to constraints in the 248 nm setup, it was not possible to measure the deposition rate at higher fluence without changing the spot size
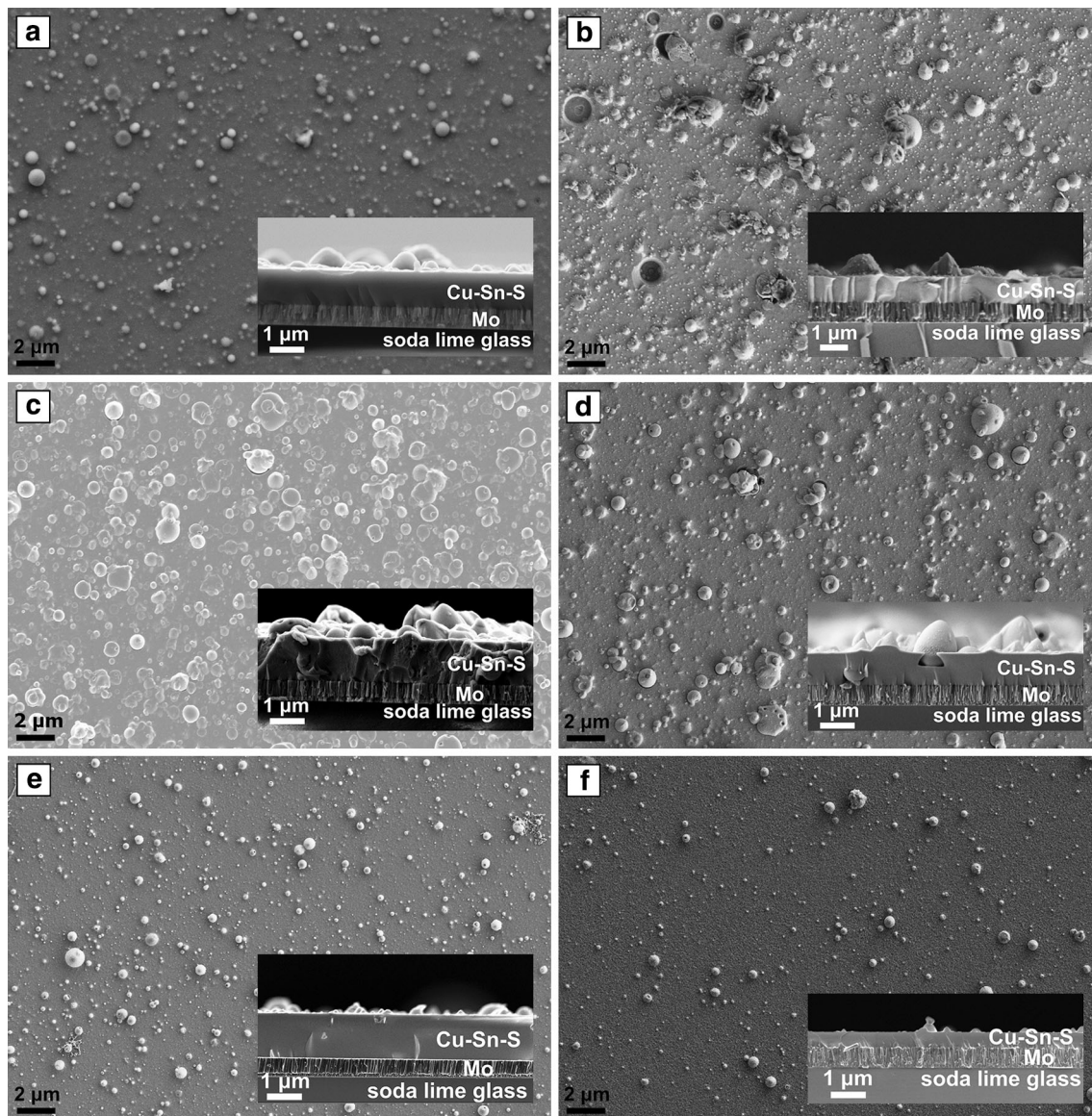
Fig. 3 SEM images (*top* and *side view*) of as-deposited films on Mo-coated soda-lime glass made at room temperature with 355 nm (**a**, **c**, **e**) and 248 nm (**b**, **d**, **f**) laser pulses. **a** 355 nm SnS-rich CTS 1.4 J/cm^2, **b** 248 nm SnS-rich CTS 1.8 J/cm^2, **c** 355 nm CTS 1.6 J/cm^2, **d** 248 nm CTS 1.6 J/cm^2, **e** 355 nm CTS 0.2 J/cm^2, **f** 248 nm CTS 0.2 J/cm^2 (note that this film was not used for EDX as it was too thin). While the 355-nm film shown in (**a**) was made at 1.4 J/cm^2, this film was highly similar to a series of films made at 2.3 J/cm^2 by the same laser. Image (**c**) was taken with the backscattered electron detector, while the others were taken with the more surface-sensitive secondary electron detectors

several microns in diameter. Our findings indicate that at a given fluence, the surface morphology of the as-deposited CTS films does not vary significantly from 355 to 248 nm. On the other hand, a decrease in the laser fluence to 0.2 J/cm^2 results in a decrease in the size and density of the droplets at both wavelengths (Fig. 3e–f).

The size distribution of the droplets extracted from SEM images in Fig. 3c–f is shown in Fig. 4. Note that we could not accurately identify small (<200 nm) particulates nor overlapping droplets by this method. The incidence of large droplets is also determined with a considerable uncertainty

in the histograms as they were relatively rare. Nonetheless, Fig. 4 shows that there is no reduction in droplet area density for the 248-nm laser compared to the 355-nm laser. At high laser fluence, the distribution profile is broad, while at low fluence, the average size of the droplets decreases. The data suggest that the size and density of the droplets are strongly dependent on the laser energy and, for a given fluence, less dependent on the UV irradiation wavelength. This will be discussed in Sect. 4.

No diffraction peaks were observed beside Mo and MoO$_x$ in X-ray diffractograms of the as-deposited films,
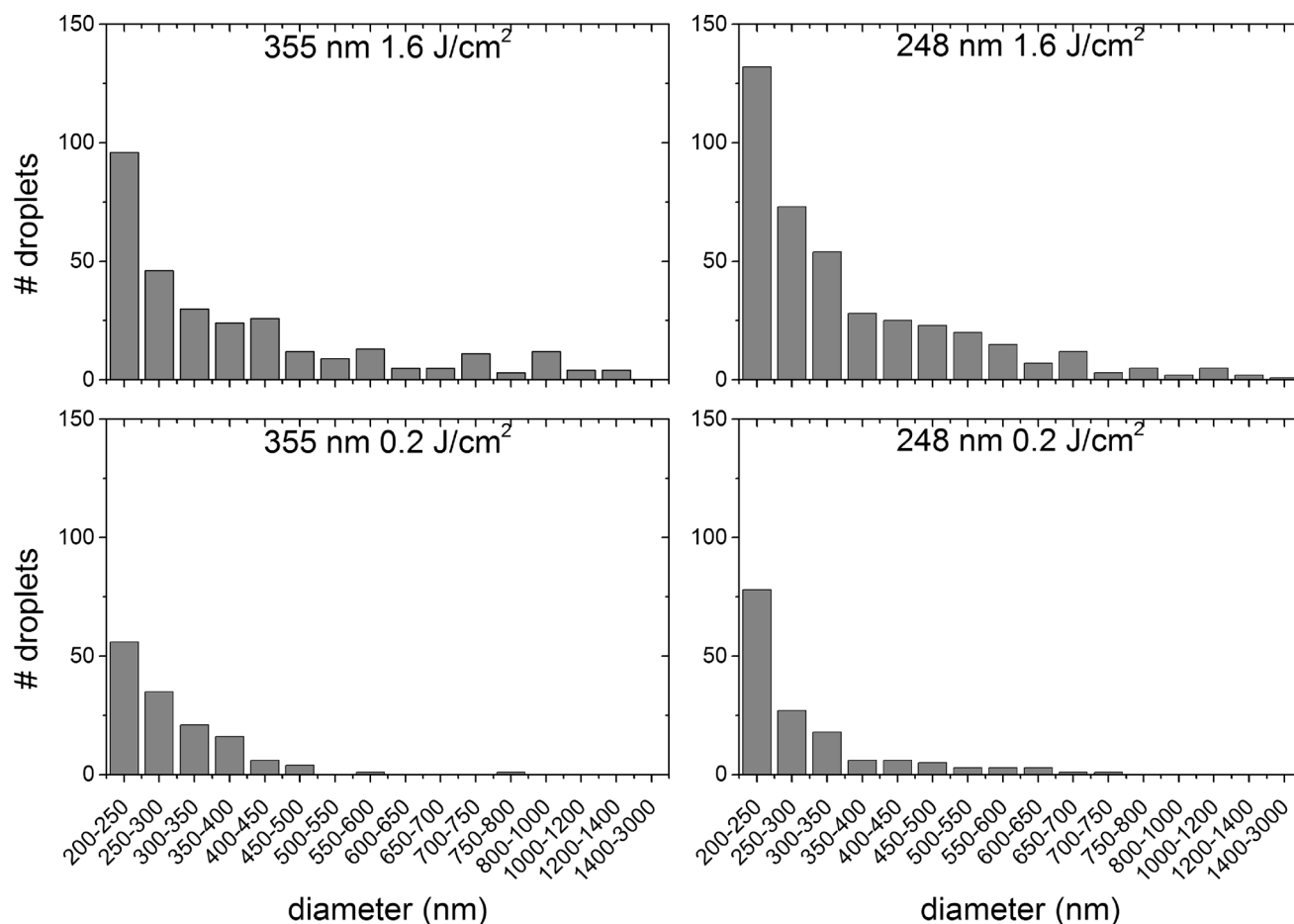
Fig. 4 Distribution of droplet size at 0.2 and 1.6 J/cm^2 with the 355- and 248-nm laser in a film made from the non-SnS-enriched target. Smaller droplets were present but could not be accurately quantified

with the image processing software. Large droplets were rare and are therefore not accurately portrayed in the histograms

indicating that the films were mostly amorphous (X-ray data not shown).

3.3 Composition

Sulfur content The CTS films deposited at high fluence (1.5–1.6 J/cm^2) show S deficiency, and the deficiency appears to be larger at 355 nm than at 248 nm (Table 2). In contrast, the S content increased markedly in the films made at low fluence (0.5 J/cm^2 with the 355 nm and 0.2 J/cm^2 with the 248-nm laser). Thus, the S content increased from $S/(Cu + Sn) = 0.8 \pm 0.2$ in the target to $S/(Cu + Sn) = 1.5 \pm 0.6$ in the film made at 0.5 J/cm^2 by the 248-nm laser.

Metal content The Cu/Sn ratio of the target is maintained within the error bar in the CTS films made at 1.6 J/cm^2 by the 355-nm laser (Table 2). In comparison, the CTS film deposited at 248 nm at a similar fluence has a somewhat lower Cu concentration, though still within the error bar. The low-fluence depositions resulted in CTS films with a significant Cu deficiency at both wavelengths.

The Cu/Sn ratio varies from 1.1 ± 0.1 for films made at 0.2–0.5 J/cm^2 at 355 nm to only 0.4 ± 0.1 for a film made at 0.5 J/cm^2 at 248 nm. These values should be compared with the Cu/Sn ratio in the target of 2.3 ± 0.5. As a general trend, we observe that as the incident laser energy is reduced, incongruent evaporation becomes dominant, and the Cu content in the as-deposited films decreases progressively (see Sect. 4). We have previously reported a similar but less dramatic increase in the S and Sn content of films made at low fluence with the 355-nm laser [8].

Composition of SnS-rich films The composition of the SnS-rich films does not vary much for films made at fluences between 0.7 and 2.3 J/cm^2 with the 355-nm laser or for films made at 1–1.8 J/cm^2 for the 248-nm laser (data not shown). In general, the films appear S- and Sn-poor compared to the target, but highly Sn-rich (Cu/Sn ~ 0.6) as well as somewhat S-poor compared to the desired stoichiometry of Cu_2SnS_3.

Composition of droplets The chemical composition versus the diameter of the droplets of the CTS films deposited at 1.6 J/cm^2 at 248 nm is shown in Fig. 5. EDX measurements

were carried out on a random selection of individual droplets with an average diameter larger than 1 µm. Figure 5 shows a significant deficiency of S and Sn and, consequently, enrichment of Cu in the Cu–Sn–S droplets. Despite the scattering of the data due to the relatively high uncertainty of the EDX analysis, we note that the deficiency of S and Sn increases as the droplet size decreases. The underlying film denoted by the "matrix" in Fig. 5 shows enrichment in the Sn content relative to the average target composition, which may derive from Sn loss from the droplets or from more efficient ablation of the Sn-rich phases in the target compared to the Cu-rich phases. The underlying film matrix is still slightly S deficient relative to the target, suggesting that sulfur losses occur both by evaporation from the film and by sulfur-deficient droplet solidification into the film.

It should be noted that the spot size was increased from 2.2 to 5 mm^2 in order to deposit films at low fluence due to the low deposition rate. The change in spot size may have had some influence on the off-axis composition, as the ablation plume becomes more forward-directed when the spot size is increased. However, we have in the present work considered the on-axis composition.

4 Discussion

Our ablation studies of CTS and SnS-rich CTS films indicate that the number of droplets is significantly reduced at lower laser fluence, while the irradiation wavelength does not significantly influence the surface morphology of the as-deposited CTS films. We observe a reduction in the average size of the droplets at low laser fluence accompanied by a change to non-stoichiometric material transfer with an increase in the S and Sn content. This trade-off
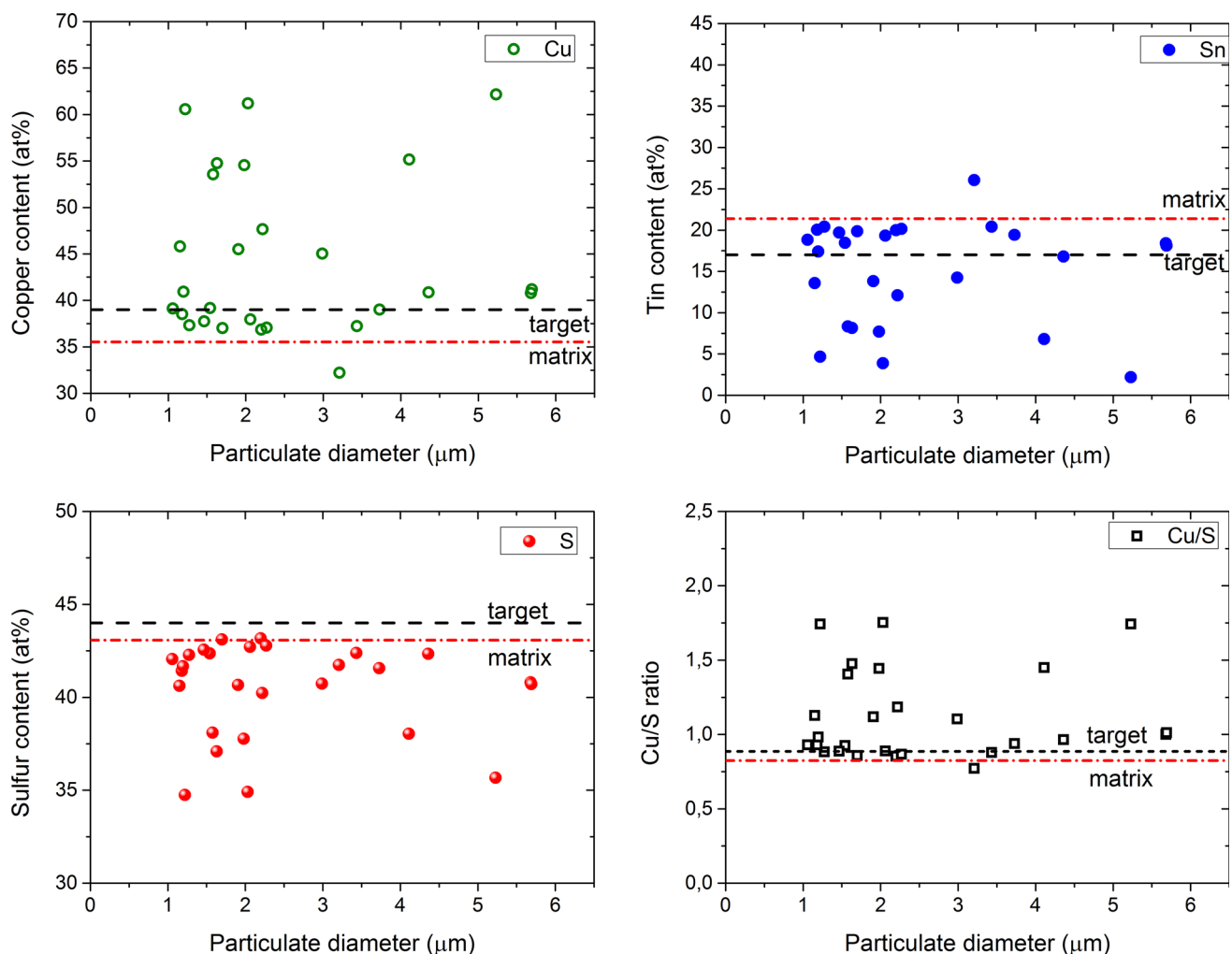
Fig. 5 Compositional analysis of the droplets as a function of droplet diameter for a film made from the non-SnS-enriched CTS target at 1.6 J/cm^2 at 248 nm (note that this target was Cu-rich and S-poor relative to the ideal composition as measured by our EDX analysis; see also Table 2). The Cu, Sn, S content, as well as the Cu/S ratio are given for a random selection of droplets with an average diameter larger than 1 µm. The composition of the target is indicated as "target", while the composition of the underlying film is indicated by "matrix"

⚛ Springer

between congruent material transfer and the amount of droplets on the films depending on fluence was previously mentioned in the literature, e.g., by Lowndes [11].

An incongruent transfer at low fluence has been observed for other materials (e.g., $SrTiO_3$ [32, 33] and YBCO [34]), and different explanatory models have been offered [11, 33, 34]. Venkatesan et al. [34] pointed out that the non-stoichiometric transfer of the material in the low-fluence regime is correlated with preferential evaporation of the elements with high vapor pressure and low cohesive energy in the multicomponent target. In the case of CTS, Cu has a higher cohesive energy (3.5 eV/atom) than Sn (3.12 eV/atom) (Table 3) [35]. While the cohesive energy of atoms in alloys has only been investigated by a few groups, alloyed atoms nevertheless show a cohesive energy similar to the pure elements [10]. Therefore, it may be expected that in the evaporative regime, the CTS films are Cu-deficient, as seen in the low-fluence films, as this is the least volatile element and thus the most difficult one to ablate.

In the high-fluence regime, ablation results in a distribution of droplets of the order of micrometer size embedded in the CTS films, independent on the irradiation wavelength. In this regime, the transfer of the ablated material is nearly stoichiometric. The films deposited at 355 nm are slightly Cu- and Sn-rich, while the films deposited at 248 nm are slightly Cu-poor. The lower Cu content of the 248-nm films may be linked to the lower intensity of the 248-nm laser pulses, since this would lead to a higher evaporative component for a given fluence. Interestingly, Kautek et al. [18] saw a similar trend in YBCO films made at 266 and 355 nm: The element transfer was incongruent at somewhat higher fluence at 266 nm than at 355 nm, even though in their experiment, both lasers had the same pulse length.

Our observation of a transition from a Cu-poor to a Cu-rich regime with increasing fluence with the 355-nm laser is similar to the transition from Sr-rich to Ti-rich $SrTiO_3$ seen by Ohnishi et al. [32] with increasing fluence. For the deposition of a bimetallic material in an oxygen background gas, it was possible for Onishi et al. to identify a fluence that perfectly balanced the Sr:Ti ratio. In contrast, for the tri-component chalcogenide CTS, it may be that no fluence exists that ensures perfectly stoichiometric transfer. However, we see that it is possible tune the ratio of Sn to Cu by fluence adjustment and to compensate for any S deficiency using a post-deposition sulfurization step, as performed for CZTS films by Moriya et al. [20].

Detailed characterization of the droplets embedded in the CTS film deposited at 1.6 J/cm^2 at 248 nm reveals a large depletion in S and Sn relative to Cu in the droplets. The degree of depletion increases with decreasing droplet size. Sulaiman et al. [13] have observed that both Cu- and Sn-rich droplets were transferred onto films of CZTS made by PLD at 355 nm without a detailed qualitative analysis. Chen and Hall [14] have shown that in binary metallic systems of Nb–Al and Nb–Cr, the droplets are usually deficient in the element with high vapor pressure and the deficiency of the volatile elements increases with decreasing droplet size. In the Cu–Sn–S system, the vapor pressure of Cu and Sn is much lower than that of S (see Table 3). As a result, preferential evaporation of S is likely and would result in Cu- and Sn-rich droplets. However, the EDX analysis indicates a deficiency of Sn in the solidified molten droplets in addition to an S deficiency. Since SnS is far more volatile than Sn (Table 3), it is likely that the Sn deficiency is caused by the evaporation of SnS, as proposed by Weber et al. [30] in an investigation of Sn loss from heated films of CZTS.

We do not see a droplet reduction with a change between the two UV laser wavelengths 355 and 248 nm. As described in the introduction, droplet reduction might have been expected if the target absorption of the 248-nm laser was higher than the 355-nm laser so that subsurface boiling would be reduced, or if the 248 nm light was able to more efficiently break up the ejected droplets. As discussed in Sect. 3.1, the absorption of different UV wavelengths in the target is not easily predicted, and the increased photon energy at 248 nm may be offset by the longer pulse length, leading to a lower pulse power. The combined effect of the differences between the lasers in wavelength and pulse length seems to have little influence on this particular material.

For the fabrication of the thin-film absorber layers of CTS for thin-film solar cells, it is desirable to have Cu-poor films [36] and a uniform composition. Since the composition of the droplets can be different to the underlying film, it is important to minimize their occurrence. We observe that splashing and associated Cu-rich droplets can be minimized by reducing the fluence, although the droplet reduction has to be balanced against the appropriate composition. Additional strategies to reduce droplets are to use off-axis deposition, a mechanical velocity filter, or a voltage across the ablation plume [11, 19]. However, these

Table 3 Cohesive energy and temperature at which the vapor pressure is 1 Pa for the constituent elements of CTS as well as SnS and Cu_2SnS_3

	Cohesive energy (eV/atom) [35]	Temperature at which the vapor pressure is 1 Pa (°C)
Cu	3.5	963 [31]
Sn	3.12	951 [31]
S	2.86	102 [31]
SnS	NA	590 [38, 39]
Cu_2SnS_3	NA	higher than SnS [30]

methods mean that the deposition process becomes far more complex.

5 Conclusion

We have reported on the fabrication of copper tin sulfide (CTS) and SnS-rich CTS thin films in vacuum for two UV wavelengths, 355 and 248 nm. The deposition rate was about four times higher at 355 nm than at 248 nm for both CTS and SnS-rich CTS. The morphology studies of the as-deposited films showed that the area density of the droplets was not reduced by increasing the photon energy from 355 to 248 nm.

For both lasers, the laser fluence significantly affects the density and average size of the droplets. At high fluence (1.6 J/cm^2), UV irradiation leads to near-congruent transfer of the ablated material. Droplets produced by the 248-nm KrF-excimer laser ablation at high fluence were mainly S- and Sn-poor, and the deficiency seemed more pronounced with decreasing droplet size. A reduction in the laser fluence down to 0.2 J/cm^2 resulted in smaller droplets and lower droplet area density for both lasers.

The low-fluence regime leads to incongruent evaporation of films with typically large copper deficiency and therefore films that were S- and Sn-rich relative to the target. The Cu deficiency was most pronounced for the 248-nm laser, possibly due to the lower intensity of the 248-nm laser pulses.

Films deposited by either laser from the SnS-rich CTS target were Sn-rich relative to the desired composition for solar cell absorber layers. Films deposited from the CTS target at 1.6 J/cm^2 by either laser were somewhat Cu-rich for solar cells (we found Cu/Sn $\sim$ 2.0 compared to Cu/Sn $\sim$ 1.7–1.9 in successful solar cells [36, 37]). However, by reducing the fluence somewhat, it will be possible to reach the optimal Cu/Sn ratio with both the 248- and the 355-nm laser.

Overall, our study illustrates the commonly observed trade-off in PLD between reduction in the droplet density and change in the composition with a reduction in the laser fluence.

References

1. D.B. Mitzi, O. Gunawan, T.K. Todorov, D.A.R. Barkhouse, Philos. Trans. R. Soc. A **371**, 20110432 (2013)
2. S. Tajima, T. Itoh, H. Hazama, K. Ohishi, R. Asahi, Appl. Phys. Express **8**, 082302 (2015)
3. T.A. Kuku, O.A. Fakolujo, Sol. Energy Mater. **16**, 199 (1987)
4. P.A. Fernandes, P.M.P. Salomé, A.F. da Cunha, Phys. Status Solidi C **7**(3–4), 901 (2010)
5. P. Zawadzki, L.L. Baranowski, H. Peng, E.S. Toberer, D.S. Ginley, W. Tumas, A. Zakutayev, S. Lany, Appl. Phys. Lett. **103**, 253902 (2013)
6. N. Aihara, H. Araki, A. Takeuchi, K. Jimbo, H. Katagiri, Phys. Status Solidi C **10**, 1086 (2013)
7. M. Nakashima, J. Fujimoto, T. Yamaguchi, M. Izaki, Appl. Phys. Express **8**, 042303 (2015)
8. R.B. Ettlinger, A. Cazzaniga, S. Canulescu, N. Pryds, J. Schou, Appl. Surf. Sci. **336**, 385 (2015)
9. S.A. Vanalakar, G.L. Agawane, A.S. Kamble, C.W. Hong, P.S. Patil, J.H. Kim, Sol. Energy Mater. Sol. Cells **138**, 1 (2015)
10. J. Schou, Appl. Surf. Sci. **255**, 5191 (2009)
11. D.H. Lowndes, in *Laser Ablation Desorption, Experimental Methods in the Physical Sciences*, vol. 30, ed. by J.C. Miller, R.F. Haglund (Academic Press, New York, 1998), pp. 475–571
12. K. Ito, in *Copper Zinc Tin Sulfide-Based Thin Film Solar Cells*, 1st edn., ed. by K. Ito (Wiley, Chichester, West Sussex, 2015), pp. 34–35
13. N.S. Che Sulaiman, C.H. Nee, S.L. Yap, Y.S. Lee, T.Y. Tou, S.S. Yap, Appl. Surf. Sci. **354**, 42 (2015)
14. L.-C. Chen, E.L. Hall, Mater. Res. Soc. Symp. Proc. **285**, 519 (1993)
15. W.O. Siew, S.S. Yap, C. Ladam, Ø. Dahl, T.W. Reenaas, T.Y. Tou, Appl. Phys. A **104**, 877 (2011)
16. N.J. Ianno, L. McConville, N. Shaikh, S. Pittal, P.G. Snyder, Thin Solid Films **220**, 92 (1992)
17. G. Koren, A. Gupta, R.J. Baseman, M.I. Lutwyche, R.B. Laibowitz, Appl. Phys. Lett. **55**, 2450 (1989)
18. W. Kautek, B. Roas, L. Schultz, Thin Solid Films **191**, 317 (1990)
19. L.-C. Chen, in *Pulsed Laser Deposition. Thin Film*, 1st edn., ed. by D.B. Crisey, G.K. Hubler (Wiley, New York, 1994), pp. 167–198
20. K. Moriya, K. Tanaka, H. Uchiki, Jpn. J. Appl. Phys. **47**, 602 (2008)
21. S.M. Pawar, A.V. Moholkar, I.K. Kim, S.W. Shin, J.H. Moon, J.I. Rhee, J.H. Kim, Curr. Appl. Phys. **10**, 565 (2010)
22. K. Ujimoto, T. Yoshimura, A. Ashida, N. Fujimura, Jpn. J. Appl. Phys. **52**, 045803 (2013)
23. D. Drouin, A.R. Couture, D. Joly, X. Tastet, V. Aimez, R. Gauvin, Scanning **29**, 92 (2007)
24. L.I. Berger, in *CRC Handbook of Chemistry and Physics*, 96th edn., ed. by W.M. Haynes, T.J. Bruno, D.R. Lide (CRC Press, Boca Raton, 2015), pp. 12-80–12-93
25. W.M. Haynes, T.J. Bruno, D.R. Lide (eds.), *CRC Handbook of Chemistry and Physics*, 96th edn. (CRC Press, Boca Raton, 2015), pp. 4–43–4–101
26. L.A. Burton, D. Colombara, R.D. Abellon, F.C. Grozema, L.M. Peter, T.J. Savenije, G. Dennler, A. Walsh, Chem. Mater. **25**, 4908–4916 (2013)
27. O. Madelung, U. Rössler, M. Schulz (eds), *Springer Materials Series Landolt-Börnstein - Gr. III Condensed Matter, Subvolume 41C, Non-tetrahedrally Bonded Elements and Binary Compounds I* (Springer, Berlin, 1998), pp. 1–2
28. A. Crovetto, R. Chen, B. Ettlinger, A.C. Cazzaniga, J. Schou, O. Hansen, C. Persson (2016) (submitted)
29. O. Madelung, U. Rössler, M. Schulz (eds.), *Non-tetrahedrally Bonded Elements and Binary Compounds I* (Springer, Berlin, 1998), pp. 1–8
30. A. Weber, R. Mainz, H.W. Schock, J. Appl. Phys. **107**, 013516 (2010)
31. W.M. Haynes, T.J. Bruno, D.R. Lide (eds.), *CRC Handbook of Chemistry and Physics*, 96th edn. (CRC Press, Boca Raton, 2015), pp. 6-88–6-116

32. T. Ohnishi, T. Yamamoto, S. Meguro, H. Koinuma, M. Lippmaa, J. Phys. Conf. Ser. **59**, 514 (2007)
33. B. Dam, J.H. Rector, J. Johansson, J. Huijbregtse, D.G. De Groot, J. Appl. Phys. **83**, 3386 (1998)
34. T. Venkatesan, X.D. Wu, A. Inam, J.B. Wachtman, Appl. Phys. Lett. **52**, 1193 (1988)
35. C. Kittel, *Introduction to Solid State Physics*, 3rd edn. (Wiley, New York, 1966) p. 78

36. A. Kanai, K. Toyonaga, K. Chino, H. Katagiri, H. Araki, Jpn. J. Appl. Phys. **54**, 08KC06 (2015)
37. M. Nakashima, T. Yamaguchi, H. Itani, J. Sasano, M. Izaki, Phys. Status Solidi C **12**, 761 (2015)
38. B. Richards, Trans. Faraday Soc. **51**, 1193 (1955)
39. V. Piacente, S. Foglia, P. Scardala, J. Alloys Compd. **177**, 17 (1991)

Chapter 7

Growth and fundamental properties of CZTS

Let it grow, let it grow
Let it blossom, let it flow
In the sun, the rain, the snow
Love is lovely, let it grow
Eric Clapton, 1974

7.1 Study 7.1: Optical properties of CZTS grown by pulsed laser deposition in a single-step process

- <u>Crovetto A</u>, Cazzaniga A, Ettlinger R B, Schou J and Hansen O 2015 Optical properties and surface characterization of pulsed laser-deposited Cu_2ZnSnS_4 by spectroscopic ellipsometry *Thin Solid Films* **582** 203–207

This study, carried out in the early days of my PhD project, investigates the optical properties of CZTS films deposited by pulsed laser deposition at different temperatures. Note that, in this study, the CZTS films were *not* post-annealed and contained detectable amounts of seconday phases. Therefore, they are certainly not device-grade CZTS films. Nevertheless, this study clearly shows the evolution of the dielectric function of CZTS as the films turn from amorphous (low deposition temperature) to polycrystalline (high deposition temperature). Additionally, I demonstrate that characterization by spectroscopic ellipsometry can clarify some properties (size, density, and dielectric function) of the droplets usually present in pulsed-laser-deposited films, consistently with the results of direct characterization techniques such as atomic force microscopy (AFM) and Raman spectroscopy.

My contribution (detailed):
• Preliminary characterization by Raman, SEM, AFM, and mechanical profilometry • Ellipsometry measurement, optical modeling, and data analysis • Writing the whole manuscript

Coauthors' contribution (brief):
• A. Cazzaniga: growth of CZTS films by PLD and XRD measurement with data analysis
• R. B. Ettlinger, J.Schou, O. Hansen: discussions and commenting the manuscript

7.2 Study 7.2: CZTS films by annealing CZTS and ZnS precursors grown by pulsed laser deposition

- Cazzaniga A, <u>Crovetto A</u>, Ettlinger R B, Canulescu S, Hansen O, Pryds N and Schou J 2015 ZnS top layer for enhancement of the crystallinity of CZTS absorber during the annealing *2015 IEEE 42nd Photovoltaic Specialist Conference (PVSC)* (IEEE) pp 1–4

This study, also belonging to the early days of our research project, was mostly carried out by PhD student Andrea Cazzaniga. It is based on the observation that the Zn content in his early CZTS films deposited by PLD was not sufficient to achieve the optimal Zn-rich stoichiometry for high-efficiency solar cells. Further, the deposition temperature in those early studies was 300°C, instead of room temperature as in the later films (Study 2.1). Therefore he tested a ZnS cap layer deposited on top of the CZTS precursors with the goal of simultaneously enrich the films in Zn and prevent loss of the volatile compounds at the relatively high deposition temperature. This was before the stoichiometry dependence on laser fluence became apparent, and before optimization of the laser spot size and laser rastering pattern on the PLD target [192]. We also found out later that the thickness of the ZnS layer deposited in this study was too large and resulted in obvious segregation of a ZnS phase on top of the CZTS film after annealing. Nevertheless, the intensity of both the XRD and Raman peaks increased with the ZnS cap layer, meaning that, if the ZnS cap thickness is carefully tuned, such a cap layer can be a way to fine-tune the stoichiometry of CZTS and improve its crystalline properties.

My contribution (detailed):
• Fabrication of Mo back contact • Potassium cyanide (KCN) etching of the samples • Raman characterization

7.3 Study 7.3: Synthesis of ligand-free CZTS nanoparticles via a facile hot injection route

- Mirbagheri N, Engberg S, <u>Crovetto A</u>, Simonsen S B, Hansen O, Lam Y M and Schou J 2016 Synthesis of ligand-free CZTS nanoparticles via a facile hot injection route *Nanotechnology* **27** 185603

This study is has a very different background compared to all the other studies presented in this thesis. While the main overall focus in the CHALSOL research project has been on pulsed laser deposition of CZTS, an alternative non-vacuum track was attempted in the work of PhD student Sara Engberg. This specific study was mostly carried out by Naghmehalsadat Mirbagheri within the background of Sara's PhD project. It shows the synthesis of phase-pure and very large CZTS nanoparticles in a polar solvent. Using a polar solvent has some significant advantages compared to non-polar solvents, as it avoids formation of long carbon chain ligands on the surface of the nanoparticles which contribute to carbon impurities in the deposited films. The dream is to eventually use water - a carbon-free polar solvent with obvious cost advantages - as a solvent in the synthesis of CZTS nanoparticles.

My contribution (detailed):
• Raman and XPS characterization and analysis • Solar cell fabrication (except for synthesis, deposition and annealing of CZTS) • Quantum efficiency measurement and analysis • Discussions and commenting the manuscript

Optical properties and surface characterization of pulsed laser-deposited Cu$_2$ZnSnS$_4$ by spectroscopic ellipsometry ☆

Andrea Crovetto [a,*], Andrea Cazzaniga [b], Rebecca B. Ettlinger [b], Jørgen Schou [b], Ole Hansen [a,c]

[a] DTU Nanotech, Technical University of Denmark, DK-2800 Kgs. Lyngby, Denmark
[b] DTU Fotonik, Technical University of Denmark, DK-4000 Roskilde, Denmark
[c] CINF, Center for Individual Nanoparticle Functionality, Technical University of Denmark, DK-2800 Kgs. Lyngby, Denmark

A B S T R A C T

Cu$_2$ZnSnS$_4$ films prepared by pulsed laser deposition at different temperatures are characterized by spectroscopic ellipsometry. The focus is on confirming results from direct measurement techniques, by finding appropriate models of the surface overlayer for data fitting, and extracting the dielectric function of the films. It is found that the surface overlayer changes with film thickness and deposition temperature. Adopting different ellipsometry measurements and modeling strategies for each film, dielectric functions are extracted and compared. As the deposition temperature is increased, the dielectric functions exhibit additional critical points related to optical transitions in the material other than absorption across the fundamental band gap. In the case of a thin film <200 nm thick, surface features observed by scanning electron microscopy and atomic force microscopy are accurately reproduced by ellipsometry data fitting.

© 2014 Elsevier B.V. All rights reserved.

1. Introduction

Cu$_2$ZnSnS$_4$ (CZTS) is a promising candidate to replace commonly used thin-film solar cell absorbers Cu(In,Ga)Se$_2$ (CIGS) and CdTe, which contain expensive or toxic materials. Unlike CIGS- and CdTe-based solar cells, which have surpassed 20% power-conversion efficiencies on the laboratory scale, the current records for CZTS are 8.4% in the case of a sulfur-pure material [1] and 12.6% if S is alloyed with Se [2]. In order to improve the efficiency, both technological issues and a still incomplete understanding of the material need to be addressed. This includes for example the spectral optical properties of CZTS, which can help clarify its band structure and absorption behavior but have seldom been reported in the literature. Levcenko et al. [3] showed the dielectric function of bulk CZTS crystals using ellipsometry and a two-phase (substrate-layer) model. Li et al. [4] extracted the dielectric function of nanocrystalline films from transmittance spectra using a Tauc–Lorentz oscillator. Sun et al. [5] derived the absorption coefficient and band-gap energy of CZTS films from ellipsometry measurements. Finally, Li et al. [6] obtained the dielectric function of a CZTS film from ellipsometry data taken at multiple angles of incidence from both sides of the sample; the data was fitted with a dielectric function of arbitrary shape, without underlying physical assumptions. In this study we characterize CZTS films by spectroscopic ellipsometry, focusing on cross-checking results from direct measurement techniques and on determining the dielectric function in films exhibiting different levels of crystallization.

2. Experimental details

Films of CZTS were deposited on fused silica substrates by pulsed laser deposition (PLD) at different temperatures: two samples at 25 °C (with different thicknesses, named C-25 t and C-25 T), one at 350 °C (C-350) and one at 425 °C (C-425). A sintered Cu$_2$ZnSnS$_4$ target was used (PVD Products). The laser wavelength, fluence and pulse repetition rate were 248 nm, 3 J/cm^2 and 15 Hz, respectively. The background pressure was 7×10^{-7} mbar and the target-to-substrate distance was 40 mm. The film surface was imaged with a scanning electron microscope (SEM) equipped with a field emission gun and an in-lens secondary electron detector (FE-SEM, Supra 40VP, Zeiss) by tilting the sample to 45°. Energy dispersive X-ray spectroscopy (EDX) was performed in the same instrument using a silicon drift detector (X-Max^N 50, Oxford Instruments) and a beam voltage of 15 kV. Surface roughness was measured by stylus profiling (Dektak 8, Veeco) and atomic force microscopy (AFM, Dimension 3100, Bruker AXS) using tapping mode. The root-mean-square surface roughness (R$_q$) is employed in this work. X-ray diffraction (XRD) patterns were collected with a Bruker D8 powder diffractometer in Bragg–Brentano configuration using Cu-Kα radiation. Raman spectra were obtained at a laser wavelength of 455 nm, laser power of 0.4 mW and spot size of 1 μm^2 in the backscattering configuration (DXR Raman Microscope, Thermo Scientific).

Ellipsometric measurements were performed in the spectral range of 0.7–5.9 eV on a rotating compensator spectroscopic ellipsometer (M-2000, J.A. Woollam Co.) using seven angles of incidence (from 45 to 75°) and a collimated beam.

3. Results and discussion

3.1. Preliminary analysis

Energy dispersive X-ray spectroscopy (EDX) demonstrated that all films are Cu- and Sn-rich.

The films deposited at 25 °C showed no XRD peaks (Fig. 1) and no crystal grain contrast in the scanning electron microscope (SEM) images (Fig. 2(a,b)). However, the peaks associated with CZTS were present in their Raman spectra (Fig. 3). Since Raman spectroscopy is more sensitive to the crystal short-range order than XRD [7] it can be assumed that these films have very small grains and/or are only partially crystallized. At 350 °C a nanocrystalline grain structure becomes visible in the SEM and is detected by XRD, with an average grain diameter of 50 nm (partially visible in Fig. 2(c)). At 425 °C the film is crystalline with an average grain diameter of about 200 nm (estimate based on morphology, Fig. 2(d)).

3.2. Analysis of surface overlayer

The surface overlayer is often difficult to model when fitting ellipsometry data [8] so it is helpful to gain some knowledge from other techniques. As shown in the SEM images in Fig. 2, the film surface is heterogeneous for all our samples. Except for C-425, the films have some localized protrusions, typically in the form of nanospheres (inset graph in Fig. 2(a)) on top of a relatively smooth surface. Surface roughnesses, measured by a stylus profiler and AFM, are shown in Table 1. The overall surface roughness increases with film thickness but appears to be independent of the temperature, i.e. of the degree of crystallization and grain size. However, if the roughness is measured over an area without nanospheres (denoted film roughness in Table 1), the value increases with temperature until, at 425 °C, it is impossible to make a distinction between the two definitions.

To verify if the surface region contains various phases besides being rough, Raman spectroscopy was employed. From ellipsometry measurements the absorption coefficient α of our CZTS films at the Raman laser wavelength of 455 nm is in the $1.5–2.0 \times 10^5$ cm^{-1} range. The Raman information depth is defined as the depth d such that $2d\alpha = 1$, i.e. half the optical penetration depth because the optical path of backscattered light in the material is doubled. Hence in our CZTS films

Fig. 1. XRD patterns of the four CZTS films. Only one pattern is shown for the C-25 t and C-25 T samples, as their differences are negligible. Phase analysis is performed based on peak position and on comparison with Raman spectra. A Cu$_3$SnS$_4$ peak is identified as a shoulder in one of the SnS peaks.

60% of the Raman signal originates within 25–35 nm below the surface, making the technique very surface sensitive at this wavelength. The laser spot size was directed onto one of the bigger nanostructures (the only one clearly visible with an optical microscope) and the focus was adjusted first to the film surface, then to the top of the structure. The results are shown in the inset graph of Fig. 3 for the C-25 t film, but similar results have been obtained for the other films in this study. When the laser is focused on the film surface the only visible peaks are the two main CZTS peaks (289 and 334 cm^{-1}) and a small peak at 316 cm^{-1} which could be Cu$_3$SnS$_4$ or SnS$_2$. When the focus is moved to the top of the structure, the relative intensity of the two CZTS peaks is redistributed, the peak at 316 cm^{-1} disappears and a broad peak centered at 475 cm^{-1} appears, probably corresponding to a disordered Cu$_{2-x}$S phase. This is supported by EDX spot analysis performed on the larger nanostructures, which consistently show an increase in the Cu fraction by 30–50% (relative) with respect to spot analysis on the smooth surface. To conclude, the surface overlayer consists both of a complex topography and of a different phase mix with respect to the underlying film.

3.3. Ellipsometry analysis

3.3.1. Optical modeling

Results from characterization techniques presented in the previous sections have been used as a starting point in building the optical layer stacks shown in Fig. 4 for ellipsometry data fitting. Based on the magnitude of the X-ray peaks from the substrate, the sampling depth of our EDX experiments is roughly estimated to be around 500 nm, whereas the sampling depth of the XRD measurements is a few μm at all incidence angles. Therefore, EDX and XRD can help identify phases, and hence the dielectric function of the bulk homogeneous film layer defined in the model. We expect to have a dominant CZTS component and smaller contributions from SnS and Cu$_3$SnS$_4$ (at least in C-350 and C-425). SEM imaging with secondary electrons and Raman spectroscopy have both sampling depths of a few tens of nm in our experiments. Therefore, SEM images have been used to define the morphology of the surface overlayer in the optical model, i.e. a mix of air and a solid phase (Fig. 4). Raman spectroscopy, on the other hand, allows to confirm whether the dielectric functions of the surface overlayer and of the near-surface region are realistic. As previously mentioned, we expect a major contribution from Cu$_{2-x}$S. Raman experiments have also been performed on the cross sections of the two thicker films (C-25 T and C-425) to complement XRD for bulk phase analysis. The intensity ratios of the peaks in cross-sectional spectra are very similar to the ones in the corresponding surface spectra shown in Fig. 3, so it is assumed that the phase mix in the bulk of the film is not depth-dependent and hence the bulk film layer in the optical model should not be defined as a graded layer. All phases detected by XRD were detected by Raman spectroscopy, and the latter provided the additional information that Cu$_3$SnS$_4$ is also present in the C-25 t sample and possibly in the C-350 sample (Fig. 3).

Based on the above discussion, the bulk film layer in the optical model should ideally be modeled as a mix of all phases expected in the bulk. As a first approximation, it could be a CZTS/SnS mix. However, a high correlation error was consistently found in the mixing ratio and dielectric function parameters, even when using literature dielectric functions of CZTS and SnS as initial parameters in the fitting algorithm. Therefore, it was decided to keep the film layer as a single-phase material in the model. It is then clear that the fitted dielectric functions are, to some degree, a mix of the dielectric functions of all phases present in the bulk. However, based on XRD and Raman measurements, we expect CZTS to be the main component.

3.3.2. Sample grown at 25 °C (thin)

The C-25 t sample is the simplest to analyze due to its lower surface roughness and its lack of long-range crystal order, which makes its
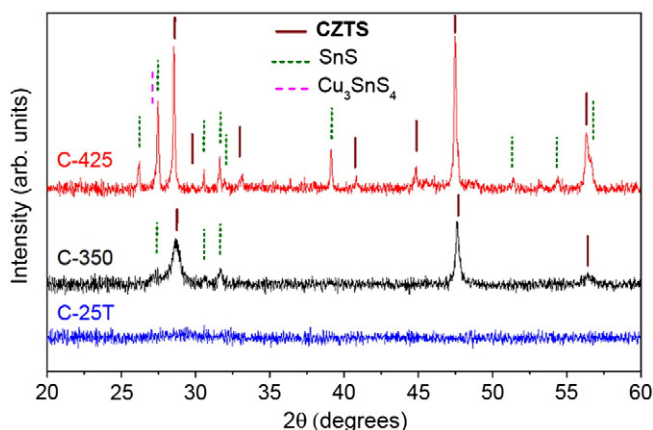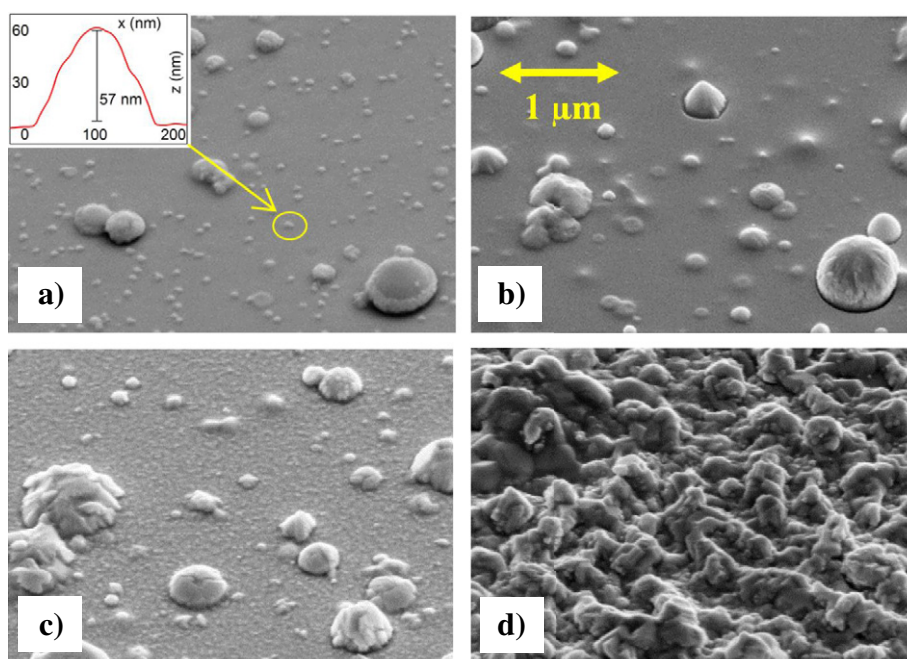
Fig. 2. SEM images of CZTS films (beam voltage: 5 kV, magnification: 50,000×) with a 45° tilt. The scale is the same in all images. a) C-25 t, where the inset graph shows an AFM scan of one of the smaller nanostructures, about 57 nm in height; b) C-25 T; and c) C-350, where a nanocrystalline grain structure becomes visible; d) C-425, where surface characteristics are completely changed.

dielectric function simpler to model. The optical model used to fit the data consists of: a mixed air-solid phase overlayer (the mix between the two being a fitting parameter), a homogeneous film, and a fused silica substrate (Fig. 4(a)). The fused silica substrate is fitted in all samples with a Sellmeier model [8]. The optical functions of the film and of the overlayer are both parameterized with a Tauc–Lorentz expression, typical of amorphous materials [9], but they are kept independent from each other. The overlayer is defined as partially
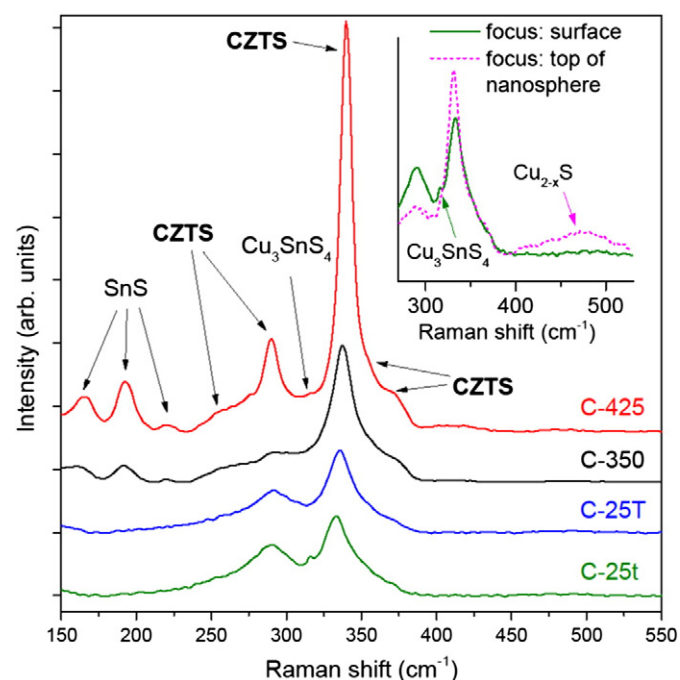
depolarizing, with the depolarization fraction being a fitting parameter. It is found that, if only the three higher incidence angles (65°, 70°, and 75°) are used, the mean square error (MSE) is twice more than that obtained if only the three lower angles are used (45°, 50°, and 55°), and it also results in generally higher correlated errors and larger deviation of the known parameters from their expected values. The same occurs if all available angles are used. Therefore, only the three lower angles are fitted (Fig. 5). The resulting topographic characteristics are shown in Table 1: they are in good agreement with the measurements from direct techniques also shown in Table 1. The surface overlayer is 53 nm thick (in good agreement with the inset in Fig. 2(a)) and consists of a mix of air (90%) and a solid phase (10%). This roughly corresponds to what is visible in the SEM image (Fig. 2(a)). The Tauc band gap of the CZTS film is 1.527 ± 0.003 eV, consistent with typical values reported in the literature [1,5]. The Tauc gap of the overlayer material is 2.07 ± 0.09 eV, which is consistent with a $Cu_{2-x}S$ phase since band gap energies between 1.7 eV and 2.7 eV have been reported for amorphous $Cu_{2-x}S$ [10,11].

3.3.3. Sample grown at 25 °C (thick)

The C-25 T sample is modeled with the same layer stack but this time the dielectric function of the CZTS film layer is a free parameter to vary without any pre-determined oscillator (Fig. 4(b)). The only physical assumptions are Kramers–Kronig consistency and an initial shape before fitting, chosen to be the Tauc–Lorentz function of sample C-25 t. This gives a large number of fitting parameters, and it is found that correlation errors and consistency with thickness and roughness measurements are minimized using five incidence angles (45°–65°). The resulting dielectric function is similar to a Tauc–Lorentz function (comparison between the two gives MSE = 0.13) with a 1.573 eV band-gap energy.

3.3.4. Sample grown at 350 °C

For the C-350 sample seven incidence angles are used and the fitting dielectric function is a free parameter to vary with the same physical assumptions as before. Besides the mixed layer, the optimal overlayer structure includes a roughness layer between the mixed layer and the film, which has a strong influence on the final MSE (Fig. 4(c)). This could physically represent the small film roughness due to

Fig. 3. Raman spectra of the four CZTS films. Phase analysis is performed based on peak position. Inset graph: two Raman spectra taken on the C-25 t sample. When the laser is focused on top of a nanosphere instead of on the film surface, a Cu_3SnS_4 peak disappears and a $Cu_{2-x}S$ peak appears.

Table 1

Topographic characteristics of CZTS films, measured with a profiler, AFM, and ellipsometry.

Sample	Film thickness [nm]		Overall roughness [nm]		Film roughness [nm]		Overlayer thickness [nm]	MSE
	Profiler	Ellipsometry	AFM	Profiler	AFM	Ellipsometry	Ellipsometry	
C-25 t	190	195	15	15	0.9	0	53	4.0
C-25 T	750	733	57	60	1.2	0	74	12.2
C-350	390	379	35	44	2.6	13	180	5.5
C-425	760	770	96	101	96	n.a.	n.a.	2.7

nanocrystallinity, as shown in Fig. 2(c) and Table 1. Despite the low MSE, the fitted thickness of the roughness layer is larger than expected from AFM and the correlation error is high, possibly because of a contribution from the smaller-sized nanospheres to this layer. The Tauc bandgap energy of the film is estimated to be 1.1 eV.

3.3.5. Sample grown at 425 °C

Modeling the surface overlayer of the C-425 sample did not give meaningful results. This is probably due to the strong depolarization effect of the rough inhomogeneous surface (Fig. 2(d)). To avoid the problem, the ellipsometry measurement was performed from the glass side of the sample (Fig. 4(d)), only fitting the spectral region above 2.2 eV where light is completely absorbed in the film and reflections from the surface overlayer are not contributing to the detected signal. Seven angles of incidence are used and the dielectric function is again fitted freely starting from the C-350 dielectric function.

3.3.6. Dielectric functions

The dielectric functions of the bulk film layer as obtained from the previous analysis are shown in Fig. 6. Those obtained for the two samples deposited at 25 °C have very similar shapes and band gap energies. This fact suggests that film thickness does not significantly influence the extracted dielectric functions of the material and the initial assumption

of a non-graded layer is confirmed. Also, since the bulk film layer was accurately modeled by a dielectric function featuring a single Tauc–Lorentz oscillator, significant contributions from phases other than CZTS are unlikely. As the deposition temperature is increased, the dielectric functions exhibit more complex dispersion due to the increased crystalline order. Unlike in amorphous materials, the selection rule of wave-vector conservation must be applied to optical absorption in crystalline solids, which gives rise to critical point structures at photon energies corresponding to singularities in the joint density of states for a specific wave vector. Absorption is enhanced in the low- or high-energy neighborhood of a critical point according to its classification [12], therefore critical points can in principle be resolved by the analysis of the imaginary part of the dielectric function $\varepsilon_2(E)$. The critical point structures we observe are similar to those reported in two other ellipsometry studies for a single-phase CZTS film [6] and for a CZTS bulk crystal [3], which in turn are in reasonable agreement with theoretical predictions [13]. The C-425 sample exhibits a rather sharp M_1 critical point [12] just below 3 eV, probably corresponding to a critical point of the same type found at 2.92 eV by [6] and at 2.82 eV by [3]. The absorption onset observed in the C-425 sample just above 4 eV may correspond to the M_0 critical point found at 3.92 eV by [6] and at 3.86 eV by [3]. In the 4.5–6.0 eV spectral region, $\varepsilon_2(E)$ in the C-425 sample has four inflection points, possibly arising from a number
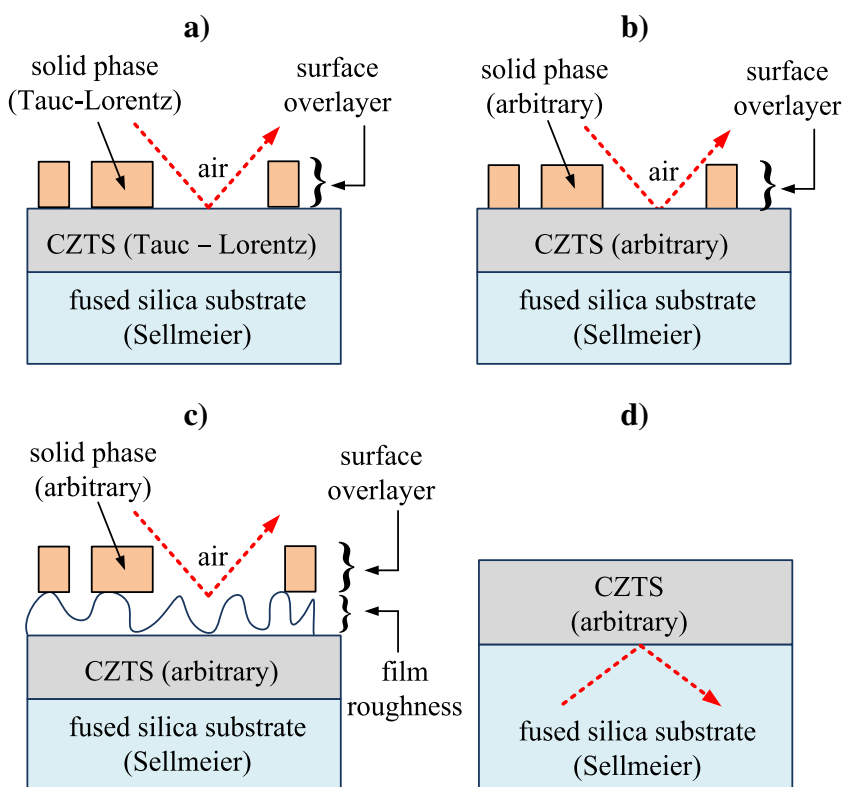

Fig. 4. Layer stacks used as optical models for fitting ellipsometry data. a) C-25 t, b) C-25 T, c) C-350, and d) C-425. The type of dielectric function used to model each layer is specified in parenthesis. The dashed red lines denote the incident and reflected light in the measurement.
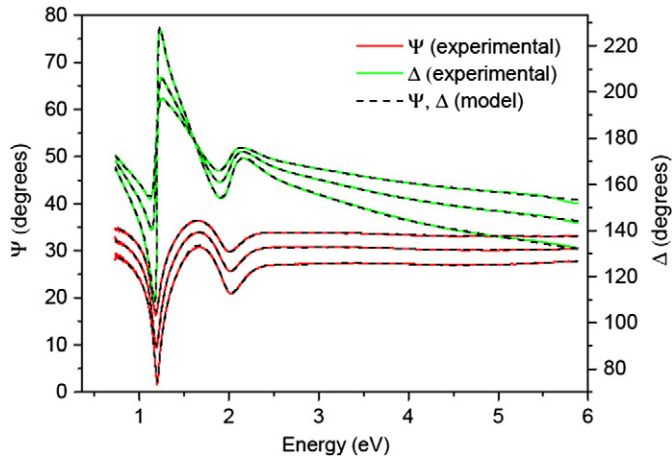
Fig. 5. Spectral magnitude (Ψ) and phase (Δ) of the ratio between p- and s-type polarization reflection coefficients, measured by ellipsometry at 45, 50 and 55° on the C-25 t sample. Solid colored lines: measured spectra. Dashed lines: fitted spectra. The MSE is 4.0.

of broad excitonic critical points as assumed in [6]. The C-350 sample is different from the C-425 sample in the following: 1) broader critical point features, 2) larger values of $\varepsilon_2(E)$ at all photon energies, and 3) red shift (by 0.3–0.5 eV) of the critical point features. The first two
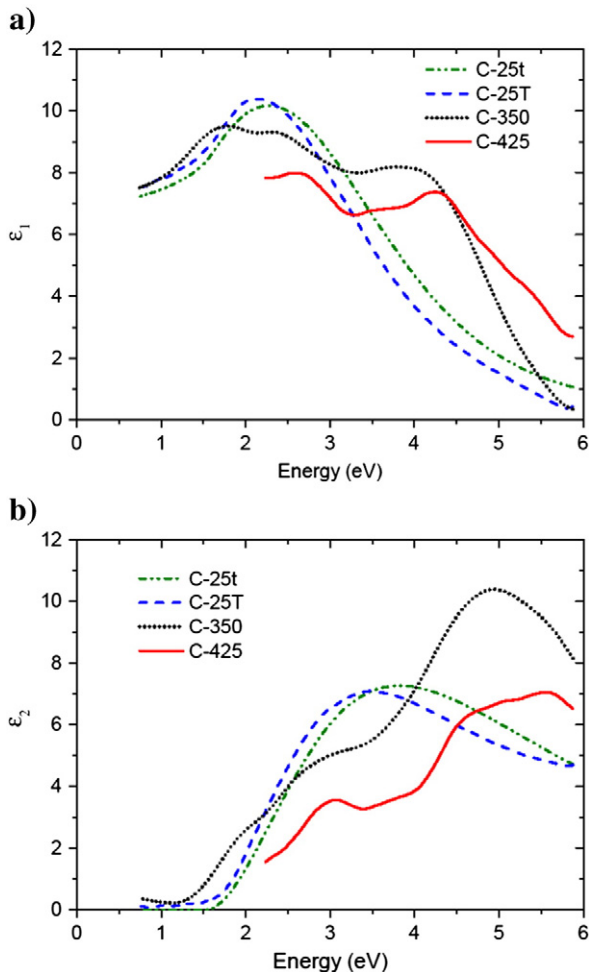

Fig. 6. a) Real part and b) imaginary parts of the dielectric functions $\varepsilon = \varepsilon_1 + i\,\varepsilon_2$ extracted by spectroscopic ellipsometry for the four CZTS films. Only the spectral region above 2.2 eV is fitted in the C-425 film due to complications arising when the surface overlayer contributes to the spectrum.

differences are probably due to the C-350 film being only partially crystallized, which partially removes the selection rule of wave-vector conservation in optical transitions. The third difference could be due to a global shift of the valence band with respect to the conduction band in the Brillouin zone, thereby shifting the characteristic energy of all optical transitions. It is difficult to estimate how much the presence of SnS and Cu_3SnS_4 in the film bulk affects the dielectric functions of the C-350 and C-425 films. Nevertheless, the critical points previously reported for single-phase CZTS have also been identified in our samples. Hence, the effect of secondary phases is not believed to be strong enough to distort the main features of CZTS dielectric functions.

4. Conclusions

Cu_2ZnSnS_4 films were deposited by PLD in a range of temperatures and thicknesses. From AFM and Raman measurements, it was found that the surface overlayer featured both a complex surface topography and a different phase mix than the underlying film, which can complicate ellipsometry data interpretation. A satisfactory model was proposed for a thin film deposited at room temperature, which was able to accurately reproduce results from topographic measurements and corroborate assumptions from phase analysis. Even though the surface overlayer in the other films is too complex to be able to identify surface phases, dielectric functions were extracted for all films with the exception of the spectral region <2.2 eV for the film deposited at 425°. The dielectric functions of two films with different thicknesses deposited at room temperature were compatible with an amorphous material with 1.5–1.6 eV band-gap energy and showed no significant thickness dependency. As the deposition temperature was increased, the dielectric functions of the films exhibited additional critical points related to strong optical transitions at specific points of the Brillouin zone. The inclusion of secondary phases in the bulk of the films did not prevent identification of critical points previously reported for CZTS.

References

[1] B. Shin, O. Gunawan, Y. Zhu, N.A. Bojarczuk, S.J. Chey, S. Guha, Thin film solar cell with 8.4% power conversion efficiency using an earth-abundant Cu_2ZnSnS_4 absorber, Prog. Photovoltaics Res. Appl. 21 (2011) 72.
[2] W. Wang, M.T. Winkler, O. Gunawan, T. Gokmen, T.K. Todorov, Y. Zhu, D. Mitzi, Device characteristics of CZTSSe thin-film solar cells with 12.6% efficiency, Adv. Energy Mater. 4 (2014) 1301465.
[3] S. Levcenko, G. Gurieva, M. Guc, A. Nateprov, Optical constants of Cu_2ZnSnS_4 bulk crystals, Mold. J. Phys. Sci. 8 (2009) 173.
[4] W. Li, K. Jiang, J. Zhang, X. Chen, Z. Hu, S. Chen, L. Sun, J. Chu, Temperature dependence of phonon modes, dielectric functions, and interband electronic transitions in Cu_2ZnSnS_4 semiconductor films, Phys. Chem. Chem. Phys. 14 (2012) 9936.
[5] L. Sun, J. He, Y. Chen, F. Yue, P. Yang, J. Chu, Comparative study on Cu_2ZnSnS_4 thin films deposited by sputtering and pulsed laser deposition from a single quaternary sulfide target, J. Cryst. Growth 361 (2012) 147.
[6] J. Li, H. Du, J. Yarbrough, A. Norman, K. Jones, G. Teeter, F.L.J. Terry, D. Levi, Spectral optical properties of Cu_2ZnSnS_4 thin film between 0.73 and 6.5 eV. Opt. Express 20 (Suppl. 2) (2012) A327.
[7] J. Alvarez-Garcia, V. Izquierdo-Roca, A. Perez-Rodriguez, Raman spectroscopy on thin films for solar cells, in: D. Abou-Ras, T. Kirchartz, U. Rau (Eds.), Advanced Characterization Techniques for Thin Film Solar Cells, Wiley-VCH Verlag, Wenheim, 2011, p. 365.
[8] H. Fujiwara, Spectroscopic Ellipsometry — Principles and Applications, Wiley, 2007.
[9] J. Tauc, R. Grigorovici, A. Vancu, Optical properties and electronic structure of amorphous germanium, Phys. Status Solidi 15 (1966) 627.
[10] S.V. Bagul, S.D. Chavhan, R. Sharma, Growth and characterization of Cu_xS (x = 1.0, 1.76, and 2.0) thin films grown by solution growth technique (SGT), J. Phys. Chem. Solids 68 (2007) 1623.
[11] F. Zhuge, X. Li, X. Gao, X. Gan, F. Zhou, Synthesis of stable amorphous Cu_2S thin film by successive ion layer adsorption and reaction method, Mater. Lett. 63 (2009) 652.
[12] C.F. Klingshirn, Semiconductor Optics, Springer-Verlag, Berlin Heidelberg, 1995.
[13] H. Zhao, C. Persson, Optical properties of $Cu(In,Ga)Se_2$ and $Cu_2ZnSn(S,Se)_4$, Thin Solid Films 519 (2011) 7508.

ZnS top layer for enhancement of the crystallinity of CZTS absorber during the annealing

Andrea Cazzaniga[1]*, Andrea Crovetto[2], Rebecca Bolt Ettlinger[1], Stela Canulescu[1], Ole Hansen[2], Nini Pryds[3]
and Jørgen Schou[1]

1)   DTU Fotonik, Technical University of Denmark, 4000 Roskilde, Denmark.

2)   DTU Nanotech, Technical University of Denmark, 2800 Kgs. Lyngby, Denmark

3)   DTU Energy, Technical University of Denmark, 4000 Roskilde, Denmark.

Abstract — **Pulsed Laser Deposition (PLD) of thin films of Cu_2ZnSnS_4 (CZTS) has not yet led to solar cells with high efficiency. The reason for the relative low efficiency is discussed and a way to overcome this issue is presented. The present thin film absorbers of CZTS suffer from loss of volatile Zn during the plasma-assisted transfer with PLD. This can be compensated by adding a thin layer of ZnS (~ 80 nm) on top of the CZTS layer before the annealing. In this work the stack ordering of the two layers CZTS and ZnS is investigated, indicating that the configuration with ZnS on top of a CZTS film gives a better crystalline quality of CZTS after the annealing, as demonstrated by X-ray diffraction and Raman spectroscopy.**

Index Terms — **kesterite materials, photovoltaic solar cells, CZTS, earth-abundant materials.**

I. INTRODUCTION

The world-scale demand for electricity supply at a Terawatt scale implies a need for an inexpensive PV technology based on earth abundant and non-toxic materials [1]. Therefore, substantial efforts are currently devoted to exploit the full potential of the absorber layer $Cu_2ZnSn(S,Se)_4$ (CZTS), which has a similar structure and similar band-gap as $Cu(In,Ga)Se_2$ and is fully made from earth-abundant materials. The record efficiency of CZTS solar cells has been greatly improved during the last few years, reaching 12.6% with a sulfo-selenide blend [2]. While these results are very encouraging, a Se-free absorber layer would be preferable since the production of selenide-based CZT(S,Se) typically involves solution-processing with the toxic and explosive hydrazine. Regarding the pure sulfide Cu_2ZnSnS_4, the record efficiency is only 8.4% [3], and the main limiting factor is a comparatively low open circuit voltage of only 661 mV for an absorber material with a bandgap of 1.5 eV. The reason for such low open circuit voltage is related to defects in the absorber layer [4] and band alignment at the interface with the CdS buffer layer [5]. Because of the complex stoichiometry, many shallow and deep defects are expected to affect the band-structure of the kesterite CZTS, of which some are associated with low formation energies of few hundreds of meV [6]. According to

Ref. [7], one finds, for the case of Cu-poor and Zn-rich stoichiometry, which is known to provide the best performing absorber layer, that the lowest energy defect is a Cu_{Zn} anti-site. This defect has an acceptor level 0.12 eV above valence band maximum (VBM). The Cu vacancy would constitute a much shallower acceptor level (at just 0.02 eV above the VBM), but has a higher formation energy between 0.6 to 0.8 eV and cannot exist under equilibrium conditions. Therefore, a non-equilibrium growth mechanism was envisaged [7] as a way to promote the formation of Cu vacancies over Cu-to-Zn anti-sites and thereby increasing the open circuit voltage. Pulsed Laser Deposition (PLD) is a highly non-equilibrium technique where intense laser pulses are directed into a vacuum chamber onto a target to induce ablation and produce a plasma plume. The plume ions and atoms are then collected onto a substrate, such that a thin film is deposited. The high kinetic energy of the deposited species (tens of eV) is known to enhance the crystallinity of the films even at modest substrate temperatures [8]. The advantage of PLD is usually that, even for complex materials, the stoichiometry from a single target is preserved in the film. Following this idea, several groups [9]-[12] have attempted to use PLD for producing CZTS films by laser ablation of a single stoichiometric target. However, due to the narrow range of stoichiometry of CZTS and the high volatility of S and Zn in vacuum, it is very difficult to obtain the desired stoichiometry from ablation of a single target. Here we suggest producing thin films of CZTS by sequential deposition of CZTS and ZnS films followed by annealing in sulfurized atmosphere. The use of a ZnS top layer has the purpose of enriching the stoichiometry of the CZTS layer up to a desired point. Furthermore, the cap layer prevents S and SnS evaporation during the first stage of the annealing, when CZTS is not yet formed.

Three different precursor configurations are investigated: one type of absorber film is produced by using only the CZTS target (sample named **"CZTS"**), one has a thin ZnS layer at the bottom of the CZTS (sample named "**ZnS/CZTS**") and the last one has a ZnS layer on top of the CZTS (sample named

"**CZTS/ZnS**"). Note that the name of the samples refers only to the precursor structure, *i.e.* before the annealing treatment. The thickness of the ZnS layer is chosen to provide an overall Zn-rich composition with a Cu/Zn ratio in the range from 1.7 to 1.9.

II. EXPERIMENTAL

Thin films of CZTS were deposited on molybdenum coated soda lime glass (SLG) under high vacuum (p <10^{-6} mbar) at a substrate temperature of 300 ^{o}C in a PLD setup, as in Fig. 1. The substrates were cleaned sequentially by ultrasonic treatment for 3 minutes in ethanol and acetone. The laser beam from a KrF excimer laser (248 nm) with a repetition rate of 13 Hz was partly focused onto a beam-spot of 2.2 mm^2 with an angle of incidence of 45° with respect to the target normal and a target-substrate distance of 40 mm. The laser fluence was set to 0.8 J/cm^{-1}, which is found to minimize droplet formation during the ablation process. The targets used are powder-sintered disks provided by PDV Products with exact stoichiometry Cu_2ZnSnS_4 and ZnS. Annealing for 10 minutes was done in a tube furnace in a N_2 and sulfur vapor atmosphere at 560° C in a graphite box placed in the hot zone of the furnace with the samples and 250 mg of sulfur powder. X-ray diffraction patterns were collected with a Bruker D8 diffractometer in Bragg-Brentano configuration in the 2-θ interval 20° to 60°. Raman fluorescence spectra were recorded at room temperature using a Raman Spectrometer (Thermo Scientific DXR Raman microscope) with a diode laser (455 nm at 0.4 mW). The signal was collected in backscattering geometry with a magnification of 100x, leading to a spot size of one micron in diameter.
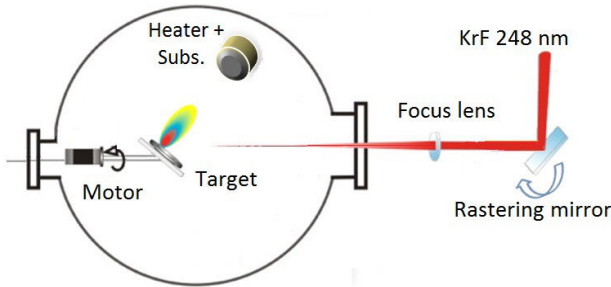

Fig. 1: Schematic of the PLD setup. The rastering mirror scans the laser onto the rotating target to assure uniformity of the ablation of the target.

III. RESULTS

The XRD patterns of the three films after annealing are shown in Fig. 2. As seen, the film produced from the stacked precursor with a ZnS top layer has more intense reflections along all its crystallographic directions, particularly along the (112) plane. Traces of Cu_2S are detected at 33.1^{o} and 44.2^{o}, as

confirmed by Raman investigations shown in Fig.3. As a matter of fact, the identification of the material as kesterite CZTS from the XRD pattern is not unambiguous. The XRD pattern of CZTS zinc-blende structure cannot be distinguished from that of the two other phases ZnS and Cu_2SnS_3. As a consequence, it is necessary to perform Raman investigations to check the formation of CZTS [12].
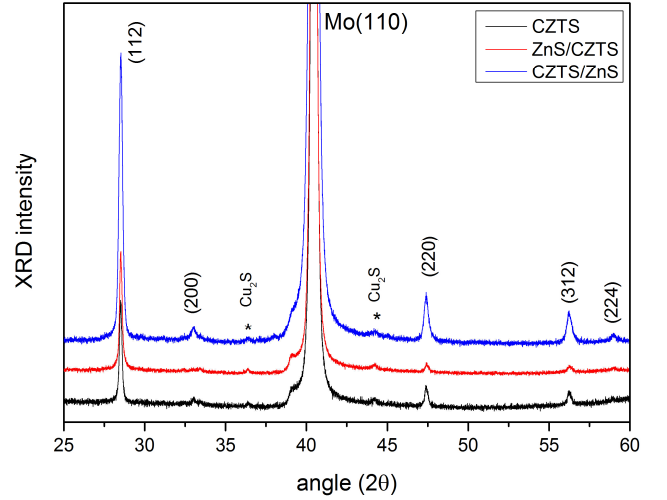
Fig.2: θ − 2θ scan of the films produced. Due to different thickness among the samples (200-250 nm for samples "CZTS" and "ZnS/CZTS", 500-550 nm for sample "CZTS/ZnS"), each pattern is normalized with respect to the main peak at 41°.

The Raman spectra are shown in Figs. 3 and 4, and the results are reproducible for different spots on each sample. As anticipated, traces of Cu_2S phase visible with the XRD are confirmed by Raman spectra, as seen in fig. 3.
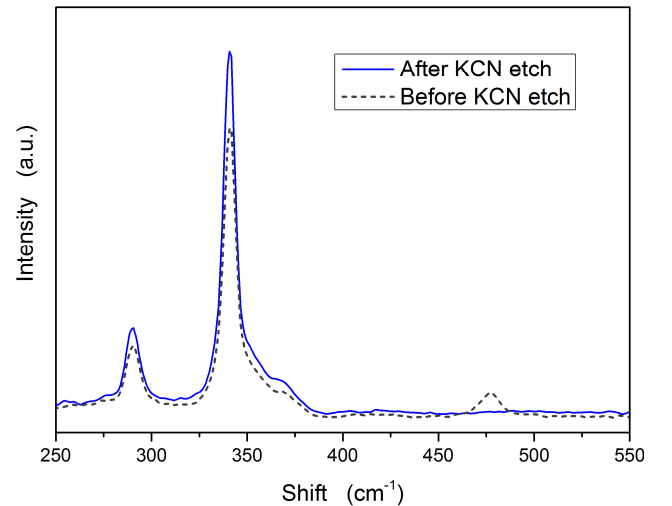
Fig.3: Raman signal of the (Mo/CZTS/ZnS) film before and after chemical etching with KCN. The peak at 478 cm^{-1} is related to Cu_2S.

Interestingly, only the sample "CZTS/ZnS" shows traces of Cu_2S under Raman investigation. Since Raman is a very surface sensitive analysis, the Cu_2S signal originates only from the surface in this sample. In the two other films we assume that Cu_2S is present mostly in the bulk. In order to remove copper-sulfide secondary phases we performed a standard KCN etching on the "CZTS/ZnS" film. As can be seen in Fig. 3, the KCN etching successfully removes the Cu_2S inclusions adjacent to the surface. In Fig. 4 we compare the Raman signals of all the samples. The samples made from the "CZTS" and "CZTS/ZnS" precursors have two well defined peaks at 287 and 337 cm^{-1}, which are unambiguously attributed to the CZTS phase [12,13]. It is also seen that the intensity of the main peak is higher for the "CZTS/ZnS". The Raman signal from the "ZnS/CZTS" is weaker, and the signal at 287 cm^{-1} can hardly be seen, as compared with the two other samples. The reason for the difference is not clear, but it is evident that, while adding ZnS is helpful for turning the stoichiometry from Cu-rich and **Zn-poor** to Cu-poor and **Zn-rich**, the effect of adding ZnS on top is not only improving the stoichiometry, but is also beneficial for crystal structure. Due to its high bandgap of more than 3 eV, ZnS is hardly visible with the excitation wavelength of 455 nm [13]. Therefore its presence as secondary phases or inclusions cannot be ruled out by our analysis. With regard to Cu_2SnS_3, which also has a phase that is not discernable from CZTS in the XRD-pattern, no sign is detected in our Raman spectra.
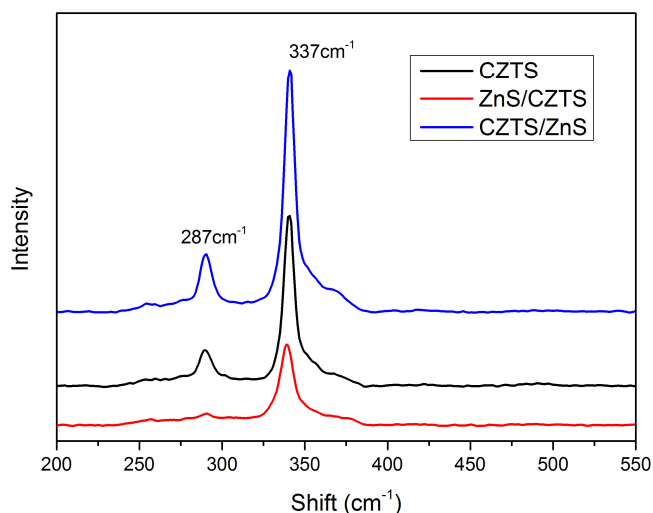

Fig.4: Comparison of Raman spectra from the three different samples. The blue line refers to the KCN etched surface.

IV. CONCLUSIONS

Films of CZTS were produced by annealing stacks of chalcogenide precursors prepared with PLD and subsequently annealed in a sulfurized atmosphere. Due to high volatility of sulfur and zinc in vacuum, the as-deposited CZTS films are under-stoichiometric in S and Zn content with respect to the target composition. In order to compensate for these losses and to obtain the desired Zn-rich stoichiometry, a layer of ZnS was added to the CZTS precursor layer. The top or bottom position of the ZnS is found to significantly affect the crystalline properties of the films after the annealing. The sample prepared with the sequence CZTS/ZnS is found to have, after the annealing, brighter reflections in the XRD pattern and is ,significantly more oriented in the (112) direction than the two other samples investigated. All the films contain grains of Cu_2S, a detrimental compound for solar cells, but for the CZTS/ZnS film, those are only located on the top surface, such that we could easily remove them with standard KCN etching. After KCN etching, no secondary phases are detected in the "CZTS/ZnS" film (apart from ZnS which is below the detection limit of our experiments). On the other hand, the film produced with the opposite ordering of the precursors "ZnS/CZTS" and the simple "CZTS" precursor, both give an inferior intensity of the XRD signal and of the Raman spectrum. More investigations are required to understand why a ZnS top layer promotes the diffusion of Cu_2S towards the top surface of the film during the annealing.

In summary, adding a layer of ZnS is not only beneficial for reaching a Cu-poor and Zn-rich composition, but the top position of this layer also leads to an enhanced crystal growth during the annealing and to confinement of Cu_2S secondary phases at the top. The PLD technique can provide us with good absorbers, if the Zn loss during the ablation is compensated. The results obtained in the present work demonstrate that the highest crystallinity is obtained with a top layer of ZnS on the CZTS layer.

REFERENCES

[1] T. Unhold and H. W. Schock, "*Non-conventional (Non-Silicon - Based) Photovoltaic Materials*", Annu. Rev. Mater. Res. 2011. 41: 297–321;

[2] W. Wang, M. Winkler, O. Gunawan, T. Gokmen, T. Todorov, Y. Zhu and D.Mitzi, "*Device Characteristics of CZTSSe Thin-Film Solar Cells with 12.6% Efficiency*", Adv. Energy Mater., 4: 1301465, 2013;

[3] B. Shin, O. Gunawan, Y. Zhu, N. Bojarczuk, S. Jay, and S. Guha, "*Thin film solar cell with 8.4% power conversion efficiency using an earth-abundant Cu2ZnSnS4 absorber*", Prog. Photovolt: Res. Appl. , 2013, 21:72–76;

[4] T. Gokmen, O. Gunawan, T. Todorov and D. Mitzi, "*Band tailing and efficiency limitation in kesterite solar cells*" Appl. Phys. Lett. 103, 103506 , 2013;

[5] R. Haight, A. Barkhouse, O. Gunawan, B. Shin, M. Hopstaken and D. Mitzi, "*Band alignment at the Cu2ZnSn(SSe)4 / CdS interface*", Appl. Phys. Lett., 98, 253502 , 2011;

[6] S. Chen, X. G. Gong, A. Walsh, and S. Wei, "*Defect physics of the kesterite thin-film solar cell absorber Cu2ZnSnS4*", Appl. Phys. Lett., 96, 021902, 2010;

[7] A. Walsh, S. Chen, S. Wei, and X. Gong, "*Kesterite Thin-Film Solar Cells: Advances in Materials Modelling of Cu2ZnSnS4*", Adv. Energy Mater., 2, 400–409, 2010;

[8] R. Eason, "*Pulsed Laser Deposition of Thin Films: Applications-Led Growth of Functional Materials*", New York, Wiley ed., 2006;

[9] K. Sekiguchi, K. Tanaka, K. Moriya, H. Uchiki, "*Epitaxial growth of Cu2ZnSnS4 thin films by pulsed laser deposition*", Phys. Stat. Sol., 3, 8, 2618– 2621, 2006;

[10] K. Moirya et al., "*Cu2ZnSnS4 thin films annealed in H2S atmosphere prepared by pulsed laser deposition*", Jap. J. of Appl. Phys., 47, 1, 602–604, 2008;

[11] A.V. Moholkar, S. Shinde, G. Agawane, S. Jo, K. Rajpure, P. Patil, C. Bhosale, J.H. Kim, "*Studies of compositional dependent CZTS thin film solar cells by pulsed laser deposition technique*", J. of All. and Comp., 544, 145–151, 20012;

[12] L. Sun, J. He, H. Kong, F. Yue, P. Yang, J. Chu, "*Structure, composition and optical properties of Cu2ZnSnS4 thin films deposited by Pulsed Laser Deposition*", Sol. En. Mat. & Solar Cells, 95, 10, 2907–2913, 2011;

[13] P. Fernandes, A. Salome' and F. Cunha, "*Growth and Raman scattering characterization of Cu2ZnSnS4 thin films*", Thin Solid Films, 517, 7, 2519–2523, 2009;

[14] M. Dimitrievska, A. Fairbrother, X. Fontané, T. Jawhari, E. Saucedo and A. Pérez-Rodríguez, "*Multi-wavelength excitation Raman scattering study of polycrystalline kesterite Cu2ZnSnS4 thin films*", Appl. Phys. Lett., 104, 2, 021901, 2014;

Synthesis of ligand-free CZTS nanoparticles via a facile hot injection route

N Mirbagheri[1], S Engberg[1], A Crovetto[2], S B Simonsen[3], O Hansen[2,4], Y M Lam[5] and J Schou[1]

[1] DTU Fotonik, Department of Photonics Engineering, Technical University of Denmark, DK-4000 Roskilde, Denmark
[2] DTU Nanotech, Department of Micro- and Nanotechnology, Technical University of Denmark, DK-2800 Kgs. Lyngby, Denmark
[3] DTU Energy, Department of Energy Conversion and Storage, Technical University of Denmark, DK-4000 Roskilde, Denmark
[4] CINF, Center for Individual Nanoparticle Functionality, Department of Physics, Technical University of Denmark, DK-2800 Kgs. Lyngby, Denmark
[5] School of Materials Science and Engineering, Nanyang Technological University, 50 Nanyang Avenue 639798, Singapore

E-mail: sleen@fotonik.dtu.dk

CrossMark

Abstract

Single-phase, ligand-free Cu_2ZnSnS_4 (CZTS) nanoparticles that can be dispersed in polar solvents are desirable for thin film solar cell fabrication, since water can be used as the solvent for the nanoparticle ink. In this work, ligand-free nanoparticles were synthesized using a simple hot injection method and the precursor concentration in the reaction medium was tuned to control the final product. The as-synthesized nanoparticles were characterized using various techniques, and were found to have a near-stoichiometric composition and a phase-pure kesterite crystal structure. No secondary phases were detected with Raman spectroscopy or scanning transmission electron microscopy energy dispersive x-ray spectroscopy. Furthermore, high resolution transmission electron microscopy showed large-sized nanoparticles with an average diameter of 23 nm $\pm$ 11 nm. This approach avoids all organic materials and toxic solvents that otherwise could hinder grain growth and limit the deposition techniques. In addition the synthesis route presented here results in nanoparticles of a large size compared to other ligand-free CZTS nanoparticles, due to the high boiling point of the solvents selected. Large particle size in CZTS nanoparticle solar cells may lead to a promising device performance. The results obtained demonstrate the suitability of the synthesized nanoparticles for application in low cost thin film solar cells.

S Online supplementary data available from stacks.iop.org/NANO/27/185603/mmedia

Keywords: CZTS, large nanoparticles, ligand-free, synthesis

(Some figures may appear in colour only in the online journal)

1. Introduction

With the growing power consumption and increase in environmental pollution caused by human activity, research and applications of alternative energy sources such as solar cells have received more attention than ever before. Among different types of solar cells, second-generation solar cells based on thin film technology have attracted considerable research effort in the last decade, mainly due to the increasing demand for earth abundant and inexpensive materials, [1, 2]. The quaternary compound of copper zinc tin sulfide, Cu_2ZnSnS_4 (CZTS), has become particularly interesting,

[3, 4]. This non-toxic compound offers a direct band gap energy of approximately 1.5 eV and a large above band edge absorption coefficient of $\sim 10^4 \, \mathrm{cm^{-1}}$, and thus has the potential to efficiently harvest solar energy, [5].

Cost-effective solar cell production not only requires the use of earth abundant materials, such as CZTS, but also needs economical fabrication processes. Fabrication processes of CZTS absorber layers can be generally classified into vacuum- and non-vacuum-based techniques. Non-vacuum processes have the advantage of low cost and high throughput compared to vacuum-based techniques [6]. The non-vacuum-based techniques follow the general solution-processing route, where an ink of some sort is deposited as a thin film, followed by a thermal treatment to obtain large grains. The ink for CZTS absorber layer formation is based on either a molecular ink or a nanoparticle ink, where the molecular inks consist of Cu–Zn–Sn–S precursor salts in the right composition, and the nanoparticle inks of small CZTS grains already crystallized into the desired phase. The molecular inks are leading in power conversion efficiency, η, ($\eta = 12.6\%$ ($\mathrm{Cu_2ZnSn(S_xSe_{1-x})_4}$ (CZTSSe) in hydrazine) [7], $\eta = 8.6\%$ ($\mathrm{Cu_2ZnSnSe_4}$ (CZTSe) in water/ethanol) [8], $\eta = 5\%$ (CZTS in water/ethanol) [9]), but the devices made from the nanoparticle inks are not far behind ($\eta = 9\%$ (CZTSSe in hexanethiol) [10], $\eta = 2.5\%$ (CZTS in toluene) [11], $\eta = 4.8\%$ (wurtzite CZTS in N, N-dimethylformamide (DMF)) [12]). The nanoparticle ink approaches have the potential to control phase formation, particle size and surface properties of the synthesized nanoparticles, [3, 13, 14]. Synthesis of CZTS nanoparticles is most commonly carried out in the organic, non-polar solvent oleylamine, [15, 16]. The resulting solution is then utilized as a nanoparticle ink for CZTS film formation using facile and cost-effective liquid coating methods such as spray coating [17], spin coating [18], and drop-casting [19]. The CZTS nanoparticles synthesized in organic, non-polar solvents bear long-chain carbon ligands as stabilizers, and are therefore hydrophobic. Hence, organic solvents, which are often expensive and toxic, are needed for the preparation of the nanoparticle ink. In addition, the stabilizers are left behind as hydrocarbon impurities in the produced CZTS film, and can act as an insulating barrier that adversely affects the efficiency of the prepared absorber layer, [3, 20, 21]. Different approaches, such as growing larger nanoparticles to minimize the surface to volume ratio of the particles [22], or exchange of the long stabilizing ligands at the surface of CZTS nanoparticles with shorter carbon chain ligands [23, 24], have been suggested to resolve this problem. However, these approaches suffer from the added complexity of the synthesis process, which eventually can affect the cost of solar cell fabrication, [3, 21].

Alternatively, the use of polar solvents for the synthesis of CZTS nanoparticles using solution-based approaches has been reported; the methods can be divided into either the solvothermal method or the hot-injection method, [25–27]. These approaches offer a facile and efficient method for the synthesis of ligand-free CZTS nanoparticles, which, in contrast to the nanoparticles capped with long hydrocarbon chains, can be dispersed in environmental-friendly polar solvents to form nanoparticle inks. For example, Kush *et al* [27] reported a simple hydrothermal synthesis of ligand-free CZTS nanoparticles (2–4 nm in diameter) in water. The nanoparticles were then used for the preparation of hydrophilic CZTS ink without employing any organic solvent. The as-prepared ink, which was reported to be stable for a week, was easily applied to a substrate to form a uniform thin film. In another work, Zaberca *et al* [26] synthesized ligand-free CZTS nanoparticles in ethylene glycol using the solvothermal method. The as-synthesized sample, composed of nanoparticles with sizes ranging from 5 to 10 nm, was used for the fabrication of low-defect, crack-free, sintered absorber layers.

When considering the device performance of pure sulfide-phase kesterite CZTS nanoparticle solar cells, the record efficiency device ($\eta = 2.5\%$) consisted of large-sized, ligand-coated nanoparticles of 60 nm, [11]. The annealing process is more challenging without selenium, and we hypothesize that larger particles are advantageous in these selenium-free devices. The best ligand-less device ($\eta = 1.94\%$) had an average particle size of 10 nm, and was made using the solvothermal method, with which it seems challenging to synthesize larger particles, [28].

Besides the hydrocarbon impurities, the elemental composition ratio of CZTS nanoparticles can significantly affect the efficiency of the fabricated CZTS absorber layer. It has previously been found that CZTS thin film solar cells with high conversion efficiency can be prepared with Cu/(Zn + Sn) and Zn/Sn composition ratios of 0.76–0.90 and 1.1–1.3, respectively, [29].

In this work, a simple and cost-effective hot injection method, inspired by the solvothermal synthesis approach, was employed for the synthesis of ligand-free CZTS nanoparticles with a larger particle size and targeted elemental composition. The influence of the amount of metal precursors on the elemental composition, phase purity, and crystalline phase composition of the synthesized nanoparticles was also investigated.

2. Experiment

2.1. Chemicals

Copper(II) chloride dihydrate ($\mathrm{CuCl_2 \cdot 2H_2O}$, 99.999%), zinc acetate ($\mathrm{Zn(OAc)_2}$, 99.99%), tin(IV) chloride pentahydrate ($\mathrm{SnCl_4 \cdot 5H_2O}$, 98%), sulfur (S, 99.98%), diethylene glycol ($\mathrm{C_4H_{10}O_3}$, DEG, 99%), and triethylenetetramine ($\mathrm{C_6H_{18}N_4}$, TETA, 97%) were purchased from Sigma Aldrich and were used without further purification. Isopropanol (99.8%) and ethanol (96%) were purchased from Merck Millipore and VWR Chemicals, respectively. Deionized (DI) water was provided from Milli-Q-Water (Millipore Corp, 18.2 $\mathrm{M\Omega \, cm^{-1}}$ at 25 °C).

2.2. Material synthesis

Synthesis of CZTS nanoparticles was performed through the hot injection method. In a typical synthesis, calculated

amounts of $CuCl_2 \cdot 2H_2O$, $Zn(OAc)_2$ and $SnCl_4 \cdot 5H_2O$ were mixed with 7 ml DEG in a round-bottom flask equipped with a reflux condenser. The reaction mixture was degassed for 20 min under stirring at room temperature and then the temperature was increased to 220 °C while purging with nitrogen. Afterwards, a solution containing 1 mmol S, 0.5 ml TETA and 1 ml DEG was quickly injected to the flask while stirring the solution (S was first dissolved in TETA and then DEG was added to this solution). The mixture was kept under stirring at 220 °C for 2 h, and thereafter the resulting mixture was allowed to naturally cool down to room temperature. The mixture was then dispersed in a solution of 10 ml DI water and 10 ml ethanol and the new mixture was transferred to a 50 ml conical centrifuge tube. After ultrasonicating the collected product at a frequency of 42 kHz for 10 min, the mixture was centrifuged at 6000 rpm for 10 min and the obtained precipitate was extracted. The precipitate was subsequently rinsed through dispersing in a solution mixture containing 5 ml DI water and 5 ml ethanol, followed by centrifuging at 6000 rpm for 10 min. This procedure showed high reproducibility for synthesis of CZTS nanoparticles.

2.3. Sample preparation

The as-synthesized CZTS nanoparticles were dispersed in a solution containing 5 ml DI water and 5 ml ethanol and ultrasonicated until a homogeneous ink was obtained. The prepared ink was deposited on a quartz or silicon substrate through a simple drop casting method, in which a drop of ink was casted over the substrate and dried with nitrogen at room temperature. This procedure was repeated three times in order to obtain a uniform and thick film of the nanoparticles on the substrate for energy dispersive x-ray spectroscopy (EDX), x-ray diffraction (XRD), Raman, and x-ray photoelectron spectroscopy (XPS) measurements.

The sample for bright-field transmission electron microscopy (TEM) and selected area diffraction (SAD) was prepared by dispersing a small amount of the synthesized nanoparticles in isopropanol using sonication for one hour. Droplets of hexane were then added to the mixture and the solution was sonicated for another 30 min. Afterwards, a droplet of the prepared ink was placed onto a Ni TEM grid with amorphous holey SiO_2 and air-dried. The sample for dark-field TEM imaging and high annular angle dark field (HAADF) scanning transmission electron microscopy (STEM) analysis was prepared by mixing the synthesized nanoparticles with droplets of hexane followed by grinding of the mixture in a ceramic mortar to obtain a fine paste. The obtained paste was then dispersed in ethanol by sonication for two hours. A droplet of the prepared suspension was added to an Au TEM grid with a holey carbon support film and air-dried.

2.4. Material characterization

The elemental composition, crystal structure and phase of the samples were determined using EDX, XRD, and Raman spectroscopy, respectively. EDX experiments were performed with an accelerating voltage of 15 kV with a Bruker Quantax 70 system integrated into a Hitachi TM3000 scanning electron microscope. The uncertainties of the elemental composition ratios given in the table 1 were calculated based on the standard deviation obtained for each element in the sample. XRD measurements were carried out in the 2θ range from 20° to 65° using a Bruker D8 Advance diffractometer at 40 kV, 40 mA using Cu K_α radiation ($\lambda = 1.5418$ Å) in Bragg–Brentano configuration, a step size of 0.01°, and a step time of 0.013 s. XRD peaks were identified manually after baseline subtraction using the program EVA and the peak patterns were matched to the relevant Joint Committee on Powder Diffraction Standards (JCPDS) files. Raman spectroscopic measurements on single spots were carried out using a DXR Raman microscope from Thermo Scientific in backscattering configuration equipped with a laser beam of wavelength 455 nm, a laser power of 0.4 mW, and a spot size of 1 μm^2. Raman line-scans were performed over a length of 32 μm with a step size of 2 μm under the same conditions as applied for single-spot measurements.

Bright-field TEM imaging and SAD were performed by using a JEM 2100 equipped with a LaB_6 source operated at 200 kV. High resolution TEM, dark-field TEM and STEM were performed in combination with EDX by using a JEM 3000F equipped with a field emission gun operated at 300 kV, a HAADF STEM detector, and an Oxford Instruments EDX detector with an ultra-thin window. The HAADF STEM analysis was performed with nominal probe size of 0.5 nm and camera length of 15 cm. From the acquired TEM images, particle sizes were measured by manually outlining the particle perimeters, using the software ImageJ and converting the measured projected particle areas to particle diameters using a circular approximation. The particle size measurement was challenged by particle agglomeration so that the particle perimeter was not always clearly defined. This problem increases with the thickness of the agglomerate, and the measurements were therefore preferentially performed at the thin regions of the agglomerates observed in bright-field TEM images. In addition, dark-field TEM images were analysed to make sure not to exclude larger particles in the thicker agglomerate regions. The measured diameters are presented in the form of particle size distributions with an optimum bin size calculated according to the work reported by Diaconis *et al* [30]. The error on the average particle size was estimated to be 13% by considering 10% TEM magnification calibration error and the error that arose from the manual determination of the single particle size.

The surface composition and oxidation state of the elements were determined using an XPS Thermo Scientific K-Alpha instrument with monochromatized Al K_α x-ray source ($h\upsilon = 1486.68$ eV). The sample surface was cleaned by a mild sputtering treatment using 200 eV Ar+ and low current settings for 5 min, and all binding energies were calibrated using the C 1s peak at 284.55 eV as a reference. The Fourier transform infrared (FTIR) measurement was carried out for powder samples, and measured in air atmosphere on a Bruker Tensor 27 spectrometer after background correction. The external quantum efficiency (EQE) was

3

Table 1. Elemental composition of a selection of samples (A–H) synthesized by changing the amount of metal precursors in the reaction medium.

Synthesized sample	Metal precursors used for synthesis (mmol)			Elemental composition determined by SEM–EDX	Cu/(Zn + Sn)	Zn/Sn
	$CuCl_2 \times 2H_2O$	$Zn(OAc)_2$	$SnCl_4 \times 5H_2O$			
A	0.50	0.40	0.25	$Cu_{2.5}Zn_{0.5}Sn_{1.0}S_{3.4}$	1.6 ± 0.2	0.54 ± 0.08
B	0.50	0.60	0.25	$Cu_{2.2}Zn_{0.9}Sn_{1.0}S_{3.0}$	1.1 ± 0.1	0.9 ± 0.1
C	0.40	0.60	0.25	$Cu_{2.0}Zn_{0.9}Sn_{1.0}S_{3.1}$	1.1 ± 0.2	0.9 ± 0.1
D	0.40	0.60	0.20	$Cu_{2.3}Zn_{1.5}Sn_{1.0}S_{4.1}$	0.9 ± 0.1	1.5 ± 0.2
E	0.40	0.45	0.20	$Cu_{2.3}Zn_{1.3}Sn_{1.0}S_{4.0}$	1.02 ± 0.09	1.3 ± 0.1
F	0.40	0.45	0.23	$Cu_{2.1}Zn_{1.1}Sn_{1.0}S_{3.6}$	1.01 ± 0.09	1.07 ± 0.09
G	0.35	0.50	0.23	$Cu_{1.9}Zn_{1.3}Sn_{1.0}S_{3.6}$	0.82 ± 0.08	1.3 ± 0.1
H	0.35	0.45	0.23	$Cu_{2.1}Zn_{1.1}Sn_{1.0}S_{3.6}$	0.95 ± 0.09	1.1 ± 0.09
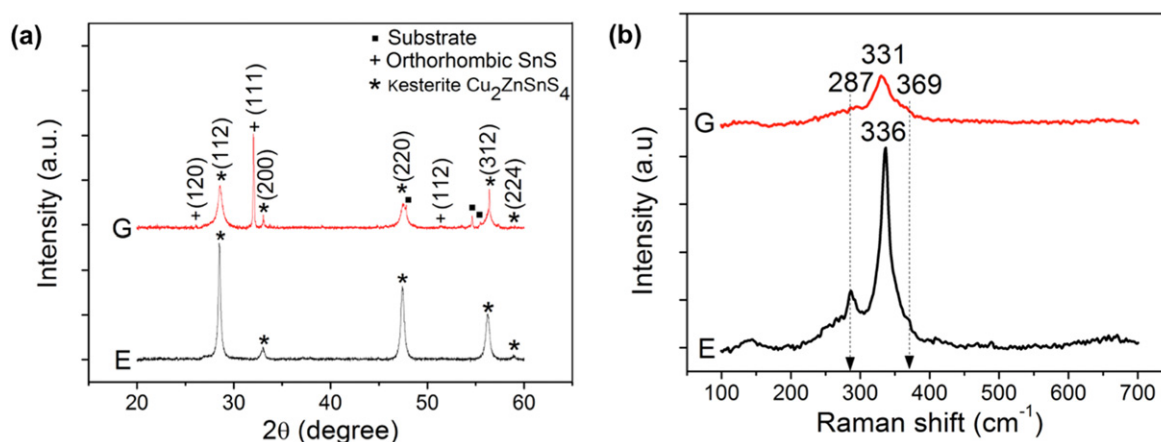
Figure 1. (a) XRD and (b) Raman spectra of sample E (black line) and sample G (red line) deposited on a silicon substrate. The characteristic CZTS Raman peaks appear at 287 and 336 cm^{-1} for sample E, whereas the main peak is shifted to 331 cm^{-1} for sample G.

measured using a homemade setup on a conventional soda lime glass/Mo/CZTS/CdS/ZnO/Al–ZnO/Al solar cell device. Light from a halogen lamp was monochromated and focused onto a 0.5 mm diameter spot on this solar cell. The output current was measured in 10 nm wavelength steps at zero voltage bias and calibrated with a standard Si photodiode to yield the quantum efficiency of the device. The absorbance spectrum was measured with a Varian Cary 50 UV–Vis spectrophotometer for liquid samples.

3. Results and discussion

Table 1 represents the elemental composition of the CZTS nanoparticles (samples A–H) synthesized from reaction mixtures containing different amounts of metal precursors. As can be seen from this table, the experimental conditions used for preparation of sample G resulted in CZTS nanoparticles with Cu/(Zn+Sn) and Zn/Sn composition ratios lying within the desired range of 0.76–0.90 and 1.1–1.3, respectively, which were previously reported as the ideal composition ratios for CZTS films with a high photovoltaic performance, [29]. However, the XRD pattern of the synthesized material (figure 1(a), red line) revealed the presence of orthorhombic

SnS secondary phase (JCPDS data file no.: 39-0354) along with the kesterite CZTS phase (JCPDS data file no.: 26-0575). The XRD measurements of all the synthesized materials in table 1 (figure 1(a) and figure S1, supplementary information), showed that only the conditions used for the synthesis of sample E resulted in the formation of nanoparticles with pure kesterite structure (figure 1(a), black line). However, it should be noted that the Cu/(Zn + Sn) composition ratio of sample E was slightly above the desired range of 0.76–0.90.

Further investigation on the phase composition of the synthesized nanoparticles was carried out using Raman spectroscopy as a complementary technique to XRD. Figure 1(b) shows the Raman spectra of the as-deposited films of samples E and G. The Raman spectrum of sample E (figure 1(b), black line) shows the CZTS characteristic Raman peaks consisting of strong peaks at 287 and 336 cm^{-1} along with a broad peak within the range of 368–373 cm^{-1}, [31]. The Raman spectrum of sample G (figure 1(b), red line) supports the formation of CZTS, though in this case the peak at 336 cm^{-1} is shifted to 331 cm^{-1}, which indicates the existence of Cu–Zn disorder within the CZTS lattice of this sample, [32]. The narrower Raman peaks observed for sample E revealed a higher crystallinity of this CZTS when compared
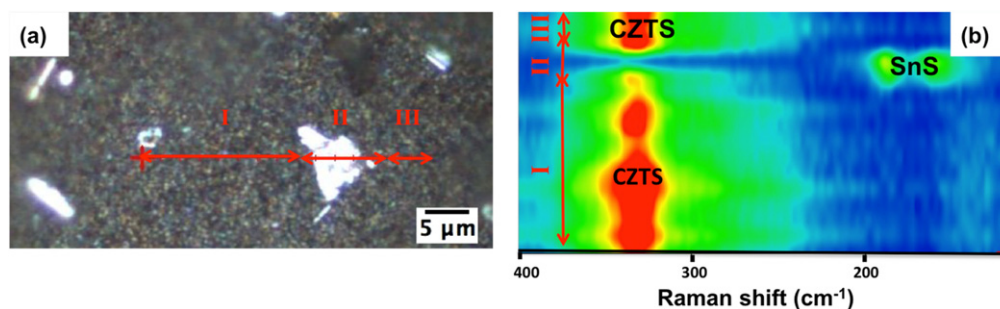
4

Figure 2. (a) Typical image of the surface of sample G showing bright regions as surface heterogeneities, and (b) the corresponding Raman map of the area indicated by red lines in (a).
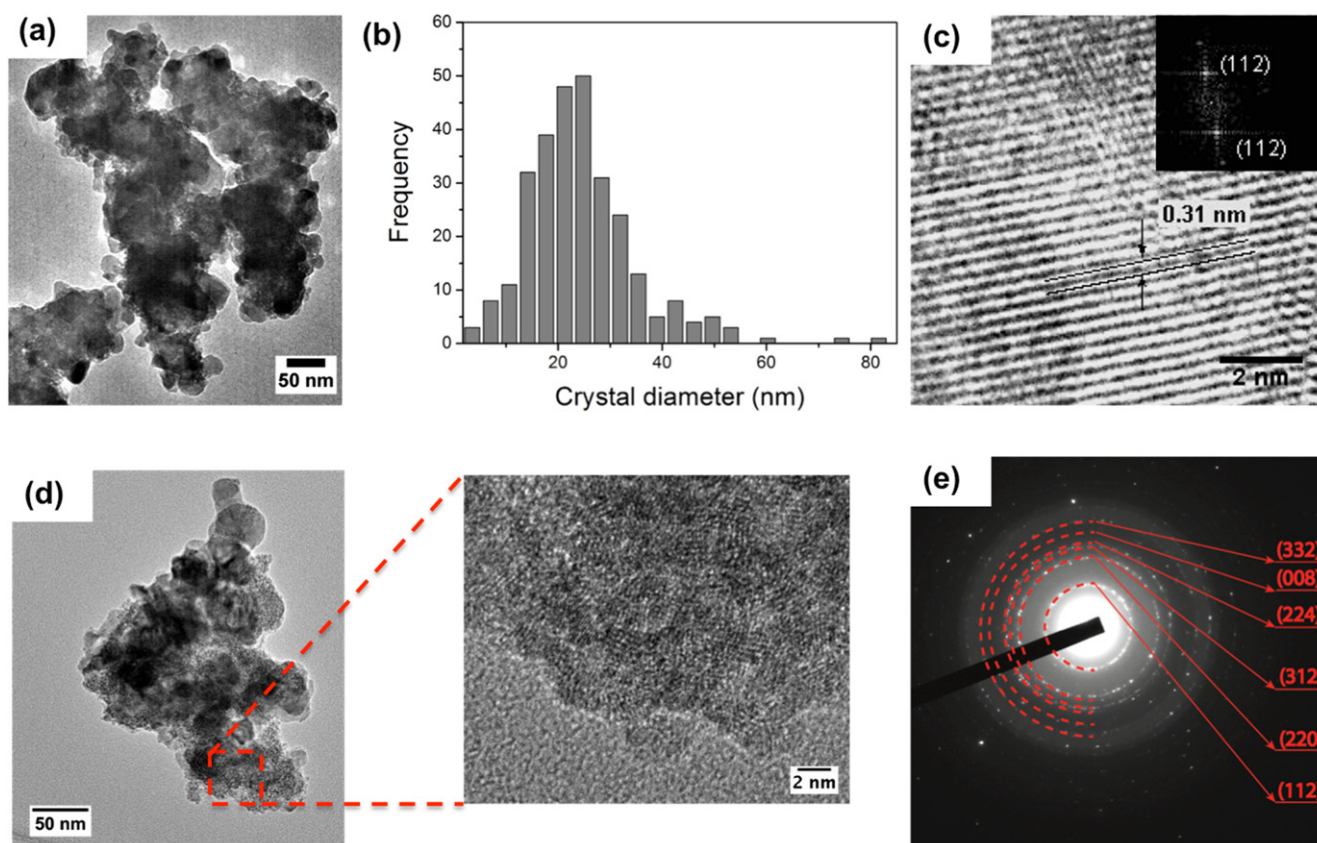

Figure 3. (a) TEM image, (b) size distribution histogram obtained for 287 nanoparticles, (c) high resolution TEM image, (d) bright-field TEM image and high resolution TEM image of the area indicated by a red square, and (e) SAD pattern of the as-synthesized CZTS nanoparticles of sample E. Inset of (c) shows a fast Fourier transform of the high resolution TEM image indicating lattice fringes that can be ascribed to the (112) plane of the kesterite.

to sample G. In addition, the Raman microscopy showed heterogeneity on the surface of sample G with a number of bright spots or faceted structures (figure 2(a)). A Raman map (figure 2(b)) of part of the sample containing these structures (indicated as region I, II, and III in figure 2(a)) showed Raman peaks corresponding to the CZTS phase in regions I and III, whereas Raman peaks consistent with the orthorhombic SnS secondary phase were obtained in region II. These data agree well with the obtained XRD patterns for samples E and G. As both the XRD and Raman measurements demonstrated the good crystalline nature of the synthesized CZTS nanoparticles of sample E, and considering the near-stoichiometric

composition obtained for this sample, we chose this sample for further chemical and optical characterization.

The morphology, crystal structure and size of nanoparticles of sample E were investigated using TEM. As can be seen in figure 3(a), the synthesized nanoparticles are irregular and have faceted morphologies with a high tendency of being aggregated. The diameter of the synthesized nanoparticles (figure 3(a) and figure S2 in supplementary information) was found to be within the range of 2.5–81.5 nm with an average particle size of 23 nm and a standard deviation of 11 nm (figure 3(b)), which is among the largest CZTS nanoparticles synthesized in organic polar solvent, [26, 28, 33–35]. To
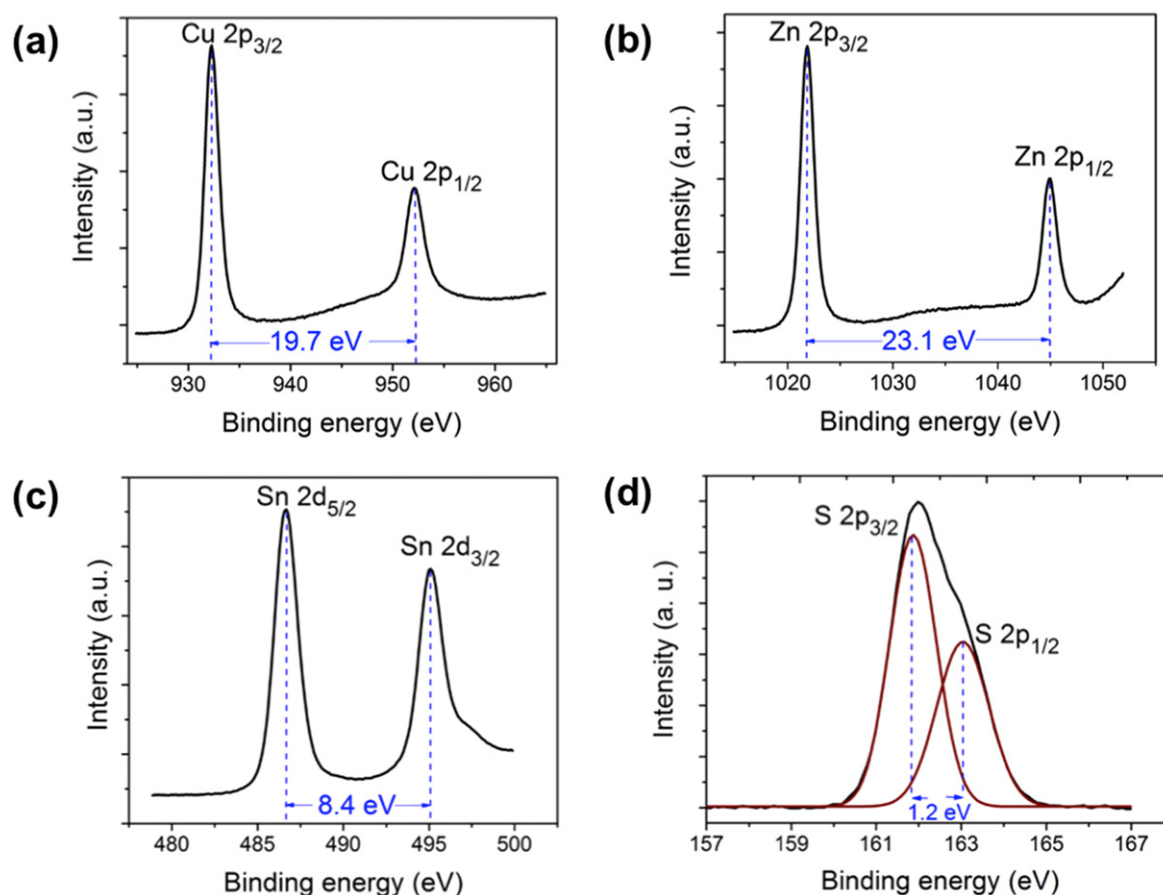
Figure 4. XPS spectra of the as-synthesized CZTS nanoparticles of sample E: (a) Cu 2p, (b) Zn 2p, (c) Sn 2d and (d) S 2p signals.

observe the full particle size range, it was necessary to record images at different magnifications. The smallest particles were for instance only observed in HRTEM images (such as the insert in figure 3(d)). It should therefore be noted, that although representative images were aimed for, the particle size distribution (figure 3(b)) will necessarily be biased by the number of recorded images at each magnification. High resolution TEM image (figure 3(c)) and the corresponding fast fourier transform pattern (figure 3(c), inset) showed lattice fringes with an inter-planar spacing of 3.1 Å, which can be ascribed to the (112) plane of the kesterite CZTS (JCPDS data file no.: 26-0575). High resolution TEM imaging also helped us to identify some parts of the sample that at lower magnifications at first sight looked like amorphous structures (the area indicated by a red square in figure 3(d)). High resolution TEM images (figure 3(d)) of these areas, however, showed that they were composed of small nanoparticles (figure 3(d), close-up). Figure 3(e) shows the SAD pattern of the synthesized nanoparticles, which also matched well with the kesterite CZTS phase and correspond to (112), (220), (312), (224), (008) and (332) planes (JCPDS data file no.: 26-0575). These data are consistent with the obtained XRD pattern of this sample and confirm the phase purity of sample E. In order to further clarify the elemental composition and distribution of the synthesized nanoparticles, the STEM–EDX elemental nanoscale mapping was conducted (figure S3,

supplementary information). The obtained elemental maps confirmed the homogeneous distribution of the four constituent elements of CZTS among the nanoparticles. In addition the obtained STEM–EDX elemental maps revealed the absence of ZnS secondary phase in sample E.

In order to identify the oxidation state of copper, zinc, tin and sulfur elements in the synthesized CZTS nanoparticles of sample E, XPS measurements were carried out on sample E (figure 4). Figure 4(a) shows the Cu 2p core level spectrum at binding energy of 932.28 and 951.98 eV corresponding to Cu $2p_{3/2}$ and $2p_{1/2}$, respectively. The absence of the satellite Cu $2p_{3/2}$ peak at 933.7 eV is indicative of the absence of Cu (II) in this sample, [36]. The peak splitting of 19.7 eV between Cu $2p_{1/2}$ and $2p_{3/2}$ peaks along with calculated Auger parameter of the copper electrons revealed that the oxidation state of copper is +1, [37, 38]. The resolved peaks in figure 4(b) at 1021.88 and 1044.98 eV with peak splitting of 23.1 eV are attributed to Zn $2p_{3/2}$ and $2p_{1/2}$ levels, respectively, and indicate the presence of Zn^{2+} in this sample, [37]. The Sn $3d_{5/2}$ and $3d_{3/2}$ core level peaks at 486.68 and 495.08 eV with peak separation of 8.4 eV demonstrate Sn is in the form of Sn^{4+} (figure 4(c)), [37]. Finally, the observed S $p_{3/2}$ and $2p_{1/2}$ peaks at 161.88 and 163.08 eV confirm the presence of S as S^{2-} (figure 4(d)), [37]. The obtained elemental oxidation states are in good agreement with the oxidation states of Cu, Zn, Sn and S in a typical CZTS nanoparticle.
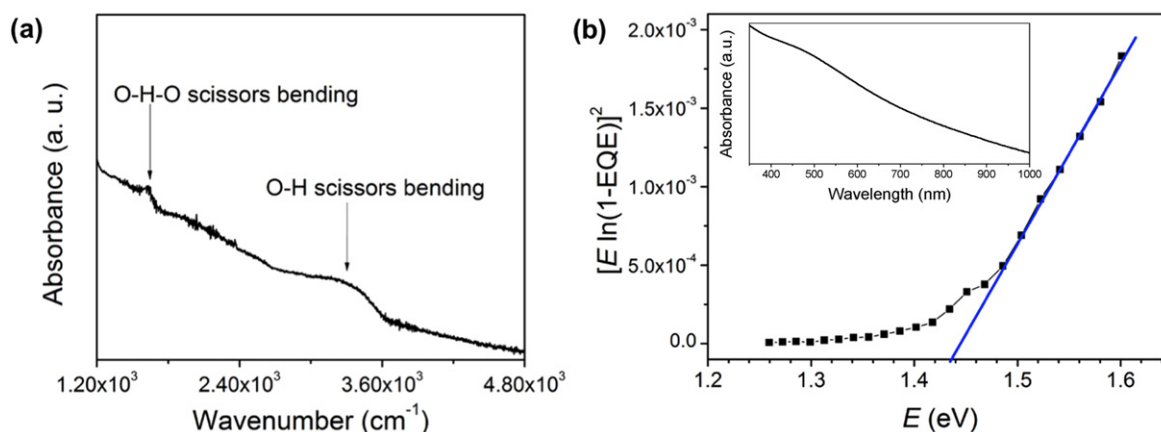
Figure 5. (a) FTIR spectrum, and (b) plot of $[E \ln (1 - \mathrm{EQE})]^2$ versus photon energy (E) of the as-synthesized CZTS nanoparticles of sample E. The band gap is determined by extrapolating the linear region of the $[E \ln (1 - \mathrm{EQE})]^2$ plot to find the intersect with the *x*-axis. The inset in (b) shows the UV–Vis spectrum.

The absence of hydrocarbon ligands (capping ligands) at the CZTS nanoparticles of sample E was confirmed by using FTIR spectroscopy, which did not show any signal in the range of $2800-3000\ \mathrm{cm}^{-1}$ corresponding to the C–H vibrational frequency of the DEG and TETA solvents (figure 5(a)). The broad band at $3000-3700\ \mathrm{cm}^{-1}$ and the band at $1635\ \mathrm{cm}^{-1}$ are attributed to the O–H stretching and O–H–O scissors bending of water molecules in the sample, respectively (figure 5(a)), [39]. The optical band gap of the CZTS nanoparticles of sample E was estimated by measuring the EQE of a fabricated CZTS thin film solar cell. Extrapolating the linear region of the plot of $[E \ln(1 - \mathrm{EQE})]^2$ versus the incident photon energy (E) [40], (figure 5(b)) indicates that the synthesized nanoparticles have a band gap of $\sim$1.44 eV. The obtained band gap is in good agreement with the previously reported optimum band gap appropriate for the fabrication of the absorber layer, [41, 42]. For the sake of completeness, we have included the absorbance spectrum of the synthesized nanoparticles (figure 5(b), inset).

the elemental composition of the synthesized nanoparticles was very close to the experimentally observed ideal composition, [29]. The as-synthesized CZTS nanoparticles can be easily dispersed in cheap, stable and environmentally friendly polar solvents, such as water, in order to prepare CZTS ink and form absorber layers without employing any predeposition treatments.

4. Conclusion

In summary, we employed a simple and cost-effective method for the synthesis of single-phase ligand-free CZTS nanoparticles with desired elemental composition in an organic polar solvent. The obtained results indicate that the as-synthesized CZTS nanoparticles have the appropriate crystalline phase, elemental oxidation state, band gap energy and particle size of the as-synthesized CZTS nanoparticles for solar cell applications. A comparison of the average size of the synthesized nanoparticles with literature data shows that the nanoparticles synthesized in this work are among the largest CZTS nanoparticles that have been synthesized in organic polar solvents. This is an important advantage of the presented synthesis method since large nanoparticles can potentially form large CZTS grains (after the annealing process), which implies that the film may possess less grain boundaries (recombination centers) per unit area. In addition,

References

[1] Bagnall D M and Boreland M 2008 *Energy Policy* **36** 4390
[2] Butler D 2008 *Nature* **454** 558
[3] Zhou H, Hsu W-C, Duan H-S, Bob B, Yang W, Song T-B, Hsu C-J and Yang Y 2013 *Energy Environ. Sci.* **6** 2822
[4] Walsh A, Chen S, Wei S-H and Gong X-G 2012 *Adv. Energy Mater.* **2** 400
[5] Ito K and Nakazawa T 1988 *Japan. J. Appl. Phys.* **27** 2094
[6] Hibberd C J, Chassaing E, Liu W, Mitzi D B, Lincot D and Tiwari A N 2010 *Prog. Photovolt.* **18** 434
[7] Wang W, Winkler M T, Gunawan O, Gokmen T, Todorov T K, Zhu Y and Mitzi D B 2014 *Adv. Energy Mater.* **4** 1301465
[8] Larramona G, Bourdais S, Jacob A, Chone C, Muto T, Cuccaro Y, Delatouche B, Moisan C, Pere D and Dennler G 2014 *J. Phys. Chem. Lett.* **5** 3763
[9] Larramona G, Bourdais S P, Jacob A, Choné C, Muto T, Cuccaro Y, Delatouche B, Moisan C, Péré D and Dennler G 2014 *RSC Adv.* **4** 14655

7

[10] Miskin C K, Yang W-C, Hages C J, Carter N J, Joglekar C S, Stach E A and Agrawal R 2015 *Prog. Photovolt.* **23** 654

[11] Mkawi E M, Ibrahim K, Ali M K M, Farrukh M A and Allam N K 2014 *Chem. Phys. Lett.* **608** 393

[12] Zhou F, Song N, Huang J, Yan C, Liu F, Sun K, Stride J A, Hao X and Green M A 2015 *J. Mater. Chem.* A **3** 23185

[13] Mitzi D B, Gunawan O, Todorov T K, Wang K and Guha S 2011 *Sol. Energy Mater. Sol. Cells* **95** 1421

[14] Rajesh G, Muthukumarasamy N, Subramanian E P, Venkatraman M R, Agilan S, Ragavendran V, Thambidurai M, Velumani S, Yi J and Velauthapillai D 2015 *Superlattices Microstruct.* **77** 305

[15] Guo Q, Ford G M, Yang W-C, Walker B C, Stach E A, Hillhouse H W and Agrawal R 2010 *J. Am. Chem. Soc.* **132** 17384

[16] Kameyama T, Osaki T, Okazaki K-I, Shibayama T, Kudo A, Kuwabata S and Torimoto T 2010 *J. Mater. Chem.* **20** 5319

[17] Carrete A, Shavel A, Fontane X, Montserrat J, Fan J, Ibanez M, Saucedo E, Perez-Rodriguez A and Cabot A 2013 *J. Am. Chem. Soc.* **135** 15982

[18] Ilari G M, Fella C M, Ziegler C, Uhl A R, Romanyuk Y E and Tiwari A N 2012 *Sol. Energy Mater. Sol. Cells* **104** 125

[19] Guo Q, Hillhouse H W and Agrawal R 2009 *J. Am. Chem. Soc.* **131** 11672

[20] Kim Y, Woo K, Kim I, Cho Y S, Jeong S and Moon J 2013 *Nanoscale* **5** 10183

[21] Azimi H, Hou Y and Brabec C J 2014 *Energy Environ. Sci.* **7** 1829

[22] Engberg S, Li Z, Lek J Y, Lam Y M and Schou J 2015 *RSC Adv.* **5** 96593

[23] van Embden J, Chesman A S R, Della Gaspera E, Duffy N W, Watkins S E and Jasieniak J J 2014 *J. Am. Chem. Soc.* **136** 5237

[24] Huang W, Li Q, Chen Y, Xia Y, Huang H, Dun C, Li Y and Carroll D L 2014 *Sol. Energy Mater. Sol. Cells* **127** 188

[25] Zaberca O, Gillorin A, Durand B and Chane-Ching J Y 2011 *J. Mater. Chem.* **21** 6483

[26] Zaberca O, Oftinger F, Chane-Ching J Y, Datas L, Lafond A, Puech P, Balocchi A, Lagarde D and Marie X 2012 *Nanotechnology* **23** 185402

[27] Kush P, Ujjain S K, Mehra N C, Jha P, Sharma R K and Deka S 2013 *ChemPhysChem* **14** 2793

[28] Tian Q, Xu X, Han L, Tang M, Zou R, Chen Z, Yu M, Yang J and Hu J 2012 *CrystEngCommun* **14** 3847

[29] Katagiri H 2015 Sulfurization of physical vapor-deposited precursor layers *Copper Zinc Tin Sulfide-Based Thin Film Solar Cells* ed K Ito (Chichester: Wiley) p 192

[30] Freedman D and Diaconis P 1981 *Z. Wahrscheinlichkeitstheor. Verwandte Geb.* **57** 453

[31] Dimitrievska M, Fairbrother A, Fontane X, Jawhari T, Izquierdo-Roca V, Saucedo E and Perez-Rodriguez A 2014 *Appl. Phys. Lett.* **104** 021901

[32] Fontane X, Izquierdo-Roca V, Saucedo E, Schorr S, Yukhymchuk V O, Valakh M Y, Perez-Rodriguez A and Morante J R 2012 *J. Alloys Compd.* **539** 190

[33] Cao M and Shen Y 2011 *J. Cryst. Growth* **318** 1117

[34] Zhou Y-L, Zhou W-H, Du Y-F, Li M and Wu S-X 2011 *Mater. Lett.* **65** 1535

[35] Flynn B, Wang W, Chang C-h and Herman G S 2012 *Phys. Status Solidi* A **209** 2186

[36] Fan J, Dai Y, Li Y, Zheng N, Guo J, Yan X and Stucky G D 2009 *J. Am. Chem. Soc.* **131** 15568

[37] Riha S C, Parkinson B A and Prieto A L 2009 *J. Am. Chem. Soc.* **131** 12054

[38] Vaccarello D, Tapley A and Ding Z 2013 *RSC Adv* **3** 3512

[39] Mojet B L, Ebbesen S D and Lefferts L 2010 *Chem. Soc. Rev.* **39** 4643

[40] Zoppi G, Forbes I, Miles R W, Dale P J, Scragg J J and Peter L M 2009 *Prog. Photovolt.: Res. Appl.* **17** 315

[41] Persson C 2010 *J. Appl. Phys.* **107** 053710

[42] Ito K 2015 An overview of CZTS-based thin-film solar cells *Copper Zinc Tin Sulfide-Based Thin Film Solar Cells* ed K Ito (Chichester: Wiley) p 29

Chapter 8

The take-home messages

All'alba vincerò. Vinceroòò. Vincerooooooò.
Giacomo Puccini, 1924

Here I want to finally formulate my PhD "thesis" in the literal meaning of the word. Actually I have more than just a single thesis but please, if you are still awake, try to resist a few minutes more, as they are definitely fewer than the famous 95 by Martin Luther.

8.1 Why is CZTS(e) worse than CIGS?

To try to answer this question, I made Table 8.1 to show the solar cell parameters of the best CIGS, CZTSe, CZTSSe, and CZTS solar cells. Because the maximum achievable solar cell parameters depend on the absorber's band gap due to the Shockley-Queisser limit, absolute values can be difficult to compare. Therefore, I also made Table 8.2. The upper part of the table shows the fraction of J_{sc}, V_{oc}, and FF achieved by those devices with respect to their Shockley-Queisser limitation. The lower part of the table shows the ratio between those fractions for different pairs of solar cells. I think the ratios shown in the lower part of the table are the most logical way of comparing one absorber to another. A ratio lower than 100% for absorber "x" versus absorber "y" means that "x" has a deficit with respect to "y".

An important note: nearly all the papers I have seen that compare CIGS with CZTS(e) or CZTS with CZTSe do not use the ratio-based approach that I propose in the lower part of Table 8.2 when comparing the voltage losses of two materials. Instead people usually look at the *difference* between the actual V_{oc} and the absorber's band gap ("V_{oc}-deficit"). The typical conclusion is that, if a material has a larger "V_{oc}-deficit" than another, it has a more serious voltage problem. I have concluded I do not like this approach for a simple reason. Ultimately, the efficiency of the solar cell is a linear function of J_{sc}, a linear function of V_{oc}, and a linear function of FF (Equation 1.9). Clear goals can be set for improvement of those three quantities, as their ultimate goal is their respective Shockley Queisser limit. Therefore, I think the highest-impact areas for improvement of the efficiency should be evaluated by looking at what fraction of those goals has been achieved by the current state-of-the-art, rather than by the offset (difference) from those goals. Take a 0.9 eV band gap material with a 0.4 eV "V_{oc}-deficit" and a 1.8 eV material with a 0.6 eV "V_{oc}-deficit". According to the common difference-based view, the first material should have less severe voltage losses than the second. However, the efficiency of the first material is only 56% of what it could be with no voltage losses. The efficiency of the second material, on the other hand, is 67% of what it could be with no voltage losses. Therefore, the difference-based method is an unjust method, because the only thing that

matters in the end - the efficiency - is proportional to the ratio between V_{oc}, J_{sc}, and FF and their physical limit - not the difference.

From Table 8.2, the most obvious pattern of CZTS(e) device parameters versus CIGS device parameters is the huge lag in open circuit voltage (69% - red bold font), as unanimously recognized by the research community. The J_{sc} and FF deficits are actually not that bad. Even though the FF deficit seems larger than the J_{sc} deficit, the maximum achievable FF is limited by the actual V_{oc} and not just by its own Shockley-Queisser limit. Therefore a considerable part of the FF deficit is simply due to the large V_{oc} deficit and will improve if V_{oc} is improved.

As explained in Section 1.3, voltage losses are related to recombination. But where? And how to mitigate it? A good strategy can be: (1) to look at E_A to identify the dominant recombination path; (2) to try and understand the materials- and/or device parameters that make that recombination path dominant; (3) once the problem is defined, try to change those parameters for the better. Let's go through this path:

1. in CZTS(e) with a low S content, E_A is very close to the bulk band gap. The residual difference is very likely to be due to the presence of tail states, from which the carriers recombine. Therefore, the dominant recombination path is likely to take place in the bulk or in the depletion region [79].

2. a feature that differentiates CZTS(e) from CIGS is the shorter carrier lifetimes in the former [45]. The diffusion length of electrons is still rather large (more than a μm) in state-of-the-art cells due to the high electron mobility [36], so J_{sc} losses are minimized. However, short lifetimes are a sign of strong recombination in the absorber and will degrade V_{oc} if recombination takes place in the bulk or in the depletion region (Equations 1.12, 1.13). The reason for shorter lifetimes in CZTS(e) is probably a higher density of deep defects in CZTS(e) with respect to CIGS. In CIGS some dangerous deep defects (such as In_{Cu}) are luckily removed from the band gap by the self-healing action of the material, which finds it energetically favorable to form the ($2V_{Cu}+In_{Cu}$) cluster instead. That cluster does not result in deep levels (Section 1.5). It is becoming more and more clear that CZTS(e) does not have such favorable self-healing capabilities. Therefore, some way to passivate those deep defects seems to be necessary.

3. since many of the deep bulk defects involve Sn [84], an option is to substitute Sn, completely or partially, with another element that does not form abundant, deep defects. This approach has given very promising results with partial substitution of Sn by Ge, which allowed a significant reduction of the V_{oc} deficit of CZTSe solar cells [193]. Another approach could be the growth of CZTS(e) under non-equilibrium conditions, where the rules for defect formation are not necessarily those given by thermodynamics. With some optimism, it might be possible to find a non-equilibrium route to synthesizing CZTS(e) without the occurrence of detrimental defects or detrimental secondary phases. However, there is a very large number of possible defects in the CZTS(e) material simply for statistical reasons. Furthermore, growth of CZTS without occurrence of detrimental secondary phases is very challenging due to the narrow stability region of CZTS(e). Another problem is the lack of predictive tools for the formation pathways of materials under non-equilibrium conditions. For these reasons, I see the non-equilibrium strategy as a lottery, where I believe that the amount of luck needed to succeed is very very high at this development stage.

A final note: the tail states themselves have been accused as the one of the main culprits for the large V_{oc} deficit in CZTS(e) solar cells. However, I do not believe them to be the major problem in CZTS(e) solar cells with a low S content. That is because it has

absorber	E_g (eV)	η (%)	J_{sc} (mA/cm^2)	V_{oc} (V)	FF (%)	n_d	$E_{A,def}$ (eV)	R_s ($\Omega\,cm^2$)
CIGS [194]	1.13	22.6	37.8	741	80.6	1.35	≈ 0	0.32
CZTSe [36]	1.0	11.6	40.6	423	67.3	1.57	<0.05	0.32
CZTSSe [18]	1.13	12.6	35.2	513	69.8	1.45	0.11	0.72
CZTS(1) [17]	1.47	9.1	20.8	701	62.5	n.a.	0.27	5.2
CZTS(2) [43]	1.45	8.4	19.5	661	65.8	1.5	0.4	4.5

Table 8.1: Device parameters of some state-of-the-art CIGS, CZTSe, CZTSSe, and CZTS solar cells. The "recombiation energy deficit" $E_{A,def}$ is defined as the difference between the absorber band gap E_g and the activation energy of the dominant recombination path E_A.

absorber	J_{sc} fraction of SQ limit achieved (%)	V_{oc} fraction of SQ limit achieved (%)	FF fraction of SQ limit achieved (%)
CIGS	87	84	93
CZTSe	84	55	79
CZTSSe	81	58	80
CZTS(1)	69	58	70
CZTS(2)	64	56	73

absorbers compared	J_{sc} mismatch (%)	V_{oc} mismatch (%)	FF mismatch (%)
CZTSSe versus CIGS	93	**69**	87
CZTS(1) versus CZTSSe	**85**	100	87
CZTS(2) versus CZTSSe	**78**	96	92
CZTS(1) versus CZTSe	**82**	106	89
CZTS(2) versus CZTSe	**75**	101	93

Table 8.2: Top part of the table: fraction of the Shockley-Queisser (SQ) limit for short circuit current, open circuit voltage, and fill factor achieved by state-of-the-art CIGS, CZTSe, CZTSSe, and CZTS solar cells. Bottom part of the table: ratios between the achieved fractions of the SQ limit ("mismatch") of different pairs of state-of-the-art CIGS, CZTSe, CZTSSe, and CZTS solar cells.

been demonstrated that it is possible to reduce the depth of the tail states in CZTSe to values very similar to the tail states in CIGS. Indeed, an offset of only 0.02 eV between the maximum of the PL peak and the optical band gap of CZTSe has been obtained in one of the best CZTSe solar cells [36], but its V_{oc} deficit is still very large: 55% with respect to the Shockley-Queisser limit (Table 8.2). Therefore I doubt that tail states (including those associated with structural disorder) are the main voltage-limiting issue of CZTSe solar cells. If I had one shot with a magic wand, I would remove the deep defects instead. If the bulk recombination problem is eventually solved, I believe that optimal grain boundary passivation will be the next challenge. Grain boundaries in CZTS(e) do not appear to be as benign as in CIGS, their behavior varies from study to study, and their physics is largely undiscovered.

8.2 Why is CZTS worse than CZTSe?

As I mentioned in the first chapter, I don't believe CZTSe will solve the problems of humanity but (pure-sulfide) CZTS might. Therefore, I want to take a specific look at why CZTS doesn't perform as well as CZTSe in solar cells. Table 8.2 yields a surprising result: the main problem of CZTS with respect to CZTSe is the short circuit current (black bold font). The fill factor is somewhat unsatisfactory and the open circuit voltage

is generally at the same level as CZTS(e) with a low S content, if not above. This may sound like a very strange conclusion for a material dominated by voltage losses, which is often accused of a larger "V_{oc} deficit" than CZTSe. However, if I convinced you with my "pro-ratio" argument in the previous section, this conclusion follows necessarily, *when CZTS is compared to CZTSe.*

An interesting situation opens up then. There are a lot of researchers trying to solve the V_{oc} problem on CZTS(e) with a low S content by working on the bulk properties of the material. This is of course also the main problem of CZTS, in absolute terms. However, if you are working on CZTS, should you focus on the same things as the CZTSe guys? My answer is: no. I think it's a much better investment to focus on the heterointerface, which in practice means finding a new buffer layer. These are the reasons:

1. E_A is always significantly lower than the band gap in CZTS solar cells with a CdS buffer layer. However, it was proven that E_A could reach a value roughly equal to the absorber's band gap minus the depth of the bulk tail states by switching to a different buffer layer [15]. This is strong evidence in favor of interface recombination as the main recombination path in CZTS solar cells with the traditional CdS buffer layer. Therefore, the CdS buffer layer is actually the limiting factor of the open circuit voltage in CZTS solar cells.

2. even though some images of epitaxial interfaces have been shown in the presence of Cd interdiffusion, the interface between CZTS and CdS is likely to be very defective due to the large lattice mismatch (7%) of the two materials. This increases the interface recombination velocity according to Equation 1.14, thus increasing J_{00} for interface recombination. Since interface recombination is the dominant recombination path, a defective interface is a factor limiting V_{oc} in the present generation of CZTS solar cells. A buffer layer material with better lattice matching with CZTS is therefore desirable.

3. as shown in Study 4.3, band gap narrowing is predicted to occur at CZTS surfaces, even though the effect is absent from CZTSe surfaces. This effect can be removed by an appropriate choice of the heterojunction partner of CZTS. While CdS fails according to theory, Zn-based buffers are expected to do the job (Study 4.3).

4. even though it seems possible to achieve a favorable CBO at the CZTS/CdS interface, interdiffusion is likely to play an important role in reaching that kind of band alignment. In particular, interdiffusion of Zn and enrichment of the interface with Zn are often documented, especially after thermal treatments that otherwise improve the interface quality [42,81]. Because ZnS is a high band gap phase with a very large spike-like CBO with CZTS, its segregation is likely to be one of the causes of the high series resistance always observed in CZTS solar cells [79].

5. as shown in Section 1.6, CZTS (more than CZTSe) is hard to dope n-type and its bands are often found to be bent upward instead of downward on bare surfaces. This means that type inversion at the heterointerface is, most likely, an issue. How can one live with this (possibly fundamental) limitation? The advantage of an inverted interface is that is quenches interface recombination of the electrons photogenerated in CZTS due to the very low hole population at the heterointerface. Therefore, CIGS solar cells can live with rather defective interfaces as long as the CBO is optimal and the heterointerface is inverted. However, CZTS probably cannot. Then, it is clear that the future of CZTS solar cell technology will depend on whether a very high-quality heterointerface can be formed. By "high-quality" I mean a low value of the interface recombination velocities of holes and electrons S_p and

S_n. This requires development of a tailored buffer layer material. Another option would be development of a proper chemical etch to modify the surface properties, or other kinds of surface modifications. For example, KCN etching has been shown to promote inversion in CZTS [168].

6. in the best CZTS solar cells with a CdS buffer layer, the buffer layer is always at least twice as thick as in the best CZTS(e) solar cells [18, 36]. Therefore, the buffer layer has a large impact on the current deficit just because of parasitic light absorption. This is clearly seen by comparing the EQE of CZTS- and CZTSe solar cells in the short wavelength region. Therefore, a higher band gap buffer material would have a higher impact in CZTS solar cells than in CZTSe solar cells.

7. finally, I would like to draw some attention to the strange empirical result that the CdS layer must be about twice as thick in CZTS solar cells than in CZTSe solar cells. Of course, one reason is that CZTS generally has a rougher morphology, so a thicker layer may be necessary to coat it. I do not believe in this explanation, though. I have looked at a number of CdS films on CZTS and I would be surprised to see that 25 nm of properly deposited CdS are not enough to completely coat a CZTS film. To find an alternative explanation, I would like to refer back to the role of the buffer layer in Section 1.4. One of the roles identified there was that a sufficiently thick CdS layer decreased the electric field between the heterointerface and the n-type layers due to the more gradual band bending. The lower field resulted in less tunneling-enhanced recombination [115]. How does this relate to kesterite solar cells? CZTS is limited by interface recombination but CZTSe is not, so tunneling effects can be probably tolerated more in CZTSe because they do not belong to the dominant recombination path. A thicker CdS layer in CZTS may therefore be necessary to keep the electric field low enough in order for interface recombination not to be even more devastating (through tunneling effects) than it already is. Note that predominance of tunneling-enhanced interface recombination in CZTS solar cells was already inferred by device simulation work [195].

Once an appropriate buffer layer is found and the main recombination path is shifted to the bulk, I expect that the main problem will be the combination of: (i) higher density of expected mid-gap defects in CZTS than in CZTSe, and (ii) deeper tail states in CZTS compared to CZTSe. Problem (i) seems to be about as severe in CZTS as in CZTSe because their electron lifetimes are often measured to be similar (Section 1.6). Problem (ii) is certainly more severe in CZTS than in CZTSe, as the tail states in CZTS are deeper (Section 1.6). As mentioned in Section 1.3, the density of defect clusters has already been correlated to the V_{oc} and FF of CZTS devices. I am convinced that further decreasing that density of defect clusters will be one of the keys to V_{oc} improvement in CZTS solar cells after a proper buffer layer material has been found. That should both improve E_A, hopefully up to a value very close to the CZTS band gap, and decrease tunneling-enhanced interface recombination of the CZTS side, which is favored by the large density of those tail states through which tunneling can occur.

8.3 On the future of pulsed laser deposition of CZTS

Now a few words about the deposition technique used for CZTS in this research project. I am confident that even the most dedicated advocate of PLD will agree with me (and with my colleague Andrea Cazzaniga, who just wrote a whole thesis about it [192]) that the industrial future of CZTS does not belong to PLD. However, mass production and fundamental understanding are two very different things. If PLD is not appropriate for

the former, can it contribute to the latter? To better phrase the question: can PLD do something that other deposition techniques cannot do? As long as the fabrication method of CZTS consists of deposition of nearly amorphous precursors followed by annealing in a S-containing atmosphere, I don't see great advantages, as most of the action occurs in the annealing furnace. However, if non-equilibrium methods should ever be explored for deposition of CZTS, PLD might be one of the best methods available. While there are other plasma-assisted deposition methods where film growth occurs under non-thermal conditions, PLD has the advantage that the energetic species in the plasma reach the substrate with a narrow energy range [196]. This is very different from, say, sputtering, where the energy of the species has a broad distribution. With sputtering, some species may hit the growing film with thermal energies and other species may carry kinetic energies in excess of several hundred eV [197]. Therefore, PLD offers better control over the degree of non-equilibrium. A problem related to PLD is the deposition of large "droplets" in parallel with gradual film growth. As shown in Study 6.2, those droplets are often Cu-rich, which means that they probably contain harmful phases for CZTS solar cells as discussed in Section 1.4. Perhaps even more importantly, I do not know of any successful attempt so far at growing CZTS(e) with a non-equilibrium technique without a subsequent (thermal) annealing step.

8.4   Finding the perfect materials for photovoltaics

Even the king of silicon solar cells Martin Green states in 2016 that *"it is inconceivable, to this author at least, that standard silicon modules, even when developed to their full potential, represent the ultimate photovoltaic solution"* [5]. As mentioned in Chapter 1, the solar cell materials are not the major part of the investment in a solar plant project. Therefore, the future of solar cells probably lies in efficiency increase rather than in cost reductions. Besides that, even silicon does have some issues when used in solar cells: it has a slightly lower efficiency limit than direct-band gap materials, it is constrained to rigid modules and it requires very high temperatures and a high energy cost in the production phase. It seems then as if the "perfect material" for photovoltaics is yet to be found, or at least yet to be developed to its full potential.

An important question is: should there be any preference for materials in a certain band gap range? If the material is to be used as the only absorber in a in single-junction solar cell, the highest efficiency can be achieved with band gaps in the 1.1-1.5 eV range. However, there are already many contenders to the throne of silicon in single-junction solar cells. Even if a better material could be found and developed to perfection, any improvement to the current (Si-based) state-of-the-art is not going to be a revolutionary step, simply because the state-of-the-art is already very close to the maximum efficiency theoretically achievable and Si solar cell costs are already very low.

The situation is very different for higher band gap materials. Photovoltaic materials in the 1.6-2.0 eV range used in a tandem solar cell architecture together with Si boost the maximum theoretical solar cell efficiency from 29% to 43% [5]. However, there is a lack of reasonably cheap materials with a good photovoltaic performance in the 1.6-2.0 eV range. The implications of finding a good high-band gap photovoltaic material are not limited to photovoltaics itself but may have crucial roles in other energy applications. For example, the much-researched water splitting reaction into hydrogen and oxygen is presently limited by the lack of an appropriate semiconductor that can output a relatively high photovoltage. If a single material is used to drive the reaction, the ideal band gap of such a material is about 2.2 eV. If a tandem architecture is employed, silicon would be a good choice in combination with a 1.8-2.0 eV thin film absorber material; such a device should then be coupled with efficient catalysts for hydrogen and oxygen evolution [198].

The development of high-band gap semiconductors with advantageous photovoltaic properties is therefore of crucial technological importance, but currently available materials cannot compare with the performance level and cost effectiveness reached by silicon in the lower band gap range. We then face the extremely-scientifically-exciting prospect that such materials are yet to be discovered and brought to glory. How can we find the perfect materials though? My belief is that the relatively young field of computational materials science can be of great help. Unfortunately, I have the impression that a long list of people in the experimental sciences are still very suspicious about the results of those atomistic simulations. Some reasons behind "computational atheism" may be (i) feelings rather than facts, (ii) incomplete understanding of what the calculation hypotheses are and what results can be used for, or (iii) belief in their poor accuracy, even though quantities that used to be determined inaccurately ten years ago might be determined with fantastic accuracy now.

Despite being an experimentalist myself I want to note that, within the results of this thesis, first-principles calculations allowed physical understanding of the double absorption onset in Cu_2SnS_3 and prediction of a surface state in CZTS, but not in CZTSe, which might be responsible for the interface losses of CZTS. Another striking success of calculations over experiment was the prediction of a 1.0 eV band gap for CZTSe [21, 199], at a time when experimentalists were still scratching their head over measured values lying anywhere between 1.0 and 1.5 eV. Ironically, it is precisely the quantities that used to be predicted with huge errors (band gaps and similar non-ground state properties) that can now (in some cases) be calculated with even better accuracy than actual measurements. Such a high accuracy comes of course with large computational costs, as discussed in Study 6.1. However, the situation cannot but improve, simply because of the steady increase in computational power available out there.

I think a next big step for computational materials science is to provide experimentalists with its best guess as to which new, undiscovered photovoltaic materials should work well in solar cells. While the concept of "materials-by-design" has been around for a while, it has not been widely applied to photovoltaic materials. I suspect the reason is the historical inaccuracy in the prediction of band gaps and the non-trivial issue of deciding the screening criteria. Clearly, the "obvious" selection criteria for new thin-film photovoltaic materials (optimal band gap and high absorption coefficient) are certainly a necessary condition for the success of a new material, but, even more certainly, not sufficient. The example of CZTS shows how many things can go wrong: deep defects, detrimental secondary phases, defect compensation, non-optimal device structure, defective interfaces and so on. Despite such an intricate puzzle, here is where I have found the area of photovoltaics that interests me the most. I would like to help computational material scientists define both a prioritized list of material properties to be checked in screening algorithms and the acceptable error in the determination of those properties. Then I would like to try and synthesize the most promising materials, fabricate a "minimal solar cell example" out of them, and identify their main problems. I believe that the increasingly predictive character of first-principles calculations will ultimately be the most effective method in finding suitable candidates for the materials that will solve our energy problems.

8.5   A message to CZTS

Sorry to say that, dear CZTS, but you really have some massive recombination problems. I don't know if, with all possible efforts, you are going to reach 25% efficiency. I sincerely hope you will surprise all of us. Don't take it personally if some of your former fans should betray you and replace you with some never-heard-of absorber material that is impossible to pronounce. You have forced us to really try hard and understand what is wrong with you. The good news is: after all the hard time you gave us, now we can probably spot all the flaws of those new materials right away. For now, it looks like IBM can, at least [200]. Amen.

Appendix A

Establishing a CZTS solar cell fabrication process flow at the Technical University of Denmark

Some blame the management some the employees
And everybody knows it's the Industrial Disease
Dire Straits, 1982

I recently read somewhere that a famous psychologist published his "CV of failures" showing all the positions he applied for and didn't get, all the exams he failed and stuff like that. I loved it. I then did some more research as I wanted to include it somehow in this chapter, and the thing turned out to be inspired by an article in *Nature* [201]. Not bad. On the one hand, my warped European mind makes it tempting to label the advertisement of this kind of things as typical American rhetoric in the lines of "you have to fail to succeed". On the other hand, it is also true that many European minds have given up on dreaming and are just looking for excuses to criticize.

So, now that I am done presenting the tip of the iceberg of my work, I would like to briefly present the remaining two and a half years, in which I did not produce anything of scientific interest. However, if anybody new to the field should ever read this chapter, I do not exclude that some time will be saved out there. Therefore, ladies and gentlemen, I shall now announce the coming of the PhD failures, or at least of the not so scientifically interesting work - strategically placed in an appendix. Welcome.

As mentioned earlier in this thesis, there was no previous experience at DTU or in the country of Denmark on chalcogenide solar cells (CZTS, CIGS or CdTe). The people who arranged the CHALSOL research project were specialists in the physics of PLD and in the deposition/characterization of some materials by PLD, combined with one extra guy (who happens to be my supervisor) expert in Si-based semiconductor devices. Therefore, the four PhD students employed in this project had to figure out nearly all by themselves. In my case, I had to establish a process flow that included all the layers in the CZTS device stack excluding CZTS itself. This is ordinary business for groups who are already working on chalcogenide solar cells, but in my case it took about two years of work.

A.1 Mo back contact

After reading a classic paper on sputtered Mo for CIGS solar cells [145] plus some trial-and-error development, I ended up depositing the baseline Mo back contact by DC sputtering in the form of a bilayer. Before actually depositing the film, I would clean a 10×10 cm^2 SLG substrate in acetone in an ultrasonic bath, dry it with N$_2$ and then load it into the

sputtering chamber. The first layer, in contact with the SLG substrate, would be deposited at a pressure of 10 mTorr. This layer is needed to achieve good adhesion with the glass due to the low stress and high porosity of Mo deposited at high pressure. However, the resistivity of such a Mo film is much higher (about one order of magnitude) than when sputtered at a lower pressure. Therefore, I would deposit the second layer at a pressure of 3 mTorr to achieve a low sheet resistance (about 0.5 Ω/sq for the double layer) without sacrificing adhesion. After film deposition, I would cut the glass/Mo substrate into small chips (usually 1.5×3 cm^2) from the glass side with a programmable saw with a diamond blade. This is the maximum size that can be processed in the PLD chamber used for deposition of CZTS precursors.

Note: at an earlier stage I would deposit the second layer at an even lower pressure (1 mTorr) to achieve an even lower sheet resistance. However, such Mo films would often delaminate from the glass substrate upon annealing of CZTS, so I switched to 3 mTorr and Mo delamination never occurred again. Note, however, that CZTS delamination from Mo is still an issue in our baseline solar cell fabrication process, and a possible solution will be proposed later.

A.2 CdS buffer

After deposition of CZTS on one of the glass/Mo chips (either by PLD or by nanoparticle-based methods) and subsequent annealing in a S-containing atmosphere, I would pick up the annealed films by the annealing furnace and dip them in DI water immediately after breaking the vacuum in the furnace. A DI water treatment is believed to be beneficial for CZTS surfaces [202,203]. It looks like oxidation of CZTS passivates its grain boundaries by formation of a benign oxide phase (Section 1.4 and [121]) and also passivates a detrimental NaS$_2$ surface phase [203] that impedes growth of a high-quality CdS layer. With the samples still dipped in water, I would walk to a chemistry lab. There an oil bath had been pre-heated to 80°C and the precursors of the CBD solution had been prepared. I use the same chemicals and concentrations as the baseline CdS recipe at NREL [115]. I would make the CBD solution by mixing the chemicals in a beaker at room temperature under mild magnetic stirring, fix the CZTS samples using plastic clamps, dip them into the solution, and dip the beaker with the continuously stirred solution and the samples into the oil bath. The equilibrium temperature of the solution in the oil bath is about 60°C, and a 100 nm film is achieved after about 20 minutes. I would then rinse the films in DI water, remove CdS from the back side of the glass with diluted HCl, and dry the samples in N$_2$. The choice of a relatively low deposition temperature was based on the results of the B.Sc. thesis of Tobias Mouritzen, who observed that the density of unwanted colloidal precipitate in the CdS films decreased (at constant film thickness) by decreasing the deposition temperature. Tobias also related the density of the precipitate to stirring speed and sample position in the solution, so those factors were also optimized accordingly.

I want to make a final point. In the chemical bath deposition technique, explained very well in a reference book [111], the type of substrate is extremely important, because a film will only form on a substrate if it is energetically favorable to do so. The energy required to form a film depends on the details of the interaction between the species in the solution and the substrate, so the material present on the substrate surface can to a great extent determine what the film will look like, or if there will be any film at all. For this reason, I strongly discourage anyone from optimizing a CBD process on a substrate that is not the substrate to be used in the actual device fabrication process. I have observed, both when depositing CdS and CeO$_2$ by CBD, that bare glass substrates are more difficult to coat than metal substrates (a Mo film on glass), oxides (ZnO:Al or In$_2$O$_3$:Sn films on glass) or CZTS itself. In all the mentioned cases, I could see clear differences in the deposition rate,

coverage, pinhole density, grain size, and precipitate density depending on the substrate. Therefore, if the goal is to deposit CdS on CZTS, I suggest using CZTS as a substrate in test deposition runs.

A.3 ZnO/ZnO:Al window

While it didn't take a very long learning curve to grow Mo, CdS, and ZnO films of *reasonable* quality in the beginning of my PhD project, I spent the whole first year of my PhD project trying to sputter ZnO:Al films of comparable quality to typical films reported in the literature with no success. I was aiming roughly for sheet resistance below 50 Ω/sq and optical transmission above 80%. These first attempts were one failure after another. I could never get a film below 2 kΩ/sq at thicknesses around 100 nm. On top of that, I could not obtain films with at least somewhat reproducible electrical properties. Running exactly the same deposition recipe one week later would often result in films with a sheet resistance that differed by three orders of magnitude with respect to the original. After one year and almost one hundred attempted processes I decided to give up and look elsewhere. Our project partners referred me to a senior researcher called Eugen Stamate, whom I shall thank extensively later on in the Acknowledgments. I described my needs to Eugen - substrate heating, Ar and O_2 gas supplies, and a shutter - and he found the necessary parts in one of his labs called "the magic room". He gave me a crash course on vacuum systems for dummies, and I assembled the setup under his guidance. At the second test deposition run, the films were already below 100 Ω/sq with good optical transmission. I played a bit with substrate temperature, moved from a DC to an RF power supply, and noticed that there was still room for improvement. The rest of the optimization was the result of the systematic work done by M.Sc. student Tobias Ottsen. Now the standard films used in our baseline solar cell fabrication process are about 200 nm thick and have a sheet resistance of about 15-20 Ω/sq when deposited on fused silica glass, with transmission above 80%. As discusses in Study 5.1, the electrical properties of ZnO:Al depend quite strongly on the position of the substrate with respect to the magnetron axis in our setup. However, because of the small substrate size allowed in the pulsed laser deposition setup, this is not really a problem, as the substrates can be placed in the region where the best electrical properties are achieved.

What was wrong with the initial sputtering setup? I can name two things that were very different from the current setup assembled with Eugen. (i) the original setup contained six cathodes, each of which contained a target of a different material. As the setup was shared between many users, all targets were replaced on a weekly basis according to the users' wishes. (ii) the target-substrate distance was 16 cm, compared to about 3 cm in the current setup. Typical distances used by other groups for ZnO:Al are in the 3-8 cm range. My guess is that the electrical properties of ZnO:Al films deposited with the original setup were not optimal due to the presence of a number of other previously deposited materials on the chamber's walls, plus the other sputtering targets. Unfortunately some elements, most notably N, result in acceptor defects in ZnO [204] and their inclusion in the growing ZnO:Al film (due to degassing, resputtering or other effects) would most likely decrease its n-type conductivity. Due to the large target-substrate distance, the deposition rate was very low and I speculate that this contributed to an unacceptably high volume density of those impurities in the growing ZnO:Al films. This can also explain why the electrical properties were not reproducible, as the impurity content of the ZnO:Al films probably depended on the recent history of the chamber.

Going back to the current baseline solar cell fabrication process, the (weakly-doped) ZnO layer in our devices actually also contains Al, as it is deposited from the same ZnO/Al_2O_3 target as the ZnO:Al films. However, its sheet resistance is much higher

than in the ZnO:Al layer, because a fraction of O_2 would be intentionally added to the background Ar gas during the sputtering process. It was found by M.Sc. student Tobias Ottsen that 10% O_2 in Ar is sufficient to obtain a sheet resistance that is too high to be measured with a standard setup (more than hundreds MΩ/sq) when the substrate is kept at room temperature at a deposition pressure of 5 mTorr. After deposition of the resistive ZnO layer, the target would be sputtered for 50 min in pure Ar with the shutter closed. This would restore the conditions where highly conductive ZnO:Al films can be produced. The subsequent deposition process of the lateral transport ZnO:Al layer would be carried out still at 5 mTorr and at substrate temperature of 150°C.

A.4 Back-end processing

By this point in the process flow, many chips would have been cut in smaller pieces for different reasons, and mostly because the low throughput of PLD forced us to use the few films we had both to make devices and to do fundamental characterization. Also, relatively steep compositional gradients were obtained by PLD in different areas of the chips. Taking all this into account, it seemed unrealistic to settle on a fixed solar cell size and therefore I never designed a shadow mask to evaporate a properly dimensioned contact grid. Instead, I designed a shadow mask with many small dots (around 1 mm in diameter), so that I could evaporate many dot contacts onto the chips, use one of them for each solar cell as a simple front contact, and have some flexibility in defining the solar cell areas wherever I wanted. Those dot contacts would be deposited by evaporating 1 μm Al through the shadow mask. A part of this strategy is the measurement of a PL intensity map on the whole chip before depositing the dot contacts, in order to identify which areas of the chip were the most promising and depositing the contacts accordingly. Indeed, very large gradients in PL intensity would often occur, as will be shown in a later figure.

After deposition of the dot contacts, I would define the solar cell areas by scribing sharp lines with a knife, which would ideally remove all the layers except for Mo/MoS$_2$. Here the choice of the knife was important, as I found that knives with a very thin blade would often result in device shunting. Making electrical contact with the metal back contact is not as straightforward in thin-film solar cells as in wafer-based solar cells where the substrate *is* the solar cell and the back and front contact are simply the back and the front side of the wafer. In thin film solar cells, both the front and the back contact are on the front side of the glass substrate. The problem is how to access the back contact. What most people (including myself) seem to do is to scratch all layers off with a knife somewhere outside the solar cell areas, and expose the back contact. However, while all layers from CZTS upward are easily removed with this method, the MoS$_2$ layer adheres well to Mo. Because MoS$_2$ is a semiconductor and not a metal, it is advantageous to remove it to obtain a low-resistance contact. In practice this can be done by welding, or alternatively by sanding the MoS$_2$ off by hand with some abrasive material, in the hope that the underlying Mo layer will be spared in some spots. Coating the resulting mess with silver paste gives reasonable hope that a direct Ag-Mo contact is formed somewhere. Many of our earlier solar cells had a very high series resistance, and now I am guessing it was because I was not aware of the problem of the MoS$_2$ layer and would simply contact the exposed Mo/MoS$_2$ bilayer after scracthing off the other layers.

A.5 Why are our in-house CZTS solar cells worse than state-of-the-art CZTS solar cells?

In Table A.1 I show some device parameters of the following solar cells: (i) our best "in-house" solar cell by PLD, with all process steps carried out at DTU; (ii) our best solar cell

solar cell	η	J_{sc}	V_{oc}	FF	n_d	R_s	R_{sh}	t_{CZTS}	t_{CdS}	t_{ZnO}
	%	mA/cm^2	V	%		$\Omega\,$cm^2	$\Omega\,$cm^2	nm	nm	nm
in-house	2.6	12.8	530	37.0	4.3	7.2	200	450	100	70
DTU-UNSW	5.2	17.6	616	47.9	3.7	6.8	1500	400	60	50
Toyota [17]	9.1	20.8	701	62.5	n.a.	5.2	1300	1200	100	0
IBM [43]	8.4	19.5	661	65.8	1.5	4.5	800	600	90	80

Table A.1: Device parameters of our best in-house solar cell, of the best DTU-UNSW solar cell, and of two of the best CZTS solar cells ever made. All device parameters were extracted from the illuminated JV curves. t_{CZTS}, t_{CdS}, and t_{ZnO} are the thicknesses of CZTS, CdS, and ZnO respectively.

by PLD produced in collaboration with UNSW - labeled "DTU-UNSW" - where UNSW took care of all process steps from CZTS post-annealing onward (this solar cell is the subject of Study 2.1); (iii) the current world-record CZTS solar cell by Toyota; (iv) the former world-record CZTS solar cell by IBM.

The flaws of the DTU-UNSW solar cell with respect to state-of-the-art CZTS solar cells have already been discussed in Study 2.1. Here I will focus on the flaws of the in-house solar cell with respect to the DTU-UNSW solar cell. The appearance of both solar cells is shown in Figure A.1(b) through cross-sectional SEM images of the finished devices. The most obvious difference is the thickness of the MoS$_2$ layer: 50 nm in the in-house solar cell and almost 400 nm in the DTU-UNSW solar cell. Note that the Mo film used in both solar cells was deposited at DTU with the same recipe. Therefore, it seems as if the CZTS annealing step of the DTU-UNSW solar cell is able to maintain a S-rich atmosphere for a longer time, which allows further sulfurization of Mo by the S gas. Even though insufficient S supply during annealing may result in the CZTS-back contact decomposition reaction [44], no obvious secondary phases were detected at the back contact in the in-house solar cell.

A.5.1 Fill factor

A major problem, with respect to both the DTU-UNSW solar cell and to state-of-the-art solar cells, is the very low fill factor. This is due to the combination of three features. A first feature is a rather high series resistance R_s, similar to the DTU-UNSW solar cell. As quantified and discussed in Study 2.1, I believe this is mostly due to the lack of a properly designed contact grid. Indeed, the in-house solar cell features just an evaporated Al dot contact. A second feature is a low shunt resistance R_{sh}. Note that what is interpreted as shunt resistance in the fit of an illuminated JV curve does not necessarily correspond to an actual shunt resistance. In our case, the slope of the JV curve at zero bias is much larger in the illuminated curve than in the dark curve (Figure A.2(a)). This hints to the fact that the low value of the shunt resistance is most likely due to voltage-dependent collection, i.e., to a gradual increase of the recombination current with increasing forward bias already near short circuit conditions [53]. The third feature is a very high diode ideality factor n_d. This may be due to a number of recombination mechanisms that saturate with increasing forward bias. Some of them, such as tunneling-enhanced recombination and recombination through defect clusters, are illustrated in [53]. Here I tend to exclude tunneling from the CdS side as a major effect because the CdS layer is quite thick in our in-house solar cell (Table A.1), which should keep the electric field low in a weakly doped buffer. Conversely, a large density of defect clusters in CZTS could be a major cause. An increasing density of donor-acceptor defect clusters was already shown to be correlated with the decrease in fill factor from a state-of-the-art solar cell to lower-performance solar cells, all fabricated the same group [104]. To this likely explanation I add another possibility, which is not often considered, i.e., a cliff-like CBO at the CZTS/CdS interface, even in the absence of interface recombination. In this case, the fill factor may degrade significantly even if the
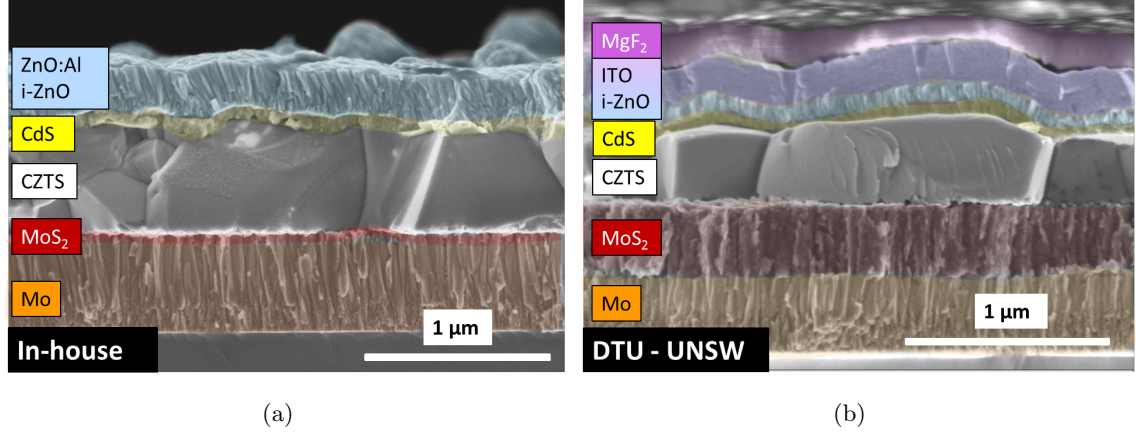
(a)   (b)

Figure A.1: (a): Cross-sectional SEM image of the second-best in-house CZTS solar cell (2.2% efficiency). (b): Cross-sectional SEM image of the best DTU-UNSW solar cell (5.2% efficiency).
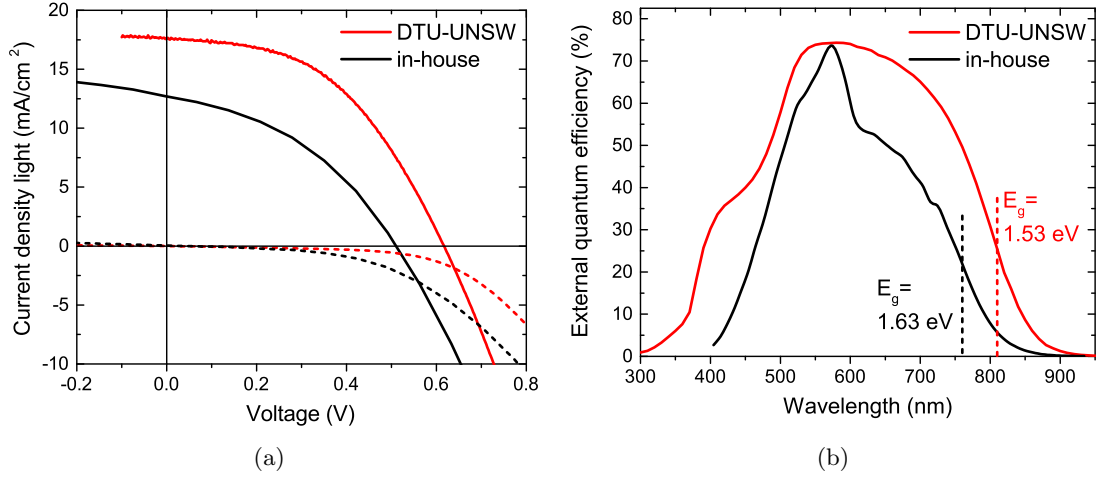

(a)   (b)

Figure A.2: (a): JV curves under AM1.5 illumination (solid lines) and in the dark (dashed lines) for the best in-house and the best DTU-UNSW solar cells. (b): External quantum efficiency of the best in-house and the best DTU-UNSW solar cells. The measurement was taken without (with) white bias light in the case of the in-house (DTU-UNSW) solar cell. The band gap of CZTS in the two solar cells is estimated from the position of the inflection point of the EQE [205].

open circuit voltage remains the same as with a moderate spike. I show this by SCAPS device simulation in Figure A.3(a). My interpretation of the result is as follows. The CZTS band bending, and thus the gradient of the electron quasi-Fermi level *on the CZTS side*, is smaller in the cliff-like configuration than in the spike-like configuration, so an appreciable recombination current starts to flow at a smaller forward bias. However, the gradient of the electron quasi-Fermi level *over the whole device* is about the same in both configurations, resulting in similar V_{oc}.

A.5.2   Short-circuit current

A second major problem is the low short-circuit current. A first factor is, of course, the limited thickness of the CZTS absorber (450 nm). As shown in Study 2.1, this should account for less than 2 mA/cm^2 loss compared to a sufficiently thick absorber. A second factor is the lack of an anti-reflection coating, which should improve the short-circuit current by about 1.5 mA/cm^2 based on previous experience. More fundamental losses can be investigated by analysis of the EQE in Figure A.2(b). A first anomaly is the sharp peak close to the band gap of CdS, between 500 nm and 600 nm. I have been wondering
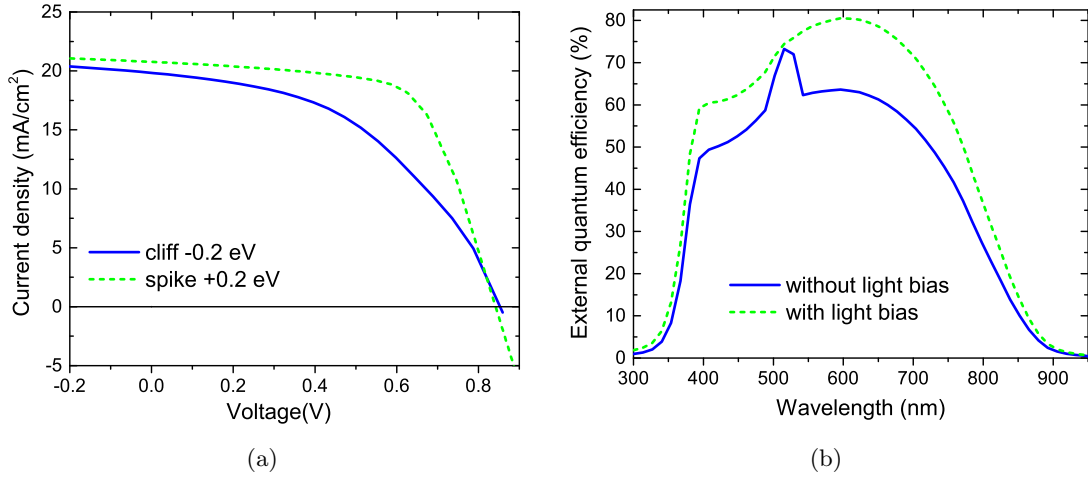
Figure A.3: (a): Simulated JV curve of a hypothetical CZTS solar cell under AM1.5 illumination without any recombination at the CZTS/CdS interface. The fill factor is degraded simply when the CBO of the interface is decreased from a moderate spike to a moderate cliff. (b): Simulated external quantum efficiency of a hypothetical CZTS solar cell with and without white light bias. The particular feature visible in the experimental EQE of the in-house solar cell (Figure A.2(b)) is qualitatively reproduced.

about the origin of that peak for a long time and I have found a possible explanation. As mentioned in Section 1.4, the CdS layer in CZTS or CIGS solar cells is believed to be a heavily compensated material with a large density of acceptor defects compensating the dominant donors. Those acceptors are mostly occupied by electrons in the dark but they become mostly unoccupied under an illuminating spectrum that contains photons with energy above the CdS band gap (Section 1.4). This changes the electrostatics of the heterojunction between the dark and illuminated cases and leads to the phenomenon of light-dark JV curve crossover, which is very pronounced in our solar cells (Figure A.2(a)). Since the EQE is normally measured by sweeping monochromatic light under otherwise dark conditions, the current collection efficiency is also expected to change depending on whether the photon energy of the monochromatic light is below or above the band gap of CdS. This effect can be eliminated by adding background white light during the whole EQE measurement, as shown for example in [206]. In the case of Figure A.2(b), the in-house solar cell was measured without bias light (not possible with our own in-house setup), whereas the DTU-UNSW solar cell was measured under white light bias. With this difference in mind, by adding a sufficient density of compensating acceptors in CdS I could reproduce the strange peak in the EQE by a SCAPS device simulation, as shown in Figure A.2(b). The peak disappears as soon as a background white light of sufficient intensity is turned on in the simulation (Figure A.2(b)).

Besides this funny detail, it is evident from Figure A.2(b) that both the short-wavelength collection and the long-wavelength collection are worse in our in-house solar cell. I find it very unlikely that parasitic absorption in CdS is the main reason for the short-wavelength EQE deficit with respect to the DTU-UNSW cell and to state-of-the-art cells. This is because one of the best CZTS solar cells ever made [43] employs a CdS layer of the same thickness as ours and has a much better short-wavelength response. I do not have a clear idea for the origin of the problem, but I suspect it may be related to sub-optimal electronic properties of the bulk CdS layer, e.g. low mobility and high defect density, resulting in a low hole lifetime in CdS. This is possibly related to the presence of unwanted phases during the chemical bath deposition of CdS due to homogeneous precipitation from the CBD solution [111]. Based on the experiments presented in the B.Sc. thesis of Tobias Mouritzen, I designed the baseline CdS deposition recipe to avoid precisely that. However, when inspecting a cross-sectional SEM image of the in-house solar cell (Figure A.1(a)) some
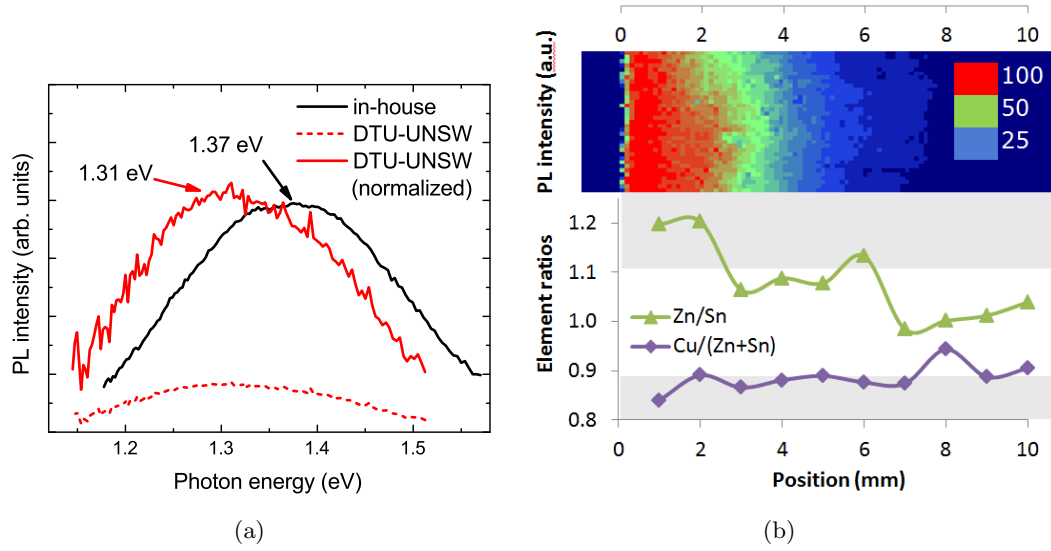
Figure A.4: (a): PL spectrum of a typical spot of the best in-house and the best DTU-UNSW solar cells. The original peak PL intensity for the DTU-UNSW solar cell is about ten times less than for the in-house solar cell and it has been normalized for clearer comparison. The peak positions for the two solar cells are indicated. (b) top: PL intensity map, over a 10 mm-wide region, for a CZTS film deposited and annealed with the in-house process. (b) bottom: Corresponding compositional linescan by EDX, showing the correlation between optimal stoichiometry and PL intensity. The optimal range of the elemental ratios for CZTS solar cells is colored in grey, after [35].

larger particulate covered with ZnO/ZnO:Al is still visible.

The differences in the long wavelength region of the EQE can be interpreted in two ways. The first is simply a band gap difference between the two solar cells. By taking the inflection point of the EQE as a measure of the band gap [205] we find a value of 1.63 eV for the in-house solar cell and 1.53 eV for the DTU-UNSW solar cell (Figure A.2(b)). The difference of 0.10 eV in the two band gaps is partially reflected in the difference of 0.06 eV in the PL peak of the two absorbers, shown in Figure A.4(a). Therefore it is likely that a higher band gap can explain, at least in part, the worse long wavelength response. Increased Zn/Cu cation ordering in CZTS results in a higher band gap [95], and the ordering parameter can be increased by a slower cooling rate after CZTS annealing. Then, the difference can be explained by the fact that the in-house solar cell was left to cool naturally below 300°C, whereas the DTU-UNSW solar cell was cooled down rapidly.

Still, I find it unlikely that band gap differences are the only reason for the different long-wavelength behavior of the two devices. This is because the in-house solar cell has a relatively low "shunt resistance" under illumination (voltage-dependent collection rather than shunt resistance), which is probably a sign of a short collection length (sum of the depletion region and the diffusion length in CZTS). A coexisting factor could be interface recombination at the back contact, which means that a large fraction of electrons generated deep into the absorber recombine at the wrong contact. It is difficult to conclude anything here, but I would exclude a short diffusion length as a major cause. This is because the peak intensity of the steady-state PL signal, measured on completed devices, is about 10 times higher in our in-house solar cell than in the DTU-UNSW solar cell. Therefore, the electron lifetime is expected to actually be higher in the in-house solar cell. One may speculate that back contact recombination is more severe in the in-house solar cell because of the much thinner MoS_2 layer (50 nm compared to almost 400 nm in the DTU-UNSW solar cell). $MoSe_2$ is believed to help form an ohmic back contact in CIGS solar cells [148] and an insufficient MoS_2 thickness in CZTS solar cells may lead to a larger back contact hole barrier, which efficiently collects the electrons close to the back contact.

A.5.3 Open-circuit voltage

The open circuit voltage seems to be the least severe problem in the in-house solar cell. Note, however, that this may be a slightly misleading indication, as the band gap of the in-house solar cell, as deduced from EQE, is particularly high (Figure A.2(b)), and therefore the upper limit of the achievable open circuit voltage is probably higher than in typical CZTS solar cells. In any case, the electron lifetime in CZTS seems to be higher in the in-house solar cell than in the DTU-UNSW solar cell, as judged by the intensity of their respective PL peaks (Figure A.4(a)). Therefore, it seems reasonable to assume that the in-house solar cell has relatively favorable CZTS bulk properties but it suffers from more severe interface recombination problems, which is in general expected to be the dominant recombination path of all decent CZTS/CdS solar cells made by anyone so far (Study 4.3). I do not have strong evidence of any particular mechanism that should increase the interface recombination rate of the in-house solar cell with respect to the CTZS-UNSW solar cell. However, based on the poor short-wavelength response of the in-house solar cell, I suspect that our in-house CdS films are more defective than in state-of-the-art solar cells, as discussed in the previous section. Unfortunately, if CdS has a high defect density in the bulk, there is no reason to think that there is also a high defect density at the interface, which would increase the interface recombination velocity. I doubt, however, that CdS is the only layer to be blamed for enhanced interface recombination. This is because some solar cells were fabricated at UNSW from CZTS precursors annealed at DTU (but with CdS deposited with the UNSW recipe), and they all had efficiencies below 1.5%. This said, I do not have any specific idea of why our annealing process would favor interface recombination and it is also possible that the low efficiency was a result of CZTS aging, even though the films were vacuum packed right after annealing and opened just before CdS deposition.

I would like to close this section by showing the correlation between the Zn/Sn and Cu/(Zn+Sn) ratios and the PL intensity in our CZTS films. As mentioned many times in this thesis, one of the absolute truths of CZTS solar cells is that those two ratios must be about 1.2 and about 0.8 respectively to obtain the highest efficiency. Due to the spatially non-uniform materials transfer in the PLD process, our CZTS films often have very pronounced compositional gradients. If the elemental ratios are determined by EDX on different spots over a region where a significant gradient exists, and the integrated PL intensity is mapped in the same region, something interesting happens. The more the elemental ratios deviate from their optimal value, the lower the intensity of the PL peak. This demonstrates that the defects and secondary phases present under non-optimal stoichiometry can indeed kill radiative recombination between the conduction band and the valence band (and related tail states).

A.5.4 What to do?

The "easy" fixes first. A common problem we have experienced in our in-house process has been delamination of CZTS from Mo after annealing. Based on the discussion in Section 1.4, it is likely that adhesion can be improved if the c-axis of MoS_2 can be forced to lie parallel to the substrate plane. As discussed earlier, there is some evidence that this can be achieved by increasing porosity of the Mo layer, which can easily be done in a sputtered film simply by increasing the deposition pressure. Therefore I would try to increase the pressure of the second Mo layer from 3 mTorr to, say, 6 mTorr. This comes at the cost of a higher sheet resistance (estimate: from 0.5 Ω/sq to 1.0 Ω/sq). However, it seems as if the Mo sheet resistance is not the factor limiting the series resistance of our solar cells (Study 2.1). Therefore, a moderate increase in Mo sheet resistance can probably be tolerated without any significant consequence on the device. Adhesion improvement would

allow fabrication of thicker absorbers, with an immediate gain in short circuit current and probably on open circuit voltage due to decreased back contact recombination. Another "easy" fix is replacement of the dot top contact with a properly dimensioned contact grid. I expect this addition to decrease the series resistance of the solar cell to a value comparable to state-of-the-art CZTS solar cells. Finally, I would try to decrease the sheet resistance of ZnO from hundreds of MΩ/sq to, say 50 kΩ/sq with the goal of achieving a higher carrier concentration in ZnO. This can easily be done in our sputtering setup, simply by decreasing the O_2 partial pressure during deposition. I got this idea by reading a study on the effect of the ZnO sheet resistance on CIGS solar cells [128]. From p-n junction theory, band bending in CZTS is expected to increase for increasing doping density of the heterojunction partners [53]. As we have seen in Section 1.6, large band bending is very much needed in CZTS, as it is does not seem to occur "naturally" as in CIGS.

Any other possible remedy critically relies on the existence of a solid and reproducible process for CZTS precursors deposition and subsequent annealing. However, especially the precursors deposition step suffers from the inherent instability of the PLD process due to window coating and the state of the target [192]. These issues have been solved only in part by the work of PhD student Andrea Cazzaniga. With an unforgiving material such as CZTS, it has become clear to us that it is unrealistic to think that PLD can provide precursors of reproducible quality. Lack of reproducibility and the low throughput of PLD (in particular of our PLD setup) are then immense disadvantages that have so far prevented any systematic study of the influence of the remaining layers on solar cell efficiency. Throughout my PhD project, the way I have done "process optimization" of the bottom and top layers has been by looking at their bulk properties without any relation to the actual solar cell device. Therefore, I would try to minimize sheet resistance and maximize adhesion of Mo; to maximize surface coverage and minimize homogeneously precipitated particulate in CdS; to achieve a high sheet resistance in ZnO; and to achieve the best trade-off between transmission and sheet resistance in ZnO:Al. However, those films must eventually stand the test of actual devices, and especially CdS does not have easily measurable "success criteria" such as sheet resistance or optical transmission. I honestly regard our 2.6% efficient solar cell as a little miracle, considering that it was never possible to optimize the device based on feedback from previous devices. In any case, there is strong evidence that at least the CdS deposition process must be improved, and probably also the CZTS annealing process. Saying how is currently out of my reach.

A.6 Appendix Study: 2.2% efficient CZTS solar cells by pulsed laser deposition

- <u>Crovetto A</u>, Cazzaniga A, Pure-sulfide CZTS solar cells by pulsed laser deposition, *presented at the 6th European Kesterite Workshop, Newcastle, UK, November 2015*

I decided to include this study - a poster presented at the European Kesterite Workshop in 2015 - as it is our only in-house solar cell result presented publicly to the community so far. In the poster, we summarize the key findings that led to the achievement of the our first solar cells by PLD with efficiency worth reporting, i.e., the stoichiometry dependence on laser fluence and the disappearance of droplets upon post-annealing. The efficiency of our in-house solar cells was later improved to 2.6%.

Contributions (brief):
• A. Crovetto: solar cell fabrication (except for CZTS deposition and annealing), all characterization (except for composition versus fluence) • A. Cazzaniga: process development and deposition of CZTS by pulsed laser deposition with subsequent annealing, composition versus fluence measurement and analysis

Pure-sulfide CZTS solar cells by pulsed laser deposition

Andrea Crovetto[1], Andrea Cazzaniga[2]

[1]DTU Nanotech, Technical University of Denmark [2]DTU Fotonik, Technical University of Denmark

Deposition parameters	Target	Annealed in	Device structure
• Temperature: 25°C • Base pressure: 10^{-7} mbar • Laser: Excimer KrF • 248 nm, 20 ns pulse @10Hz	Compound Cu_2ZnSnS_4 **(Cu/Zn = 1.8)**	100 mbar N2 200 mg S 570°C 10 min	**Mo** – 600 nm - DC sputtering **CZTS** – 800 nm - pulsed laser deposition **CdS** – 70 nm - chemical bath deposition **ZnO/AZO** – 70/250 nm - RF sputtering

??? Why pulsed laser deposition ???

PROS	CONS
1. Many tunable parameters 2. Kinetic energy of ablated species promotes surface mobility at the substrate 3. Non-equilibrium deposition conditions → **control over defect formation?**	1. Complex physics 2. Expensive production method 3. Radially inhomogeneous flux of species 4. Ejection of micro-particulate **(solved after annealing!)**

Pulsed laser deposition setup

Laser fluence = pulse energy / beam area

Pulse energy: constant over 1 hour deposition time

Beam area: tuned by changing the **lens-target distance**

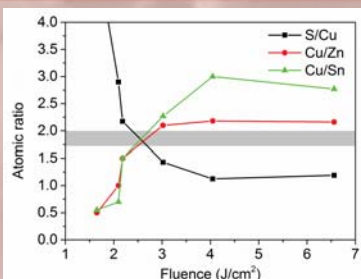Very low fluence:
evaporation
Very high fluence:
ablation

Influence of laser fluence on composition

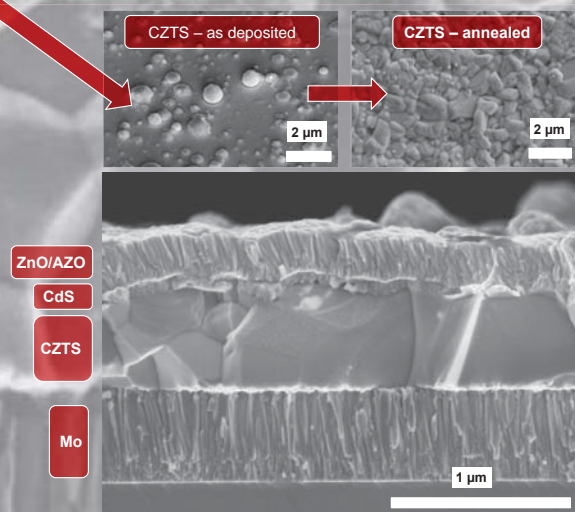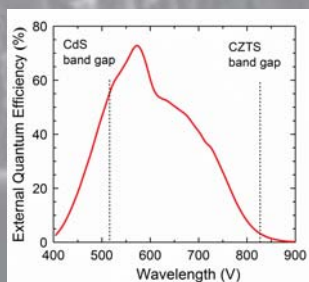**Copper** has the lowest vapour pressure among the 4 elements

⬇

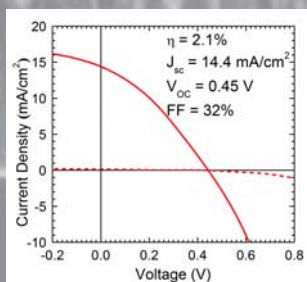**Tuning laser fluence = tuning %Cu**

At optimal lens position:

Cu: **22.6%**;   Zn: **14.7%**;   Sn: **12.2%**;   S: **50.5%**

Cu /(Zn+Sn) = **0.84**;   Zn/Sn = **1.20**;   Cu/Sn = **1.85**

CZTS – as deposited   CZTS – annealed

2 µm   2 µm

ZnO/AZO
CdS
CZTS
Mo

1 µm

η = 2.1%
J_{sc} = 14.4 mA/cm²
V_{oc} = 0.45 V
FF = 32%

CdS band gap   CZTS band gap

Conclusions

Solar cell devices	CZTS processing
1. J_{sc} and V_{oc} are relatively close to best devices 2. Fill factor is very low 3. Extreme light-dark crossover	1. Compact morphology with large grains 2. Micro-particulate disappears after annealing 3. Radial compositional inhomogeneities

Acknowledgements

Oh I get by with a little help from my friends
Oh I get high with a little help from my friends
The Beatles, 1967

For some reason, I have always had the belief that this would be the most read chapter of any PhD thesis. I will then do my best and write this section (at least parts of it) before anything else in this thesis. And I am really taking my time here! Right now it is March 29th 2016 and I am chilling in a nearly horizontal position in Sydney, Australia. My hand-in date, August 31st, feels no more than a distant bugaboo. If I know myself well enough, the next page I will write is going to be around August 15th or something like that.[1]

Before I start with my cheesy acknowledgements, let me note that I am aware that it is not particularly popular to write cheesy acknowledgements in Denmark (and, when we are talking about a PhD thesis, probably not even in South America, home of *telenovelas*), but honestly I couldn't care less. I value feelings and gratitude, so I am going to write my 3 pages of acknowledgements anyway.

The first person I would like to thank is (perhaps not surprisingly) my main supervisor Ole Hansen. Even though PhD students cannot refrain from politely saying thanks to their supervisor *without whom none of this would have been possible*, I hope everyone will believe me that I am truly grateful to Ole. He selected me for a PhD project just a few weeks after I had kept questioning his scientific claims in a Denmark vs. Italy email duel. He never tried to direct my research, as long as he thought it made sense. Whenever he had to assess me from 1 to 100 based on *any* criteria, he would always give me a 100 (I doubt my mom would do that, and she is an Italian mother). He is both the most encyclopedic professor I know and the one with the best overview, navigating at view pretty much all over the place in the physical sciences. He is also possibly the fastest email replier I know when it's about something important. Thank you Ole.

I will also spend a few words about the captain of our research project, and my co-supervisor, Jørgen Schou. Even though I haven't worked much with him in practice, he really is the one without whom this would not have been possible as he brought the cash home for this project. Please let me also emphasize that Jørgen is possibly the most envied supervisor at conferences, where he relentlessly shows his vintage dance moves to the young PhD/postdoc crowd, three or four hours past the bedtime of most senior conference guys.[2] If I have to associate the phrase "forever young" to someone, my first pick would be Jørgen.

The person who truly saved my PhD project from certain failure is Eugen Stamate, a.k.a. "my unofficial supervisor", a guy who is famous in Denmark for not being a criminal.[3] If that is a journalist's conclusion, you must be a pretty good guy. In fact Eugen clearly

---

[1]Note from August 16th: Section 1.1 is more or less finished

[2]I believe Jørgen is about 70 years old

[3]http://politiken.dk/oekonomi/arbejdsmarked/ECE2336219/eugen-stamate-er-rumaener-men-han-er-ikke-kriminel/

reminds us of how easy it is for a few lucky ones to be outrageously good-hearted without even trying. I really hope I will continue collaborating with Eugen, not only because he is a master in plasma physics and technology, but also because one can't help trying being a nicer person when around him, just to feel a bit less inadequate in comparison. Besides saving my PhD, which alone would secure him a considerable share of my fortune if I ever should amass a fortune, he really is one of the unsung heroes of our times. If you are in charge of giving funding to research and you are reading this, please give money to Eugen. He will do great things with it.[4]

A big hug to my fellow foot soldiers Sara Engberg, Rebecca Ettlinger, and Andrea Cazzaniga (Cazza). I have had a lot of fun with you guys in the lab, at conferences, out on the town, and especially when exchanging samples in Copenhagen in the evening over a beer, a light dinner or a swim in the sea. We have had some good honest chats, good results, less good results, not so good frustration, but always a good time together. I hope you will get to do what you like best now, and hopefully a PhD degree will help.

I am also very excited to acknowledge my great scientific collaborators, found here and there around the department and around the world: Ronghzhen Chen (Royal Institute of Technology, Sweden) and Clas Persson (University of Oslo, Norway), who provided fantastic theoretical insights on the Cu_2SnS_3 dielectric functions; Daniel Kjær (CAPRES A/S, Denmark), who helped with more than a few micro-four-point-probe measurements; Mattias Palsgaard, Mads Brandbyge (DTU Nanotech) and Kurt Stokbro (Quantumwise A/S) who did an innovative band alignment study upon my insistent requests; Xiaojing Hao, Kaiwen Sun, Fangzhou Zhou and especially Chang Yan (University of New South Wales, Sydney, Australia), who took me in their group as a visiting research fellow and showed me a great deal of the magic behind their $> 8\%$ efficiency CZTS solar cells. Speaking of Sydney, I would have probably starved to death or spent half of my savings on food during my (way too short) research stay in Sydney if it hadn't been for my beloved Chinese gang consisting of Carol and Jiang Hui,[5] who fed me every single day and every single night with amazing Chinese delicacies. [6]

I would like to thank the Silicon Microtechnology crew at DTU Nanotech, that is, Thomas Pedersen, Rasmus Davidsen, and Maksym Plakhotnyuk. Those three guys are some of the most helpful around and they have provided technical assistance with a million things, trivial and less trivial.

People at the Danchip clean room facilities have also made a lot of these results possible. First and foremost "min ven" Jesper Hanberg, who trained me on nearly all the machines I needed at Danchip, plus the ones I didn't know I didn't need. Poor Jesper had to deal with me and my problems a lot, and I must say I have noticed a correlation between the number of visits to his office and the amount of white hair on his head. Sorry about that Jesper. At Danchip, warm thanks also to Mikkel, Jonas, Søren, Katharina, and Berit for their valuable help.

My gratitude goes to the Nanocarbon group (Peter Bøggild) and to the Nanoprobes group (Anja Boisen), who have kindly allowed me to use their Raman setups to help me understand when our nominally CZTS films were not really CZTS films.

I shall also properly acknowledge the most welcome surprise of this project: my amazing master/bachelor students and interns. In chronological order, Edo, Philip, Tobias O, Tomas, Lasse, Mathias, Lars, and Tobias M. Guys, thanks to you I have realized I love being a supervisor, chilling out and eating watermelon in the sun while you all work hard in the lab - best deal ever. Through various paths, you all did a great job in the end. Please come to my PhD defense and cheer for me or remember I can still lower your grade.

---

[4]such as discovering new plasma effects and saving the life of other PhD students

[5]You may know Jiang Hui as the King of Karaoke

[6]OK, maybe I need more time to learn to appreciate pork feet

Let me also thank *en passant* some extra people who have provided much-needed help in specific situations (mostly for free): Stela Canulescu, Basil Uthuppu, Beniamino Iandolo, Radu Malureanu, Stronzo Bestiale, Emil Højlund, Karen and Wolfgang Pantleon, and Juan Maria García Lastra. I really appreciated it.

Doing something not too scientific on a regular basis has kept me in a decent mental shape throughout this PhD project. That "something" is, first and foremost, my biggest passion, music. So, thanks to the musicians I shared a stage with in the last three years, especially Emil and Alexandra from Concept Dylan[7] and the Rechoired crew, who keep reminding me of my previous life in which I disliked physics and wanted to become a rockstar. A couple of Saturday nights per year you almost make me believe that I actually *am* a rockstar. That's better than nothing.

In the few periods of time when I was neither a rockstar nor a scientist, a number of really great people made sure that life would still be somewhat cool. With that I mean my dear A-Team including the latest wild card Abhay, and my dear roommates that made me feel at home in my many homes: Josh, Elena, Yann, Lindsay, Juliane, and Miranda.

As always with whatever I do, my nearest family (mamma, papá, Peto, zio e zia) has supported me. That's undoubtedly a privilege not everyone has, so even though I don't say it often I would like to tell my family how much I appreciate that they have always let me do things my own way and paid a couple of bills on my behalf in the process.

Finally, I wish to apologize with all my collaborators for picking just one of them as my real favorite. Yes, it's really bad style but I can't help it. I am talking about the one who personally wrote the true masterpiece of this thesis, over which I have no claim of authorship, that is, the Danish abstract. This highly skilled coauthor also happens to have a spacious living room, which witnessed some of the most inspired writing of this thesis.[8] I am of course talking about the one and only, the biggest catch in Copenhagen, Bettina. You are awesome.

Finally, thanks to *you* for reading this thesis, or at least parts of it. I hope it stimulated some good thinking. You are always welcome to contact me in any way.

---

[7] https://www.facebook.com/Concept-Dylan-1575181296060346/
[8] The footnotes of the Acknowledgments

Peer-reviewed publications

Tak for kaffe
Danish slang

Related to PhD project

Published

1. <u>Crovetto A</u>, Yan C, Zhou F, Stride J, Schou J, Hao X, Hansen O 2016 Lattice-matched Cu_2ZnSnS_4/CeO_2 solar cell with open circuit voltage boost *Applied Physics Letters*, in press

2. <u>Crovetto A</u>, Chen R, Ettlinger R B, Cazzaniga A C, Schou J, Persson C and Hansen O 2016 Dielectric function and double absorption onset in monoclinic Cu_2SnS_3: Origin of experimental features explained by first-principles calculations *Solar Energy Materials and Solar Cells* **154** 121–129

3. <u>Crovetto A</u>, Ottsen T S, Stamate E, Kjær D, Schou J and Hansen O 2016 On performance limitations and property correlations of Al-doped ZnO deposited by radio-frequency sputtering *Journal of Physics D: Applied Physics* **49** 295101

4. Mirbagheri N, Engberg S, <u>Crovetto A</u>, Simonsen S B, Hansen O, Lam Y M and Schou J 2016 Synthesis of ligand-free CZTS nanoparticles via a facile hot injection route *Nanotechnology* **27** 185603

5. Ettlinger R B, <u>Crovetto A</u>, Canulescu S, Cazzaniga A, Ravnkilde L, Youngman T, Hansen O, Pryds N and Schou J 2016 Formation of copper tin sulfide films by pulsed laser deposition at 248 and 355 nm *Applied Physics A* **122** 466

6. Palsgaard M L N, <u>Crovetto A</u>, Gunst T, Markussen T, Hansen O, Stokbro K and Brandbyge M, 2016 Semiconductor band alignment from first principles: a new nonequilibrium Green's function method applied to the CZTS/CdS interface for photovoltaics, *2016 International Conference on Simulation of Semiconductor Processes and Devices (SISPAD)* pp 377–380

7. Cazzaniga A, <u>Crovetto A</u>, Ettlinger R B, Canulescu S, Hansen O, Pryds N and Schou J 2015 ZnS top layer for enhancement of the crystallinity of CZTS absorber during the annealing *2015 IEEE 42nd Photovoltaic Specialist Conference (PVSC)* (IEEE) pp 1–4

8. <u>Crovetto A</u>, Cazzaniga A, Ettlinger R B, Schou J and Hansen O 2015 Optical properties and surface characterization of pulsed laser-deposited Cu_2ZnSnS_4 by spectroscopic ellipsometry *Thin Solid Films* **582** 203–207

Submitted

9. Cazzaniga A*, <u>Crovetto A*</u>, Yan C, Sun K, Hao X, Estelrich J R, Canulescu S, Stamate E, Pryds N, Hansen O and Schou J, Ultra-thin Cu_2ZnSnS_4 solar cell prepared by pulsed laser deposition, submitted. *: contributed equally

10. <u>Crovetto A</u>, Palsgaard M L N, Gunst T, Markussen T, Stokbro K, Brandbyge M and Hansen O, Interface gap narrowing behind open circuit voltage losses in Cu_2ZnSnS_4 solar cells, submitted

11. <u>Crovetto A</u>, Huss-Hansen M K and Hansen O, How the relative permittivity of heterojunction solar cell materials influences solar cell performance, submitted

Related to M.Sc. project

12. Li S, <u>Crovetto A</u>, Peng Z, Zhang A, Hansen O, Wang M, Li X and Wang F 2016 Bi-resonant structure with piezoelectric PVDF films for energy harvesting from random vibration sources at low frequency *Sensors and Actuators A*, **247** 547–554

13. <u>Crovetto A</u>, Wang F and Hansen O 2014 Modeling and Optimization of an Electrostatic Energy Harvesting Device *Journal of Microelectromechanical Systems* **23** 1141–1155

14. <u>Crovetto A</u>, Wang F and Hansen O 2013 An electret-based energy harvesting device with a wafer-level fabrication process *Journal of Micromechanics and Microengineering* **23** 114010

15. <u>Crovetto A</u>, Wang F, Triches M and Hansen O 2012 MEMS fabricated energy harvesting device with 2D resonant structure *Proceedings PowerMEMS* pp 125–128

16. Triches M, Wang F, <u>Crovetto A</u>, Lei A, You Q, Zhang X and Hansen O 2012 A MEMS Energy Harvesting Device for Vibration with Low Acceleration *Procedia Engineering* vol 47 pp 770–773

B.Sc. and M.Sc. theses of supervised students

- Huss-Hansen M K 2015 Modelling and simulation of Cu_2ZnSnS_4 solar cells, *B.Sc. thesis*, DTU Nanotech, Technical University of Denmark

- Kildebro L 2015 CZTS solar cell technology, *B.Sc. thesis*, DTU Nanotech, Technical University of Denmark

- Mouritzen T L 2015 Fabrication of buffer layers for CZTS solar cells, *B.Sc. thesis*, DTU Nanotech, Technical University of Denmark

- Ottsen T S 2015 Sputter deposition of aluminum doped zinc oxide for CZTS application, *M.Sc. thesis*, DTU Nanotech, Technical University of Denmark

- Ravnkilde L and Youngman T H 2015 Characterization of CZTS and CTS thin-film solar cells, *B.Sc. thesis*, DTU Nanotech, Technical University of Denmark

- Rasmussen P L 2015 CZTS solar cell technology, *B.Sc. thesis*, DTU Nanotech, Technical University of Denmark

Bibliography

[1] Kiehl J 2011 *Science* **331** 158–9

[2] Green M A, Emery K, Hishikawa Y, Warta W and Dunlop E D 2016 *Progress in Photovoltaics: Research and Applications* **24** 905–913

[3] Nelson J 2003 *The Physics of Solar Cells* (Imperial College Press)

[4] Hegedus S and Luque A 2011 Achievements and Challenges of Solar Electricity from Photovoltaics *Handbook of Photovoltaic Science and Engineering* (Chichester, UK: John Wiley & Sons, Ltd) pp 1–38

[5] Green M A 2016 *Nature Energy* **1** 15015

[6] Jäger-Waldau A 2014 PV Status Report JRC 92477

[7] 2016 Module prices for selected models in Germany *Photon International* 42

[8] Polman A, Knight M, Garnett E C, Ehrler B and Sinke W C 2016 *Science* **352** aad4424

[9] Green M A 2006 *Progress in Photovoltaics: Research and Applications* **14** 383–392

[10] Friedlmeier T M, Jackson P, Bauer A, Hariskos D, Kiowski O, Menner R, Wuerz R and Powalla M 2016 *Thin Solid Films*

[11] 2005 Rare Earth Elements—Critical Resources for High Technology — USGS Fact Sheet 087-02

[12] Vesborg P C K and Jaramillo T F 2012 *RSC Advances* **2** 7933

[13] Directive 2011/65/EU of the European Parliament and of the Council of 8 June 2011 on the restriction of the use of certain hazardous substances in electrical and electronic equipment (recast)

[14] Green M A, Ho-Baillie A and Snaith H J 2014 *Nature Photonics* **8** 506–514

[15] Platzer-Björkman C, Frisk C, Larsen J K, Ericson T, Li S Y, Scragg J J S, Keller J, Larsson F and Törndahl T 2015 *Applied Physics Letters* **107** 243904

[16] Song N, Young M, Liu F, Erslev P, Wilson S, Harvey S P, Teeter G, Huang Y, Hao X and Green M A 2015 *Applied Physics Letters* **106** 252102

[17] Tajima S, Itoh T, Hazama H, Ohishi K and Asahi R 2015 *Applied Physics Express* **8** 082302

[18] Wang W, Winkler M T, Gunawan O, Gokmen T, Todorov T K, Zhu Y and Mitzi D B 2013 *Advanced Energy Materials* **4** 1301465

[19] Best Research-Cell Efficiencies http://www.nrel.gov/ncpv/images/efficiency_chart.jpg

[20] Schorr S, Hoebler H J and Tovar M 2007 *European Journal of Mineralogy* **19** 65–73

[21] Persson C 2010 *Journal of Applied Physics* **107** 053710

[22] Chen S, Yang J, Gong X, Walsh A and Wei S 2010 *Physical Review B* **81** 245204

[23] Bär M, Schubert B A, Marsen B, Schorr S, Wilks R G, Weinhardt L, Pookpanratana S, Blum M, Krause S, Zhang Y, Yang W, Unold T, Heske C and Schock H W 2011 *Physical Review B* **84** 035308

[24] Shockley W and Queisser H J 1961 *Journal of Applied Physics* **32** 510

[25] Reference Solar Spectral Irradiance: Air Mass 1.5 http://rredc.nrel.gov/solar/spectra/am1.5/

[26] Bremner S, Yi C, Almansouri I, Ho-Baillie A and Green M 2016 *Solar Energy* **135** 750–757

[27] Katagiri H, Jimbo K, Maw W S, Oishi K, Yamazaki M, Araki H and Takeuchi A 2009 *Thin Solid Films* **517** 2455–2460

[28] Katagiri H 2012 Survey of development of CZTS-based thin film solar cells *2012 IEEE 3rd International Conference on Photonics* (IEEE) pp 345–349

[29] Delbos S 2012 *EPJ Photovoltaics* **3** 35004

[30] Mitzi D B, Gunawan O, Todorov T K and Barkhouse D A R 2013 *Philosophical transactions. Series A, Mathematical, physical, and engineering sciences* **371** 20110432

[31] Fella C M, Romanyuk Y E and Tiwari A N 2013 *Solar Energy Materials and Solar Cells* **119** 276–277

[32] Bourdais S, Choné C, Delatouche B, Jacob A, Larramona G, Moisan C, Lafond A, Donatini F, Rey G, Siebentritt S, Walsh A and Dennler G 2016 *Advanced Energy Materials* 1502276

[33] Ito K and Nakazawa T 1988 *Japanese Journal of Applied Physics* **27** 2094–2097

[34] Katagiri H, Sasaguchi N, Hando S, Hoshino S, Ohashi J and Yokota T 1997 *Solar Energy Materials and Solar Cells* **49** 407–414

[35] Katagiri H, Jimbo K, Tahara M, Araki H and Oishi K 2009 The Influence of the Composition Ratio on CZTS-based Thin Film Solar Cells *MRS Proceedings* vol 1165 (Cambridge University Press) pp 1165–M04–01

[36] Lee Y S, Gershon T, Gunawan O, Todorov T K, Gokmen T, Virgus Y and Guha S 2015 *Advanced Energy Materials* **5** 1401372

[37] Hiroi H, Sakai N, Iwata Y, Kato T and Sugimoto H 2015 Impact of buffer layer on kesterite solar cells *2015 IEEE 42nd Photovoltaic Specialist Conference (PVSC)* (IEEE) pp 1–4

[38] Haass S G, Diethelm M, Werner M, Bissig B, Romanyuk Y E and Tiwari A N 2015 *Advanced Energy Materials* **5** 1500712

[39] Larramona G, Levcenko S, Bourdais S, Jacob A, Choné C, Delatouche B, Moisan C, Just J, Unold T and Dennler G 2015 *Advanced Energy Materials* **5** 1501404

[40] Xin H, Vorpahl S M, Collord A D, Braly I L, Uhl A R, Krueger B W, Ginger D S and Hillhouse H W 2015 *Phys. Chem. Chem. Phys.* **17** 23859–23866

[41] Hiroi H, Sakai N, Kato T and Sugimoto H 2013 High voltage Cu_2ZnSnS_4 submodules by hybrid buffer layer *2013 IEEE 39th Photovoltaic Specialists Conference (PVSC)* (IEEE) pp 0863–0866

[42] Sun K, Yan C, Liu F, Huang J, Zhou F, Stride J A, Green M and Hao X 2016 *Advanced Energy Materials*

[43] Shin B, Gunawan O, Zhu Y, Bojarczuk N A, Chey S J and Guha S 2013 *Progress in Photovoltaics: Research and Applications* **21** 72–76

[44] Scragg J J, Kubart T, Wätjen J T, Ericson T, Linnarsson M K and Platzer-Björkman C 2013 *Chemistry of Materials* **25** 3162–3171

[45] Repins I L, Moutinho H, Choi S G, Kanevce A, Kuciauskas D, Dippo P, Beall C L, Carapella J, DeHart C, Huang B and Wei S H 2013 *Journal of Applied Physics* **114** 084507

[46] Schubert B A, Marsen B, Cinque S, Unold T, Klenk R, Schorr S and Schock H W 2011 *Progress in Photovoltaics: Research and Applications* **19** 93–96

[47] Moriya K, Tanaka K and Uchiki H 2007 *Japanese Journal of Applied Physics* **46** 5780–5781

[48] Moholkar A, Shinde S, Agawane G, Jo S, Rajpure K, Patil P, Bhosale C and Kim J 2012 *Journal of Alloys and Compounds* **544** 145–151

[49] Jin X, Yuan C, Zhang L, Jiang G, Liu W and Zhu C 2016 *Solar Energy Materials and Solar Cells* **155** 216–225

[50] Vanalakar S, Agawane G, Shin S, Suryawanshi M, Gurav K, Jeon K, Patil P, Jeong C, Kim J and Kim J 2015 *Journal of Alloys and Compounds* **619** 109–121

[51] Mitchell K, Potter R, Ermer J, Wieting R, Eberspacher C, Tanner D P, Knapp K and Gay R 1987 High efficiency thin film tandem PV modules *Conference Record of the IEEE Photovoltaic Specialists Conference* (IEEE) pp 13–18

[52] Sze S and Ng K K 2004 *Physics of semiconductor devices* (Wiley)

[53] Scheer R and Schock H W 2011 *Chalcogenide Photovoltaics* (Weinheim, Germany: Wiley-VCH Verlag)

[54] Li S Y, Hägglund C, Ren Y, Scragg J J, Larsen J K, Frisk C, Rudisch K, Englund S and Platzer-Björkman C 2016 *Solar Energy Materials and Solar Cells* **149** 170–178

[55] Frisk C, Yi Ren Y, Shuyi Li S and Platzer-Bjorkman C 2015 CZTS solar cell device simulations with varying absorber thickness *2015 IEEE 42nd Photovoltaic Specialist Conference (PVSC)* (IEEE) pp 1–3

[56] Winkler M T, Wang W, Gunawan O, Hovel H J, Todorov T K and Mitzi D B 2014 *Energy & Environmental Science* **7** 1029

[57] Wurfel U, Cuevas A and Wurfel P 2015 *IEEE Journal of Photovoltaics* **5** 461–469

[58] Lundberg O, Bodegård M, Malmström J and Stolt L 2003 *Progress in Photovoltaics: Research and Applications* **11** 77–88

[59] Ellmer K 2012 *Nature Photonics* **6** 809–817

[60] Gunawan O, Gokmen T and Mitzi D B 2015 Loss Mechanisms in Kesterite Solar Cells *Copper Zinc Tin Sulfide-Based Thin-Film Solar Cells* ed Ito K (Wiley) chap 17

[61] Scheer R 2009 *Journal of Applied Physics* **105** 104505

[62] Sah C, Noyce R and Shockley W 1957 *Proceedings of the IRE* **45** 1228–1243

[63] Hegedus S S and Shafarman W N 2004 *Progress in Photovoltaics: Research and Applications* **12** 155–176

[64] Green M A 1998 *Solar Cells: Operating Principles, Technology and System Applications* (University of New South Wales)

[65] Rau U and Schock H 1999 *Applied Physics A: Materials Science & Processing* **69** 131–147

[66] Hages C J, Carter N J, Agrawal R and Unold T 2014 *Journal of Applied Physics* **115** 234504

[67] Westley Miller D, Warren C W, Gunawan O, Gokmen T, Mitzi D B and Cohen J D 2012 *Applied Physics Letters* **101** 142106

[68] Gershon T, Shin B, Bojarczuk N, Gokmen T, Lu S and Guha S 2013 *Journal of Applied Physics* **114** 154905

[69] Haight R, Barkhouse A, Gunawan O, Shin B, Copel M, Hopstaken M and Mitzi D B 2011 *Applied Physics Letters* **98** 253502

[70] Sites J and Mauk P 1989 *Solar Cells* **27** 411–417

[71] Green M A 1981 *Solid-State Electronics* **24** 788–789

[72] Würfel P 2005 *Physics of solar cells* (Wenheim: Wiley-VCH Verlag GmbH & Co. KGaA)

[73] Olekseyuk I, Dudchak I and Piskach L 2004 *Journal of Alloys and Compounds* **368** 135–143

[74] Siebentritt S and Schorr S 2012 *Progress in Photovoltaics: Research and Applications* **20** 512–519

[75] Choubrac L, Lafond A, Guillot-Deudon C, Moëlo Y and Jobic S 2012 *Inorganic Chemistry* **51** 3346–3348

[76] Lafond A, Choubrac L, Guillot-Deudon C, Deniard P and Jobic S 2012 *Zeitschrift für anorganische und allgemeine Chemie* **638** 2571–2577

[77] Valle Rios L E, Neldner K, Gurieva G and Schorr S 2016 *Journal of Alloys and Compounds* **657** 408–413

[78] Just J, Sutter-Fella C M, Lützenkirchen-Hecht D, Frahm R, Schorr S and Unold T 2016 *Phys. Chem. Chem. Phys.* **18** 15988–15994

[79] Redinger A, Mousel M, Wolter M H, Valle N and Siebentritt S 2013 *Thin Solid Films* **535** 291–295

[80] Li W, Chen J, Yan C and Hao X 2015 *Journal of Alloys and Compounds* **632** 178–184

[81] Tajima S, Asahi R, Isheim D, Seidman D N, Itoh T, Hasegawa M and Ohishi K 2014 *Applied Physics Letters* **105** 093901

[82] Fairbrother A, García-Hemme E, Izquierdo-Roca V, Fontané X, Pulgarín-Agudelo F A, Vigil-Galán O, Pérez-Rodríguez A and Saucedo E 2012 *Journal of the American Chemical Society* **134** 8018–21

[83] Barkhouse D A R, Gunawan O, Gokmen T, Todorov T K and Mitzi D B 2012 *Progress in Photovoltaics: Research and Applications* **20** 6–11

[84] Chen S, Walsh A, Gong X G and Wei S H 2013 *Advanced Materials* **25** 1522–1539

[85] Gunawan O, Gokmen T, Warren C W, Cohen J D, Todorov T K, Barkhouse D A R, Bag S, Tang J, Shin B and Mitzi D B 2012 *Applied Physics Letters* **100** 253905

[86] Levcenko S, Just J, Redinger A, Larramona G, Bourdais S, Dennler G, Jacob A and Unold T 2016 *Physical Review Applied* **5** 024004

[87] Islam M M, Halim M A, Sakurai T, Sakai N, Kato T, Sugimoto H, Tampo H, Shibata H, Niki S and Akimoto K 2015 *Applied Physics Letters* **106** 243905

[88] Chen R and Persson C 2012 *Journal of Applied Physics* **112** 103708

[89] Yee Y S, Magyari-Köpe B, Nishi Y, Bent S F and Clemens B M 2015 *Physical Review B* **92** 195201

[90] Scragg J J, Ericson T, Fontané X, Izquierdo-Roca V, Pérez-Rodríguez A, Kubart T, Edoff M and Platzer-Björkman C 2014 *Progress in Photovoltaics: Research and Applications* **22** 10–17

[91] Rudisch K, Ren Y, Platzer-Björkman C and Scragg J 2016 *Applied Physics Letters* **108** 231902

[92] Scragg J J S, Choubrac L, Lafond A, Ericson T and Platzer-Björkman C 2014 *Applied Physics Letters* **104** 041911

[93] Rey G, Redinger A, Sendler J, Weiss T P, Thevenin M, Guennou M, El Adib B and Siebentritt S 2014 *Applied Physics Letters* **105** 112106

[94] Scragg J J S, Larsen J K, Kumar M, Persson C, Sendler J, Siebentritt S and Platzer Björkman C 2016 *physica status solidi (b)* **253** 247–254

[95] Valentini M, Malerba C, Menchini F, Tedeschi D, Polimeni A, Capizzi M and Mittiga A 2016 *Applied Physics Letters* **108** 211909

[96] Gokmen T, Gunawan O, Todorov T K and Mitzi D B 2013 *Applied Physics Letters* **103** 103506

[97] Siebentritt S, Rey G, Finger A, Regesch D, Sendler J, Weiss T P and Bertram T 2015 *Solar Energy Materials and Solar Cells*, in press

[98] Mattheis J, Rau U and Werner J H 2007 *Journal of Applied Physics* **101** 113519

[99] Dirnstorfer I, Wagner M, Hofmann D M, Lampert M D, Karg F and Meyer B K 1998 *physica status solidi (a)* **168** 163–175

[100] Larsen J K, Burger K, Gutay L and Siebentritt S 2011 Temperature dependence of potential fluctuations in chalcopyrites *2011 37th IEEE Photovoltaic Specialists Conference* (IEEE) pp 000396–000401

[101] Rey G, Weiss T, Sendler J, Finger A, Spindler C, Werner F, Melchiorre M, Hála M, Guennou M and Siebentritt S 2016 *Solar Energy Materials and Solar Cells* **151** 131–138

[102] Gokmen T, Gunawan O and Mitzi D B 2014 *Applied Physics Letters* **105** 033903

[103] Frisk C, Ericson T, Li S Y, Szaniawski P, Olsson J and Platzer-Björkman C 2016 *Solar Energy Materials and Solar Cells* **144** 364–370

[104] Gershon T, Shin B, Gokmen T, Lu S, Bojarczuk N and Guha S 2013 *Applied Physics Letters* **103** 193903

[105] Burgelman M, Nollet P and Degrave S 2000 *Thin Solid Films* **361-362** 527–532

[106] Liu F, Lai Y, Liu J, Wang B, Kuang S, Zhang Z, Li J and Liu Y 2010 *Journal of Alloys and Compounds* **493** 305–308

[107] Nakanishi T and Ito K 1994 *Solar Energy Materials and Solar Cells* **35** 171–178

[108] Misic B, Pieters B E, Theisen J P, Gerber A and Rau U 2015 *physica status solidi (a)* **212** 541–546

[109] Bikowski A, Welzel T and Ellmer K 2013 *Journal of Applied Physics* **114** 223716

[110] Hironiwa D, Matsuo N, Sakai N, Katou T and Sugimoto H 2014 *Japanese Journal of Applied Physics* **53** 106502

[111] Hodes G 2002 *Chemical solution deposition of semiconductor films* (New York, Basel: Marcel Dekker)

[112] Olsen L, Eschbach P and Kundu S 2002 Role of buffer layers in CIS-based solar cells *Conference Record of the Twenty-Ninth IEEE Photovoltaic Specialists Conference, 2002.* (IEEE) pp 652–655

[113] Wada T 1997 *Solar Energy Materials and Solar Cells* **49** 249–260

[114] Nakada T and Kunioka A 1999 *Applied Physics Letters* **74** 2444

[115] Contreras M A, Romero M J, To B, Hasoon F, Noufi R, Ward S and Ramanathan K 2002 *Thin Solid Films* **403** 204–211

[116] Orgassa K, Rau U, Nguyen Q, Werner Schock H and Werner J H 2002 *Progress in Photovoltaics: Research and Applications* **10** 457–463

[117] Ibdah A R, Aryal P, Pradhan P, Rajan G, Li J, Rockett A A, Marsillac S and Collins R W 2014 Solar cells with thin $Cu(In_{1-x}Ga_x)Se_2$ absorbers: Optical analysis and quantum efficiency simulations *2014 IEEE 40th Photovoltaic Specialist Conference (PVSC)* (IEEE) pp 0373–0378

[118] Minemoto T, Matsui T, Takakura H, Hamakawa Y, Negami T, Hashimoto Y, Uenoyama T and Kitagawa M 2001 *Solar Energy Materials and Solar Cells* **67** 83–88
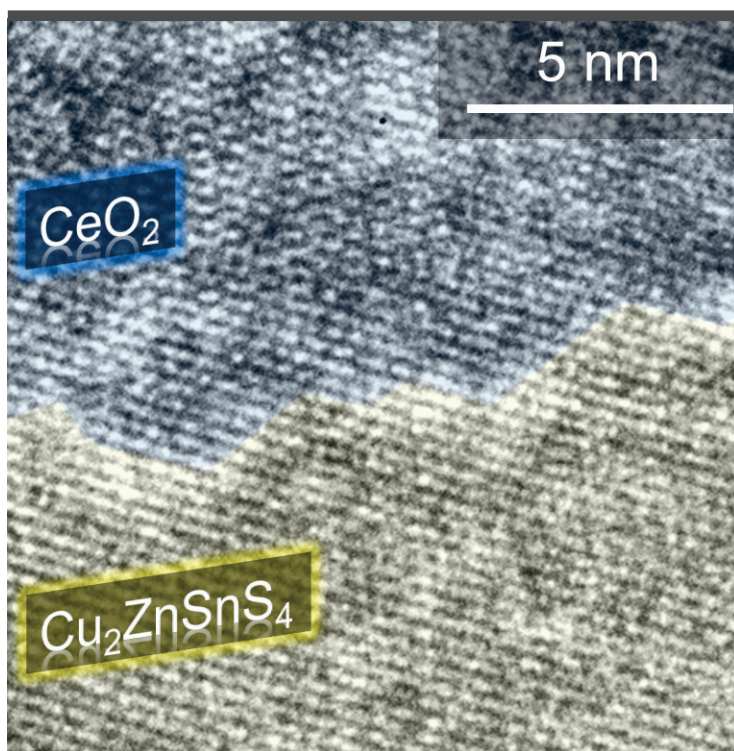
[119] Morkel M, Weinhardt L, Lohmueller B, Heske C, Umbach E, Riedl W, Zweigart S and Karg F 2001 *Applied Physics Letters* **79** 4482

[120] Schock H W and Noufi R 2000 *Progress in Photovoltaics: Research and Applications* **8** 151–160

[121] Sardashti K, Haight R, Gokmen T, Wang W, Chang L Y, Mitzi D B and Kummel A C 2015 *Advanced Energy Materials* **5** 1402180

[122] Larsen J, Ren Y, Ross N, Särhammar E, Li S Y and Platzer-Björkman C 2016 *Thin Solid Films*

[123] Nakada T 2000 *Thin Solid Films* **361** 346–352

[124] Klenk R 2001 *Thin Solid Films* **387** 135–140

[125] Shafarman W N, Siebentritt S and Stolt L 2010 Cu(InGa)Se$_2$ Solar Cells *Handbook of Photovoltaic Science and Engineering* ed Luque A and Hegedus S (Chichester, UK: John Wiley & Sons, Ltd) chap 13

[126] Janotti A and Van de Walle C G 2007 *Physical Review B* **76** 165202

[127] Hála M, Fujii S, Redinger A, Inoue Y, Rey G, Thevenin M, Deprédurand V, Weiss T P, Bertram T and Siebentritt S 2015 *Progress in Photovoltaics: Research and Applications* **23** 1630–1641

[128] Williams B L, Zardetto V, Kniknie B, Verheijen M A, Kessels W M and Creatore M 2016 *Solar Energy Materials and Solar Cells* **157** 798–807

[129] Cooray N F, Kushiya K, Fujimaki A, Sugiyama I, Miura T, Okumura D, Sato M, Ooshita M and Yamase O 1997 *Solar Energy Materials and Solar Cells* **49** 291–297

[130] Hsu C, Ko T and Huang Y 2008 *Journal of the European Ceramic Society* **28** 3065–3070

[131] Bikowski A, Rengachari M, Nie M, Wanderka N, Stender P, Schmitz G and Ellmer K 2015 *APL Materials* **3** 060701

[132] Hedström J, Ohlsen H, Bodegård M, Kylner A, Stolt L, Hariskos D, Ruckh M and Schock H 1993 ZnO/CdS/Cu(In,Ga)Se$_2$ thin film solar cells with improved performance *Conference Record of the Twenty Third IEEE Photovoltaic Specialists Conference)* (IEEE) pp 364–371

[133] Gershon T, Shin B, Bojarczuk N, Hopstaken M, Mitzi D B and Guha S 2014 *Advanced Energy Materials* **5** 1400849

[134] Jackson P, Würz R, Rau U, Mattheis J, Kurth M, Schlötzer T, Bilger G and Werner J H 2007 *Progress in Photovoltaics: Research and Applications* **15** 507–519

[135] Li J B, Chawla V and Clemens B M 2012 *Advanced Materials* **24** 720–723

[136] Kim G, Kim J, Jo W, Son D H, Kim D H and Kang J K 2014 *Nanoscale Research Letters* **9** 10

[137] Haight R, Shao X, Wang W and Mitzi D B 2014 *Applied Physics Letters* **104** 033902

[138] Du H, Romero M J, Repins I, Teeter G, Noufi R and Al-Jassim M M 2011 Nanoscale measurements of the surface photovoltage in Cu(In,Ga)Se$_2$, Cu$_2$ZnSnS$_4$, and Cu$_2$ZnSnSe$_4$ thin films: The role of the surface electronics on the efficiency of solar cells *37th IEEE Photovoltaic Specialists Conference* (IEEE) pp 001983–001986

[139] Li J, Mitzi D B and Shenoy V B 2011 *ACS Nano* **5** 8613–8619

[140] Xu P, Chen S, Huang B, Xiang H J, Gong X G and Wei S H 2013 *Physical Review B* **88** 045427

[141] Bär M, Schubert B A, Marsen B, Krause S, Pookpanratana S, Unold T, Weinhardt L, Heske C and Schock H W 2011 *Applied Physics Letters* **99** 112103

[142] Scragg J J, Dale P J, Colombara D and Peter L M 2012 *Chemphyschem : a European journal of chemical physics and physical chemistry* **13** 3035–46

[143] Scragg J J, Wätjen J T, Edoff M, Ericson T, Kubart T and Platzer-Björkman C 2012 *Journal of the American Chemical Society* **134** 19330–19333

[144] Redinger A, Berg D M, Dale P J and Siebentritt S 2011 *Journal of the American Chemical Society* **133** 3320–3323

[145] Scofield J H, Duda A, Albin D, Ballard B and Predecki P 1995 *Thin Solid Films* **260** 26–31

[146] Tai K F, Gunawan O, Kuwahara M, Chen S, Mhaisalkar S G, Huan C H A and Mitzi D B 2016 *Advanced Energy Materials* **6** 1501609

[147] Gunawan O, Gokmen T and Mitzi D B 2014 *Journal of Applied Physics* **116** 084504

[148] Wada T, Kohara N, Nishiwaki S and Negami T 2001 *Thin Solid Films* **387** 118–122

[149] Brammertz G, Oueslati S, Buffiere M, Bekaert J, El Anzeery H, Messaoud K B, Sahayaraj S, Nuytten T, Koble C, Meuris M and Poortmans J 2015 *IEEE Journal of Photovoltaics* **5** 649–655

[150] Hiroi H, Iwata Y, Adachi S, Sugimoto H and Yamada A 2016 *IEEE Journal of Photovoltaics* **PP** 1–4

[151] Salvador M, Vorpahl S M, Xin H, Williamson W, Shao G, Karatay D U, Hillhouse H W, Ginger D S 2014 *Nano Letters* **14** 6926–6230

[152] Eisgruber I, Granata J, Sites J, Hou J and Kessler J 1998 *Solar Energy Materials and Solar Cells* **53** 367–377

[153] Pudov A O, Kanevce A, Al-Thani H A, Sites J R and Hasoon F S 2005 *Journal of Applied Physics* **97** 064901

[154] Zhang S B, Wei S H and Zunger A 1998 *Journal of Applied Physics* **83** 3192

[155] Ericson T, Scragg J J, Hultqvist A, Watjen J T, Szaniawski P, Torndahl T and Platzer-Bjorkman C 2014 *IEEE Journal of Photovoltaics* **4** 465–469

[156] Gloeckler M and Sites J 2005 *Thin Solid Films* **480-481** 241–245

[157] Liu F, Yan C, Huang J, Sun K, Zhou F, Stride J A, Green M A, Hao X 2016 *Advanced Energy Materials* **6** 1600706

[158] Lindahl J, Keller J, Donzel-Gargand O, Szaniawski P, Edoff M and Törndahl T 2016 *Solar Energy Materials and Solar Cells* **144** 684–690

[159] Su Z, Tan J M R, Li X, Zeng X, Batabyal S K and Wong L H 2015 *Advanced Energy Materials* **5** 1500682

[160] Malerba C 2014 *Cu_2ZnSnS_4 thin films and solar cells: material and device characterization* PhD thesis University of Trento

[161] Winer W 1967 *Wear* **10** 422–452

[162] Yoon J H, Kim J H, Kim W M, Park J K, Baik Y J, Seong T Y and Jeong J h 2014 *Progress in Photovoltaics: Research and Applications* **22** 90–96

[163] Siebentritt S 2013 *Thin Solid Films* **535** 1–4

[164] Polizzotti A, Repins I L, Noufi R, Wei S H and Mitzi D B 2013 *Energy & Environmental Science* **6** 3171–3182

[165] Li J, Du H, Yarbrough J, Norman A, Jones K, Teeter G, Terry F L and Levi D 2012 *Optics express* **20 Suppl 2** A327–32

[166] Baer M, Nishiwaki S, Weinhardt L, Pookpanratana S, Fuchs O, Blum M, Yang W, Denlinger J D, Shafarman W N and Heske C 2008 *Applied Physics Letters* **93** 244103

[167] Persson C and Zunger A 2003 *Physical Review Letters* **91** 266401

[168] Bär M, Schubert B A, Marsen B, Wilks R G, Pookpanratana S, Blum M, Krause S, Unold T, Yang W, Weinhardt L, Heske C and Schock H W 2011 *Applied Physics Letters* **99** 222105

[169] Yan C, Liu F, Song N, Ng B K, Stride J A, Tadich A and Hao X 2014 *Applied Physics Letters* **104** 173901

[170] Nagoya A, Asahi R and Kresse G 2011 *Journal of physics. Condensed matter* **23** 404203

[171] Jaffe J and Zunger A 2001 *Physical Review B* **64** 241304

[172] Li Y H, Walsh A, Chen S, Yin W J, Yang J H, Li J, Da Silva J L F, Gong X G and Wei S H 2009 *Applied Physics Letters* **94** 212109

[173] Gokmen T, Gunawan O and Mitzi D B 2013 *Journal of Applied Physics* **114** 114511

[174] Hempel H, Redinger A, Repins I, Moisan C, Larramona G, Dennler G, Handwerg M, Fischer S F, Eichberger R and Unold T 2016 *Journal of Applied Physics* **120** 175302

[175] Chen S, Walsh A, Yang J H, Gong X G, Sun L, Yang P X, Chu J H and Wei S H 2011 *Physical Review B* **83** 125201

[176] Goh G K L, Tay C S S, Chan K Y S and Gosvami N 2006 *Journal of Electroceramics* **16** 575–579

[177] Izaki M, Saito T, Chigane M, Ishikawa M, Katayama J, Inoue M and Yamashita M 2001 *Journal of Materials Chemistry* **11** 1972–1974

[178] Kobayashi Y and Fujiwara Y 2006 *Journal of Alloys and Compounds* **408-412** 1157–1160

[179] Lau G K, Zhang T S and Goh G K L 2010 *Journal of Nanoscience and Nanotechnology* **10** 4733–4737

[180] Parikh H and De Guire M R 2009 *Journal of the Ceramic Society of Japan* **117** 228–235

[181] Tang L 2009 *Modification of solid oxide fuel cell anodes with cerium oxide coatings* PhD thesis Case Western Reserve University

[182] Unuma H, Kanehama T, Yamamoto K, Watanabe K, Ogata T and Sugawara M 2003 *Journal of Materials Science* **38** 255–259

[183] Gillen R, Clark S J and Robertson J 2013 *Physical Review B* **87** 125116

[184] Hinuma Y, Grüneis A, Kresse G and Oba F 2014 *Physical Review B* **90** 155405

[185] Ellmer K, Klein A and Rech B 2008 *Transparent Conductive Zin Oxide: Basics and Applications in Thin Film Solar Cells* (Berlin Heidelberg: Springer-Verlag)

[186] Morkoç H 2009 *Zinc oxide : fundamentals, materials and device technology*

[187] Janotti A and Van de Walle C G 2009 *Reports on Progress in Physics* **72** 126501

[188] Ellmer K 2000 *Journal of Physics D: Applied Physics* **33** R17–R32

[189] Petersen D H, Hansen O, Lin R and Nielsen P F 2008 *Journal of Applied Physics* **104** 013710

[190] Nakashima M, Fujimoto J, Yamaguchi T and Izaki M 2015 *Applied Physics Express* **8** 042303

[191] de Wild J, Robert E V C, El Adib B and Dale P J 2015 *MRS Proceedings* **1771** mrss15–2135683

[192] Cazzaniga A C 2016 *Fabrication of thin film CZTS solar cells with Pulsed Laser Deposition* PhD thesis Technical University of Denmark

[193] Collord A D and Hillhouse H W 2016 *Chemistry of Materials* **28** 2067–2073

[194] Jackson P, Wuerz R, Hariskos D, Lotter E, Witte W and Powalla M 2016 *physica status solidi (RRL) - Rapid Research Letters* **10** 583–586

[195] Courel M, Andrade-Arvizu J A and Vigil-Galán O 2014 *Applied Physics Letters* **105** 233501

[196] Willmott P R 2004 *Progress in Surface Science* **76** 163–217

[197] Welzel T and Ellmer K 2013 *Journal of Physics D: Applied Physics* **46** 315202

[198] Prévot M S and Sivula K 2013 *The Journal of Physical Chemistry C* **117** 17879–17893

[199] Chen S, Gong X G, Walsh A and Wei S H 2009 *Applied Physics Letters* **94** 041903

[200] Gershon T, Sardashti K, Gunawan O, Mankad R, Singh S, Lee Y S, Ott J A, Kummel A and Haight R 2016 *Advanced Energy Materials* 1601182

[201] Stefan M 2010 *Nature* **468** 467–467

[202] Katagiri H, Jimbo K, Yamada S, Kamimura T, Maw W S, Fukano T, Ito T and Motohiro T 2008 *Applied Physics Express* **1** 041201

[203] Ren Y, Scragg J J S, Edoff M, Larsen J K and Platzer-Björkman C 2016 *ACS Applied Materials & Interfaces* **8** 18600–18607

[204] Park C H, Zhang S B and Wei S H 2002 *Physical Review B* **66** 073202

[205] Todorov T K, Tang J, Bag S, Gunawan O, Gokmen T, Zhu Y and Mitzi D B 2013 *Advanced Energy Materials* **3** 34–38

[206] Yan C, Liu F, Sun K, Song N, Stride J A, Zhou F, Hao X and Green M 2016 *Solar Energy Materials and Solar Cells* **144** 700–706

CeO$_2$

Cu$_2$ZnSnS$_4$

5 nm

DTU Nanotech
Department of Micro- and Nanotechnology